Lawrence Berkeley National Laboratory
Recent Work

Title

EFFECT OF OPGANIC ADSORBATES ON THE INITIAL STAGE OF ELECTROLYTIC METAL DEPOSITION: DEVELOPMENT AND USE OF A SPECTROSCOPIC ELLIPSOMETER

Permalink

https://escholarship.org/uc/item/63f3c3x9

Authors

Farmer, J.C.
Muller, R.H.

Publication Date

1983-03-01

eScholarship.org Powered by the California Digital Library
University of California

LBL-15607
c.2

Lawrence Berkeley Laboratory
UNIVERSITY OF CALIFORNIA

RECEIVED
LAWRENCE
BERKELEY LABORATORY
MAY 17 1983
LIBRARY AND
DOCUMENTS SECTION

Materials & Molecular Research Division

EFFECT OF ORGANIC ADSORBATES ON THE INITIAL STAGE OF ELECTROLYTIC METAL DEPOSITION: DEVELOPMENT AND USE OF A SPECTROSCOPIC ELLIPSOMETER

Joseph Collin Farmer* and Rolf H. Muller

(*Ph.D. Thesis)

March 1983

TWO-WEEK LOAN COPY

This is a Library Circulating Copy which may be borrowed for two weeks. For a personal retention copy, call Tech. Info. Division, Ext. 6782.

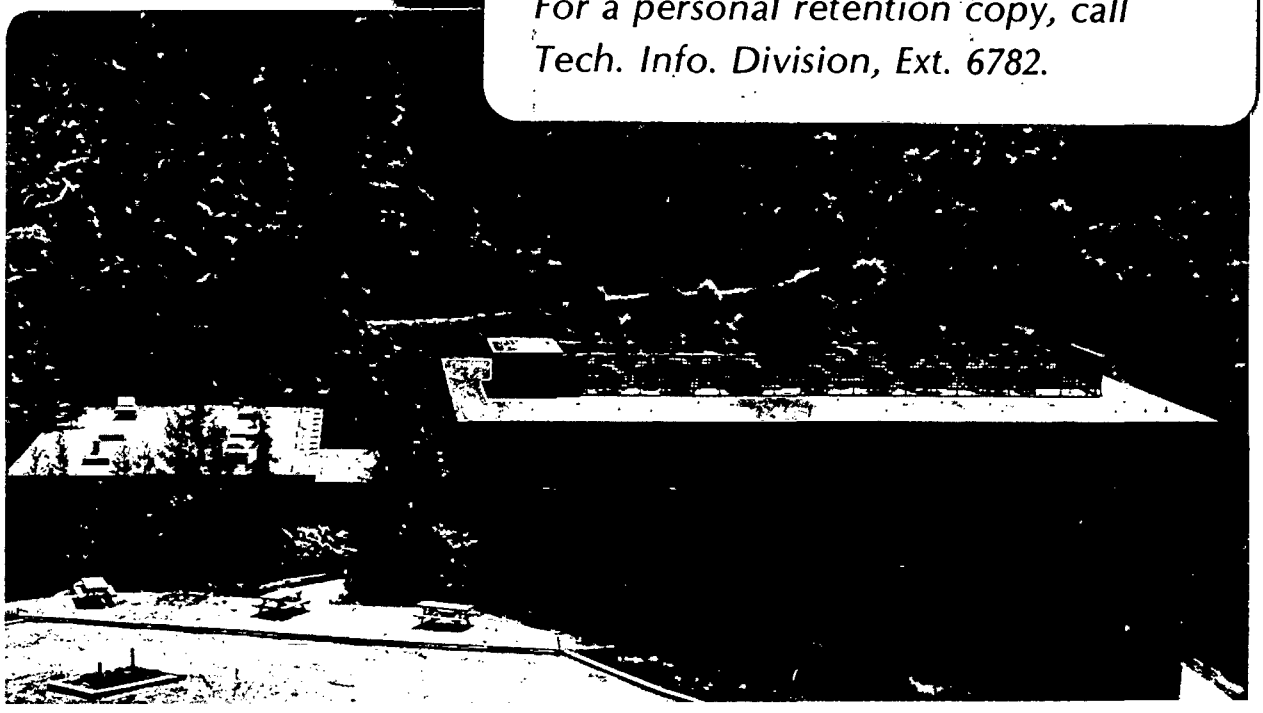

Prepared for the U.S. Department of Energy under Contract DE-AC03-76SF00098

LBL-15607
c.2

DISCLAIMER

This document was prepared as an account of work sponsored by the United States Government. While this document is believed to contain correct information, neither the United States Government nor any agency thereof, nor the Regents of the University of California, nor any of their employees, makes any warranty, express or implied, or assumes any legal responsibility for the accuracy, completeness, or usefulness of any information, apparatus, product, or process disclosed, or represents that its use would not infringe privately owned rights. Reference herein to any specific commercial product, process, or service by its trade name, trademark, manufacturer, or otherwise, does not necessarily constitute or imply its endorsement, recommendation, or favoring by the United States Government or any agency thereof, or the Regents of the University of California. The views and opinions of authors expressed herein do not necessarily state or reflect those of the United States Government or any agency thereof or the Regents of the University of California.

LBL-15607

EFFECT OF ORGANIC ADSORBATES ON THE INITIAL STAGE OF ELECTROLYTIC METAL DEPOSITION: DEVELOPMENT AND USE OF A SPECTROSCOPIC ELLIPSOMETER

Joseph Collin Farmer

(Ph.D. Thesis)

with Rolf H. Muller

Lawrence Berkeley Laboratory
Materials and Molecular Research Division
and
Department of Chemical Engineering
University of California, Berkeley
Berkeley, California 94720

March 1983

"The United States Department of Energy has the right to use this thesis for any purpose whatsoever including the right to reproduce all or any part thereof."

This work was supported by the Director, Office of Energy Research, Office of Basic Energy Sciences, Materials Sciences Division of the U.S. Department of Energy under contract no. DE-AC03-76SF00098.

Effect of Organic Adsorbates
on the Initial Stage of Electrolytic Metal Deposition:
Development and Use of a Spectroscopic Ellipsometer

Copyright © 1983

by

Joseph Collin Farmer

LBL-15607

EFFECT OF ORGANIC ADSORBATES ON THE INITIAL STAGE OF ELECTROLYTIC METAL DEPOSITION: DEVELOPMENT AND USE OF A SPECTROSCOPIC ELLIPSOMETER

Joseph Collin Farmer

with Rolf H. Muller

Lawrence Berkeley Laboratory
Materials and Molecular Research Division
and
Department of Chemical Engineering
University of California, Berkeley
Berkeley, California 94720

ABSTRACT

A study was performed to define the functional role of surface active agents during the initial stage of electrocrystallization. The system selected for investigation involved Cu as the electrode substrate, Pb as the deposited metal, and rhodamine-B chloride as the model inhibitor. The strong absorption band of rhodamine-B in the visible spectrum made it detectable by optical techniques in submonolayer amounts on the electrode. Deposit thicknesses investigated ranged from a single monolayer (the underpotential deposit, UPD) to thicknesses of about 1,000 Angstroms. It has been found that 1) the free energy of Pb electrosorption is about 7 kcal/mol; 2) the Pb adatom in the underpotential layer is completely discharged; and 3) in the absence of rhodamine-B, a Pb monolayer completely covers the Cu surface before three-dimensional nucleation of the bulk Pb phase; 4) the bulk phase

which forms on the monolayer consists of a granular, porous layer covered by large dendritic islands; 5) addition of rhodamine-B prevents complete formation of the Pb monolayer and results in more compact bulk deposits than are possible in its absence; 6) rhodamine-B inhibits dendrite growth; 7) rhodamine-B is simultaneously reduced with the Pb^{++} ion and is depleted from the electrode surface, which results in a mass transfer controlled inhibitory effect; and 8) the dye species responsible for inhibition has a preferential normal orientation on the electrode surface.

A self-compensating, magneto-optic spectroscopic ellipsometer was developed for this in situ study. It combined the advantages of rapid spectral scannning with the inherent accuracy of a compensating instrument operated in the polarizer-compensator-sample-analyzer configuration. Wavelength could be varied continuously over the visible-UV (370-720 nm) at a maximum rate of 114 nm/s by rotating a continuously variable interference filter. A microcomputer was used to collect spectroscopic data, perform digital filtering, calibrate the Faraday cells over the spectral range used, and interpret data in terms of physically significant quantities.

To support interpretations of ellipsometry data, light scattering measurements from electrode surfaces during deposit formation were also done. Deposits were then studied ex situ by scanning electron microscopy (SEM) and energy dispersive analysis of x-rays (EDAX).

Contents

Chapter 1: Extended Summary of Dissertation

Abstract 1

Introduction 1

Objectives 3

A Brief Background on Ellipsometry:
Principles and Practice 4

Criteria for Model Electrochemical System 7

Types of Information Obtainable by Spectroscopic
Ellipsometry 10

Modeling First Order Optical Effects:
Micromorphological Differences 14

Modeling Second Order Optical Effects:
Inhibitor Coverage and Orientation 20

Ellipsometry and Light Scattering During
Cyclic Voltammetry 23

Scanning Electron Micrographs: A Complementary Study 27

Summary of Contributions and Conclusions 29

Other Projects and Future Work 32

References 34

Figure Captions 41

Figures 43

Chapter 2: Development of the Automatic, Self-Nulling, Spectral
Scanning Ellipsometer: A Description of Hardware

Abstract 52

Introduction 53

Systems 54

I. Optics 54

II. Electronics 55

III. Computer System 57

Component Details 60

I. Spectral Scanning Source 60

II. Argon Laser Source 64

III. Extended Red Photomultiplier 69

IV. Electronics Considerations for Spectroscopic Measurements 70

V. Three-Reflection Fresnel Rhomb 72

Required Calibrations 73

I. Spectral Dependence of the Verdet Coefficient 73

II. Wavelength Calibration of the Encoder 74

Complications Due to Non-Idealities Instrument 75

References 79

Tables 82

Figure Captions 84

Figures 87

Appendices 104

Chapter 3: Software for the LSI-11 Data Acquisition System

Abstract 122

Introduction 122

Fixed-Wavelength Data Acquisition 125

I. SCAN 125

II. EDR002 125

III. DECOD2 126

IV. TRNSLT 127

V. PLOT01 128

Spectroscopic Data Acquisition 129

I. SEV002 130

II. RECALL 131

III. FIXPCA 131

IV. SHIFT 131

VI. FCSMTH 133

VII. FCAVG2 133

VIII. DSCONV 134

IX. RISURF 134

X. RISMTH 134

XI. RIGEN1 135

XII. DYERI 135

XIII. MINUS 135

XIV. NORMAL 135

Spectroscopic Simulators 136

I. EMASES 136

II. BRUGMN 136

III. CSMSES 136

IV. AISPEC 137

Single Parameter Modeling Routines 137

I. EMAFIT 137

II. CSMFIT 138

Programs for Tektronix 4662 Plotter 138

Multiple Parameter Optimization Routines 139

I. OHGOGO 139

II. GOGOGO 139

III. WLGOGO 140

IV. AIGOGO 141

Simple Calculations of Delta and Psi 141

I. FLMTST 141

II. EMATST 141

III. CSFIT 141

IV. PSIDEL 141

TI-59 Programs 142

References 143

Chapter 4: Selection of Substrate, Deposit and Surface Active Dye.

Abstract 144

Introduction 145

Experimental 147

Terminology 149

Results and Discussion: Dyes 150

I. Cationic Dyes 150

II. Neutral Dyes 151

III. Anionic Dyes 153

IV. Classification of Dyes Studies 153

V. Differences in Rhodamine-Type Dyes 155

Results and Discussion: Substrates 155

I. Platinum 155

II. Gold 156

III. Copper 156

IV. Free Energies of Adsorption on Cu and Au 157

Coulombic Efficiencies of Pb Deposition on Cu 157

Conclusions 158

References 160

Figure Captions 164

Figures 167

Chapter 5: Micromorphological Changes of Lead Electrodeposits on Silver and Copper Observed by Ellipsometry and Light Scattering During Cyclic Voltammetry

Abstract 194

Introduction 194

Experimental Procedure 197

Results 199

Optical Model of the Initial Stage of Deposit Formation 201

Applications and Theory of Light Scattering from Microrough Surfaces 212

Analysis of Adsorption Isotherm Data 212

The Charge Balance 216

Conclusions 217

References 218

Tables 225

Figure Captions 236

Figures 240

Nomenclature 263

Chapter 6: The Effect of Rhodamine-B on Lead Electrodeposition

Abstract 267

Introduction 267

Experimental 268

I. Selection of Electrochemical System for Study 268

II. Automatic Spectroscopic Ellipsometer 271

III. Electrochemical Cells 272

IV. Potentiostat 275

V. Electrode Preparation 275

VI. Electrolyte Preparation 275

Results 276

Discussion 285

Conclusions 286

References 287

Tables 291

Figure Captions 294

Figures 300

Chapter 7: Modeling First Order Optical Effects:
Deposit Micromorphology

Abstract 342

Introduction 344

Experimental 345

Single Layer Deposit Models 346

I. Compact Film Models 347

II. Effective Media Models 348

III. Coherent Superposition Model 349

Multilayer Models 351

I. Description 351

(1) First Layer 351

(2) Third Layer 352

II. Results of Early Three-Layer Model Simultations 353

III. Strategy for Using Spectroscopic Simulators 354

IV. Optimization of the Three-Layer Model 355

V. Calculation of Parameters and Variances 357

Conclusions 359

References 362

Tables 364

Figure Captions 365

Figures 371

Chapter 8: Modeling Second Order Effects:
Rhodamine-B Adsorption

Abstract 411

Introduction 412

Optical Models of the Dye Monolayer 413

I. Drude's Model 417

II. Strachan's Model 419

III. Sivukin's Model 420

IV. Anisotropic Film 421

V. Coverage and Orientation from the Anisotropic Film Model 425

Simulated Spectroscopic Ellipsometer Measurements 432

Empirical Interpretation of Experimental Spectroscopic Measurements 434

Conclusions 436

References 438

Figure Captions 440

Figures 444

Chapter 9: Scanning Electron Microscopy Complementing Ellipsometry of Thin Lead Deposits

Abstract 469

Introduction 469

Results 471

Conclusions 475

References 476

Figure Captions 477

Figures 479

Acknowledgments 494

Chapter 1

EFFECT OF ORGANIC ADSORBATES ON THE INITIAL STAGE OF ELECTROLYTIC METAL DEPOSITION: DEVELOPMENT AND USE OF A SPECTROSCOPIC ELLIPSOMETER

SUMMARY

Abstract

This chapter is an overview of the dissertation. Work presented in subsequent chapters is summarized and related to ideas found in the literature. Chapter 2 contains instrumentation details and Chapter 3 a description of necessary software. Experimental results pertaining to insitu investigations of Pb electrodeposition and the effect of rhodamine-B on this process are discussed in the remaining chapters.

Introduction

There are several reasons for investigating the effect of organic adsorbates on electrodeposition: (1) organic impurities occur naturally in practical electrolytes and may alter deposit morphology and increase the required cell potential; (2) organic materials are often added to electrolyte solutions to serve as brightening and leveling agents; and (3) organics are used to prevent corrosion of metal surfaces. Here, such organics will be referred to as "inhibitors."

More speculation exists in regard to the role of inhibitors during the initial stage of electrodeposition than actual experimental observation (1,2). Therein lies the importance of this work. We focused our attention on the period of deposit growth from development of the first monolayer (underpotential deposit, UPD) to formation of bulk deposits about 1000 Angstroms thick. Particular attention was paid to inhibitor induced differences in (1) the UPD preceeding bulk deposition, (2) bulk deposit micromorphology, and (3) inhibitor coverages and orientations on the electrode surface during deposition.

Of the alternative approaches considered for this fundamental electrodeposition study, spectroscopic ellipsometry was the only insitu technique allowing measurement of all the surface changes of interest. Consequently, a novel, self-nulling, spectral scanning ellipsometer was developed. This instrument is completely automated, computerized, and probably the fastest, most versatile, and most accurate ellipsometer in use today.

As a first system for study, we selected a combination of inhibitor, deposit, and substrate such that the materials were optically different, yet compatible electrochemically. Such a combination gave unambiguous data for interpretation, an important consideration since we were developing a technique while simultaneously performing a fundamental investigation. The components, selected on the basis of optical and electrochemical criteria, were (1) rhodamine-B chloride as inhibitor, (2) Pb as deposit, and (3) Cu as the electrode substrate. The

supporting electrolyte was composed of 1 M $NaClO_4$, acidified to a pH of 3 by using perchloric acid. Inhibitor concentrations were typically 10 micromolar and Pb^{++} ion concentrations were either 0.5 or 5.0 millimolar. These concentrations increased the time constant of the physical phenomena that we studied to match the experimental capabilities of our instrumentation. In this special case, the inhibitory action of the rhodamine-B was kinetic in nature; this dye molecule was simultaneously reduced on the electrode surface with Pb^{++} ion. All candidate inhibitors investigated were reduced on the electrode prior to Pb deposition. From the literature and discussions with persons in the industry, it seems that this is the rule for inhibitors and not the exception (1,2).

Objectives

The objectives of this project were:

(1) to develop a spectroscopic self-nulling ellipsometer based upon the earlier concepts of Muller (3) and Layer (4).

(2) to apply this instrument to an electrodeposition study from monolayer coverage to deposit thicknesses of about 1000 Angstroms.

(3) from this study, determine inhibitor induced variations in

   a. UPD coverage preceeding bulk deposition.

   b. micromorphology of the bulk deposit.

(4) determine inhibitor coverages and orientations on electrode surfaces.

A Brief Background on Ellipsometry: Principles and Practice

Theoretical aspects of ellipsometry are covered in depth by many authors throughout the literature, and the reader is referred to these references for details (5-7). However, a brief discussion is presented here as a review for the reader already familiar with the technique.

In classical electrodynamics, a beam of light is thought of as an electromagnetic wave propagating through space and represented by an electric field vector, oscillating transverse to the direction of propagation (Fig. 1). This electric field vector can be decomposed into two components, an "s" component and a "p" component. The s-component is oriented normal to the plane of incidence (formed by the incident and reflected beams); the p-component lies in the plane of incidence. The phase difference (delta) and the amplitude ratio (tan(psi)) of these two components are used to characterize the state of polarization and represent the two measured parameters. The tip of the resultant electric field vector traces a helix as it propagates through space. When this helix is projected onto a plane normal to the wave vector, it appears as an ellipse. This is the most general case of polarization of light, and has two limiting cases, those of linear and circular polarization.

Ellipsometry involves the measurement of changes in delta and psi due to reflection. These changes are then interpreted in terms of (1) the complex refractive indices of the substrate and film materials, (2)

the thicknesses of films covering the surface, (3) inhomogeneities of these films, and (4) anisotropies existing in the films. We speak of films as plural since one usually has to resort to multiple film models to explain experimental ellipsometry measurements.

More information is contained in spectroscopic ellipsometry measurements than in measurements at a fixed wavelength. A spectroscopic ellipsometer exploits differences in the spectral dependence of the complex refractive indices of the substrate and film components. The real part of the complex refractive index is related to the electronic polarizability of the medium; the imaginary part is known as the "extinction coefficient" and is related to the absorption of light by the medium. For example, if one has a species with a strong absorption band adsorbed on a metal surface, spectroscopic ellipsometry measurements will show peaks in plots of delta and psi against wavelength. The extinction coefficient passes through a maximum at the absorption band peak wavelength. Such effects give very clear definition to light absorbing monolayers. Micromorphological variations in thin deposits are just as dramatic if similar differences exist between deposit and substrate optical properties.

Our instrument is basically a polarizer-compensator-sample-analyzer (PCA or PCSA) optical configuration with a light source that is continuously swept through the spectrum from approximately 350 nm to 750 nm (Chapter 2). Automatic and self-nulling (self-compensating), it tracks spectral differences in the surface as the light source wavelength is

swept. Wavelength, delta, and psi, together with time, current, and potential are all collected, stored, and interpreted by a microcomputer (Chapter 3).

In the PCA arrangement (Fig. 2), the elliptic polarization state of the incident beam (between components #6 & #7) is manipulated by a sequence of linear polarizers (#4 & #5), followed by an achromatic quarter-wave retarder (#6, also called the compensator), so that after reflection by the sample (#7) the beam is again linearly polarized (between #7 & #8). Subsequent polarizers (#8 & #9) extinguish the beam detected by a photomultiplier (#11). This nulling is controlled automatically and magneto-optically by Faraday cells (#5 & #8). Modulation currents having 90 degree phase separation are applied to the Faraday cells and generate two modulation signals on a single photomultiplier; these signals are separated by two phase sensitive detectors, each referenced to the modulation current of one of the Faraday cells. Derived error signals are then used in a feed-back control scheme to adjust the dc current outputs from two fast, high-current, bipolar operational amplifiers. These dc currents, fed to the Faraday cells, are proportional to delta and psi, with the Faraday cell core Verdet coefficients being a part of the proportionality constants. Polarizing elements on the incident beam are referred to as "polarizers" while those on the reflected beam are referred to as "analyzers."

Criteria for Model Electrochemical System

The model electrochemical system selected for this study had to meet certain optical and electrochemical criteria, which helped assure that collected data be sufficiently unambiguous to allow interpretation.

As optical criteria, we decided that the deposit or substrate should show characteristic absorption in the spectral range accessible to the optical instrumentation; the absorption band of the inhibitor should be distinguishable from that of the surface.

Electrochemically, the substrate electrode had to be inert at the pH and potential of interest (8). Since we elected to use different metals for the substrate and deposit, it was necessary to pick a combination that did not form alloys electrochemically at the interface, as this would confound the effects that we were primarily interested in. The deposit should form at potentials anodic to those where hydrogen evolution problems degrade the optical signal. The organic inhibitor should demonstrate significant and observable interference with the metal ion being deposited. Originally, we had hoped to find organic compounds which were inert on the cathode during deposition; however, we found that compounds which chemisorbed to the surface were first electrochemically reduced prior to the onset of deposition. Electrochemical reduction and incorporation into deposits are common problems among organic additives for electrochemical systems (9). Electrode potential, partly dictated by the metal ion deposited, had to be sufficiently

cathodic to prevent interference of anions such as chloride.

Using these criteria as a guideline, the system selected for most of the experimental investigations involved Cu as the electrode substrate, Pb as the deposited metal, and rhodamine-B chloride as the model inhibitor.

Cu is stable to dissolution and oxidation at the reversible potential for Pb deposition from acidic aqueous solutions (10). Furthermore, it has been found that Pb forms a distinct underpotential deposit on Cu substrates (11, 12). Cu also has a distinctive absorption edge in the visible (550 nm), which is believed to be due to electronic transitions from the filled "d" bands into the "sp" conduction bands (13-15). In contrast to Cu, Pb has flat optical properties throughout the optical range of the spectroscopic ellipsometer.

Rhodamine-B chloride was found to induce very large surface overpotentials when depositing Pb on various substrates; the cathodic peak in the Pb cyclic voltammetry was shifted cathodically on the first sweep by roughly 125 millivolts (Chapter 4). Also, rhodamine-B could be observed on electrode surfaces with the spectroscopic ellipsometer. Being a laser dye, this compound was available in high purity at low cost from commercial suppliers; spectroscopic features of this compound are relatively well known. Both Plieth (16) and Schmidt (17) have done reflection spectroscopy of rhodamine-B on Ag and Pt surfaces, respectively. Similar experiments were repeated with the spectroscopic ellipsometer as

a means of instrumentation validation (Chapter 8). Rhodamine-B is cationic and carries with it Cl^- anion, however, Pb^{++} ion is deposited at potentials sufficiently cathodic to the point-of-zero-charge to prevent Cl^- specific adsorption on the cathode. This was verified by running experiments aimed at determining the effects of Cl^- alone on the Pb cyclic voltammograms.

Since Au also has optical properties in the visible which are distinctive, it too was considered as a substrate (18). However, we discovered from cyclic voltammetry that Pb and Au form an alloy electrochemically, as do Pb and Pt (see Chapter 4). Alloys of Pb and Au at elevated temperatures are well known, and may exist at temperatures as low as a few hundred degrees centigrade (19,20). Postulation of surface alloys formed electrochemically is not unreasonable (21). Similar anodic stripping peaks in the Pb/Au cyclic voltammogram were observed by Hamelin have been interpreted as differences in the UPD potential on different crystal faces of the polycrystalline substrate (22). Another disadvantage of the Au substrate is related to its optical properties. For metal adatom adsorption on Au, optical changes due to the adatom may be obscured by optical changes in the substrate (23).

Zn was also considered as a deposit for study since it may be of more practical importance in future secondary batteries than Pb, with specific reference to the zinc-nickel system. However, the more cathodic reduction potential of Zn gave rise to more extensive hydrogen evolution, which degraded the optical signal of the ellipsometer. Also,

upon simultaneous deposition of Zn and Ag alloys were formed (24). Similar alloy formation problems are believed to exist with the Zn/Cu system.

Rhodamine-B was selected over several other candidate inhibitors since it caused the most significant shifts in the potentials for Pb deposition (Chapter 4) and since it had been studied previously as an adsorbate by reflection spectroscopy. The structural formulae, ionicities, solute adsorption wavelength maxima, and induced cathodic shifts in the Pb voltammogram deposition peak are given for rhodamine-B and two other inhibitors in Fig. 3.

Types of Information Obtainable by Spectroscopic Ellipsometry

Historically, spectroscopic ellipsometry has been used to determine both the structure and composition of thin films on various surfaces. Aspnes and Theeten have used both light scattering and spectroscopic ellipsometry to determine the microroughness of both fine-grained polycrystalline silicon films and smoother, amorphous silicon films grown by chemical vapor deposition (25). They found that the microroughness, or micromorphology, could be accurately modeled as an equivalent film using either the Bruggeman or Maxwell-Garnett effective media theories. The applicability of the Maxwell-Garnett theory to rough surfaces has also been illustrated by Azzam and Bashara (26). However, in their experiments they varied angle-of-incidence instead of wavelength, and used a diffraction grating as a model rough surface.

Physical and chemical film compositions have been determined by spectroscopic ellipsometry for magnesium oxide films (27) and silicon oxide films (28), also through the application of the Bruggeman effective theory.

Spectroscopic ellipsometry has been used for investigation of film-interface properties between passive layers and substrates in MOS and MNOS integrated circuit devices (29) and the passive film on iron (30). In the case of iron passivation, the presence of chemical species important in the passivation process was inferred from spectra on the basis of characteristic absorption bands (electronic transitions). Through personal communications with the Santa Barbara Research Center, it has been learned that Hg-Te-Cd infrared detectors (the semiconductor/passive layer interface) will be investigated by spectroscopic ellipsometry.

In this study, we have used spectroscopic ellipsometry to determine micromorphology of very thin electrodeposits of Pb on Cu (Chapters 6 and 7), and to determine the surface concentration and orientation of dye adsorbates serving as inhibitors during the deposition (Chapters 6 and 8).

We chose to categorize the measurable optical changes in the electrode surface during electrodeposition in two ways, as first and second order optical effects. First order optical effects are variations in delta and psi ranging from several degrees to tens of degrees and are

primarily due to deposit formation (Chapter 7). Second order effects are much more subtle, ranging from hundreths of a degree to a few degrees (Chapter 8); optical measurements of the presence of inhibitor and its orientation on the electrode fall in this category. Before proceeding, two spectral scans made with the newly developed spectroscopic ellipsometer are shown to illustrate first and second order optical effects. These data will be discussed in the following chapters in greater detail.

First order optical effects are illustrated by the spectroscopic measurements delta and psi shown in Figs. 4.a and 4.b, respectively. In these figures three spectral scans are superimposed, one for a bare Cu substrate, and two for Pb deposits on Cu. Both deposits contained identical quantities of Pb; however, one deposition was made in the absence of inhibitor and the second in the presence of 10 micromolar rhodamine-B. If these deposits had been compact, the deposit thickness would have been about 310 Angstroms; differences in the two spectra reflect micromorphological variations caused by the addition of rhodamine-B in one experiment. The deposit formed in the presence of rhodamine-B had optical properties essentially the same as those of an infinitely thick layer of compact Pb; the deposit formed in the absence of rhodamine-B had optical properties which could not be explained assuming a compact layer of Pb. In the "no dye added" case, the absorption edge of the bare Cu substrate was still detectable and changes in delta trended in a negative direction from the Cu spectra, instead of in

a positive direction as expected for compact Pb. Optical models were used to interpret the spectroscopic ellipsometer measurements. Interpretations are discussed in detail in Chapter 7.

Observable second order optical effects are shown for rhodamine-B adsorption on Pt (Figs. 5.a & 5.b). Though we had decided to use a Cu substrate, spectra such as these were collected to enable comparison of our spectroscopic ellipsometry data for chemisorbed rhodamine-B with data in the literature; such comparisons helped us determine the validity of our data and served as a test of the capabilities of the instrument. Another reason for collecting these spectra was that the absorption band of rhodamine-B is centered roughly on the absorption edge of Cu; Pt has flat optical properties in this region and gave a better background for observing the adsorbed dye. Two features in these spectra should be noted, relatively small delta and psi peaks centered at about 470 nm, and a pair of larger peaks closer to the rhodamine-B solute absorption band. The peak at 470 nm is believed to have been due to a tightly bound chemisorbate whose absorption band is chemically shifted towards the UV with its transition moment parallel to the electrode (pi electrons bonding it to the surface). In such an instance, if the singlet ground state electronic energies are lowered, one would expect a shift of the absorption band towards higher energies, as observed. The much larger peak near the solute absorption band is believed to have been due to a rhodamine-B species with preferential orientation of their transition moments normal to the surface; the very

slight chemical shift indicates only a weak interaction with the surface. These normally oriented species may have populated the compact double layer. Interpretation of the chemically shifted 470 nm peak is in rough agreement with independent reflection spectroscopy results of Schmidt (31).

Modeling First Order Optical Effects: Micromorphological Differences

As discussed earlier, first order optical effects are manifested in changes of delta and psi from several degrees to tens of degrees and are due to the electrodeposit. Spectroscopic ellipsometry measurements showing first order effects were interpreted in terms of micromorphological differences in thin Pb electrodeposits; the quantity of material in the deposit is known from digital coulometry done while stripping the deposit from the surface. Comparison of the charge passed during deposition and stripping gives the coulombic efficiency.

Potentiostatic step experiments were performed (Chapter 6) with the standard supporting electrolyte having a Pb^{++} ion concentration of 5 mM; the counter electrode in this instance was an ultrapure Pb wire. The Cu substrate electrode was first polarized at 0 millivolts relative to a Ag/AgCl reference, and held there for about 15 minutes. At this potential and pH no oxides of Pb or Cu are stable. Then, the potential was stepped to -600 millivolts, sufficiently cathodic to deposit Pb on the surface. Ellipsometric spectra were taken of the thin layer Pb deposits, before significant dissolution could occur at open circuit.

Deposits were stripped after taking spectra in order to determine the coulombic efficiency (always greater than 95 percent) and to determine losses to corrosion (always less than 5 percent).

In these experiments, we studied three levels of passed charge. All three deposits were made with and without 10 micromolar rhodamine-B present in the bulk electrolyte. The three levels of passed charge were equivalent to compact film thicknesses of 310, 600, and 1100 Angstroms. Optically, all deposits made with rhodamine-B additions appeared as infinitely thick layers of compact Pb. Trends in the spectroscopic ellipsometry measurements of deposits made without the inhibitor were more intriguing since they couldn't be predicted on the basis of compact film optical models.

The problem addressed in Chapter 7 is that of developing ellipsometry models capable of predicting the unusual spectroscopic measurements of deposits formed in the absence of rhodamine-B. By developing models which explain unusual observations such as these, insight into deposit structures which result from electrodeposition without inhibitor has been gained. Comparisons of these structures to those formed with rhodamine-B additions were made. One structural difference was found to be due to the nucleation and growth of dendritic islands; in the absence of rhodamine-B dendritic islands formed with a granular, porous deposit (about 50 percent porosity) between and below the islands. In contrast, the deposits formed in the presence of rhodamine-B were found to have no dendrites initially and were relatively compact (less than 10 percent

porosity). Quantification of the wavelength-independent adjustable parameters in these models allowed us to determine the amount of charge used for dendrite formation compared to that involved in the underlying deposit.

Models formulated to explain these first order effects were categorized in four ways: (1) compact film models, (2) effective media approximations, (3) coherent superposition models, and finally, (4) multilayer models. These models are illustrated schematically in Fig. 6.

The first and simplest conceptualization of a thin electrodeposit was as a compact, single-layer film. This compact film model was based upon the Drude equation and assumed that the film, substrate, and incident medium were all homogeneous and isotropic. It was found that the compact film model could explain ellipsometry data for Pb deposition in the presence of rhodamine-B, but was inadequate to explain data for deposition in the absence of this inhibitor.

Next, we attempted to model the entire deposit as a single, equivalent film, having the composite optical properties of a porous, granular layer. This model was inspired by light scattering and ellipsometry measurements made during cyclic voltametry (Chapter 5 and subsequent discussion).

Applicability of the Maxwell-Garnett and Bruggeman theories to granular thin-films, like the Pb deposits of concern in this work, has been substantiated by the optical density measurements of Sichel, et.

al. (32), and more recently by the work of Santucci, et. al. (33). Berreman attempted to account for uniaxial anisotropy in such granular films, but had poor success (34). Bondar presents data and theory for microrough thin films, addressing the question of anamolous absorption in discontinuous Ag films (35). Cohen has done experiments relevant to this thesis illustrating the effects of variations in incident medium refractive index on observed reflection spectra for rough surfaces (36); roughness scattering was taken as a perturbation on the ordinary interaction of light with a flat surface. Corrugations were assumed to cause induced surface dipoles which absorb and reradiate scattered light, thereby altering the reflectance change due to the surface.

We used the theories of both Maxwell-Garnett and Bruggeman as mixing rules for computation of the composite optical constants. The Maxwell-Garnett theory assumes the host medium has the same dielectric properties as the component present in the greatest amount (either electrolyte or Pb), where as the Bruggeman theory assumes that the host medium has the same optical properties as the composite material (electrolyte and Pb mixed physically). The Bruggeman theory is self-consistent at any combination of component volume fractions, and is therefore superior to the Maxwell-Garnett theory. However, the Bruggeman theory has the disadvantage of requiring one to find the roots of a complex polynomial for the general, multicomponent case. Fortunately, the quadratic formula can be used for binary systems, and one is only faced with the selection of the correct root (usually the one having the

largest modulus). The granular, porous Pb deposit considered here was a binary system, one component being Pb and the other being electrolyte. For the effective media assumption to apply, the size of the microinclusions of electrolyte (or alternatively, the size of Pb islands on the Cu) must be much less than the wavelength of the light illuminating the surface.

We found that it was impossible to explain the observed spectroscopic ellipsometry measurements with an equivalent film having thickness and porosity consistent with the amount of Pb known to be deposited (from coulometric measurements made during deposition and stripping).

The Pb deposited on the surface was then assumed to be distributed as islands and the coherent superposition model used. This modeling effort was inspired by scanning electron micrographs of the thin electrodeposits (Chapter 9 and subsequent discussion); dendritic islands were observed on the surface.

The coherent superposition model used a weighted average of the complex reflection coefficients for the bare surface and for the portion of the surface covered with deposit (Pb islands); the thickness of these islands was determined by both the quantity of deposit on the surface (charge passed) and the fraction of the surface covered by the deposit. The weighted average reflection coefficients were substituted into the ellipsometry equation used for calculating delta and psi. To use coherent superposition of reflections from the bare and deposit covered

surfaces, we had to assure that the diameter of the islands was less than the spatial coherence of the illuminating light beam (Chapter 2). In our spectroscopic ellipsometer the transverse coherence varied from 10 microns at 400 nm to 17 microns at 750 nm; the longitudinal coherence varied from 16 microns at 400 nm to 49 microns at 700 nm. Furthermore, the coherent superposition model assumed that the contribution of incoherently scattered light to the reflectance could be neglected; the total reflectance was composed of only the coherent component (37). This condition was fulfilled by use of a detector having a very small acceptance solid angle. Smith and Muller used this technique to simulate Ag_2O islands on Ag anodes (38).

Islands were first assumed to be compact Pb, but were later given porosity by employing the Maxwell-Garnett and Bruggeman relationships. The compact island model also failed to explain the data. By giving the islands some porosity, the agreement was somewhat better, but still unsatisfactory.

Because of our failure to achieve agreement between theory and experiment with the forementioned single-layer models, we had to employ multilayer models (39). Success was achieved by assuming three layers, all having different micromorphologies. The first layer was assumed to be a compact film (UPD), covered by a granular, porous deposit extending further into the electrolyte (Bruggeman theory). The thicknesses of these layers were much smaller than the incident beam wavelength. A third layer was composed of relatively large, dendritic islands having

diameters smaller than the spatial coherence of the incident beam, but larger than its wavelength (coherent superposition model). Apparent refractive indices were calculated at interfaces of the multilayer film. This multilayer film model is consistent with ellipsometry measurements, as well as SEM, light scattering, and digital coulometry data.

Modeling Second Order Optical Effects: Inhibitor Coverage and Orientation

Second order optical effects are subtle changes in delta and psi that range from hundreths of a degree to a few degrees, and may contain information relevant to rhodamine-B coverage and orientation on electrode surfaces. This information can be interpreted with concepts summarized by Bootsma (40).

Organic adsorbates like rhodamine-B (dyes) exhibit strong birefringence due to the electronic transition moment responsible for light absorption (41, 42). A spectroscopic simulator based upon a uniaxial anisotropic film model has permitted rhodamine-B orientation on the electrode to be inferred by taking into account this birefringence (Chapters 3, 6,and 8). The film's thickness was determined by the size of the adsorbed molecule; surface coverage was varied by changing the film optical constants (extinction coefficient) from those of the bulk electrolyte (zero coverage) to those of the adsorbate (complete monolayer).

Rhodamine-B dye has a well established structure, and the electronic transition moment responsible for light absorption is believed to

lie in the plane of the three conjugated aromatic rings making up the heart of the molecule. One can think of the dye molecule geometrically as it is illustrated in Fig. 7; the hexagonal boxes represent the aromatic rings and the arrow represents the electronic transition moment. Recalling the visualization of light as an electromagnetic wave, the electric field vector component parallel to the transition moment will be preferentially attenuated (absorbed). If a dye molecule is randomly oriented in a bulk liquid phase, the medium is isotropic. However, a well ordered monolayer of the same species will exhibit birefringence if transition moments of all molecules in the layer are aligned either normal or parallel to the surface. When transition moments are normal to the surface (parallel to the z-axis in Fig. 7), the extraordinary extinction coefficient, k_e, will be large while the ordinary extinction coefficient, k_o, will be very small (approximately zero). Alternatively, in the case of parallel orientation, k_e will be zero and k_o will be large. By assigning reasonable values of the ordinary and extraordinary complex refractive indices, consistent with an assumed orientation, we found that empirical rules could be established for the qualitative interpretation of spectroscopic ellipsometry measurements in terms of molecular orientation.

The thickness and volumetric surface concentration of the adsorbate monolayer(s) were calculated from bond lengths, knowledge of the molecular structure, and by assuming that molecules were preferentially aligned on surface. Additionally, intelligent guesses were made

regarding values of extraordinary and ordinary extinction coefficients of the adsorbate layer through extrapolation of absorption spectra data for the dissolved dye. This extrapolation accounted for differences in the dye volumetric concentration in the adsorbate layer compared to its concentration in the bulk solution, a primary effect; enhancements of the extrapolated extinction coefficients resulting from preferential orientation were considered, but had only an insignificant, secondary effect.

Since trends in the simulated peaks were qualitatively the same for all substrates considered, empirical rules for the interpretation of spectroscopic ellipsometry of dye adsorbate layers were established. It was found that with the electronic transition moment normal to the surface, resulting peaks in the plots of delta against wavelength were always negative relative to their background, and had amplitudes of about -5 degrees; corresponding changes in psi were smaller by an order-of-magnitude, and could be either positive or negative relative to background. For the parallel orientation, peaks in delta were always positive relative to background, having amplitudes of approximately +0.5 degrees, roughly an order of magnitude less response than for the normal orientation; corresponding changes in psi were of the same order-of-magnitude as the changes in delta, but were always negative relative to background. The assumed angle-of-incidence was 75 degrees in these calculations; the relative sensitivity of the ellipsometer to the two orientations might be different at other inclinations. The thickness

and optical constants of the birefringent dye layer responsible for inhibition of Pb deposition on Cu were also calculated by optimization (Chapters 3 and 6).

Ellipsometry and Light Scattering During Cyclic Voltametry

In addition to making spectroscopic measurements of thin Pb deposits and rhodamine-B adsorbate layers at potentiostatic and open circuit conditions, potentiodynamic experiments were also performed (Chapters 5 and 6). Changes in surface optical properties (delta, psi, and scattered light intensity) were followed during cyclic voltametry. Ellipsometry and light scattering measurements were made at a single, fixed wavelength (usually 515 nm).

Incentives for this type of experiment were to (1) separate optical effects due to formation of the first monolayer, the UPD, from those due to bulk deposition, (2) eliminate uncertainties regarding the interpretation of first order optical effects, and (3) look for inhibitor effects on both the UPD and bulk deposit. By ramping the electrode potential (Chapters 5 and 6), rather than stepping it (Chapter 9), formation of the UPD and bulk deposit were separated in time; this unique experimental approach allowed optical changes attributable to the two layers to be differentiated.

The unusual trend in spectroscopic measurements of delta was attributed to the formation of dendrites and the granular, porous nature of underlying deposit. By performing simultaneous cyclic voltametry and

ellipsometry this optical behavior was correlated with the Pb bulk deposition peak and shown to be reversible upon stripping (Chapter 5). Trends in delta and psi corresponding to the UPD peak were interpretable as the spreading of monolayer thick islands (patches) on the Cu surface; the surface was completely covered by the UPD monolayer before formation of the porous bulk deposit (also Chapter 5). During cyclic voltametry, it was shown that the effect of rhodamine-B on deposit micromorphology (leveling action) was the same as discussed previously in regard to the spectroscopic ellipsometry measurements (Chapter 6). This leveling action disappeared after the first potential cycle; the failure of rhodamine-B to serve as a leveling agent during repeated potential cycling is believed to have been due to its depletion electroreduction from the electrode surface during the first potential cycle (Chapters 4 and 6).

Reduction of leveling agents and inhibitors during electrochemical metal deposition is common (43). However, it is noteworthy that other investigators have found that the Pb underpotential on Ag inhibits the electroreduction of nitrobenzene (44) and oxygen (45) from acidic solutions, probably due to blocking of active sites.

With depletion of rhodamine-B from the electrode surface and from the electrolyte closest to the electrode, a mass transfer boundary layer for the rhodamine-B formed. Related mass transfer effects have been experienced with additives used in nickel depostion on rotating disk electrodes (45.a). After relaxation of the mass transfer boundary layer,

both the double layer and the electrode surface were repopulated with adsorbed rhodamine-B. Repopulation of the electrode with rhodamine-B were observed by spectroscopic ellipsometry; changes in delta and psi peak amplitudes have been correlated with time dependent changes in the dye-induced overpotential required for Pb deposition (Chapter 6). Dye-induced overpotential was observed in cyclic voltamograms (Chapter 3).

Light scattering has been used successfully in conjunction with ellipsometry and reflectance measurements to characterize microrough aluminum films vapor deposited on silicon (46) and fused polycrystalline aluminum oxide surfaces (47). The work on aluminum oxide illustrates how rms roughness and correlation distance can be extracted from light scattering measurements. Simultaneous ellipsometry and light scattering was done on granular Ag_2O film to confirm ellipsometric interpretations regarding the anodic nucleation and growth of Ag_2O particles on Ag electrodes (48). Extensive theory exists for light scattering from rough surfaces which could be applied to the interpretation of experimental data (49-53).

To help substantiate the interpretation of unusual ellipsometry measurements as being due to a granular, porous deposit (rather than other unexpected optical changes in the surface), measurements of laser light scattered from the electrode surface during cyclic voltametry were made (Chapter 5). These experiments were similar to those done earlier for anodic Ag_2O films (54). They were performed early in the study, and were done on a Ag substrate in the same cell used in the Ag_2O

experiments. Our literature references on the formation of a Pb UPD on Ag during cyclic voltametry influenced our choice of substrate (54,55), as did the availability of the existing light scattering cell. Since we wanted to contrast UPD and bulk deposit effects in these experiments, the Pb^{++} ion concentration was adjusted to give UPD and bulk deposit current peaks of comparable amplitudes, and optical effects of the same order of magnitude. The Pb^{++} ion concentration used was 0.5 millimolar. An increase in scattered light intensity was found to be coincident with the Pb bulk deposition peak; the scattered light intensity returned to its initial level upon stripping the Pb from the surface. No increase in scattered light intensity was observed with formation of the UPD layer. The optical features which caused the unusual trend in ellipsometer measurements were most likely the same as those responsible for the increased light scattering, and are believed to have been a fine, granular dispersion of Pb covering the compact Pb monolayer.

Separation of the UPD and bulk deposit properties was significant in that it has allowed us to prove three-dimensional nucleation occurs immediately following formation of a complete Pb monolayer (UPD), with the nuclei sitting on the monolayer. This conclusion was deduced from both ellipsometry and scattering measurements made during cyclic voltametry. Other investigators have attempted to prove this, but only through exsitu experiments using Auger spectroscopy (57), X-ray fluorescence (58), and scanning electron microscopy (59). From this study we also determined the apparent optical constants, thickness, and Gibbs

free energy of adsorption for the Pb underpotential on Ag and Cu substrates (see Chapters 4 and 5). The micromorphology (volume fraction electrolyte) of the initially deposited Pb granular layer on the UPD was also determined.

Scanning Electron Micrographs: A Complementary Study

Incorporation of the coherent superposition model into the interpretation of our ellipsometry data was inspired by scanning electron micrographs of the Pb electrodeposits made in the absence of inhibitor (Chapter 9). These micrographs show the growth of dendritic islands during potentiostatic Pb deposition on Cu. After about 1 minute of deposition at -600 mV (Ag/AgCl ref.), comparable to Figs. 4.a and 4.b, these islands had a size of about 10 microns and covered less than 7 percent of the surface.

Interestingly enough, these large islands had a relatively insignificant effect on spectroscopic ellipsometry measurements and were not primarily responsible for the unusual trends in delta discussed above. The ellipsometer was more sensitive to the fine, granular deposit distributed between islands and detected by light scattering. Though existence of Pb between dendritic islands was verified by EDAX (energy dispersive analysis of X-ray emission), such fine granular deposit could not be quantified by EDAX or satisfactorily resolved by SEM (due to its dielectric nature after exposure to air). These SEM and EDAX studies

were analogous to the X-ray fluorescence study conducted by Vossos and Mark (60).

Unfortunately, in transferring the Pb covered surface from the electrochemical cell to the SEM vacuum chamber, exposure to air occurred. The deposit oxidized immediately, producing a surface which was dielectric in nature. Dielectric samples were plasma coated with Au to prevent surface charging and to allow SEM imaging. The Au coating was of the same thickness as the Pb deposit lying between islands. Pb/Au alloy formation may also have occured, as well as changes in micromorphology due to dehydration and oxidation. Complications may have also arisen from actual changes in micromorphology due to deposit dehydration and oxidation during transfer.

For structures having dimensions less than the source wavelength, more credence is given to the ellipsometry data than that obtained by SEM. The ellipsometry data allowed quantification of the amount of material in the deposit lying between islands by fitting adjustable parameters in optical models. Qualitative knowledge regarding the large dendritic islands, which had diameters greater than the wavelength of the source, was obtained from SEM photographs. However, the charge involved in these islands was deduced from the total deposited charge, measured by digital coulometry, and the the quantity of Pb contained in the underlying deposit, determined from the ellipsometry data. These islands could not be quantified directly by ellipsometry due to the relative insensitivity of the instrument to them.

Potential-step, fixed-wavelength elllipsometry measurements were performed while the deposits for the SEM studies were being formed. These data complement the spectroscopic ellipsometry measurements of the thin Pb deposits already discussed and also show unusual trends in measured values delta, indicative of multilayer, non-homogeneous deposits (also Chapter 9). Spectroscopic ellipsometry of the oxidized Pb deposits formed in the presence of rhodamine-B indicate that this inhibitor was incorporated into the deposit.

Summary of Contributions and Conclusions

1. A novel fast-scanning spectroscopic ellipsometer was developed (Chapter 2).

2. A microcomputer was interfaced for collection, reduction, storage, and interpretation of data (Chapter 3).

3. Spectral simulators (models) used in conjunction with graphics capabilities of the system allow "on the spot" interpretation of spectroscopic ellipsometry data (Chapters 3, 7 and 8).

4. Computerized data acquisition has made possible subtraction of spectral scans; difference spectra can be generated quickly and efficiently. Second order optical effects would be difficult or impossible to resolve without spectral subtraction, digital filtering, and averaging of multiple scans.

5. The spectroscopic ellipsometer was utilized in a fundamental study which was directed at understanding the role of inhibitors during the initial stage of electrodeposition (Chapters 5 and 6).

6. In the absence of inhibitors, bulk Pb deposition on Ag and Cu was found to be preceded by the formation of a complete monolayer of Pb adatoms (UPD layer).

7. In the absence of inhibitors, the bulk Pb electrodeposit had a complicated structure consisting of dendritic islands growing on a granular, porous layer (Chapter 5).

8. Optical modeling indicates that the ellipsometer was primarily sensitive to the fine, granular deposit between islands, which is virtually unresolvable by the SEM (Chapters 7 and 9).

9. Pb electrodeposits formed in the presence of rhodamine-B, a reducible inhibitor, were more compact (Chapter 6). Rhodamine-B was incorporated into the pores of the electrodeposit.

10. Rhodamine-B adsorbate coverage and orientation relevant to inhibition of of Pb electrodeposition were measured by spectroscopic ellipsometry (Chapter 6).

11. Data were interpreted based upon uniaxial anisotropic film model (Chapters 3 and 8).

12. From cyclic voltammetry with ellipsometry at a fixed wavelength, it was demonstrated that leveling action (inhibitory effect) ceases

after the surface concentration is depleted; leveling action resumes with relaxation of the mass transfer boundary layer (Chapter 6).

13. From integration of the anodic UPD peak, it was found that the UPD coverage (stripped) was incomplete prior to bulk deposition when rhodamine-B was added to the electrolyte.

14. The UPD formed at more cathodic potentials when rhodamine-B was present in the electrolyte.

The observed differences in the apparent deposit porosities resulting from rhodamine-B additions are attributed to an increase in nucleation density on the surface and inhibition of dendrite growth by the dye. Since potentials required for Pb deposition are more cathodic in the presence of rhodamine-B than in its absence, the equilibrium size of two-dimensional nuclei on the electrode surface (UPD islands of Pb) would have a much smaller diameter when formed with rhodamine-B present (61). Therefore, for comparable quantities of underpotentially deposited charge, with and without rhodamine-B, a greater number of UPD islands of smaller diameter would have been formed in the presence of adsorbed rhodamine-B. Assuming that subsequent bulk Pb deposition could have occurred only on previously deposited UPD, the nucleation density resulting from rhodamine-B addition would have been enhanced. Furthermore, selective rhodamine-B reduction at points of high activity would have promoted Pb^{++} reduction and deposition at lower activity sites; the

dye would be preferentially reduced on dendrite tips extending into the bulk electrolyte, whereas Pb^{++} would have diffused closer to the surface for reduction, due to its higher mobility (compare the molecular weights and charge of these two cations).

Other Projects and Suggestions for Future Work

1. A project was done with W. J. Plieth using simultaneous light scattering and ellipsometry to verify previous ellipsomtric data interpretations by Muller and Smith regarding the nucleation and growth of Ag_2O particles.

2. Data was inadvertently obtained on electrochemically formed Pb/Au surface alloys. Spectroscopic ellipsometry and simultaneous cyclic voltammetry and ellipsometry at different wavelengths are ideally suited for studies of such surfaces. Stoichiometry of the alloy phases could be determined optically by application of the Bruggeman theory.

3. A paper has been written proposing that molecular orientations and concentrations at liquid-liquid interfaces be measured by a spectroscopic ellipsometer, using either the transmission or reflection mode. If dyes were used in a model extraction system, variations in interfacial structure could be monitored as bulk concentrations changed. Data interpretation would be analogous to that described in this thesis.

4. Sputter roughening of thin Pb films on Cu could be studied in UHV (ultra-high vacuum) by the same techniques of spectroscopic ellipsometry described in this thesis. In particular, reference is made to the section on micromorphological determinations by spectroscopic ellipsometer. If Auger spectroscopy with ellipsometry are ever used together for depth profiling, such information would be of crucial importance. One might also monitor scattered light from the surface during argon beam sputtering, using this as an indication of the degree of roughening. Note that the Auger lines of Cu and Pb are well separated, and that Pb sputters much more easily than the underlying substrate. Sputter rates could be calibrated by ellipsometry.

5. The variations in surface concentration of rhodamine-B during electrodeposition could be measured by spectroscopic ellipsometry under flow conditions; Reynolds number effects on mass transfer controlled inhibitor effects could be measured directly.

6. Light scattering measurements during laser annealling could give insight into the dynamics of the process, as of yet undetermined.

References

1. Harrison, J. A., Thirsk, H. R., "The Fundamentals of Metal Deposition," ELECTROANALYTICAL CHEMISTRY, Vol. 5, A. J. Bard, ed., Marcel Dekker, New York, 1971, p. 139.

2. Lundquist, J., W. R. Grace Company, Columbia, MD, personal communication, October, 1982.

3. Mathieu, H. J., McClure, D. E., Muller, R. H., "Fast Self-nulling Ellipsometer," Rev. Sci. Instrum., 45, 798 (1974).

4. Layer, H. P., "Circuit Design for an Electronic Self-nulling Ellipsometer," Surf. Sci., 16, 177 (1969).

5. Azzam, R. M. A., Bashara, N. M., ELLIPSOMETRY AND POLARIZED LIGHT, North- Holland, New York, 1977.

6. Muller, R. H. "Principles of Ellipsometry," ADVANCES IN ELECTROCHEMISTRY, Vol. 9, R. H., Muller, ed., Wiley, New York, 1973.

7. Rzhanov, A. V., Svitashev, K. K., "Ellipsometric Techniques to Study Surfaces and Thin Films," ADVANCES IN ELECTRONICS AND ELECTRON PHYSICS, Vol. 49, Academic Press, 1979.

8. See 1, p. 129.

9. See 1, p. 139.

10. Pourbaix, M., ATLAS OF ELECTROCHEMICAL EQUILIBRIA IN AQUEOUS SOLUTIONS, Pergamon Press, New York, 1966, p. 384.

11. Kolb, D. M., "Physical and Electrochemical Properties of Metal Monolayers on Metallic Substrates," ADVANCES IN ELECTROCHEMISTRY

AND ELECTROCHEMICAL ENGINEERING, Vol. 11, John Wiley & Sons, New York, (1978), pp. 125-271.

12. Schmidt, E., Gygax, H. R., "Chronoamperometrische Untersuchung Metallischer Monoschichten," J. Electroanal. Chem., 12, 300 (1966).

13. Hass, G., Hadley, L., "Optical Properties of Metals," AMERICAN INSTITUTE OF PHYSICS HANDBOOK, 2nd ed., Gray, D. E., ed., McGraw-Hill, New York, 1963, pp. 6-103 to 6-122.

14. Johnson, P. B., Christy, R. W., "Optical Constants of the Noble Metals," Phys. Rev. B, 6, 4370 (1972).

15. Kolb, D. M., Kotz, R., "Optical Properties and Electronic Structure of Copper Atoms Adsorbed on a Platinum Electrode," Surf. Sci., 64, 698 (1977).

16. Plieth, W. J., Gruschinske, P., Hensel, H. J., "Electronic Changes of Light Absorption by the Electric Field of the Electrolytic Double Layer," Ber. Bunsenges. Phys. Chem., 82, 615 (1978).

17. Schmidt, S., Reich, R., Ber. Bunsenges. Phys. Chem., 76, 549 (1972).

18. Aspnes, D. E., Kinsbron, E., Bacon, D. D., "Optical Properties of Au: Sample Effects," Phys. Rev. B, 21, 3290 (1980).

19. Hansen, M., CONSTITUTION OF BINARY ALLOYS, McGraw-Hill, New York, pp. 222-223.

20. Elliott, R. P., See 19, Supplement No. 1, 1965, pg. 98.

21. Budinok, A., "Underpotential Effects in the Process of Electrodeposition of CuCd Alloy on a Cu(111) Single Crystal," J. Electroanal. Chem., 123, 365 (1981).

22. Hamelin, A., Katayama, A., "Lead Underpotential Deposition on Gold Single-Crystal Surfaces: The (100) Face and Its Vicinal Faces," J. Electroanal. Chem., 117, 221 (1981).

23. See 11.

24. Adzic, G. McBreen, J. Chu, M. G., "Adsorption and Alloy Formation of Zinc Layers on Silver," J. Electrochem. Soc., 128, 1691 (1981).

25. Aspnes, D. E., Theeten, J. B., "Investigation of Effective-media Models of Microscopic Surface Roughness by Spectroscopic Ellipsometry," Phys. Rev. B, 20, 3292 (1979).

26. Azzam, R. M. A., Bashara, N. M., "Polarization Characteristics of Scattered Radiation from a Diffraction Grating by Ellipsometry with Application to Surface Roughness," Phys. Rev. B, 5, 4721 (1972).

27. Kotz, R., Hayden, B., Schweizer, E., Bradshaw, A. M., "The Application of Spectroscopic Ellipsometry to the Oxidation of Magnesium," Surf. Sci., 112, 229 (1981).

28. Aspnes, D. E., Theeten, J. B., "Spectroscopic Analysis of the Interface Between Si and Its Thermally Grown Oxide," J. Electrochem. Soc., 127, 1359 (1980).

29. Theeten, J. B., Aspnes, D. E., "The Determination of Interface Layers by Spectroscopic Ellipsometry," Thin Solid Films, 60, 183 (1979).

30. Chen, Chia-Tien, Cahan, B. D., "The Nature of the Passive Film on Iron," J. Electrochem. Soc., 129, 17 (1982).

31. See 17.

32. Sichel, E. K., Gittleman, J. I., and Abeles, B., "Optical Properties of Granular Magnesium Films," Thin Solid Films, 51, 89 (1978).

33. Santucci, S., Picozzi, P., Paoletti, L., Tangucci, F., "Optical Properties of Granular Metal Films: The Au/Ag System," Thin Solid Films, 79, 133 (1981).

34. Berreman, D. W., "Reflectance and Ellipsometry when Submicroscopic Particles Bestrew a Surface," J. Opt. Soc. Am., 60, 499 (1970).

35. Bondar, E. A., "The Anamolous Absorption of Discontinuous Silver Films and the Polarizability of Small Particles," Thin Solid Films, 81, 121 (1981).

36. Cohen, D. K., Sari, S. O., Scherkoske, K. D., "Interfacial Scattering and Electrodynamics due to Roughness at Silver Surfaces," Surf. Sci., 101, 355 (1980).

37. Ohlidal, I., Lukes, F., Navratil, K., "Rough Silicon Surfaces Studied by Optical Methods," Surf. Sci., 45, 91 (1974).

38. Muller, R. H., Smith, C. G., "Use of Film Formation Models for the Interpretation of Ellipsometer Observations," Surf. Sci., 96, 375 (1980).

39. Mathieu, H. J., "Computer Programs for Ellipsometry II," Lawrence Berkeley Laboratory, Berkeley, CA, LBL-2517 (1973).

40. Bootsma, G. A., Meyer, F., "Ellipsometry in the Submonolayer Region," Surf. Sci., 14, 52 (1969).

41. Plieth, W. J., Schaefer, G., "Modulation Spectroscopic Investigation of the Electrochemical Aspects of Adsorbed Layers of Organic Molecules," Surf. Sci., 37, 67 (1973).

42. Plieth, W. J., Gruschinske, P., Hensel, H. J., "Electronic Changes of Light Absorption by the Electric Field of the Electrolytic Double Layer," Ber. Bunsenges. Phys. Chem., 82, 615 (1978).

43. See 1.

44. Kokkinidis, G., Juttner, K., "The Electrocatalytic Influence of Underpotential Lead Adsorbates on the Reduction of Nitrobenzene and Nitrosobenzene on Silver Single Crystal Surfaces in Methanolic Solutions," Electrochim. Acta, 26, 971 (1981).

45. Zwetanora, A., Juttner, K., "The Electrocatalytic Influence of Underpotential Lead and Thallium Adsorbates on the Cathodic Reduction of Oxygen on (111), (100), and (110) Silver Single-crystal Surfaces," J. Electrochem. Soc., 119, 149 (1981).

45a. See 1, pp. 139-141.

46. Smith, T., "Effect of Surface Roughness on Ellipsometry of Aluminum," Surf. Sci., 56, 252 (1976).

47. Hensler, D. H., "Light Scattering from Fused Polycrystalline Aluminum Oxide Surfaces," Appl. Opt., 11, 11 (1972).

48. Muller, R. H., Plieth, W. J., Farmer, J. C., "Nucleation and Growth of Silver Oxide Films: Light Scattering and Ellipsometry Measurements," Lawrence Berkeley Laboratory, Berkeley, CA, LBL-12965 (1981).

49. Bousquet, P., Flory, F., Roche, P., "Scattering from Multilayer Thin Films: Theory and Experiment," J. Opt. Soc. Am., 71, 1115 (1981).

50. Jakeman, E., "Fresnel Scattering by a Corrugated Random Surface with Fractal Slope," J. Opt. Soc. Am., 72, 1034 (1982).

51. Marvin, A., Toigo, F., Celli, V., "Light Scattering from Rough Surfaces, General Incidence Angle and Polarization," Phys. Rev. B, 11, 2777 (1975).

52. Celli, V., Marvin, A., Toiga, F., "Light Scattering from Rough Surfaces," Phys. Rev. B, 11, 1779 (1975).

53. Maradudin, A. A., Mills, D. L., "Scattering and Absorption of Electromagnetic Radiation by a Semi-infinite Medium in the Presence of Surface Roughness," Phys. Rev. B, 11, 1392 (1975).

54. See 48.

55. Takayanagi, K., Kolb, D. M., Kambe, K., Lehmpfuhl, G., "Deposition of Monolayer and Bulk Lead on Ag(111) Studied in Vacuum and in an Vacuum and in an Electrochemical Cell," Surf. Sci., 100, 407 (1982).

56. See 1, pg. 113.

57. See 55.

58. Vossos, B. H., Mark, H. B., Jr., J. Electroanal. Chem., 13, 1 (1967).

59. Poretkin, V. V., Kovenski, I. M., "Initial Step of Copper Electrocrystallization in the Presence of Cadmium," Soviet Electrochem., 17, 1461 (1981).

60. See 58.

61. Plieth, W. J., "On the Electrochemical Properties of Small Clusters of Metal Atoms and their Role in the Surface Enhanced Raman Scattering," Lawrence Berkeley Laboratory, Berkeley, CA, LBL-12955 (1981).

Figures

1. Definition of s and p components of elliptically polarized electromagnetic wave.

2. Apparatus diagram showing PCSA optical configuration. Also shown as Fig. 1 in Chapter 2.

3. Structural formulae of model inhibitors also shown as Fig. 1 in Chapter 4.

4.a Spectral scans of thin Pb deposits on Cu, contrasting a deposit made with rhodamine-B to another made in the absence of this inhibitor. Measurements for the bare Cu substrate are also shown for comparison. The electrolyte concentrations used were 5 mM $Pb(NO_3)_2$, 1 M $NaClO_4$, and 10 micromolar rhodamine-B (when added), at pH 3. Also shown as Fig. 7.a in Chapter 6 and Fig. 1.a in Chapter 7.

4.b Psi vs wavelength corresponding to Fig. 4.a. Also shown as Fig. 7.b in Chapter 6 and Fig. 1.b in Chapter 7.

5.a Experimental spectroscopic ellipsometry of rhodamine-B adsorbed on Pt from 20 micromolar solution containing 5 mM $Pb(NO_3)_2$ and 1 M $NaClO_4$ at pH 3 (delta vs wavelength). Also shown as Fig. 7.a in Chapter 8.

5.b Psi vs wavelength corresponding to Fig. 5.a. Also shown as Fig. 7.b in Chapter 8.

6. Schematic representation of the various ellipsometer models used in attempts to explain experimental spectroscopic measurements of thin film Pb deposits on Cu substrates. Numbers in parenthesis indicate the number of adjustable parameters involved in each model. Four general categories of models are shown.

7. Geometric representation of rhodamine-B adsorbed on a surface (x-y plane) with normal and parallel orientations of the electronic transition moment. Also shown as Fig. 1 in Chapter 8.

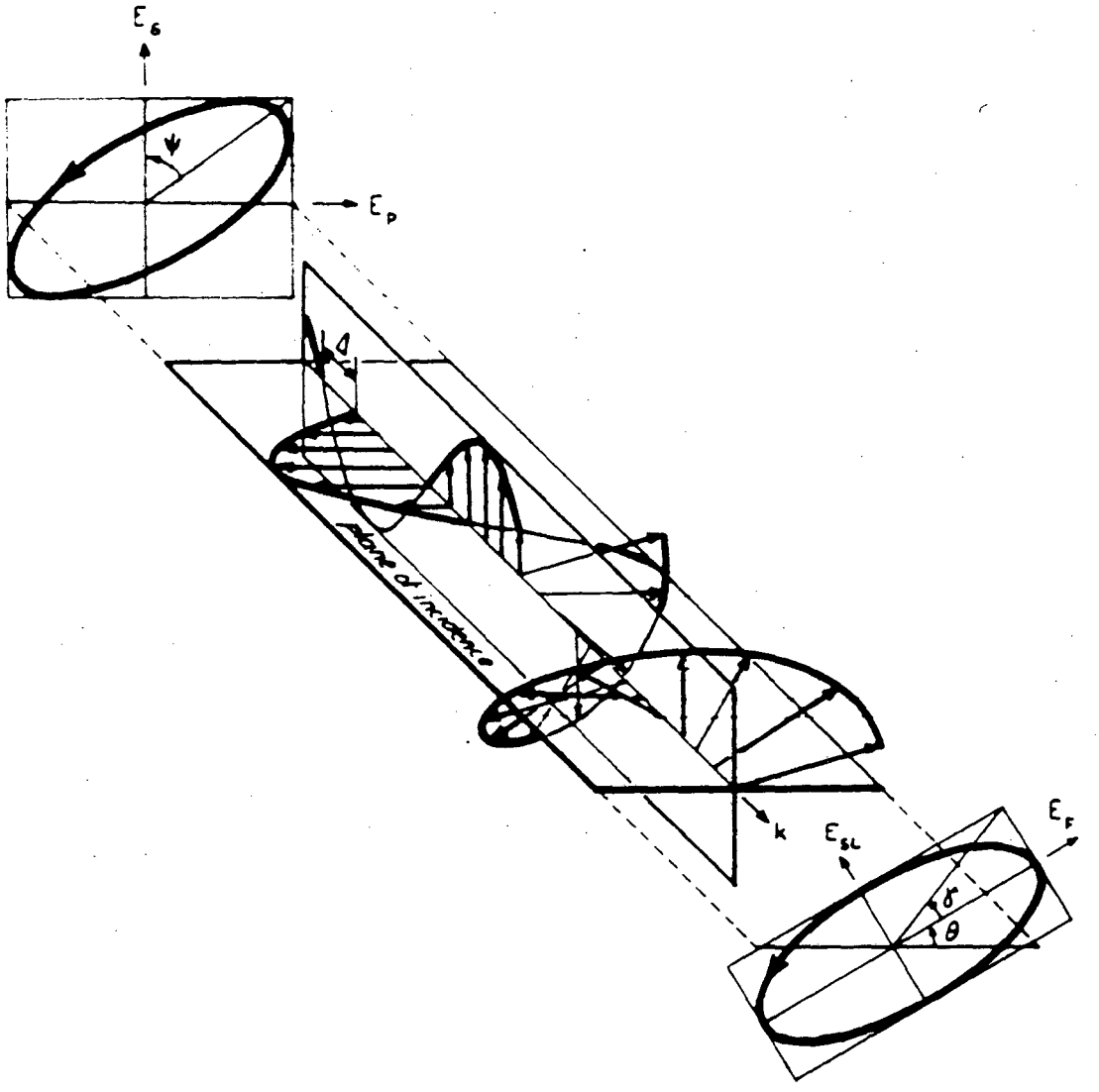

XBL 681-59A

Fig. 1

SPECTRAL SCANNING, SELF-NULLING ELLIPSOMETER OPTICS

1. high pressure Xe lamp
2. rotating interference filter
3. collimator
4. Glan-Thompson polarizer
5. Faraday cell polarizer
6. Fresnel rhomb achromatic retarder
7. electrochemical cell (or Auger)
8. analyzer Faraday cell
9. analyzer Glan-Thompson prism
10. collimator
11. spectrally "flat" detector
12. rotary incremental digital encoder
13. spectral scanner drive motor

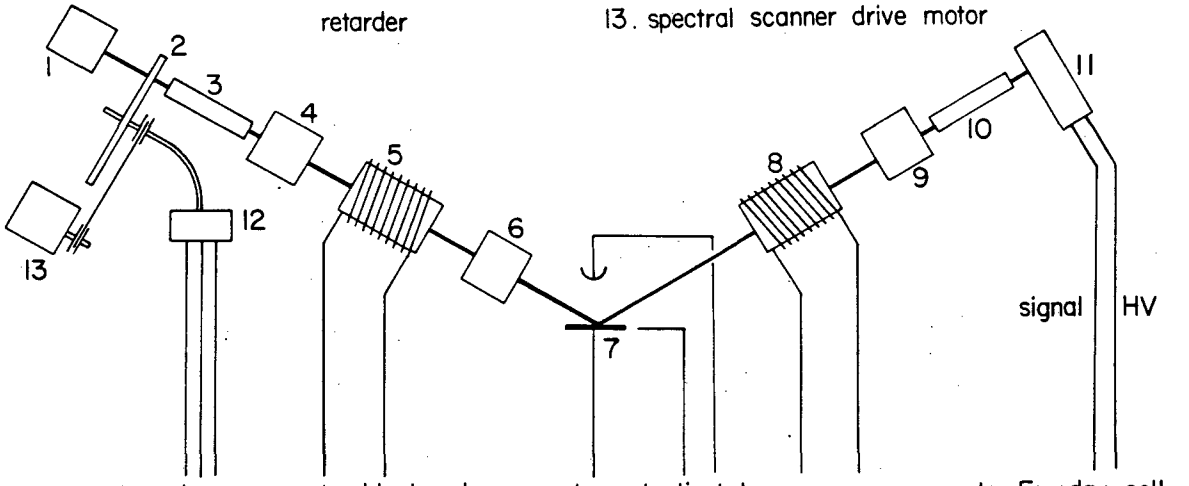

XBL 829-11871

Fig. 2

CATIONIC
555 NM
125 MV

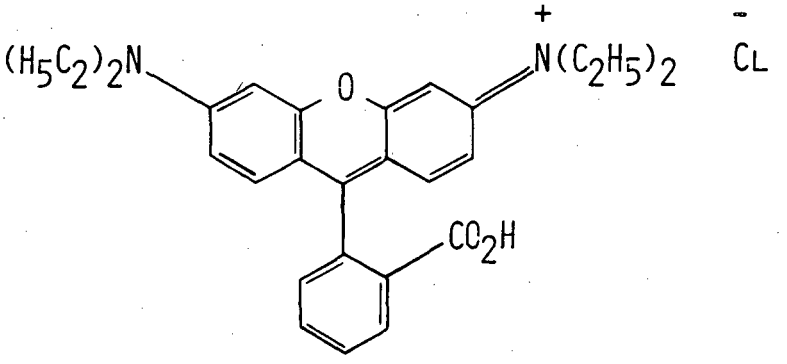

RHODAMINE-B CHLORIDE

NEUTRAL
501 NM
60 MV

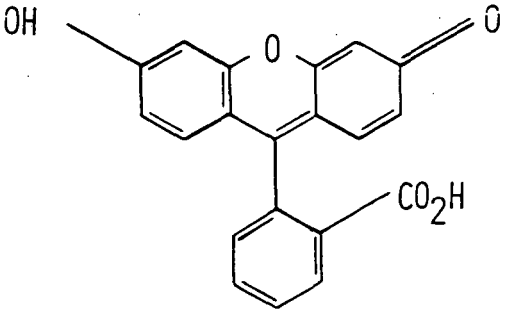

FLUORESCEIN

ANIONIC
470 NM
25 MV

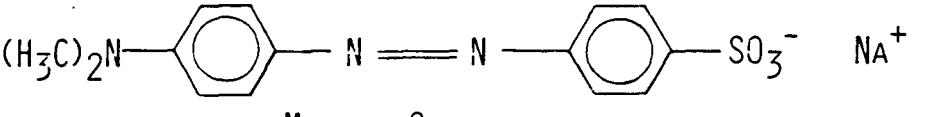

METHYL ORANGE

EXAMPLES OF MODEL INHIBITORS USED

XBL 833-8503

Fig. 3

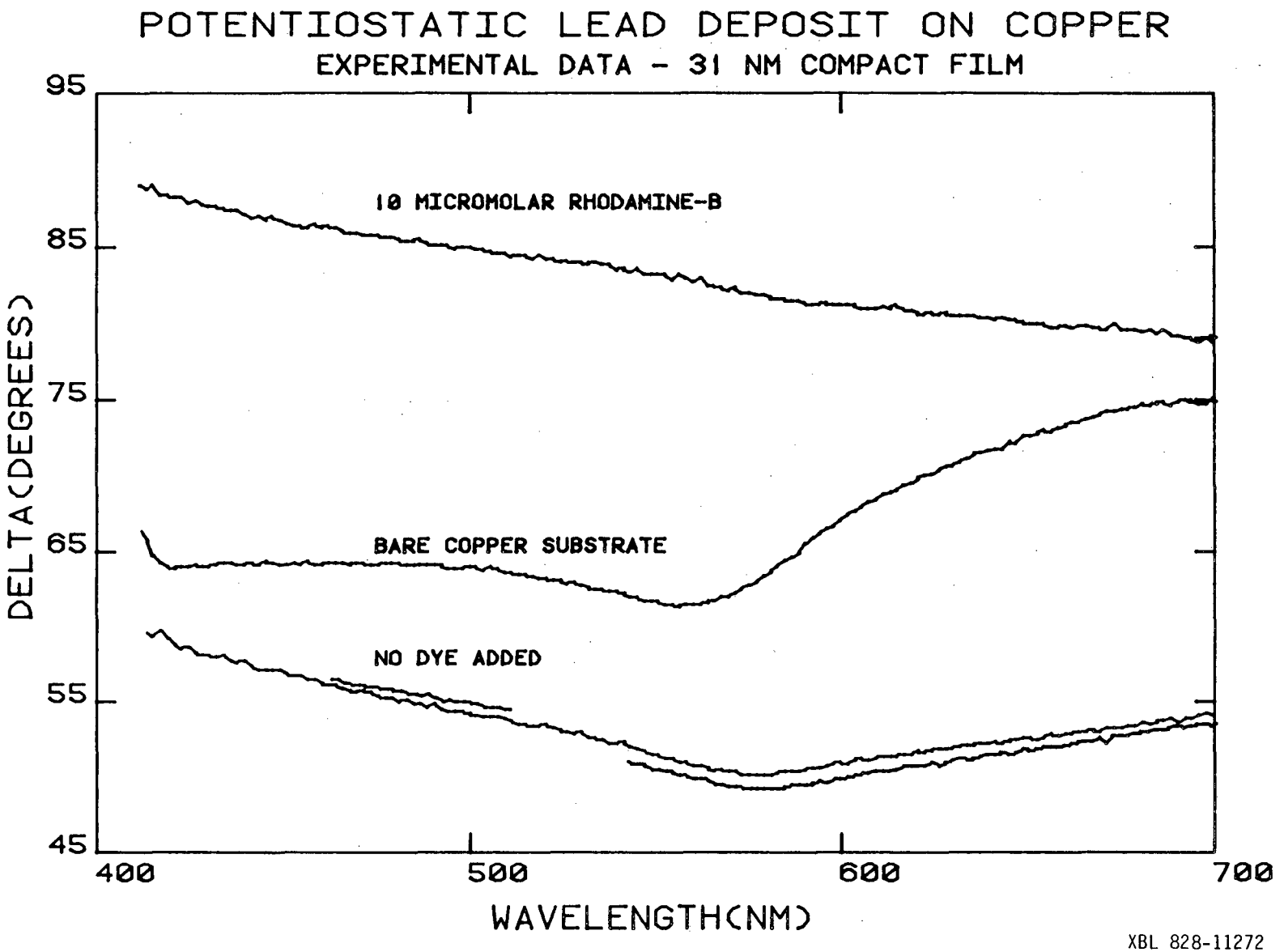

XBL 828-11272

Fig. 4.a

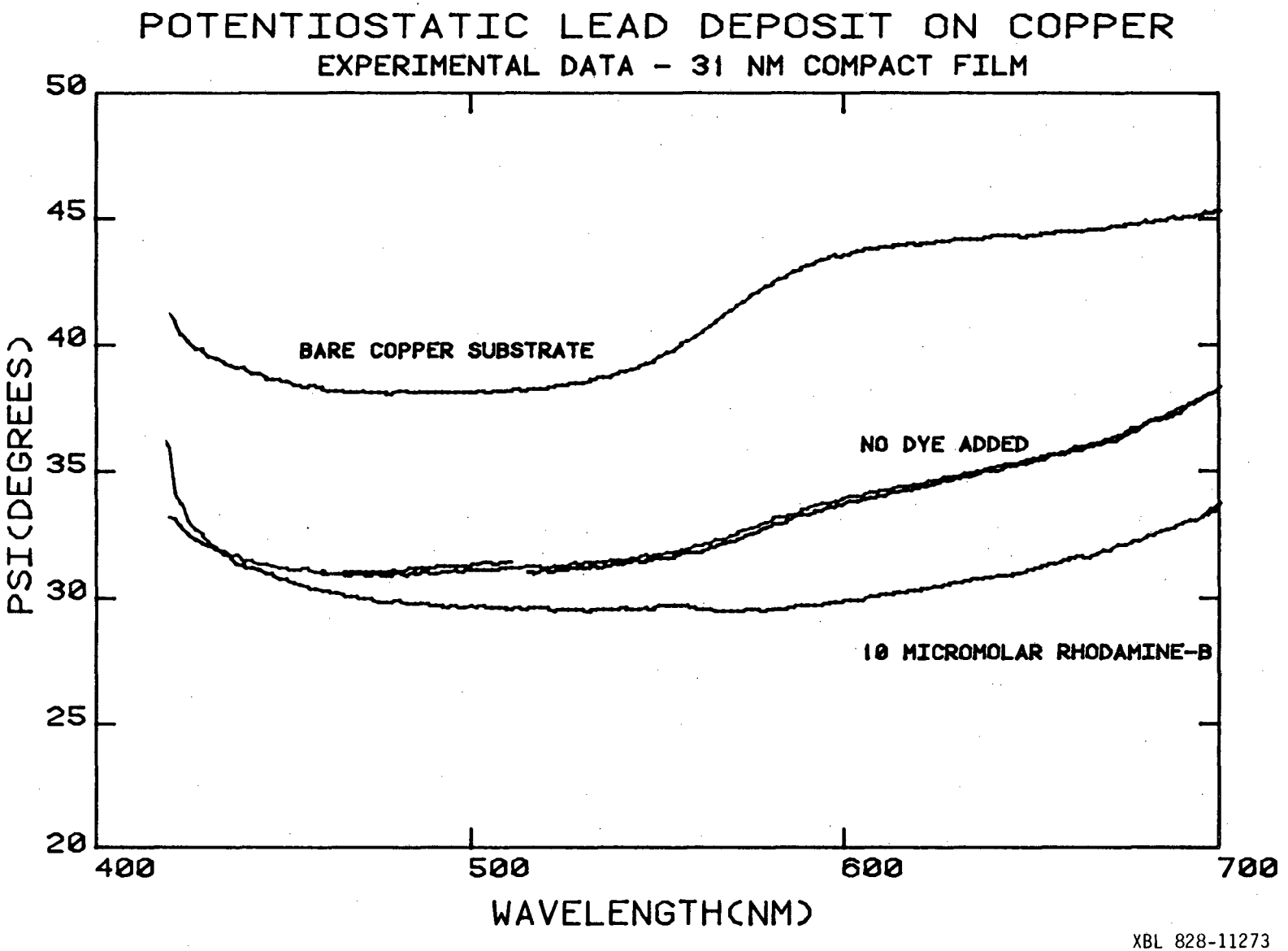
POTENTIOSTATIC LEAD DEPOSIT ON COPPER
EXPERIMENTAL DATA - 31 NM COMPACT FILM
50
45
40
35
30
25
20
PSI(DEGREES)
BARE COPPER SUBSTRATE
NO DYE ADDED
10 MICROMOLAR RHODAMINE-B
400
500
600
700
WAVELENGTH(NM)
XBL 828-11273

Fig. 4.b

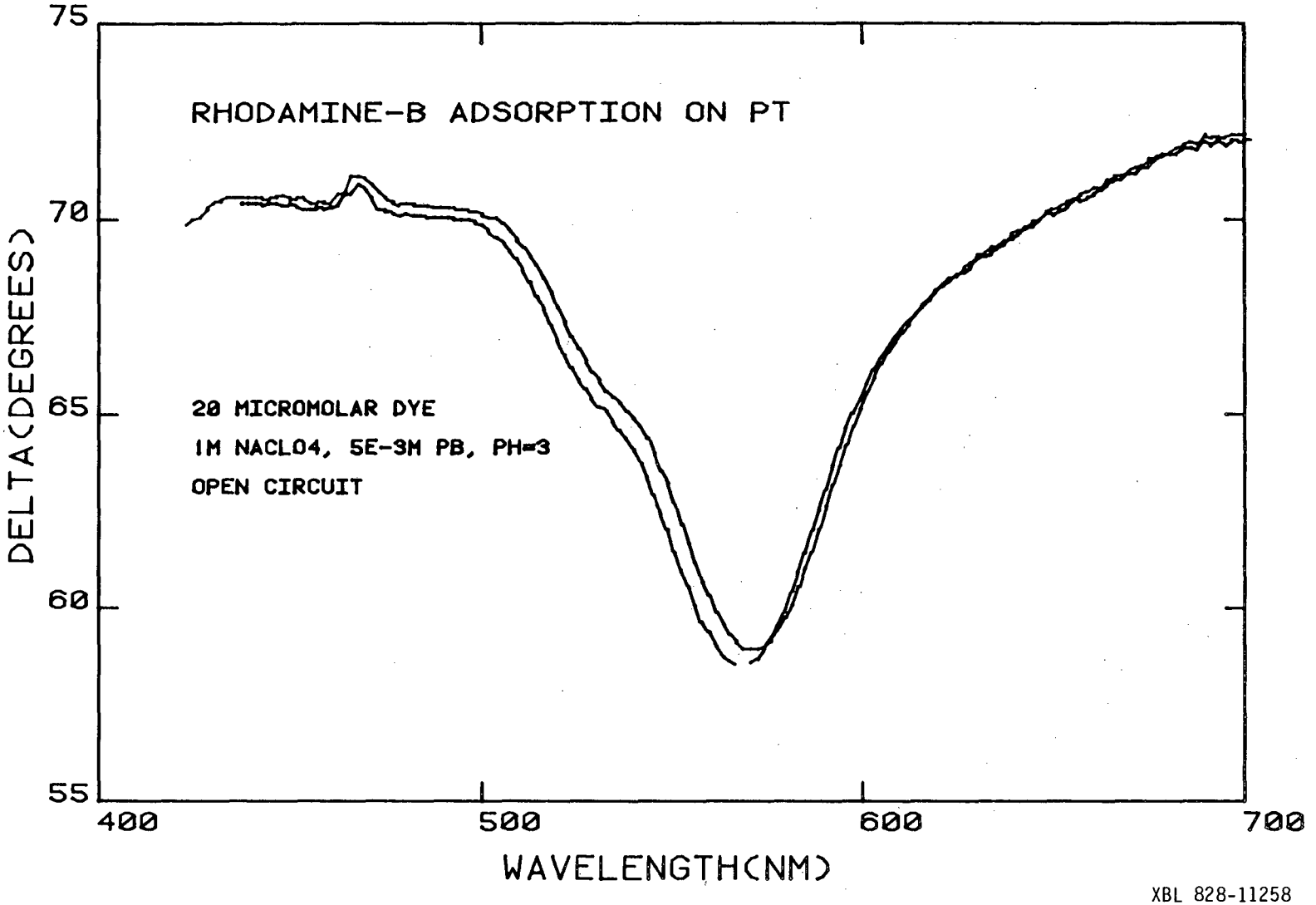

XBL 828-11258

Fig. 5.a

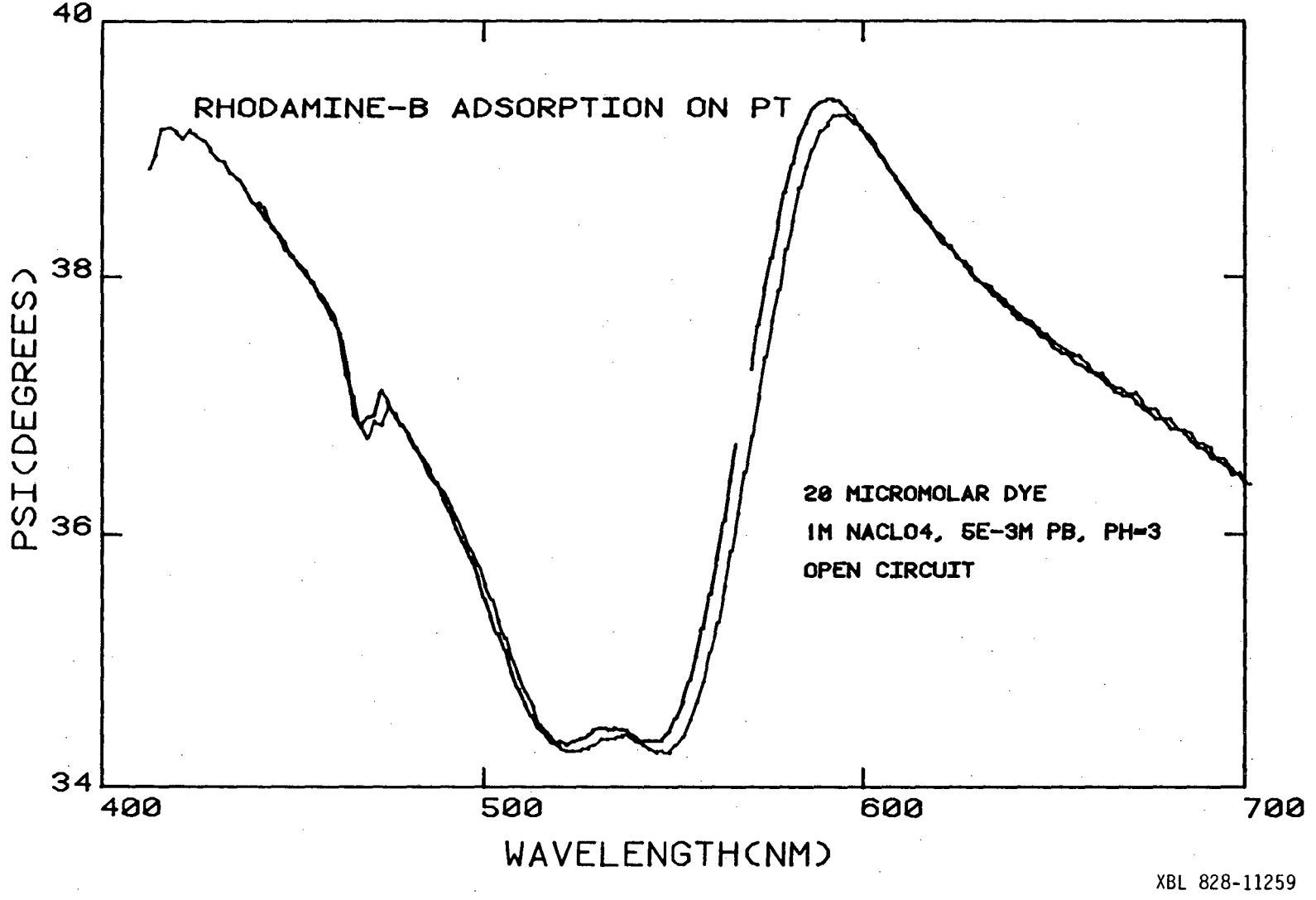
RHODAMINE-B ADSORPTION ON PT
20 MICROMOLAR DYE
1M NACLO4, 5E-3M PB, PH=3
OPEN CIRCUIT
PSI(DEGREES)
40
38
36
34
400
500
600
700
WAVELENGTH(NM)
XBL 828-11259

Fig. 5.b

MODELING FIRST ORDER OPTICAL EFFECTS

COMPACT HOMOGENEOUS FILM

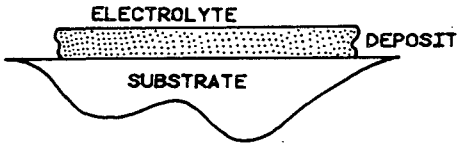

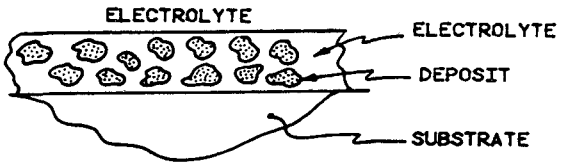

EFFECTIVE MEDIA APPROXIMATION

1. MAXWELL-GARNETT (2)
2. BRUGGEMAN (2)

COHERENT SUPERPOSITION

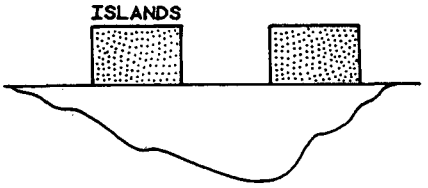

1. COMPACT ISLANDS (2)
2. POROUS ISLANDS (3)
3. ANISOTROPIC (6)

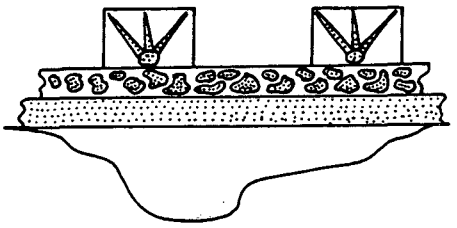

MULTILAYER MODELS

1. THREE LAYER (6)
2. TWO LAYER SIMPLIFICATION (3)

XBL 829-11873

Fig. 6

MODELING SECOND ORDER EFFECTS

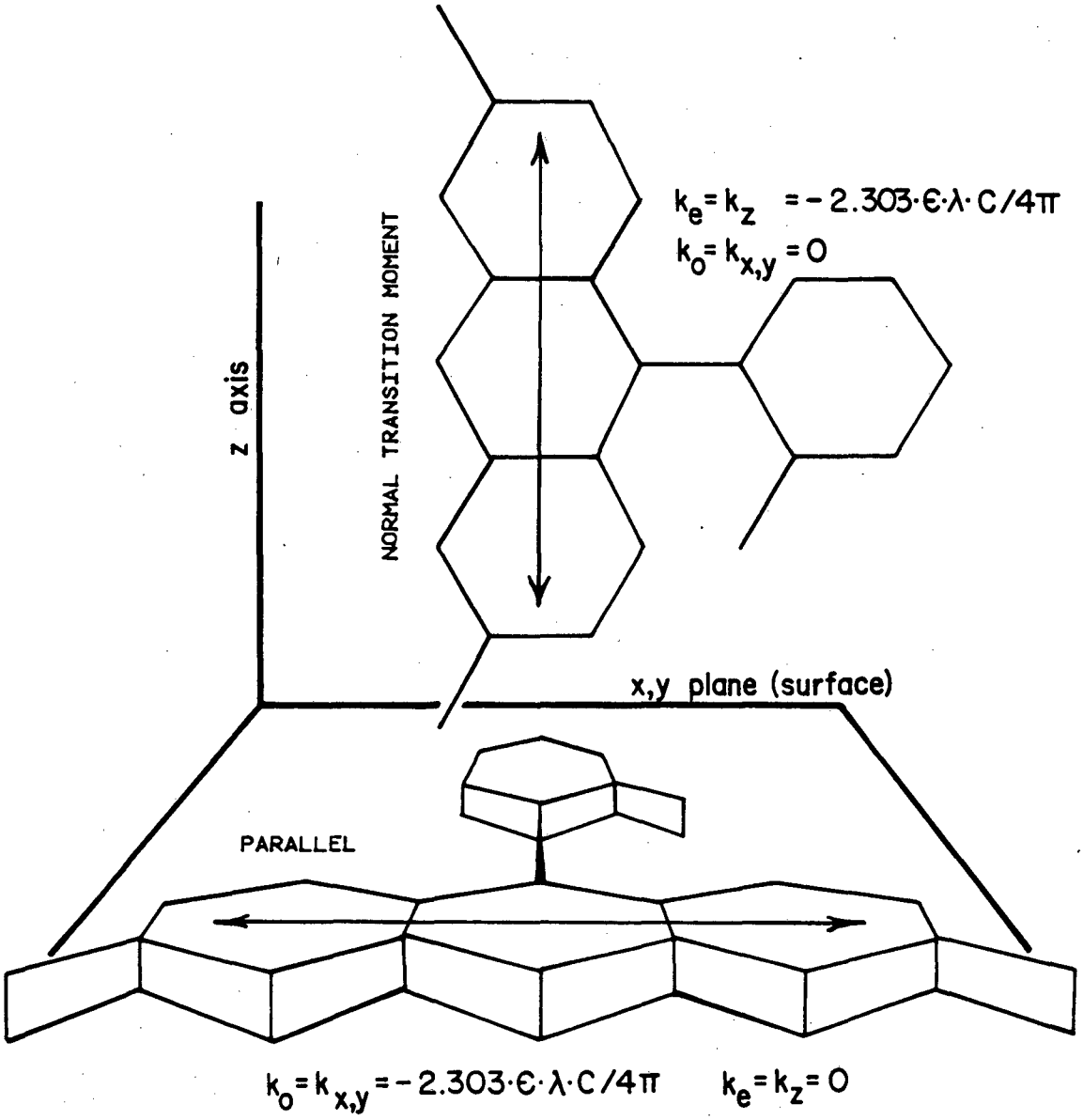

Fig. 7

Chapter 2

DEVELOPMENT OF THE AUTOMATIC, SELF-NULLING, SPECIAL SCANNING ELLIPSOMETER: A DESCRIPTION OF HARDWARE

Abstract

The automatic, magneto-optic ellipsometer reported previously (1) has been given spectral scanning capabilities in the visible-UV by using a high pressure Xe lamp and a rotating CVF (continuously variable filter) as a variable monochromatic source. A Fresnel rhomb is used as an achromatic compensator in a PCA optical component configuration. Interchangeable Faraday cell cores of various glasses extend the spectral range of the instrument. Variations in loop gain during spectral scanning and implications are discussed. An argon laser can also be used as a source for the ellipsometer, and is especially useful when making ellipsometric measurements on rough surfaces.

An LSI-11/2 has been interfaced for data acquisition. This allows (1) rapid, efficient treatment of nonlinear responses of the Faraday cells to changes in wavelength; (2) simultaneous recording of wavelength, psi, and delta (as well as electrochemical cell potential and current), and (3) "on the spot" interpretation of spectra in terms of physically significant quantities such as adatom coverages and orientations, substrate refractive indices, and deposit micromorphologies. Applications are discussed in subsequent chapters.

Introduction

The spectroscopic ellipsometer used in this work is a novel modification of the instrument constructed by Mathieu, McClure, and Muller (1), which was based upon principles proposed earlier by Layer (2). Details of the automatic self-nulling ellipsometer are reviewed here, along with modifications necessary to make possible rapid spectral scanning.

Discussion of the instrument is subdivided into three categories, optical path components (Fig. 1), electronics (Fig. 2), and computer (Fig. 3). The optical path components (Fig. 1) include sources, collimators, polarizing prisms, magneto-optic rotators, the compensator, and the photodetector; the electronic components (Fig. 2) include the Faraday cell controller, Faraday cell power supplies, the modulation amplifier, and supplies for the source and photomultiplier. The computerized data acquisition system components (Fig. 3) are the microprocessor and memory, the dual floppy disk drive, the work station (graphics terminal, printer, and interactive plotter), the analog-to-digital converter, various auxiliary boards (RAM memory, an input-output board, a pulse counter, an external clock, and a pulse generator), and a step-motor control module which makes possible computer control of some optical components.

Systems

I. Optics

The PCA (or PCSA, Polarizer-Compensator-Sample-Analyzer) configuration of optical components is used (Fig. 1 and Appendix 1). Collimated monochromatic light is linearly polarized by a Glan-Thompson prism and a Faraday cell, collectively referred to as the "polarizer." This beam then passes through a Fresnel rhomb which serves as an achromatic quarter-wave retarder, called the "compensator." Leaving the Fresnel rhomb, the beam is elliptically polarized in such a way so that after reflection from a sample surface (electrode), it is again linearly polarized (3,4). The reflected beam is then extinguished (nulled) by another sequence of polarizing components, a Faraday cell followed by a Glan-Thompson prism; these are collectively referred to as the "analyzer." After the analyzer, the light is collected by a second telescope. A photomultiplier tube is used for detection of the reflected beam intensity.

Transmission axes azimuths of the polarizer and analyzer, and the azimuth of the fast axis of the compensator are all measured from the plane of incidence formed by reflection from the sample; these azimuths are the quantities P, A, and C, respectively. When adjusted in such a way to produce a null intensity at the detector, these azimuths can be used to calculate the ellipsometer parameters delta and psi. Holding C fixed (45 or 135 degrees), the elliptic state of polarization of the beam incident on the sample is governed by P; there are two incident

beam polarizations which give linear reflected polarization. The two sets of measured azimuths, P and A represent the same values of delta and psi. Therefore, P and A are measurements of the surface optical properties.

Rotation of the polarizer and analyzer transmission axes depends upon both the manual azimuth setting of the Glan-Thompson prisms and the magneto-optic rotation induced by the Faraday cells; prism and Faraday cell rotations are additive.

II. Electronics

Incorporation of the Faraday cells into the PCA configuration allows the quantities P and A to be measured electronically, and controlled automatically (Fig. 2 and Appendix 2). Knowledge of the Faraday cell construction (solenoid turns and length), Verdet coefficient of the diamagnetic glass core, and dc current level and sense permits one to calculate the Faraday cell contribution to azimuth rotation in either pair of polarizing components. The induced rotation is linearly proportional to the dc currents; the bipolar programmable power supplies generate a voltage proportional to the current which is monitored by computer via analog-to-digital converters. The current supplied to the Faraday cells is controlled automatically by a sophisticated feed-back scheme which is sensitive to the photomultiplier output (1). Independent, simultaneous control of P and A is accomplished through quadrature phase separation of the two channels.

Modulation currents of 10 kHz and 90 degree phase difference are fed to each Faraday cell, both generating responses from the photomultiplier governed by the transfer curve shown in Fig. 4. Independent error signals for the polarizer and analyzer are derived from the photomultiplier response using two phase sensitive detectors, one referenced to the polarizer modulation current and the other referenced to the analyzer modulation current.

To more fully understand this method of control, operation of a single channel should be considered first. From the transfer curve (Fig. 4), one sees that the photomultiplier response to the Faraday cell modulation will be in phase with the modulation current and have the fundamental frequency if the dc current level (azimuth rotation) is overcompensated; undercompensation produces a response completely out of phase (180 degrees), but still having the fundamental frequency. At exact compensation (null condition) only second harmonics are generated. The phase detector (Fig. 2) performs a full-wave rectification of these responses, positive polarity for overcompensation and negative polarity for undercompensation. The error signal used to control the bipolar, dc current supply for the Faraday cell is derived by integration of the rectified phase detector output, and is positive for overcompensation, negative for undercompensation, and zero for exact compensation (integration of the second harmonic gives a zero result). When this error signal is applied to the controller input for the bipolar dc current supply, the Faraday cell is driven to the null condition.

Separation of the two error signals for the polarizer and analyzer is achieved by maintaining quadrature phase difference between their respective ac modulation currents. Consider the polarizer phase sensitive detector response to the analyzer Faraday cell modulation, referred to as a cross-modulation response (see the discussion of program CALFC1 in Chapter 3, "CROSS-TALK PARAMETERS"). The polarizer phase sensitive detector will rectify this cross-modulation with positive polarity for one half-cycle and with negative polarity for the other half cycle; after integration the contribution of this cross-modulation to the error signal is zero. This situation is contrasted to the manner in which the polarizer phase detector rectifies its own modulation signal; i.e., full-wave rectification of either positive or negative polarity, which after integration gives a corresponding net error signal of either positive or negative polarity. The converse is true for cross-modulations induced on the analyzer channel by the polarizer. In conclusion, by maintaining a 90 degree phase difference between the polarizer and analyzer modulations, one assures that cross-modulation responses appearing on their respective phase detector outputs do not contribute to the error signal derived by integration; therefore, there is quadrature separation of the two error signals.

III. Computer System

The computer system (Fig. 3 and Appendix 3) acquires data in two modes, which are categorized as the "spectral scanning" and the "potentiodynamic, fixed-wavelength" modes. The types of data acquired in the two modes are somewhat different.

In the spectral scanning mode one desires to rapidly measure delta and psi as a function of wavelength. As indicated in the foregoing discussions, delta and psi are linearly proportional to the dc currents required by the polarizer and analyzer Faraday cells to produce nulling. The bipolar power supplies producing these currents also generate electrical signals (-200 to +200 mV) proportional to the currents. These signals are monitored by the computer over two channels of an 8-channel analog-to-digital converter and are subsequently interpreted as delta and psi by software (see Chapter 3). Wavelength is swept by rotation of a continuously variable interference filter (CVF) positioned between a white light source and the polarizer, and varies linearly with the circular filter's angular position (Figs. 5 and 6). The computer monitors wavelength indirectly by measuring the angular position of the CVF as it rotates. This is done with a digital rotary incremental encoder interfaced to the computer via an addressable pulse counter (5,6). As the CVF rotates the encoder generates three pulse trains correlated with angular position, an index pulse (1 per revolution) and two other series of pulses of higher repetition rate (400 per revolution). The frequency of the high repetition pulses is measured directly by one channel of the pulse counter and used as a measure of scan rate. Angular position is determined by counting one series of high repetition pulses and using the index to reset the count every revolution; software interprets this count as wavelength on the basis of calibrations (see the discussion of SEV002 in Chapter 3, input data file WLCALC.DAT). Since the Verdet coefficient is wavelength dependent, the Faraday cells must also be calibrated over the spectral range of the

CVF; magneto-optic Faraday rotation is correlated with encoder count (see the discussion of CALFC1 in Chapter 3, "POL VERDET COEF"). Note that the instrument can also be operated as a scanning reflection spectrophotometer by monitoring the photomultiplier output instead of the Faraday cell currents as the CVF rotates, which is useful for wavelength calibration of the digital encoder (see Appendix 5, Fig. 13).

In the potentiodynamic, fixed-wavelength mode the computer only acquires data from the 8-channel analog-to-digital converter; the pulse counter is ignored since the CVF is kept stationary. As in the spectral scanning mode, two channels are dedicated for measuring Faraday cell currents (delta and psi). Additionally, two channels monitor electrochemical cell potential and current via outputs from a rack-mounted potentiostat. Occassionally it becomes advantageous to use the 515 nm line of an argon laser (Figs. 7.a and 7.b) as source when doing simultaneous ellipsometry and light-scattering measurements (Chapter 5); in this case another channel is used to follow scattered-light intensity (photomultiplier output).

Once accumulated data has filled the buffer, these data are periodically recorded on double density floppy disks in unformatted form (Chapter 3). conversion of Faraday cell currents to delta and psi is done post-experiment. Data can be obtained as high-quality graphic output from an interactive plotter (Fig. 6, item H), as numeric output from a teletype, or viewed on the graphics terminal screen with an option of hardcopy (Fig. 6, item G). The graphics terminal serves as the instrument control console.

An elaborate collection of spectra simulation programs allow the user to interpret spectroscopic ellipsometry measurements immediately after performing an experiment (Chapter 3). Since simulated and experimental data can be displayed together at the work station, the operator can fit adjustable optical model parameters visually. Similar simulations exist for fixed-wavelength data interpretation.

Component Details

I. Spectral Scanning Source

The spectroscopic mode utilizes a high pressure xenon lamp, which serves as a white source. Wavelength can be varied continuously by rotating a continuously variable interference filter (CVF) positioned between the lamp and polarizer collimating telescope (Figs. 1, 5, and 6).

In the original version of this instrument, Muller used a high pressure mercury lamp with a narrow band filter for the 546 nm line. The same lamp supply and housing (Oriel model # C-72-20) are now used for a 75 watt high pressure xenon lamp (Illumination Industries, Inc. model # W75-2002). This power supply and lamp system are current stabilized. After the installation of a new lamp, a concave reflector inside the housing and external lenses have to be adjusted so their focal point is at the polarizer collimating telescope pinhole.

As the filter revolves clockwise, the wavelength passed by the filter varies from approximately 370 nm to 720 nm over the first 180 degrees of rotation, and then decreases to 370 nm again over the second

180 degrees of rotation (Ref. 7, Table I, Appendices 5 and 6). This spectral range allows sensitivity to solid state and interfacial optical properties related to electronic transitions from about 3.4 eV (370 nm) to 1.7 eV (720 nm). It is important to realize, however, that the absorption edge of the Faraday cells limit the UV end of the range and that the photomultiplier sensitivity limits the near infrared end of the range (see specifications of Faraday cell glass cores).

Several means of scanning the source wavelength were considered. The reasons for selecting the CVF-type monochromator are given here. (1) Transmittance of the desired wavelength was relatively high compared to other types of monochromators. Transmission (through-put) varies from 35 percent at 400 nm to 50% at 720 nm, approximately. Higher transmission leads to stronger modulation signals and better signal-to-noise ratios in the self-nulling ellipsometer. (2) The CVF monochromator had a "straight-through" beam path and required minimal space when inserted into the existing ellipsometers optical path; a clearance of only 1 inch was required. (3) The CVF monochromator was easily adapted to continuous scanning by virtue of its circular geometry, linear dependence of the transmitted wavelength on angular displacement, absence of abrupt discontinuities in transmitted wavelength upon rotation, and its symmetry. These virtues allow the ellipsometer to easily track spectral variations in surfaces since Faraday cell dc current responses to the CVF rotation are gradual and continuous; the CVF rotation does not have to be reversed. (4) Since the wavelength varies linearly with rotation, spectral calibrations are

easy. (5) Each collected spectrum is replicated in a single revolution of the CVF since the spectrum is repeated twice per revolution (opposite scanning direction); this allows one to eliminate potential artifact peaks which may arise from filter imperfections. (6) This type of monochromator does not result in partial polarization of the transmitted light (since the light is normally incident on the filter).

There are disadvantages associated with the CVF-type monochromator too. (1) The resulting beam suffers from relatively poor monochromaticity due to the broad bandwidth of the transmission wavelength, which ranges from 6 nm at a peak wavelength of 400 nm to 17 nm at a wavelength of 720 nm (Table I). (2) The CVF coating can undergo degradation with age and exposure. (3) Artifact peaks can be generated in spectroscopic ellipsometry measurements due to scratches in the CVF. Fortunately, the symmetry of the two spectra taken during one complete rotation allows easy detection of such artifacts. (4) There exists a difficulty in obtaining uncut CVF replacements for the monochromator from the manufacturer. The bonded CVF is made of two 180 degree arcs cemented together, which are usually sold separately before bonding.

The CVF is rotated inside a special protective housing with a slit, referred to as an OCLI Model 1 monochromator (Optical Coatings Laboratory, Inc.; see Fig. 5, item B). The CVF axis is rotated by a variable speed electric motor (Bodine model # NSH-12R; see Fig. 5, item C). After gear reduction (180:1), the drive motor produces a maximum rotation rate of 9.8 rpm, which translates into a maximum scan rate of 114 nm per second (1 pass through the spectral range every 3 seconds) at

1:1 ratio between the motor drive and CVF shaft. However, the ellipsometer electronics fail to track such fast changes in wavelength; electronics limit the wavelength scan rate to about 23 nm per second (1 pass through the spectral range every 15 seconds). Since noise in the spectroscopic measurements increases with scan rate it is sometimes desirable to scan at slower speeds (adsorption studies). Unfortunately the drive motor becomes subject to increased chatter at low rpm, which also generates noise in spectroscopic measurements. To circumvent problems associated with chatter, reduction pullies coupled by large diameter o-rings have been incorporated into the scanner to attain very stable low rotation speeds in experiments where high noise levels obscure crucial spectral features. The digital incremental rotary encoder (Dyneer model # STRE-2014-010; see Fig. 5, item A) directly coupled to the CVF rotation shaft with a segment of flexible steel cable.

In order to determine the applicability of ellipsometry models used for the interpretation of data, such as the coherent superposition model discussed in Chapters 5 and 7, one must first have knowledge of the transverse and longitudinal coherence of the source. The longitudinal coherence (8) of a source is related to the center of the band-pass wavelengths, λ, and the bandwidth, $\delta\lambda$; it ranges in value from 16 to 49 microns for the spectral scanner. The transverse coherence (9,10), also referred to as the lateral coherence length, is related to the collimating telescope focal length, r, and the source pin-hole diameter, s; it ranges in value from 10 to 17 microns for the spectral scanner.

This formula is based upon the Van Cittert-Zernike theorem. The reader is referred to Appendix 6.

II. Argon Laser Source

For fixed wavelength measurements on rough surfaces, a Lexel Model 75.2 argon laser operated in single line mode is used (Ref. 11, Fig. 7). The plasma tube, laser head, and power supply are Lexel types 591 Ar, 523 H, and 517 PS, respectively. The 514.5 nm line is used for measurements since it is the most intense and since quarter wave plates are commercially available for this wavelength. Lexel guarantees a fundamental mode power of 100 mW and a multimode power of 120 mW for this single line. In the laboratory, a multimode power of 150 mW has been measured. Though the 514.5 nm line is usually used, several lines are available from this source; data on their relative powers are given in Table II. This laser is currently classified as Class III in terms of safety (12); details relevant to safety considerations and ellipsometric application are given here.

One has to be judicious in selection of commercial lasers. There are several transverse modes excited in lasers, but for application to ellipsometry it is desirable to have most of the power in the TEM_{00} mode. The Lexel design is believed to have better transverse mode stability than comparable Spectra Physics designs, in that there is always TEM_{00} output. Spectra Physics designs have been known to oscillate between TEM_{00} and TEM_{01} modes during operation (13).

In order to determine the degree of hazard associated with a laser source and classify it, considerations of beam diameter and divergence are also important. The diameter of the Gaussian TEM_{00} beam is taken at the 1/e2 power point, and is the diameter of an aperture stop that will pass 86.5 percent of the total laser power at the output mirror. For the laser being used, the beam diameter is 0.9 mm (514.5 nm, TEM_{00}), before beam expansion. The corresponding beam divergence is 0.8 mrad.

Though the 514.5 nm line is used, one must appreciate that this line is actually made up of a large number of longitudinal modes spaced over a frequency bandwidth of approximately 5 GHz, which translates into a total line-width of 0.0442 nm at this wavelength. The spacing between longitudinal modes is c/2L, where c is the velocity of light and L is the resonator mirror spacing (14). In this case, the cavity length, with the prism for single-line operation, is 0.64 m, so the mode spacing is about 235 MHz (about 0.0002 nm at 514.5 nm). Compared to the range of linewidths available in the spectral scanning mode (6 nm at 400 nm to 17 nm at 720 nm), the monochromaticity of the laser is better by at least three orders of magnitude.

The longitudinal coherence for the argon laser, 60 mm, is greater than that for the spectral scanning source, which is 16 to 49 microns; this could be increased to 100 m, a coherence comparable to that of the helium-neon laser, if an intra-cavity etalon were used (for longitudinal mode rejection).

Stability is crucial; recall that the lamp is current stabilized. The laser power output is stabilized by a controller internal to the

laser. Two types of operation are possible, light control and current control. Light control is used in ellipsometric measurements. A photodiode senses the output intensity and controls the the plasma tube current to achieve some desired, preset intensity. Intensity fluctuates less than ±0.2% about the setpoint. The major factors affecting the beam-pointing stability is the thermal change in the index of refraction of the quartz used in the prism wavelength selector, and thermal stresses in the resonator construction. The properties of quartz are such that, if left uncorrected, it will detune the laser at a rate of 0.2 nm per degree Centigrade and cause an angular change in the beam-pointing of 11 arcsec per degree Centigrade. This is sufficient to completely detune the laser with as little as a 10 degree Centigrade change in temperature. However, temperature compensation in this laser has reduced pointing stability problems to about 0.7 arcsec per degree Centigrade.

Errors in the angle of incidence can have significant adverse effects of ellipsometry data. Such misalignment problems have been encountered in switching from one laser line to another for ellipsometric measurements. For example, though a specimen may be aligned in the instrument for the 514.5 nm line, complete misalignment will result when tuning the prism of the laser to 488.0 nm. Alignment is not restored when retuning to the 514.5 nm line.

When used with the ellipsometer, the laser beam has to be attenuated to prevent (1) sample heating, etc. and (2) photodetector saturation. At maximum power laser induced effects have been observed

on sample surfaces; photomultiplier saturation results in a complete loss of the modulation signal. Attenuation is done through plasma tube current regulation, beam expansion, and the use of neutral density filters. Usually, it is sufficient to operate the laser at an output of 30 mW (light regulated). The beam expansion optics (telescope) increases the 0.9 mm beam diameter by roughly a factor of 5 before deflection into the polarizer optics. Then, additional attenuation as needed can be achieved by inserting neutral density filters into the incident beam optical path (typically a filter of density 0.7).

Ideally, an ellipsometer source should be depolarized since a polarized source would bias the apparent azimuth P. The laser beam is linearly polarized since the plasma tube windows are mounted at Brewster's angle to eliminate the high reflective losses from the window surfaces. Depolarization is done by inserting a mica quarter-wave retardation plate after the beam expander and translation mirrors and before the polarizer collimating telescope; a retarder for the lasing wavelength should be used (514.5 nm, 488.0 nm, etc.). The term "depolarized" in this case can be misinterpreted since the beam leaving this retarder posses circular polarization; however, exact circular polarization introduces no bias into the measured polarizer azimuth. To assure that the mica retardation plate is adjusted to the correct azimuth for circular polarization, the polarizer Glan-Thompson prism is rotated 360 degrees and the light intensity observed immediately following the polarizer. The observed intensity should not vary significantly with rotation of the polarizer if the mica retarder

azimuth is correctly adjusted for circular polarization; without the retarder, the intensity will exhibit maxima and minima with rotation. Coarse adjustment can be made visually by imaging the beam on a paper screen (never look into a laser beam); fine adjustment should be done using a photometer.

The laser is potentially very dangerous. Alignment of any optical component in the system should always be done at the lowest possible power and greatest attenuation (use extreme care). When running experiments at higher power levels, the beam path is completely enclosed in an interlocked shroud which switches off the laser if the beam path becomes exposed at any time (Fig. 7.b). For more non-routine work using the laser, suitable laser goggles are worn (Laser-Gard Serial # F2008). These goggles have an optical density of 15 at 488 nm and an optical density of 11 at 515 nm, with virtually complete transmittance above 550 nm. Note that such lasers have induced nucleate boiling inside the human eye, as well as retinal burns; both forms of damage are irreversible. Fig. 7.a is not representative of normal operation, and is only presented as an illustration of the instrument optical path.

In the spectral scanning mode discussed above, alignment of the sample surface is done by viewing the light beam image through an eyepiece substituted for the photomultiplier, tilting the surface to a point where the image is centered in the eyepiece cross-hairs with no halo. This procedure can't be used with the laser since it requires the operator to view the beam directly. Consequently, an eyepiece was modified so that the beam image and the cross-hairs are projected

together on a small paper screen, where they can be viewed safely.

III. Extended Red Photomultiplier

Over the spectral range from 370 to 720 nm typical photomultiplier responses vary more than an order-of-magnitude and have the lowest gain in the "red" portion of the spectrum. Successful extension of the automatic, self-nulling ellipsometer concept to spectroscopic applications depends upon use of a photomultiplier with spectrally flat (wavelength independent) gain characteristics over the range of interest. Such detectors are referred to as "extended red photomultipliers" since they have nearly the same gain in the red portion of the spectrum as in the blue. In this study, we found the Hamamatsu R-928 photomultiplier suitable for use in the spectroscopic, self-nulling ellipsometer. This photomultiplier has a multialkali photocathode composed of Cs, Na, K, and Sb. The spectral range extends from 185 to 930 nm. Fortunately, the peak spectral response coincides with the absorption edge of the Faraday cell glass cores (400 nm). Performance tests, conducted with a front-surface mirror, are discussed here.

Fig. 8 illustrates the variation in polarizer and analyzer azimuths as the spectral scanner CVF is rotated clockwise from 0 to 360 degrees; these null azimuths were measured by manual adjustments of the Glan-Thompson prisms giving zero dc current levels in the Faraday cells. These curves show the "expected" compensation required of the Faraday cells as the CVF is rotated with the Glan-Thompson prisms at fixed

azimuths.

Fig. 9 shows the measured compensation of the Faraday cells while the CVF was rotated with the Glan-Thompson prisms at fixed azimuths. In the upper photograph responses are shown using a photomultiplier (RCA 931-A) with spectral gain characteristics representative of common tubes; this tube has a photocathode composed of Sb and Cs. The spectral range of the RCA 931-A extends from about 300 to 650 nm with a peak response at 400 nm. Note that the analyzer response is asymmetric and that the polarizer response drops to a flat plateau in the red portion of the spectrum, due to the loss of signal. Compare these results to those of the extended red detector, the Hamamatsu R-928, where the analyzer response is symmetric and the polarizer response does not drop to a flat plateau in the red portion of the spectrum (monochromator angular position of about 60 degrees).

Using the RCA 931-A in early studies to determine the fastest achievable scan rate for the instrument, the Faraday cell responses shown in Fig. 10 were measured. Acceptable scan rates gave polarizer responses symmetric about the red limit of the CVF, similar to those shown in Fig. 9 (despite some signal loss); unacceptable scan rates gave a high degree of distortion.

IV. Electronics Considerations for Spectroscopic Measurements

The Faraday cell controller is essentially a two-channel, phase-sensitive detector which separates two superimposed signals having a 90 degree phase difference (Ref. 15 and 16, Fig. 2). These signals are

detected simultaneously by the extended red photomultiplier tube and are due to modulations of the polarizer and analyzer Faraday cells. The detected signals undergo both band-pass filtering and amplification before they reach the phase detector.

Layer anticipated that the spectral dependence of the lamp luminance, photomultiplier sensitivity, and Verdet coefficient would cause the modulation depth, Faraday cell calibration, and overall loop gain to deviate from fixed-wavelength design values, making it necessary to implement an automatic gain controller as part of the photomultiplier amplifier circuit. He proposed using detection of the second harmonic as the basis for controlling the loop gain and maintaining a wavelength-independent instrument response. Since the amplitude of the fundamental component of the signal (used as a basis for null detection) has the same functional dependence on wavelength as the second harmonic, the transfer characteristic of the fundamental component can be kept constant by maintaining the amplitude of the second harmonic constant. Here, it has been found that gain-leveling is not essential provided the computer correct data for changes in the Verdet coefficient as a function of wavelength (Chapter 3, program "CALFC1") and provided that the light beam is not attenuated to the extent of complete loss of signal. A gain-leveling circuit (ALC, auto-level control) has been incorporated into the Faraday cell controller for optional use; however, the computer is still required to correct data for the spectral dependence of the Verdet coefficient. The ALC helps minimize signal biasing at the maximum absorption wavelength of light absorbing incident

media during spectral scanning.

Electronically, three important differences exist between the spectral scanning ellipsometer discussed in this thesis and the instrument proposed by Layer. In our instrument: (1) spectral dependence of the Faraday cells is accounted for by computer, rather than by analog circuitry; (2) computerized data acquisition, allows digital filtering, subtraction, and averaging of spectral scans; and (3) each Faraday cell solenoid has two coils, an inner coil to carry the modulation current and an outer coil to carry the dc current for compensation. These differences allow much faster scan rates and greater resolution than are obtainable in an instrument like the one proposed by Layer.

V. Three-Reflection Fresnel Rhomb

Mica, quarter-wave retardation plates used as compensators in earlier versions of the PCA, automatic, self-nulling ellipsometer were not achromatic and were therefore unsuitable for spectroscopic applications. The achromatic nature of the Fresnel rhomb makes it a particularly attractive retarder for spectroscopic ellipsometry. This device exploits the difference between the phase shifts that are experienced by the p and s components of light upon total internal reflection and employs three-reflections to maintain colinearity of the incident and emergent beams. Its achromatic nature is partly attributable to special optical coatings on the prism reflecting surfaces. The basic design equation is given by Azzam and Bashara (3).

The primary problem that we have encountered with implementation of the three-reflection Fresnel rhomb into the instrument discussed here is axial skew which arises from inherent imperfections in fabrication of the device. These problems have been minimized to the extent possible by stringent specifications (Appendix 1), but are still too severe to allow four-zone measurements to be made easily; four-zone measurements require rotation of the Fresnel rhomb by 90 degrees, and amplify misalignments due to skewing of the beam.

Required Calibrations

I. Spectral Dependence of the Verdet Coefficient

The Faraday rotation introduced into a polarized beam of light by a diamagnetic glass subjected to a strong magnetic field is wavelength dependent (17-19). At a fixed magnetic field strength (constant solenoid current in a Faraday cell), the rotation increases nonlinearly as the wavelength of the beam decreases. As discussed above, we have had to take into account this spectral dependence of the polarizer and analyzer Faraday cells in the analysis of data from the self-nulling, spectroscopic ellipsometer. The LSI-11 microcomputer stores the Faraday cell solenoid current levels on floppy disk (Chapter 3, program SEV002); stored data is in ADCU units, proportional to current and magnetic field strength. Therefore, we calibrate the instrument in terms of an effective Verdet coefficient having the units of degrees per ADCU (which is equivalent to degrees per unit magnetic field strength). Such calibrations are also done with the LSI-11 (Chapter 3, program CALFC1),

and are shown in Figs. 11.a and 11.b (unsmoothed and smoothed). These effective Verdet coefficients are also stored on floppy disk and are subsequently recalled by the LSI-11 when raw data is to be converted to polarizer and analyzer azimuths (Chapter 3, program DSCONV). Azimuths are then converted to delta and psi.

An assumption implicit in the calculation and use of these effective Verdet coefficients is that the induced Faraday rotation per unit increase in solenoid current is current-independent. The validity of this assumption was substantiated by the data shown in Figs. 12.a, 12.b, and 12.c. Spectral scans were done by manually rotating the CVF and recording the Faraday cell dc current levels at various angular positions of the CVF. The procedure was repeated with ±2 degree increments of the Glan-Thompson prisms each rotation of the CVF. The increases in required Faraday cell compensation due to uniform increments of Glan-Thompson prism azimuths at specific CVF angular positions (wavelengths) were constant for both the analyzer and polarizer Faraday cells. Therefore, the effective Verdet coefficients (for the current levels investigated) were current-independent. Furthermore, it was found that Faraday cell ranges in fixed-wavelength operation could be increased from about ±25 degrees at 546 nm to more than ±40 degrees at 370 nm.

II. Wavelength Calibration of the Digital Encoder

Angular position of the CVF is determined by the LSI-11 pulse counter which is interfaced to the digital encoder of the spectral

scanner. The transmitted wavelength is correlated with angular position by linear regression (Appendix 4); wavelength is also correlated with encoder pulse count by linear regression (Appendix 5; Chapter 3, data file WLCALC.DAT). Regression line parameters are used as wavelength calibration parameters for the spectral scanning ellipsometer. The encoder count at which monochromatic (filtered) light of a known wavelength is transmitted is determined by monitoring photomultiplier output as the CVF rotates (Chapter 3, program SEV002); transmission is then plotted against encoder count. Calibrations can be checked by plotting the same transmission spectrum against wavelength (Fig. 13) instead of encoder count after appropriate regression line parameters are entered into the input data file WLCALC.DAT.

Complications Due to Nonidealities of the Instrument

The foregoing discussion is highly idealized and does not take into consideration (1) nonidealities associated with the band-pass filter used to eliminate higher order odd harmonics, whose effects are not eliminated by integration; (2) finite band width of the light source due to the use of nonideal interference filters to monochromatize the beam; (3) finite phase adjustment errors involved in tuning the phase shifter; (4) inductive interaction between the two Faraday cell solenoids; (5) magnetic field effects on the photomultiplier; and (6) magneto-optic changes of the sample induced by the Faraday cells.

Of particular interest in the spectral scanning application is the question regarding interference filter band width. In a very

overcompensated or very undercompensated state, the instrument reacts primarily to modulations related to the center line wavelength; however, near compensation the contributions of these modulations to the error signal become insignificant compared to those related to other wavelengths passed. Near compensation the instrument's response is dominated by higher-order effects such as these.

Cross-modulation problems can be especially troublesome in adsorption experiments where one has to measure very small differences in delta and psi due to monolayer coverages, and may arise from the unavoidable errors present in tuning the Faraday cell control circuit phase shifter. Though one strives to achieve a 90 degree phase difference between channels, such perfect separation is not possible.

Imperfections in the modulation wave form due to performance of the oscillator circuit and distortions introduced by both phase shifting and amplification may also give rise to nulling errors. Such distortions manifest themselves as higher-order harmonics superimposed on the fundamental and are not completely removed by band-pass filtering of the photomultiplier signal and integration of outputs from the two phase detectors.

Classical arguments for the use of ellipsometry are based upon its ability to be used for insitu observation. However, an ideal analytical tool should not alter the specimen properties during sampling and should be only sensitive to the physical properties of interest. Magnetic field and photochemical effects on samples caused by this class of ellipsometer are unknown, but should be determined. Small errors may

also result in situations where an adsorbate being studied at a liquid-solid interface exhibits optical activity while dissolved in the bulk phase. Dye adsorption studies have been conducted; corrections for the possible optical activity of the disolved dye have not been made.

When operating in the spectral scanning mode with an ambient medium which is light absorbing (dye solution), one encounters a minimum in the overall instrument loop gain due to attenuation of the beam intensity at the maximum absorption wavelength. This may result in complete, temporary signal loss (drop-out period) causing artifact peaks to appear in the collected spectroscopic measurements (Figs. 6.a and 6.b of Chapter 9). Amplitudes of such artifact peaks are correlated with increasing light absorption by the solution as the bulk dye concentration is increased. If one uses this instrument to perform adsorption isotherm measurements with dyes by increasing the bulk concentration, such artifacts may be encountered (Figs. 8.a through 8.e of Chapter 8). Artifacts due to transfer curve flattening (reduction of instrument gain) at the maximum absorption wavelength and due to variations in bulk solution optical activity may also occur and are more elusive. There are simple ways to circumvent such difficulties. To minimize bulk solution effects, electrochemical cells having very short optical paths were built. Furthermore, experiments were performed where dye surface concentrations were changed without changing the bulk concentrations, thereby maintaining constant gain from one experiment to another at the maximum absorption wavelength. Differences in spectroscopic ellipsometry measurements in such cases can only be due to

changes on the surface (Chapter 6, rhodamine-B relaxation effect).

The instrument works best with a high quality signal, which is obtained by using an intense source. However, when using an argon laser one has to be careful to avoid saturation of the photomultiplier.

Imperfections in the Fresnel rhomb contribute errors into measurements made by the spectroscopic ellipsometer presented here; however, we have not yet quantified these errors. Problems associated with both azimuthal and axial misalignment of optical components have been discussed in the literature (20, 21).

References

1. Mathieu, H.J., McClure, D.E., Muller, R.H., "Fast Self-Compensating Ellipsometer," Rev. Sci. Instrum., 45(6), 798 (1974).

2. Layer, H.P., "Circuit Design for an Electronic Self-Nulling Ellipsometer," Surf. Sci., 16, 177 (1969).

3. Azzam, R.M.A., Bashara, N.M., ELLIPSOMETRY AND POLARIZED LIGHT, North-Holland Publishing Co., New York, 1977, pp. 79, 280, 372.

4. King, R.J., Downs, M.J., "Ellipsometry Applied to Films on Dielectric Substrates," Surf. Sci., 16, 288 (1969).

5. Abe, M., Mizuno, M., "A Digital Ellipsometer," Jap. J. Appl. Phy., 18, 165 (1979).

6. 6. Breslow, D. H., "High-Performance Optical Encoders Can Have Small Size, Weight, and Cost," Electro-optical Systems Design, Sept. 1981, pp. 29-38.

7. INSTRUCTIONS FOR OCLI MONOCHROMATOR HOUSING MODEL 1, Optical Coating Laboratory, Inc., Santa Rosa, CA, 1978.

8. Fowles, G. R., Introduction to Modern Optics, 2nd ed., Holt, Rinehart, and Winston, Inc., New York, 1975, pp. 74-75.

9. Smith, C. G., "Ellipsometry of Anodic Film Growth," Ph.D. Thesis, Dept. Chem. Eng., U. C. Berkeley and Lawrence Berkeley Laboratory, Berkeley, CA, LBL-8082, 1978, pg. 56.

10. Born, M., Wolf, E., PRINCIPLES OF OPTICS, MacMillan, New York, 1964, pg. 551.

11. MANUAL MODEL 75 ION LASER, Lexel Corp., Palo Alto, CA, 1978.

12. AMERICAN NATIONAL STANDARD FOR THE SAFE USE OF LASERS, American National Standards Institute, Inc., 1430 Broadway, New York, 10018, ANSI Z136.1, Approved March 8, 1976.

13. LDV SHORT COURSE NOTES, TSI, Inc., St. Paul, MN, 1979.

14. Kogelnik, Li, "Laser Beams and Resonators," Appl. Opt., 5, 1550 (1966).

15. Brophy, J. J., BASIC ELECTRONICS FOR SCIENTISTS, McGraw-Hill, New York, 1966, pg. 286.

16. INSTRUCTION MANUAL FOR PRECISION LOCK-IN AMPLIFIER MODEL HR-8, Princeton Applied Research, Princeton, NJ, 1969.

17. Hartfield, E., Thompson, B. J., "Optical Modulators," HANDBOOK OF OPTICS, Sect. 17, Driscoll, W. G., ed., McGraw-Hill, New York.

18. "Faraday Effect and Verdet Constants of Some Optical Glasses," Schott Optical Glass Technical Information, No. 11, May 1976.

19. Borelli, N. F., "Faraday Rotation in Glasses," J. Chem. Phys., 44, 3289 (1964).

20. Bermudez, V. M., Ritz, V. H., "Wavelength-scanning polarization-modulation ellipsometry: some practical considerations," Appl. Opt., 17, 542 (1978).

21. Riedling, K., "Error Effects in the Ellipsometric Investigation of Thin Films," Thin Solid Films, 75, 355 (1981).

Table I. Spectral Characteristics of the OCLI Monochromator CVF: Bonded CVF with a 1 mm Slit Width.

Angular Position	Transmission Centerline Wavelength (1/2 PWR)	Transmission Wavelength Bandwidth (1/2 PWR)	Peak Transmission
degrees	nm	nm	percent
5	377.77	5.84	12.60
30	423.90	6.89	39.66
60	483.90	8.12	43.78
90	542.67	9.77	41.74
120	603.54	11.92	41.65
150	664.48	14.29	44.03
175	716.02	16.53	48.56
175	710.61	16.21	48.81
150	658.75	13.87	45.24
120	597.20	11.42	42.86
90	536.66	9.58	41.25
60	476.99	7.98	43.63
30	417.58	6.68	36.98
5	372.77	6.37	7.69

Table II. Fundamental Lines of Argon Laser.

Wavelength	Guaranteed Fundamental Mode Power	Guaranteed Multimode Power	Measured Power in Laboratory
nm	mW	mW	mW
528.7	5	10	.....
514.5	50	75	150
501.7	5	10	17
496.5	10	20	50
488.0	50	75	150
476.5	10	20	53
472.7	.....	.....	8
465.8	.....	.....	5
457.9	5	10	22

Figures

1. Spectral scanning, self-nulling ellipsometer optics.

2. Spectral scanning, self-nulling ellipsometer electronics.

3. LSI-11/2 ellipsometer data collection/reduction system.

4. Transfer curve for the magneto-optic, self-nulling ellipsometer.

5. Picture of the spectral scanner showing various components: (A) digital encoder; (B) OCLI monochromator housing for CVF; (C) Bodine motor with reduction pullies; (D) scan rate controller and interface; and (E) continuously variable filter, CVF.

6. Picture showing spectral scanning ellipsometer with: (A) spectral scanner; (B) polarizer collimating telescope; (C) polarizer Faraday cell; (D) three-reflection Fresnel rhomb mounted in polar rotator; (E) Auger system, not used for this study; (F) analyzer Faraday cell; (G) VT55 graphics console for LSI-11 microcomputer; (H) Tektronix plotter; and (I) racks with analog electronics.

7.a Picture showing ellipsometer with laser source, illustrating the optical path of the instrument. The components shown are: (A) argon laser; (B) laser beam expander, translator, and depolarizer; (C) polarizer collimating telescope and Glan-Thompson prism; (D) polarizer Faraday cell; (E) mica quarter-wave retardation plate compensator; and (BEAM) the laser beam entering the electrochemical cell.

7.b Picture showing ellipsometer during routine operation with the laser; the beam is covered by a protective, interlocked shroud.

8. Spectroscopic ellipsometry of a front surface mirror by manual nulling; polarizer azimuth vs CVF azimuth, which is equivalent to delta vs wavelength. The analyzer azimuth vs CVF azimuth, which is equivalent to psi vs wavelength, is also shown.

9. Comparison of typical photomultiplier (RCA 931-A) and extended red photomultiplier (Hamamatsu R928) during spectroscopic ellipsometer performance test. The extended red detector increases the spectral range of the instrument significantly. Signals monitored by dual trace oscilloscope.

10. Performance test of the spectroscopic ellipsometer showing scan rate distortion of the polarizer and analyzer signals. Determination of the maximum attainable scan rate using RCA 931-A photomultiplier; test done before installation of the extended red detector. Signals monitored by dual trace oscilloscope.

11.a Unsmoothed effective Verdet coefficients (0 to 25 degrees/ADCU) at various wavelengths (400 to 700 nm) for the polarizer and analyzer Faraday cells.

11.b Lagrangian smoothing of the curves shown in Fig. 11.a.

12.a Spectral response of the polarizer Faraday cell to various levels of of required compensation (2, 4, 6, and 10 degrees). The dynode voltage of the photomultiplier was 800 volts. Δ should read ΔP.

12.b Spectral response of the analyzer Faraday cell to various levels of required compensation (2, 4, 6, and 10 degrees). The dynode voltage of the photomultiplier was 800 volts. Δ should read ΔA.

12.c Same as 12.a, but with additional measurements at a greater photomultiplier dynode voltage (1000 volts).

13. Transmission spectra of two narrow-band filters used for wavelength calibration of the digital encoder; measurements made by the spectroscopic ellipsometer serving as a spectrophotometer. Peaks appear when the transmission of the calibration filter (436 or 577 nm) coincides with the transmission of the CVF. Transmission can be displayed against either encoder count (0 to 400) or wavelength (400 to 700 nm).

SPECTRAL SCANNING, SELF-NULLING ELLIPSOMETER OPTICS

1. high pressure Xe lamp
2. rotating interference filter
3. collimator
4. Glan-Thompson polarizer
5. Faraday cell polarizer
6. Fresnel rhomb achromatic retarder
7. electrochemical cell (or Auger)
8. analyzer Faraday cell
9. analyzer Glan-Thompson prism
10. collimator
11. spectrally "flat" detector
12. rotary incremental digital encoder
13. spectral scanner drive motor

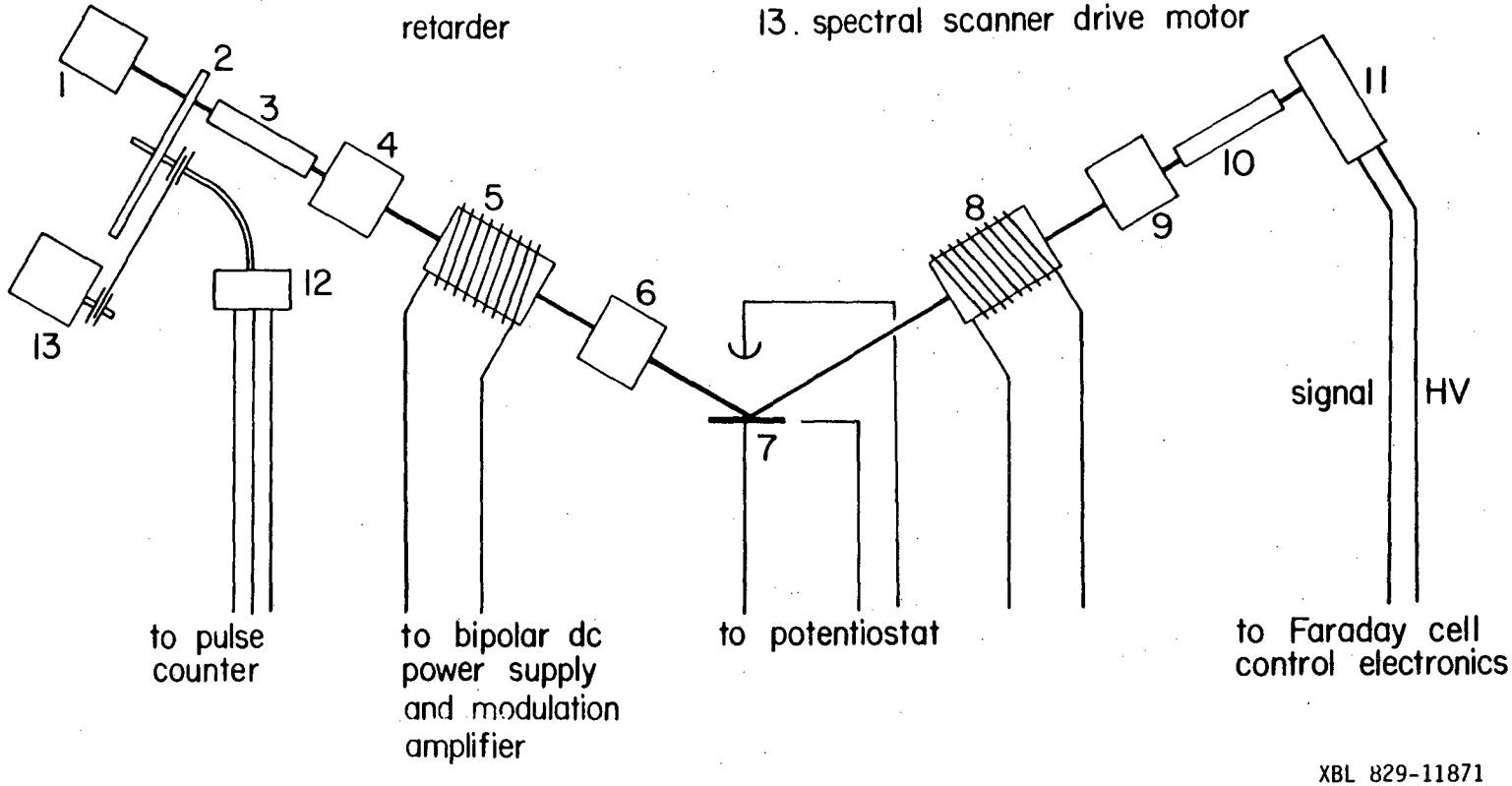

XBL 829-11871

Fig. 1

SELF-NULLING ELLIPSOMETER ELECTRONICS

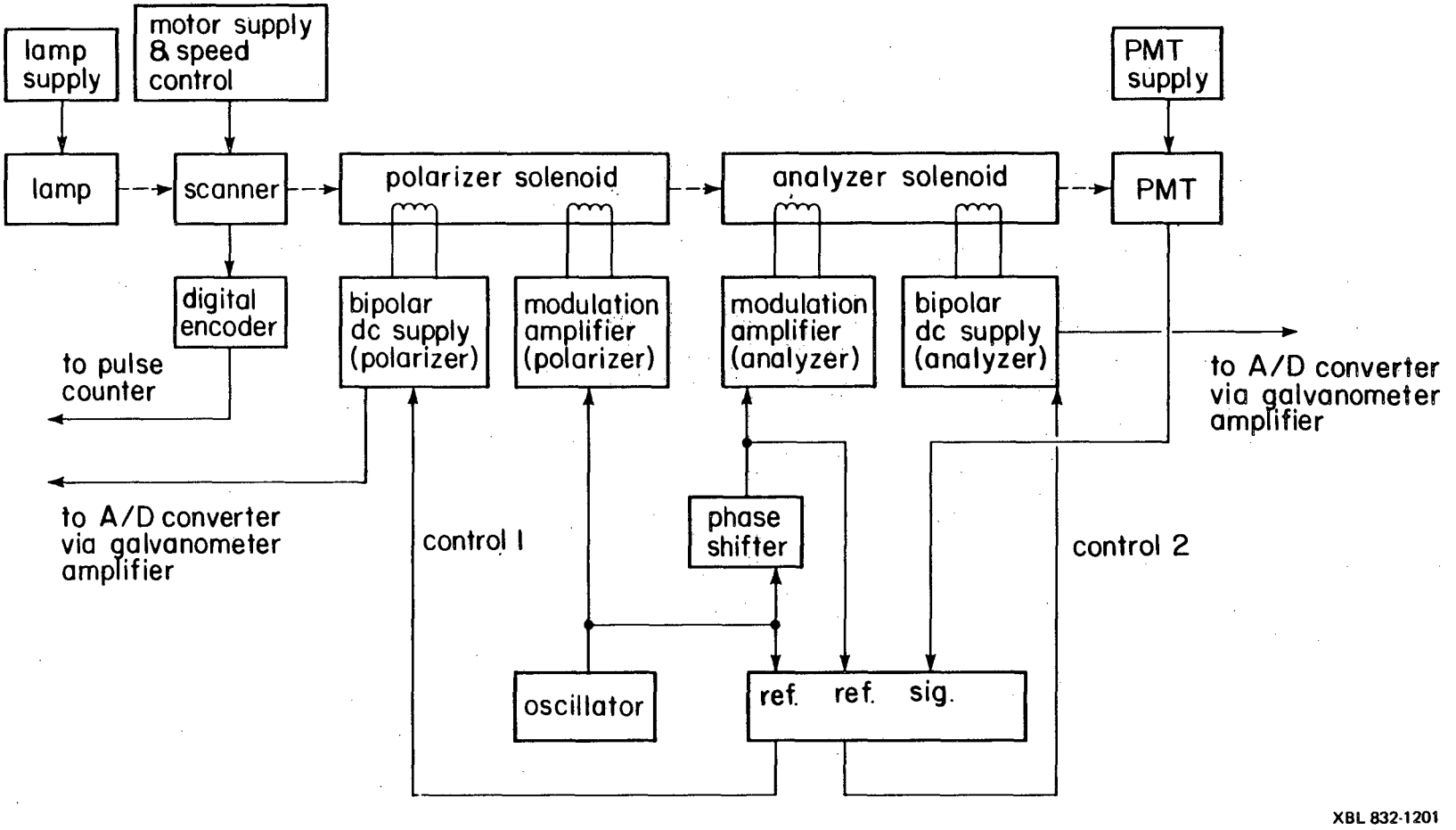

Fig. 2

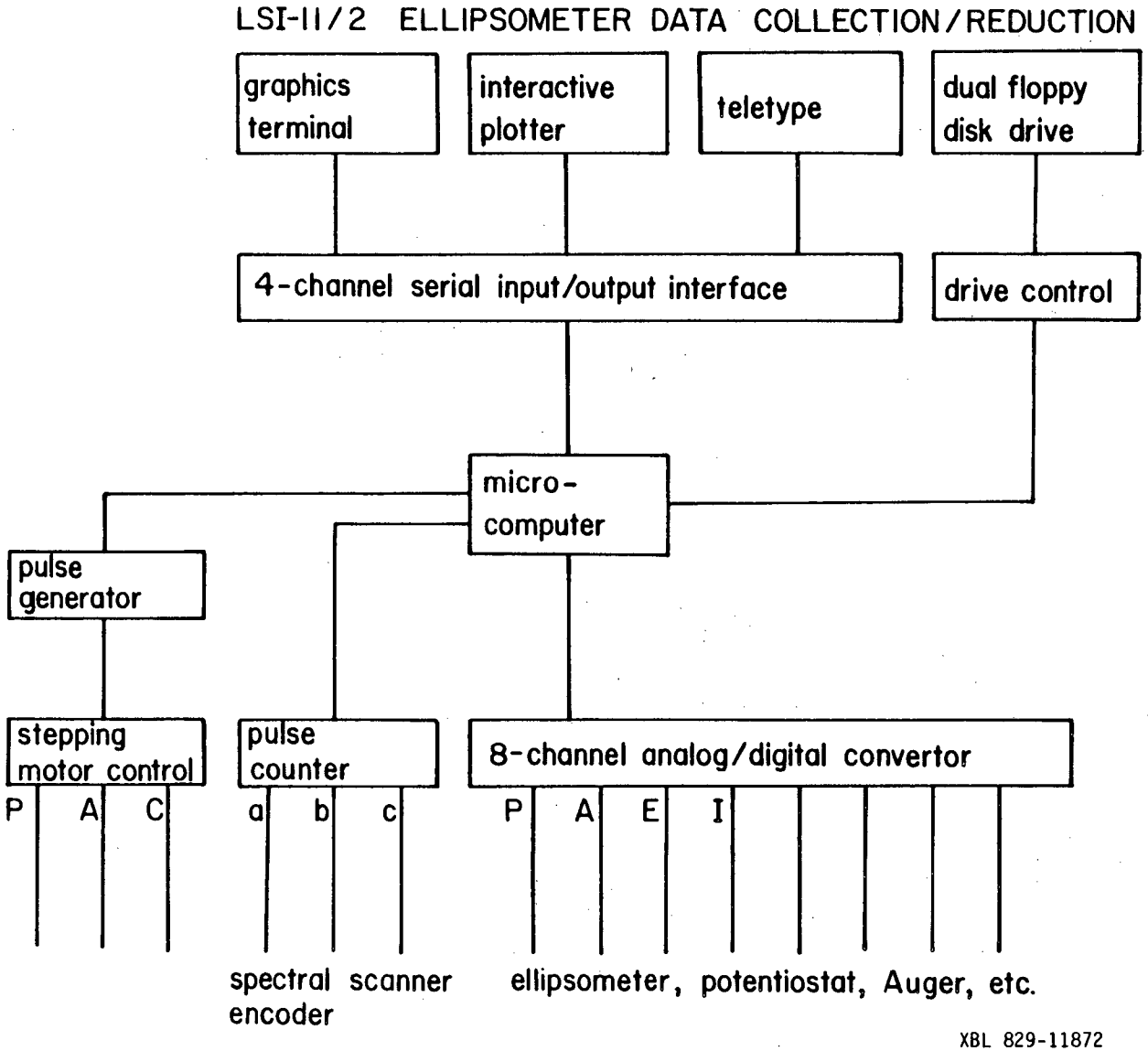
LSI-11/2 ELLIPSOMETER DATA COLLECTION/REDUCTION
graphics terminal
interactive plotter
teletype
dual floppy disk drive
4-channel serial input/output interface
drive control
micro-computer
pulse generator
stepping motor control
P A C
pulse counter
a b c
8-channel analog/digital convertor
P A E I
spectral scanner encoder
ellipsometer, potentiostat, Auger, etc.
XBL 829-11872

Fig. 3

ELLIPSOMETER TRANSFER CURVE

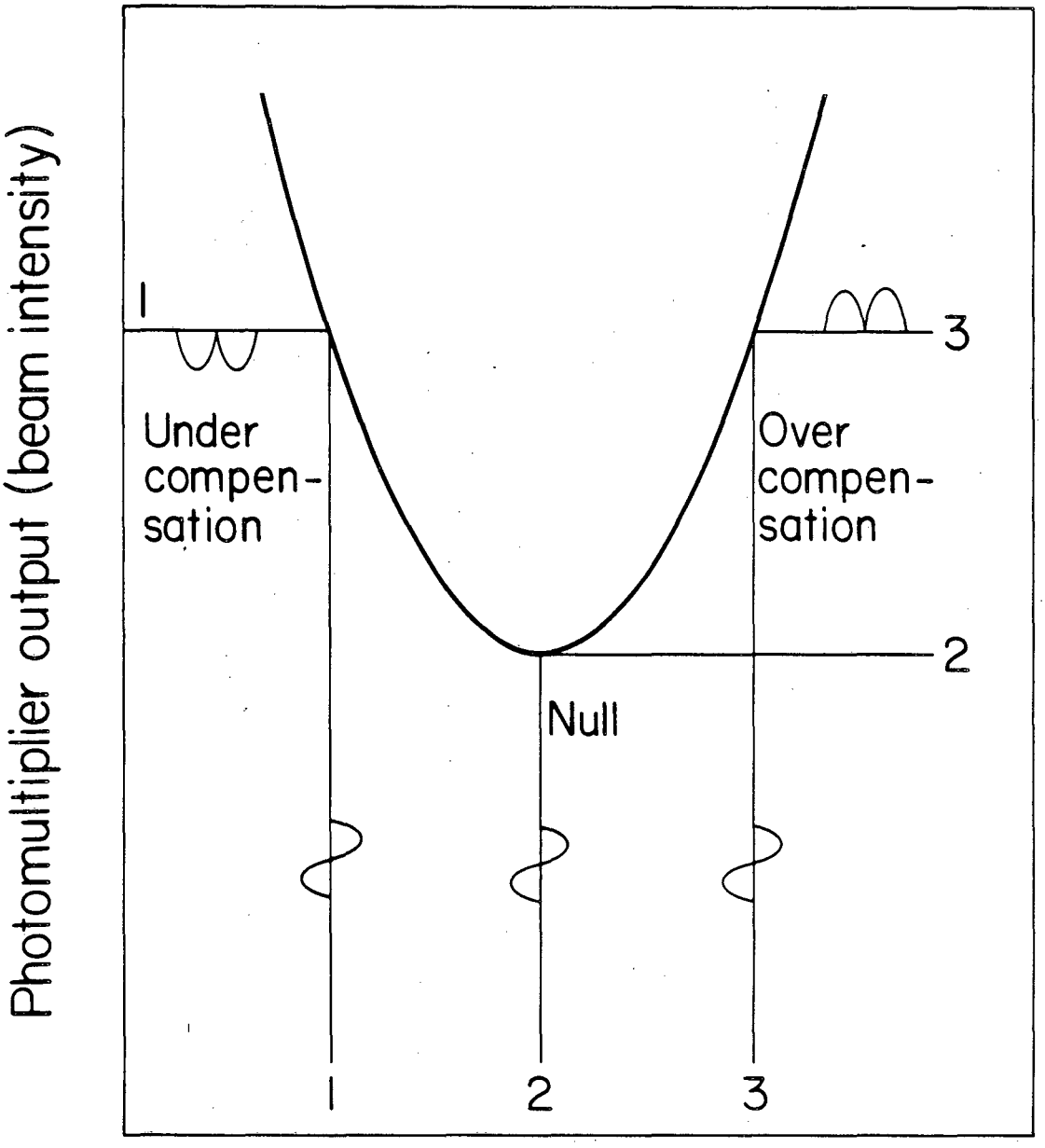

Fig. 4

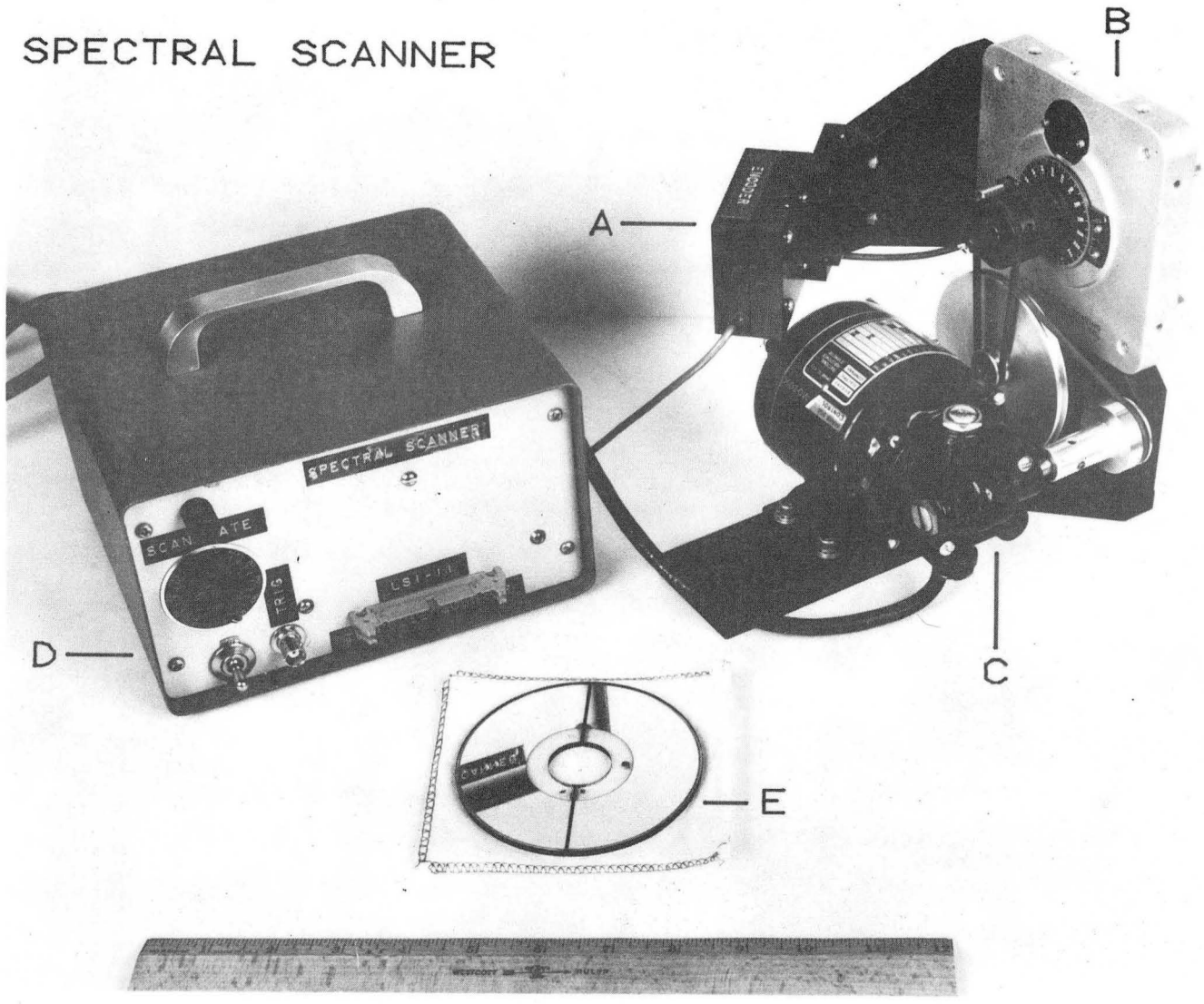

Fig. 5

XBB 820-10763A

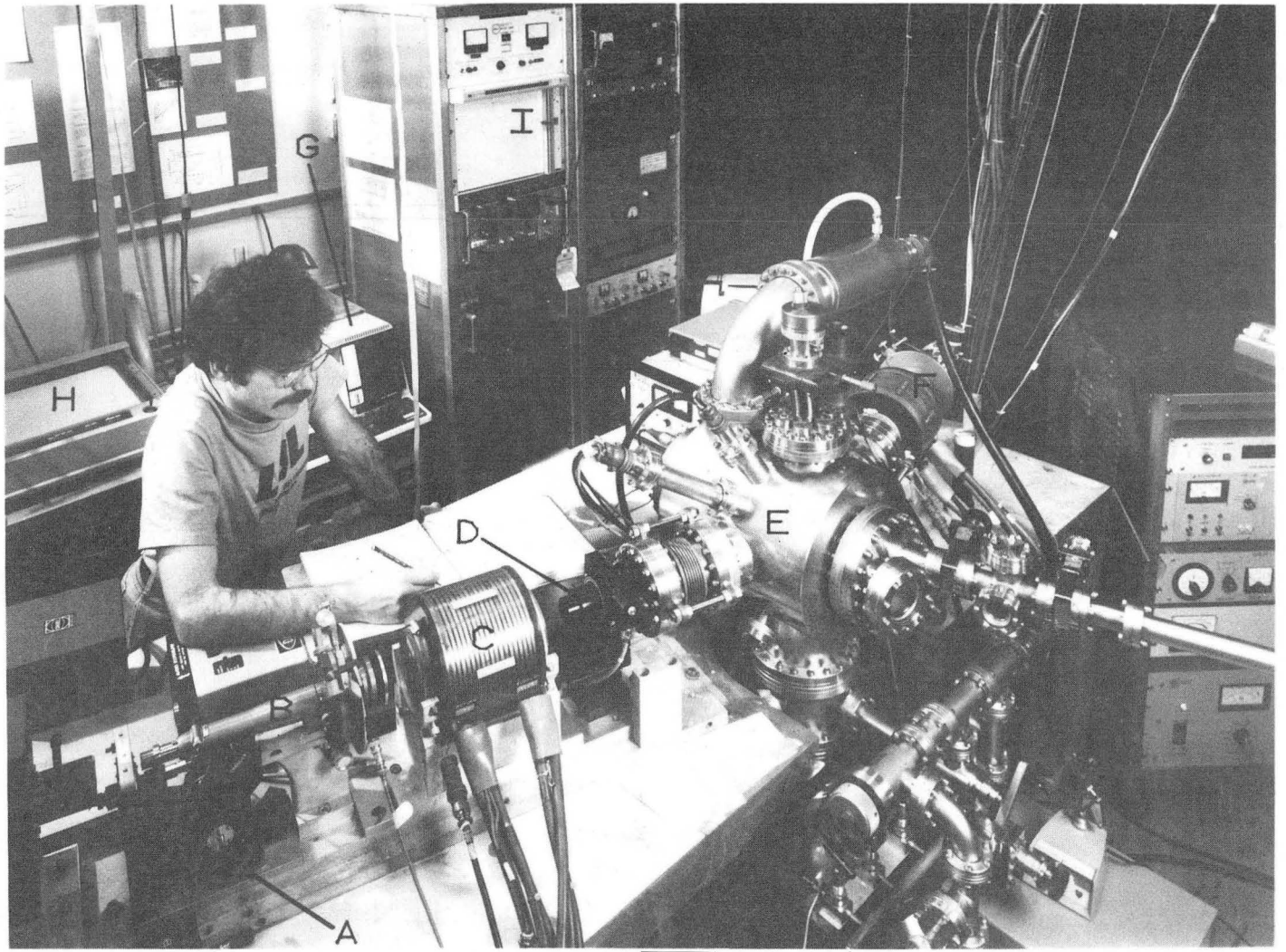

WITH SPECTRAL SCANNER

XBB 820-10887A

Fig. 6

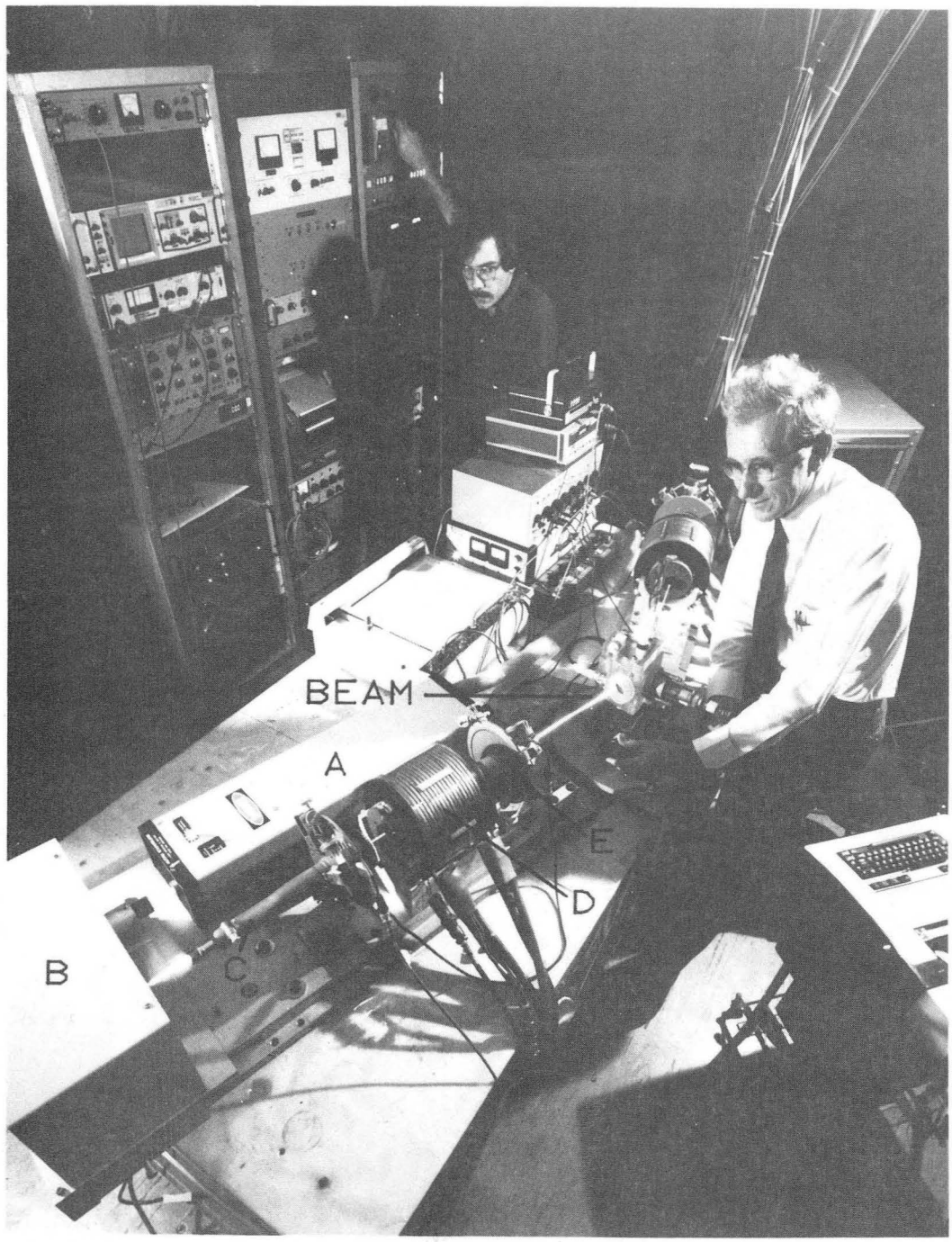

WITH LASER SOURCE

XBB 818-8176A

Fig. 7a

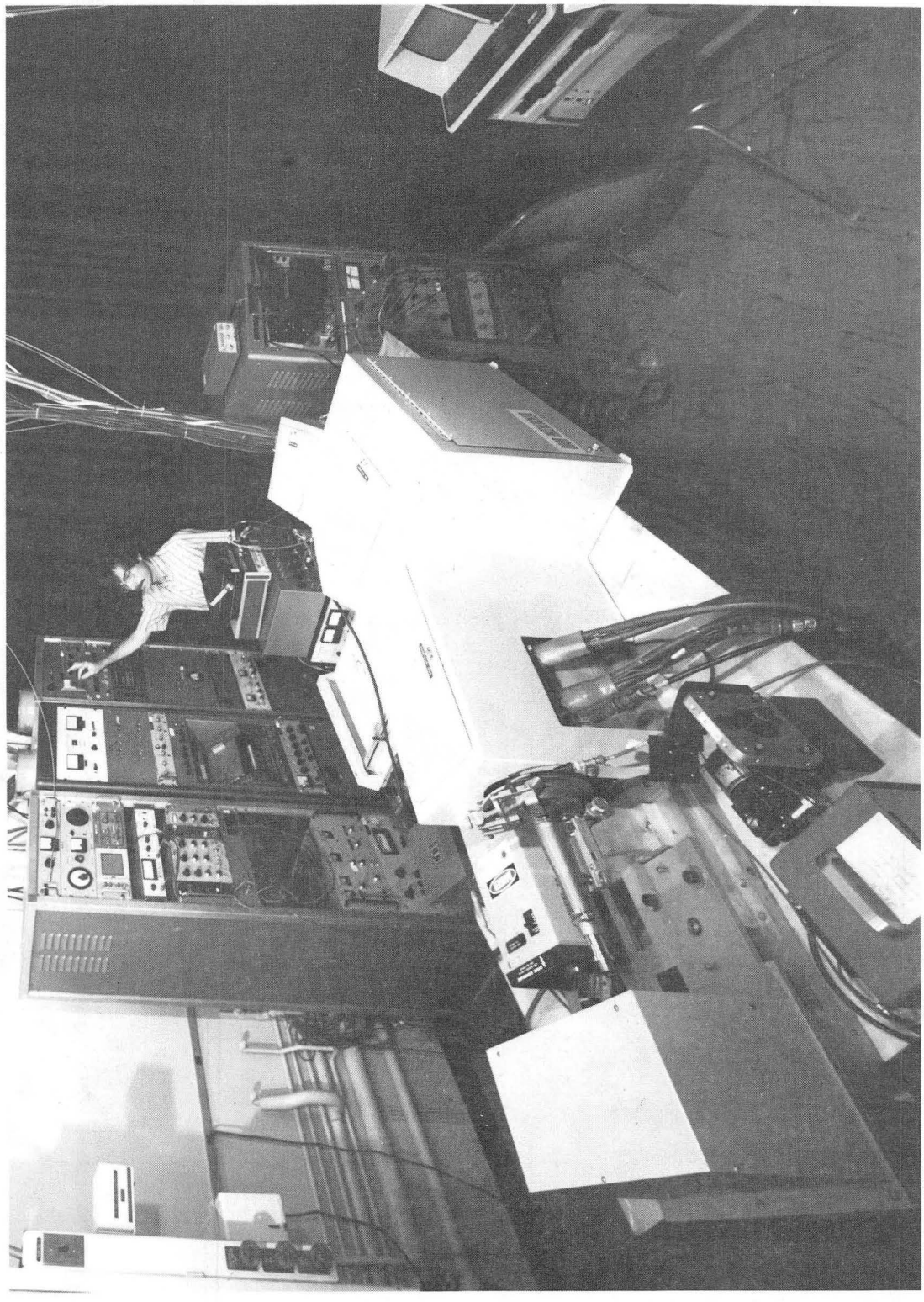

CBB 818-8180

Fig. 7b

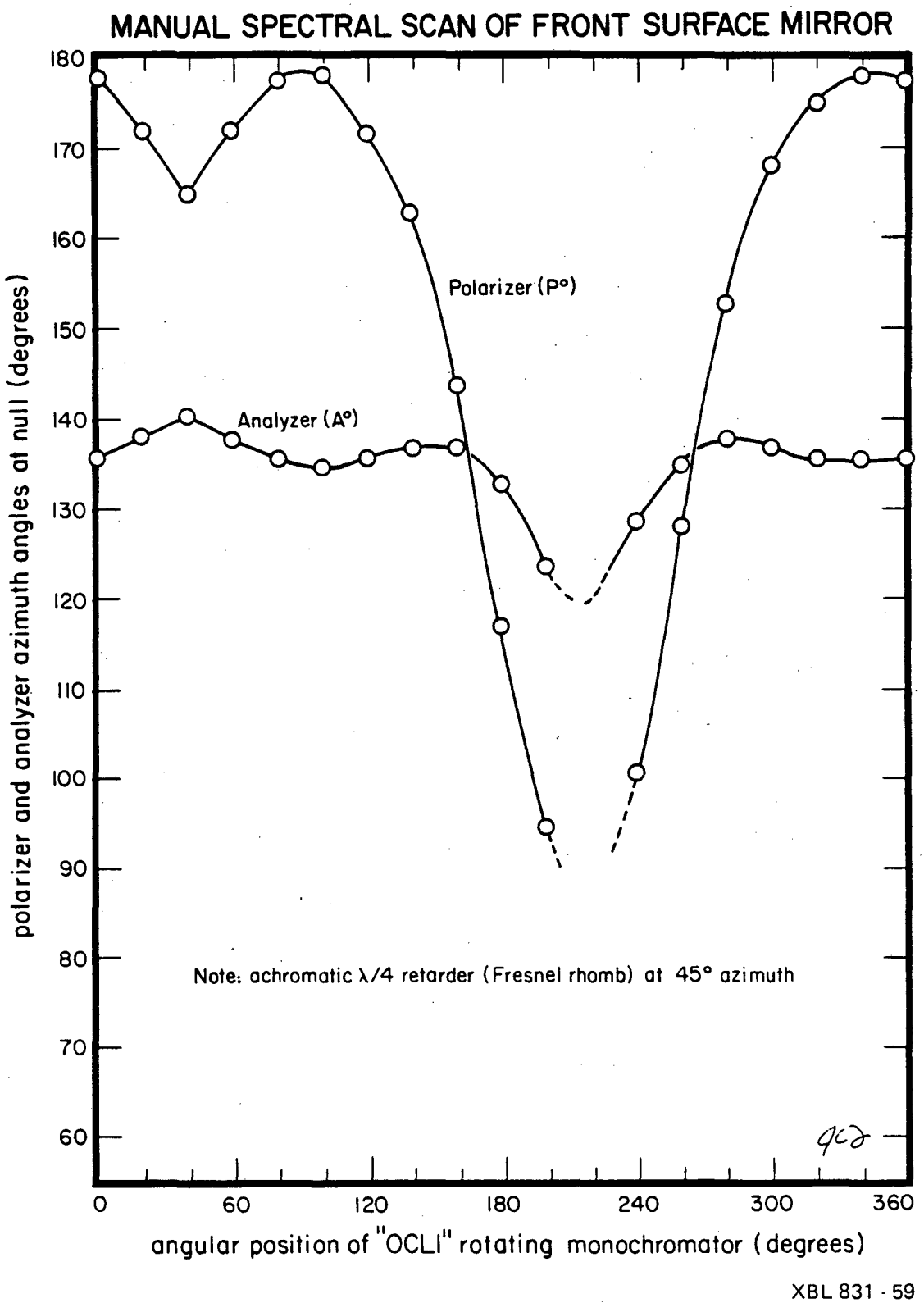
MANUAL SPECTRAL SCAN OF FRONT SURFACE MIRROR
polarizer and analyzer azimuth angles at null (degrees)
180
170
160
150
140
130
120
110
100
90
80
70
60
Polarizer (P°)
Analyzer (A°)
Note: achromatic λ/4 retarder (Fresnel rhomb) at 45° azimuth
0
60
120
180
240
300
360
angular position of "OCLI" rotating monochromator (degrees)
XBL 831 - 59

Fig. 8

COMPARISON OF PHOTODETECTORS IN SPECTRAL SCANNING MODE

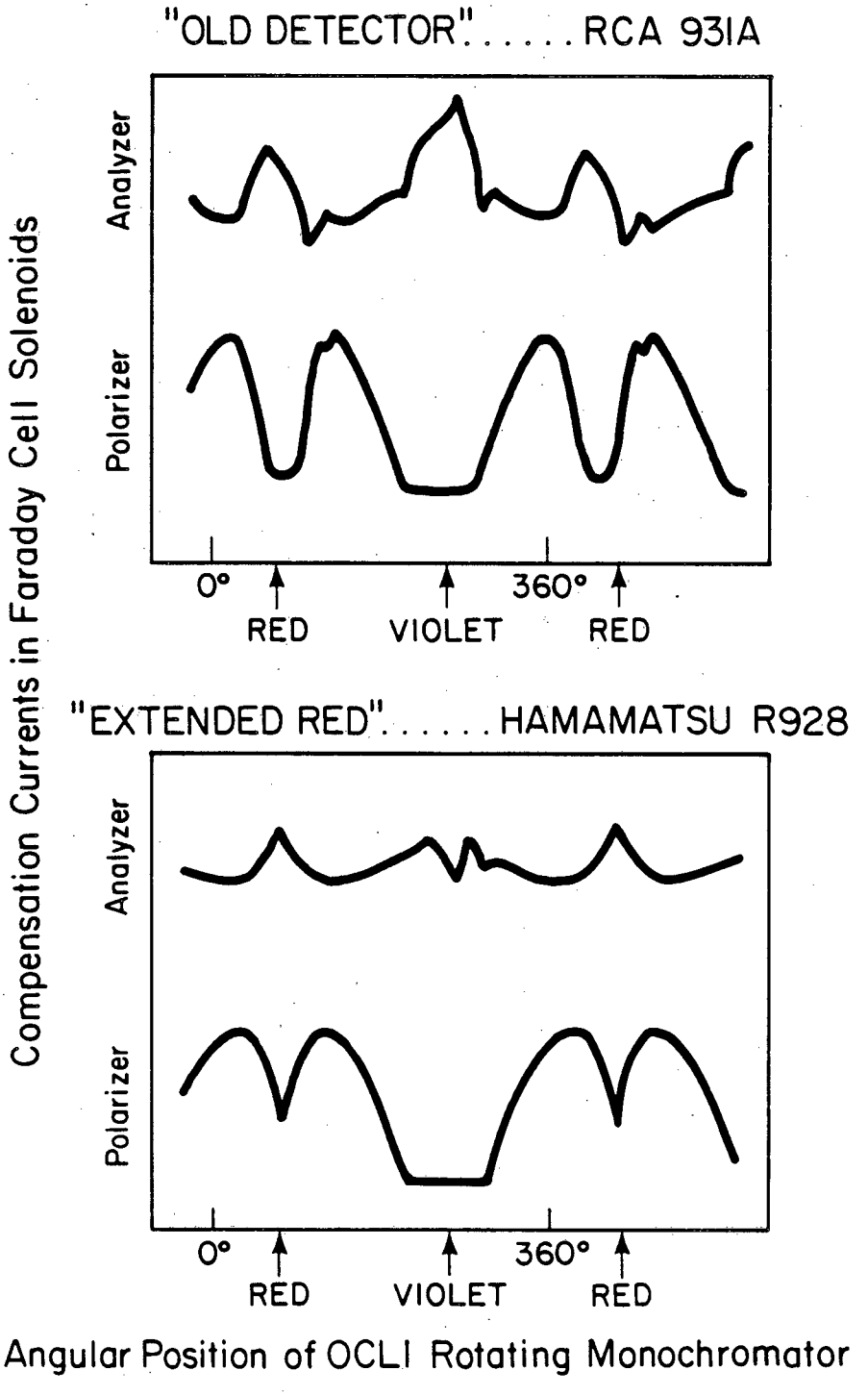

XBL 831 - 63

Fig. 9

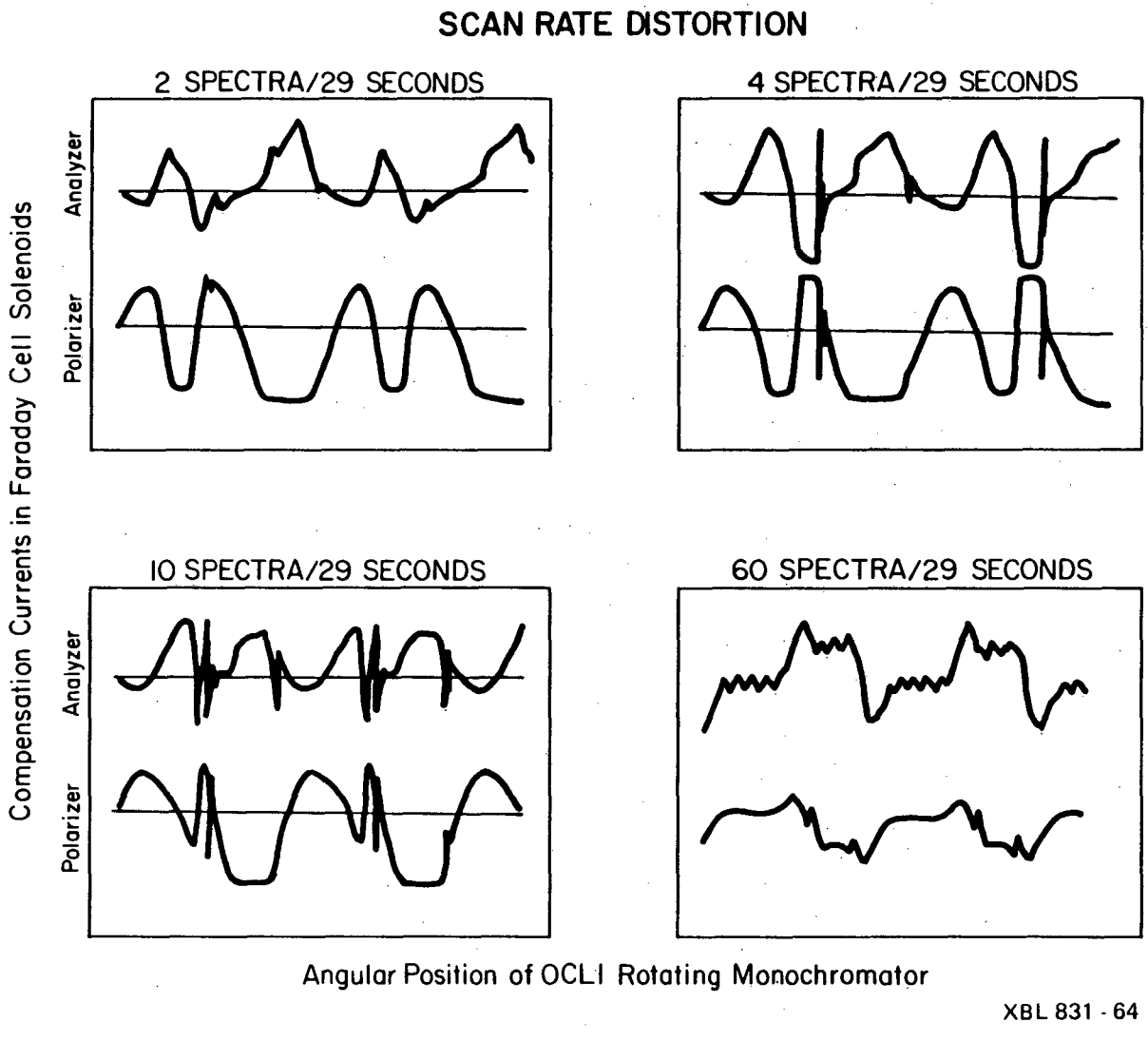
SCAN RATE DISTORTION
2 SPECTRA/29 SECONDS
4 SPECTRA/29 SECONDS
10 SPECTRA/29 SECONDS
60 SPECTRA/29 SECONDS
Analyzer
Polarizer
Analyzer
Polarizer
Compensation Currents in Faraday Cell Solenoids
Angular Position of OCLI Rotating Monochromator
XBL 831 - 64

Fig. 10

UNSMOOTHED
FARADAY CELL CALIBRATION FOR WAVELENGTH

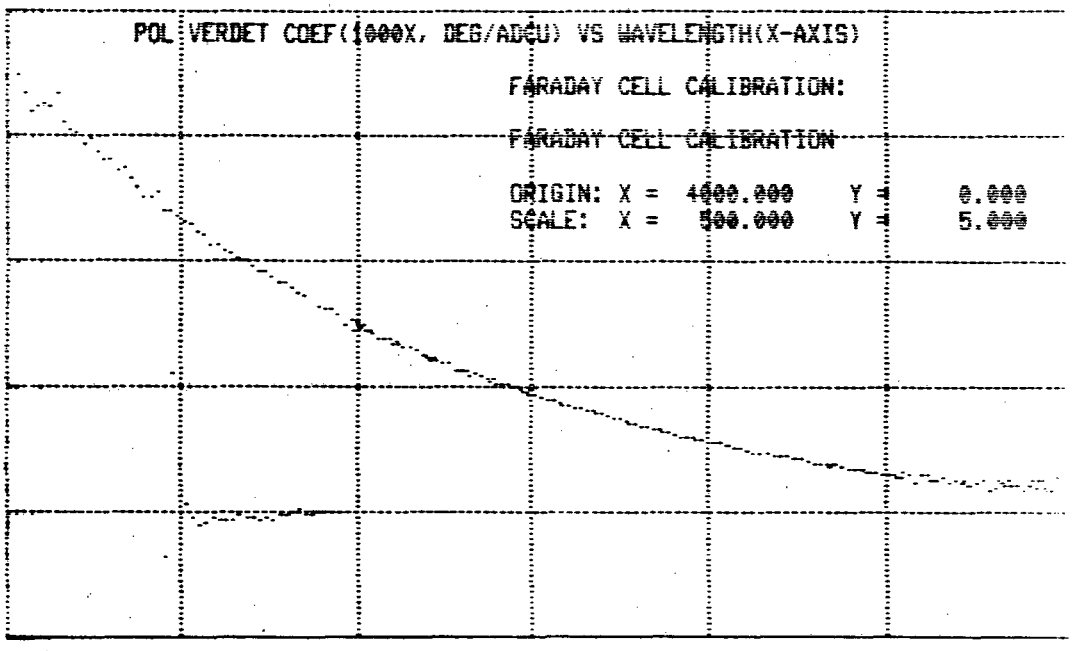

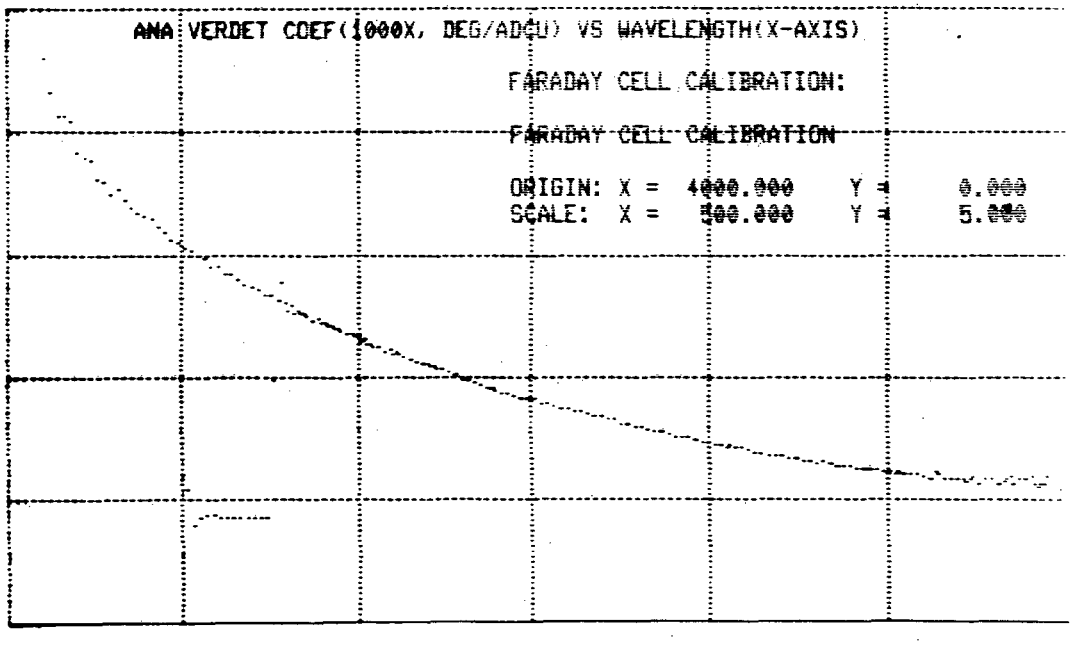

XBL 831-7914

Fig. 11.a

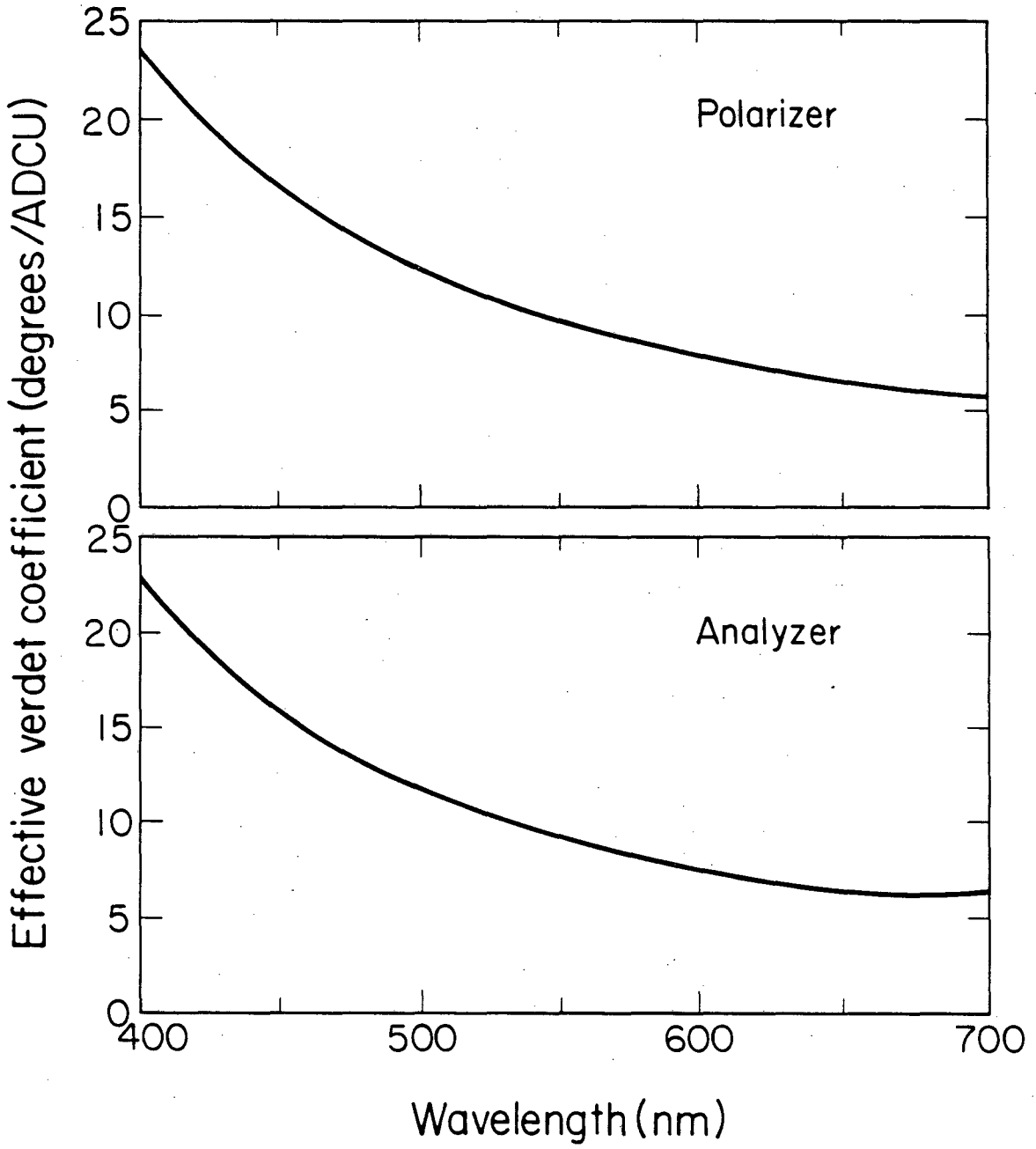
LAGRANGIAN SMOOTHING
FARADAY CELL CALIBRATION FOR WAVELENGTH
Polarizer
Analyzer
Effective verdet coefficient (degrees/ADCU)
Wavelength (nm)
0
5
10
15
20
25
400
500
600
700
XBL 832-1202

Fig. 11.b

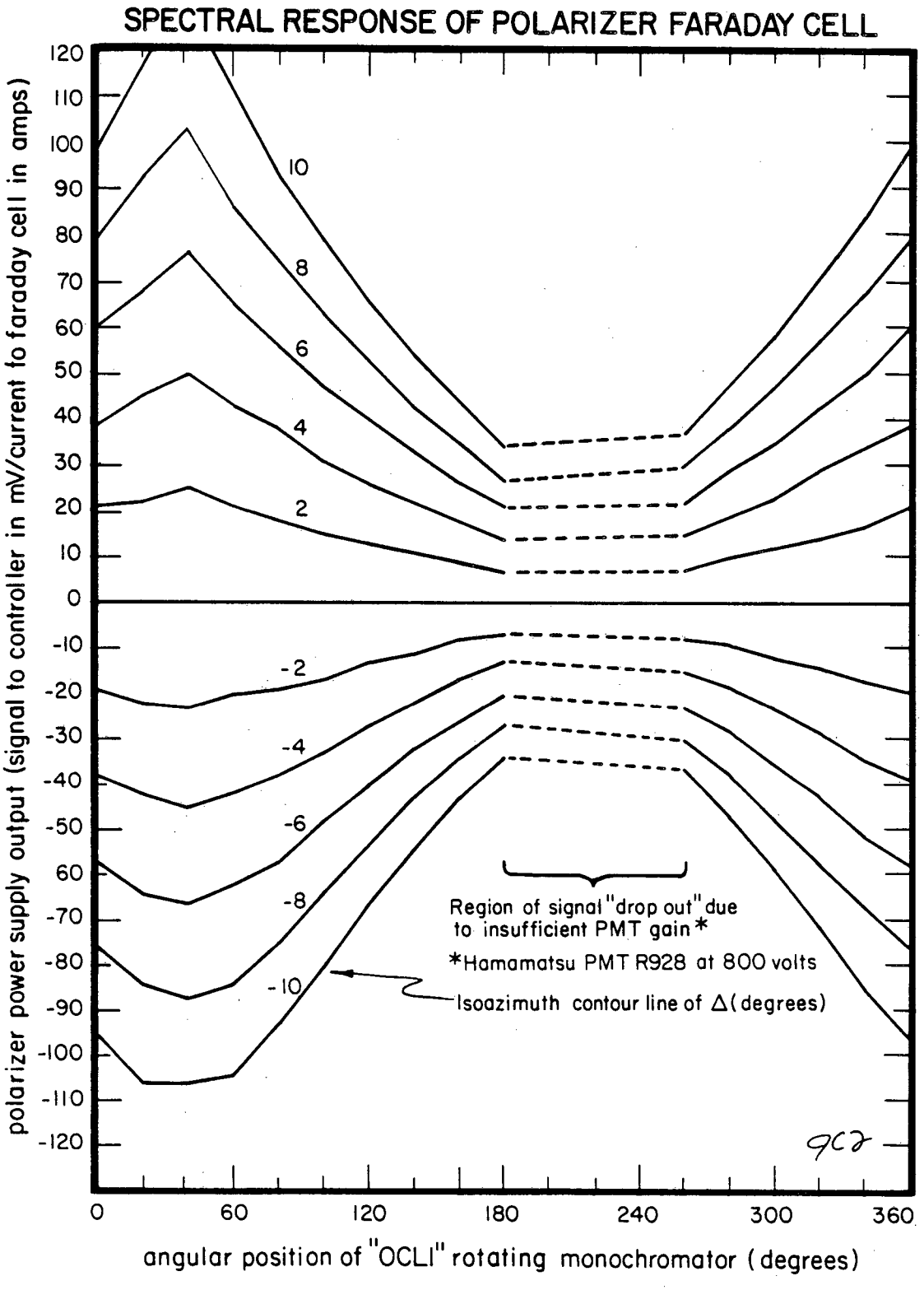
SPECTRAL RESPONSE OF POLARIZER FARADAY CELL
polarizer power supply output (signal to controller in mV/current to faraday cell in amps)
120
110
100
90
80
70
60
50
40
30
20
10
0
-10
-20
-30
-40
-50
60
-70
-80
-90
-100
-110
-120
10
8
6
4
2
-2
-4
-6
-8
-10
Region of signal "drop out" due to insufficient PMT gain*
*Hamamatsu PMT R928 at 800 volts
Isoazimuth contour line of Δ(degrees)
0
60
120
180
240
300
360
angular position of "OCLI" rotating monochromator (degrees)
XBL 831-62

Fig. 12.a

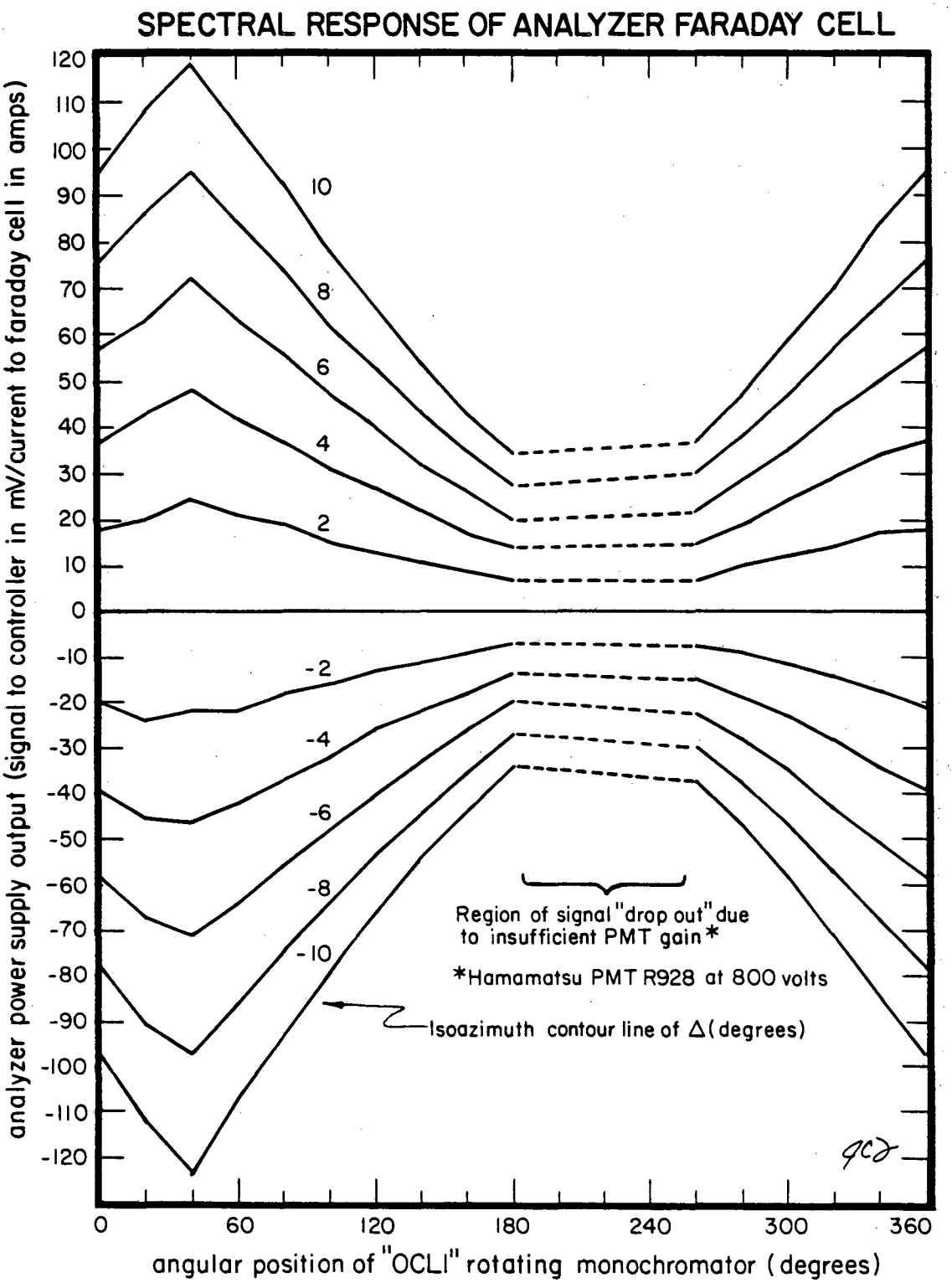
SPECTRAL RESPONSE OF ANALYZER FARADAY CELL
analyzer power supply output (signal to controller in mV/current to faraday cell in amps)
120
110
100
90
80
70
60
50
40
30
20
10
0
-10
-20
-30
-40
-50
-60
-70
-80
-90
-100
-110
-120
10
8
6
4
2
-2
-4
-6
-8
-10
Region of signal "drop out" due to insufficient PMT gain*
*Hamamatsu PMT R928 at 800 volts
Isoazimuth contour line of Δ (degrees)
0
60
120
180
240
300
360
angular position of "OCLI" rotating monochromator (degrees)
XBL 831-61

Fig. 12.b

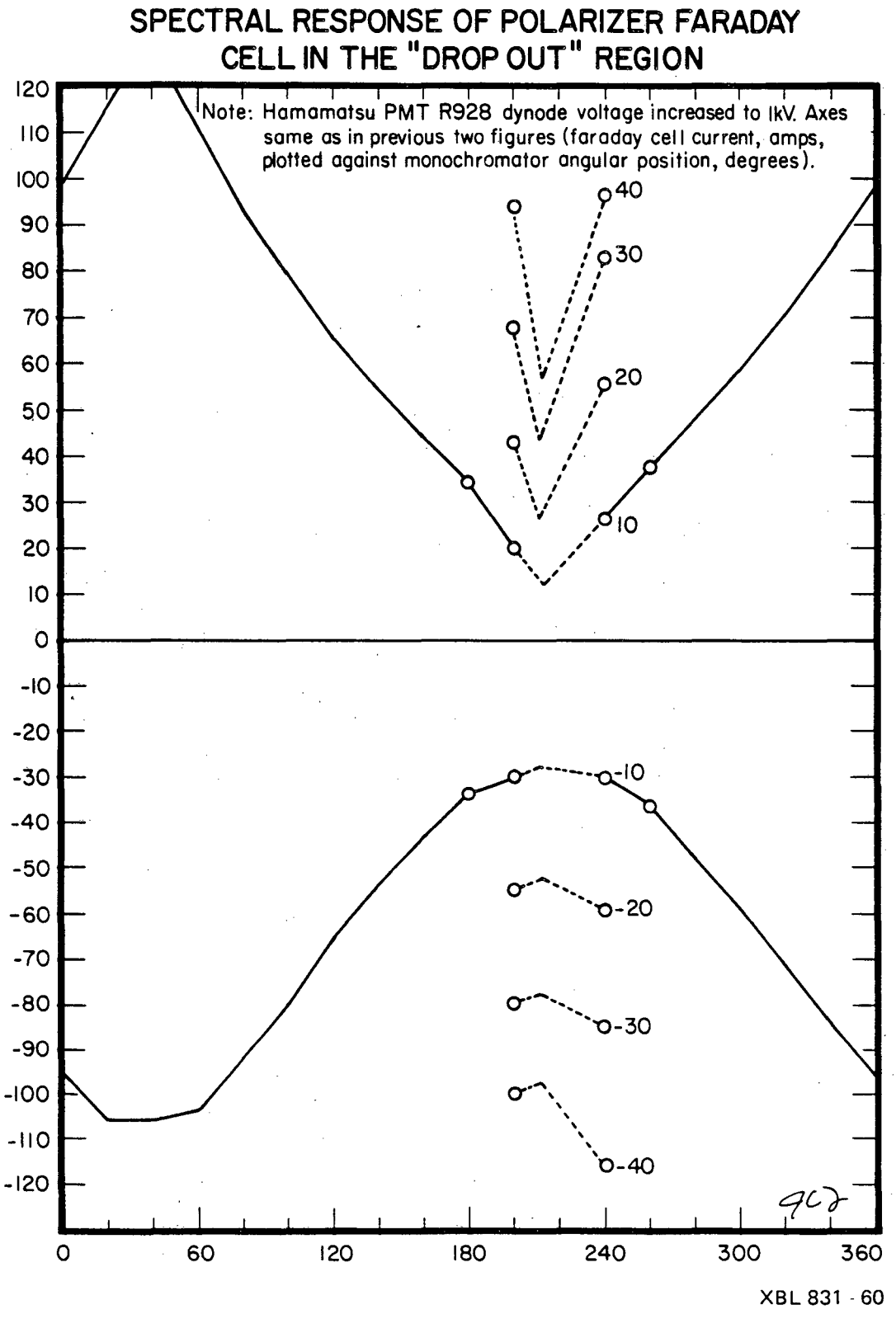
SPECTRAL RESPONSE OF POLARIZER FARADAY CELL IN THE "DROP OUT" REGION
Note: Hamamatsu PMT R928 dynode voltage increased to 1kV. Axes same as in previous two figures (faraday cell current, amps, plotted against monochromator angular position, degrees).
40
30
20
10
-10
-20
-30
-40
120
110
100
90
80
70
60
50
40
30
20
10
0
-10
-20
-30
-40
-50
-60
-70
-80
-90
-100
-110
-120
0
60
120
180
240
300
360
XBL 831 - 60

Fig. 12.c

WAVELENGTH CALIBRATION OF SPECTRAL SCANNER

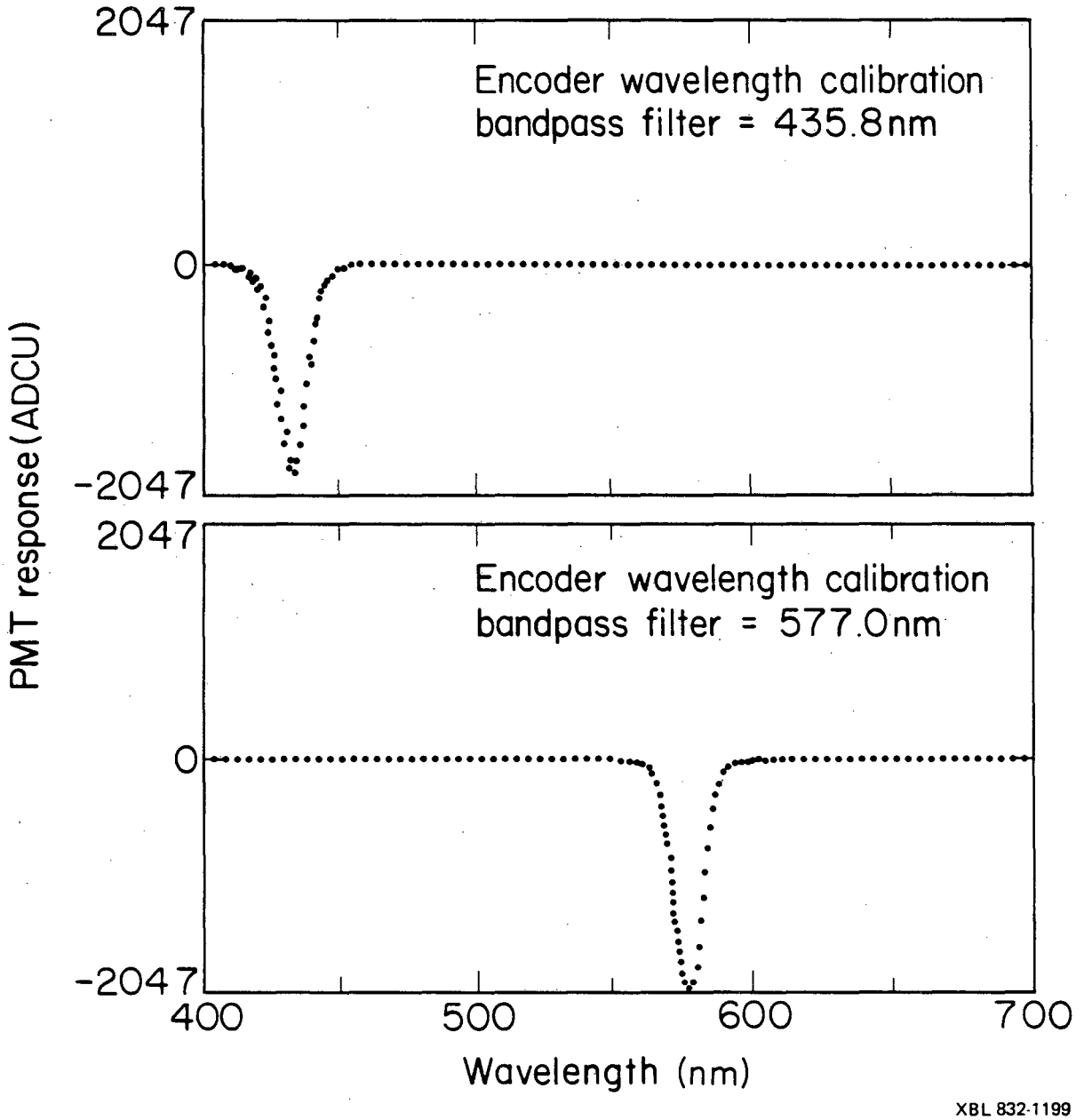

Fig. 13

Appendix 1.

Optical Components: Specifications and Commercial Suppliers

SPECTRAL SCANNING SOURCE

1. Oriel Model C-72-20 Lamp Power Supply and Housing

   Oriel Corporation of America
   15 Market Street
   Stamford, CN 06902
   203-357-1600

2. Illumination Industries Model W75-2002, 75 watt, Xenon Lamp ($48)

   LBL Purchase Requisition #0925-68; Order #1634306

   Illumination Industries, Incorporated
   825 East Evelyn
   Sunnyvale, CA 94806

3. Continuously Variable Interference Filter and Housing

a. Bonded CVF, P/N VC-180-017, W.O. # 15-3910-410, P.O. 2767906 ($922)

   LBL Purchase Requisition #221-11; Order #2767906

b. Uncut CVF, unknown identification numbers

c. OCLI Model 1 Monochromator Housing, S/N 1164 ($1024)

Typically the CVF is sold as an arc segment of 180 degrees; to have a full 360 degrees requires that two segments be bonded together ("bonded CVF"), or that a special order has to be placed ("uncut CVF") which involves unusually long delivery times. In ordering a bonded CVF, costs are itemized as follows: 180 degree arc CVF, $260 each; bonding costs, $275; and index hole fabrication cost, $125. An uncut CVF (unless OCLI has one on the shelf) can cost as much as an order of magnitude more. CVF's for the near infrared are also available that span 680 nm to 1200 nm, at a cost of about $2900 after bonding.

Ms. Marge Dougherty
Optical Coating Laboratory, Inc.
P.O. Box 1599
Santa Rosa, CA 95402
707-545-6440 x230

3. Spectral Scanner Drive Motor

NSH-12R Model 546, Variable Speed Motor ($98)

Model 911 Speed Controller with Manual Potentiometer ($172)

LBL Purchase Requisition #0809-04; Order #83727A6

This motor can be speed controlled with a variable rpm on the drive shaft ranging from 0.33 to 14 rpm. The motor itself requires 115 volts dc, and at 40 degrees Centigrade has an rpm 1/50 horsepower with a maximum speed of 1725 rpm. A 180:1 gear reduction box gives

a maximum stable speed of 9.8 rpm at a torque of 9 inch-pounds. The serial number is 546FJ2134.

Ms. Carol Gruber
Republic Supply Company
1927 Hartog Drive
San Jose, CA 95131

4. Spectral Scanner Digital Encoder

Model STRE-2014-010 Incremental Rotary Encoder ($75)

LBL Purchase Requisition #1054-92; Order #1161506

This encoder generates three TTL compatible pulse trains on three separate channels. Two channels have a repetition rate of 400 pulses per revolution, with a 90 degree phase difference to enable sense of rotation to be determined (use with up-down counter logic). The third channel has a repetition rate of 1 pulse per revolution, and is used as an index pulse. The encoder hub dimensions are compatable with a 3/16 inch o.d. shaft; this encoder was a custom fabrication and has the same encoder body and integrated circuit board dimensions as the vendors catalog model # STRE-1601.

Mr. Jack Muradliyan
Sensor Technology, Incorporated
Subsidiary of Dyneer Corporation
21012 Lassen Street
Chatsworth, CA 91311
213-882-4100

5. ADAC Model 1604/OPI-4 Pulse Counter for Encoder/LSI-11 Interface ($395)

LBL Purchase Requisition #1055-95; Order #1227606

ADAC 70 Tower Office Park
Woburn, MA 01801
617-935-6668

FIXED-WAVELENGTH SOURCE

1. Model 75.2 Argon Laser

Lexel Corporation
928 East Meadow Drive
Palo Alto, CA 94303
415-494-3241

POLARIZERS

1. Polarizing Prisms

Glan-Thompson Polarizing Prisms for Visible-UV ($250 ea.)

LBL Purchase Requisition #8719-86; Order #7601002

These polarizers have 12 mm x 12 mm square apertures and are 24 mm in length with a 15 degree angular polarized field. The magnesium fluoride antireflection coating was optimized for a maximum transmission at a wavelength of 500 nm. The spectral transmission range of these components lies between 230 nm and 2300 nm. The

extinction ratios of the two principle axes is guaranteed to be better than 300,000. The prisms are mounted in black-anodized, brass cylindrical barrels 1 inch o.d. x 1-1/4 inch length.

Karl Lambrecht, Incorporated
3959 North Lincoln Avenue
Chicago, Il 60613

COMPENSATORS

1. Achromatic Compensator for Spectral Scanning

FAD-10 3-Reflection, Fresnel Rhomb for Visible-UV ($1,465)

LBL Purchase Requisition #221-35; Order #2784606

This prism serves as an achromatic quarter-wave retarder for the spectral scanning source. The last digits of the model number indicates the aperture diameter (10mm). Prism faces have a magnesium fluoride antireflection coatings. Custom fabrication with very strict specifications for skew were required; the entrance and exit beams are coaxial and have, by specification a skew of less than 0.01 degrees.

Mr. Manfred Grindel
Continental Optical Corporation
15 Power Drive
Hauppauge, NY 11787
516-582-3388

2. Fixed-wavelength Mica Compensators for Laser

WPUM-4-25-458, 488, 515, 546, 633 ($175 ea.)

These mica plates serve as quarter-wave retarders for the laser source. There are six digits in the model number. The second and third represent the aperture diameter in mm (25 mm); the last three digits represent the wavelength in nm (458 nm, etc.).

KLC Karl Lambrecht Corporation
4204 North Lincoln Avenue
Chicago, IL 60618
312-472-5442

STEP-MOTOR DRIVEN ROTATORS FOR POLARIZERS AND COMPENSATOR

1. Step-motor Control Module

LBL Fabrication #13X382 (Electronics, Joe Katz and Richard Whiteman)

Four Rapidsyn Model 43020 Step-motor Drivers for Rapidsyn Steppers

Model 11R-01 ($101 ea.)

LBL Purchase Requisition #1054-91; Order #1144106

Rapidsyn-Dana Industrial
11901 Burke Street
Sante Fe Springs, CA 90670
213-698-2595

Nationwide Electronic Systems Counter Model CT1617 ($342 ea.)

Compatible Connectors ($9 ea.)

LBL Purchase Requisition #1059-95; Order #1479306

Nationwide Electronic Systems, Incorporated
1536 Brandy Parkway
Streamwood, IL 60103
312-289-8820

2. ADAC Model 1604/POC-4 Pulse Output Controller for LSI-11 Interfacing ($395)

LBL Purchase Requisition #1055-95; Order #1227606

ADAC
70 Tower Office Park
Woburn, MA 01801
617-935-6668

3. Step-motor Driven Optical Rotators with Collimators

LBL Fabrication (MMRD Shops, Walter Giba and Herb Rebi)

Ardel Kinematic Model RTM-175 Polar Rotators ($655 ea.)

LBL Purchase Requisition #1054-90; Order #1144006

These rotators can adjust azimuths of the polarizers and compensator remotely with an accuracy of 0.01 degrees, which is comparable to the previously used Gertner mounts. The steppers are Rapidsyn Models 11R-01.

Ardel Kinematic Corporation
125-20 18th Avenue
College Point, NY 11356
212-353-3600

MAGNETO-OPTIC POLARIZERS

1. Faraday Cell Glass Cores

Glass Rods of Optical Quality 19.9 mm dia. x 153.2 mm ($31 ea.)

LBL Purchase Requisition #221-12; Order #2767606

The numbers given below are (a) the type of glass; (b) its Verdet coefficient at 435.8 nm; and (c through e) its percent transmissions at 435.8 nm, 400 nm, and 350 nm respectively for a thickness of 25 mm (5 mm for SF6 glass). The glasses were all annealed to relieve strains; strain was given by the manufacturer in terms of induced phase shift, which for all the glasses is less than 5 x 10-6 nm per m of length (very low birefringence).

(a)	(b)	(c)	(d)	(e)
SF6	0.155	94	73	6
BK7	0.333	99.4	99.1	93
F2	0.083	99.4	99.0	75
SF2	0.093	98.6	97.0	50

Dr. Jack Shroud
Schott Optical Glass, Incorporated
York Avenue
Duryea, PA 18642
717-457-7485 x326

Schott Optical Glass, Incorporated
1400 Harbor
Fullerton, CA 92636

2. Solenoids

PHOTOMULTIPLIER

1. Hamamatsu Model R928 Extended Red Photomultiplier ($170)

LBL Purchase Requisition #1059-94; Order #1483306

This photomultiplier has relatively flat spectral response.

See the reference literature.

Hamamatsu Corporation
2444 Moorpark Avenue
Suite 217
San Jose, CA 95128
408-292-8603

Mr. Leo Fell
CECO
2115 Avenue X
Brooklyn, NY 11235

Appendix 2.

Electronics: Components and Commercial Suppliers

FARADAY CELL CONTROLLER

LBL special design #8S-9833

FARADAY CELL POWER SUPPLIES

LBL special design #8S-9813

MODULATION AMPLIFIER

McIntosh Model MC-2300 stereo amplifier, 300 Watts per channel

PHOTOMULTIPLIER SUPPLY

Power Designs Pacific, Inc. Model 3K-20, 3000 volts at 20 mA

XENON LAMP SUPPLY

Oriel Model C-72-20

GALVANOMETER AMPLIFIER

LBL special design #8S-3133

DIGITAL VOLTMETERS

LBL special design #8S-3063

POTENTIOSTATS

Princeton Applied Research Model 173 potentiostat with Model 179 digital coulometer

X-Y RECORDER

Hewlett-Packard Model 7044A recorder with time base

Appendix 3.

Computer System: Components and Commercial Suppliers

CONSUMABLE ITEMS

1. Dysan Double Density Floppy Disks 3740/1 for DSD 440 Disk Drive
   Part #800501 (10 diskettes in a box)

   Marcia Bogart
   410 Latimer Hall
   University of California, Berkeley
   Berkeley, CA 94720
   415-642-5560

2. Paper for DEC VT55 Graphics Terminal

   DEC Part #VT50K-12 ($119 per box, 12 rolls in a box)

   LBL Purchase Requisition #1056-03; Order #12604A6

   Digital Equipment Corporation - DEC
   7700 Edgewater Drive
   Oakland, CA 94621
   415-635-3000

3. Ribbon for Model 43 Teletype Printer

   Teletype Part #430035 ($6)

   UCB Purchase Order #9K5019-5480

   Teletype Corporation
   5555 Touhy Avenue
   Skokie, IL 60076

4. Paper for Model 43 Teletype Printer

Wallace Bussiness Form #E6879SPL ($27 per carton)

These forms are 11" x 12", white, and tear to a size of 8-1/2" x 11"; there are 3000 forms per carton.

Will Eggleston
Wallace Business Forms
P.O. Box 4140
Foster City, CA 94404
415-349-4313

5. Pens for Tektronix 4662 Interactive Digital Plotter

Tektronix Part #016-0589-02 (3 per foil package)

These are black pens, specified by the last two digits of the part number. Several other colors are available.

Tektronix, Inc.
Beaverton, OR

HARDWARE

1. DEC LSI-11/2 Central Processor Unit (CPU #975-64864, KEV-11 Extended Arithmetic Chip #5975-62989)

2. MSC 4601, 32K RAM, LSI-11 Add-in Memory (#5975-64865)

3. DLV-11, 4-Channel, Serial Input-output Board

4. ADAC Model 1604/OPI, 4-Channel, 16-Bit, Binary Input Pulse Counter

5. ADAC Model 1604/POC Pulse Controller Board

6. DATEL 8-Channel Analog-to-digital Convertor (#ST-LSI2)

7. DSD 440 Dual Floppy Disk Drive (Model 440 L11-2A)

8. DEC VT55 Graphics Terminal with Hardcopy

9. Teletype Model 43, 300 BAUD Printer

10. Tektronix 4662 Interactive Digital Plotter

APPENDIX 4.

Correlation of the Transmission Wavelength of CVFs with Angular Position (M°): Uncut CVF Example.

$215° < M° < 395°$

$\lambda(Å) = 20.4118\ M° - 765.7647$ $\qquad r = 0.9998$

$40° < M° < 215°$

$\lambda(Å) = -20.2397\ M° + 8037.5603$ $\qquad r = 1.0000$

Notes: 395° is equivalent to 35°.

APPENDIX 5.

Wavelength Calibration of the Spectral Scanner Digital Encoder: Uncut CVF Example.

---

x = encoder count

y = band pass wavelength (Å) of the calibration filters

Linear Regression for Segment #1 (1/2 of CVF):

x	y
-57	4047
-43	4358
+34	5770

$y = a_1x + b_1$

$a_1 = 18.7332$

$b_1 = 5137.1312$

$r_1 = 0.9996$

Linear Regression for Segment #2 (1/2 of CVF):

x	y
207	5770
283	4358
298	4047

$y = a_2x + b_2$

$a_2 = -18.8188$

$b_2 = 9668.0696$

$r_2 = 0.9999$

Appendix 5 (cont.)

Calculation of Segment Intersection Points:

$y = 18.7332\ x + 5137.1312$ (segment #1)

$y = -18.8158\ x + 9668.0696$ (segment #2)

$x = 120.6577 \sim 121$ (encoder count at intersection of two calibration lines)

Range of Applicability of Segment #1:

$x = 121$ (lower limit)

$x = 321$ (upper limit)

Notes: r_1 and r_2 are the respective correlation coefficients for segments #1 and #2. These calibration parameters are entered into WLCALC . DAT shown in Appendix 13 of Chapter 3.

APPENDIX 6.

Calculation of the Longitudinal and Transverse Coherence of the Spectral Scanning Source

---

Longitudinal Coherence:

$\ell_c = \lambda^2/\delta\lambda$

@λ = 400 nm, $\delta\lambda$ ~ 10 nm, ℓ_c ~ 16μ

@λ = 700 nm, $\delta\lambda$ ~ 10 nm, ℓ_c ~ 49μ

Transverse Coherence:

$\sigma_c = 0.16\ \lambda r/s$ r = 15 cm s = 1 mn

@λ = 400 nm, σ_c = 10μ

@λ = 700 nm, σ_c = 17μ

Chapter 3

SOFTWARE FOR THE LSI-11 DATA ACQUISITION SYSTEM

Abstract

FORTRAN software was written to make possible acquisition of both fixed-wavelength and spectroscopic data from the automatic, self-nulling ellipsometer by a LSI-11 microcomputer. Additional programs were written to aid in the interpretation of the acquired ellipsometry data. Software is categorized as being for either (a) fixed-wavelength data collection; (b) spectroscopic data collection, reduction, and simulation; (c) graphics; or (d) modeling and optimization.

The most basic ellipsometry equations have also been programmed for a Texas Instruments 59 calculator, and are presented because of their proven usefulness, convenience, and popularity.

Introduction

FORTRAN software (1,2) was written to make possible acquisition of both fixed-wavelength and spectroscopic data from the automatic, self-nulling ellipsometer by a LSI-11 microcomputer. Additional programs were written to aid in the interpretation of the acquired ellipsometry data. Software is catagorized as being for either (a) fixed-wavelength data collection; (b) spectroscopic data collection, reduction, and simulation; (c) graphics; or (d) modeling and optimization. Only main

programs are discussed in the text. Both main programs and subroutines are thoroughly documented in the appendices (presented in reference 1) by effective use of comment statements; each listing of software begins with a statement of the software objective. Subroutine listings are presented in the same appendix as the main program calling the subroutine, unless the subroutine listing has been presented in a preceding appendix.

Fixed-wavelength data are synchronized by the internal line clock of the computer and spectroscopic data are synchronized by the digital encoder of the spectral scanner (see Chapter 2). The file length (blocks) for fixed-wavelength data depends upon the duration of the experiment, whereas spectroscopic data files always require 5 blocks; the number of encoder pulses per spectral scan is always constant (400), even when several scans are averaged. Therefore, one double density floppy disk (974 blocks) can store about 190 spectroscopic data files. Spectroscopic data files can contain either raw data, delta and psi, measured substrate refractive indices, or simulated spectroscopic measurements (delta and psi generated by ellipsometry models. However, all these data are written to and read from floppy disk using the same subroutines (OUTPUT and INPUT).

This strategy allows easy manipulation of spectroscopic data. All files can be retrieved from disk and viewed by the user using a single program, RECALL (discussed subsequently). Furthermore, the user can measure delta and psi over the spectral range of the ellipsometer prior

to film formation, and subsequently convert these data into complex refractive indices. These refractive indices can then be read by simulation programs, which generate theoretical spectral scan data files comparable to experimental measurements; theoretical and experimental values of delta and psi can be plotted together using the same graphics programs so that visual comparisons can be made. Plotting can be done either on the screen of the VT55 graphics terminal or on the Tektronix 4662 digital interactive plotter. One spectroscopic data file can be easily subtracted from another so that very small changes in delta and psi can be easily seen (second order optical effects) since all files are stored and recalled similarly.

Modeling and simulation programs used to interpret ellipsometry data are based upon either (1) the Bruggeman theory, (2) the Maxwell-Garnett theory, (3) the coherent superposition of reflection coefficients, or (4) a uniaxial anisotropic film model. These basic theories were applied to both single and multilayer film models (see Chapters 5, 6, 7, and 8).

The most basic ellipsometry equations have also been programmed for a Texas Instruments 59 calculator, and are presented because of their proven usefulness, convenience, and popularity. These programs exploit the complex arithmetic capabilities of this particular calculator and require all of the memory.

Fixed-Wavelength Data Acquisition

The basic data collection programs used during a fixed-wavelength, potentiodynamic experiment are SCAN, EDR002, DECOD2, TRNSLT, and PLOT01, and will be discussed first (see appendix 1). These programs are demonstrated using a typical data storage disk (see appendix 2).

I. SCAN (appendix 3).

This program, which is actually called as a subroutine, reads the 8-channel A/D converter (3) continuously and displays all channel input levels on the VT55 screen (4). SCAN allows the LSI-11 to serve as an 8-channel digital voltmeter. Channel gains can be either 0, 1, 2, or 3 (1X, 2X, 4X, or 8X, respectively). The digital resolution of the A/D converter is limited by a maximum value of 2047 units (ADCU), which corresponds to an input voltage of 1.2445 volts at a gain of 3 (0.000608 volts per ADCU).

II. EDR002 (appendix 4 through 6).

EDR002 reads the 8-channel A/D converter at intervals specified by the user and stores the data in unformatted form on floppy disk. The user also specifies the channels to be read and their respective gains. The shortest interval between channel sampling is 1/60 seconds (1 tic); longer intervals allow digital filtering of the data (an interval of 10 tics would result in averaging 10 measurements).

Though EDR002 is a general data acquisition program and can be used to monitor any analog electrical signal, the following conventions have been adopted and should be used for monitoring the ellipsometer and potentiostat (appendix 5).

Channel Assignments

Identification	Channel	Gain
Polarizer Faraday Cell	0	3
Analyzer Faraday Cell	1	3
Cell Potential	2	3
Cell Current	3	3
Polarizer Manual Adjustment Flag	4	3
Analyzer Manual Adjustment Flag	5	3

III. DECOD2 (appendix 7).

Since EDR002 stores data in unformatted files, one cannot display these numeric data directly on the VT55 screen with the TYPE command. Data must first be read from the unformatted data file by DECOD2 and then displayed on the VT55 screen.

Values of time are not stored in the data files, but are reconstructed for individual data points on the basis of specified channel sampling intervals; this increases the storage efficiency of each floppy

disk. Early software (before optimization) was too slow to allow data collection from all 8 channels at the maximum sampling rate without a loss of data. Such losses caused errors in the reconstructed times displayed with data points. EDR002 has been optimized so that 6 channels can now be monitored simultaneously at the maximum sampling rate without any loss of data.

IV. TRNSLT (appendix 8).

TRNSLT converts the unformatted data files to polarizer azimuth, analyzer azimuth, cell potential, cell current, delta, and psi, respectively. These conversions are based upon parameters read by TRNSLT from the data file TRNSLT.DAT (appendix 9); parameters in this file are defined in the "Demonstration of TRNSLT." In the example shown the "incremental manual adjustments of the polarizer and analyzer" are both 10 degrees. During the experiment, if the Faraday cells had been required to exceed their range, the user could have adjusted the Glan-Thompson polarizers by ±10 degrees to prevent over-ranging (loss of ellipsometer signal). Inputs to either channel 5 (polarizer) or channel 6 (analyzer) should be set to zero (grounded) during the manual adjustments to alert TRNSLT so than similar corrections can be made in the reduction of data files (conversion of azimuth reading to delta and psi). The open channels will always be read as a value greater than zero, until grounded; the "flag tolerance" is the range of ADCU values which TRNSLT interprets as zero for the two "flag channels." The Fara-

day cells are calibrated by allowing them to compensate for increments of the Glan-Thompson prism azimuths; this compensation (increased dc Faraday cell current) is monitored with SCAN and recorded in terms of ADCU; polarization rotation is correlated with Faraday cell current level (in ADCU) by linear regression, which gives the "Faraday cell calibration curve equation parameters." Note that the "slope" is the effective Verdet coefficient (with the units of degrees per ADCU).

The converted data are then output to a formatted file called PLTDAT.DAT (appendix 10). The first line of this data file is the experiment identification. The columns of numbers are time (tics), polarizer azimuth (degrees), analyzer azimuth (degrees), cell potential (mV), and cell current (microamps), delta (degrees), and psi (degrees), respectively. The last column currently serves no purpose.

PLOT01 (appendix 11).

Any data stored in PLTDAT.DAT can be recalled and plotted on the VT55 screen with PLOT01. Plots are automatically scaled. However, the user can select any scaling desired, superimpose grids on the plot, label the plot, and specify any combination of the x and y axes desired; i.e., any column of PLTDAT.DAT can be plotted against any other column. In the example shown polarizer azimuth (column 1) is plotted against reconstructed time (column 0). Though time is not stored per se in the unformatted data files, it is stored as a column of numbers in PLTDAT.DAT.

Spectroscopic Data Acquisition

The basic data collection programs used during spectral scans are SEV002, RECALL, RISURF, MINUS, and DSCONV (see appendix 12). An additional program, CALFC1, is required for spectroscopic calibration of the Faraday cells (values of Verdet coefficients measured of the spectral range of the instrument). Other programs which have been written to enhance the capabilities of the instrument will also be discussed. The directory of the data storage disk used to illustrate the operation of these programs is shown in appendix 13, along with the spectral scanner calibration file WLCALC.DAT, required as an input data file by all programs discussed in this section.

From the preceding discussion, recall that EDR002 increases disk storage efficiency by storing a single parameter used to reconstruct time values for each stored set of data points. Here, in an analogous fashion, SEV002 increases disk storage efficiency by storing only a few numeric values used to reconstruct wavelengths rather than actually storing wavelength values for each data point. The parameters for wavelength reconstruction are stored in WLCALC.DAT , a single formatted data file common to all spectroscopic data files (for a given spectral scanner calibration). The six numbers in this file are two sets of intercept, slope, and regression coefficient for wavelength calibration of the spectral scanner. Linear regression is used to correlate encoder count with the center of the band-pass wavelength of the spectral scanner rotating circular filter (also called a continuously variable filter, or CVF. Two sets of regression line parameters (one per half-

revolution) are necessary since the CVF is symmetric; i.e., the spectral range of the filter is repeated twice per revolution (400 encoder counts; Chapter 2, encoder wavelength calibrations).

The plotting routine (subroutine PLOT) requires the input data file TITLE.DAT shown in appendix 14 for labeling VT55 graphics with alphanumeric characters. Almost all spectroscopic programs, SEV0002, RECALL, etc. call subroutine PLOT.

I. SEV002 (appendix 15).

This is the main spectroscopic data collection program for monitoring variations in Faraday cell current levels via two channels of the A/D converter (preset as channels 0 and 1 at gains of 3). Digital filtering is done by averaging all data collected between encoder pulses. Channels are sampled at the maximum possible speed (limited by the A/D conversion rate). The program reinitializes the pulse counter (5) every revolution after detection of the indexing pulse on a separate channel of the counter interface. Another channel monitors the pulse frequency, used as a measure of the scan rate. The program is capable of averaging multiple scans (data for a single surface can be collected and averaged for hours); this may be necessary for reduction of background noise to an extent necessary to see some spectroscopic features attributable to submonolayer films (see Chapters 6 and 8). The user is also required to store other instrument operational parameters with the data for purposes of thorough experimental documentation.

II. RECALL (appendix 16).

All spectroscopic data files, regardless of their content, are unformatted. RECALL is used to retrieve these data files and can display the information graphically on the VT55 screen or output the information in numeric form on the line printer (Model 43 teletype).

III. FIXPCA (appendix 17).

Mistakes in entering azimuths of the Glan-Thompson polarizers and the Fresnel rhomb with stored data occur. These azimuths are required when the data files are converted to delta and psi by DSCONV (to be discussed). To correct azimuth entries, one uses FIXPCA.

IV. SHIFT (appendix 18).

It is sometimes desired to use data files together (in spectroscopic simulations or subtractions) which were collected at times when different spectral scanner calibrations were in effect (which sometimes results from equipment maintenance). SHIFT allows the unformatted data files to be rearranged so that the simulators can use the same WLCALC.DAT parameters for both files.

V. CALFC1 (appendix 19).

Delta and psi are indirectly measured by the automatic, self-nulling ellipsometer as the dc current levels in the polarizer (POL) and analyzer (ANA) Faraday cells. These current levels are monitored by the microcomputer over two channels (0 and 1) of the 8-channel A/D con-

verter. In order to convert these current levels (recorded as ADCU) to polarizer and analyzer azimuths (delta and psi), proportionality constants (effective Verdet coefficients) must be known; these constants are "current-level independent" but vary in a non-linear manner with wavelength. CALFC1 generates a spectroscopic data file with wavelength dependent effective Verdet coefficients (degrees of rotation per ADCU); one constant is stored for each encoder pulse (wavelength). CALFC1 requires three spectroscopic data files as input. One spectral scan is required with the ellipsometer nulled (zero Faraday cell dc current levels) at some reference wavelength (say with the spectral scanner azimuth set at M = 120 degrees); another spectral scan is required with the polarizer Glan-Thompson prism azimuth incremented (increment unimportant), and final spectral scan with the analyzer Glan-Thompson prism azimuth incremented (increment unimportant). The effective Verdet coefficients (degrees per ADCU) are calculated by subtraction of the first spectral scan from those with incremented polarizer and analyzer azimuths and division of the resultant values (ADCU) by the increment in azimuth (degrees). These constants are stored in a file 7 blocks in length (rather than the usual 5 blocks); consequently, slightly different input/out subroutines are required for these calibration factors (subroutines INFC and OUTFC). In appendix 19 these factors are referred to as "FC RESPONSE FACTORS" and were stored in a file called "DY1FARADYDAT."

In addition to generating effective Verdet coefficients, CALFC1 also calculates "CROSS-TALK PARAMETERS" which are measures of the degree

of cross-modulation existing between the two channels of the Faraday cell controller. Ideally, increments of the polarizer azimuth should only result in changes in the polarizer Faraday cell dc current; however, due to cross-modulation, some response in the analyzer Faraday cell occurs. The analyzer "CROSS-TALK PARAMETER" is the change in analyzer response (ADCU) normalized by the change in polarizer response (ADCU) when the polarizer Glan-Thompson prism is incremented. Cross-modulation for the polarizer channel is measured in a similar manner. Through careful tuning of the Faraday cell controller (two-channel phase sensitive detector), cross-modulation between channels has been reduced to essentially zero over the entire spectral range.

VI. FCSMTH (appendix 20).

Noise present in the original spectral scans used to generate the Faraday cell calibration file is also present in the effective Verdet coefficients. To prevent propagation of these errors throughout all data converted to delta and psi (by DSCONV), the effective Verdet coefficients are smoothed by approximating the data with an nth degree Lagrangian polynomial. This is done by FCSMTH. Data can be stored in the original data file, or in a new, smoothed data file created by FCSMTH.

VII. FCAVG2 (appendix 21).

This program allows one to average both polarizer and analyzer effective Verdet coefficients, using the result for both Faraday cells.

VIII. DSCONV (appendix 22).

DSCONV recalls spectroscopic data files stored by SEV002 and converts the contents to delta and psi; effective Verdet coefficients stored by CALFC1 are also required. For the ellipsometer configuration having the plane-of-incidence parallel to the optical table, the "rotated azimuth formula option" is selected by the user. This program also allows the user to display delta and psi plotted against wavelength on the VT55 screen (by calling subroutine PLOT). The converted data can then be stored in the same file as the original data or in a new file specified by the user.

IX. RISURF (appendix 23).

Measurements of delta and psi for a bare, reflecting surface can be used to calculate the optical constants of the surface (refractive index and extinction coefficient). Files created by DSCONV can be converted to complex refractive indices at different wavelengths by RISURF. The converted data can then be stored in any new or existing spectroscopic data file. Subroutine PLOT is also used by RISURF to generate graphics on the VT55 screen.

X. RISMTH (appendix 24).

This program performs Lagrangian smoothing of spectroscopic complex refractive index data files using subroutine SMOOTH, the same routine as employed by FCSMTH.

XI. RIGEN1 (appendix 25).

Spectroscopic refractive index data files can be generated by linear regression of literature data; use of RIGEN1 requires the assumption of linear optical constants (no absorption bands or edges) over the spectral range of the data.

XII. DYERI (appendix 26).

This program can be used to generate the refractive index data file of an adsorbed dye layer on an electrode surface from (1) absorption spectra measured with the spectral scanning ellipsometer serving as a spectrophotometer and from (2) a data file having a refractive index (real part) believed to be comparable to that of the dye (see Chapter 8).

XIII. MINUS (appendix 27).

This program generates "difference spectra" by subtracting one spectroscopic ellipsometry data file from another. This program is essential for determining very small changes in delta and psi due to formation of single monolayers (see Chapter 6, dye relaxation experiment).

XIV. NORMAL (appendix 28).

This program normalizes one spectroscopic ellipsometry data file by another and is useful when measuring intensity (photomultiplier tube output) rather than polarization (Faraday cell dc current levels).

Spectroscopic Ellipsometry Simulators

Simulators are used to predict spectroscopic ellipsometry measurements on the basis of experimentally determined spectroscopic refractive index data files, literature data, and established optical theories.

I. EMASES (appendix 29).

Delta and psi are calculated at different wavelengths based upon the Maxwell-Garnett theory. This routine was used extensively in Chapter 7 to predict spectroscopic ellipsometry measurements of thin, porous Pb electrodeposits on Cu.

II. BRUGMN (appendix 30).

This program is similar to EMASES and calculates values of delta and psi at different wavelengths based upon the Bruggeman theory. This routine was also used extensively in Chapter 7 to predict spectroscopic ellipsometry measurements of thin, porous Pb electrodeposits on Cu. This program is believed to have a more sound theoretical basis than EMASES due to the self-consistency of the Bruggeman theory.

III. CSMSES (appendix 31).

Delta and psi at different wavelengths are calculated on the basis of the coherent superposition model. When a deposit is distributed as islands on a substrate the weighted average of reflection coefficients for film-covered and for bare surface are used to calculate the overall reflection coefficients, when are then used to calculate delta and psi.

See Chapters 5 and 7.

IV. AISPEC (appendix 32).

Delta and psi at different wavelengths are calculated on the basis of a uniaxial anisotropic film model. This simulator reads spectroscopic complex refractive index data files created by DYERI and RISURF to predict spectroscopic ellipsometry measurements of adsorbed dye monolayers on electrodes and was used extensively in Chapter 8.

Single Parameter Modeling Routines

I. EMAFIT (appendix 33).

The current passed during cathodic metal deposition with fixed-wavelength ellipsometry experiments is integrated by this program and values of delta and psi calculated based upon combinations of deposit thickness and porosity consistent with the charge balance. This program uses the Bruggeman theory as the theoretical basis for predicting delta and psi. EMAFIT reads PLTDAT.DAT and creates a formatted data file, EMAFIT.DAT, of the same format as PLTDAT.DAT. The columns of numbers in EMAFIT.DAT are time, calculated delta, calculated psi, the sum-of-squares error between predicted and measured values, the charge determined by integration of the current in PLTDAT.DAT, the film thickness, and the volume fraction of deposit in the composite film. This model has only one adjustable parameter which was optimized by gradually increasing the parameter value until a minimum in the sum-of-squares error was detected (column 4 of EMAFIT.DAT).

II. CSMFIT (appendix 34).

This program is similar to EMAFIT except that the theoretical basis for calculating delta and psi is the coherent superposition model. There is only one adjustable parameter; combinations of island thickness and surface coverage are coupled through the charge balance.

Programs for Graphic Output on the Tektronix 4662 Digital Plotter

Most of the figures presented in this thesis were generated with the Tektronix plotter (6) using four programs, TEK002, TEK003, AXES, and LABMOD (appendix 35). The axes of graphs are drawn and labeled by AXES (appendix 36); the alpha-numeric labeling of the axes is determined by values read from the input data file AXES.DAT (appendix 37). Program LABMOD is used to label graphics with alpha-numeric information (appendix 38). Graphic output generated by AXES from the input AXES.DAT and demonstration labels generated by LABMOD are both shown in appendix 39. TEK002 (appendix 40) plots any spectroscopic ellipsometry file (those 5 blocks in length); scaling of the plot is determined by values read from the input file RANGES.DAT (appendix 41). The graphic output generated by TEK002 is shown in appendix 42. TEK003 (appendix 43) reads the formatted data file PLTDAT.DAT (appendix 44) and draws graphs (appendix 45) identical in size to those drawn by TEK002; scaling of graphs generated by TEK003 is done via the VT55 keyboard.

Multiple Parameter Optimization Routines (appendix 46).

A unvariant search program, SEARCH (appendix 47), was written so that multiple parameter ellipsometry models could be optimized. This optimization program has been applied to several multilayer film models and a uniaxial anisotropic film model. SEARCH minimizes any function Y calculated in the objective subroutine ERROR.

I. OHGOGO (appendix 48).

OHGOGO optimizes a two-layer film model (7) where the film closest to the substrate is assumed to be compact and the second film is assumed to be porous. The complex refractive index of the second layer are calculated from the combined optical constants of the solid film material and the incident medium using the Bruggeman theory. After delta and psi are calculated for the substrate covered by the single, compact film, apparent optical constants for this film-covered surface are calculated and used as the substrate optical properties in the delta-psi calculation for the second, porous layer. The program reads the formatted input film OHGOGO.DAT and outputs the optimized model parameters to the line printer.

II. GOGOGO (appendix 49).

GOGOGO is similar to OHGOGO except that the assumed film structure consists of a compact layer closest to the substrate, covered by a second porous layer. Sitting on top of the second porous layer are islands. The Bruggeman theory is used to compute the composite optical

properties of the second layer and the coherent superposition model is applied to the third layer, which is composed of islands.

Apparent substrate optical constants are determined after the calculation of delta and psi for each layer, beginning with the inner-most compact film. A film-covered surface is treated as a simple substrate having optical properties corresponding to the values of delta and psi calculated for the film covered surface. This program was used for calculations discussed in both Chapters 5 and 6.

III. WLGOGO (appendix 50).

The multilayer model optimized by this program is identical to that optimized by GOGOGO. WLGOGO and GOGOGO are different in that WLGOGO only optimizes those parameters of the film model which are assumed to be wavelength independent. Values of delta and psi measured at several different wavelengths for a particular surface are all treated as independent observations of that surface. Consequently, model parameter variances can be determined from spectroscopic ellipsometry measurements. See Chapter 7. These variances are measures of the ability of the model to fit the experimental data; they also reflect the models sensitivity to particular parameters. Variability in model parameters from one experiment to another cannot be determined from a single experiment. Furthermore, these values do not account for errors in the alignment of optical components.

IV. AIGOGO (appendix 51).

The optical constants and thickness of a uniaxial film are optimized. This program was used in calculations discussed in Chapter 6 (dye relaxation experiment).

Simple Calculations of Delta and Psi

I. FLMTST (appendix 52).

This program calculates delta and psi for a homogeneous film model.

II. EMATST (appendix 53).

This program calculates delta and psi for a homogeneous, composite film model composed of two components. It is based upon the Bruggeman theory.

III. CSFIT (appendix 54).

This program calculates delta and psi for an island covered surface; the theoretical basis is the coherent superposition model.

IV. PSIDEL (appendix 55).

This program computes delta and psi from polarizer and analyzer azimuths entered from the VT55 keyboard; azimuths in any zone can be converted.

Ellipsometry Programs for the Texas Instruments 59 Calculator

Given the angle-of-incidence and measured values of delta and psi for a reflecting surface, the complex refractive index of the surface can be calculated (appendix 56). Values of delta and psi for a homogeneous film model can also be calculated (appendix 57). The complex arithmetic capabilities of this calculator make it attractive for such calculations (8).

References

1. Farmer, J. C., Muller, R. H., "Documentation of Software for the Self-nulling, Spectroscopic Ellipsometer Data Acquisition System," Lawrence Berkeley Laboratory, Berkeley, CA, LBL-15525, 1983.

2. RT-11 Version 3 and Version 4 Documentation, Digital Equipment Corporation, Maynard, Massachusetts, 1979-1980.

3. Instruction Manual No. 58-12140-35, DATEL Systems, Inc., 11 Cabot Blvd., Mansfield, Massachusetts, 1979.

4. VT55 Programming Manual, AA-4949B-TC, Digital Equipment Corporation, 1980.

5. Model 1604/OPI Optically Isolated Four Channel 16 Bit Binary Input Pulse Counter Instruction Manual, ADAC, Inc., 70 Tower Office Park, Woburn, Massachussetts, 1978.

6. Tektronix 4662 Digital Interactive Plotter Instruction Manual, Tektronix, Beaverton, Oregon, 1981.

7. Mathieu, H. J., "Computer Programs for Ellipsometry II," Lawrence Berkeley Laboratory, Berkeley, CA, LBL-2517, 1973.

8. TI Programmable 58/59 Master Library Manual, Texas Instruments, Inc.,

Chapter 4

SELECTION OF SUBSTRATE, DEPOSIT, AND SURFACE ACTIVE DYE BY CYCLIC VOLTAMMETRY

Abstract

Cyclic voltammetry was used to study the deposition of Pb on Pt, Au, and Cu substrates from 5 millimolar $Pb(NO_3)_2$, 1 M $NaClO_4$, at pH 3, in the presence of various organic dyes which serve as deposition inhibitors. Dyes were used because they are both light absorbing and surface active. These properties make them desirable for investigation insitu by spectroscopic ellipsometry during electrodeposition (1). Originally, 30 materials were chosen for screening, based upon literature references and availability. Of these, 14 cationic, anionic, and neutral dyes and indicators were investigated in detail and and it was found that rhodamine-B chloride induced the largest overpotential for lead deposition (125 mV cathodic shift).

This 125 mV cathodic shift of the deposition peak occurred during the first potential cycle; after subsequent cycling the peak potential was the same as prior to rhodamine-B addition to the electrolyte. After allowing the cell to remain at open circuit for several minutes, the cathodic shift (overpotential) reappeared (referred to as a relaxation phenomenon). From cyclic voltammograms of rhodamine-B in the absence of Pb^{++}, it is believed that rhodamine-B became reduced and depleted from the electrode surface during the first potential cycle, hence its inhibitory effects disappeared. At open circuit, the surface was

probably repopulated with adsorbed rhodamine-B, and inhibitor action resumed.

Prominent underpotential deposition peaks were observed on both Au and Cu. On Au the underpotential deposition (UPD) peak potential corresponded to a free energy of adsorption of approximately 17 kcal/mol; on Cu two peaks were observed for the UPD, one corresponding to a free energy of 5 kcal/mol, the second corresponding to a free energy of 7 kcal/mol. A well defined UPD peak was not observed on Pt (however, the UPD may have formed). The addition of rhodamine-B also shifted the UPD and bulk peaks to more cathodic potentials.

Anodic dissolution peaks, at potentials anodic to that of the Pb bulk stripping peak were observed on both Pt and Au and are believed to have been due to electrochemical surface alloys; more stripping peaks appeared in the cyclic voltammogram than deposition peaks, and integration indicated that the charge involved in these peaks was in excess of that required for a single monolayer.

Introduction

Few fundamental studies have been conducted to elucidate the role of organic plating additives at the cathode surface during electrodeposition (2). In this dissertation, spectroscopic ellipsometry and cyclic voltammetry have been used in a novel insitu investigation of the role of a strongly light absorbing adsorbate (rhodamine-B dye) on Pb electrodeposition. The electrochemical basis for selecting these materials is discussed in this chapter.

Pb deposition on Cu was investigated because Pb is known to form a well defined underpotential deposit (UPD) on this substrate (3); Cu is stable to dissolution at the potential and pH where Pb is deposited (4). The optical constants of Pb and Cu are also dramatically different; Cu has an electronic transition in the visible range whereas Pb does not (5). Pb on Au was studied for similar electrochemical (6) and optical (7) reasons. Pt as a substrate was chosen because optical studies of dye adsorbates on this metal were found in the literature (8,9).

Dyes were chosen for investigation because they have characteristic absorption bands which allow them to be easily detected and identified by spectroscopic ellipsometry, even when present on the electrode in submonolayer amounts. Furthermore, dyes are usually surface active.

Prior to a detailed study by spectroscopic ellipsometry, a dye had to be selected which exhibited significant inhibitory effect during the electrodeposition of Pb on suitable substrates; these candidate model inhibitors also had to absorb light in the visible range accessible to the optical instrumentation. Here, the electrochemical screening tests performed during the selection of this inhibitor are reviewed. The principal experimental technique used was cyclic voltammetry. Pb was deposited on Pt, Au, and Cu substrates from 5 millimolar $Pb(NO_3)_2$, 1 M $NaClO_4$, at pH 3, in the presence of various organic dyes which served as deposition inhibitors, some having greater effects than others.

Though many organic additives for plating and corrosion protection have been studied and reported in the literature (10-16), none met the optical criteria of having a characteristic absorption in the spectral

range of interest (370 to 720 nm). However, dyes adsorbed to electrode surfaces have been studied (17,18), but not in the context of their role as metal deposition inhibitors. These compounds, like many industrial inhibitors (19), were found to be reduced on the electrode surface. Because of the technical advantage of stable inhibitors (20) we had originally hoped to find a model inhibitor that did not undergo electroreduction during metal depostion, but stability was not essential since reducible inhibitors are used in practice (2). Because of the lack of available literature on candidate inhibitors with the desired spectroscopic features, we systematically screened a large number of laser dyes and indicators (21-26). Attention was focused on laser dyes specifically since they are available commercially in high purity at relatively low cost (27). Compounds were selected which were cationic, anionic, and neutral, representing a variety of structural types (28).

Experimental Procedure

The principal experimental technique was cyclic voltammetry. Studies on Pt electrodes were conducted in a stagnant cell (180 ml glass beaker under nitrogen). The electrodes were rectangular (5.080 cm x 0.780 cm x 0.061 cm) with a length of 1.8 cm (35% of the total area) subm in electrolyte. Prior to use, the electrodes were polished with fine grit emery cloth and boiled in HNO_3, followed by several rinses with distilled water. Both cathode and anode were Pt; the anode oxidized (turned brown) during cyclic voltammetry.

The supporting electrolyte was 1 M $NaClO_4$ acidified to a pH of about 3.00 using dilute $HClO_4$ (measured by a digital pH meter, Corning Model #130). The commercial source for the $Pb(NO_3)_2$ and $HClO_4$ was Mallinckrodt (#5744 lot #KHSM and #2766 lot #LLMN, respectively) and the source for the $NaClO_4$ was Fisher Scientific (S-360). The Pb^{++} concentration was fixed at 5 millimolar by addition of $Pb(NO_3)_2$ salt. The nitrate salt was used because of its high solubility; the nitrate anion has little effect on the electrodeposition process. The solvent was distilled, deionized water (10 megohm). Dye concentrations used during the screening tests with the Pt substrate were 2.5 micromolar; dye concentrations used for subsequent experiments with Au and Cu substates were 10 micromolar.

A Pine Instrument Company Model RDE 3 potentiostat was used to drive the electrochemical cell from +0.2 to -0.8 V (Ag/AgCl reference electrode, Corning Cat. No. 476067) at a sweep rate of 2 V/min. Data were recorded on a Hewlett-Packard Model 7044A x-y recorder with time base.

Cell temperature was monitored by thermometer, and remained between 24 and 25 degrees Centigrade.

Dyes were added from prepared solutions by a calibrated dropper (1 drop per 0.05 ml). Dye solutions were prepared so that 10 drops added to 250 ml of electrolyte would result in a net dye concentration of 1 micromolar. By transferring dyes in disolved form, a high degree of accuracy was possible in controlling dye concentrations; weighing and transferring such small quantities of dyes in solid form would result in

large errors.

Experiments on Au electrodes were performed in similar fashion. However, experiments performed on single-crystal Cu electrodes used another stagnant cell discussed in detail elsewhere (29). Here too the electrode was oriented vertically.

Terminology

Before proceeding, terminology used in qualitative descriptions of results are defined. Terminology discussed here is related to ionicity, acidity, solubility and solution color, and inhibitory effect.

Dyes are considered to be either cations or anions if they have inorganic counter ions; they are considered neutral if they have no inorganic counter ions.

Here, acidic implies a 1 M $NaClO_4$ solution with a pH of 3 or less; neutral implies a pH of between 4 and 6 (5.5); and basic implies a pH of greater than 9.

As described in the "Experimental" section, dyes were transferred in disolved form. The stock dye solutions were prepared so that 10 drops of the solution (0.05 ml per drop) added to 250 ml of electrolyte would result in a net dye concentration in the electrolyte of 10 micromolar. The stock solutions were prepared in 20 ml volumes by adding the necessary weight of solid dye. In some instances, the dyes were "completely soluble" in neutral electrolyte, whereas the electrolyte would have to be made basic in order to disolve the added dyes. If precipitates appeared in the electrolyte and if there was

slight color change of the liquid, the dye was considered to be "partially soluble." If essentially all the added dye precipitated and if there was no color in the liquid, the dye was considered to be "insoluble." Colors of the stock solutions were noted.

Inhibitory effects on Pb (on Pt) deposition were considered to be "weak" if the dye induced shift in the bulk deposition peak in the cyclic voltammogram was 25 mV or less, mild if the shift was between 40 and 60 mV, and strong if the shift exceeded 60 mV. Cationic, neutral and anionic species having strong, mild, and weak inhibitory effects are shown in Fig. 1.

Results and Discussion: Dyes

I. Cationic Dyes

Rhodamine-B chloride (Eastman #14352, lot #A6A) has a formula weight of 479 and has an absorption maximum at about 554 nm. The stock solution required 4.79 mg of dye per 20 ml of neutral 1 M $NaClO_4$; the solution color was reddish-pink and the dye was completely soluble. As the solution becomes acidic, the color becomes magenta. The inhibitor effect was very strong (Fig. 2, 125 mV).

Gentian-violet or crystal-violet (MCB E-10H-12, 1-79) has a formula weight of 408. The stock solution required 4.08 mg per 20 ml of neutral 1 M $NaClO_4$; the solution was dark purple (violet) and the dye was completely soluble. The inhibitor effect was mild (Fig. 3, 40 mV).

Both rhodamine-B and gentian-violet have chloride as a counter ion. It was found that chloride alone cannot account for the large inhibitor effect of rhodamine-B (Fig. 4, 25 mV). Fig. 4 is a cyclic voltammogram with NaCl added.

Rhodamine-116 perchlorate (Eastman #14937, lot #A6X) has a formula weight of 459 and an absorption maximum at about 525 nm. The stock solution required 4.59 gm per 20 ml of neutral 1 M $NaClO_4$; the solution was reddish-orange and the dye only partially soluble. By making the stock solution basic, the color changed to bright orange and the dye became completely soluble. The inhibitor effect was mild (Fig. 5, 50 mV).

II. Neutral Dyes

Fluorescein (Baker 5-M422, #744355) has a formula weight of 332 and an absorption maximum at about 501 nm. The heart of the fluorescein molecule is very similar to that of rhodamine-B and rhodamine-116. The stock solution required required 3.32 mg per 20 ml neutral 1 M $NaClO_4$; the solution was almost colorless and the dye only partially soluble. By making the stock solution basic, the color changed dramatically to a bright yellowish-green and the dye became completely soluble. The inhibitor effect was mild to strong (Fig. 6, 60 mV).

Cresol-red (MCB) has a formula weight of 382. The stock solution required 3.82 mg of dye per 20 ml of neutral 1 M $NaClO_4$; the dye was only partially soluble. By making the stock solution basic, the color changed to magenta and the dye became completely soluble. The inhibitor

effect was mild (Fig. 7, 45 mV).

m-Cresol-purple (Eastman #2118, lot #A7X) has a formula weight of 382. The stock solution required 3.82 mg per 20 ml of neutral 1 M $NaClO_4$; the dye was only partially soluble. By making the stock solution basic, the color changed to dark purple (violet) and the dye became completely soluble. The inhibitor effect was mild (Fig. 8, 50 mV).

Coumarin-343 (Eastman #14943, lot #A7B) has a formula weight of 285 and an absorption maximum at about 446 nm. The stock solution required 2.85 mg per 20 ml of neutral 1 M $NaClO_4$; the dye was only partially soluble and the stock solution colorless. By making the stock solution basic, the color changed to light yellow, still almost colorless, and the dye became completely soluble. The inhibitor effect was mild (Fig. 9, 40 mV).

Methyl-red (MCB E-10-J-13, 11-79) has a formula weight of 269. The stock solution required 2.69 mg per 20 ml of neutral 1 M $NaClO_4$; the dye was completely soluble and the solution color was yellow. The inhibitor effect was very weak (Fig. 10, 10 mV).

Coumarin-30 (Eastman #11986, lot #C5B) has a formula weight of 347 and an absorption maximum at about 413 nm. The stock solution required 3.47 mg per 20 ml of neutral 1 M $NaClO_4$; the dye was insoluble and the solution colorless. By making the solution basic, the color changed to light yellow, still almost colorless, and the dye became partially soluble. The inhibitor effect could not be determined with any degree of certainty.

Coumarin was colorless and insoluble in neutral 1 M $NaClO_4$; it was still colorless in basic solution and was only partially soluble. The inhibitor effect could not be determined with any degree of certainty.

III. Anionic Dyes

Methyl-orange (MCB B-3F-25) has a formula weight of 327. The stock solution required 3.27 mg per 20 ml of neutral 1 M $NaClO_4$; the dye was completely soluble and the color of the solution was bright orange. The inhibitor effect was weak (Fig. 11 and 12, 25 mV).

Ethyl-orange (Aldrich, 19957-7, lot #011987) has a formula weight of 333. The stock solution required 3.33 mg per 20 ml of neutral 1 M $NaClO_4$; the dye was completely soluble and the color of the solution was bright orange. The inhibitor effect was weak (Fig. 13, 25 mV).

3',3"-bis((N,N-bis(carboxy)amino)methyl)-thymolsulfonephthalein pentasodium salt, an indicator (Eastman #8068), has a formula weight of 867. The stock solution required 4.33 mg per 20 ml of neutral 1 M $NaClO_4$; the indicator was completely soluble and the solution turned dark brown. The inhibitor effect was mild (Fig. 14, 45 mV).

IV. Classification of Dyes Studied

Dyes can be classified by their ionicity as implied above. The cationic (+) dyes studied were rhodamine-116, rhodamine-B, and gentian violet. The anionic (-) dyes were methyl-orange, ethyl-orange, and the phthalein pentasodium salt. Neutral (0) compounds were fluorescein, coumarins (343, 30, etc.), cresol-red, cresol-purple, and methyl-orange.

Classification by similarities in molecular structure is also possible. Rhodamine-B, rhodamine-116, and fluorescein have similar structures (referred to here as rhodamine-type structures). Methyl-orange and ethyl-orange are azo-type compounds; the coumarins are structurally similar, as are the cresol dyes.

The dyes can be classified as either neutral or base soluble. Neutral-soluble dyes include rhodamine-B, methyl-orange, methyl-red, gentian-violet, ethyl-orange, and phthalein pentasodium salt. Base-soluble dyes include the coumarins, fluorescein, rhodamine-116, cresol-red, methylene-violet (Fig. 15), and cresol-purple.

The stock solutions covered a beautiful range of colors, yellows, oranges, violet, green, magenta, red, and brown. Coumarins were colorless to light yellow; methyl-red was yellow; fluorescein was bright yellowish-green; methyl-orange, rhodamine-116, and ethyl-orange were all bright orange; methylene- violet, gentian-violet, and cresol-purple were all violet; and rhodamine-B and cresol-red were red to magenta. These colors were all at the pH of greatest solubility.

Probably the most useful classification here is by inhibitor effect, either weak, mild, or strong. There was clearly only one strong inhibitor, rhodamine-B chloride (125 mV, +); all others were either mild or weak. Mild inhibitors include fluorescein (60 mV, 0), rhodamine-116 (50 mV, +), m-cresol-purple (50 mV, 0), cresol-red (45 mV, 0), phthalein pentasodium salt (45 mV, -), gentian-violet (40 mV, +). Weak inhibitors were methyl-orange (25 mV, -), ethyl-orange (25 mV, -), and methyl-red (10 mV, 0).

V. Differences in Rhodamine-type Molecules

It is interesting to note that rhodamine-B (strongest inhibitor) is similar in structure to both fluorescein and rhodamine-116 (both mild inhibitors); this difference was shown not to be due to differences in counter ions (i.e., the presence of chloride). The only difference between rhodamine-B and rhodamine-116 which could account for their diffenences in inhibitory effect must be related to the hydrocarbon chain length of substituted groups on the cationic tertiary amine. If these compounds are adsorbed on the cathode as cations (cationic amine bonded to the electrode), the attached hydrocarbon chains would sterically block adjacent surface sites. More sites are blocked by the longer substituted chain (on rhodamine-B); this increased blocking would greatly decrease the Pb current density to the surface, until the dye becomes reduced and displaced. Perhaps Fluorescein is bonded to the suface via a (C-O-M) bond.

Cyclic voltammetry of rhodamine-B on Pt in the absence of Pb^{++} indicates the irreversible electroreduction at potentials cathodic to 0 mV (Ag/AgCl ref.) may occur (Fig. 16). This belief is further supported by studies performed on Au discussed subsequently.

Results and Discussion: Substrates

I. Platinum

Several cathodic and anodic peaks were observed in the cyclic voltammogram for Pb deposition on polycrystaline Pt which are believed

to have been due to underpotential, bulk, and alloy formation. During the cathodic potential sweep (Figs. 2 through 15, broken curves) the bulk deposition peak was centered at -500 mV (Ag/AgCl reference) and had a shoulder at -450 mV, perhaps due to either formation of an alloy or the UPD. During the anodic sweep the bulk Pb stripping peak was centered at -325 mV; a smaller peak observed near -250 mV may have been the Pb UPD; the broad peak between -100 and 0 mV may have been due to the stripping of an alloy phase.

II. Gold

Pb cyclic voltammetry on polycrystalline Au electrodes is shown in Fig. 17; the effect of rhodamine-B on Pb deposition was as strong with Au substrates as with Pt substrates (Figs. 18.a-b). There were cathodic peaks at -175 mV and -450 mV, believed have been the Pb UPD and bulk deposit, respectively. There were more anodic than cathodic peaks; there were peaks at -350 mV and -200 mV believed to have been the Pb bulk deposit and an alloy of Pb and Au, respectively. The shoulder on the -200 mV peak (at -150 mV) is believed to have been due to the UPD. Rhodamine-B is reduced on Au, as illustrated in Figs. 19.a-19.c.

III. Copper

Similar data for Pb deposition on Cu(111) with and without rhodamine-B were obtained (Figs. 20.a and 20.b). It is interesting to note that in the absence of rhodamine-B two UPD peaks were seen (Fig. 21.a); a 2 micromolar addition gave a cyclic voltammogram with only one prominent UPD peak, which was shifted to more cathodic potentials. The

UPD peak shift showed a relaxation phenomenon with repeated potential cycling, as does the bulk peak. In the absence of rhodamine-B and on polycrystalline Cu cathodic peaks were observed at -250, -290, and -430 mV, and are believed to have been due to two UPD deposits and the bulk deposit, respectively. The two UPD deposits may have been due to electrosorption on two different types of surface sites. Anodic peaks were observed at -330, -220, and -200 to 0 mV, and are believed to have been due to bulk, UPD, and alloy Pb phases, respectively (Fig. 21.b).

IV. Free Energies of Adsorption on Cu and Au

Using the methods described in Chapter 5 and cyclic voltammetry data can be used to infer the Gibbs free energy of adsorption. The Pb UPD peaks on Cu without rhodamine-B appeared at potentials (half-coverage under-potentials of 115 and 155 mV) corresponding to free energies of 5.3 and 7.1 kcal/mol. In the presence of rhodamine-B, making the same assumptions, the single peak would imply a free energy of about 4.6 kcal/mol. It is interesting to note that only one UPD peak was reported in the literature (41); this may have been due to impurities (which were introduced here intentionally). The results for the Au substrate imply a much higher free energy of adsorption, about 17.1 kcal/mol. The tendency of Pb and Au to alloy may be related to this very negative free energy (compared to that of Cu).

V. Coulombic Efficienies of Pb Deposition on Cu

Potential step experiments were performed (Figs. 22.a through 22.c) to determine the coulombic efficiency for Pb deposition from the 5

millimolar Pb(NO3)2 solution. Efficiency was measured by stripping the deposit, comparing the charge recovered by stripping to that deposited. Efficiences below -600 mV were greater than 90%. Later studies gave even higher coulombic efficiences and did not exhibit the dramatic decrease in efficiencey with pulse length. The decreasing efficiency with increasing potential was probably due to greater rates of water decomposition at the higher potentials. At long deposition times (increasing pulse length) the Pb^{++} concentration at the electrode surface probably became depleted, water decomposition enhanced, and efficiency lowered.

Conclusions

Originally, 30 cationic, anionic, and neutral dyes and indicators were chosen for screening, based upon literature references and availability. Of these, 14 were investivaged in detail, and it was found that rhodamine-B chloride induced the largest overpotential for lead deposition (125 mV cathodic shift).

This -125 mV shift of the cathodic depostion peak occured during the first potential cycle; after subsequent cycling the peak potential was the same as prior to rhodamine-B addition to the electrolyte. After allowing the cell to remain at open circuit for several minutes, the cathodic shift (overpotential) reappeared (referred to as a relaxation phenomena). From cyclic voltammetry of rhodamine-B in the absence of Pb^{++}, it is believed that rhodamine-B became reduced and depleted from the electrode surface during the first potential cycle, hence its

inhibitory effect disappeared. At open circuit, the surface was probably repopulated with adsorbed rhodamine-B, and the inhibitor action resumed.

Prominent underpotential deposition peaks were observed on both Au and Cu. On Au the underpotential deposition (UPD) peak potential corresponded to a free energy of adsorption of approximately 17 kcal/mol; on Cu two peaks were observed for the UPD, one corresponding to a free energy of 5 kcal/mol, the second corresponding to a free energy of 7 kcal/mol. A well defined UPD peak was not observed on Pt (however, the UPD may have formed over a broader potential range). The addition of rhodamine-B also shifted the UPD and bulk peaks to more cathodic potentials.

Dissolution peaks, at potentials anodic to that of the Pb bulk stripping peak, were observed on both Pt and Au and are believed to have been due to electrochemical surface alloys; more stripping peaks appear in the cyclic voltammogram than cathodic peaks, and integration indicated that the charge involved in these peaks was in excess of that required for a single monolayer.

References

1. Farmer, J. C., Muller, R. H., "Effect of Rhodamine-B on Pb Electrodeposition on Ag and Cu," Electrochem. Soc. Meeting, San Francisco, CA, May 8-13, 1983 (this thesis, Chapter 6).

2. Harrison, J. A., Thirsk, H. R., "The Fundamental of Metal Deposition," ELECTROANALYTICAL CHEMISTRY, Vol. 5, Bard, A. J., ed., Marrel Dekker, New York, 1971, p. 139.

3. Schmidt, E., Gygax, H. R., "Chronoamperometrische Untersuchung Metallischer Monoschichten," J. Electroanal. Chem., 12, 300 (1966).

4. See 3.

5. Hass, G., Hadley, L., "Optical Properties of Metals," AMERICAN INSTITUTE OF PHYSICS HANDBOOK, 2nd ed., Gray, D. E., ed., McGraw-Hill, New York, 6-103 to 6-122 (1971).

6. Adzic, R., Yeager, E., Cahan, B. D., "Optical and Electrochemical Studies of Lead on Gold Evaporated and Single-Crystal Electrodes," J. Electrochem. Soc., 121, 474 (1974).

7. Aspnes, D. E., Kinsborn, E., Bacon, D. D., "Optical Properties of Gold Electrode Surface Covered with Metal Monolayer," Surf. Sci., 47, 622 (1975).

8. Plieth, W. J., Gruschinske, P., Hensel, H. J., "Electronic Changes of Light Absorption by the Electric Field of the Electrolytic Double Layer," Ber. Bunsenges. Phys. Chem. 82, 615 (1978).

9. Schmidt, S, Reich, R., Ber. Bunsenges. Phys. Chem., 76, 599 (1972).

10. Nechaev, E. A., Shaidullin, R. Ya., "Effect of Organic Materials on Cadmium Electrodepostion from Acidic Solutions," Soviet Electrochem.,

11. Pyzik, G., Lipkowski, J., "On the Mechanism of Ion Transfer Across the Monolayers of Organic Surfactants. The Mechanism of Cu(II) Deposition at Hg Electrodes Covered by Monolayers of Aliphatic Alcohols," J. Electro. Anal. Chem., 123, 351 (1981).

12. Sarma, R. L., Nageswar, S., "Electrodeposition of Copper on the Copper (100) Face in the Presence of 2-Mercaptoethanol," J. Appl. Electrochem., 12, 329 (1982).

13. Loshkarev, M. A., Danilov, F. I., "Individual and Joint Adsorption of the Components of Brightner Composition DKhTI-102 For Zinc Plating Electrolytes," Soviet Electrochem., 16, 857 (1980).

14. Shukla, R. K., Jha, S. K., Srivastava, S. C., "Studies of the Effects of Addition Agents on the Electrodepostion of Ni-Co-Zn Alloy from Borate Bath," Surf. Tech., 17, 157 (1982).

15. Dinnappa, R. K., Mayanna, S. M., "Benzoic Acid and Substituted Benzoic Acid and Substituted Benzoic Acid as Interfacial Corrosion Inhibitors for Copper in $HCLO_4$," J. Appl. Electrochem., 11, 11 (1981).

16. Hobbins, N. D., Roberts, R. F., "An Ellipsometric Study of Thin Films Formed on Copper By Aqueous Benzotriazole and Benzimidazole," Surf. Tech., 9, 235 (1979).

17. Plieth, W. J., Gruschinske, P., "Modulations-Reflexions-Spectroskopie zur Untersuchung der Kinetik der Methyleneblau-Redukton," Berichte der Bunsen-Gesellschaft fur Physikalische Chemie (Fruher Zeitschrift fur Elektrochemie) 76, 486 (1972).

18. Plieth, W. J., Naegele, K., "Eine Mehrfachreflexionszelle zur Optischen Untersuchung von Elektrodenprozessen," Electrochimica Acta, 20, 421 (1976).

19. See 2.

20. Zavgorodnyaya, E. F., Lubyanova, V. I., Degtyareva, Z. E., "Behavior of Zinc Oxide Cathodes in Alkaline Solutions Containing Certain Organic Substances," Soviet Electrochem., 16, 867 (1980).

21. Strome, F. C., "The Dye Laser," Eastman Organic Chemical Bulletin, Eastman-Kodak, Rochester, NY 14650, Vol. 46, No. 2 (1974).

22. Webb, J. P., Webster, F. G., Plourde, B. E., "Sixteen New Infrared Laser Dyes Excited by a Simple Linear Flashlamp," Eastman-Kodak, Rochester, NY 14650, Vol. 46., No. 3 (1974).

23. "Dyes for Lasers," Data Release, Eastman-Kodak, Rochester, NY 14650 (1974).

24. Snavely, B. B., "Flashlamp-Excited Organic Dye Lasers," Proceed. IEEE, 57, 1374 (1969).

25. Gacoin, P., Flamant, P., "High Efficiency Cresyl Violet Laser," Opt. Comm., 5, 351 (1972).

26. Bass, M., Deutsch, T. F., Weber, M. J., "Dye Lasers," Raytheon Co., Waltham, Massachusetts (1971).

27. EASTMAN ORGANIC CHEMICALS CATALOG, No. 50, Eastman-Kodak, Rochester, NY 14650, 1980-81, pp. 59, 185.

28. Schwartz, A. M., Perry, J. W., SURFACE ACTIVE AGENTS, THEIR CHEMISTRY AND TECHNOLOGY, Interscience, New York, 1949, pp. 14-17, 151-157, 468-471.

29. Farmer, J. C., Muller, R. H., "Nucleation of Pb Electrodeposits on Ag and Cu," Electrochem. Soc. Meeting, San Francisco, CA, May 8-13, 1983 (this thesis, Chapter 5).

Figures

1. Examples of three different inhibitors studied, representing cationic, neutral, and anionic species. The absorption maximum wavelength and shift in Pb deposition peak potential are given for each inhibitor.
2. The effect of rhodamine-B on Pb deposition with a Pt substrate.
3. The effect of gentian-violet on Pb deposition with a Pt substrate.
4. The effect of chloride anion on Pb deposition with a Pt substrate.
5. The effect of rhodamine-116 on Pb deposition with a Pt substrate.
6. The effect of fluorescein on Pb deposition with a Pt substrate.
7. The effect of cresol-red on Pb deposition with a Pt substrate.
8. The effect of cresol-purple on Pb deposition with a Pt substrate.
9. The effect of coumarin-343 on Pb deposition with a Pt substrate.
10. The effect of methyl-red on Pb deposition with a Pt substrate.
11. The effect of methyl-orange on Pb deposition with a Pt substrate.
12. The effect of methyl-orange on Pb deposition with a Pt substrate. A replicate experiment of that performed and shown in Fig. 11.
13. The effect of ethyl-orange on Pb deposition with a Pt substrate.
14. The effect of 3',3"-bis((N,N-bis(carboxymethyl)amino)methyl)-thymolsulfonephthalein pentasodium salt on Pb deposition with a Pt substrate.

15. The effect of methylene-violet on Pb deposition with a Pt substrate.

16. The electroreduction of rhodamine-B on Pt substrate in the absence of Pb^{++}.

17. Cyclic voltammetry of Pb on Au substrate at different sweep rates illustrating the formation of the underpotential and bulk deposits and showing dissolution of additional phases believed to be alloys. Numbers indicate differences in sweep rate in V/min.

18.a The effect of rhodamine-B on Pb deposition with Au substrate.

18.b Repopulation of electrode surface with rhodamine-B after relaxation period at open circuit; a continuation of experiment shown in Fig. 18.a.

19.a Electroreduction of rhodamine-B (200 micromolar) on Au electrode in the absence of Pb^{++} at potential sweep rates of 2, 4, and 8 V/min.

19.b Electroreduction of rhodamine-B on Au electrode in the absence of Pb^{++} at a potential sweep rate of 4 V/min and two different concentration levels, 200 and 400 micromolar.

19.c Electroreduction of rhodamine-B (400 micromolar) on Au electrode in the absence of Pb^{++} at a potential sweep rate of 4 V/min.

20.a The effect of rhodamine-B on Pb deposition with a Cu(111) substrate during the first potential cycle. The solid line represents a cyclic voltammogram without rhodamine-B; the broken line is in the presence of rhodamine-B.

20.b The effect of rhodamine-B on Pb deposition with a Cu(111) substrate after multiple potential cycles.

21.a Cyclic voltammetry of Pb on a polycrystaline Cu substrate at 2 V/min sweep rate showing two UPD peaks.

21.b Digital coulommetry of Pb on a polycrystaline Cu substrate for multiple potential cycles.

22.a Digital coulommetry during potentiostatic step experiments, Pb deposition on polycrystaline Cu.

22.b Accumulated charge from experiments of 22.a plotted against step potential for two step durations, 10 and 30 seconds.

22.c Coulombic efficiency from experiments of 22.a plotted against step potential for two step durations, 10 and 30 seconds.

CATIONIC
555 NM
125 MV

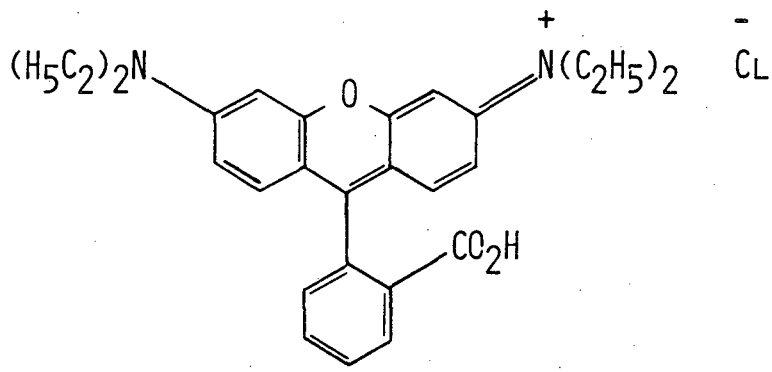

RHODAMINE-B CHLORIDE

NEUTRAL
501 NM
60 MV

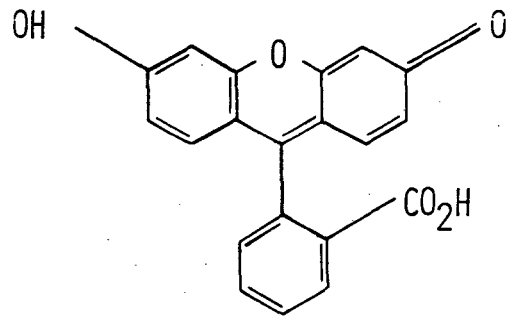

FLUORESCEIN

ANIONIC
470 NM
25 MV

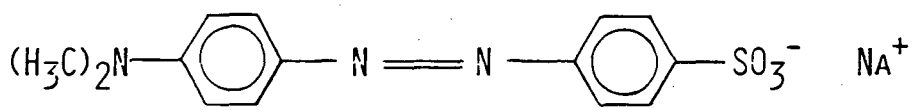

METHYL ORANGE

EXAMPLES OF MODEL INHIBITORS USED

XBL 833-8503

Fig. 1

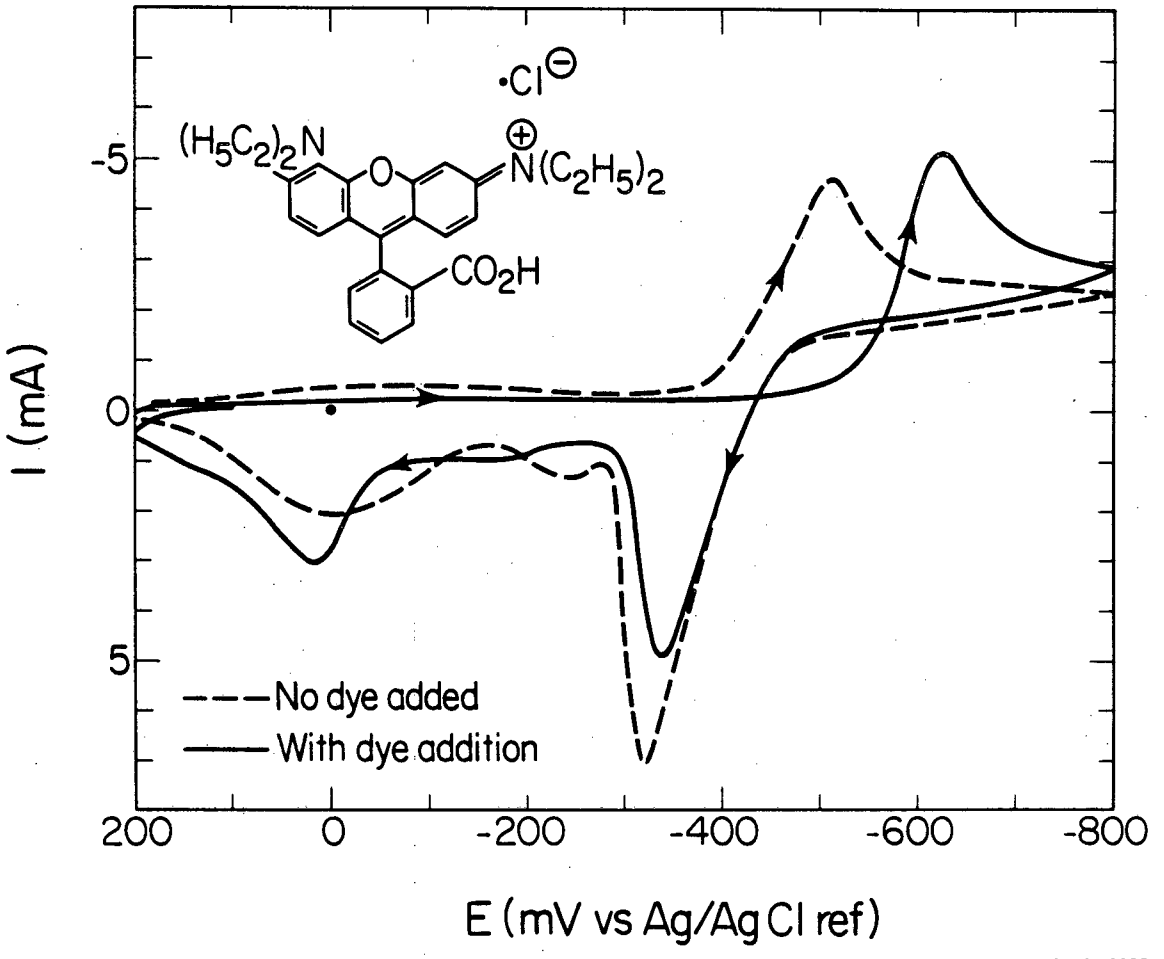
·Cl⊖
(H5C2)2N
⊕N(C2H5)2
CO2H
-5
0
5
I (mA)
No dye added
With dye addition
200
0
-200
-400
-600
-800
E (mV vs Ag/Ag Cl ref)
XBL 8212-12388

Fig. 2

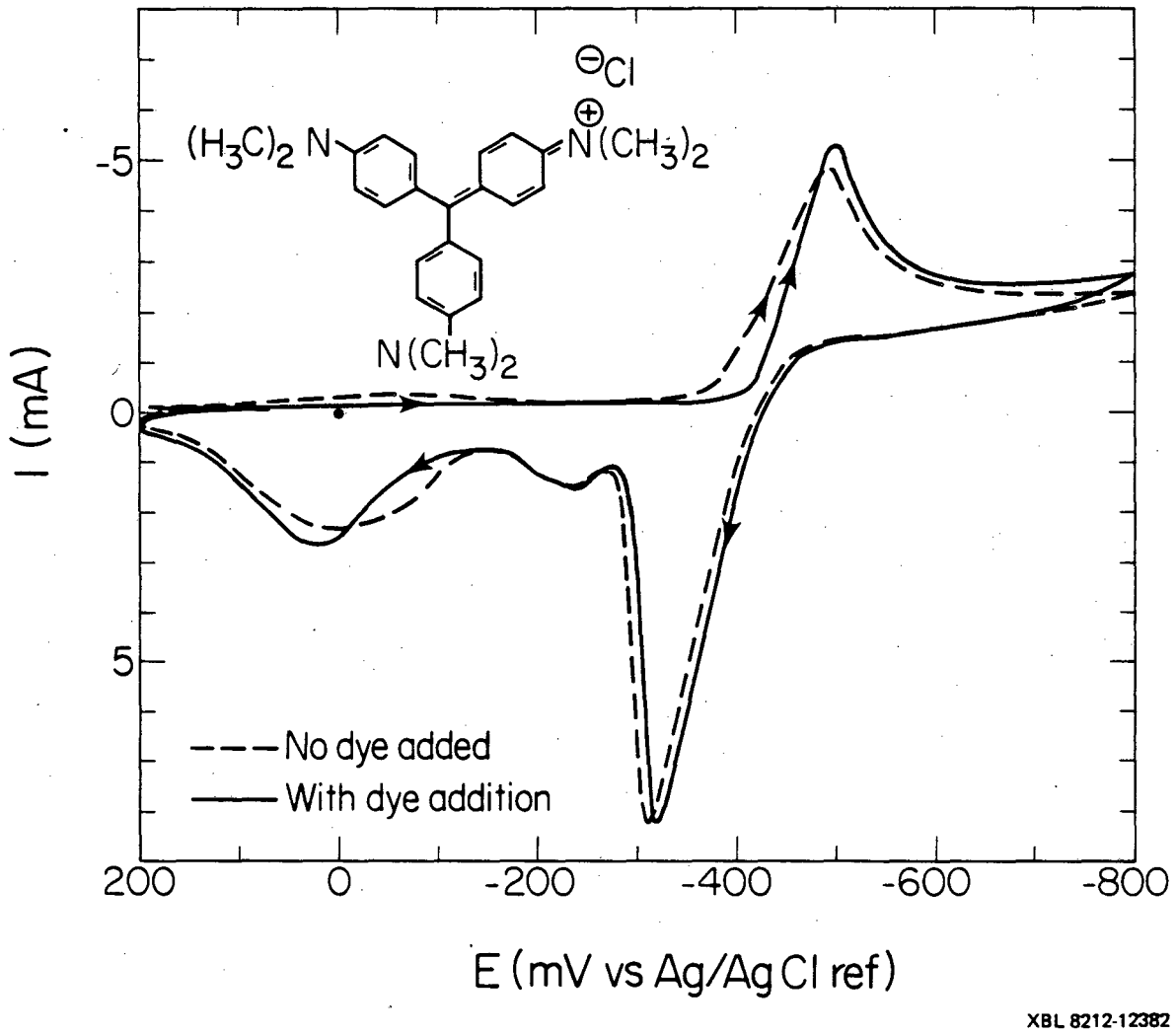
$\ominus$Cl
$\oplus$
$(H_3C)_2$ N
N$(CH_3)_2$
N$(CH_3)_2$
-5
0
5
I (mA)
200
0
-200
-400
-600
-800
E (mV vs Ag/Ag Cl ref)
No dye added
With dye addition
XBL 8212-12382

Fig. 3

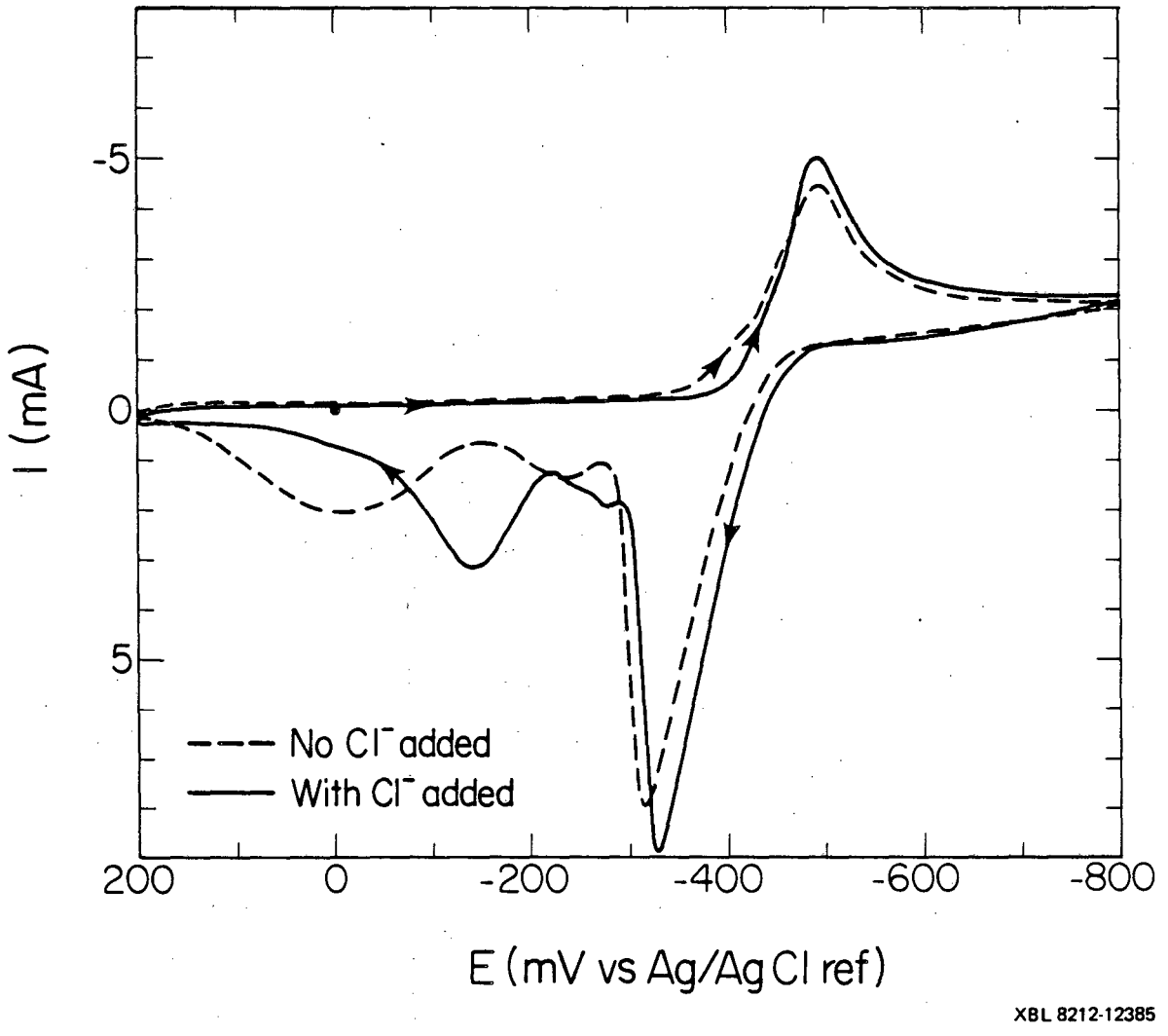
-5
0
5
I (mA)
200
0
-200
-400
-600
-800
E (mV vs Ag/Ag Cl ref)
No Cl⁻ added
With Cl⁻ added
XBL 8212-12385

Fig. 4

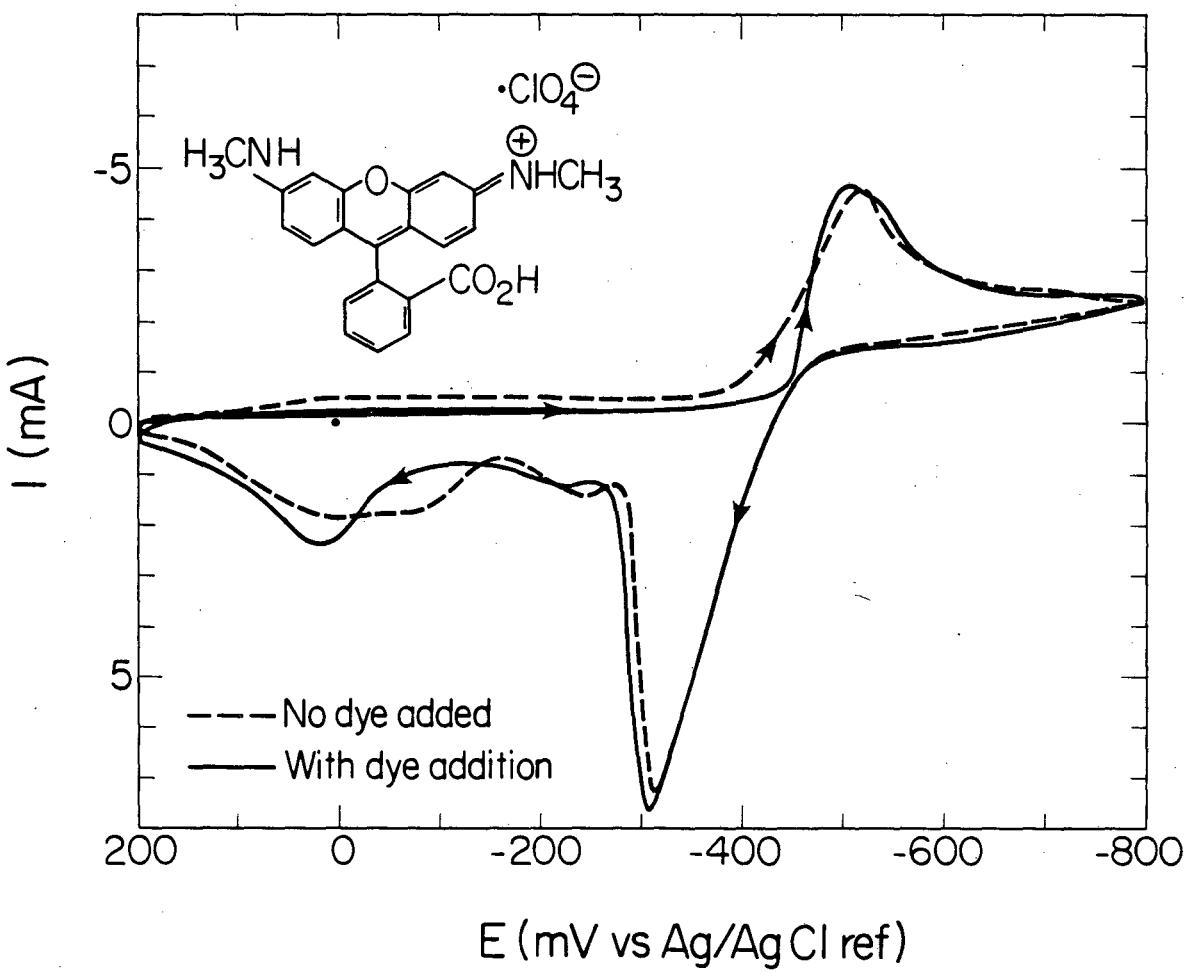
·ClO4⊖
H3CNH
⊕
NHCH3
CO2H
-5
0
5
I (mA)
No dye added
With dye addition
200
0
-200
-400
-600
-800
E (mV vs Ag/Ag Cl ref)
XBL 8212-12387

Fig. 5

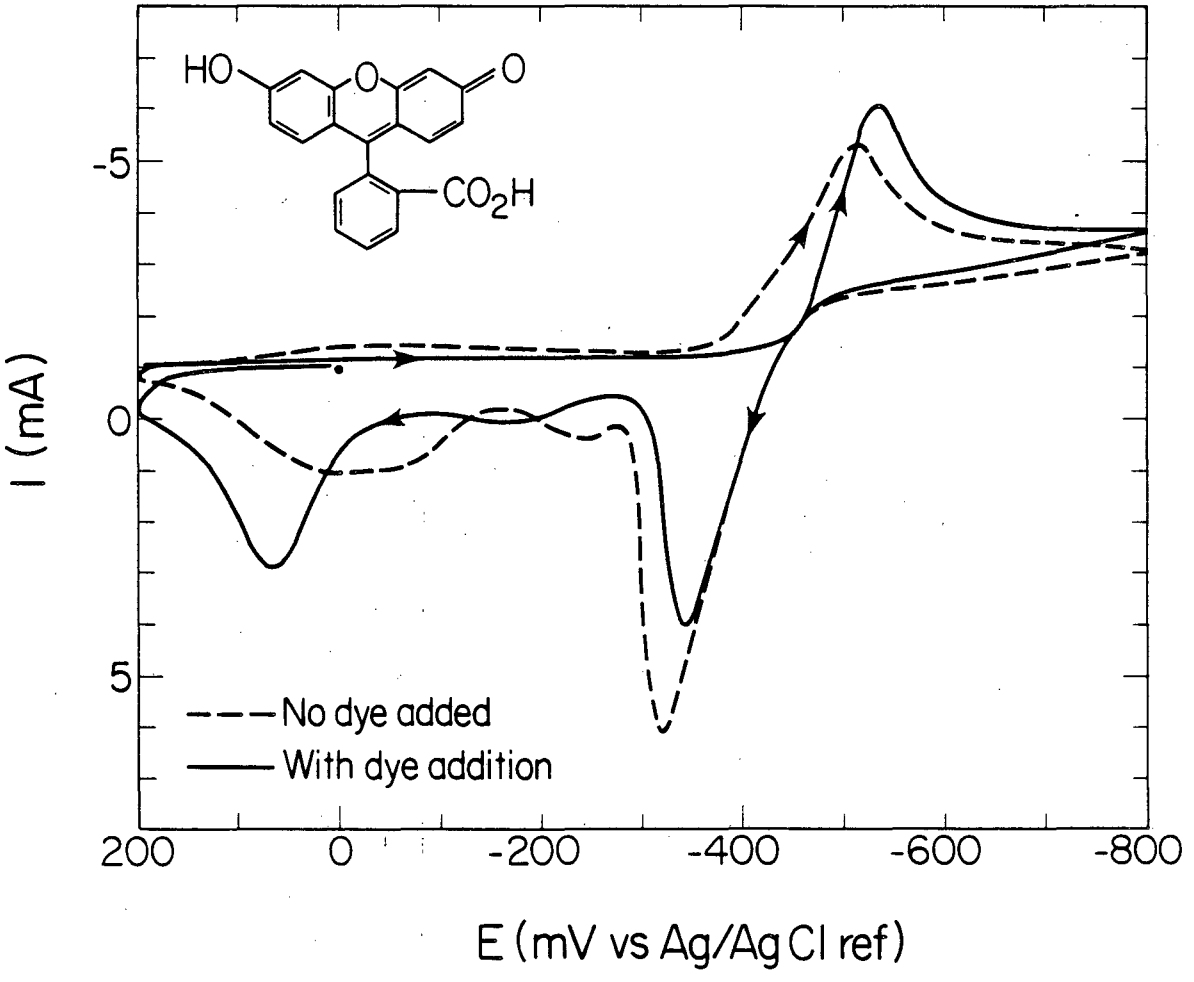
HO
O
O
CO_2H
-5
0
5
I (mA)
No dye added
With dye addition
200
0
-200
-400
-600
-800
E (mV vs Ag/Ag Cl ref)
XBL 8212-12386

Fig. 6

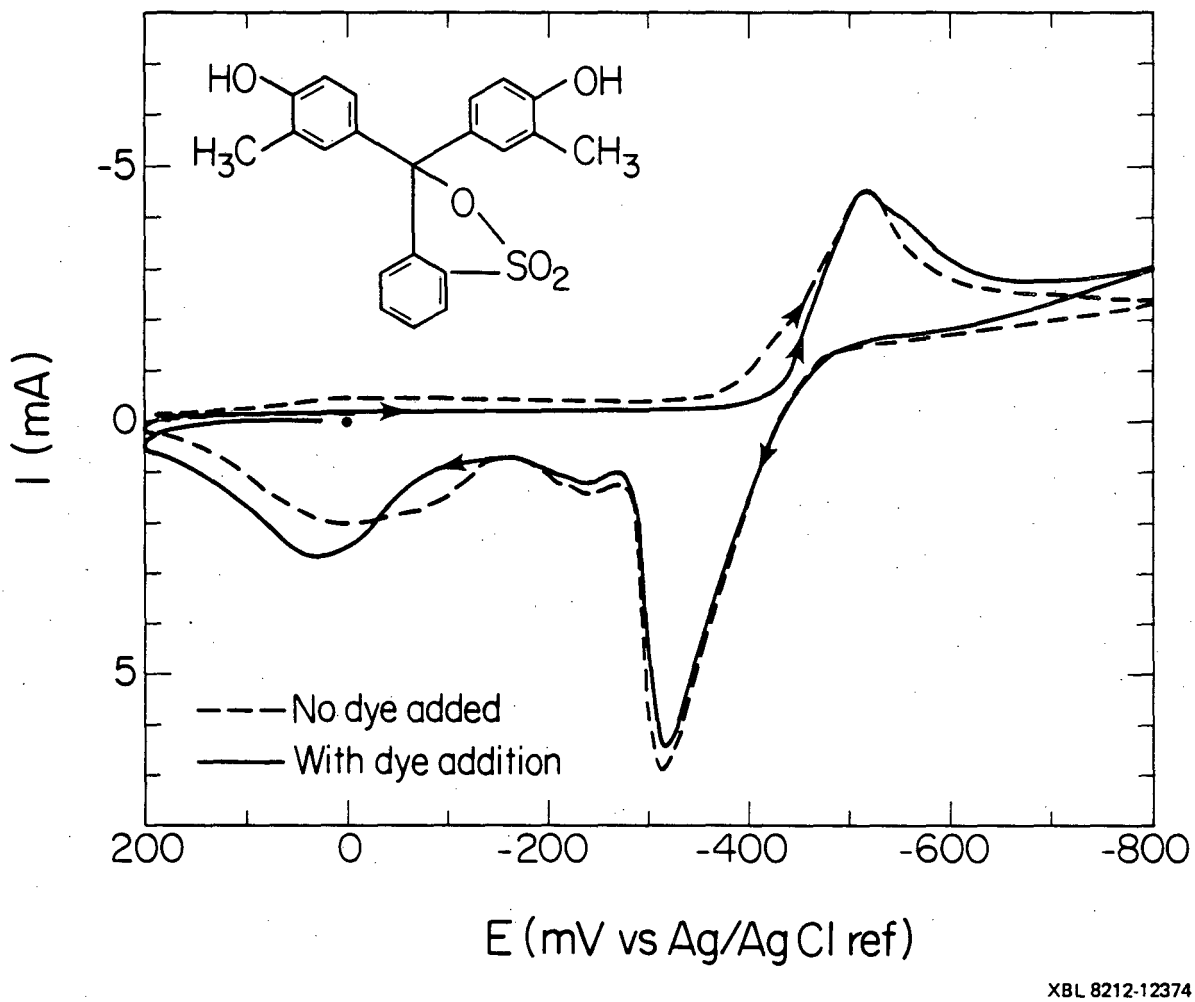
HO
OH
H_3C
CH_3
O
SO_2
-5
0
5
I (mA)
No dye added
With dye addition
200
0
-200
-400
-600
-800
E (mV vs Ag/Ag Cl ref)
XBL 8212-12374

Fig. 7

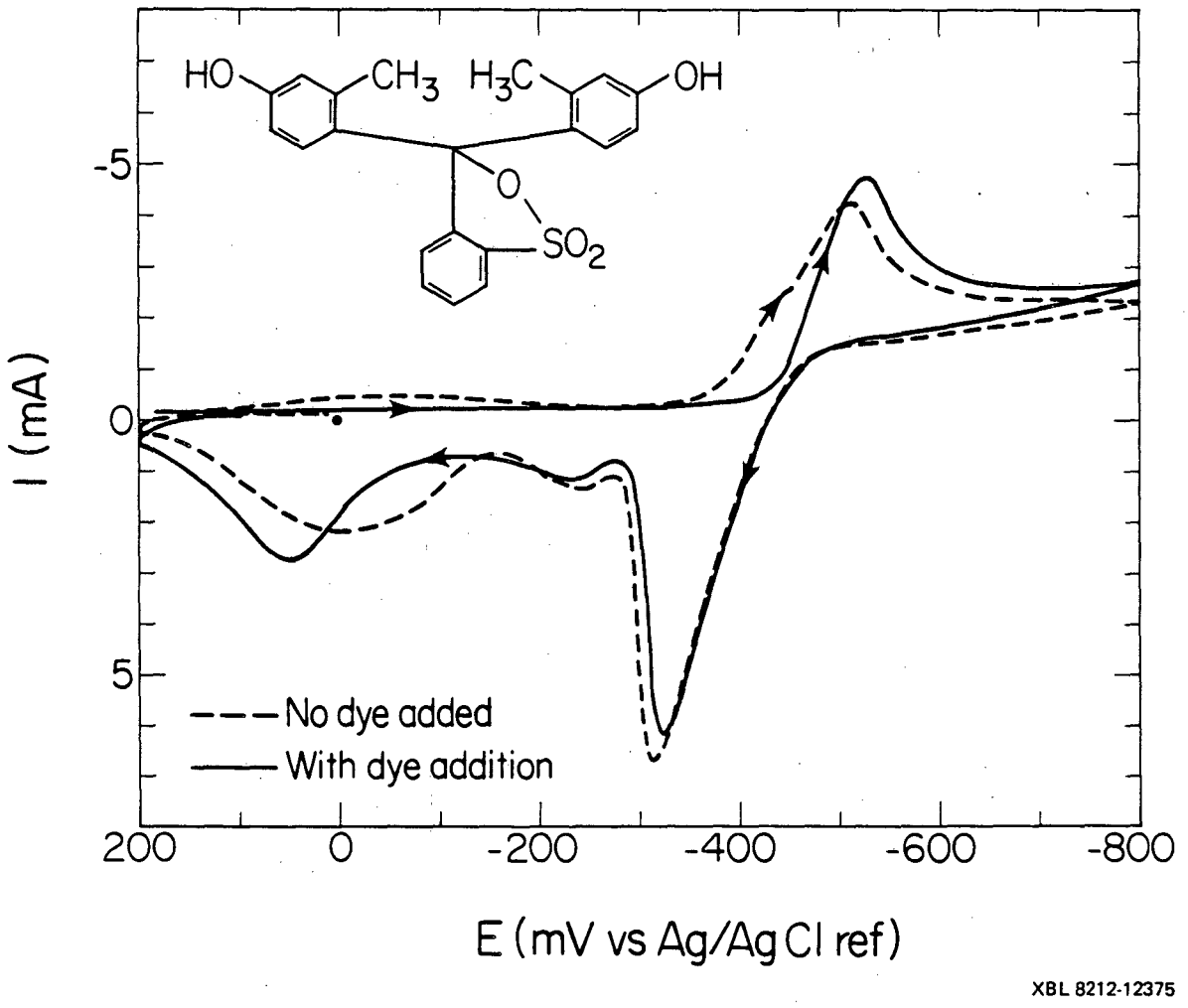
HO
CH3
H3C
OH
O
SO2
-5
0
5
I (mA)
No dye added
With dye addition
200
0
-200
-400
-600
-800
E (mV vs Ag/Ag Cl ref)
XBL 8212-12375

Fig. 8

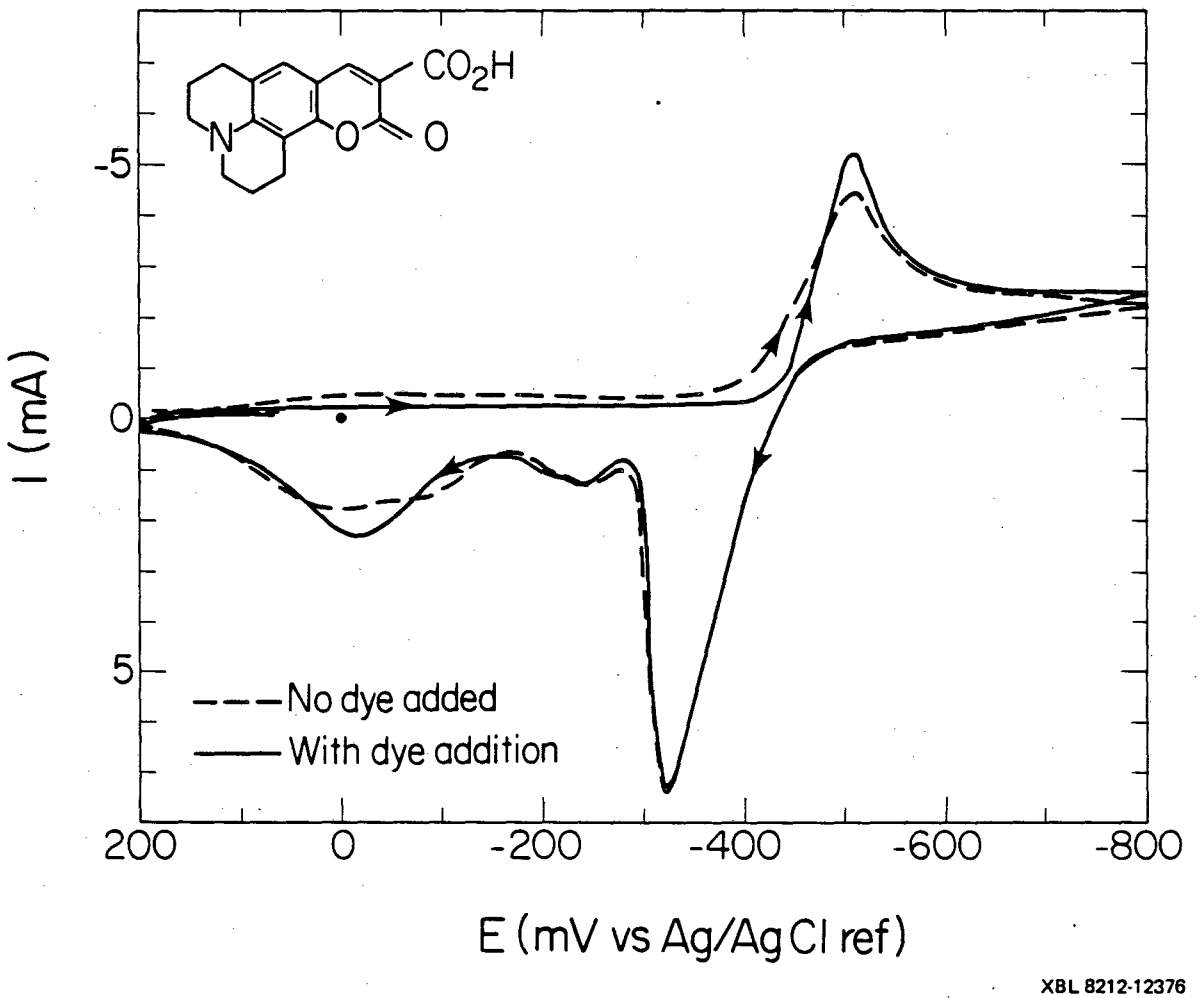
CO2H
O
N
O
-5
0
5
I (mA)
---No dye added
——With dye addition
200
0
-200
-400
-600
-800
E (mV vs Ag/Ag Cl ref)
XBL 8212-12376

Fig. 9

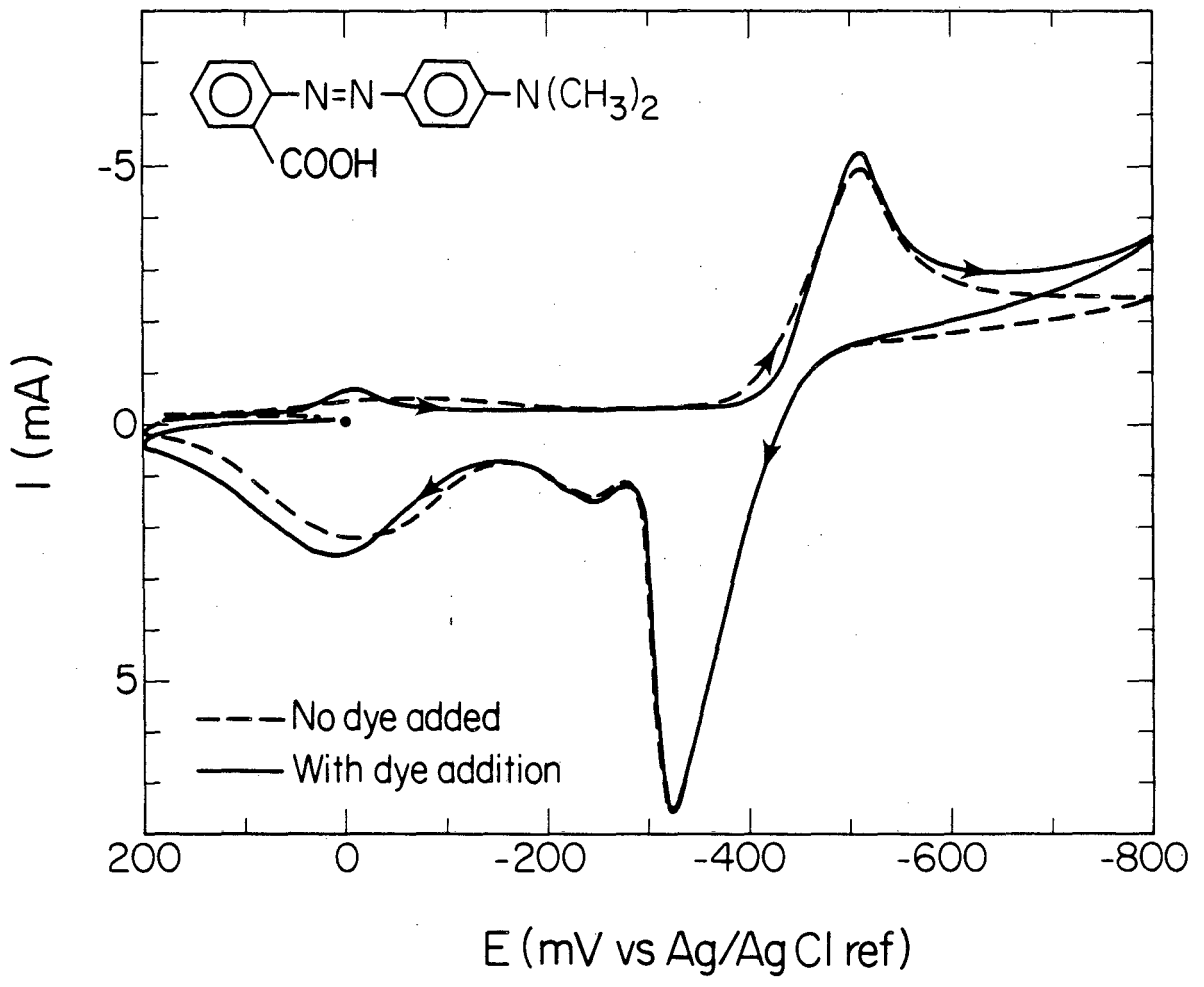
N=N
N(CH3)2
COOH
-5
0
5
I (mA)
No dye added
With dye addition
200
0
-200
-400
-600
-800
E (mV vs Ag/Ag Cl ref)
XBL 8212-12381

Fig. 10

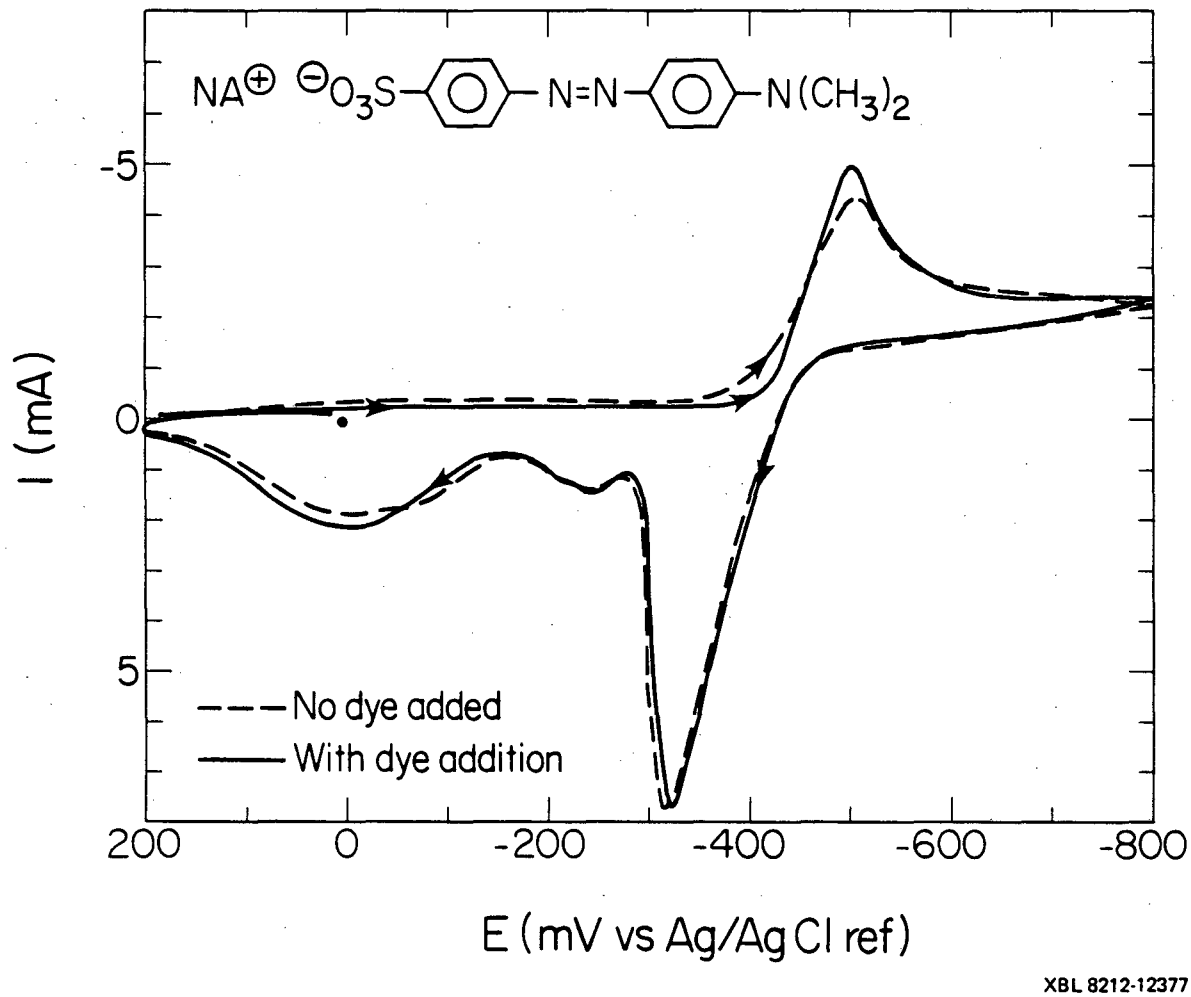
NA⊕ ⊖O3S— —N=N— —N(CH3)2
-5
0
5
I (mA)
200
0
-200
-400
-600
-800
E (mV vs Ag/Ag Cl ref)
No dye added
With dye addition
XBL 8212-12377

Fig. 11

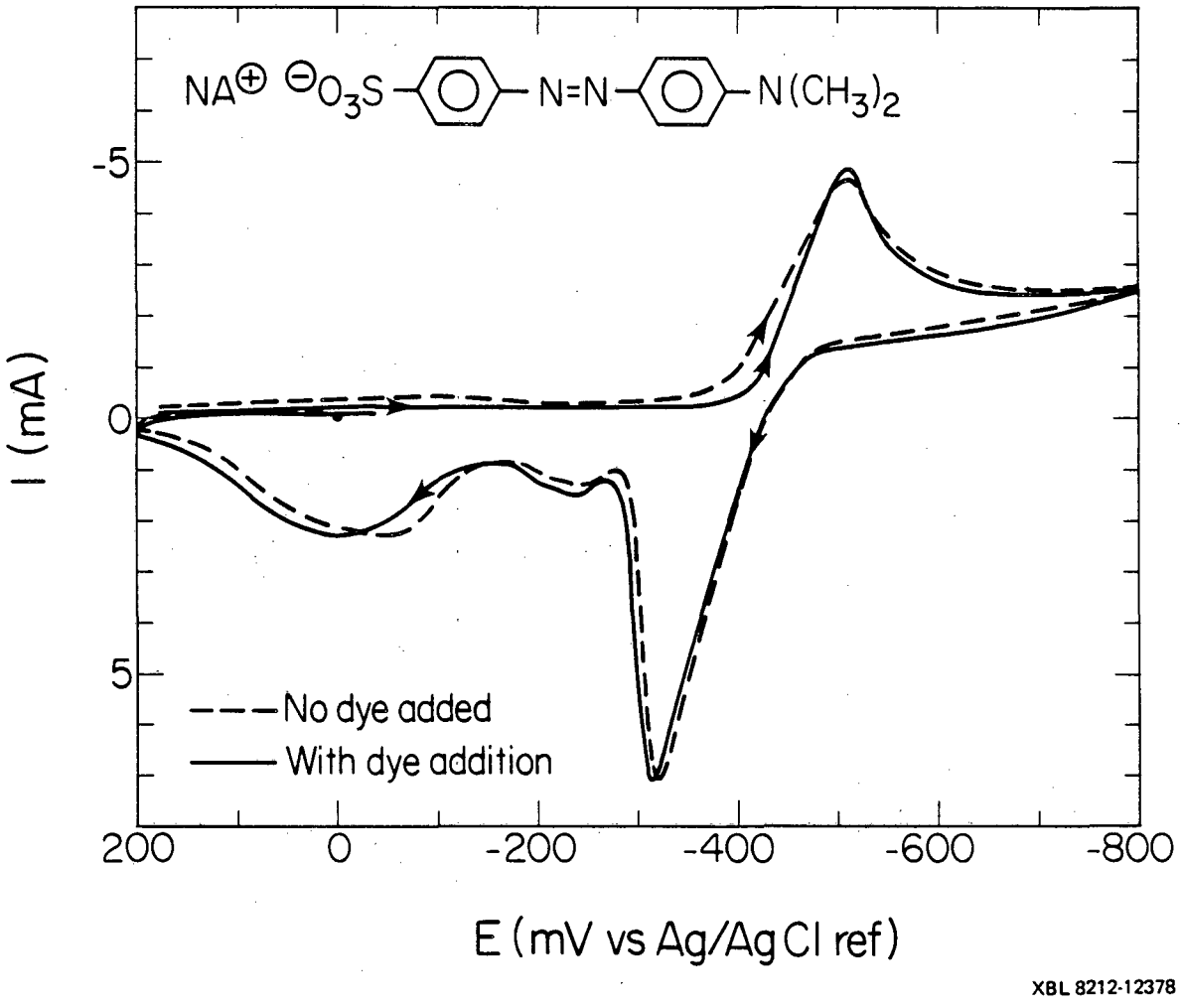
NA⊕ ⊖O3S
N=N
N(CH3)2
-5
0
5
I (mA)
No dye added
With dye addition
200
0
-200
-400
-600
-800
E (mV vs Ag/Ag Cl ref)
XBL 8212-12378

Fig. 12

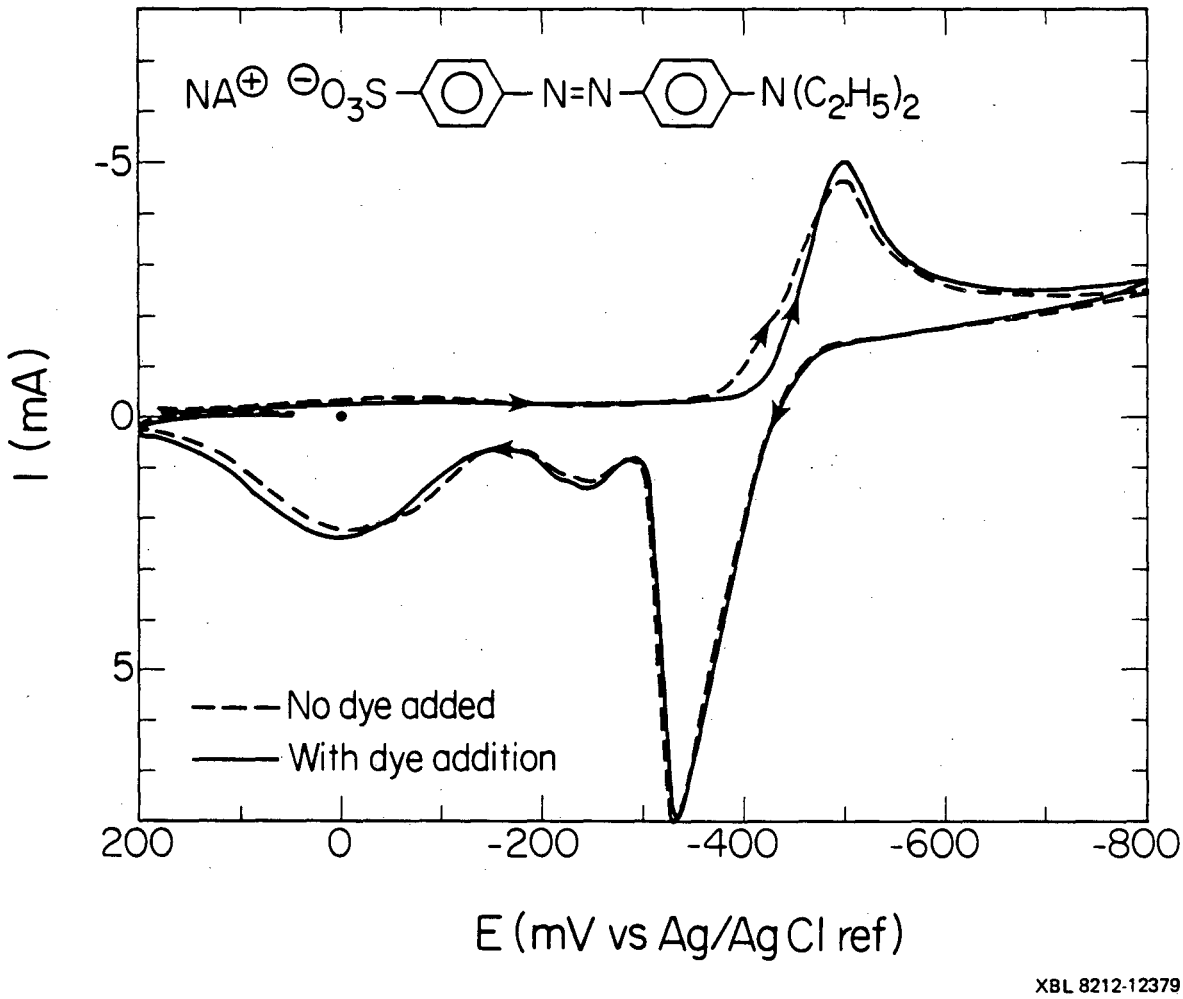
NA⊕ ⊖O3S
N=N
N(C2H5)2
-5
0
5
I (mA)
No dye added
With dye addition
200
0
-200
-400
-600
-800
E (mV vs Ag/Ag Cl ref)
XBL 8212-12379

Fig. 13

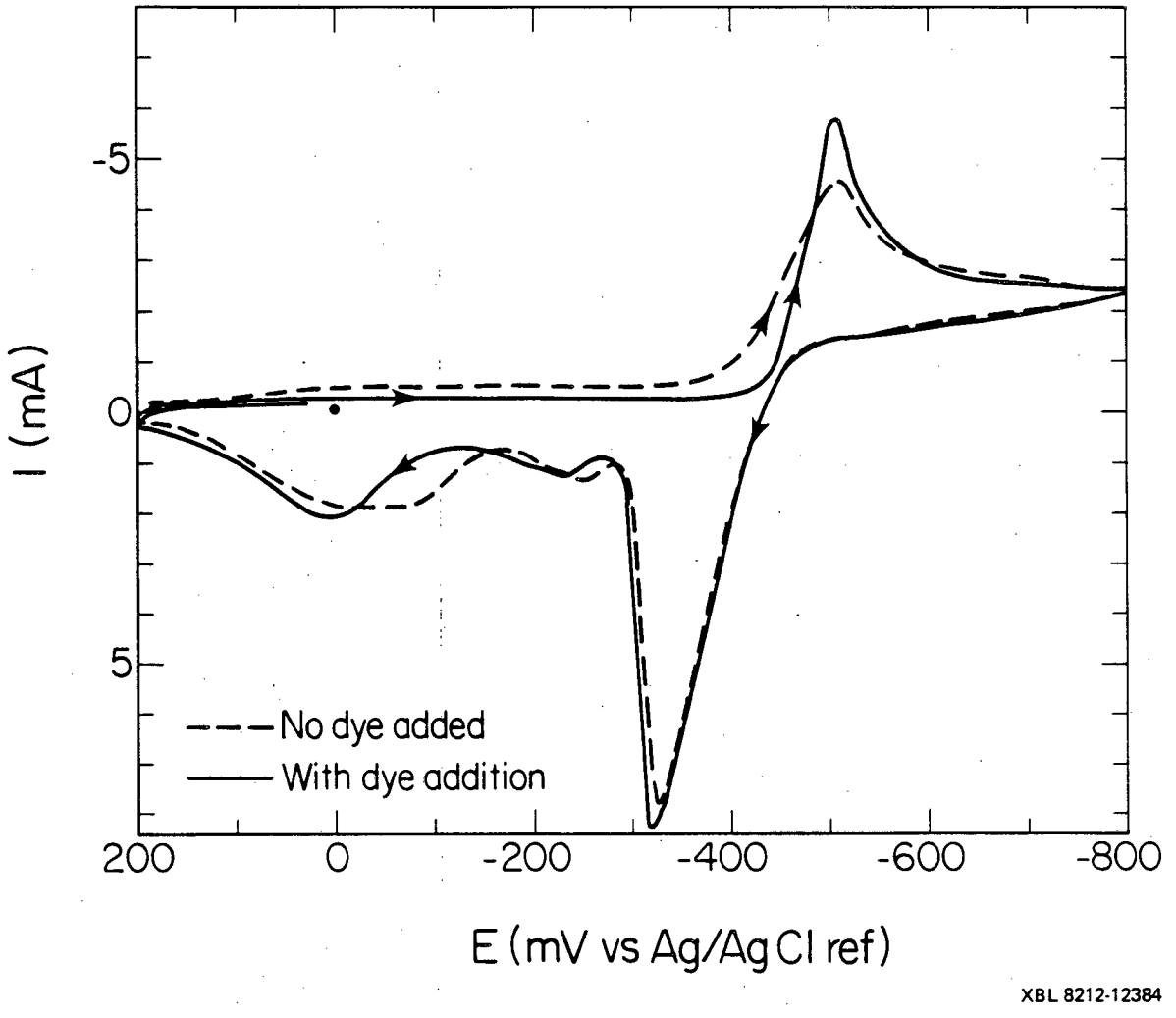
-5
0
5
I (mA)
No dye added
With dye addition
200
0
-200
-400
-600
-800
E (mV vs Ag/Ag Cl ref)
XBL 8212-12384

Fig. 14

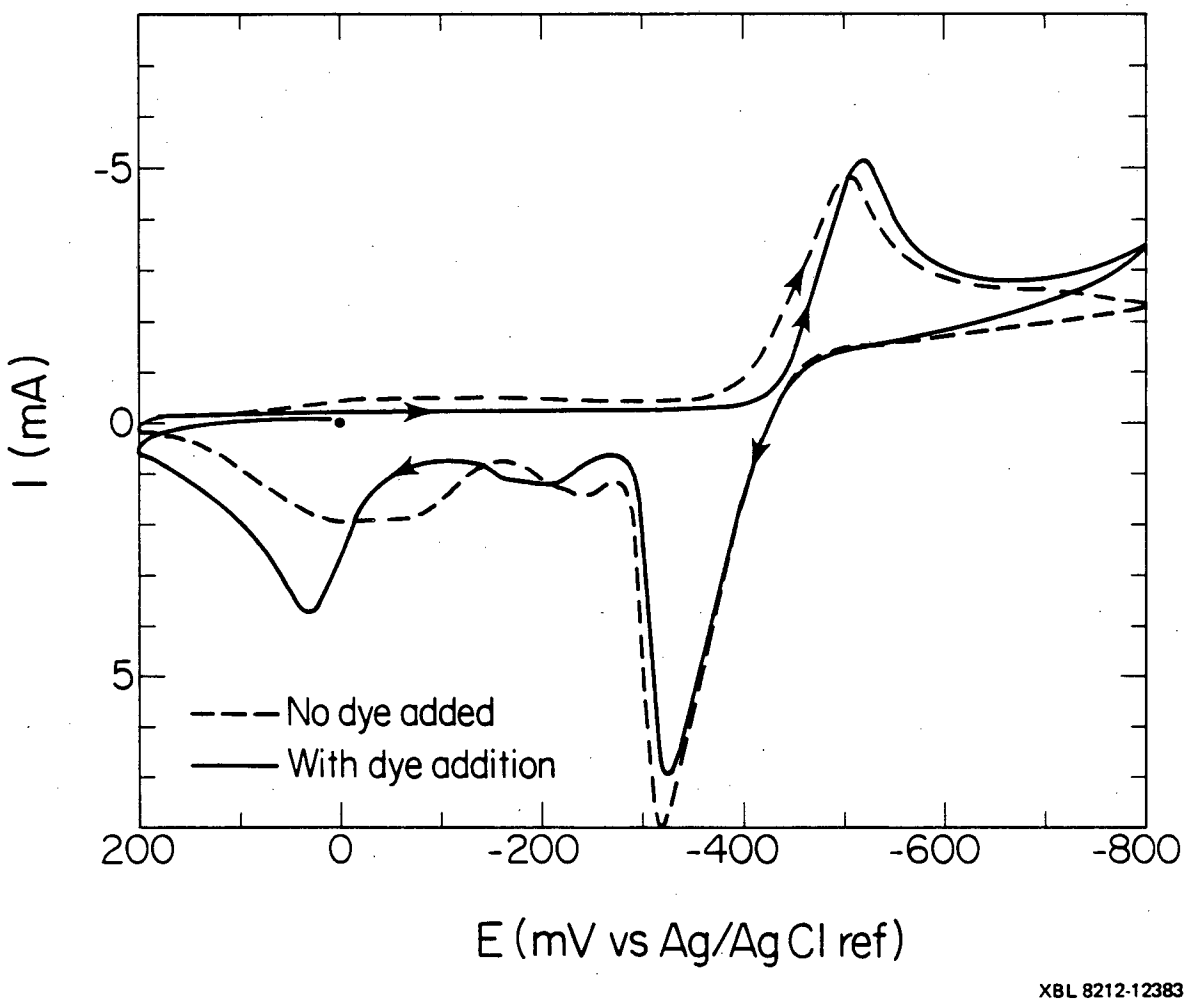
-5
0
5
I (mA)
No dye added
With dye addition
200
0
-200
-400
-600
-800
E (mV vs Ag/Ag Cl ref)
XBL 8212-12383

Fig. 15

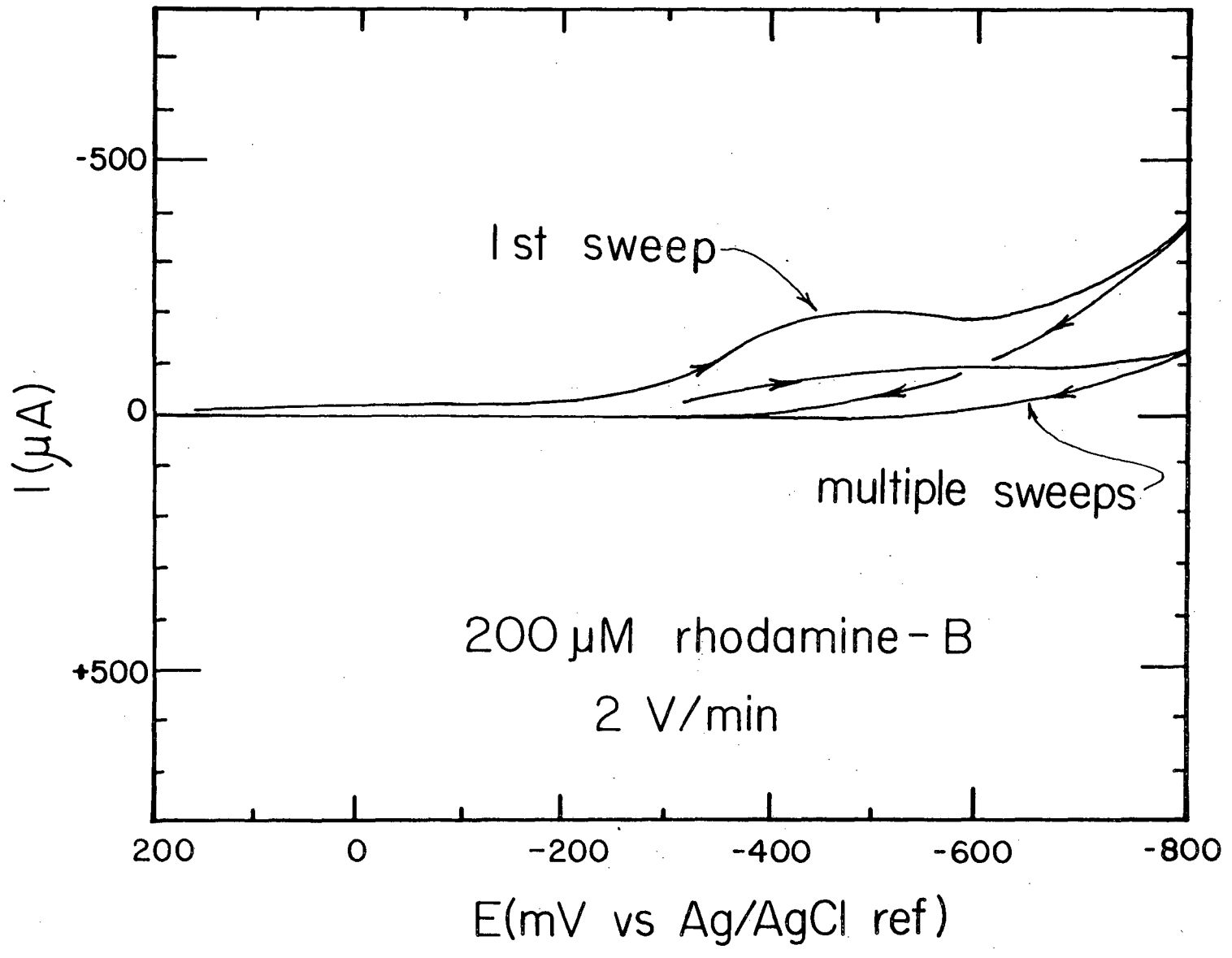

XBL 833-8505

Fig. 16

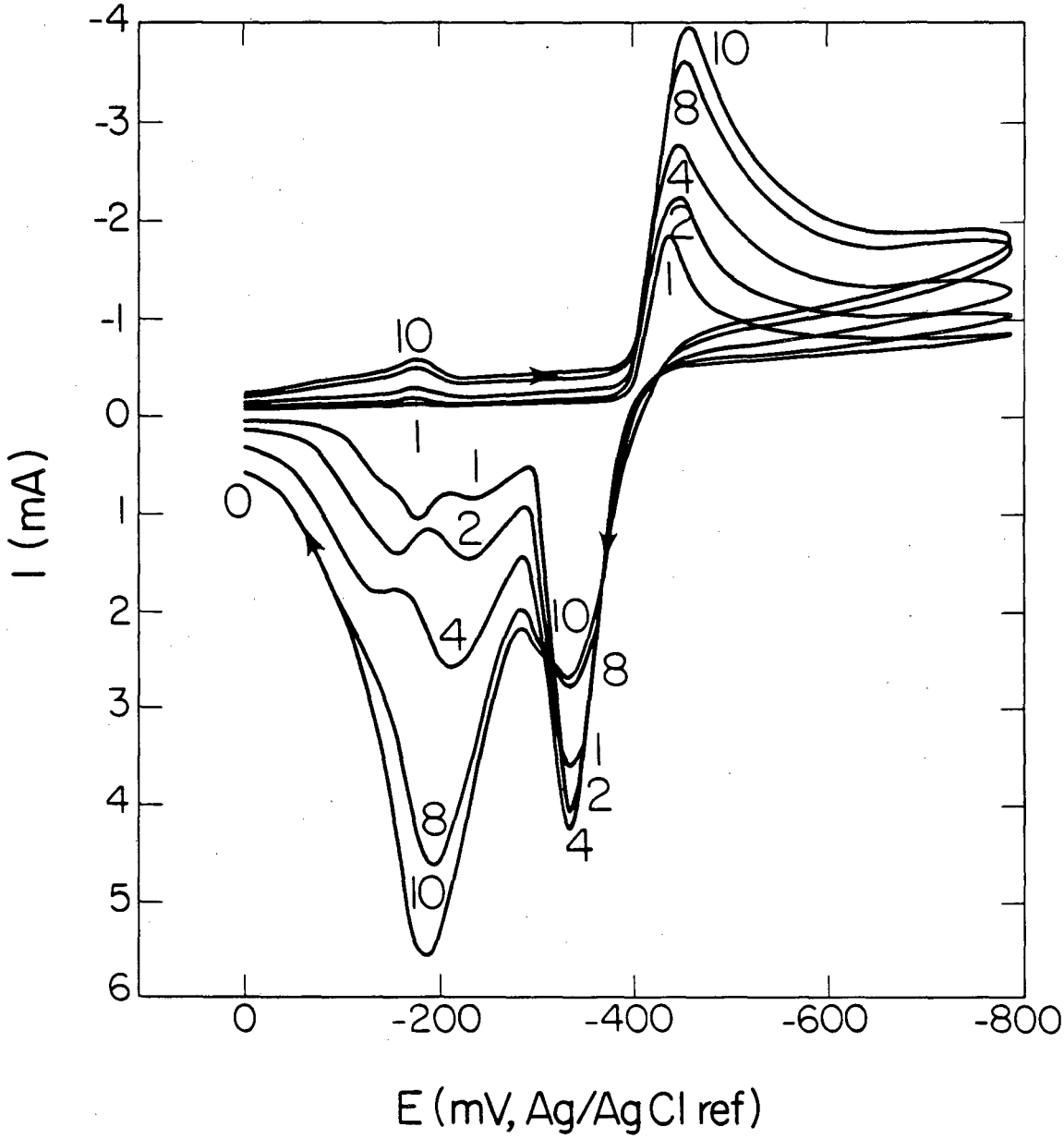

XBL 8212-12392

Fig. 17

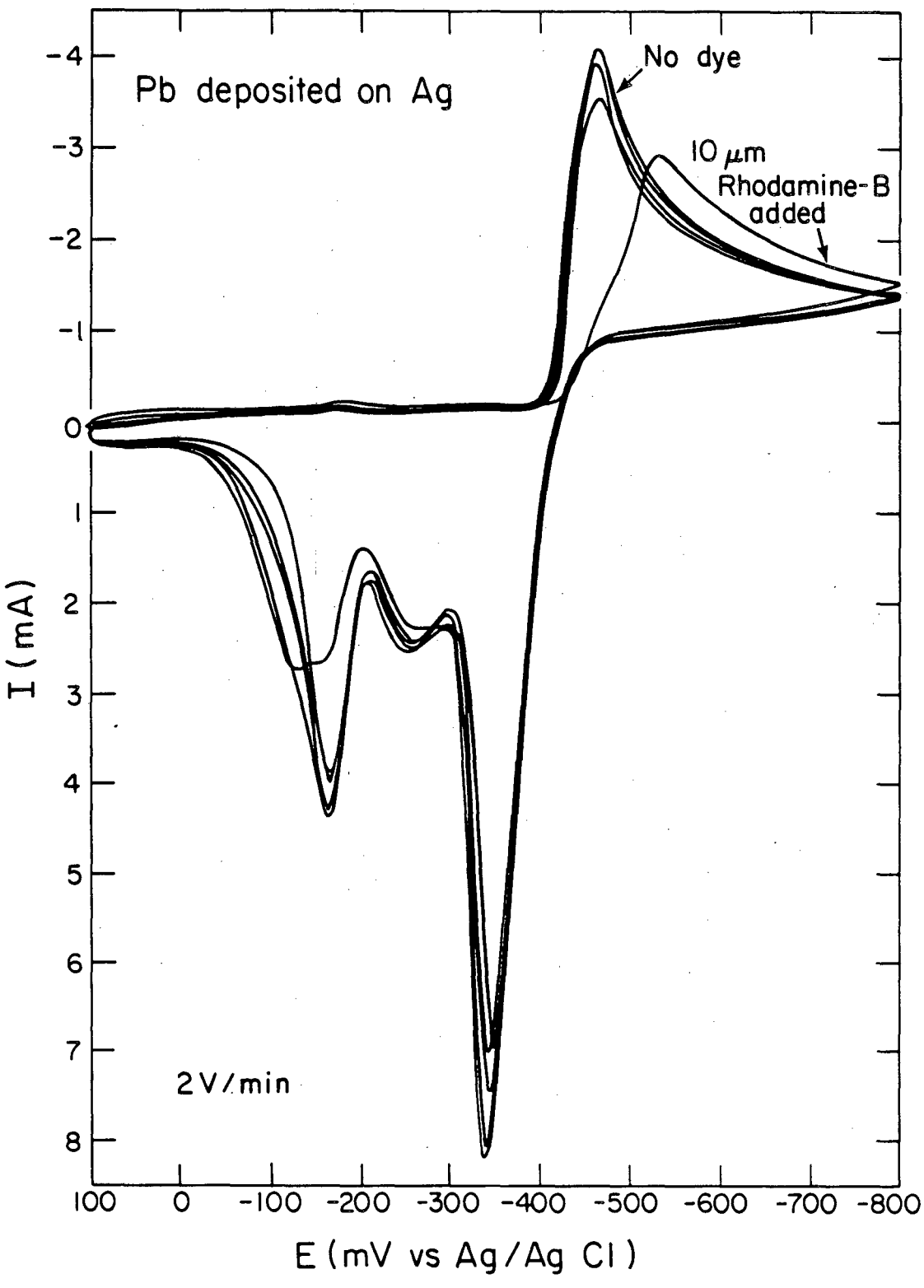

XBL 831 - 32

Fig. 18.a

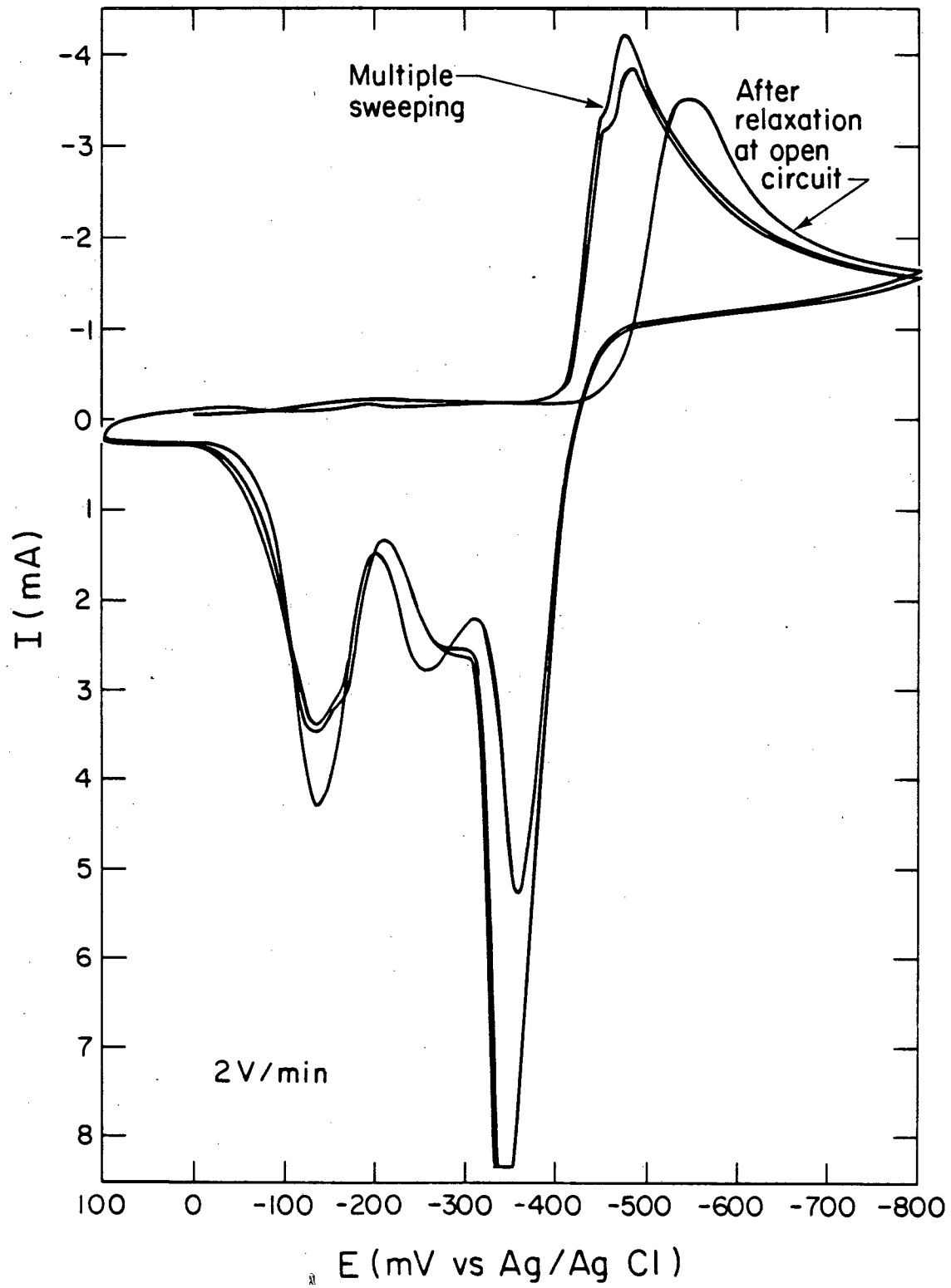

XBL 831 - 33

Fig. 18.b

ELECTRODEDUCTION OF RHODAMINE-B

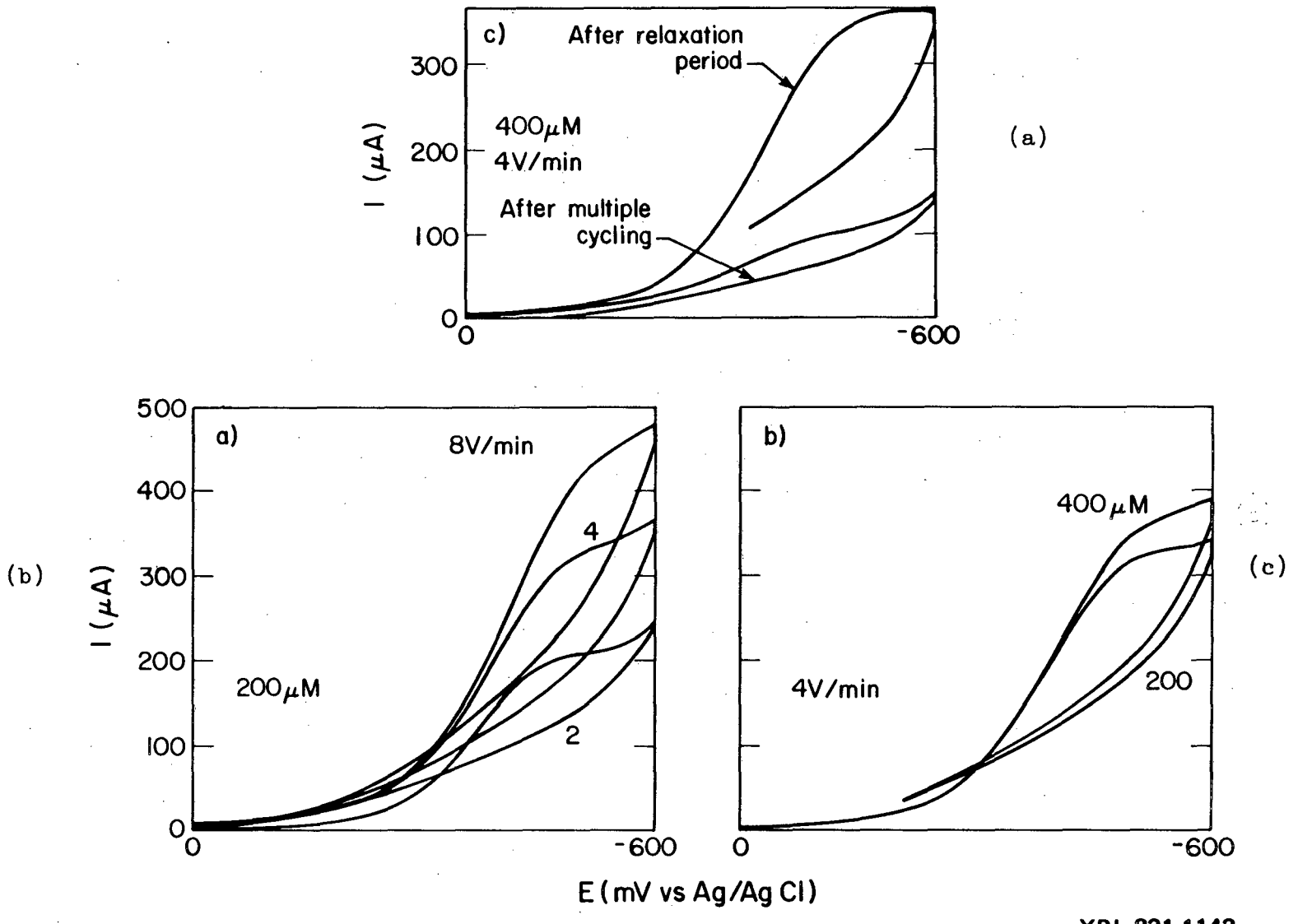

XBL 831-1142

Fig. 19.a-c

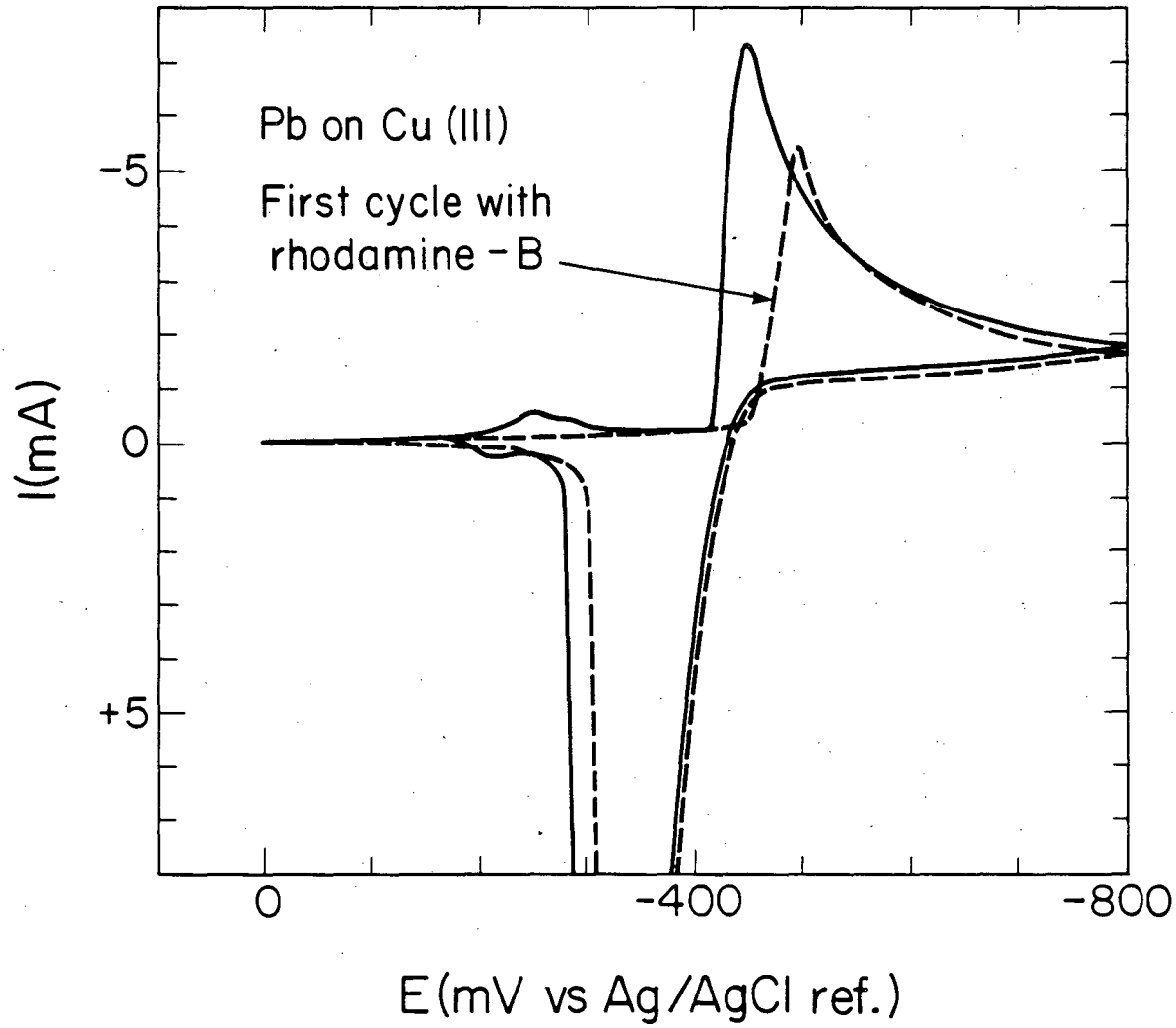
Pb on Cu (111)
First cycle with
rhodamine - B
-5
0
+5
I(mA)
0
-400
-800
E(mV vs Ag/AgCl ref.)
XBL 831-1126

Fig. 20.a

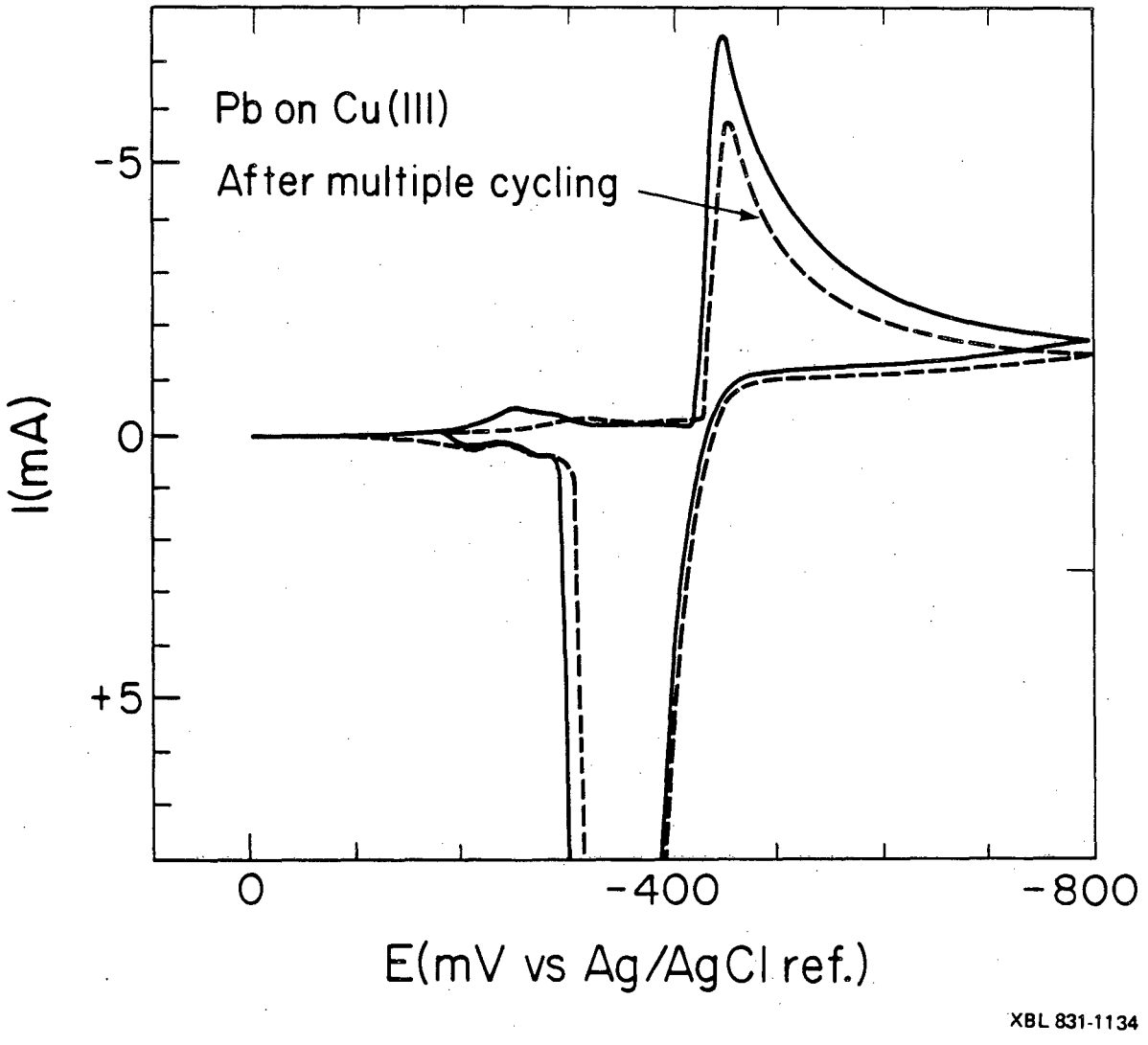
Pb on Cu(111)
After multiple cycling
-5
0
+5
I(mA)
0
-400
-800
E(mV vs Ag/AgCl ref.)
XBL 831-1134

Fig. 20.b

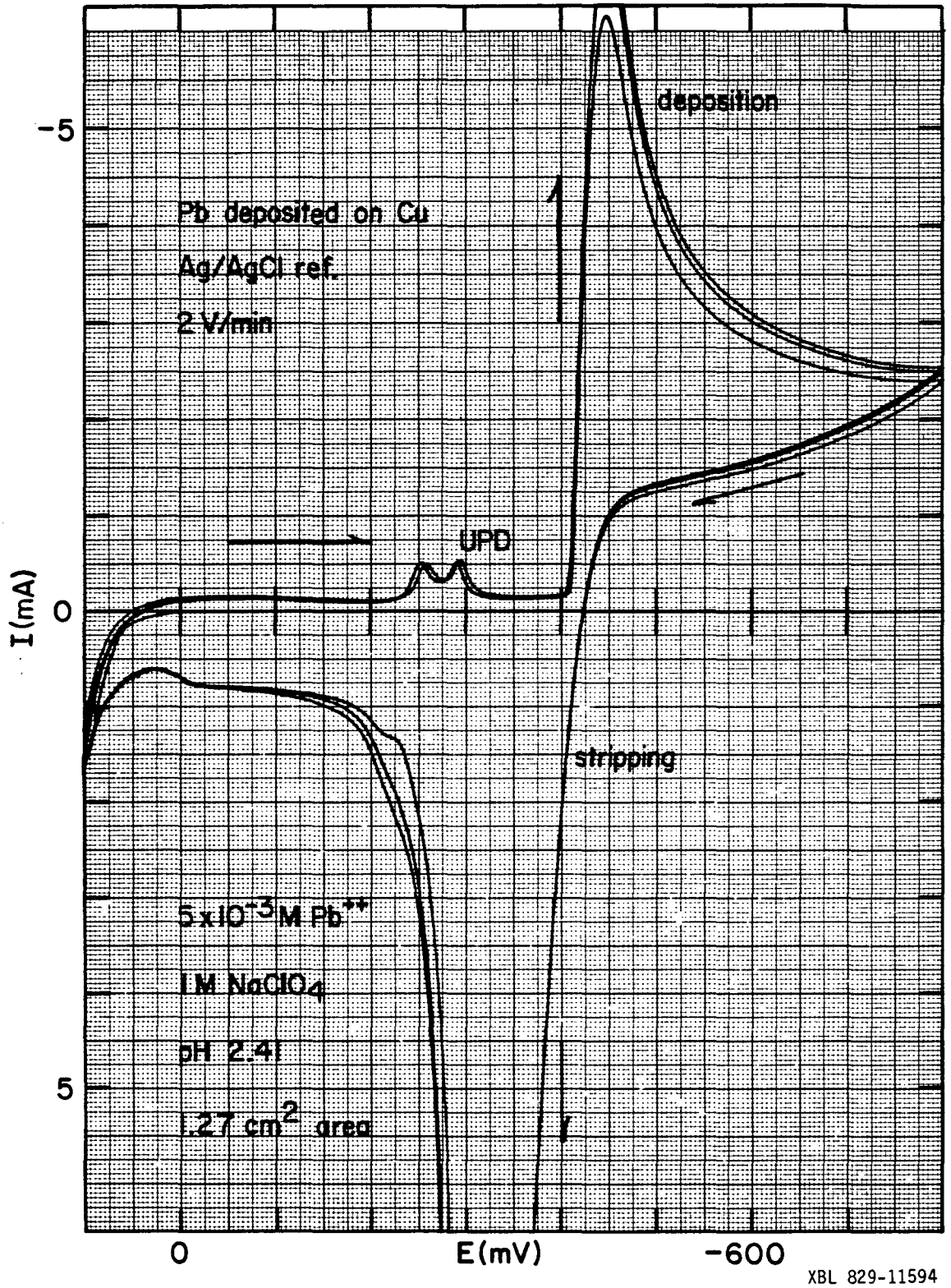
deposition
Pb deposited on Cu
Ag/AgCl ref.
2 V/min
UPD
stripping
5×10^{-3} M Pb^{++}
1 M $NaClO_4$
pH 2.4
1.27 cm^2 area
-5
0
5
I(mA)
0
E(mV)
-600
XBL 829-11594

Fig. 21.a

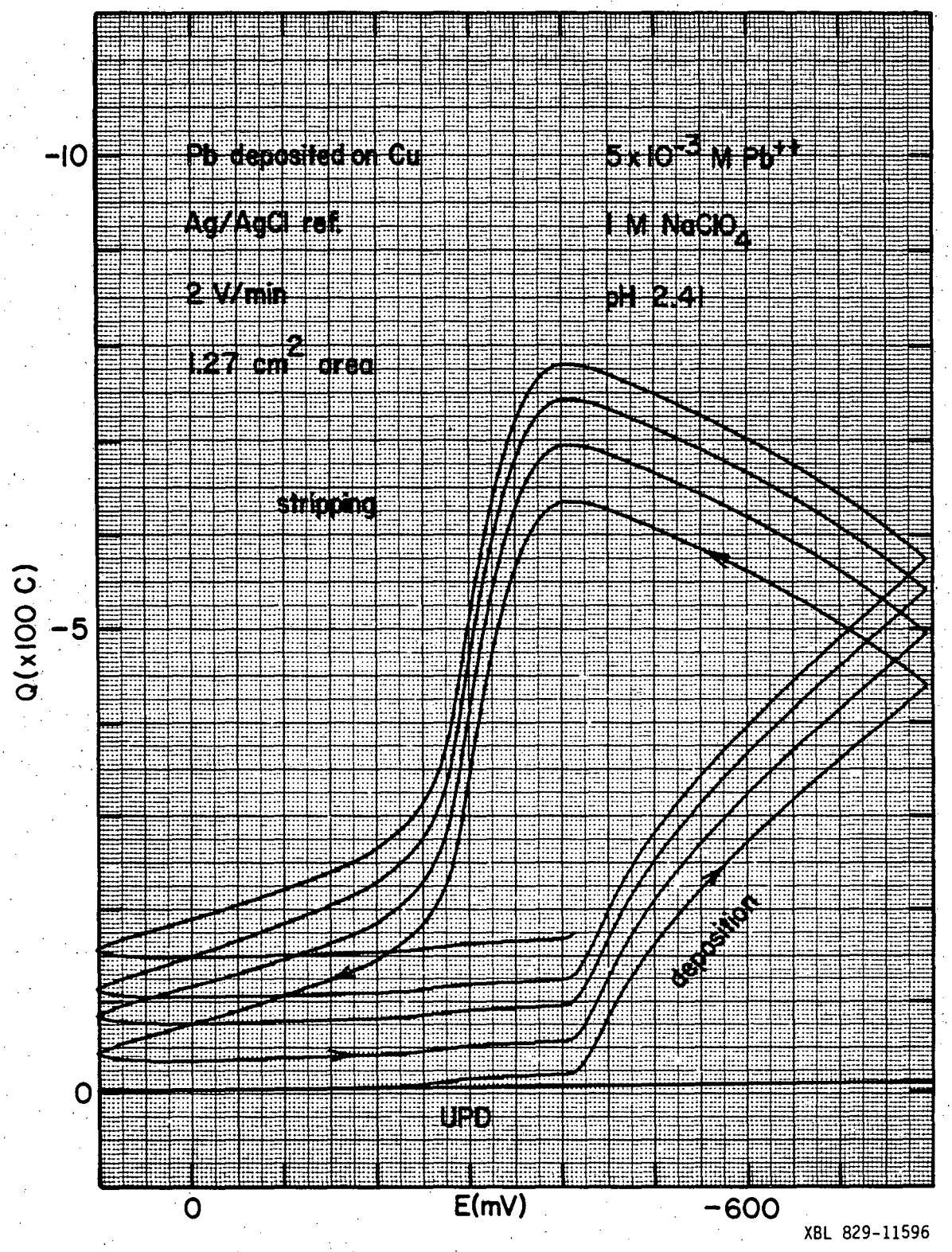
Pb deposited on Cu
Ag/AgCl ref.
2 V/min
1.27 cm² area
5 x 10⁻³ M Pb⁺⁺
1 M NaClO₄
pH 2.41
stripping
deposition
UPD
Q(x100 C)
-10
-5
0
0
E(mV)
-600
XBL 829-11596

Fig. 21.b

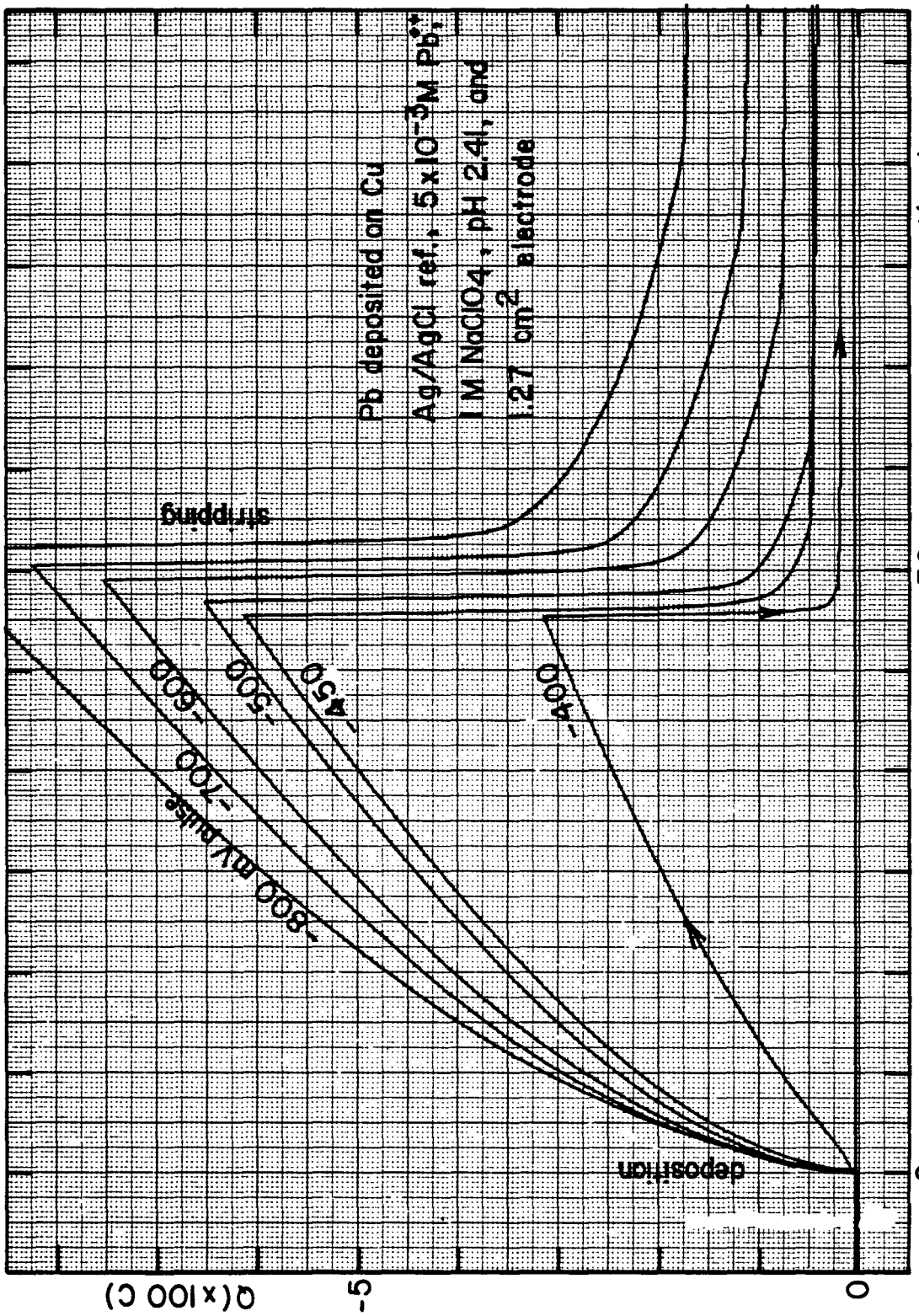

XBL 829-11595

Fig. 22.a

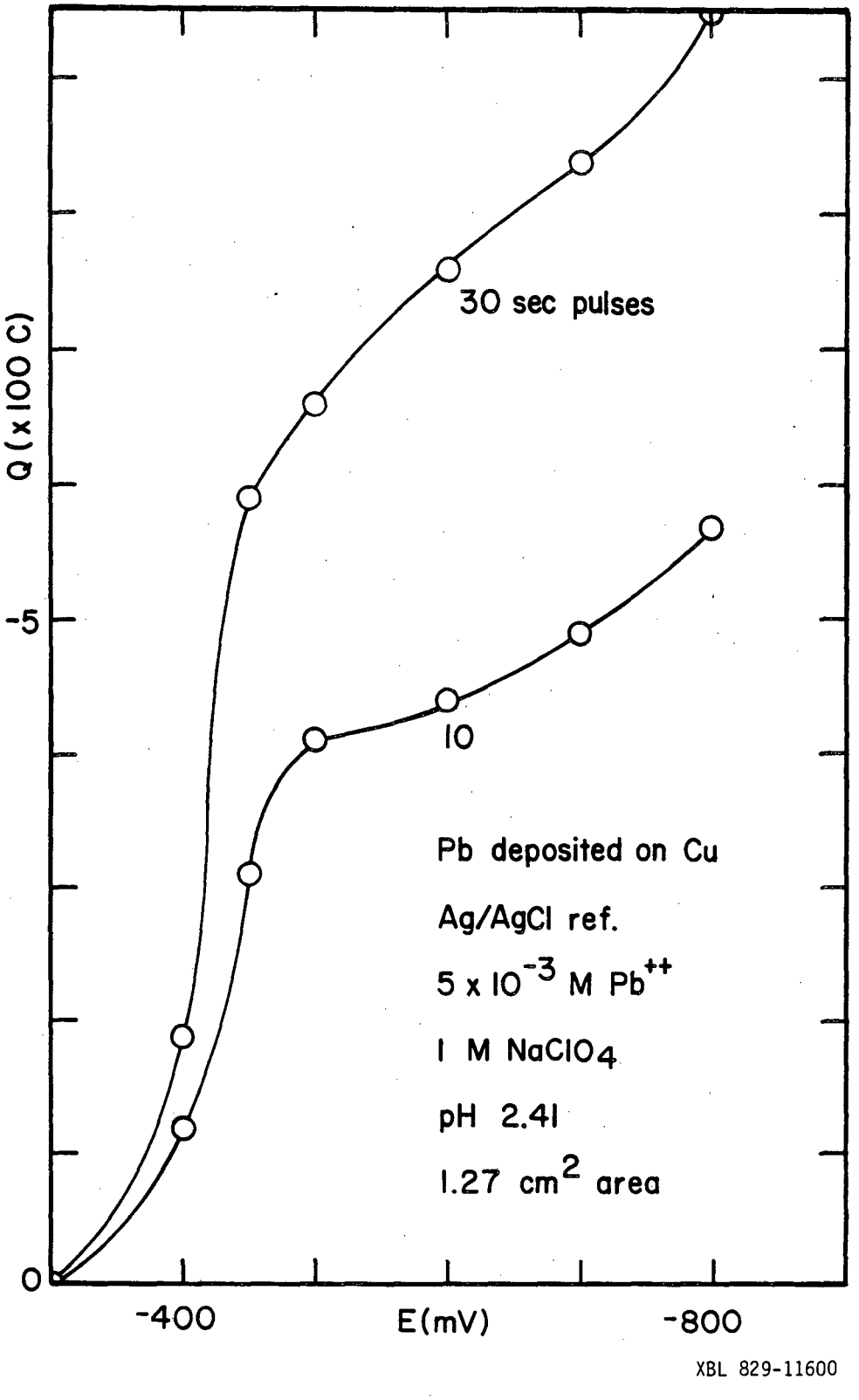
Q (x 100 C)
-5
0
-400
E(mV)
-800
30 sec pulses
10
Pb deposited on Cu
Ag/AgCl ref.
5 x 10^-3 M Pb^++
1 M NaClO4
pH 2.41
1.27 cm^2 area
XBL 829-11600

Fig. 22.b

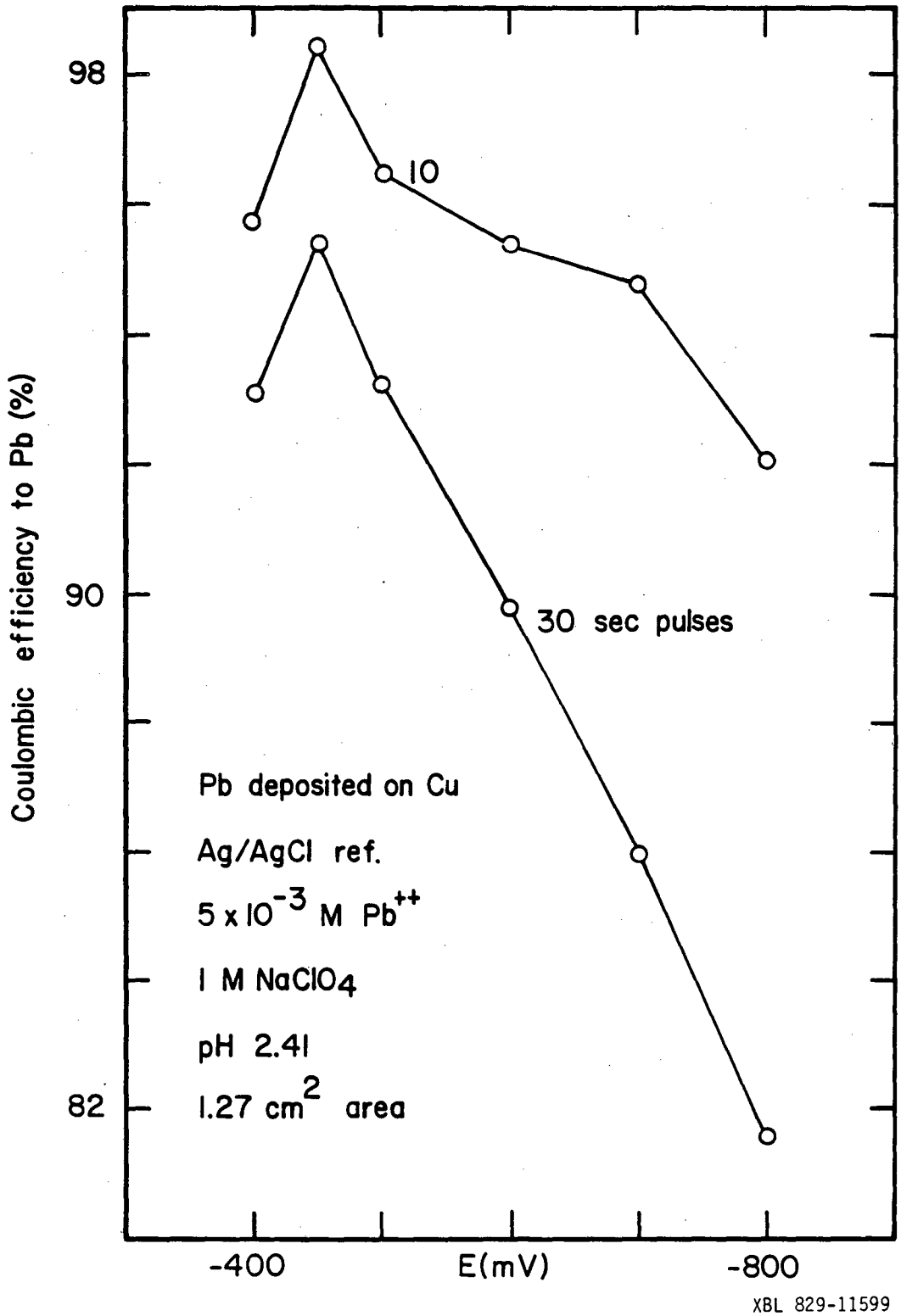
98
90
82
Coulombic efficiency to Pb (%)
10
30 sec pulses
Pb deposited on Cu
Ag/AgCl ref.
5 x 10^-3 M Pb^++
1 M NaClO4
pH 2.41
1.27 cm^2 area
-400
E(mV)
-800
XBL 829-11599

Fig. 22.c

Chapter 5

MICROMORPHOLOGICAL CHANGES OF LEAD ELECTRODEPOSITS ON SILVER AND COPPER OBSERVED BY ELLIPSOMETRY AND LIGHT SCATTERING DURING CYCLIC VOLTAMMETRY: NO ADDITIVES

Abstract

Initial stages in the deposition of Pb from 0.5 and 5.0 mM $Pb(NO_3)_2$ and from 1 M $NaClO_4$ (pH 3) have been investigated by ellipsometry and light scattering during cyclic voltammetry. Optical constants, thickness, valence, and free energy of adsorption of the underpotential deposit have been determined. An optical model fitting experimental data for fractional coverage is presented which implies island-like growth. The bulk deposit (less than 20 Angstroms thick) immediately following formation of the underpotential monolayer is of a particulate, porous nature.

Introduction

The initial stages of Pb electrocrystallization on Ag(111) and Cu(111) single crystals were studied electrochemically and optically. Particular attention has been given to the transition from the first monolayer, the underpotential deposit (UPD), to the bulk deposit. The electrolyte was an acidic 1 M $NaClO_4$ solution (pH 3) containing 0.5 or 5.0 mM $Pb(NO_3)_2$.

We chose to study Pb deposition on Ag and Cu here because of the well known underpotential layer which forms on these substrates (1-3).

There are also significant differences in the optical constants of Pb and the chosen substrates, making detection of small amounts of Pb on the electrode surface by ellipsometry possible (4-6).

Changes in the optical properties of the cathode (delta and psi) were followed during cyclic voltammetry with the ellipsometer at a single, fixed wavelength. Intensity of the laser light scattered from the surface during cyclic voltammetry was also measured. By ramping the electrode potential (rather than stepping it) formation of the first monolayer and formation of the bulk deposit were separated in time, thereby allowing optical changes attributable to the two layers to be differentiated.

Separation of the UPD and bulk deposit properties was significant in that it has allowed us to prove in situ that three-dimensional nucleation occurs on top of a complete Pb monolayer (UPD), immediately following its formation. This conclusion was derived from interpretations of the ellipsometry data, and was substantiated by light scattering results. We have determined the apparent optical constants and thickness of the underpotential layer, and have used an optical model capable of accurately predicting sub-monolayer coverages, given only the optical properties of the substrate and complete monolayer. The thickness of the UPD was determined to be between 4 and 5 Angstroms; the atomic diameter is about 3.5 Angstroms. The micromorphology of the initially deposited Pb nuclei on the underpotential layer was also determined. It was found that during this initial stage of deposition (layers from about 10 to 200 Angstroms thick) deposits are 25 to 40

volume percent porous. Nucleation of this granular, porous layer on the first monolayer coincides with the onset of significant light scattering; no increase of light scattering is observed during UPD formation. Other investigators have attempted to prove that three-dimensional nucleation occurs on a completely formed monolayer, but only through exsitu experiments using Auger spectroscopy (7), X-ray fluorescence (8), and scanning electron microscopy (9). We believe that this study is the first insitu confirmation of this electrodeposition mechanism.

Schmidt and Gygax (10) determined the Gibbs free energy of adsorption for Pb electrosorption on polycrystalline Ag and Cu. This can be done simply by integration of the cathodic UPD peak in the cyclic voltammogram, determining coverage as a function of potential. We too have used our data to extract adsorption isotherm data for the Pb underpotential, but on single crystal Ag and Cu. We have found that two electrons are involved in the electrosorption of a single Pb atom to the Cu and Ag surfaces, implying complete discharge. A simple Langmuir-type adsorption isotherm (Frumkin isotherm with g=0) is adequate to describe this electrosorption process. The Gibbs free energy of adsorption is about 7 kcal/mol, which is higher than that obtained by Schmidt and Gygax on polycrystalline substrates (5 kcal/mol). There exists no significant difference in the valence or adsorption free energies on Cu and Ag. The computed coverages were determined to be sweep rate independent.

Experimental Procedure

Experiments were run potentiodynamically while simultaneously acquiring ellipsometer measurements of the electrode surface. Simultaneous cyclic voltammetry, ellipsometry, and light scattering was performed. A Pine Instrument Company bipotentiostat (model RDE 3) was used to drive the electrochemical cell and an automatic, self-nulling ellipsometer was used to follow optical changes in the surface (11). The potential was swept from 200 to -800 mV at sweep rates varying from 0.1 to 1.5 volts per minute. In these experiments the ellipsometer source wavelength was 515 nm.

These experiments were all conducted in an acrylic electrochemical cell used for earlier investigations of anodic silver oxidation (12). The cell had two quartz windows which allowed ellipsometry of the electrode surface at a 75 degree angle-of-incidence. The volume of electrolyte required to fill this cell was approximately 250 ml. It had ports for introduction and draining of electrolyte, for a nitrogen purge stream, and for a reference electrode capillary. A Pt counter electrode was used and positioned so as not to interfere with the working electrode. It first oxidized and subsequently evolved oxygen.

Ag(111) and Cu(111) working electrodes were used. The single-crystal surfaces were approximately 1.20 cm x 2.85 cm (3.42 cm^2), and were mounted in epoxy. Threaded contacts on the backs of electrodes allowed them to be screwed into position.

Electrodes were all polished mechanically, ultimately using 0.05 micron aluminum oxide powder suspended in water. This was followed by

ultra cleaning, chemical polishing (for Ag surfaces only), a period of soaking in the acidic electrolyte, and pre-electrolysis. The chemical polishing of both single crystal and polycrystalline Ag was done as follows (13,14). First, the electrode was soaked from 2 to 5 minutes in an aqueous solution of CrO_3 and HCl (24 grams CrO_3, 20 ml HCl, 1000 ml water). It was then rinsed with water and transferred to an ammonium hydroxide solution (500 ml of 25% NH_4OH, 1000 ml water) for 10 to 15 seconds. Finally, the electrode was rinsed and dipped in a nitric acid solution (70 ml of 65% HNO_3, 1000 ml water) for about 5 seconds. Before placing the electrode into the electrochemical cell it was rinsed in an abundance of distilled water. Oxides formed on the surface during transfer to the cell were unstable at the pH and potential used for the experiments; these oxides were removed by a pre-electrolysis period in the electrolyte at a potentials anodic to that for Pb deposition (15,16). No significant electrochemical or ellipsometric effects were observed between Ag electrodes polished mechanically and chemically and those polished by only mechanical means. The only incentive for chemical polishing was to generate smoother surfaces for light scattering experiments. When scattering experiments were completed the chemical polishing step was omitted.

A double-junction, Ag/AgCl reference electrode was used (E = 0.2 vs NHE, Dow-Corning catalog no. 476067). The inner compartment was filled with 4 M KCl saturated with AgCl, which was in equilibrium with the actual reference electrode element. This compartment was separated by a porous glass plug from an outer compartment filled with a second

electrolyte, 1 M KNO_3 (KNO_3 from factory). A slow flow of KNO_3 solution through a second porous glass plug into the test solution helped minimize diffusion potentials. Usually a double junction reference electrode such as this serves the purpose of isolating ions of the reference electrode from that of the test solution; in this instance the choice of reference electrode was based upon availability.

A second cell was used for light scattering studies (Fig. 8), and has been described elsewhere (17). This cell used high-purity, polycrystalline Ag sheets rather than single crystals. The electrode was 0.5 cm x 5.0 cm x 0.2 cm and was 60% immersed in electrolyte. It was located in a cylindrical glass cell of 4 cm diameter and illuminated with the beam from an argon laser (515 nm line) at an angle-of-incidence of 75 degrees.

All experiments used a supporting electrolyte of 1 M $NaClO_4$ at pH 3. Pb^{++} ion was introduced into the electrolyte as a nitrate at concentrations of either 0.5 or 5.0 mM. The pH was adjusted to the desired level by adding small amounts of dilute $HClO_4$, and measured to a high degree of accuracy using a digital pH meter (Corning model no. 130).

Results

Experimental data for the deposition of Pb on Ag(111) from a 0.5 mM solution at a sweep rate of 0.1 V/min are shown in Figs. 1.a through 1.e: (1.a) a plot of current against potential; (1.b) a time profile of potential; (1.c) a time profile of current; (1.d) a time profile of

delta; and (1.e) a time profile of psi. Comparable data are shown for potentiodynamic Pb deposition on Cu(111) at concentrations of 0.5 and 5.0 mM and a sweep rate of 1.5 V/min in Figs. 2.a-e and Figs. 3.a-e, respectively.

In each experiment, changes in delta and psi correlated with the cathodic UPD peaks are interpretable as the formation of a complete monolayer of Pb on the substrate. Unexpected changes in delta and psi correlated with the cathodic bulk deposition peaks cannot be interpreted as compact layers of Pb. A porous, particulate Pb deposit must be assumed in order to account for these unusual observations.

It is important to note that the changes of optical properties correlated with the cathodic peaks were reversible upon anodic stripping. The bulk deposit is first stripped, and delta and psi returned to values corresponding to a complete Pb monolayer covering the substrate. Next, the UPD is stripped and delta and psi returned to values corresponding to a bare substrate.

Measurements of the intensity of scattered laser light from the electrode surface during cyclic voltammetry are shown in Figs. 4.a through 4.d. The lower oscillogram trace in each frame represents the current response of the cell, the upper trace being the scattered light intensity. Cathodic peaks are shown with negative amplitudes, while anodic peaks have positive amplitudes. In each experiment, an increase in scattered ligh intensity was correlated with the onset of bulk deposition; the scattered light intensity returned to its initial level upon stripping the Pb from the surface. No increase in scattered light

intensity was observed with formation of the UPD layer. Fig. 4.b shows the stability of the scattering centers upon current interruption (the potential sweep is stopped and the cell is open circuit); 4.c shows a gradual increase in scattered light when the potential sweep is held constant at its most cathodic level; and 4.d shows stripping of the deposit formed during a previous polarization, Fig. 4.b. Light scattering, like the changes in ellipsometry measurements, was reversible. The optical features causing the unusual trend in ellipsometer measurements were most likely the same as those responsible for the increased light scattering. These features are believed to have been very small, dendritic, Pb islands formed on a Pb monolayer, completely covering the substrate.

Optical Model of the Initial Stage of Deposit Formation

The general theory for sub-monolayer ellipsometry has been reviewed by Bootsma (18,19). He discussed various approaches for modeling a layer of adatoms on a substrate, including: (1) Drude approximation; (2) Strachan's model; (3) Sivukin's model; (4) extrapolated macroscopic theory; and (5) application of the Bruggeman theory to apparent refractive index. Others have written on this topic and have paid particular attention to the anisotropic nature of the adsorbate layer (20-23). Anisotropy is addressed specifically Chapter 8.

Here, it is shown that one can also apply the coherent superposition model (24,25) to the UPD monolayer as it forms. This model is compared to the application of the Bruggeman theory. In the

coherent superposition model it is assumed that the surface is partially bare and partially covered with "patches" or "islands" of a thin film. Reflection coefficients are computed for both the bare and film covered surface from Eqns. 1 through 7; the bare surface is a limiting case.

$$r_\nu = \frac{r_{1\nu} + r_{2\nu} \exp(-iD)}{1 + r_{1\nu}\, r_{2\nu} \exp(-iD)} \tag{1}$$

$$r_{1p} = \tan(\phi - \hat{\phi}_f)/\tan(\phi + \hat{\phi}_f) \tag{2}$$

$$-r_{1s} = \sin(\phi - \hat{\phi}_f)/\sin(\phi + \hat{\phi}_f) \tag{3}$$

$$r_{2p} = \tan(\hat{\phi}_f - \hat{\phi}_s)/\tan(\hat{\phi}_f + \hat{\phi}_s) \tag{4}$$

$$-r_{2s} = \sin(\hat{\phi}_f - \hat{\phi}_s)/\sin(\hat{\phi}_f + \hat{\phi}_s) \tag{5}$$

$$D = 4\pi(d/\lambda_0)\ \hat{n}_f \cos(\hat{\phi}_f) \tag{6}$$

$$n_a \sin \phi = \hat{n}_f \sin \hat{\phi}_f = \hat{n}_s \sin \hat{\phi}_s \qquad (7)$$

Then, provided that the diameters of these islands are less than the transverse coherence of the light (Eqn. 8), a coherent superposition of the polarization states resulting from the reflection on bare and covered surface elements can be used.

$$\sigma_c = \frac{0.16\ f\ \lambda}{D_d} \qquad (8)$$

Overall reflection coefficients for both the "s" and "p" polarizations can be calculated by taking a weighted average of the reflection coefficients for the bare surface and the film covered surface (Eqn. 9).

$$r_\nu = \theta_f \cdot r_{\nu,f} + (1-\theta_f) \cdot r_{\nu,s} \qquad (9)$$

These average reflection coefficients are then used to calculate the ratio of p and s components given by Eqn. 10

$$\rho = \frac{r_p}{r_s} \qquad (10)$$

This ratio is then substituted into Eqn. 11, the ellipsometry equation, which is solved for the phase and amplitude (delta and tan(psi)).

$$\rho = \tan(\psi)\exp(-i\Delta) \qquad (11)$$

Application of this "island" concept to the underpotential deposit assumed that: (1) metal adatoms adsorbed to the surface, as two-dimensional clusters or individually, can be treated as an equivalent thin-film islands of some apparent thickness and complex refractive index; (2) the optical constants and thickness of individual islands are the same as those of the complete monolayer; (3) the overall reflectance of the surface is due to a coherent superposition of beams reflected from island-covered and bare portions of the electrode; and (4) the optical constants of the individual islands and the substrate are potential independent over the range where the UPD is formed. The second assumption implies that there is negligible interaction between individual islands as the monolayer approaches complete coverage; optical properties are assumed to be independent of coverage.

As an alternative, the Bruggeman theory can be used to compute the apparent refractive index of the underpotential layer at submonolayer coverages by mixing electrolyte and adatom optical properties. This model assumes that electrolyte ions and adatoms composing the UPD monolayer exist as a homogeneous, isotropic film covering the surface (a diffuse layer of adatoms weakly interacting with the surface).

Figs. 5.a and 5.b contrast the coherent superposition model and the Bruggeman model to some experimental data points. The Bruggeman model could not explain the experimental measurements, whereas the coherent

superposition model could.

The bulk deposit which formed on the first monolayer of Pb adatoms was found to be a granular, porous layer and could be adequately described by application of the Bruggeman theory (26). The effect of porosity on deposit optical properties was calculated by mixing the optical properties of metallic Pb with those of bulk electrolyte (physical mixing). This approach is analogous to that of others who have treated microrough surfaces as equivalent films (26-28).

The most general form for mixing the dielectric properties of a thin film is given in Eqn. 12 (29).

$$\frac{\hat{\varepsilon} - \hat{\varepsilon}_h}{\hat{\varepsilon} + 2\hat{\varepsilon}_h} = \sum_{i=1}^{n} \theta_i \frac{\hat{\varepsilon}_i - \hat{\varepsilon}_h}{\hat{\varepsilon}_i + 2\hat{\varepsilon}_h} \qquad (12)$$

Each term in the summation represents a weighted contribution of the polarizability of individual components of the composite film (mixed material) and are related to the molecular polarizability of the individual components through the Claussius-Mossetti equation (30)

$$\frac{\hat{\varepsilon}_i - 1}{\hat{\varepsilon}_i + 2} = \frac{4}{3}\pi N_i \alpha_i \qquad (13)$$

The porous deposit is a special case for the use of Eqn. 12 in that it is a binary system, a mixture of Pb and electrolyte. Eqn. 12 is simplified for the binary case as

$$\theta_{Pb} \frac{\hat{\varepsilon}_{Pb} - \hat{\varepsilon}_f}{\hat{\varepsilon}_{Pb} + 2\hat{\varepsilon}_f} + (1 - \theta_{Pb}) \frac{\hat{\varepsilon}_{soln} - \hat{\varepsilon}_f}{\hat{\varepsilon}_{soln} + 2\hat{\varepsilon}_f} = 0 \qquad (14)$$

This simplification is important in that the complex dielectric constant of the composite film material (considered to be the host medium in Eqn. 12) can be determined by solving the resulting complex quadratic equation. The general multicomponent case requires finding "n" roots of an "n-th" degree complex polynomial, a formidable task. Eqns. 15 through 18 are used to compute the complex refractive index of the Bruggeman equivalent medium.

$$\hat{A} = \frac{1}{2} [\hat{\varepsilon}_{Pb}(1 - 3\,\theta_{Pb}) + \hat{\varepsilon}_{soln}\,(3\,\theta_{Pb} - 2)] \qquad (15)$$

$$\hat{B} = -\frac{1}{2}[\hat{\varepsilon}_{Pb}\,\hat{\varepsilon}_{soln}] \qquad (16)$$

$$\hat{\varepsilon}_f = \frac{1}{2} [-\hat{A} \pm (\hat{A}^2 - 4\hat{B})^{1/2}] \qquad (17)$$

$$\hat{n}_f = \hat{\varepsilon}_f^{\,1/2} \qquad (18)$$

The complex refractive index of Eqn. 18 is used in the ellipsometry equations discussed above to calculate delta and psi. It is important to note that one has to select one of two roots from the solution of the complex quadratic equation; the root with the largest modulus is used (31).

To model both the UPD monolayer and the bulk deposit collectively a two-film model was used, analogous to the approach of Smith and Muller (32,33). First, a value of the complex reflection coefficient ratio due to the UPD layer on the electrode was calculated (Eqn. 10). This was done using the apparent optical properties of the UPD. Then, using this ratio and Eqns. 19 through 21 an apparent substrate refractive index was calculated, which included both the effects of the substrate and the UPD monolayer. The Bruggeman theory was used to compute the apparent film refractive index of the composite film material. These optical constants were then used in the ellipsometry equations, with a specified thickness, to calculate values of delta and psi.

$$\tan \hat{\phi}' = \left(\frac{1+\rho}{1-\rho}\right)/\tan \phi \qquad (19)$$

$$\sin \hat{\phi}' = \tan \hat{\phi}'/[1 + \tan^2 \hat{\phi}']^{1/2} \qquad (20)$$

$$\hat{n}_s = n_s - ik_s = n_a \sin\phi / \sin\hat{\phi}' \tag{21}$$

By minimizing the sum-of-squares error between the model predictions and measured values of delta and psi, optimum values of the adjustable model parameters were determined (34,35). Parameters fitted were (1) UPD complex refractive index, (2) apparent thickness of the UPD, (3) porosity of the bulk deposit, and (4) the thickness of the bulk deposit. Fine tuning of the metallic optical constants was done initially to compensate for the large uncertainty in literature and experimental values of Pb optical constants. Eqn. 22 defines the sum-of-squares error for the model is defined by Eqn. 22.

$$S_{\Delta,\psi} = \sum_{i=1}^{N'} (\Delta_{M,i} - \Delta_{C,i})^2 + \sum_{i=1}^{N'} (\Psi_{M,i} - \Psi_{C,i})^2 \tag{22}$$

The parameter variance is then defined by Eqn. 23.

$$SE(p) = \frac{\sigma^2}{\frac{1}{2}\frac{\partial^2 S_{\Delta,\psi}}{\partial p^2}} \tag{23}$$

Parameter confidence intervals (Eqn. 24) were calculated from this variance and the student-t statistic for "2N'-P" degrees of freedom, where "N'" is the number of delta-psi measurements and "P" is the number of adjustable model parameters.

$$\delta(p) = t(2N' - P, 1 - 2\alpha)[SE(p)]^{1/2} \tag{24}$$

Both the parameter variance and the model variance were required and estimated numerically with Eqns. 25 and 26, respectively.

Eqn. (25) is the model variance.

$$\sigma^2 \sim S_{MIN}/df = S_{MIN}/(2N' - P) \tag{25}$$

$$\frac{1}{2}\frac{\partial^2 S_{\Delta,\psi}}{\partial p^2} \sim \frac{S_{(+)} + S_{(-)} - 2\,S_{MIN}}{2(\Delta p)^2} \tag{26}$$

Separate optimizations were performed to estimate UPD and bulk optical properties. This was possible since potential ramping separates formation of the two layers in time.

During formation of the Pb UPD on Ag; 19 values of current, delta, and psi were measured and logged by computer. These measurements were used collectively to estimate the three model parameters pertaining to the UPD (complex refractive index and thickness). The optical constants and thicknesses for the Pb UPD layers on Ag(111) and Cu(111), calculated for a wavelength of 515 nm, are given in Table I. Stated errors ignore the sensitivity of these parameters to errors in the substrate and incident medium refractive indices. Model predictions for the Pb UPD on Ag(111) and Cu(111) are compared to experimental observations in Figs. 6.a and 6.b, respectively. Experimental observations are given

numerically in Tables II.A and II.B.

Estimates of the parameters pertaining to the bulk deposit are more uncertain. Confidence intervals for these parameters could have been estimated only by averaging comparable values of delta and psi from replicate experiments (or multiple sweeps). Modeling results for the bulk Pb deposit are presented in Table III for the potential cycles shown in Figs. 1.a through 1.e, 2.a through 2.e, and 3.a through 3.e. From these results it was concluded that the bulk deposit formed in the experiments conducted at 0.5 mM was approximately 30% porous and had a thickness of about 10 Angstroms; the bulk deposit formed in the experiment conducted at 5.0 mM was approximately 40% porous and had a thickness of about 200 Angstroms.

The calculations described here were done with the computer programs and data files discussed in Chapter 3. Data were collected by a LSI-11 microcomputer using program EDR002 and converted to current, delta, and psi using program TRNSLT. The reduced data were stored in a formatted data file called PLTDAT.DAT.

Both the UPD optical constants and thickness were calculated by the optimization routine OHGOGO by matching measured values of delta and psi with predicted values at complete monolayer coverage. Sub-monolayer predictions were generated with EMATST and CSMTST using the optical constants generated by OHGOGO. Program EMATST, based upon the Bruggeman theory, was used to predict delta and psi for the UPD (Fig. 5.a); program CSMTST, based upon the coherent superposition model, was used to predict delta and psi for the UPD shown in Figs. 5.b, 6.a, and 6.b.

Variances of the three parameters involved in the coherent superposition model were computed by CSMERR and were based upon all available data for formation of the UPD monolayer, from zero to complete coverage.

These programs rely on several subroutines. FILM computes delta and psi for a homogeneous, isotropic film given: the film thickness; the complex refractive indices of the substrate, film, and incident medium; the angle of incidence; and the source wavelength. Subroutine EMA computes the apparent film refractive index of a binary mixture based on the Bruggeman theory. Subroutine REFIND calculates the apparent substrate complex refractive index when multiple film calculations are required. Subroutine CSFILM calculates delta and psi from the weighted average of the reflection coefficients for the coherent superposition model.

It is traditional when doing ellipsometry in the sub-monolayer region to present measured values of delta and psi as differences from baseline values, since changes are small compared to absolute values (Eqns. 27 and 28).

$$\delta\Delta = \Delta - \Delta_0 \tag{27}$$

$$\delta\psi = \psi - \psi_0 \tag{28}$$

Applications and Theory of Light Scattering from Microrough Surfaces

Extensive theory exists for correlating surface roughness with light scattering (36-40). Light scattering has been used in conjunction with ellipsometry and reflectance measurements to characterize microrough aluminum oxide surfaces (41), and for the confirmation of ellipsometric interpretations regarding the nucleation and growth of anodic silver oxide films (42). In nickel deposition light scattering measurements have been used to determine rms roughness and correlation distance (43). Here, light scattering was used only to substantiate ellipsometric interpretations regarding the formation of submicroscopic particulate (granular, porous) Pb deposits on electrode surfaces (see Figs. 4.a through 4.c). The maximum increase in light scattering corresponds to a film thickness (particle diameter) of about 20 Angstroms. Light scattering is correlated with bulk deposition and is reversible. The cell used for measurement is shown in Fig. 8.

Analysis of the Adsorption Isotherm Data

Conway, Kozlowska, and Dahr have presented general theories of adsorption at liquid-solid interfaces and the proper selection of standard states (44). Ross has applied the Frumkin adsorption isotherm (g=0) to the case of H_2 adsorption on Pt single crystals; data were taken from cyclic voltammograms (45). Conway and Kozlowska have discussed the effects of sweep rate, etc. on the UPD peak in the voltammetry data (46).

The general form of the Frumkin adsorption isotherm is given in Eqn. 29 below (47).

$$\frac{\theta}{1-\theta} = C \exp\left[-\frac{zFV}{RT}\right] \exp\left[\frac{-\Delta G^{\circ}_{ADS} - g\theta RT}{RT}\right] \tag{29}$$

If the interaction parameter is negligible (g=0), Eqn. 29 simplifies to Eqn. 30 which is linear in potential.

$$\ell n \left(\frac{\theta}{1-\theta}\right) = -\frac{zF}{RT}(U-U_{1/2}) \tag{30}$$

The Gibbs free energy of adsorption is related to the underpotential at half monolayer coverage ($U_{1/2}$) through Eqn. 31.

$$\Delta G^{\circ}_{ADS} = -zFU_{1/2} \tag{31}$$

Since Eqn. 30 is linear in potential (underpotential scale), it can be applied to experimental data easily by using regression analysis (48-50). Eqn. 32 is used for data reduction; the slope and intercept (m and b, respectively) are then related to the Gibbs free energy of adsorption, the half coverage underpotential, and the apparent valence through Eqns. 33, 34, and 35, respectively.

$$\ell n \left(\frac{\theta}{1-\theta}\right) = m \cdot U + b \tag{32}$$

$$G^{\circ}_{ADS} = -bRT \tag{33}$$

$$U_{1/2} = -b/m \tag{34}$$

$$z = -m\ RT/F \tag{35}$$

Rigorous analysis relates the error in these physical quantities (Eqns. 36 through 38) to the uncertainties in the regression line slope and intercept (Eqns. 39 and 40), and to the model variance (Eqn. 41).

$$\delta(\Delta G^{\circ}_{ADS}) = F \left[(U_{1/2} \cdot \delta z)^2 + (z \cdot \delta U_{1/2})^2 \right]^{1/2} \tag{36}$$

$$\delta(U_{1/2}) = U_{1/2} \left[\left(\frac{\delta b}{b}\right)^2 + \left(\frac{\delta m}{m}\right)^2 \right]^{1/2} \tag{37}$$

$$\delta(z) = \frac{RT}{F} |\delta m| \qquad \text{also written as } \delta z \tag{38}$$

$$\delta m = S \cdot t(N-2, 1-2\alpha) \left[\sum_{i=1}^{N} (U_i - \overline{U})^2 \right]^{-1/2} \tag{39}$$

$$\delta b = S \cdot t(N-2, 1-2\alpha) \left[\left(\sum_{i=1}^{N} U_i^2 \right) \div \left(N \sum_{i=1}^{N} (U_i - \overline{U})^2 \right) \right]^{1/2} \tag{40}$$

$$S = \left[\sum_{i=1}^{N} \left(\ell n\left(\frac{\theta_i}{1-\theta_i}\right) - \ell n\left(\frac{\theta_u}{1-\theta_u}\right) \right)^2 \frac{1}{N-2} \right]^{1/2} \tag{41}$$

Results of the linear regression and error analysis are presented in Table IV. The data for the Pb UPD on Ag(111) and Cu(111) were first analyzed separately; then together. The non-integer apparent valences have no statistical significance and are believed to be due to integration errors. The coverage, which was determined by integration of the cathodic UPD peak, could not be determined accurately at low values since the current was of the same amplitude as the background noise. Therefore, it was assumed that the valence was approximately 2; inspection of the experimental data plotted in Fig. 7.a shows that the half-coverage underpotential is about 155 mV (for both substrates) which corresponds to a Gibbs free energy of adsorption of 7.14 kcal/mol. Theoretical predictions of coverage at different potentials were made by

substituting these values into the adsorption isotherm equation. These predictions are represented by the broken line in Fig. 7.a and agree with experimental data, except at very low coverages where significant integration errors exist. The data were also linearized and plotted in Fig. 7.b for comparison to model predictions, shown as a solid line. Note that double layer charging was subtracted from the integrated current used to calculate the coverage.

There is a popular concept of partial discharge associated with electrosorption bonds (51). The results presented here regarding the Pb UPD do not support this concept.

The Charge Balance

Eqn. 42 was used to calculate the charge passed to the working electrode during deposition. This charge was used to calculate the coverage of Pb adatoms on the electrode surface. The actual charge required for a complete UPD monolayer was within 25% of the expected amount; the discrepancy is probably due to the finite surface roughness which was not considered in the charge balance. See Table V.

$$Q = \int_0^t i\,(t)\cdot A\cdot dt = \frac{(x\cdot y\cdot d_q)\rho_{Pb}}{MW_{Pb}}\; z_{Pb} e\, N_{AVG} \qquad (42)$$

The deposit thickness and its volume fraction Pb, determined from ellipsometry measurements, were used to compute the total Pb on the electrode surface. This quantity was then compared to the amount thought to be present based upon the charge passed; the ellipsometer

measurements consistently indicated less Pb on the surface than the charge balance (a discrepancy ranging from 10 to 50 percent). This might have been due to poor current distribution on the electrode with Pb preferentially deposited around the edge of the electrode, while the ellipsometry measurement was performed at the center.

Conclusions

This work illustrates how the initial stages of electrodeposition can be elucidated using simultaneous ellipsometry and cyclic voltammetry, and simultaneous light scattering measurements and cyclic voltammetry. The advantage of this experimental approach lies in the separation of the UPD and bulk deposit optical properties in time by ramping the potential.

From this study, we have concluded that three-dimensional nucleation occurs on the UPD monolayer. The optical constants of the UPD monolayer and its apparent thickness have been determined. An optical model which fits the data very well and involves the formation of monolayer islands has been applied to UPD growth. The micromorphology of the bulk deposit formed on the UPD has been quantified.

The Gibbs free energy of adsorption and apparent valence for the Pb UPD on Ag(111) and Cu(111) have been determined (valence of 2, free energy of 7 kcal/mol) and are different from the values found in the literature.

References

1. Kolb, D. M., "Physical and Electrochemical Properties of Metal Monolayers on Metallic Substrates," ADVANCES IN ELECTROCHEMISTRY AND ELECTROCHEMICAL ENGINEERING, Vol. 11, John Wiley & Sons, New York, 1978, pp. 125-271.

2. Schmidt, E., Gygax, H. R., "Chronoamperometrische Untersuchung Metallischer Monoschichten," J. Electroanal. Chem., 12, 300 (1966).

3. Harrison, J. A., Thirsk, H. R., "The Fundamentals of Metal Deposition," ELECTROANALYTICAL CHEMISTRY, Vol. 5, A. J. Bard, ed., Marcel Dekker, New York, 113 (1971).

4. Hass, G., Hadley, L., "Optical Properties of Metals," AMERICAN INSTITUTE OF PHYSICS HANDBOOK, 2nd ed., Gray, D. E., ed., McGraw-Hill, New York, 6-103 to 6-122 (1963).

5. Johnson, P. B., Christy, R. W., "Optical Constants of the Noble Metals," Phys. Rev. B, 6, 4370 (1972).

6. Adzic, R., Yeager, E., Cahan, B.D., "Optical and Electrochemical Studies of Underpotential Deposition of Lead on Gold Evaporated and Single-Crystal Electrodes," J. Electrochem. Soc., 121, 474 (1974).

7. Takayanagi, K., Kolb, D. M., Kambe, K., Lehmpfuhl, G., "Deposition of Monolayer and Bulk Lead on Ag(111) Studied in Vacuum and in an Electrochemical Cell," Surf. Sci, 100, 407 (1982).

8. Vassos, B. H., Mark, H. B., Jr., J. Electroanal. Chem., 13, 1 (1967).

9. Povetkin, V. V., Kovenskii, I. M., "Initial Step of Copper Electrocrystallization in the Presence of Cadmium, "Soviet Electrochem., 17, 1461 (1981).

10. See 2.

11. Mathieu, H. J., McClure, D. E., Muller, R. H., "Fast self-compensating ellipsometer," Rev. Sci. Instrum., 45, 798 (1974).

12. Muller, R. H., Plieth, W. J., Farmer, J. C., "Nucleation and Growth of Anodic Silver Oxide Films: Light Scattering and Ellipsometry Measurements," Lawrence Berkeley Laboratory, LBL-12965 (1981).

13. Petzow, G., METALLOGRAPHISCHES ATZEN, Gebruder Borntraeger, Berlin, english translation by ASM (1976).

14. See 12.

15. Delahay, P., Pourbaix, M., Rysselberghe, P., "Potential-pH Diagram of Silver," J. Electrochem. Soc., 98, 65 (1951).

16. Pourbaix, M., "Atlas of Electrochemical Equilibria in Aqueous Solutions," Pergamon Press, New York (1966).

17. See 12.

18. Bootsma, G. A., Meyer, F., "Ellipsometry in the Sub-monolayer Region," Surf. Sci., 14, 52 (1969).

19. Bootsma, G. A., Hanekamp, L. J., Gijzeman, O. L. J., "4. Chemisorption Investigated by Ellipsometry," Proceedings of the 5th International Summer Institute for Surface Science," Howe, R., Vanselow, R., eds., Springer-Verlag, Berlin (1982).

20. Brodski, A. M., Urbakh, M. I., "Dependence of the Reflection of Light from Metals on the Characteristics of Adatoms: Microscopic Description of the Optical Properties of the Adatom," Soviet Electrochem., 38, 1553 (1979).

21. Plieth, W., Bruckner, H., Hensel, H. J., "Anisotropy of the Dielectric Properties of the Solid/Electrolyte Interface," Surf. Sci., 101, 261 (1980).

22. Takamura, T., Takamura, K., "Application of the Optical Reflection Method to the Study of Electrosorption, Anodic Oxide, and Underpotential Deposition," ....., ..., 179 (....).

23. Takamura, K., Watanabe, F., "An Interpretation on the Origin of the Specular Reflectance Change Caused by the Sub-monolayer Formation of Foreign Metals on Some Precious Metal Electrodes," Electrochim. Acta, 26, 979 (1981).

24. Muller, R. H., Smith, C. G., "Use of Film Formation Models fot the Interpretation of Ellipsometer Observations," Surf. Sci., 96, 375 (1980).

25. Ohlidal, I., Lukes, F., Navratil, K., "Rough Silicon Surfaces Studied by Optical Methods," Surf. Sci., 45, 91 (1974).

26. Aspnes, D. E., Theeten, J. B., "Investigation of Effective-media Models of Microscopic Surface Roughness by Spectroscopic Ellipsometry," Phys. Rev. B, 20, 3292 (1979).

27. Brudewski, K., "Ellipsometric Investigation of a Substrate-Thin Film System with Rough Boundaries Using the Equivalent Film

Theory," Thin Solid Films, 61, 183 (1979).

28. Smith, T., Smith, P., Mansfield, F., "Ellipsometry Interpretation for Electrochemistry," J. Electrochem. Soc., 126, 799 (1979).

29. See 26.

30. Lorrain, P., Corson, D., ELECTROMAGNETIC FIELDS AND WAVES, 2nd ed., W. H. Freeman, San Francisco, 115 (1970).

31. Kahan, W., personal communication, Department of Computer Science and Mathematics, University of California, Berkeley, August, 1982.

32. Smith, C. G., "Ellipsometry of Anodic Film Growth," Ph.D. Thesis, Department of Chemical Engineering, University of California, Berkeley, LBL-8082 (1978).

33. See 24.

34. Hendrix, C., "An R/D Technical Education Course in Recent Advances in Statistics, Lecture No. 2," Union Carbide Technical Center, So. Chas., WV, April 18, 1978.

35. Box, G. E. P., Coutie, G. A., "Application of Digital Computers in the Exploration of Functional Relationships," Proceedings of the Institution of Electrical Engineers, Vol. 103, Part B, Supplement No. 1, 100 (1956).

36. Marvin, A., Toigo, F., Celli, V., "Light Scattering from Rough Surfaces, General Incidence Angle and Polarization," Phys. Rev. B, 11, 2777 (1975).

37. Celli, V., Marvin, A., Toiga, F., "Light Scattering from Rough Surfaces," Phys. Rev. B, 11, 1779 (1975).

38. Maradudin, A. A., Mills, D. L., "Scattering and Absorption of Electromagnetic Radiation by a Semi-infinite Medium in the Presence of Surface Roughness," Phys. Rev. B, 11, 1392 (1975).

39. Jakeman, E., "Fresnel Scattering by a Corrugated Random Surface with Fractal Slope," J. Opt. Soc. Am., 72, 1034 (1982).

40. Bousquet, P., Flory, F., Roche, P., "Scattering from Multilayer Thin Films: Theory and Experiment," J. Opt. Soc. Am., 71, 1115 (1981).

41. Hensler, D. H., "Light Scattering from Fused Polycrystalline Aluminum Oxide Surfaces," Appl. Opt., 11, 11 (1972).

42. See 12.

43. See 28.

44. Conway, B. E., Angerstein-Kozlowska, H., Dhar, H. P., "On the Selection of Standard States in Adsorption Isotherms," Electrochim. Acta, 19, 455 (1974).

45. Ross, P. N., Jr., "Studies of Adsorption at Well-ordered Electrode Surfaces Using Low Energy Electron Diffraction," Proceedings of the 5th International Summer Institute for Surface Sciences," Howe, R., Vanselow, R., eds., Springer-Verlag, Berlin (1982).

46. Conway, B. E., Angerstein-Kozlowska, H., "Interaction Effects in Electrodeposited Monolayers and the Role of the 'Electrosorption

Valency' Factor," J. Electroanal. Chem., 113, 63 (1980).

47. See 44.

48. Draper, N. R., Smith, H., APPLIED REGRESSION ANALYSIS, Wiley, New York, 7-17 (1966).

49. Burr, I. W., APPLIED STATISTICAL METHODS, Academic Press, New York, 436 (1974).

50. Dixon, W. J., Massey, F. J., Jr., INTRODUCTION TO STATISTICAL ANALYSIS, McGraw-Hill, New York (1969).

51. Mola, Eduardo, E., "Electrosorption Bond Theory in the Hartree-Fock Approximation," Electrochim. Acta, 26, 1253 (1981).

Table I. Optical Properties of the Pb UPD at θ=1.

Substrates		$Ag(111)_1$	$Cu(111)_1$	$Cu(111)_2$
Ambient refractive index	n_A	1.340	1.340	1.340
UPD refractive index	n_{UPD}	1.285±0.007	1.225±0.066	0.952±0.417
UPD extinction coef.	k_{UPD}	4.080±0.040	3.520±0.041	3.898±0.021
UPD thickness	d_{UPD}	5.149±0.026	4.030±0.178	4.777±1.101
Substrate refractive index	n_s	0.174	0.788	0.853
Substrate extinction coef.	k_s	3.215	2.408	2.347

Conditions:

λ = 5145 , θ = 75°, T = 25°C, 0.5 and 5.0 mM Pb^{++}, 1M $NaClO_4$, pH 3

Note:

Errors given for 95% level of confidence and based upon 37 degrees of freedom, assuming applicability of the coherent superposition model. These errors do not take into account errors introduced by uncertainty in n_a and n_s, both determined experimentally. $Cu(111)_1$ at 0.5 mM and $Cu(111)_2$ at 5.0 mM Pb^{++} respectively.

Table II.A. Data for Pb UPD on Ag(111).

t(sec)	U(mV)‡	θ	$\ell n(\frac{\theta}{1-\theta})$	Δ°	ψ°	δΔ°	δψ°
148	198	0	-∞	71.445	43.738	0	0
150	193			71.340	43.728	-0.011	-0.010
152	187	0.015	-4.177381	71.424	43.696	-0.042	-0.042
154	182	0.044	-3.089731	71.466	43.728	0.000	-0.010
156	176	0.088	-2.338820	71.445	43.707	-0.021	-0.031
158	171	0.147	-1.759757	71.549	43.686	0.083	-0.052
160	165	0.240	-1.155331	71.507	43.655	0.041	-0.083
162	160	0.368	-0.542481	71.654	43.613	0.188	-0.125
164	155	0.498	-0.009542	71.759	43.560	0.293	-0.178
166	150	0.606	0.428222	71.696	43.498	0.230	-0.240
168	144	0.689	0.795158	71.801	43.456	0.335	-0.282
170	139	0.756	1.130275	71.821	43.466	0.355	-0.272
172	133	0.813	1.466744	71.884	43.403	0.418	-0.335
174	128	0.862	1.832707	71.947	43.393	0.418	-0.345
176	123	0.905	2.248414	71.905	43.383	0.439	-0.355
178	117	0.938	2.720549	71.884	43.372	0.418	-0.366
180	112	0.964	3.272731	71.884	43.341	0.418	-0.397
182	107	0.980	3.908851	71.926	43.351	0.460	-0.387
184	101	0.990	4.630358	71.905	43.351	0.439	-0.387
186	96	0.996	5.604699	71.968	43.341	0.502	-0.397
188	91	0.999	7.180542	71.947	43.330	0.481	-0.408
190	86	1	+∞	71.905	43.309	0.481	-0.408

‡ E° = -456 ± 2 mV(Ag/AgCl ref.)

Table II.B. Data for Pb UPD on Cu(111).

t(sec)	U(mV)‡	θ	$\ell n(\frac{\theta}{1-\theta})$	Δ°	ψ°	δΔ°	δψ°
7.2	236	0	-∞	59.377	38.729	0	0
7.4	230	0.002	-6.381277	59.377	38.729	0	0
7.6	225	0.004	-5.52036	59.377	38.729	0	0
7.8	219	0.005	-5.384475	59.377	38.741	0	0.012
8.0	212	0.005	-5.327193	59.424	38.753	0.047	0.024
8.2	208	0.011	-4.527167	59.401	38.471	0.024	0.012
8.4	201	0.027	-3.589674	59.447	38.717	0.070	-0.012
8.6	195	0.051	-2.932453	59.447	38.717	0.070	-0.012
8.8	190	0.085	-2.372676	59.447	38.717	0.070	-0.012
9.0	184	0.142	-1.795334	59.471	38.717	0.094	-0.012
9.2	178	0.212	-1.313231	59.518	38.717	0.141	-0.012
9.4	172	0.279	-0.947876	59.518	38.694	0.141	-0.035
9.6	167	0.354	-0.603588	59.541	38.694	0.164	-0.035
9.8	161	0.435	-0.261780	59.564	38.682	0.187	-0.047
10.0	155	0.515	0.060849	59.634	38.659	0.257	-0.070
10.2	148	0.594	0.382045	59.658	38.647	0.281	-0.082
10.4	144	0.675	0.728522	59.681	38.624	0.304	-0.106
10.6	138	0.753	1.115357	59.775	38.612	0.398	-0.117
10.8	133	0.824	1.544160	59.798	38.589	0.421	-0.140
11.0	127	0.881	2.005935	59.821	38.601	0.444	-0.128
11.2	121	0.923	2.480317	59.891	38.566	0.514	-0.163
11.4	116	0.953	3.007560	59.938	38.577	0.561	-0.152
11.6	110	0.977	3.738404	59.961	38.566	0.584	-0.163
11.8	104	0.992	4.761394	59.985	38.566	0.608	-0.163
12.0	98	0.998	6.002495	59.961	38.542	0.584	-0.187
12.2	93	1	∞	60.008	38.542	0.631	-0.187

‡E° = -454 ± 2 mV (Ag/AgCl ref.)

Table III. Optical Properties of Bulk Pb Deposits.[†]

t(sec)	$E^{\ddagger}$(mV)	Q(mC)	d_q(Å)	Δ_M°	ψ_M°	Δ_C	ψ_C	d(Å)	θ_{Pb}	n_{Pb}	k_{Pb}
					Ag(111), 0.5 mM Pb[‡], 0.1 V/min						
219*	-443	1.55	3.52	72.06	43.27	72.06	43.27	5.53	1	1.30	4.27
300	-490	12.93	29	71.90	41.85	71.58	41.97	16	0.75	2.05	4.27
413	-663	18.35	42	71.62	41.13	71.30	41.18	26	0.75	2.10	4.27

[†]1 M $NaClO_4$ supporting electrolyte at pH 3
‡Ag/AgCl reference electrode
*underpotential deposit

Table III. Optical Properties of Bulk Pb Deposits.[†] (Continued)

t(sec)	$E^{\ddagger}$(mV)	Q(mC)	d_q(Å)	Δ_M°	ψ_M°	Δ_C	ψ_C	d(Å)	θ_{Pb}	n_{Pb}	k_{Pb}
					Cu(111), 0.5 mM Pb[‡], 0.5 V/min						
18*	-452	1.58	3.52	60.31	38.44	60.32	38.43	5.05	1	1.35	4.03
24	-592	2.20	5	60.56	38.22	60.52	38.13	6	0.71	1.95	4.27
30	-746	3.14	7	60.61	38.11	60.61	38.11	6	0.71	1.95	4.27
46	-476			60.61	37.90	60.51	38.14	6	0.71	1.95	4.27
48	-438	4.47	10	60.83	37.84	60.82	37.80	12	0.73	1.98	4.24

[†]1 M $NaClO_4$ supporting electrolyte at pH 3
[‡]Ag/AgCl reference electrode
*underpotential deposit

Table III. Optical Properties of Bulk Pb Deposits.† (Continued)

t(sec)	E‡(mV)	Q(mC)	d_q(Å)	Δ_M°	ψ_M°	Δ_C	ψ_C	d(Å)	θ_{Pb}	n_{Pb}	k_{Pb}
					Cu(111), 5.0 mM Pb‡, 1.5 V/min						
17*	-422	2	3.52	59.34	38.04	59.32	37.97	4.79	1	0.95	3.99
23	-576	28	49	56.59	36.17	56.52	36.09	76	0.56	1.90	4.30
40	-606	80	141	58.00	33.95	58.01	34.03	170	0.60	1.94	4.26
45	-478	91	160	58.55	33.56	58.63	33.16	194	0.61	1.99	4.28

†1 M $NaClO_4$ supporting electrolyte at pH 3
‡Ag/AgCl reference electrode
*underpotential deposit

Table IV. Linear Regression Analysis of Adsorption Isotherm Data.

QUANTITY	UNITS	Ag(111)	Cu(111)	Ag(111)+Cu(111)
ΔG°_{ADS}	kcal/mol	-8.75	-7.75	-7.90
$U_{1/2}$	mV	151	156	155
z		2.52	2.15	2.21
m	mV^{-1}	-0.098.26	-0.083678	-0.086188
b		14.783091	13.090754	13.339047
$\delta(\Delta G^{\circ}_{ADS})$	kcal/mol	1.23	0.87	0.88
$\delta(U_{1/2})$	mV	17	13	15
δz		0.21	0.12	0.12
δm	mV^{-1}	0.008001	0.004746	0.004523
δb		1.134927	0.800944	0.706471
S		0.485484	0.437346	0.572739
R		-0.989448	-0.992104	-0.986668

Note: $N-2 = 17$, $1-\frac{\alpha}{2} = 0.95$, and $t(17, 0.95) \sim 2.11$

$N-2 = 36$, $1-\frac{\alpha}{2} = 0.95$, and $t(36,0.95) \sim 2.02$

Table V.A. Charge Balance for UPD.

SUBSTRATE	Q(mc)	Q/1.27
Ag(111)	1.55	1.22
Cu(111)	1.58	1.24

Table V.B. Agreement of Charge Balance for Bulk Deposit with Optical Data.

SUBSTRATE	Pb^{++} mM	time sec	coulombic efficiency %	d_q Å	θ_{Pb} vol. fract.	d Å	$\frac{\theta_{Pb} \cdot d}{d_q}$
Ag(111)	0.5	300		29	0.75	16	0.41
		413	50	42	0.75	26	0.46
Cu(111)	0.5	24		5	0.71	6	0.85
		30		7	0.71	6	0.61
		46		9	0.71	6	0.47
		48	95	10	0.73	12	0.88
Cu(111)	5.0	23		49	0.56	76	0.87
		40		141	0.60	170	0.72
		45	96	160	0.61	194	0.74

Table V.C. Charge Balance for UPD.

Quantities

Monolayer Dimensions for UPD

$d_q = 3.52 \times 10^{-8}$ cm (Pb atomic diameter)

$x = 1.20$ cm (electrode dimension)

$y = 2.85$ cm

Constants

$N_{AVG} = 6.0221 \times 10^{23}$ Atoms/mol

$e = 1.6019 \times 10^{-19}$ coul/e^-

$z_{Pb} = 2e^-$/Atom

$\rho_{Pb} = 11.3437$ gm/cm^3

$MW_{Pb} = 207.20$ gm/mol

Table V.C. Charge Balance for UPD. (Continued)

Sample Calculation

$$Q = \int_0^t i(t) \cdot A \cdot dt = \frac{(x \cdot y \cdot d_q)\ \rho_{Pb}\ z_{Pb}\ e\ N_{AVG}}{MW_{Pb}}$$

$$Q = \frac{(3.52 \times 10^{-8} \times 1.20 \times 2.85)(11.34)(2)(1.60 \times 10^{-19})(6.02 \times 10^{23})}{(207.20)}$$

$Q = 1.27 \times 10^{-3}$ coul per monolayer

Figures

1.a Cyclic voltammogram for Pb deposition on Ag(111) from 1 M $NaClO_4$, 0.5 mM $Pb(NO_3)_2$, pH 3. Potential is given relative to a Ag/AgCl reference electrode. The counter electrode was a sheet of Pt and the experiment was conducted in an acrylic cell.

1.b Potential ramp corresponding to Fig. 1.a from +150 mV to -660 mV at a sweep rate of 0.15 V/min.

1.c The current response to Fig. 1.b. The electrode area was 3.42 sq. cm (1.2 cm x 2.8 cm, mounted in epoxy resin).

1.d Ellipsometer response to Fig. 1.b at a source wavelength of 515 nm and an angle of incidence of 75 degrees. Delta vs time.

1.e Ellipsometer response to Fig. 1.b at a source wavelength of 515 nm and an angle of incidence of 75 degrees. Psi vs time.

2.a Cyclic voltammogram analogous to 1.a, except for Pb deposition on Cu(111) at a sweep rate of about 2 V/min.

2.b Potential ramp corresponding to Fig. 2.a from 0 to -800 mV at about 2 V/min.

2.c Current response corresponding to Fig. 2.b. Electrode dimensions were comparable to 1.c.

2.d Ellipsometer response to Fig. 2.b at a source wavelength of 515 nm and an angle of incidence of 75 degrees. Delta vs time.

2.e Ellipsometer response to Fig. 2.b at a source wavelength of 515 nm and an angle of incidence of 75 degrees. Psi vs time.

3.a Cyclic voltammogram similar to 2.a, except at 5 mM $Pb(NO_3)_2$ concentration (instead of 0.5 mM).

3.b Potential ramp corresponding to Fig. 3.a from 0 to -800 mV at about 2 V/min.

3.c Current response corresponding to Fig. 3.b. Electrode dimensions were same as for 2.c.

3.d Ellipsometer response to Fig. 3.b at a source wavelength of 515 nm and an angle of incidence of 75 degrees. Delta vs time.

3.e Ellipsometer response to Fig. 3.b at a source wavelength of 515 nm and an angle of incidence of 75 degrees. Psi vs time.

4.a Potential and current plotted against time comparable to the cyclic voltammogram shown in Fig. 1.a.

4.b Light scattering data at conditions similar to that of Fig. 1.a, except that the experiments were conducted on polycrystalline Ag in a specially designed light scattering cell. The electrodes were rectangular sheets submersed in the electrolyte. The top trace is the scattered light intensity (increasing in the positive direction). The bottom trace is the current response to the potential ramp (cathodic peaks have negative amplitudes). The first cathodic peak is the UPD deposition, the second being bulk Pb deposition. The source was an argon laser at 515 nm.

4.c Identical to 4.b, except at the maximum potential level, the cell was left at open circuit conditions.

4.d Stripping the deposit formed during the experiment shown in Fig. 4.c.

5.a Experimental data compared to Bruggeman model predictions for the Pb UPD on Ag(111). Delta and psi as a function of coverage. The optical constants were not optimized, but were simply computed for the last data point obtained at complete coverage.

5.b Similar to 5.a, except the submonolayer coverages are based upon the coherent superposition of reflection coefficients for the UPD and bare Ag(111) electrode.

6.a Optimized coherent superposition model for Ag(111) used for estimation of the UPD optical constants given in Table I.

6.b Optimized coherent superposition model for Cu(111) used for estimation of the UPD optical constants given in Table I. Note the deviation from the model prediction for delta at coverages greater than 0.85.

7.a Pb Langmuirian Electrosorption on Ag(111) and Cu(111), a comparison of the model preditions for a free energy of adsorption of 7 kcal/mol and a valence of 2 to experimental data. Coverages were computed from integration of the cyclic voltammogram UPD peaks of Figs. 1.a and 2.a. Coverage plotted against potential.

7.b Linearization of the data shown in Fig. 7.a.

8. A photograph of the light scattering cell with photomultiplier detector and fiber optics probe. The fiber optics probe could be automatically scanned through different scattering angles. The

angle of collection of scattered light was 15 degrees off specular, towards the surface normal. Courtesy of W. Plieth.

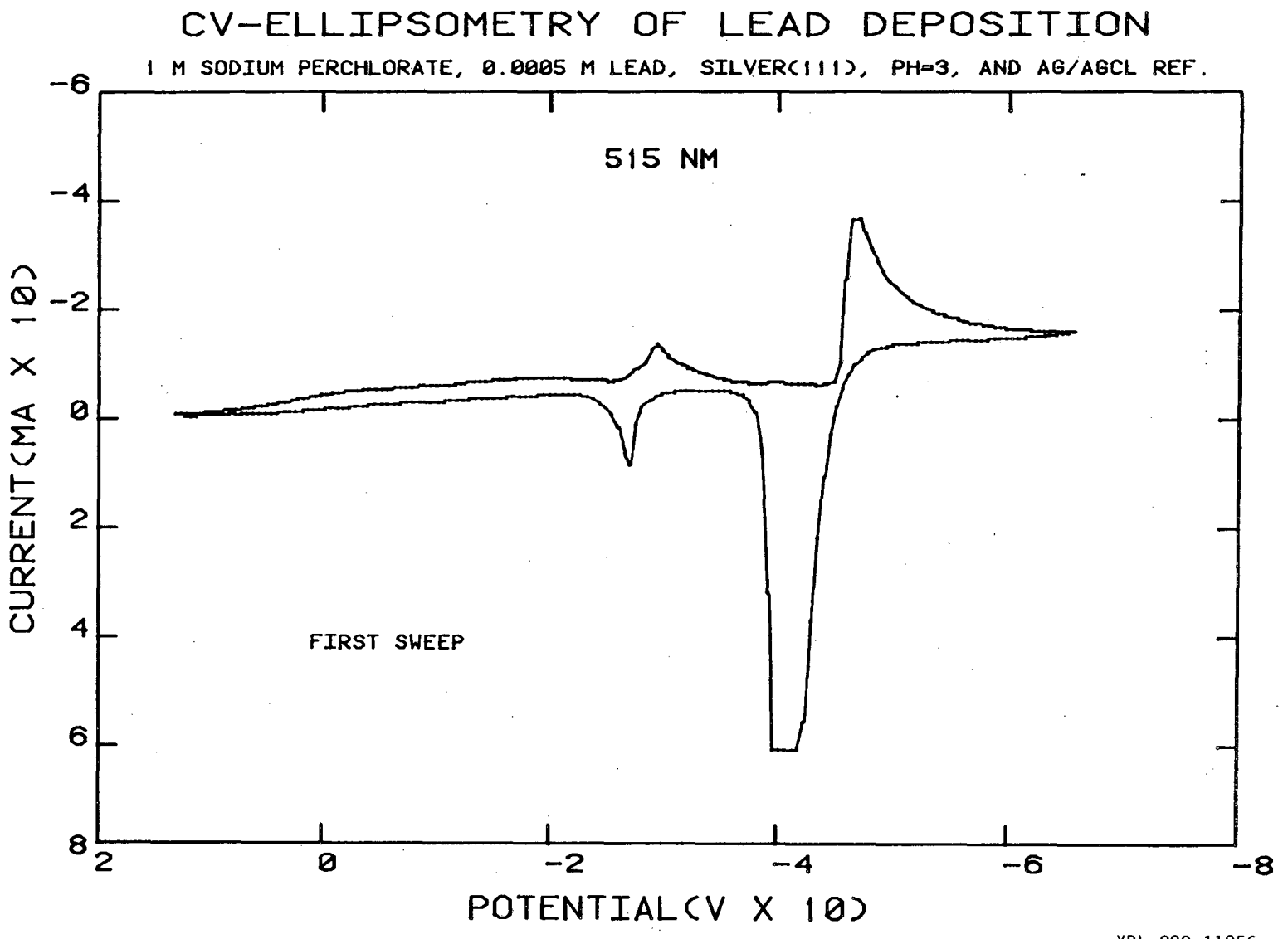

XBL 829-11856

Fig. 1.a

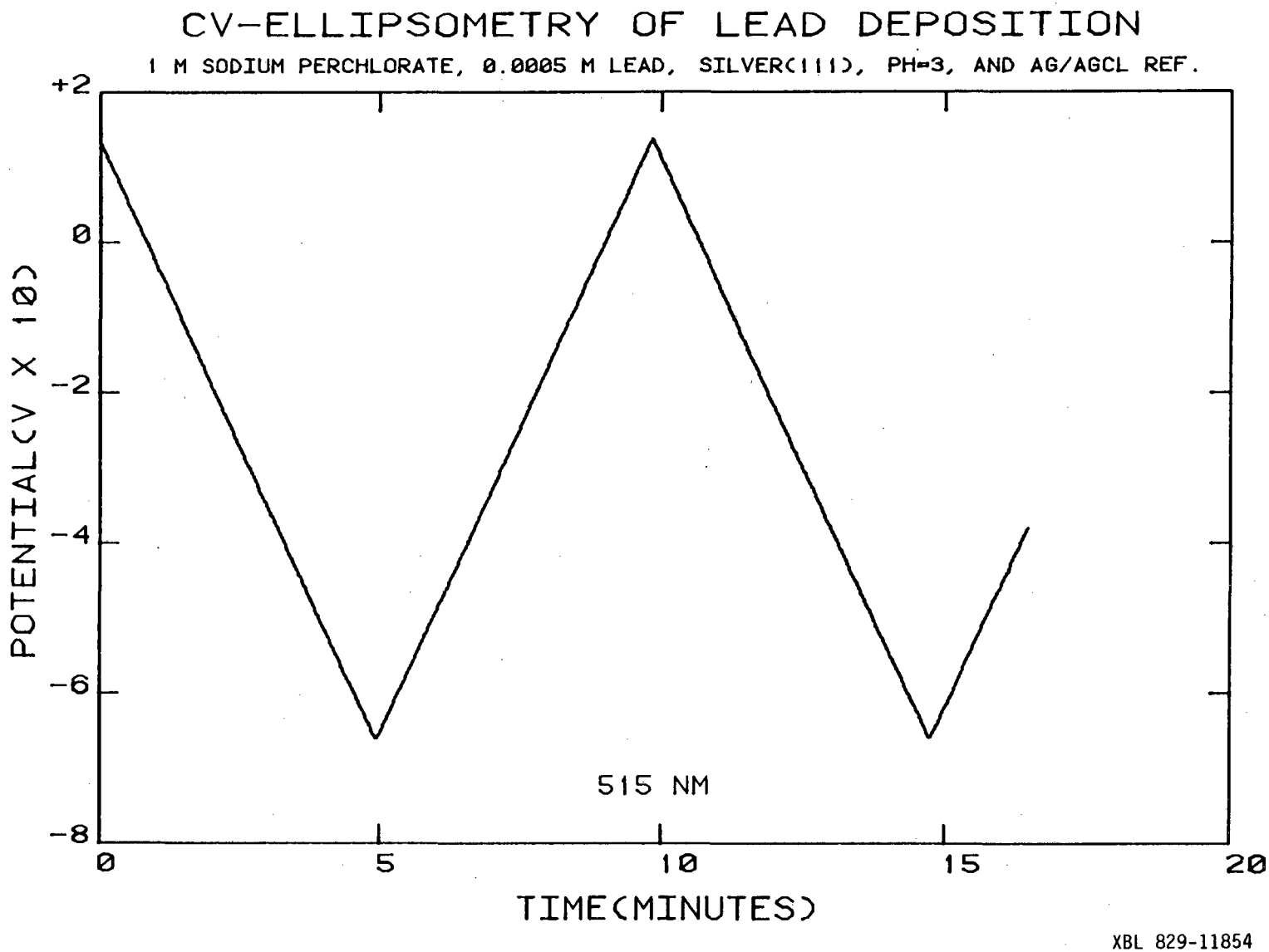

XBL 829-11854

Fig. 1.b

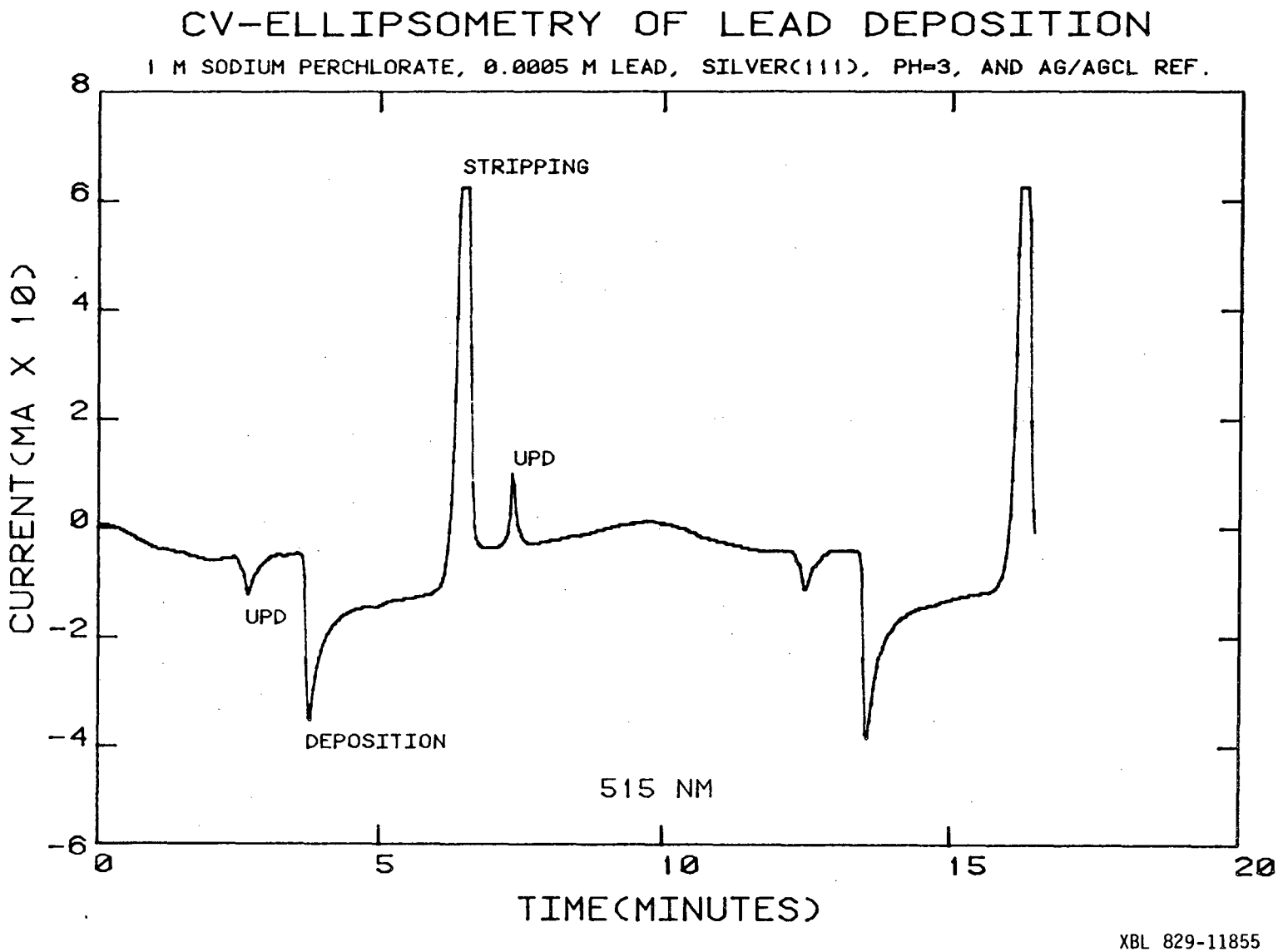

XBL 829-11855

Fig. 1.c

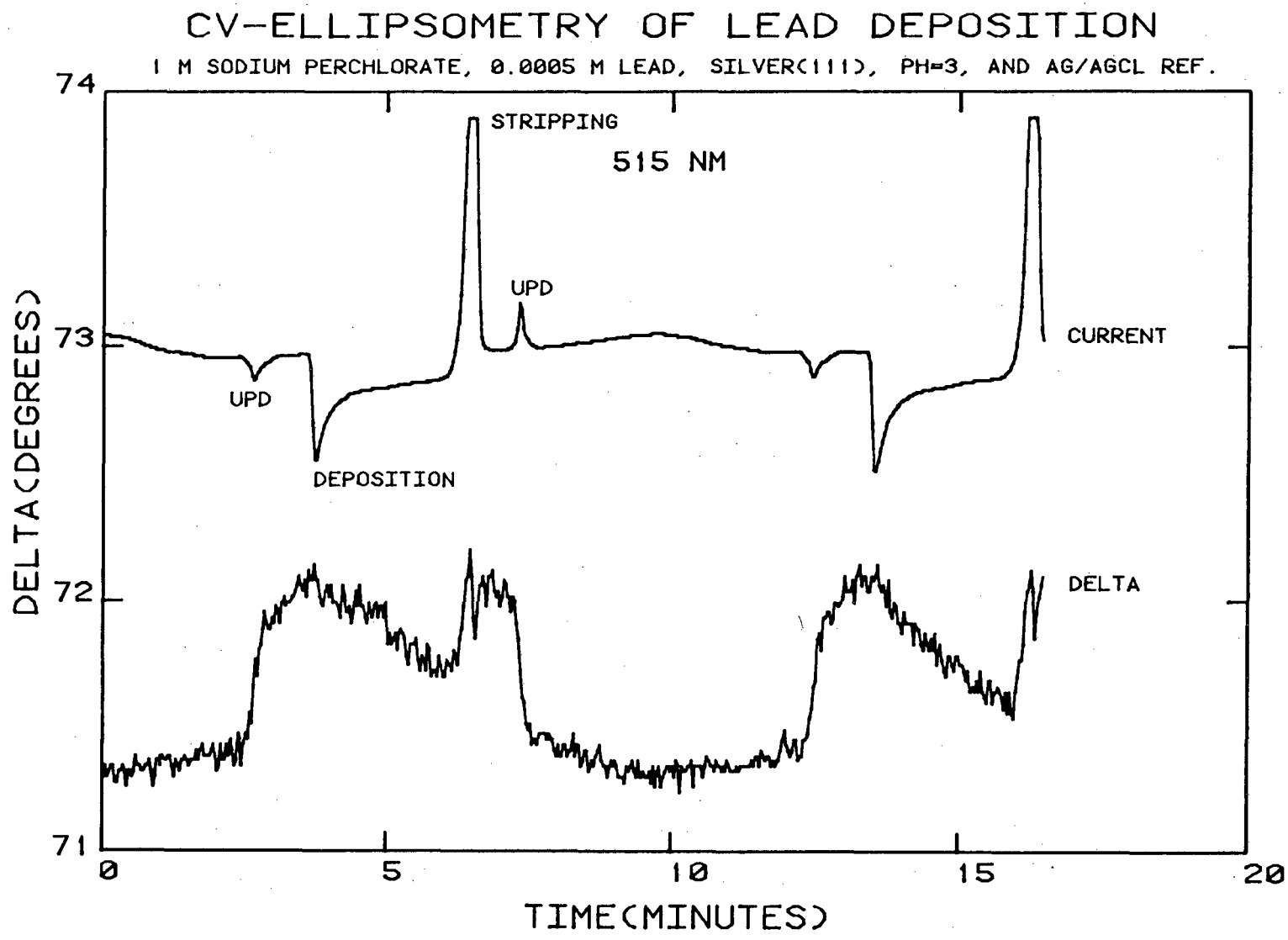

XBL 829-11857

Fig. 1.d

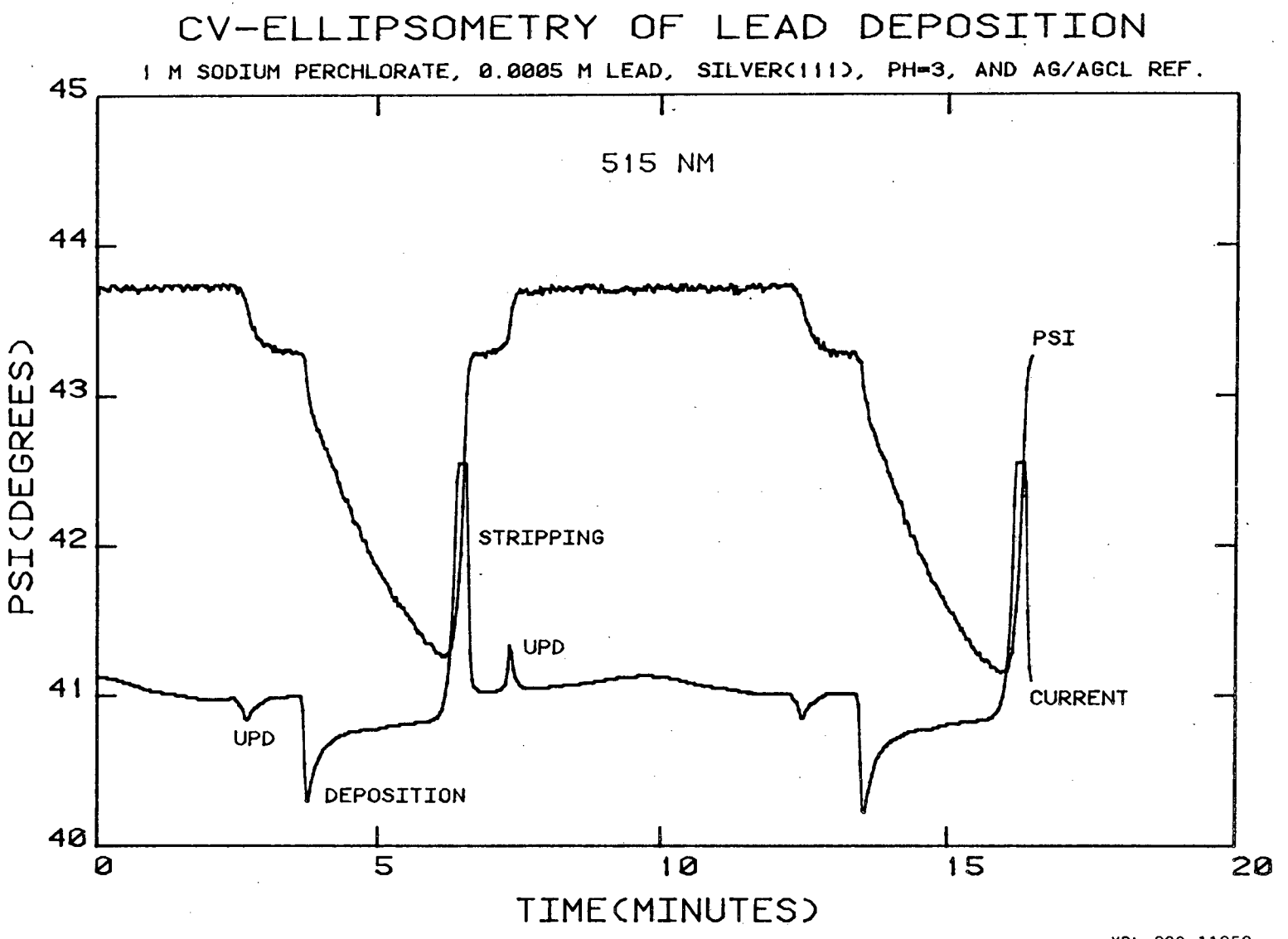

XBL 829-11858

Fig. 1.e

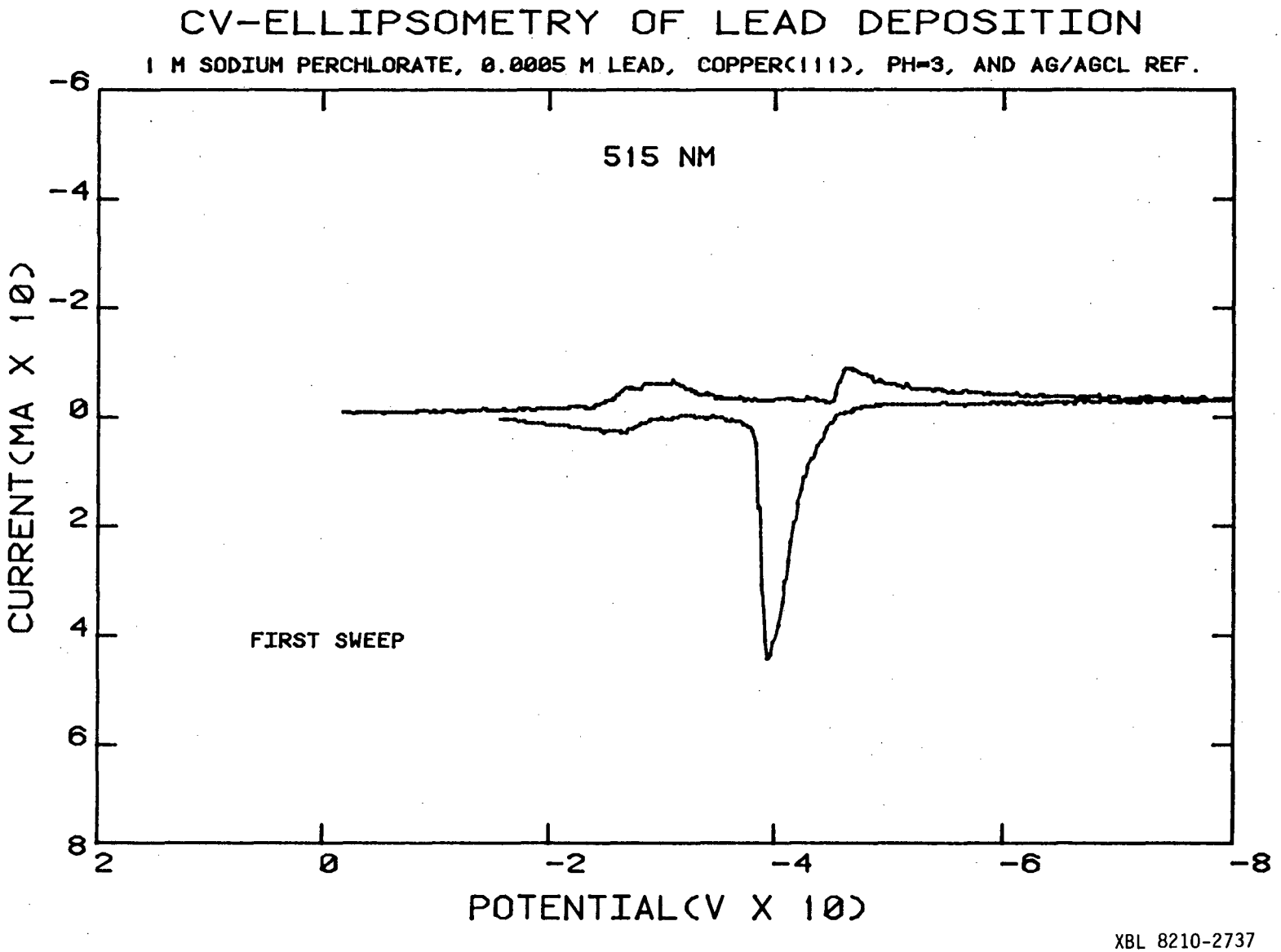

XBL 8210-2737

Fig. 2.a

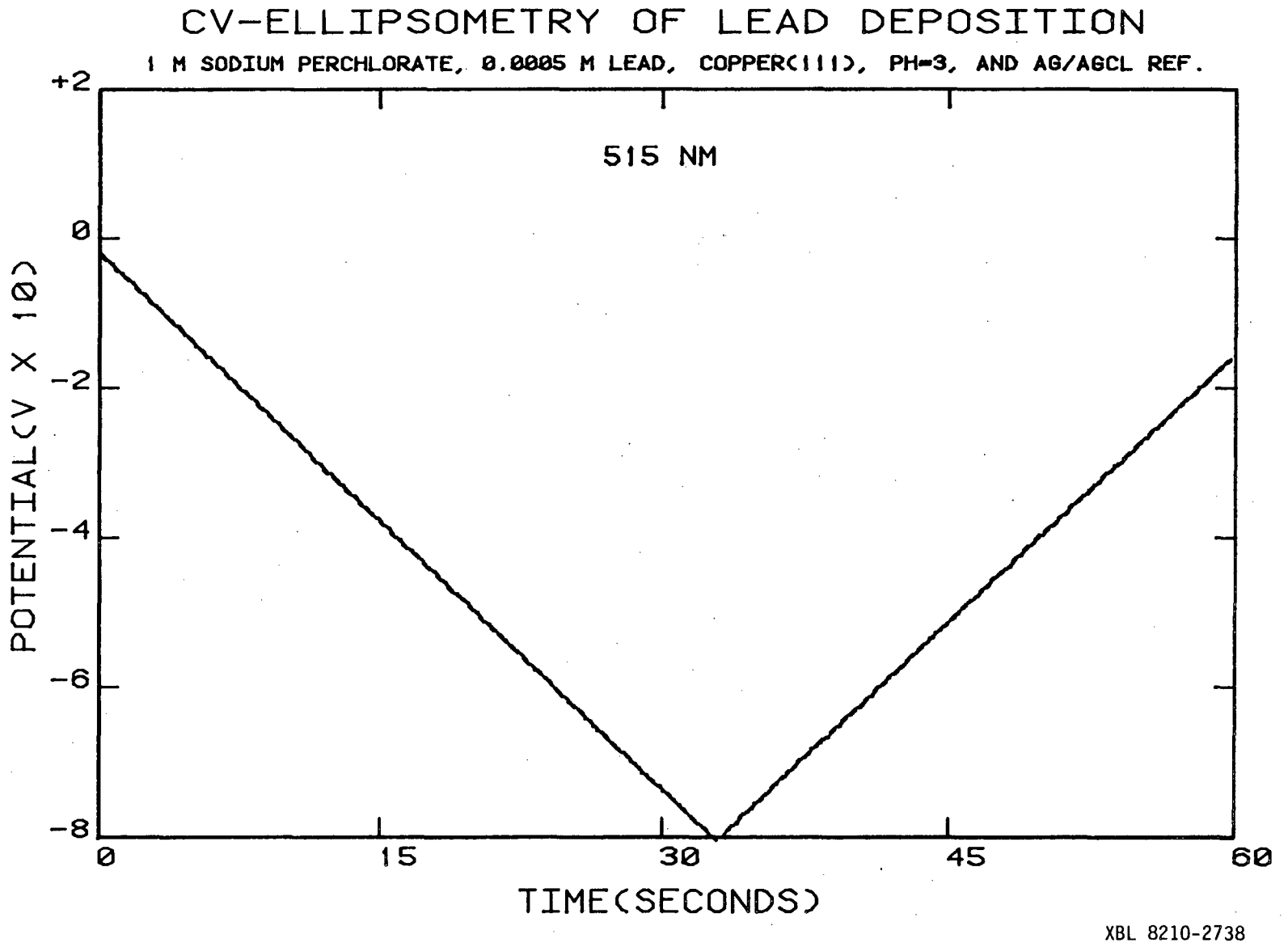

XBL 8210-2738

Fig. 2.b

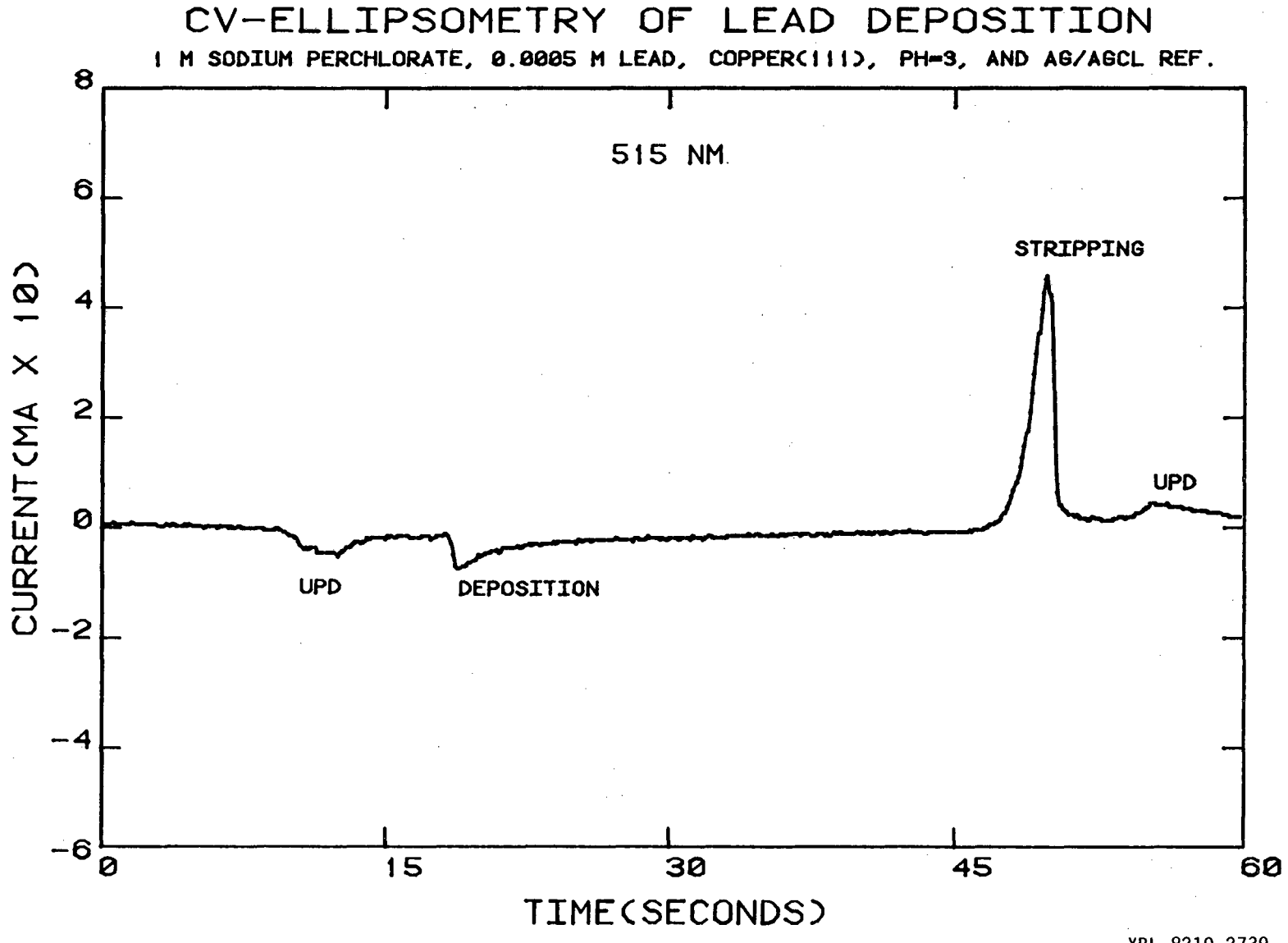

XBL 8210-2739

Fig. 2.c

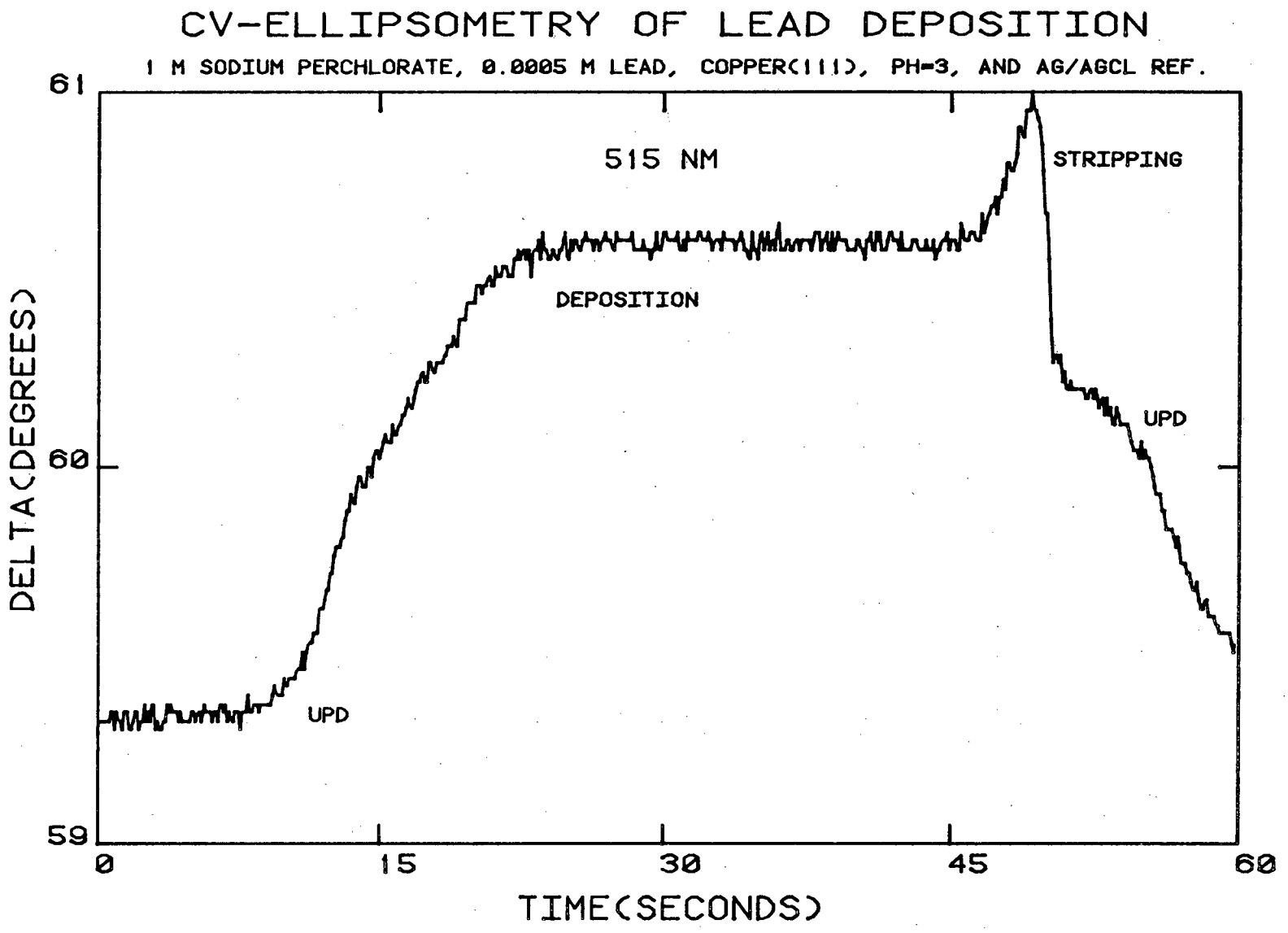

XBL 8210-2740

Fig. 2.d

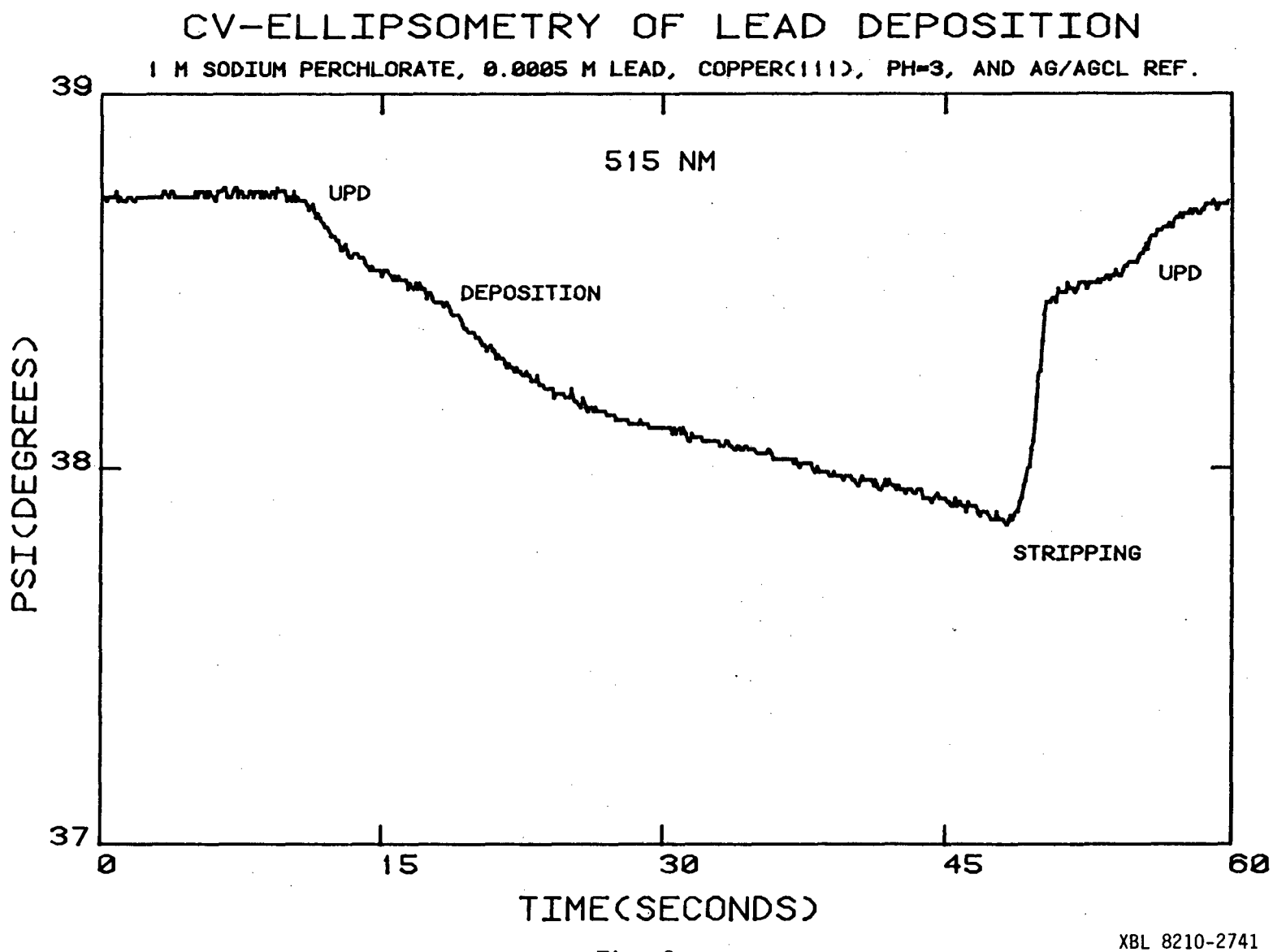

Fig. 2.e

XBL 8210-2741

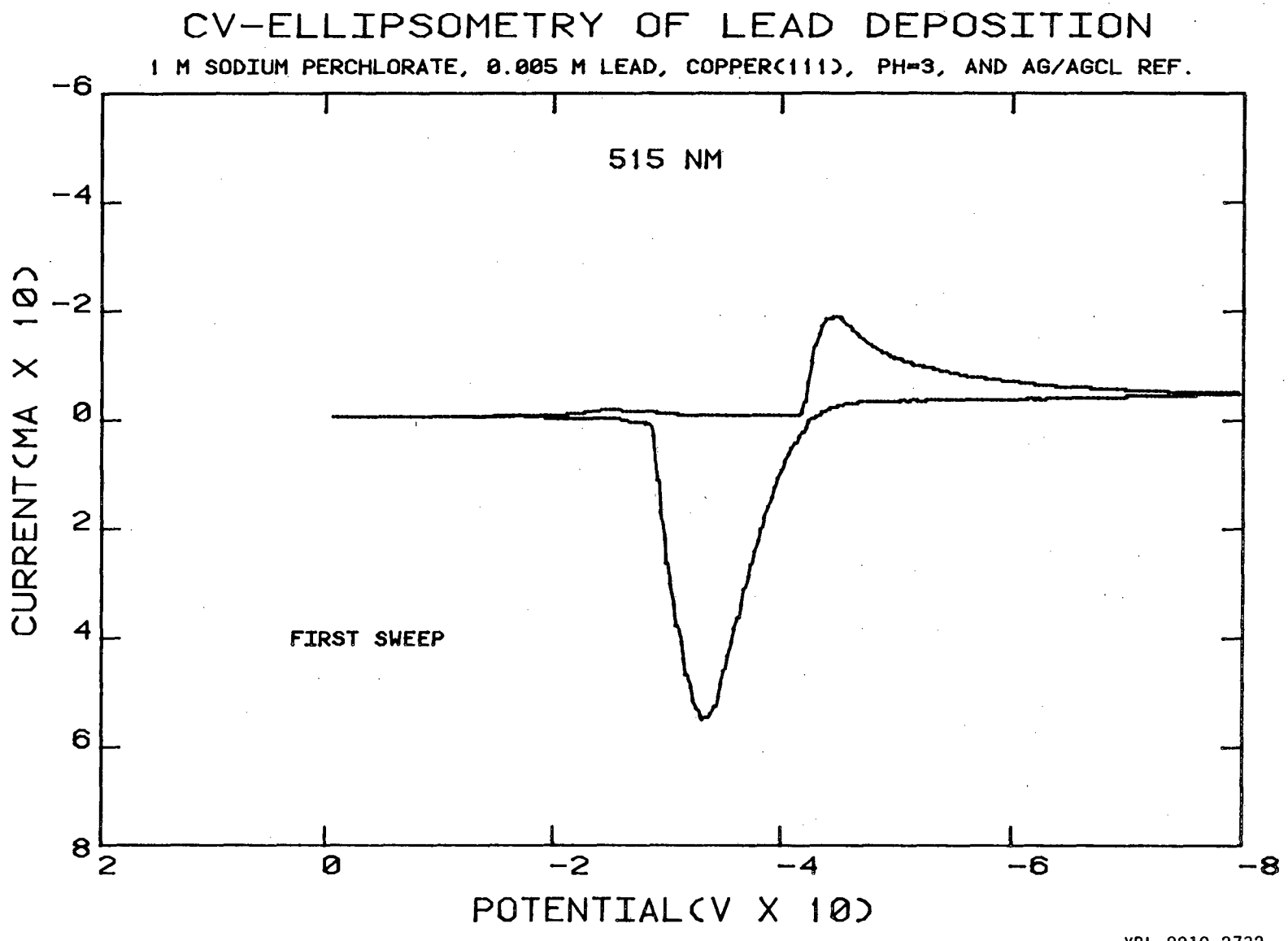

Fig. 3.a

XBL 8210-2732

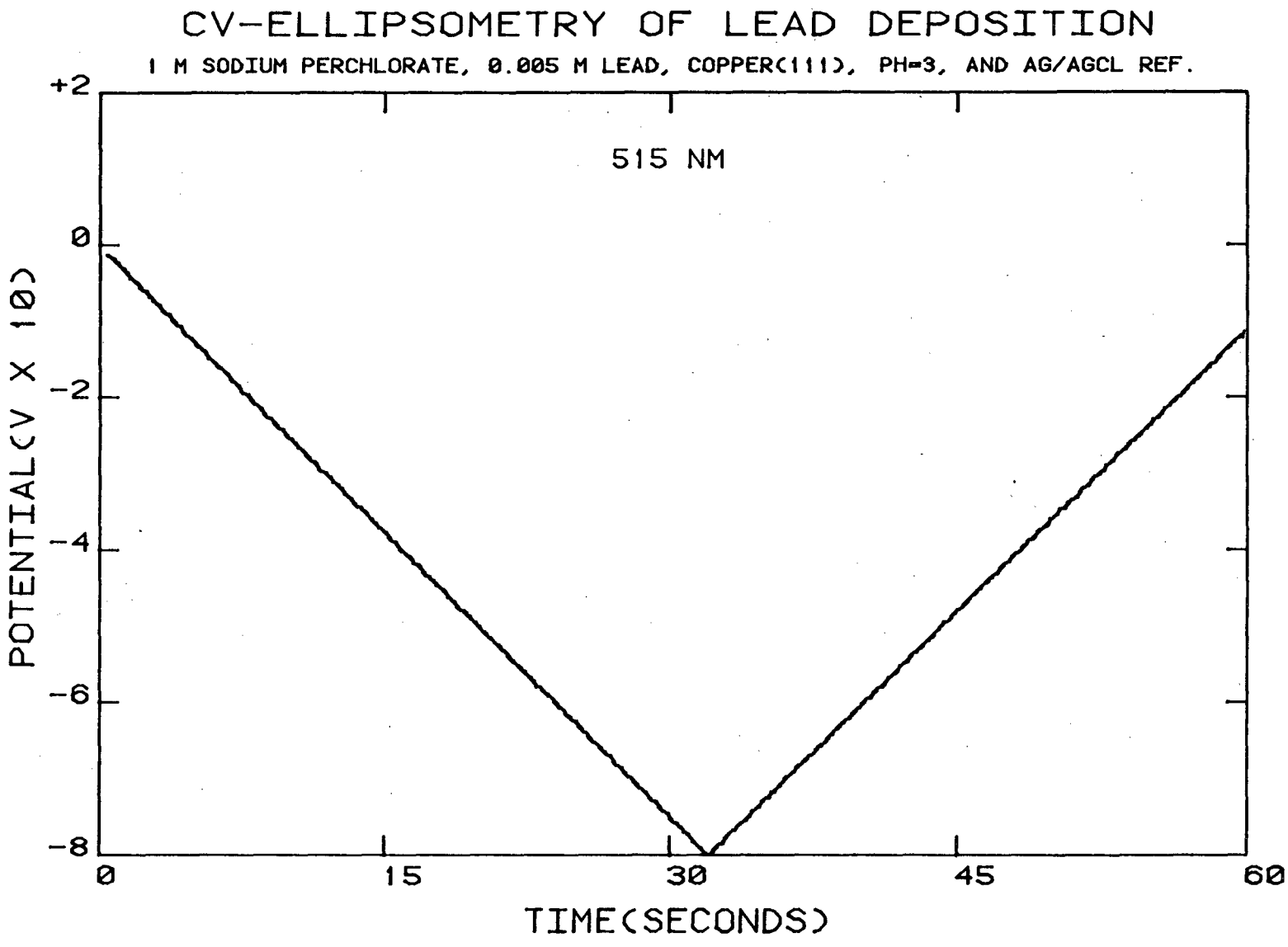

Fig. 3.b

XBL 8210-2733

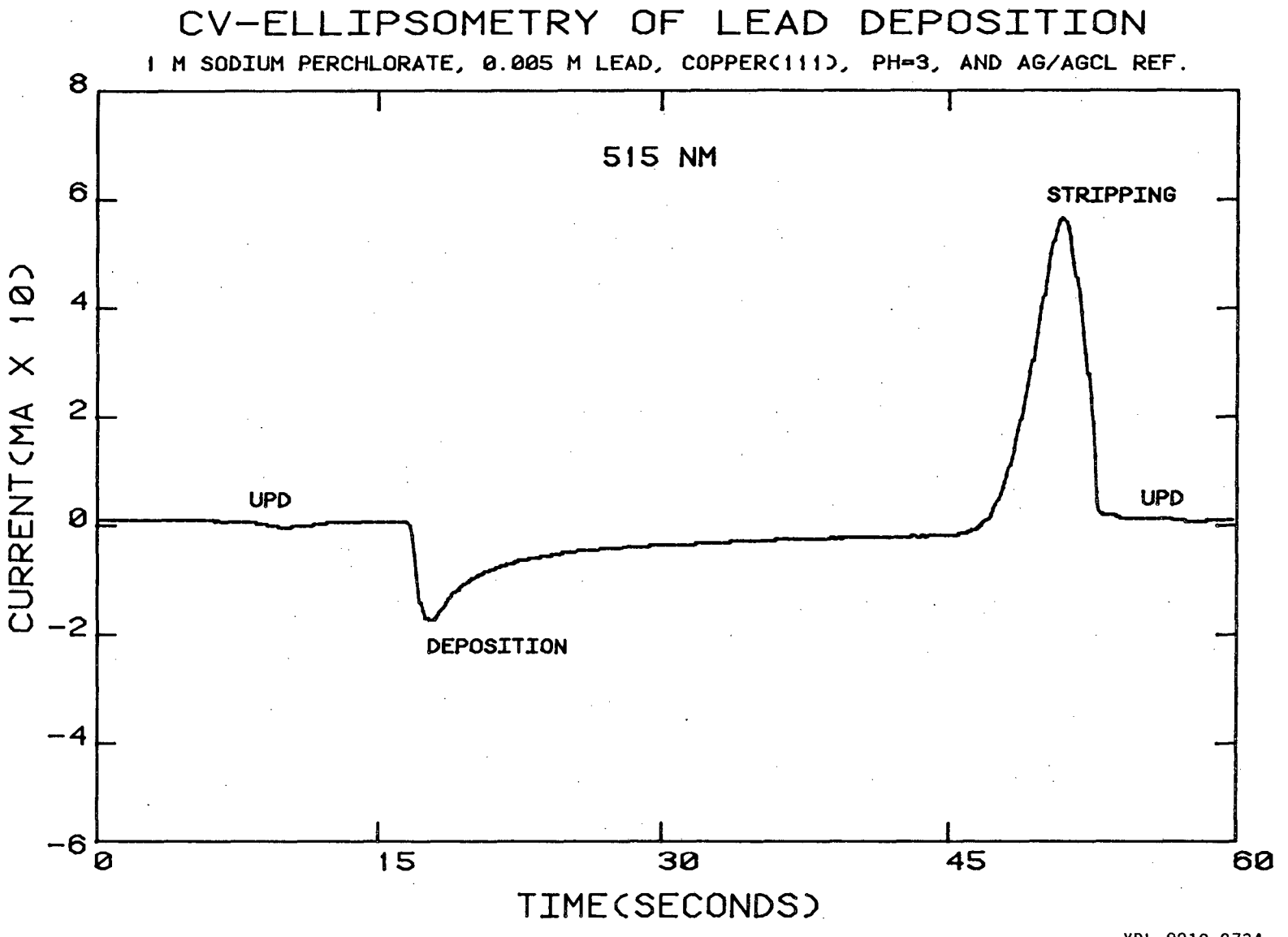

Fig. 3.c

XBL 8210-2734

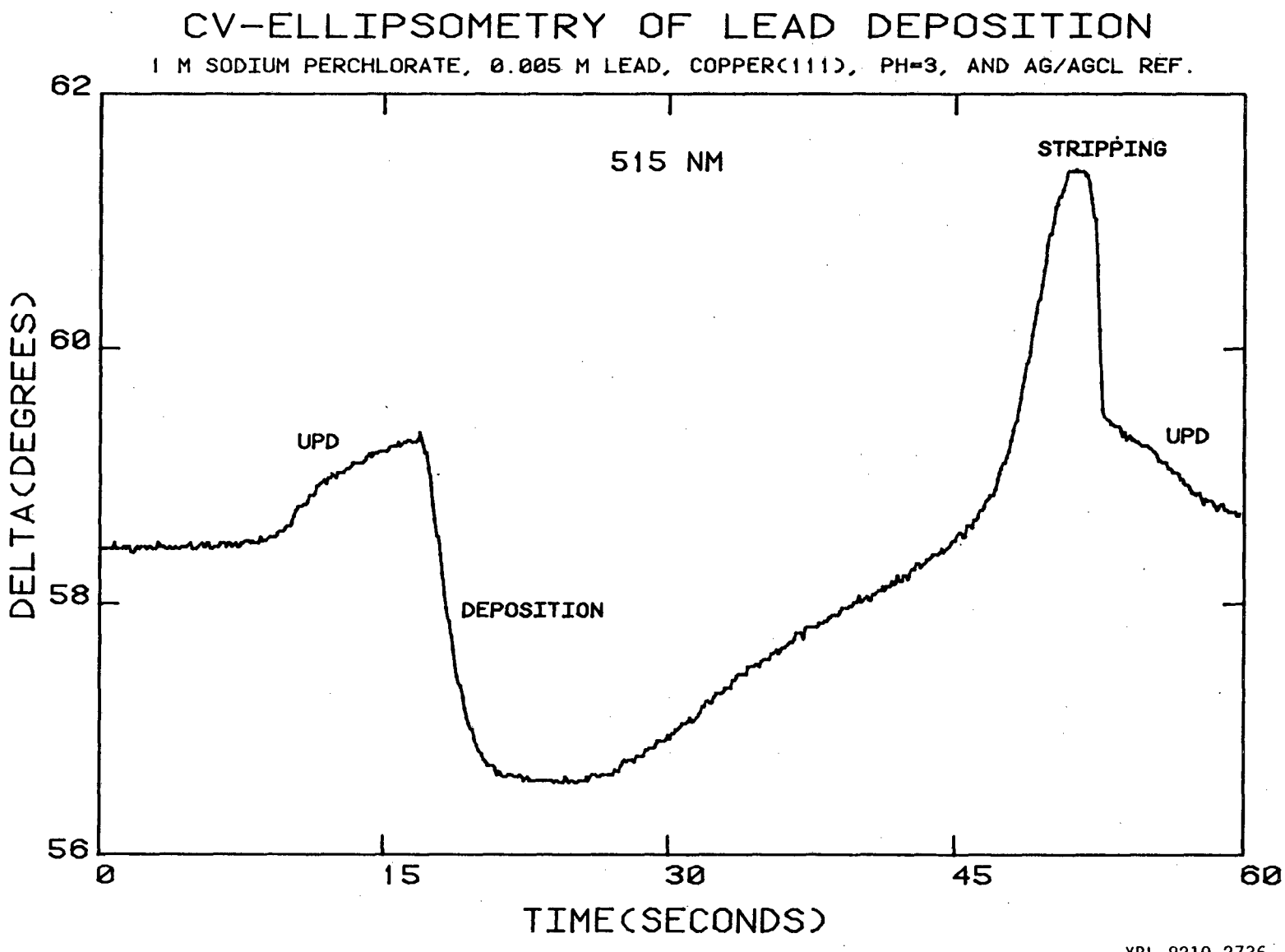

Fig. 3.d

XBL 8210-2736

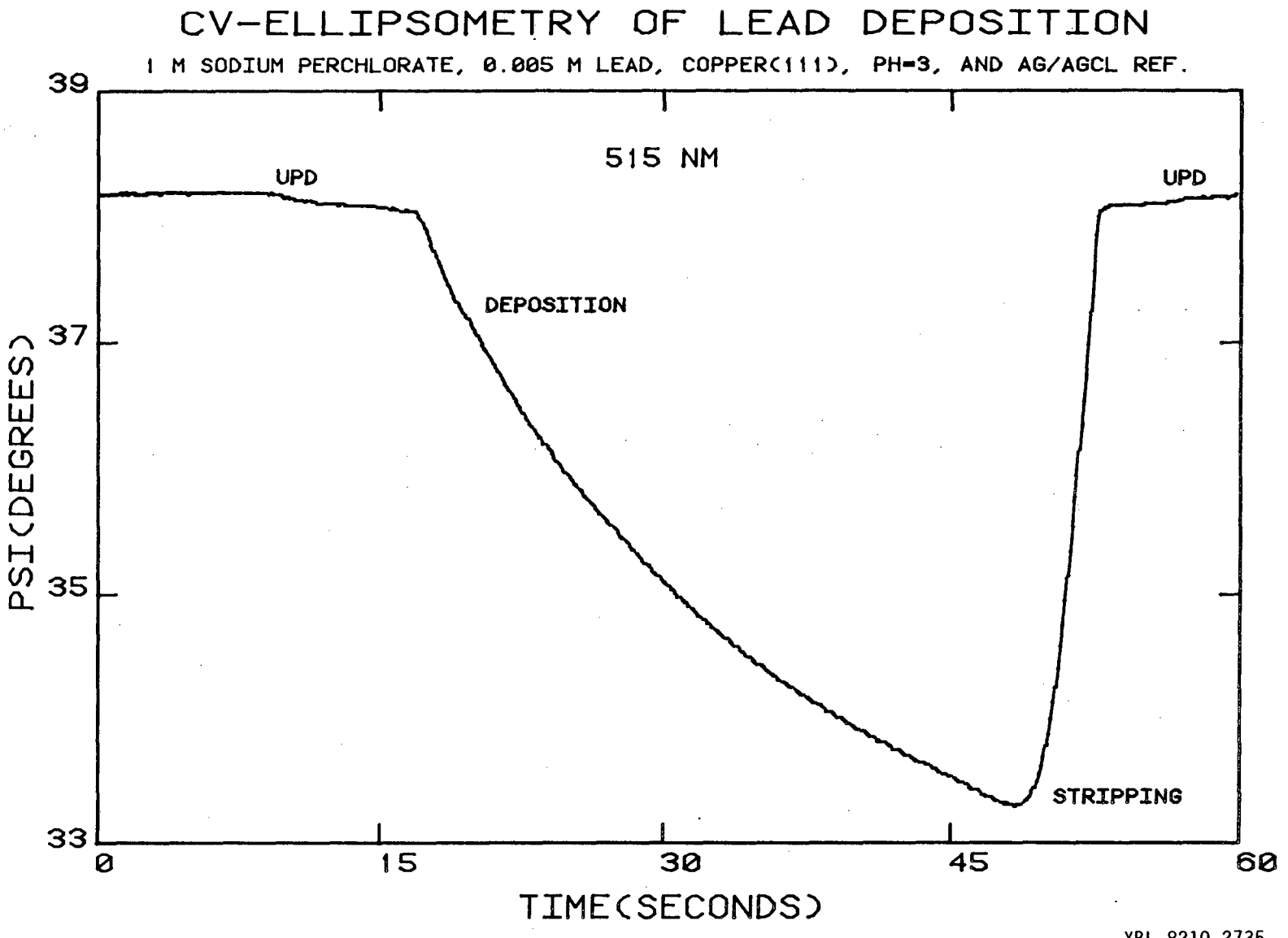

Fig. 3.e

XBL 8210-2735

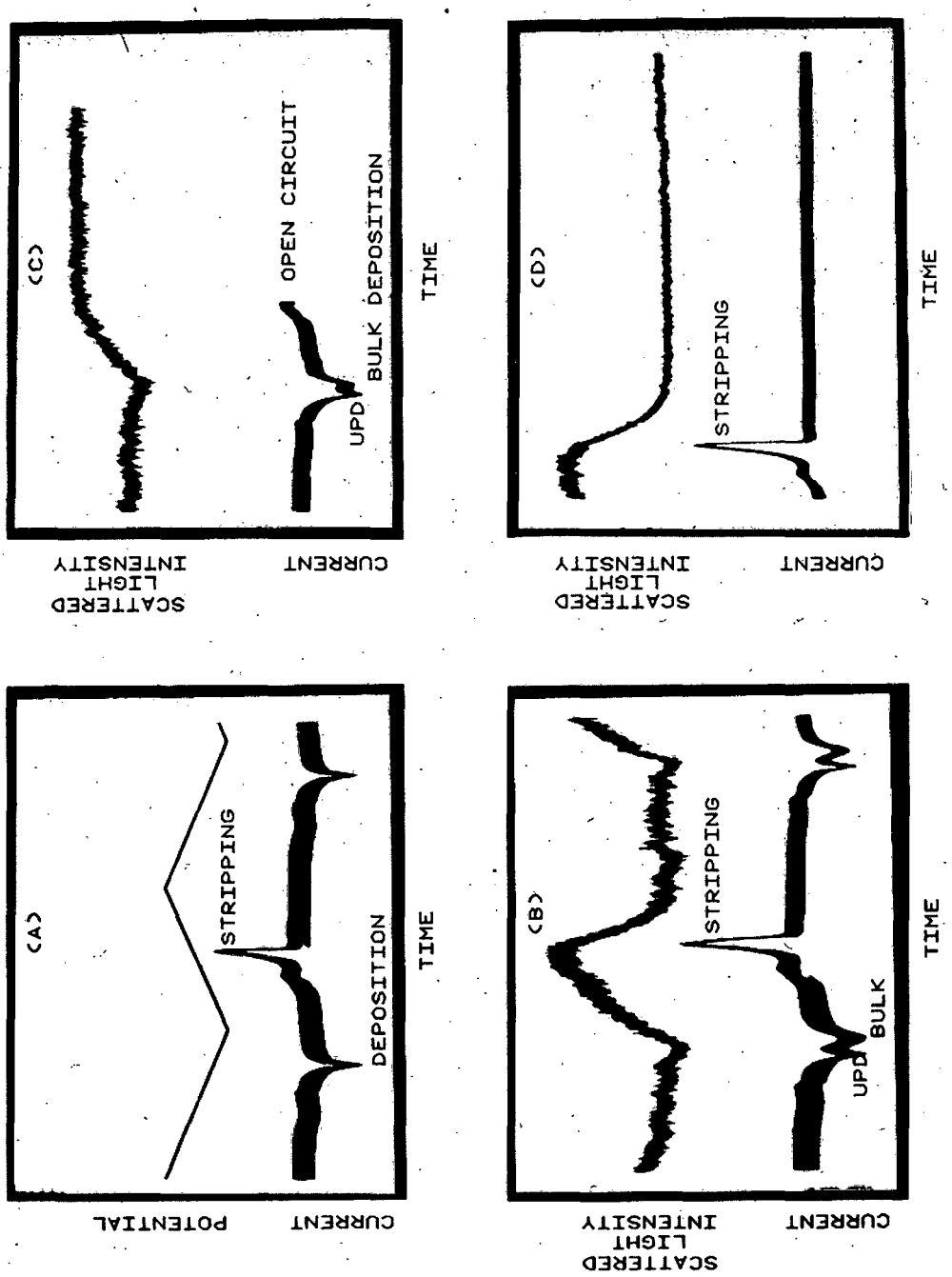

XBB 831-905

Fig. 4

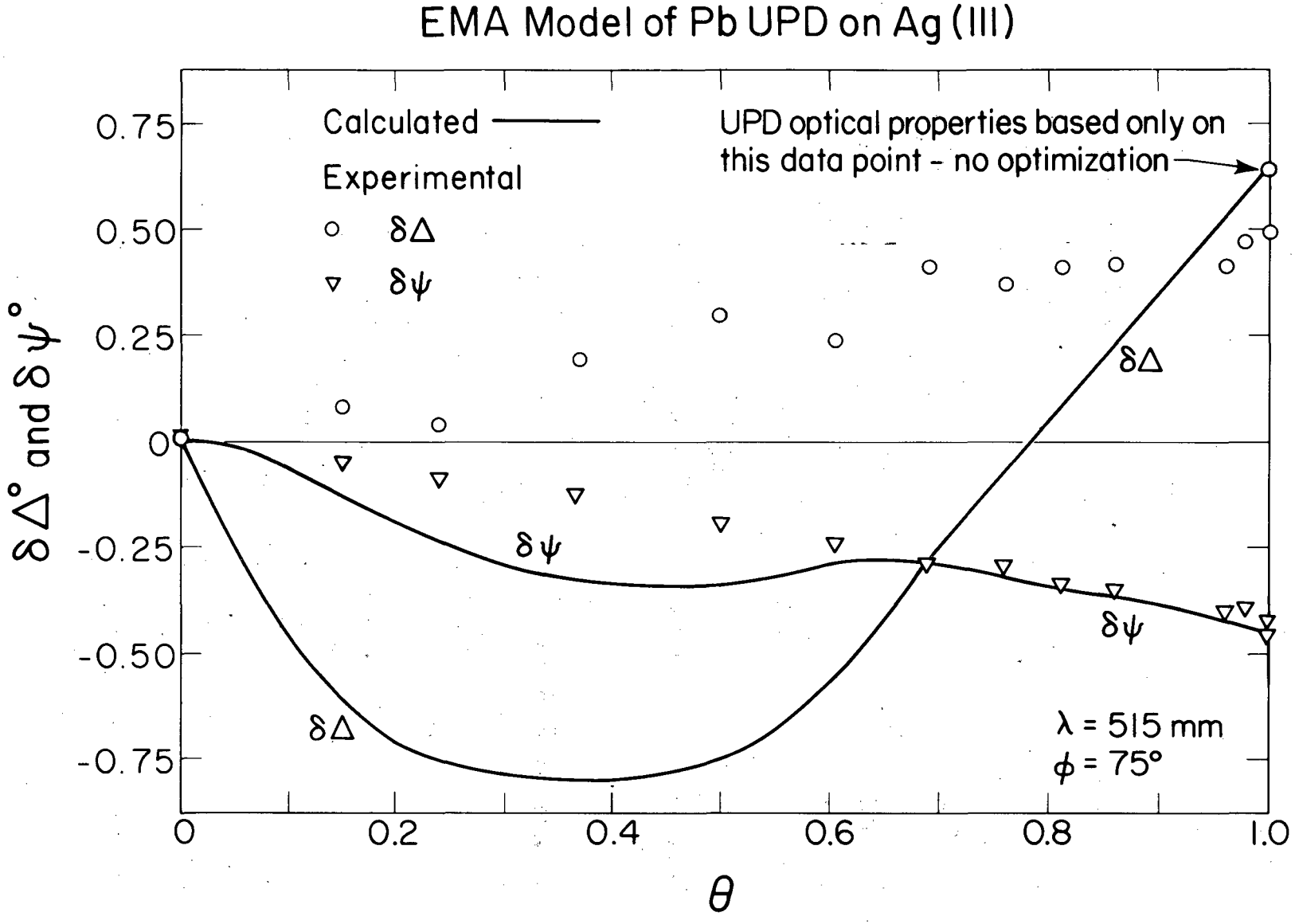

XBL 8212-12368

Fig. 5.a

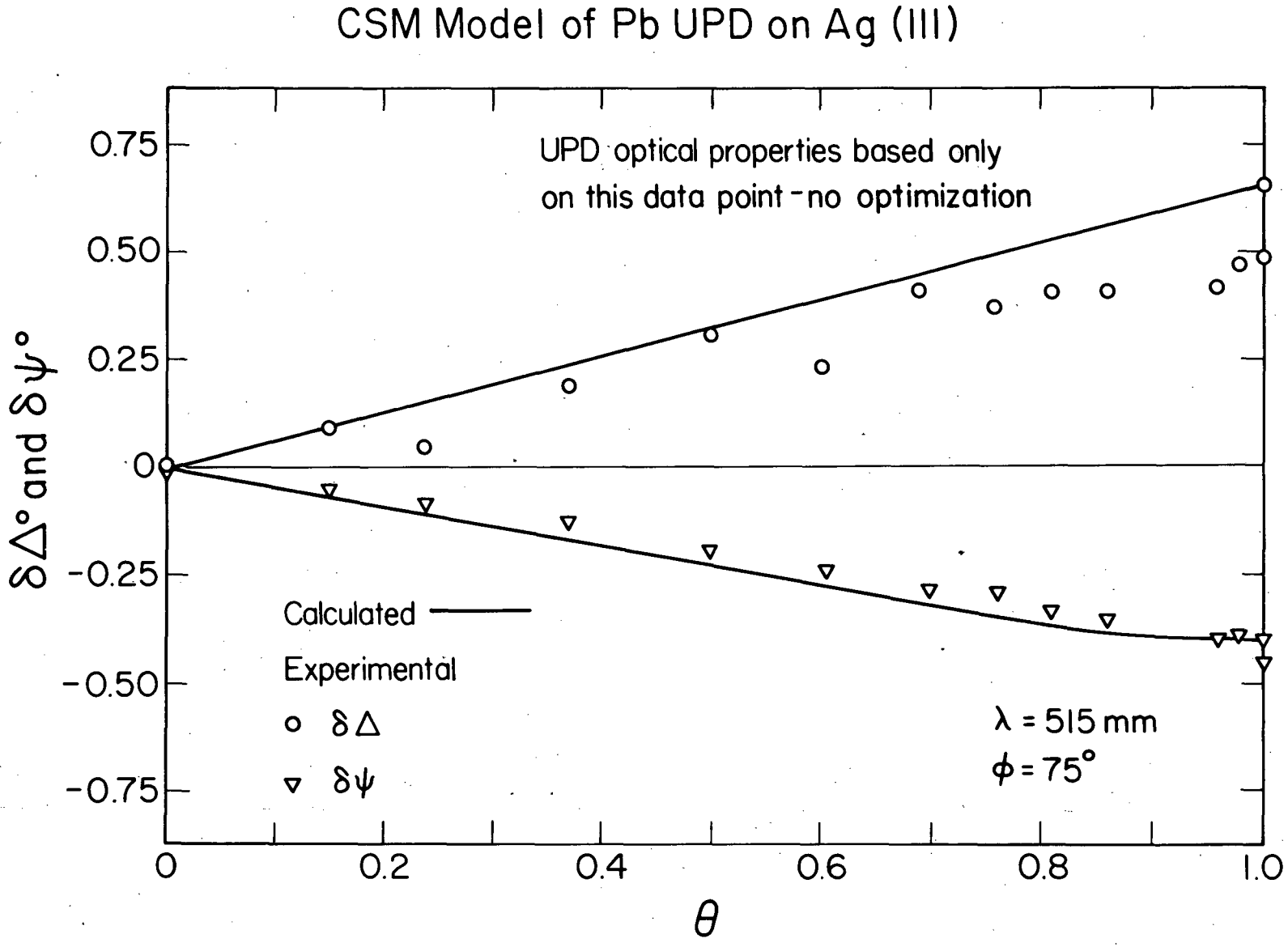

Fig. 5.b

XBL 8212-12371

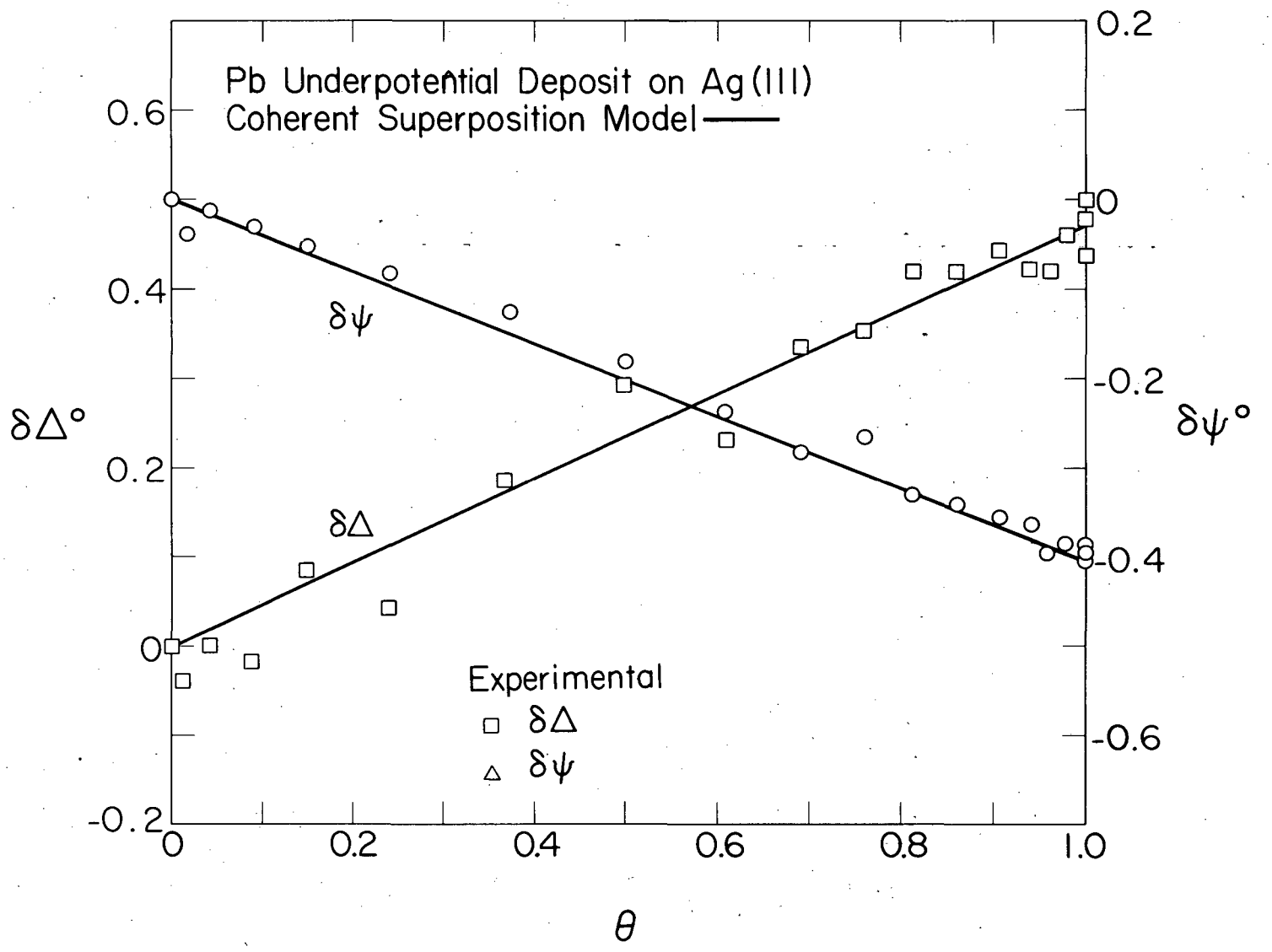

Fig. 6.a

XBL 8212-12373

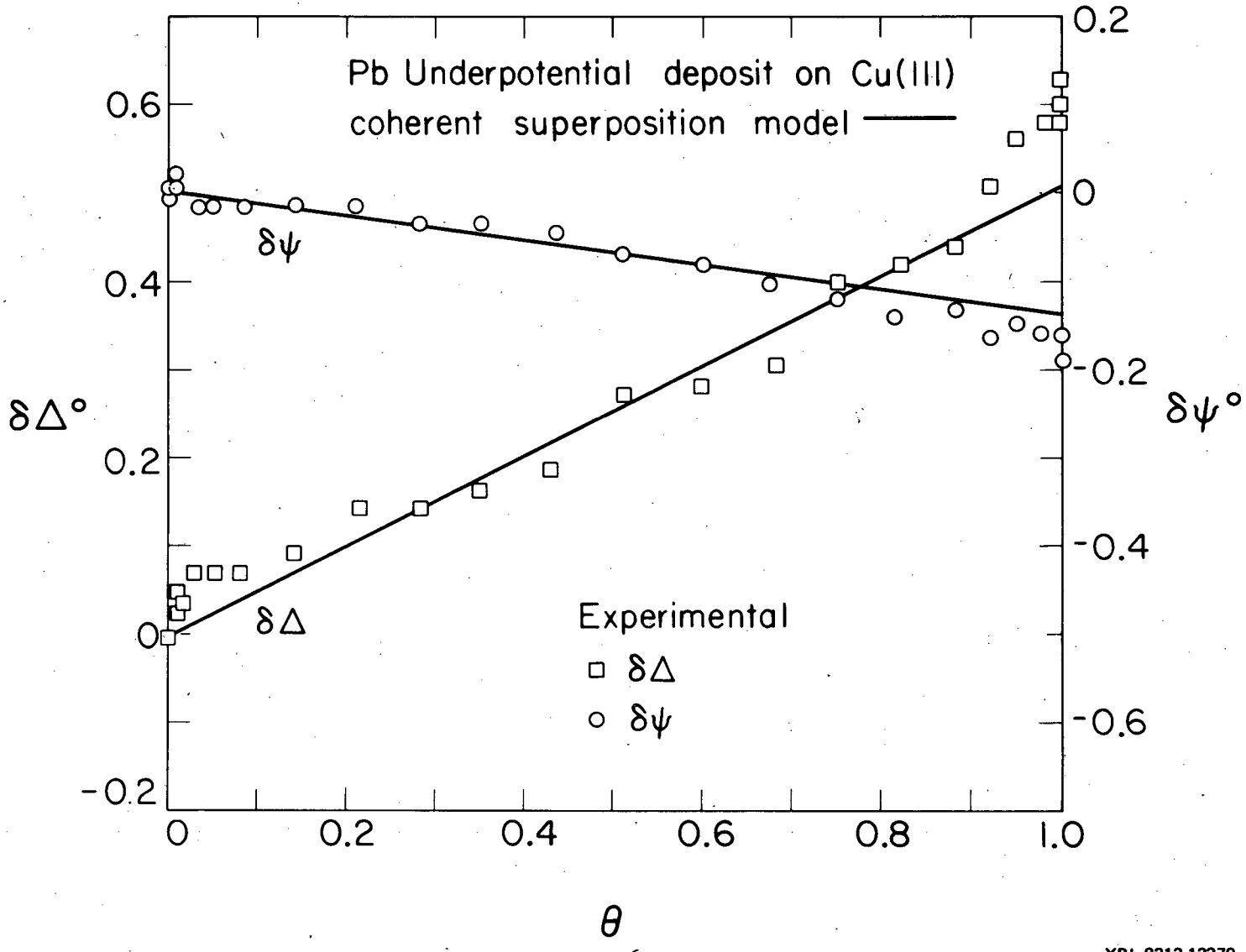

Fig. 6.b

XBL 8212-12370

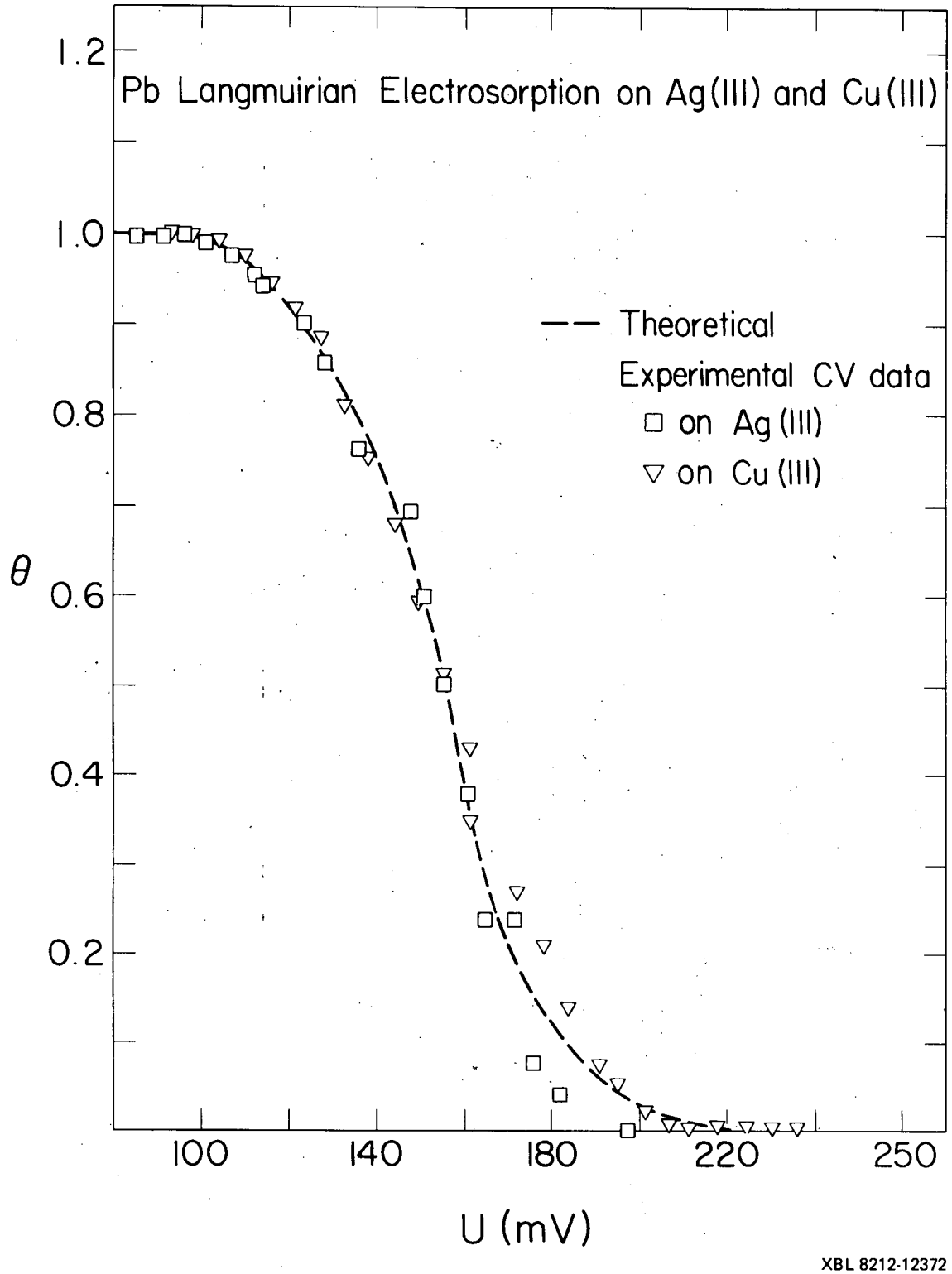
Pb Langmuirian Electrosorption on Ag(111) and Cu(111)
Theoretical
Experimental CV data
□ on Ag (111)
▽ on Cu (111)
θ
1.2
1.0
0.8
0.6
0.4
0.2
100
140
180
220
250
U (mV)
XBL 8212-12372

Fig. 7.a

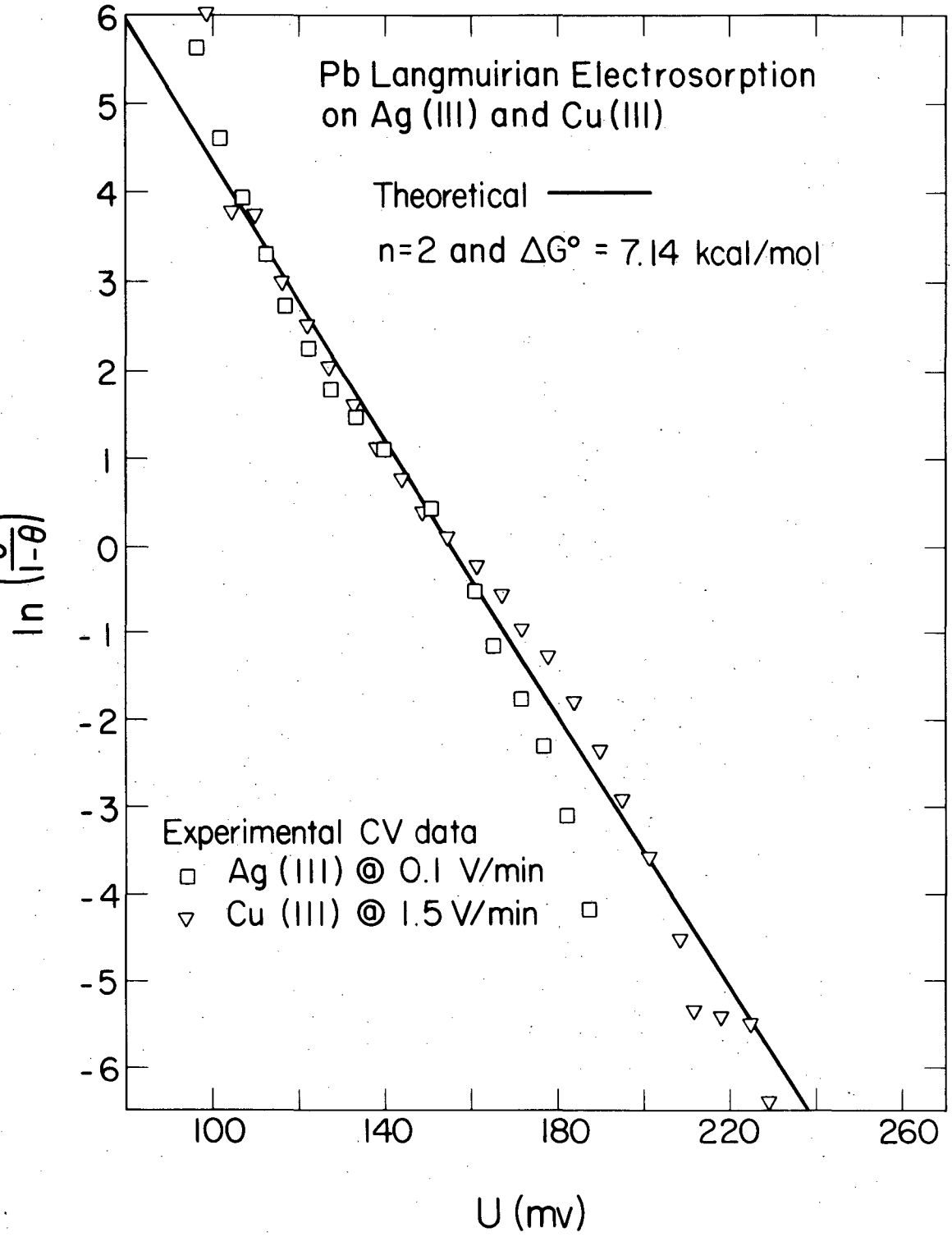
Pb Langmuirian Electrosorption
on Ag (111) and Cu (111)
Theoretical
n=2 and ΔG° = 7.14 kcal/mol
Experimental CV data
Ag (111) @ 0.1 V/min
Cu (111) @ 1.5 V/min
ln (θ/(1-θ))
U (mv)
6
5
4
3
2
1
0
-1
-2
-3
-4
-5
-6
100
140
180
220
260
XBL 8212-12369

Fig. 7.b

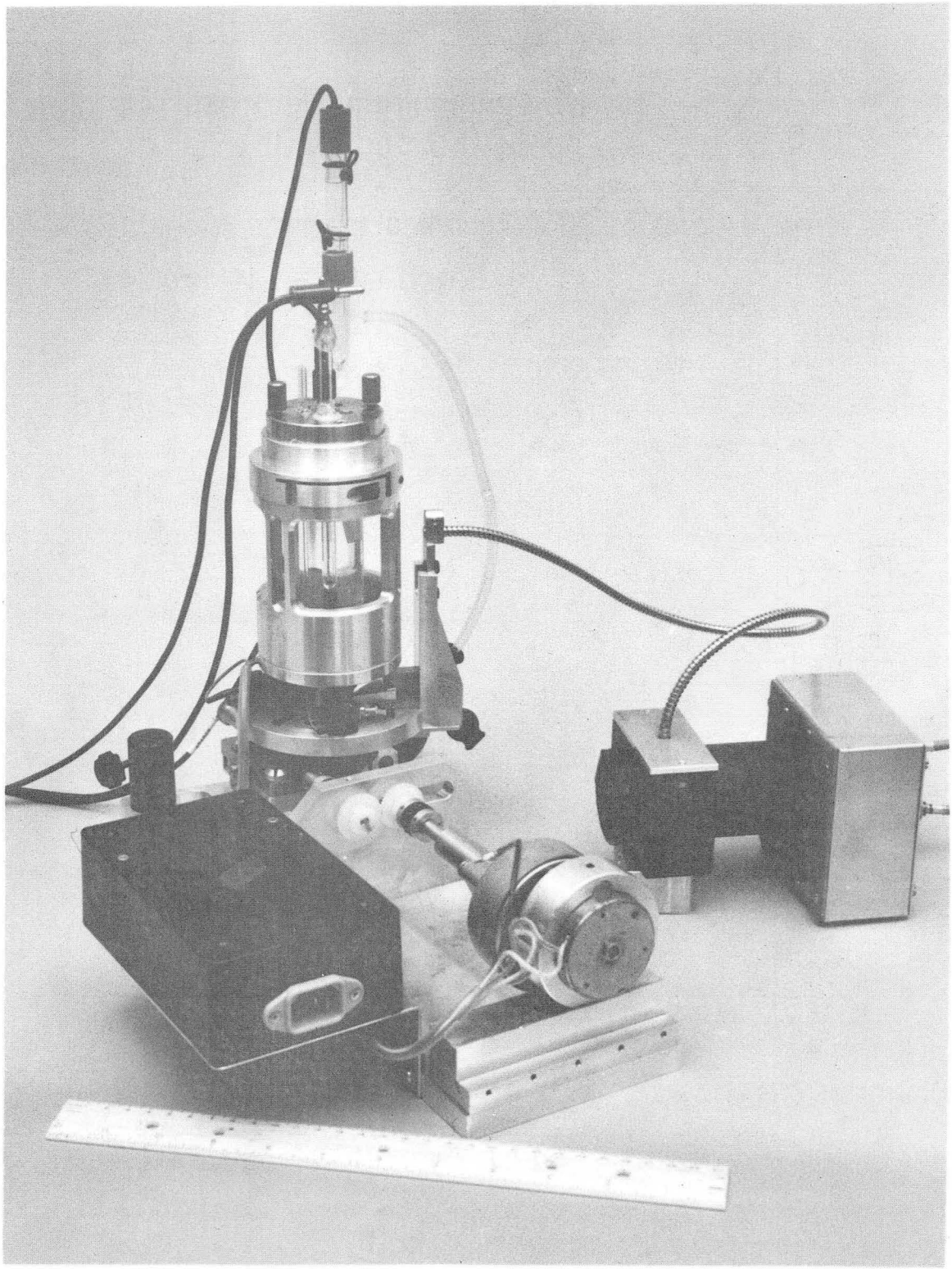

CBB 818-8182

Fig. 8

NOMENCLATURE

ρ	ratio of complex reflection coefficients
ψ	relative amplitude ratio of p and s electric field waves after reflection, relative to the incident waves (degrees)
Δ	relative phase difference between p and s electric field waves after reflection, relative to the incident waves (degrees)
r_ν	Fresnel reflection coefficient for the "ν" polarized wave, where ν = s or ν = p.
ϕ	angle of incidence at ambient medium - film interface (degrees)
d	film thickness based upon ellipsometry data (Å)
λ_o	vacuum source wavelength (Å)
n_a	ambient medium refractive index
$\hat{n}_f$	complex film refractive index
$\hat{n}_s$	complex substrate refractive index
$\hat{\varepsilon}$	complex dielectric constant of the effective medium
$\hat{\varepsilon}_h$	complex dielectric constant of the host medium
$\hat{\varepsilon}_i$	complex dielectric constant of component "i" making up the effective medium
θ_i	volume fraction of component "i" in the effective medium
N_i	atomic number density of component "i" in the effective medium
α_i	molecular polarizability of component "i" in the effective medium
θ_{Pb}	volume fraction of Pb in porous, thin-film, electrochemical deposit
$\hat{\varepsilon}_{Pb}$	complex dielectric constant of Pb

$\hat{\varepsilon}_{soln}$	complex dielectric constant of electrolyte
$\hat{\varepsilon}_f$	effective thin-film deposit complex dielectric constant
$\hat{A},\hat{B}$	complex parameters for quadratic equation defining
θ_f	fraction of surface covered by film of refractive index $\hat{n}_f$
σ_c	lateral coherence length
f	focal length of the collimating telescope (mm)
λ	source wavelength (λ)
D_d	pinhole diameter following light source (mm)
Δ_o	initial value of Δ, before deposition (degrees)
ψ_o	initial value of ψ, before deposition (degrees)
$S_{\Delta,\psi}$	sum-of-squares error between theoretical ellipsometer parameters and those measured experimentally
$\Delta_{M,i}$	the "ith" measured value of Δ in a particular data set
$\psi_{M,i}$	the "ith" measured value of ψ in a particular data set
$\Delta_{C,i}$	the calculated value of Δ corresponding to $\Delta_{M,i}$
$\psi_{C,i}$	the calculated value of ψ corresponding to $\psi_{M,i}$
SE(p)	the variance of parameter "p"
σ^2	the variance of the model predictions for Δ and ψ
$\delta(p)$	the error in parameter "p" at an "1-2 " level of confidence
$t(2N'-P,1-2\alpha)$	the t-statistic for "2N'-P" degrees-of-freedom at a "1-2α" level of condidence
N'	the number of pairs of Δ and ψ measurements
P	the number of model parameters to be fit
S_{MIN}	the minimum value of $S_{\Delta,\psi}$ corresponding to a selection of "p" values giving a "best fit"

$S_{(+)}$	a value of $S_{\Delta,\psi}$ computed at a parameter value of "p+Δp"
$S_{(-)}$	a value of $S_{\Delta,\psi}$ computed at a parameter value of "p-Δp"
θ	fractional coverage of electrode substrate by UPD monolayer
V	electrode potential (V)
F	Faraday constant (23.04064 kcal/mol·V)
RT	constant (0.592 kcal/mol)
ΔG°_{ADS}	Gibbs free energy of adsorption for UPD monolayer (kcal/mol)
g	interaction parameter
C	concentration
U	underpotential (V) relative to E°, the Nearnst potential
$U_{1/2}$	the underpotential corresponding to θ = 0.5 (V)
z	apparant valence of metal adatom before electrosorption in UPD monolayer
m	linear regression line slope (V^{-1})
b	linear regression line intercept
$\delta(\ )$	denotes the error of the quantity inside the parentheses[‡]
θ_i	the UPD monolayer coverage measured experimentally at underpotential U_i
θ_u	the electrosorption model prediction of θ corresponding to the experimental underpotential U_i
N	the number of data points defining the experimentally determined electrosorption isotherm
S	the sum-of-squares error between the experimental data and the electrosorption model predictions
$\bar{U}$	the mean underpotential (V)

[‡]except in the case of $\delta\Delta$ and $\delta\psi$

Q	the total charge passed to the working electrode coul
t	time (sec)
A	the electrode area (cm^2)
x	electrode dimension (cm)
y	electrode dimension (cm)
d_q	deposit thickness based upon charge (Å)
ρ_{Pb}	the density of Pb (11.3437 gm/cm^3)
e	electronic charge (1.6019×10^{-19} $coul/e^-$)
N_{AVG}	Avagadro's Number (6.0221×10^{23} atoms/mol)
MW_{Pb}	atomic weight of Pb (207.20 gm/mol)
$i(t)$	time varying current density during cyclic voltammetry (A/cm^2)

Chapter 6

THE EFFECT OF RHODAMINE-B ON LEAD ELECTRODEPOSITION ON SILVER AND COPPER

Abstract

Rhodamine-B chloride has been found to have significant inhibitory effects on the electrodeposition of Pb from 1 M $NaClO_4$ (pH 3). These effects have been studied by ellipsometry during cyclic voltammetry. The dye shifts the bulk deposition peak to more cathodic potentials during the first potential cycle, prevents complete formation of the Pb underpotential deposit preceding bulk deposition, and eventually leads to more compact bulk deposits than are possible in its absence (porosities of 10% and 50%, respectively). Dye effects disappear after subsequent cycling and reappear after readsorption during relaxation periods at open circuit. Dye depletion and readsorption on the surface have been observed with the spectroscopic ellipsometer.

Introduction

Surface active agents (additives, inhibitors) have long been used on an empirical basis to control surface finish in electrolytic metal deposition; uncontrolled impurities may cause similar effects. Few fundamental studies have been undertaken to clearly define the functional role of these agents during the initial stages of electrocrystallization, despite the great technical importance of their use (1). The objectives of this work were (a) to correlate variations

in adsorbate coverage and orientation on the electrode with differences in overpotential, and (b) to determine the effect of this material on the micromorphology of the deposit. Deposit thicknesses investigated ranged from a single monolayer (the underpotential deposit, UPD) to thicknesses of about 1,000 Angstroms (100 nm). The principal experimental techniques used were cyclic voltammetry and ellipsometry (both spectroscopic and fixed-wavelength). A self-compensating instrument with rapid spectral scanning capabilities for the visible range and automated data collection was built for this purpose; this instrument is discussed in Chapter 2 and elsewhere (2,3).

Experimental

I. Selection of Electrochemical System for Study

The materials used in this study were selected to satisfy electrochemical and optical criteria. Using such criteria as a guideline, the system selected for most of the experimental investigations involved Cu as the electrode substrate, Pb as the deposited metal, and rhodamine-B chloride as the model inhibitor. The supporting electrolyte was composed of 1 M $NaClO_4$, acidified to a pH of 3 by use of $HClO_4$. Inhibitor concentrations were typically 10 micromolar and Pb^{++} ion concentration was 5.0 M, unless otherwise stated.

These materials have optical constants which are distinguishable over the spectral range accessible to the optical instrumentation (370 to 720 nm). Cu has a distinctive absorption in the visible (around 550

nm), which is believed to be due to electronic transitions from the filled "d" bands into the "sp" conduction bands (4-10). In contrast to Cu, Pb shows no such characteristic in the visible and has relatively linear optical constants (11-14). Dissolved rhodamine-B has a characteristic absorption band at about 555 nm believed to be due to an electronic transition from a singlet ground state to an excited triplet state (15). The electronic transition moment related to this absorption process lies parallel to the three conjugated rings of the rhodamine-B molecule. Rhodamine-B probably adsorbs on the surface with a preferential orientation of the transition moment, resulting in a very birefringent (dichroic) adsorbate layer. This birefringence, and its spectral dependence, can be interpreted in terms of molecular orientation on the surface (16). Preliminary studies of rhodamine-B adsorption on Pt and Ag were conducted with the newly developed spectroscopic ellipsometer and have proven that monolayers of adsorbed dye are detectable (Chapter 8). These studies were inspired by earlier investigations of rhodamine-B adsorption on Pt (17) and Ag (18) by reflection spectroscopy.

Electrochemically, the substrate had to be inert under the conditions of interest (19). Cu is stable to dissolution and oxidation at the reversible potential for Pb deposition from acidic solutions (20) and it has been found that Pb forms a well defined underpotential deposit on Cu substrates (21).

Since we elected to use different metals for the substrate and deposit, it was necessary to pick a combination that did not form alloys

electrochemically at the interface; such behavior would have confounded the effects of interest. Since Au has optical properties in the visible which are distinctive, it was considered as a substrate (22). However, it was discovered from cyclic voltammetry that Pb and Au form an alloy electrochemically, as do Pb and Pt (Chapter 4). Another disadvantage of a Au substrate is related to its optical properties; optical changes due to adatoms may be obscured by optical changes in the substrate (23). Zn may be of more practical importance in future secondary batteries than Pb^{++} ion, with specific reference to the zinc-nickel system. However, Zn is known to alloy with Ag and Cu (24,25).

The deposit should form at potentials anodic to those where hydrogen evolution problems degrade the optical signal; minimal hydrogen evolution was desired. This was another reason that Zn^{++} ion was not used in this initial study.

The choice of rhodamine-B resulted from screening studies with over 30 materials, 14 of which were indicators or laser dyes. Dyes were investigated because they are strongly light absorbing and can therefore be detected in small amounts on the electrode surface; they adsorb strongly on the surface; they are well characterized both optically and structurally; and they are available in high purity from commercial suppliers. Of the compounds investigated, rhodamine-B was found to induce the largest increase in Pb bulk deposition overpotential (125 mV cathodic shift). Furthermore, it was found that rhodamine-B was adsorbed with sufficiently great affinity for the surface to be relatively insensitive to other impurities unavoidably present.

However, rhodamine-B was reduced on the electrode during metal deposition.

Originally, we had hoped to find organic compounds which would be inert on the cathode during deposition; however, we found that compounds which chemisorb to the surface were reduced electrochemically prior to the onset of metal deposition. Electrochemical reduction and incorporation into deposits are common problems among organic additives for electrochemical systems (26,27).

The electrode potential, dictated by the metal ion deposited, Pb^{++}, was sufficiently cathodic to prevent significant interference of the Cl^{-} anion introduced with the rhodamine-B cation. Pb adatoms also inhibit other cathodic reactions, such as oxygen reduction, making Pb electrodeposition insensitive to the presence of such species (28,29).

II. Automatic Spectroscopic Ellipsometer

The ellipsometer used in this study was of novel design and is described in detail in Chapter 2 and elsewhere (2). It was based upon the polarizer-compensator-sample-analyzer optical configuration, was self-nulling by use of the magneto-optic polarizer and analyzer, and could be operated in either a spectroscopic or fixed wavelength mode. The spectral range is 370 nm to 720 nm and the angle-of-incidence used was 75 degrees. One complete range of spectroscopic measurements (delta and psi at different wavelengths) could be made in 3 to 4 seconds, though improved signal-to-noise ratios are obtained with slower scanning (one scan per 15 seconds) or by averaging multiple scans. Slower

scanning was essential to observe dye adsorption on the surface (second order optical effects), whereas faster scanning gave sufficient signal quality for resolution of deposit micromorphological differences (first order effects). Data acquisition was fully computerized with a LSI-11/02 microcomputer system.

III. Electrochemical Cells

For the experiments described here with Cu substrates, specially designed Teflon electrochemical cells were used (Figs. 1 and 2). These cells had a liquid volume of 2 ml when completely assembled, and were pie-shaped (2" high, 1-3/16" deep in the direction normal to electrode, and 1-1/4" wide in the direction parallel to electrode).

Two quartz windows were oriented normal to the incident and reflected light beams used to measure changes in the optical properties of the working electrode. These windows were polished and annealed and were made of optical quality quartz (1/16" x 9/16" o.d.). They were held in place by external, anodized aluminum plates which pressed them against circular Teflon edges surrounding the window ports, forming a liquid-tight seal. The effective aperture (clearance) for the beam was about 1/3" in diameter.

The working electrodes were machined from solid pieces of oxide-free Cu; the electrode surface exposed to the electrolyte was 1/2" in diameter. This electrode was a disk 1/2" in diameter and 15/1000" thick with threaded posts (1/4" diameter, 20 threads per inch) for mounting into the Teflon cell. Lengths of the posts varied, depending upon

application. Those electrodes fabricated for use in both the electrochemical cell and an ultra high vacuum (UHV) Auger spectrometer had posts 1/3" in length; those used only in the electrochemical cell had lengths of 7/8". The liquid-tight seal around the electrode was made with leached Viton o-rings and metal-teflon seals. Electrode-edge effects were eliminated (to some extent) by wrapping the edge tightly with Teflon tape and press-fitting it into the electrochemical cell. This assembly allowed interchangeability and freedom from impurities introduced by epoxy resins.

The counter electrode was made of specially fabricated Pb wire (made at Lawrence Berkeley Laboratory, 99.999% purity, 0.064" to 0.066" o.d.) inserted through holes in the top of the Teflon cell, and externally sealed with small viton o-rings. To increase the counter electrode surface area and assure uniform current distribution, the Pb wire was wound into a flat spiral inside the cell (after it was pulled through a small hole); this disk was parallel to the working electrode. Since experiments had to be performed below the solubility of Pb in the electrolyte, some minor problems were encountered from dissolution of the Pb wire; the Pb^{++} concentration increased slightly over extended periods of time due to corrosion dissolution of the counter electrode. The Pb wire was covered with an oxide film (white) when inserted into the cell; this oxide was removed by chemical dissolution and cathodic polarization against a temporary auxiliary Pb wire electrode in an initial electrolyte charge. Then the Cu working electrode was inserted, with subsequent replacement of electrolyte.

The reference electrode was a Dow-Corning double-junction Ag/AgCl reference electrode (cat. no. 476067) and was inserted into a Teflon reference electrode compartment, a white cylinder 2" o.d. with a height of 2-1/4". The reference electrode was held in place by inserting it through a hole (1/2" i.d.) in a threaded Teflon cap (3/4" diameter, 16 threads per inch) and then through a Viton o-ring. The cap, reference electrode, and o-ring were then threaded into the reference electrode compartment. The liquid reservoir inside this compartment was 5/8" i.d. and had a liquid hold-up of about 2 ml after assembly. The reference electrode compartment was in communication with the electrochemical cell via a Teflon capillary (0.064" o.d.), inserted into the bottom of the compartment reservoir and into the top of the cell.

Two syringes (15 ml each) were used for electrolyte transfer into the cell, one used to supply electrolyte, the second being used to withdraw excess electrolyte. Electrolyte was first introduced into the electrochemical cell and forced through the capillary connecting the cell and reference electrode compartment, and finally into the second syringe; by reversing flow direction trapped nitrogen from the purge could be displaced from the system and collected in either syringe (Fig. 1). The syringes were also in communication with the cell via Teflon capillaries, as was the nitrogen purge stream.

Another electrochemical cell system was used for the experiments performed with the Ag(111) substrates. The cell was acrylic, the counter electrode was Pt, and the electrode was mounted in epoxy. These experiments were conducted early in the program using a cell described

in Chapter 5 elsewhere (32).

IV. Potentiostat

A PAR (Princeton Applied Research) Model 173 potentiostat with a PAR Model 173 potentiostat with a PAR Model 179 plug-in digital coulometer was used to control the cell potential. The ramp potential was generated by a Pine Instrument Company Model RDE 3 potentiostat and applied to the PAR potentiostat external signal input. The reference electrode was connected to the PAR potentiostat electrometer probe input via a PAR potentiostat electrometer probe. The LSI-11 microcomputer system interfaced to the spectroscopic ellipsometer was used to monitor cell potential and current simultaneous with measured values of delta and psi (measured as Faraday cell current levels) via an 8-channel analog-to-digital converter (Chapter 3, program EDR002).

V. Electrode Preparation

Electrodes were polished mechanically with emery paper, followed by Al_2O_3 paste. The final powder size used for the paste was 0.05 micron. The thin oxide formed on the electrode surface before installation in the electrochemical cell was removed by prepolarization in the acidic electrolyte.

VI. Electrolyte Preparation

The electrolyte was prepared from singly distilled, deionized water (10 megohm) and reagent grade salts. Pre-electrolysis was done before introducing the electrolyte into the electrochemical cell. The

electrolyte was nitrogen stripped for about 15 minutes prior to experiments, and the cell was purged with nitrogen before the electrolyte was introduced into the cell.

Results

Simultaneous cyclic voltammetry and ellipsometry were performed with and without dye additions to the electrolyte (Figs. 3.a-d and Figs. 4.a-d, respectively). As stated previously, the electrolyte consisted of 5 mM $Pb(NO_3)_2$, 1 M $NaClO_4$ at pH 3, with either no inhibitor or 10 micromolar rhodamine-B additions. The substrate was polycrystalline, oxide-free Cu. Results in the absence of dye are first discussed (Figs. 3.a-d). Figs. 3.c and 3.d show the ellipsometer response to the cathodic potential ramp shown in Fig. 3.a (+100 to -800 mV vs 4 M Ag/AgCl reference, 2 V/min). The observed change in delta, corresponding to the cathodic current peak (Fig. 3.b), was negative relative to its initial value. This negative deviation was contrary to that expected for formation of a compact layer of Pb on a Cu substrate, and was explained by a microporous bulk deposit (on a compact Pb monolayer). Prior to anodic stripping, this deposit was approximately 510 Angstroms thick and was about 45% porous (based upon the Bruggeman model (33)). A comparable experiment was done with rhodamine-B added to the electrolyte at 10 micromolar concentration (Figs. 4.a-d). The time profile for delta analogous to Fig. 3.c is shown in Fig. 4.c. During the first potential cycle, optical measurements indicate that the bulk Pb deposit was about 300 Angstroms thick, and was only 10% porous. However, with depletion of dye at the electrode surface, deposits formed

during subsequent potential cycles were more porous (2nd cycle, 420 Angstroms thick, 34% porous). The observed effect of rhodamine-B on deposit porosity reappears after relaxation periods at open circuit conditions.

These interpretations regarding ellipsometry during cyclic voltammetry are summarized in Table I and Fig. 5. The theoretical porosities and thicknesses were computed by a multiple film model program (Ref. 32, Chapter 3, program GOGOGO). A porous Pb deposit was assumed to cover a compact Pb adatom layer; Pb which was not accounted for in these two thin Pb films was distributed as dendritic Pb islands sitting on the porous deposit. This is shown pictorially as the two-layer simplification of the three-layer multiple film model (Fig. 6). These islands covered less than 7% of the surface, and had insignificant effect on the ellipsometer response (the contribution to the reflectivity had a weighting factor of less than 7%). Table II summarizes the agreement between digital coulometry measurements (d_q) and ellipsometry measurements (d); the Pb accounted for by ellipsometry was less than that accounted for in the charge balance. The differential may have been involved in the dendritic island layer.

Similar conclusions regarding the effect of rhodamine-B on deposit porosity were also derived from spectroscopic ellipsometry of Pb deposits. Fig. 7.a (delta vs wavelength) and 7.b (psi vs wavelength) show spectroscopic ellipsometer measurements of thin Pb deposits on Cu, contrasting results for a deposit made with rhodamine-B to another in the absence of inhibitor. Measurements for the bare Cu substrate are

also shown for comparison. Both deposits were formed potentiostatically at -600 mV (Ag/AgCl reference) from the same electrolyte as used in the experiments shown in Figs. 3.a through 3.d (no dye added) and Figs. 4.a through 4.d (10 micromolar rhodamine-B). Deposited Pb was measured during stripping by digital coulometry and in both cases the deposits would have been 310 Angstroms thick if they had been compact. The coulombic efficiencies between deposition and dissolution were always greater than 95%. The distinctive spectral properties of the Cu substrate were still visible through the deposit obtained without dye. The deviation of delta from values for the bare Cu surface were interpreted as a porous Pb layer (about 310 Angstroms thick and 41% porous) on the UPD. Residual Pb was accounted for in large dendritic Pb islands which began to form on the porous deposit; these islands covered less than 7% of the surface and were optically insignificant. In contrast, when the dye was added to the electrolyte, almost all of the deposited Pb was in the form of a compact layer; in this case the spectral properties of the Cu substrate were completely masked. The Pb overgrowth became progressively more compact. Spectral scans of deposits corresponding to 110 nm thick compact layers are shown in Fig. 8.a (delta vs wavelength) and Fig. 8.b (psi vs wavelength). With this greater thickness, deposits made with and without rhodamine-B had similar optical characteristics which were interpreted as compact Pb layers too thick to be measured (porosity less than 10%). At this stage of development, the Cu substrate (in both cases) had become completely overgrown with Pb and the substrate optical properties had been completely masked; the Cu absorption edge was no longer seen. All

deposits made with rhodamine-B additions, even at equivalent thicknesses of 31 nm were interpreted as compact Pb deposits.

For deposits formed in the absence of rhodamine-B, single-layer film models (compact, porous, or islands) could not account for both spectroscopic ellipsometer measurements and digital coulometry measurements. Multilayer models had to be used (Ref. 2, Chapter 7, three-layer model). Table III gives measured and calculated values of delta and psi at different wavelengths for three deposits (equivalent compact Pb layers of 31, 60, and 110 nm, respectively). The calculated values of delta and psi based upon the optimized two-layer simplification of the three-layer model are shown in Fig. 9.a and 9.b as circles superimposed on the spectroscopic ellipsometer measurements, shown as solid lines. These calculated values, corresponding to compact Pb deposits of 31, 60, and 110 nm, imply that the fractions of the total deposits distributed as dendritic islands were 42($\pm$18), 35($\pm$17), and 23($\pm$235)%, respectively (confidence interval at 95% level). Recall that a similar argument was used in the discussion of Table II.

Use of spectroscopic ellipsometry for micromorphological determinations allowed calculation of both thickness and porosity with confidence intervals for a single surface; this would not have been possible with measurements at a single wavelength (Ref. 2, Chapter 3, program WLGOGO). The variance of the ellipsometer model parameters, the thickness and porosity of the porous deposit, are given in parenthesis beside corresponding parameter values. Note that as the deposits became thicker, the thickness variance asymptotically approached infinity (the

thickness became indeterminate). Also note that the porosity of this layer was determined with a greater relative confidence than the thickness.

Confidence intervals for the model parameter p, referred to as (p), were computed from the variance SE(p) by the formula

$$\delta(p) = t(df, 1-2\alpha) \sqrt{SE(p)} \qquad (1)$$

where t(df,1-2α) is the t-statistic for 2N-P degrees-of-freedom (df) at a confidence level of 1-2α. N is the number of independent ellipsometer measurements of the surface, one measurement at each wavelength, and P is the number of model parameters. Since there were only 2 adjustable parameters in the two-layer simplification of the three-layer model and since ellipsometer measurements at 10 different wavelengths were used, there were 17 degrees-of-freedom. At a 90% level of confidence the value of the t-statistic is 1.74. Note that the wavelengths were spaced at intervals greater than the filter bandwidth of 10 nm.

Cyclic voltammetry underpotential and bulk peaks were shifted to more cathodic potentials during the first potential cycle by rhodamine-B additions; this potential shift disappeared after several uninterrupted potential cycles (Fig. 10). The potential shift reappeared after relaxation periods (10 to 60 min) at open circuit. This relaxation istributed to dye reduction on the electrode and the need to reestablish the dye layer at the surface by diffusion from the electrolyte.

Repopulation of the electrode surface with rhodamine-B adsorbate was observed with the spectroscopic ellipsometer; the subtracted ellipsometer measurements with dye addition minus measurements without are shown in Figs. 11.a and 11.b; replicate measurements are shown in Figs. 12.a and 12.b. These spectral scans were taken immediately preceding the corresponding cyclic voltammograms of Fig. 10, the relaxation time (minutes) prior to the spectroscopic ellipsometer measurements and cyclic voltammogram is indicated by the numbers on the figure labeling the different curves (10, 30, and 60).

Through optimization of adjustable parameters in a uniaxial anisotropic film model, the adsorbate layer was determined to have a thickness of about 32 Angstroms, comparable to the molecular dimensions of rhodamine-B parallel to the electronic transition moment (Fig. 13), and was also found to exhibit a high degree of birefringence which changed with relaxation time (Ref. 34, Chapter 3, program AIGOGO). This optimization minimized the error between calculated and measured values of delta and psi at different wavelengths, and was based upon the data shown in Figs. 14.a and 14.b. These values were the result of averaging and smoothing the spectral scans shown in Figs. 11.a and 12.a (delta) and Figs. 11.b and 12.b (psi). Results of the optimization are shown in Figs. 14.b and 14.c. The extraordinary refractive index, n_e, and extraordinary extinction coefficient, k_e, are shown in Fig. 14.b; the extinction coefficient exhibits a peak near the rhodamine-B absorption band, which is reasonable (no such peak appears for the refractive index). The peak amplitude increases with increasing relaxation time.

The refractive index and extinction coefficient birefringence, n_e/n_o and k_e/k_o, respectively, are shown in Fig. 14.c. The change in extinction coefficient birefringence near that absorption band wavelength indicates that the surface was repopulated with a species having its transition moment oriented normal (preferentially) to the electrode surface. The derivative-type response of n_e/n_o to k_e/k_o may have been due to relationships existing between the optical constants, or artifact generated by the instrument (the analyzer channel response to higher order harmonics generated by the polarizer channel). Summarizing, birefringence of the dye layer and changes in the birefringence with relaxation time indicate that the species responsible for inhibition (cathodic shifts in cyclic voltammetry deposition peaks) had its transition moment oriented normal to the surface and was probably bonded as a cation.

Earlier experiments were performed with simultaneous ellipsometry during cyclic voltammetry on a Ag(111) substrate which also illustrate the optical effects due to the presence of Rhodamine-B during Pb electrodeposition. In these experiments the Pb^{++} concentration was only 0.5 millimolar and the rhodamine-B concentration was 6 micromolar. Experiments were performed both with and without the dye present in the electrolyte, and at two wavelengths, one near the absorption band and another removed from the absorption band (555 and 515 nm, respectively). It had been anticipated that experiments performed near the absorption band would give maximum sensitivity to the adsorbed dye, whereas experiments performed at other wavelengths would primarily reflect

surface changes due to deposit formation.

The data at 515 nm in the absence of dye have been discussed in Chapter 5 (Fig. 15.a through 15.e) and are shown here only in contrast to similar data taken in the presence of rhodamine-B (Figs. 16.a through 16.e). The first dramatic observation was that the cathodic UPD (underpotential deposit) peak was well defined in the absence of the inhibitor, and did not appear in the voltammogram with the rhodamine-B addition (Figs. 15.a and 16.a, and Figs. 15.c and 16.c). However, an anodic stripping peak for the UPD appeared in both instances. Integration of the stripping peaks indicate that the UPD formed in the presence of rhodamine-B involved only 33% as much charge per unit area as the UPD formed without the additive present. Though no cathodic UPD peak was seen, the ellipsometer responses did indicate formation of at least a portion of the UPD layer during the cathodic sweep (Figs. 16.d and 16.e). During UPD formation in the presence of rhodamine-B the values of delta and psi changed +0.6 and -0.3 degrees, compared to changes in the absence of dye of +0.7 and -0.5 degrees, respectively. Quantification of these changes was not attempted since it was difficult to estimate the effects of the dye adsorbate on the surface optical properties during UPD formation and since the ellipsometer response was relatively noisy after dye addition. The increased noise level was attributed to a decrease in the ellipsometer gain due to light absorption by the dye in the electrolyte.

Results from the experiments performed at 555 nm, near the dye absorption wavelength, are shown in Figs. 17.a through 17.e. Figs.17.b

and 17.c show current responses to the potential ramp shown in Fig. 17.a for cyclic voltammetry without and with rhodamine-B, respectively. Results were the same as those current responses shown in Figs. 15.c and 16.c, except there was some distortion of the UPD peak during the first cathodic sweep in Fig. 17.b. This is believed to be due to some slight surface impurity which was reduced or displaced in subsequent cycles; perhaps even residual rhodamine-B contaminating the cell from previous experiments. Ellipsometer responses are shown in Fig. 17.d (delta vs wavelength) and Fig. 17.e (psi vs wavelength); data for cyclic voltammetry with and without dye are both shown in the same figures. The most dramatic observation was that delta does not return to its initial value after anodic stripping when rhodamine-B is added to the electrolyte, whereas it does when no dye is present. A similar observation was made for changes in psi. It is important to note that both delta and psi returned to initial values after anodic stripping of Pb at 515 nm, even with dye additions. This difference is believed to be due to reduction and/or displacement of the rhodamine-B during the first potential cycle, and the greater sensitivity of the ellipsometer to the rhodamine-B depletion from the surface near the absorption wavelength, 555 nm. Qualitatively, these results are consistent with trends in delta and psi observed during the dye relaxation experiments with a Cu substrate (Figs. 11.a, 11.b, 12.a, and 12.b). Unfortunately, uncertainty regarding the initial values of delta and psi do not allow quantification of the results.

Discussion

The observed differences in the apparent deposit porosities resulting from rhodamine-B additions are attributed to an increase in nucleation density on the surface and inhibition of dendrite growth. Potentials required for Pb deposition were more cathodic in the presence of rhodamine-B than in its absence. Consequently, the equilibrium size of two dimensional nuclei on the surface (UPD islands of Pb) would have had smaller diameters when formed in the presence of rhodamine-B (35). Therefore, for comparable quantities of underpotentially deposited charge, with and without rhodamine-B present, a greater number of islands of smaller diameter would have been formed in the presence of adsorbed rhodamine-B. Alternatively, a kinetic argument can be used. Perhaps the adsorbed dye molecules limited the surface diffusion of Pb adatoms on the Cu surface; such "caging" would have also resulted in more two-dimensional nuclei. Nucleation density may have been a result of incomplete monolayer formation, prior to bulk deposition. If one assumes that bulk deposition could have occurred only on adatoms in the first monolayer, which is supported by the results presented in Chapter 5, the disperse nature of the UPD layer in the presence of rhodamine-B would have necessarily enhanced nucleation density. Selective rhodamine-B reduction at points of high activity would have promoted Pb^{++} reduction at lower activity sites; the dye would have been preferentially reduced on dendrite tips extending into the bulk electrolyte, whereas Pb^{++} would have been diffused closer to the surface for reduction, due to its higher mobility.

Conclusions

Rhodamine-B acted as a deposition inhibitor for the electrodeposition of Pb on Cu (and Ag). The dye was reduced at the surface and repopulated the surface after relaxation periods at open circuit; inhibitory effects on the deposit micromorphology also disappeared until the surface was repopulated with rhodamine-B adsorbate. Birefringence of the dye layer and changes in the birefringence with relaxation indicated that the species responsible for the increase in Pb deposition overpotential had its transition moment oriented normally to the surface and was probably bonded as a cation; the thickness of the rhodamine-B adsorbate layer (32 Angstroms) was also consistent with a normal orientation of the molecule on the surface. Rhodamine-B additions resulted in less porous deposits than were possible in its absence and prevented complete UPD formation prior to bulk deposition; the incomplete first monolayer due to the presence of rhodamine-B may have increased nucleation density, which would have increased the ultimate deposit compactness.

References

1. Harrison, J. A., Thirsk, H. R., "The Fundamentals of Metal Deposition," ELECTROANALYTICAL CHEMISTRY, Vol. 5, Bard, A. J., ed., Marcel Dekker, New York, 1971, p. 139.

2. Muller, R. H., Farmer, J. C., "Fast, Self-Nulling Spectroscopic Ellipsometer: Instrumentation and Application," Intl. Conference of Ellipsometry and Other Optical Methods, Paris, France, June 7-10, 1983.

3. Muller, R. H., "Electrochemical Phase Boundaries," MATERIALS AND MOLECULAR RESEARCH ANNUAL REPORT, Lawrence Berkeley Laboratory, Berkeley, CA, LBL-15150, 1973.

4. Hass, G., Hadley, L., "Optical Properties of Metals," AMERICAN INSTITUTE OF PHYSICS HANDBOOK, 2nd ed., Gray, D. E., ed., McGraw-Hill, New York, 963, pp. 6-103 to 6-122.

5. Johnson, P. B., Christy, R. W., "Optical Constants of the Noble Metals," Phys. Rev. B, 6, 4370 (1972).

6. Kolb, D. M., Kotz, R., "Optical Properties and Electronic Structure of Copper Atoms Adsorbed on a Platinum Electrode," Surf. Sci., 64, 698, (1977).

7. See 2 and 3.

8. Adzic, R., Yeager, E., Cahan, B.D., "Optical and Electrochemical Studies of Lead on Gold Evaporated and Single-Crystal Electrodes," J. Electrochem. Soc., 121, 474 (1974).

9. Bousquet, P., "Constants Optiques et Structure des Couches Minces," J. Phys. Rad., 21, 873 (1960).

10. Smakula, Phys., 88, 114 (1939).

11. Drude, Ann. Phys., 39, 481 (1890).

12. Kent, C. V., "The Optical Constants of Liquid Alloys," Phys. Rev., 14, 459 (1919).

13. Trompette, J., "Determination des Facteurs de Reflection, de Transmission et de L'Absorption de Lames Minces d'Argent Deposses sur Quartz par Evaporation," J. Phys. Rad., 17, 124 (1956).

14. See 2 and 3.

15. Birks, J. B., PHOTOPHYSICS OF AROMATIC MOLECULES, Wiley, London, 1970.

16. Plieth, W. J., Gruschinske, P., Hensel, H. J., "Electronic Changes of Light Absorption by the Electric Field of the Electrolytic Double Layer," Ber. Bunsenges. Phys. Chem. 82, 615 (1978).

17. Schmidt, S., Reich, R., Ber. Bunsenges. Phys. Chem. 76, 599 (1972).

18. See 16.

19. See 1, p. 129.

20. Pourbaix, M., ATLAS OF ELECTROCHEMICAL EQUILIBRIA IN AQUEOUS SOLUTIONS, Pergamon Press, New York, 1966, p. 384.

21. Kolb, D. M., "Physical and Electrochemical Properties of Metal Monolayers on Metallic Substrates," ADVANCES IN ELECTROCHEMISTRY AND ELECTROCHEMICAL ENGINEERING, Vol. 11, John Wiley and Sons, New

York, (1978), pp. 125-271.

22. Aspnes, D. E., Kinsbron, E., Bacon, D. D., "Optical Properties of Au: Sample Effects," Phys. Rev. B, 21, 3290 (1980).

23. Kolb, D. M., Leutloft, D., Przasnyski, "Optical Properties of Gold Electrode Surface Covered with Metal Monolayer," Surf. Sci., 47, 622 (1975).

24. Adzic, G., McBreen, J., Chu, M. G., "Adsorption and Alloy Formation of Zinc Layers on Silver," J. Electrochem. Soc., 128, 1691 (1981).

25. Farmer, J. C., Lawrence Berkeley Laboratory, unpublished data, 1981.

26. See 1, p. 139.

27. Lundquist, J., W. R. Grace Company, personal communication, October, 1982.

28. Kokkinidis, G., Juttner, K., "The Electrocatalytic Influence of Underpotential Lead Adsorbates on the Reduction of Nitrobenzene and Nitrosobenzene on Silver Single Crystal Surfaces in Methanolic Solutions," Electrochimica Acta, 26, 971 (1981).

29. Zwetanora, A., Juttner, K., "The Electrocatalytic Influence of Underpotential Lead and Thallium Adsorbates on the Cathodic Reduction of Oxygen on (111), (100), and (110) Silver Single Crystal Surfaces," J. Electrochem. Soc., 119, 149 (1981).

30. Mathieu, H. J., McClure, D. E., Muller, R. H., "Fast Self-nulling Ellipsometer," Rev. Sci. Instrum., 45, 798 (1974).

31. Layer, H. P., "Circuit Design for an Electronic Self-nulling Ellipsometer," Surf. Sci., 6, 177 (1969).

32. Farmer, J. C., Muller, R. H., "Nucleation of Pb Electrodeposits on Ag and Cu," Electrochem. Soc. Meeting, San Francisco, CA, May 8-13, 1983 (also see Chapter 5).

33. Aspnes, D. E., Theeten, J. B., "Investigation of Effective-Media Models of Microscopic Surface Roughness by Spectroscopic Ellipsometry," Phys. Rev. B, 20, 3292 (1979).

34. Azzam, R. M. A., Bashara, N. M., ELLIPSOMETRY AND POLARIZED LIGHT, North-Holland, New York, 1977, pp. 356-357.

35. Plieth, W. J., "On the Electrochemical Properties of Small Clusters of Metal Atoms and their Role in the Surface Enhanced Raman Scattering," Lawrence Berkeley Laboratory, Berkeley, CA, LBL-12955, 1981.

Table I. Optical Properties of the Bulk Pb Deposit.

t(sec)	E(mV)	Q(mC)	d_q(Å)	Δ_M°	ψ_M°	Δ_C°	ψ_C°	d(Å)	θ_{Pb}	n	k
					NO DYE ADDED						
16	-235	0	0	65.29	38.08	65.29	38.08	0	-	0.901	2.765
23	-304	0.65	3.52	66.25	37.63	66.25	37.63	5.90	1	1.765	4.265
30	-582	30	163	58.00	36.42	57.97	36.35	75	0.38	2.1	4.2
52	-430	70	379	55.00	31.68	54.98	31.58	506	0.56	2.1	4.2
99	-573	30	163	56.80	36.42	56.80	36.35	86	0.35	2.1	4.2
123	-400	70	379	54.20	31.68	53.86	31.50	509	0.55	2.1	4.2
					10μM RHODAMINE-B						
9	-242	0	0	65.83	38.93	65.83	38.93	0	-	0.794	2.810
16	-513			67.71	38.63	67.71	38.63	2.64	1	0.815	2.820
28	-800	40	217	74.30	32.00	74.72	33.12	113	0.89	2.1	4.2
43	-439	70	379	79.79	32.00	79.74	32.04	2.96	0.85	2.1	4.2
96	-800	50	271	60.19	33.37	60.05	33.43	244	0.61	2.1	4.2
111	-388	80	433	65.00	32.00	65.19	32.36	420	0.66	2.1	4.2

Table II

Charge Balance for UPD & Bulk Pb Deposit

Electrode Surface Area = 1.33 cm^2

Calculated Charge for UPD Monolayer = 0.49 mC

Measured Charge for UPD Monolayer = 0.65 mC

Apparent Surface Roughness = 1.33

Agreement of Charge Balance for Bulk Deposit with Optical Data

t(sec)	d_q(Å)	d(Å)	θ_{Pb}	$\theta_{Pb}(d/d_q)$
		NO DYE ADDED		
30	163	75	0.38	0.17
52	379	506	0.56	0.75
99	163	86	0.35	0.18
123	379	509	0.55	0.74
		10μM RHODAMINE-B		
28	217	113	0.89	0.46
43	379	296	0.85	0.66
96	271	244	0.61	0.55
111	433	420	0.66	0.64

Table III. Spectroscopic Ellipsometry of Pb Deposits: Optimization of 2-Layer Simplification Model

	30 nm		60 nm		110 nm		
λ(nm)	Δ°	ψ°	Δ°	ψ°	Δ°	ψ°	
4248	58.69	32.99	78.01	32.55	89.84	34.62	Measured
	60.54	28.92	81.97	29.30	94.25	29.61	Calculated
4492	57.24	31.12	76.02	30.14	88.42	31.81	etc.
	56.49	31.68	75.64	31.60	87.64	31.76	
4756	55.48	30.88	73.77	29.11	86.53	30.35	
	54.28	30.97	73.63	30.16	85.84	30.30	
5155	52.73	30.99	71.42	28.81	84.44	29.42	
	51.89	30.90	71.19	29.18	83.69	29.32	
5586	50.07	31.73	69.52	28.68	82.91	28.99	
	49.59	31.48	69.44	28.60	82.44	28.85	
5998	49.97	33.58	66.95	29.04	81.14	28.84	
	49.81	33.50	66.71	28.70	80.88	28.77	
6242	51.03	34.47	65.91	29.62	79.68	29.10	
	50.91	34.38	64.95	29.25	79.47	28.99	
6504	51.85	35.35	64.99	30.59	78.06	29.85	
	52.27	35.24	63.54	30.38	77.90	29.71	
6748	52.87	36.39	64.58	31.99	76.99	30.96	
	53.69	35.99	63.04	31.78	76.79	30.81	
6991	53.45	38.11	64.09	34.43	75.53	33.65	
	55.14	36.89	63.12	34.53	75.30	33.52	
ERROR (degrees)	5.359		6.049		6.835		
THICKNESS (Å)	310	(5.8×10^{2})	500	(9.0×10^{3})	870	(2.3×10^{6})	
VOL. FRACT. Pb	0.585	(6.7×10^{-3})	0.775	(9.5×10^{-3})	0.968	(2.6×10^{-2})	

NOTE: PARAMETER VARIANCE GIVEN IN PARENTHESES

Figures

1. Flow diagram for electrochemical cell for simultaneous ellipsometry and cyclic voltammetry. Electrolyte transfer was via glass and Teflon syringes.

2. Picture of the electrochemical cell for simultaneous ellipsometry and cyclic voltammetry. The reference electrode (A) is held in a cylindrical Teflon reservoir (B). The cell (C) is made of Teflon and is mounted on an optical x-y-z translator with tilt (D). Electrolyte transfer is done with syringes (E). The beam path forms a 75 degree angle of incidence with the electrode surface. Windows (H) are quartz; metal presses (I) for holding windows are black anodized aluminum; and the electrodes (G) are either Cu, Ag, Pt, or Au and are screwed into Teflon mounts (F) using a special tool (J). The counter electrode was an ultra-pure Pb wire (99.9999% pure, made at LBL).

3.a Potential ramp from +100 to -800 mV vs Ag/AgCl at a sweep rate of 2 V/min. Used to drive working electrode during simultaneous cyclic voltammetry and ellipsometry experiment. Pb deposition on Cu from 5 mM $Pb(NO_3)_2$, 1 M $NaClO_4$, pH 3, no dye added. Experiments were performed in the cell shown in Fig. 1 and Fig. 2. The ellipsometer source wavelength was 550 nm (10 nm bandwidth) and the angle of incidence was 75 degrees.

3.b Current response corresponding to Fig. 3.a. Electrode surface area was 1.13 cm^2 (1.2 cm dia.).

3.c Ellipsometer response corresponding to Fig. 3.a. delta vs time. Note that the trend in delta is negative relative to the initial value of 65 degrees. This can not be explained by a compact deposit of Pb on Cu; porosity must be assumed to account for this unusual behavior.

3.d Ellipsometer response corresponding to Fig. 3.a. Psi vs time.

4.a Same as 3.a, but with rhodamine-B addition at 10 micromolar concentration.

4.b Same as 3.b, but with rhodamine-B addition at 10 micromolar concentration.

4.c Same as 3.b, but with rhodamine-B addition at 10 micromolar concentration. Note that the first cycle response characteric of a compact microdeposit; subsequent cycle responses are characteristic of a porous micromorphology, similar to those of all cycles shown in 3.b.

4.d Same as 3.c, but with rhodamine-B addition at 10 micromolar concentration. Psi is more indicative of the amount of Pb on the Cu surface than the porosity of the deposit. These responses are very similar to those of Fig. 3.c.

5. Calculated deposit thicknesses and porosities at different levels of deposited charge (Pb); computations based upon the data of Figs. 3 and 4, and upon the "two-layer simplification" of a "three-layer model" shown in Fig. 7. The first compact layer is the compact UPD monolayer, the second layer having the thickness and porosity

indicated in this figure, and the third layer composed of relatively large dendritic islands which cover an insignificant fraction of the surface.

6. Schematic representation of various models used in attempts to explain the unusual trends in delta noted in figures 3.c and 5.a. First order effects. The number of adjustable model parameters are shown in parenthesis.

7.a Spectral scans of thin Pb deposits on Cu, contrasting a deposit made with rhodamine-B to another made in the absence of this inhibitor. Measurements made for the bare Cu substrate are also shown for comparison. The same electrolyte concentrations were used as in Figs. 3 and 4. Deposition was done potentiostatically at -600 mV, and the Pb deposit corresponds to a compact layer of 31 nm. Delta vs wavelength.

7.b Psi vs wavelength corresponding to Fig. 7.a.

8.a Spectral scans analagous to those of 7.a, but for Pb deposits corresponding to a compact layer of 110 nm. Delta vs wavelength.

8.b Psi vs wavelength corresponding to Fig. 8.a.

9.a Simulated ellipsometer spectral scan data based upon the "two-layer simplification" superimposed on the experimental spectral scans. Circles represent the "two-layer simplification model," solid lines are simulated spectra assuming a compact deposit, and the solid lines are the experimental data. Delta vs wavelength. (See Table III).

9.b Spectral scans corresponding to 9.a. Psi vs wavelength.

10. Cyclic voltammograms at the conditions of Figs. 4.a through 4.d. Each voltammogram is the first sweep after some "relaxation" period at open circuit conditions (except "a" which was a multiple sweep experiment). Note the cathodic shifts in the deposition peaks, correlated with increasing relaxation time.

11.a Spectral scans taken at open circuit immediately preceding the corresponding cyclic voltammograms of Fig. 10 (with spectra for bare Cu subtracted; electrolyte has no dye). Delta vs wavelength. Note development of the broad band and peak structure at 60 minutes relaxation time.

11.b Spectral scan corresponding to 11.a.

12.a Replicate of 11.a

12.b Replicate of 11.b

13. Conceptual drawing of rhodamine-B adsorbate with two molecular orientations relative to the surface, the transition moment being normal or perpendicular to the electrode. Such orientations result in birefringence which can be accounted for (optically) through uniaxial anisotropic film models.

14.a Smoothed and averaged ellipsometer spectral scans (subtracted) similar to the data of Figs. 11 and 12. Scans for 10, 30 and 60 minutes of relaxation.

14.b Computed extraordinary complex refractive index as a function of wavelength (optimized values of n_e and k_e); the optimum adsorbate

layer thickness is 32 Angstroms, comparable to the molecular dimension of the dye molecule parallel to the transition moment (Fig. 13). Corresponds to spectral scans of Fig. 14. Note that there is a peak in k_e near the dissolved rhodamine-B absorption wavelength; ne does not exhibit this feature, but does have an edge.

14.c Computed birefringence of the complex refractive index as a function of wavelength (optimized values of n_e/n_o and k_e/k_o). Corresponds to spectral scans of Fig. 14.a.

15.a Cyclic voltammogram for Pb deposition on Ag(111) from electrolyte similar to that of experiments described in the previous experiments, except that the Pb concentration here is 0.5 mM. No dye added. This data has been discussed previously (Chapter 5), and is only shown here as a reference for experiments done on Ag(111) with rhodamine-B inhibitor. The counter electrode is Pt and experiments were performed in an acrylic cell. The ellipsometer source wavelength during this experiment was 515 nm. Note that this wavelength is well removed from the dye absorption band.

15.b Potential ramp during cyclic voltammogram of Fig. 15.a; +100 to -650 mv at 0.15 V/min.

15.c Current response corresponding to 15.b.

15.d Ellipsometer response corresponding to 15.c, delta vs time. The current response is shown again just as a reference for the

ellipsometer response.

15.e Ellipsometer response corresponding to 15.d, psi vs time.

16.a Cyclic voltammogram taken under identical conditions as 15.a, except here rhodamine-B was added to the electrolyte at a concentration of 6 micromolar. The ellipsometer source wavelength here too is 515 nm.

16.b Analogous to 15.b, except at the conditions of 16.a. With rhodamine-B.

16.c Analogous to 15.c, except at the conditions of 16.a. With rhodamine-B.

16.d Analogous to 15.d, except at the conditions of 16.a. With rhodamine-B.

16.e Analogous to 15.e, except at the conditions of 16.a. With rhodamine-B.

17.a Potential ramp analagous to 15.b used in cyclic voltammetry and ellipsometry experiments conducted at a source wavelength of 555 nm, near the maximum absorption wavelength for rhodamine-B.

17.b Current response to 17.a with no dye added.

17.c Current response to 17.b with 6 micromolar rhodamine-B addition.

17.d Ellipsometer response to 17.a both with and without rhodamine-B addition; delta vs time.

17.e Ellipsometer response to 17.a, both with and without rhodamine-B addition; psi vs time.

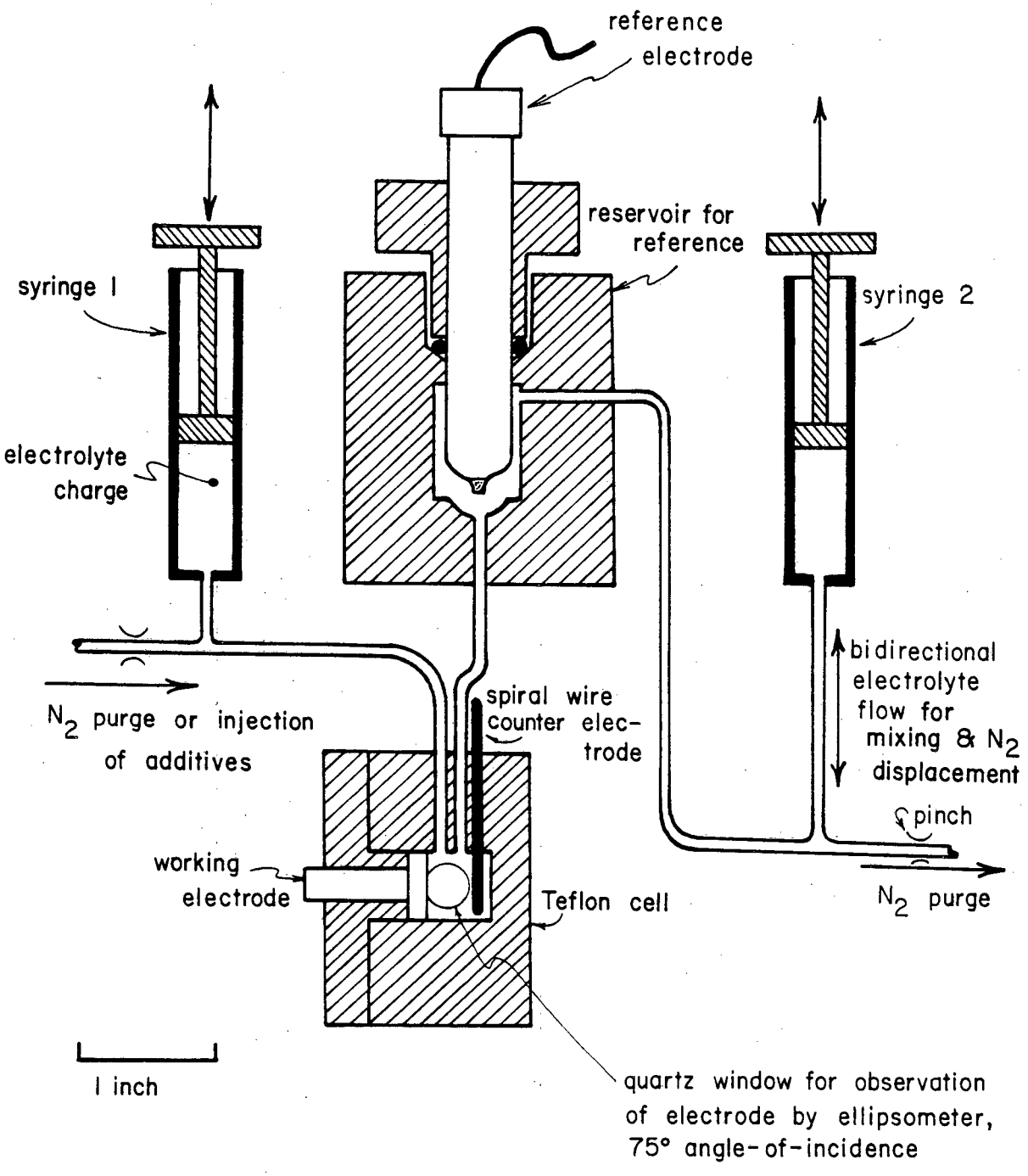

XBL 833-8506

Fig. 1

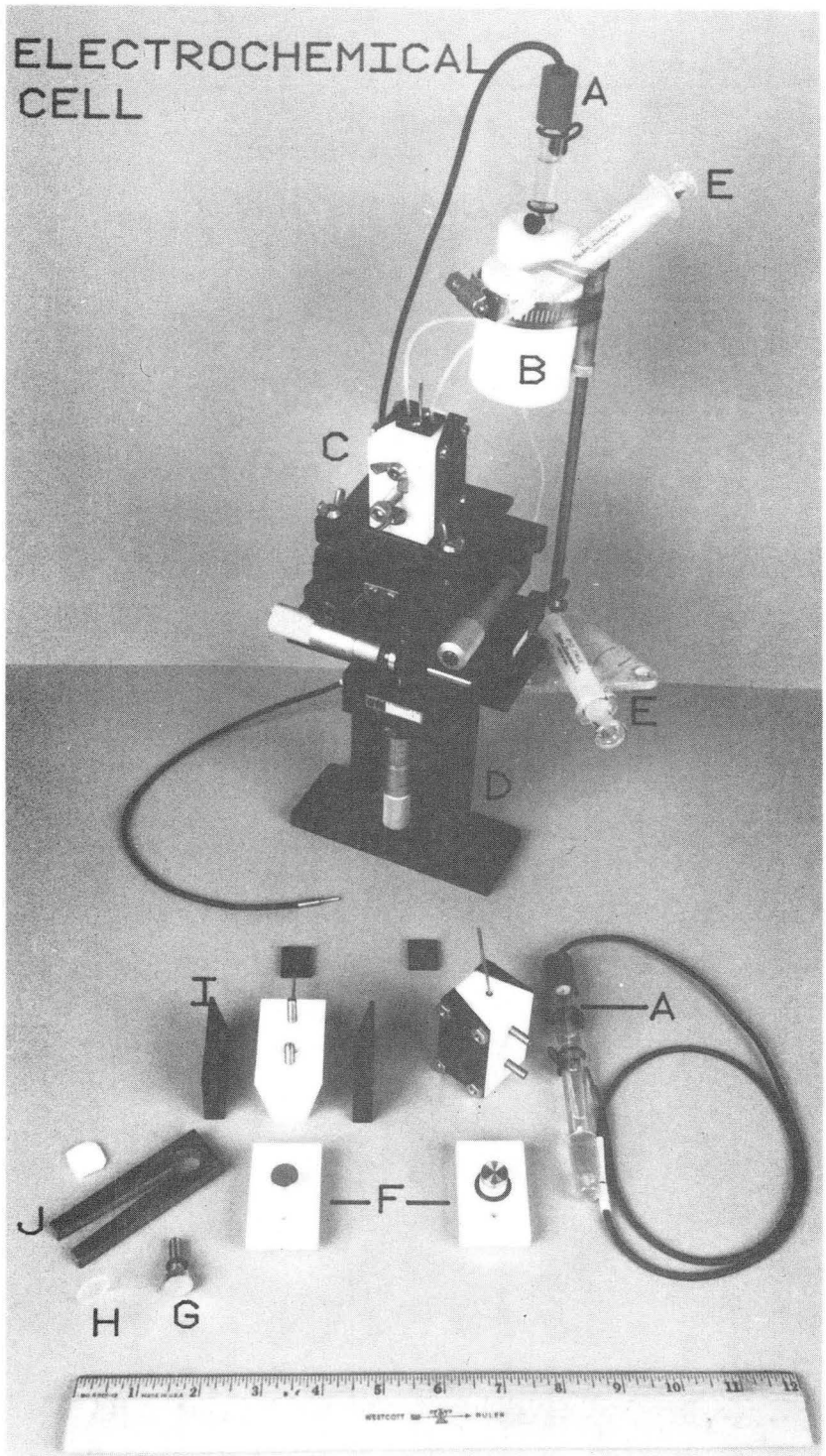

XBB 820-10765A

Fig. 2

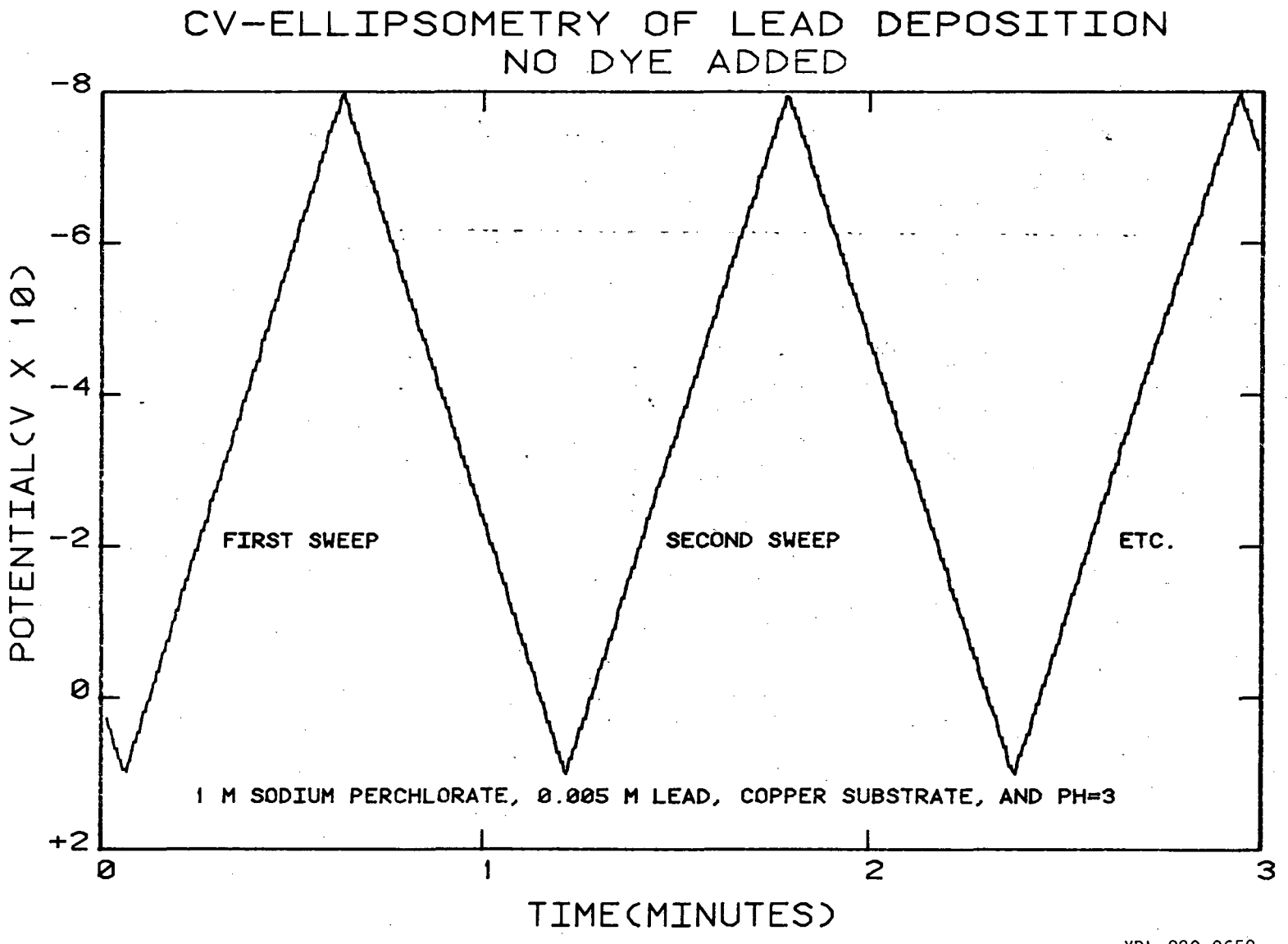

Fig. 3.a

XBL 829-9650

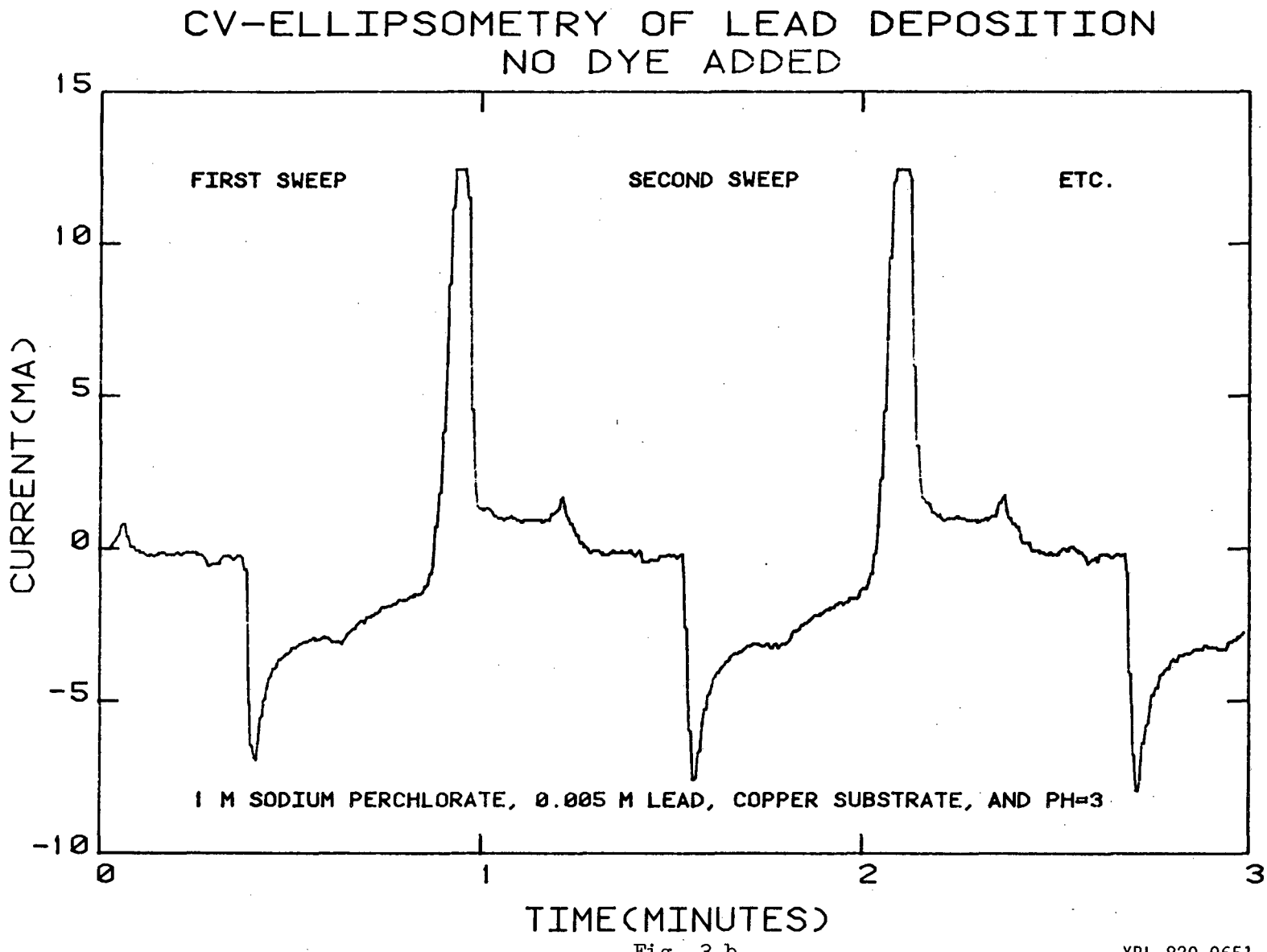

Fig. 3.b

XBL 829-9651

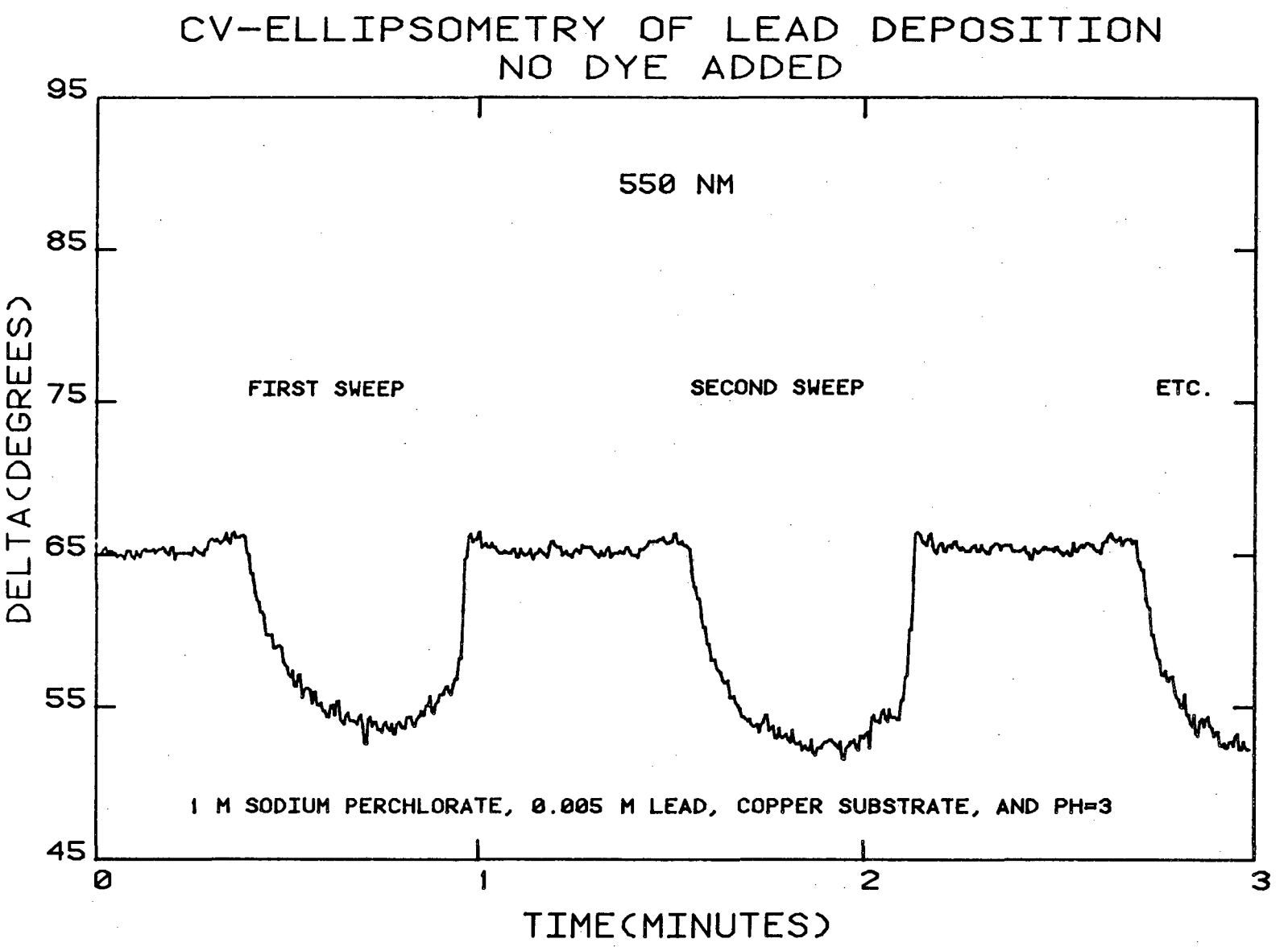

Fig. 3.c

XBL 829-9652

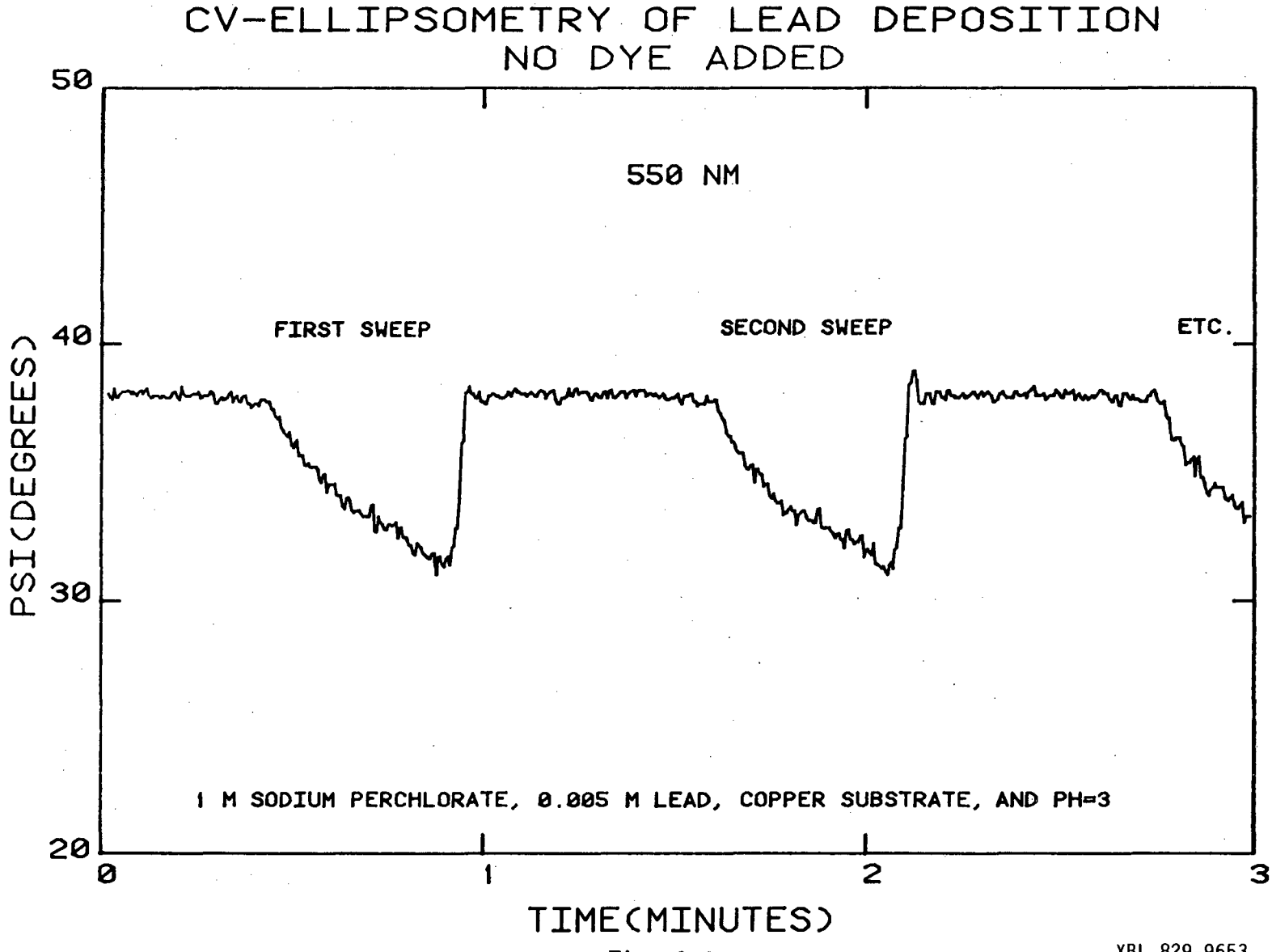

Fig. 3.d

XBL 829-9653

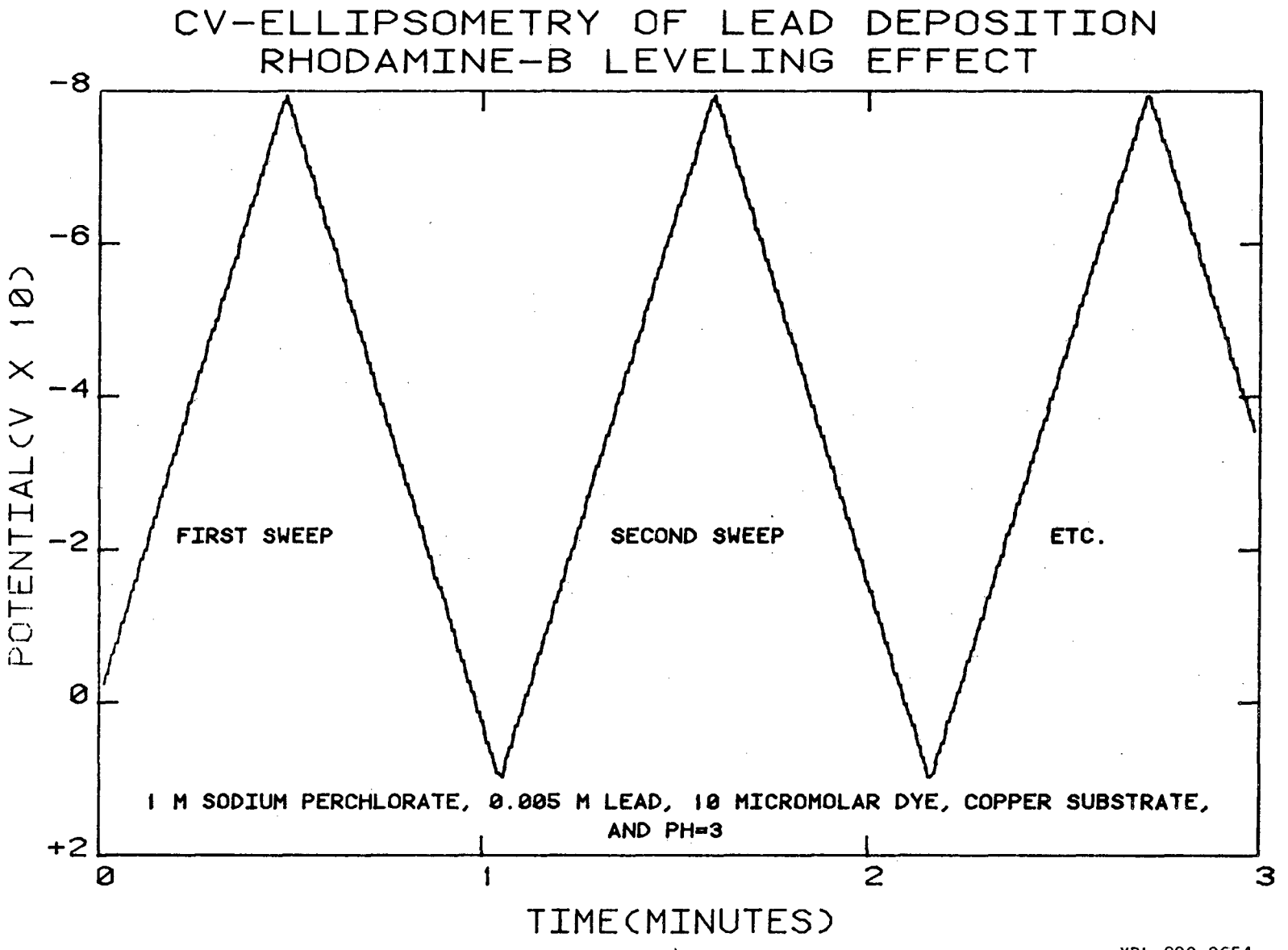

Fig. 4.a

XBL 829-9654

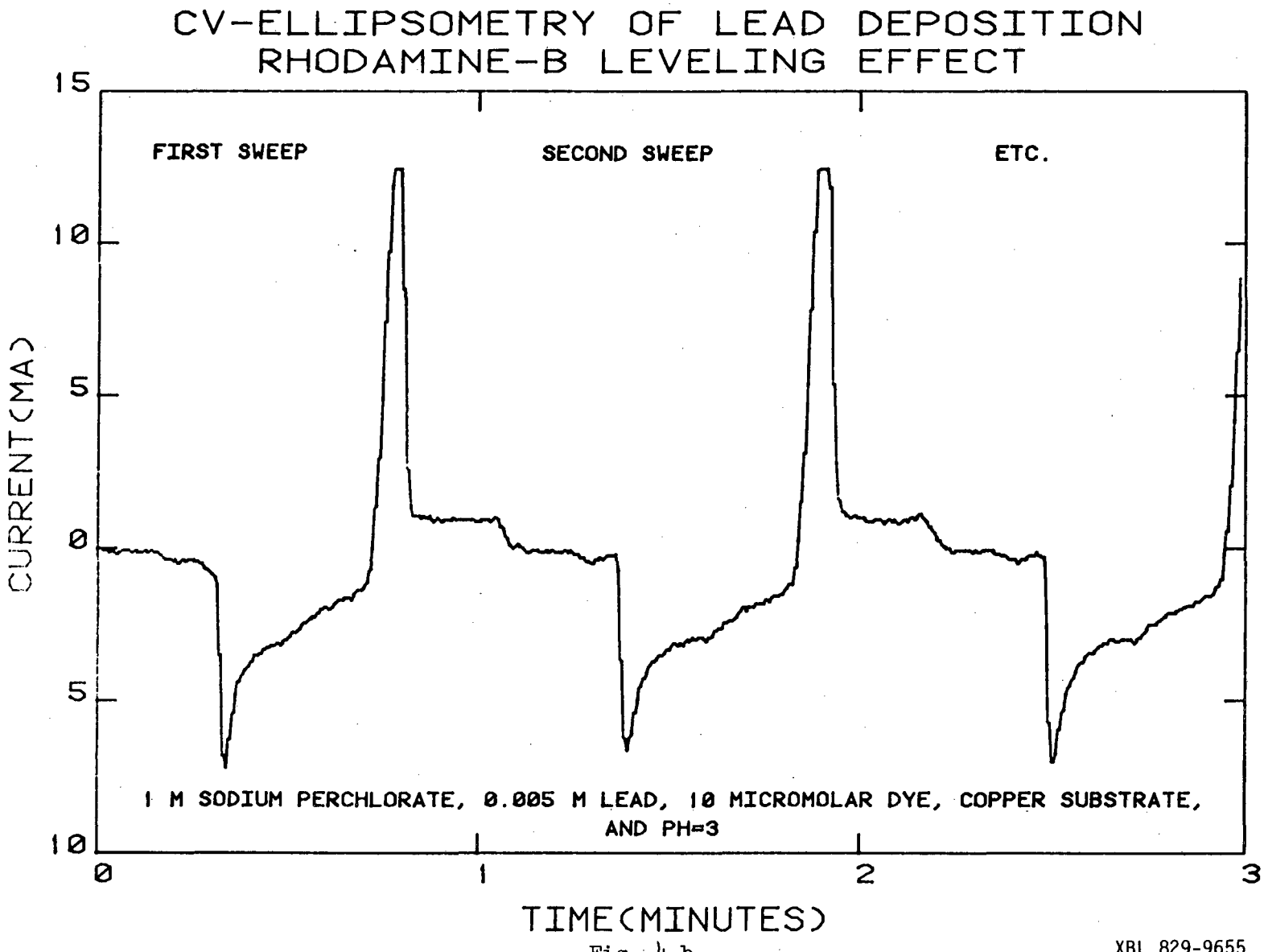

Fig. 4.b

XBL 829-9655

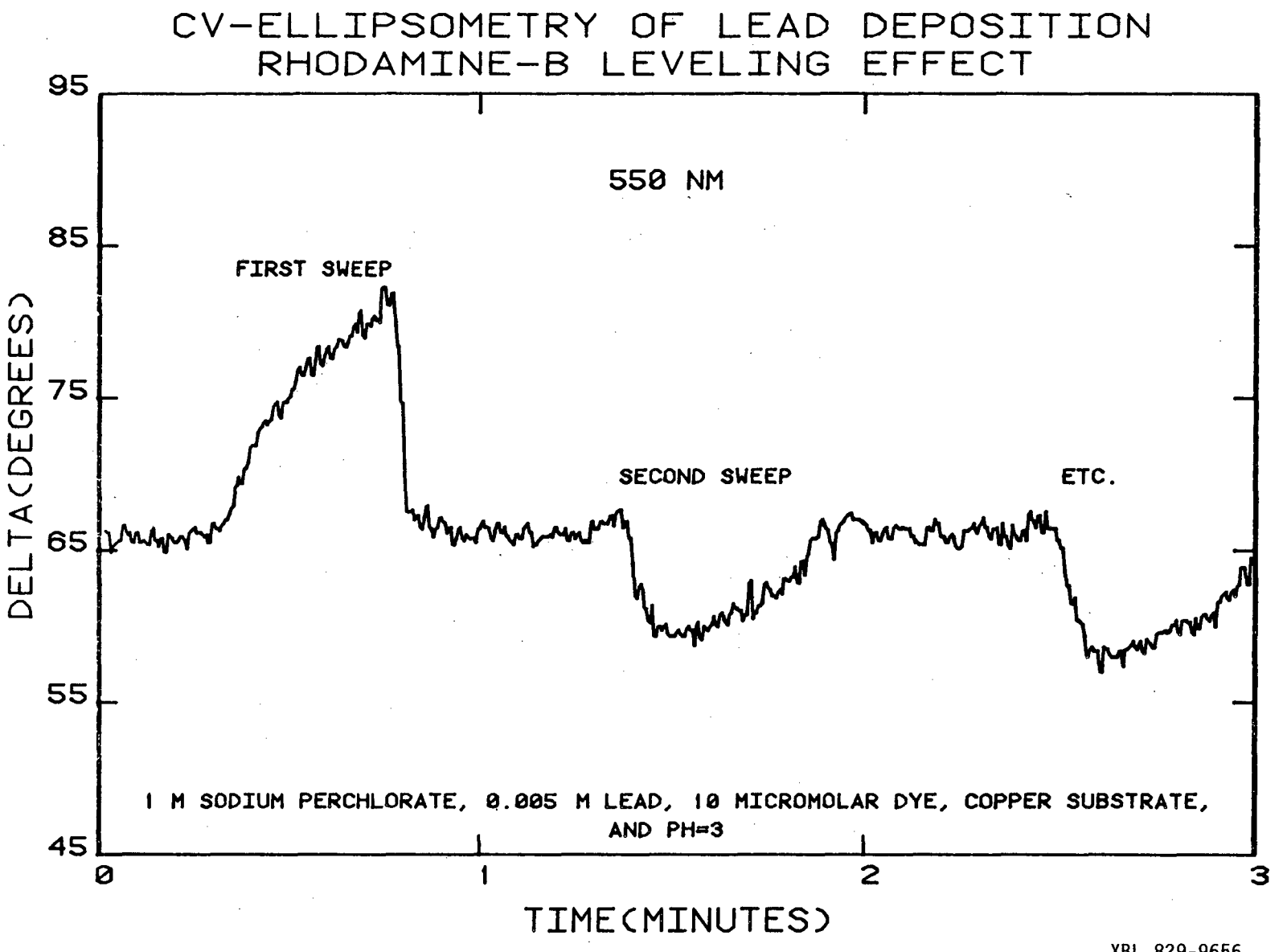

XBL 829-9656

Fig. 4.c

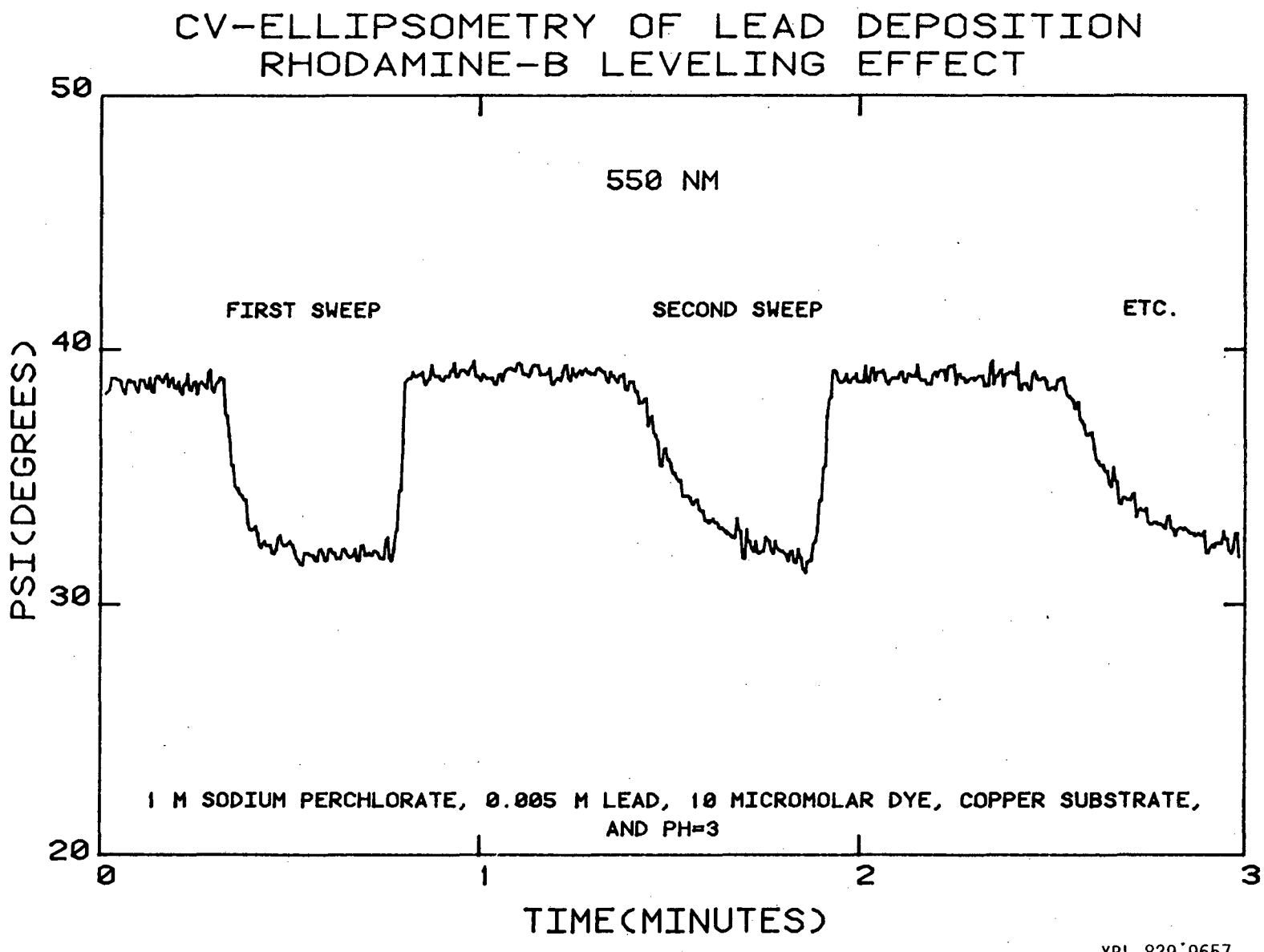

Fig. 4.d

XBL 829-9657

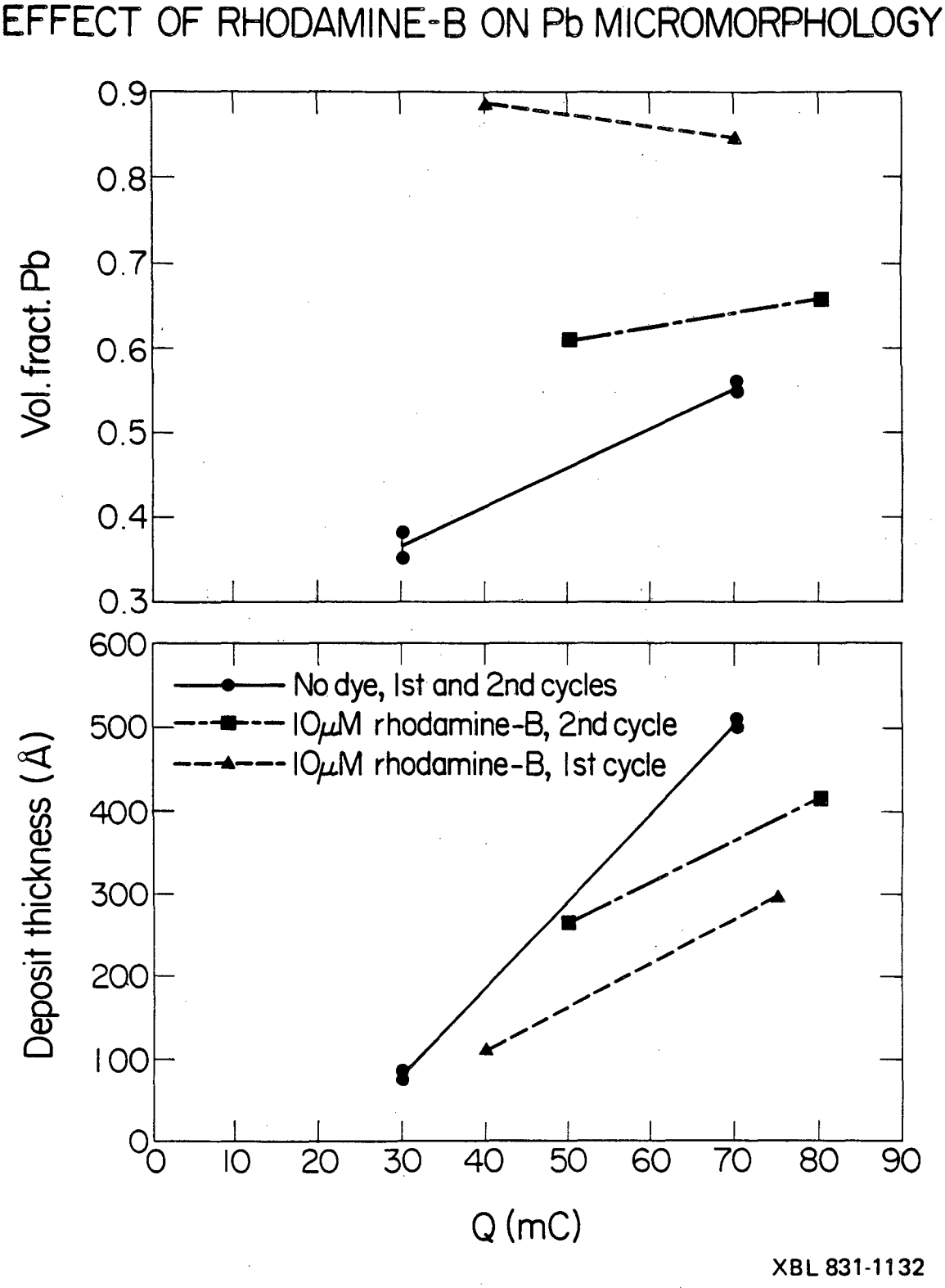
EFFECT OF RHODAMINE-B ON Pb MICROMORPHOLOGY
Vol. fract. Pb
0.9
0.8
0.7
0.6
0.5
0.4
0.3
Deposit thickness (Å)
600
500
400
300
200
100
0
No dye, 1st and 2nd cycles
10μM rhodamine-B, 2nd cycle
10μM rhodamine-B, 1st cycle
0
10
20
30
40
50
60
70
80
90
Q (mC)
XBL 831-1132

Fig. 5

MODELING FIRST ORDER OPTICAL EFFECTS

COMPACT HOMOGENEOUS FILM

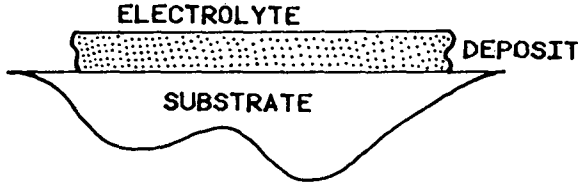

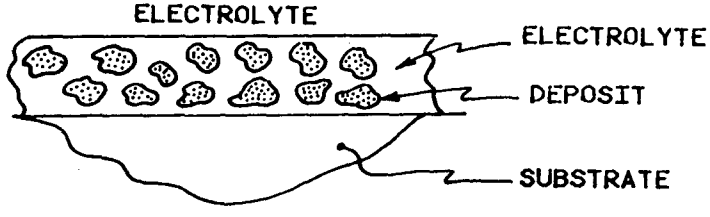

EFFECTIVE MEDIA APPROXIMATION

1. MAXWELL-GARNETT (2)
2. BRUGGEMAN (2)

COHERENT SUPERPOSITION

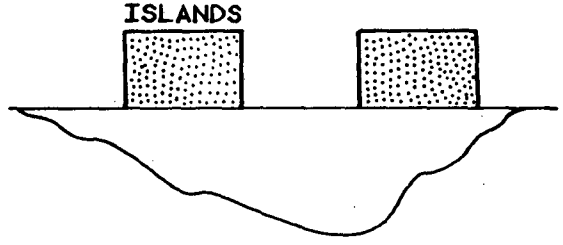

1. COMPACT ISLANDS (2)
2. POROUS ISLANDS (3)
3. ANISOTROPIC (6)

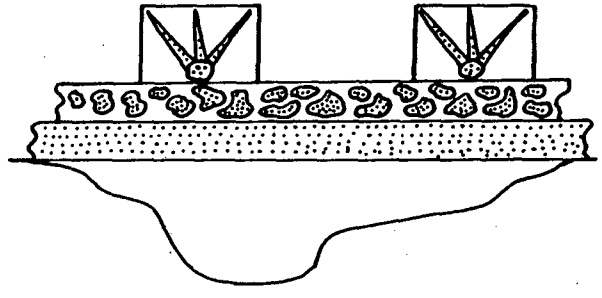

MULTILAYER MODELS

1. THREE LAYER (6)
2. TWO LAYER SIMPLIFICATION (3)

XBL 829-11873

Fig. 6

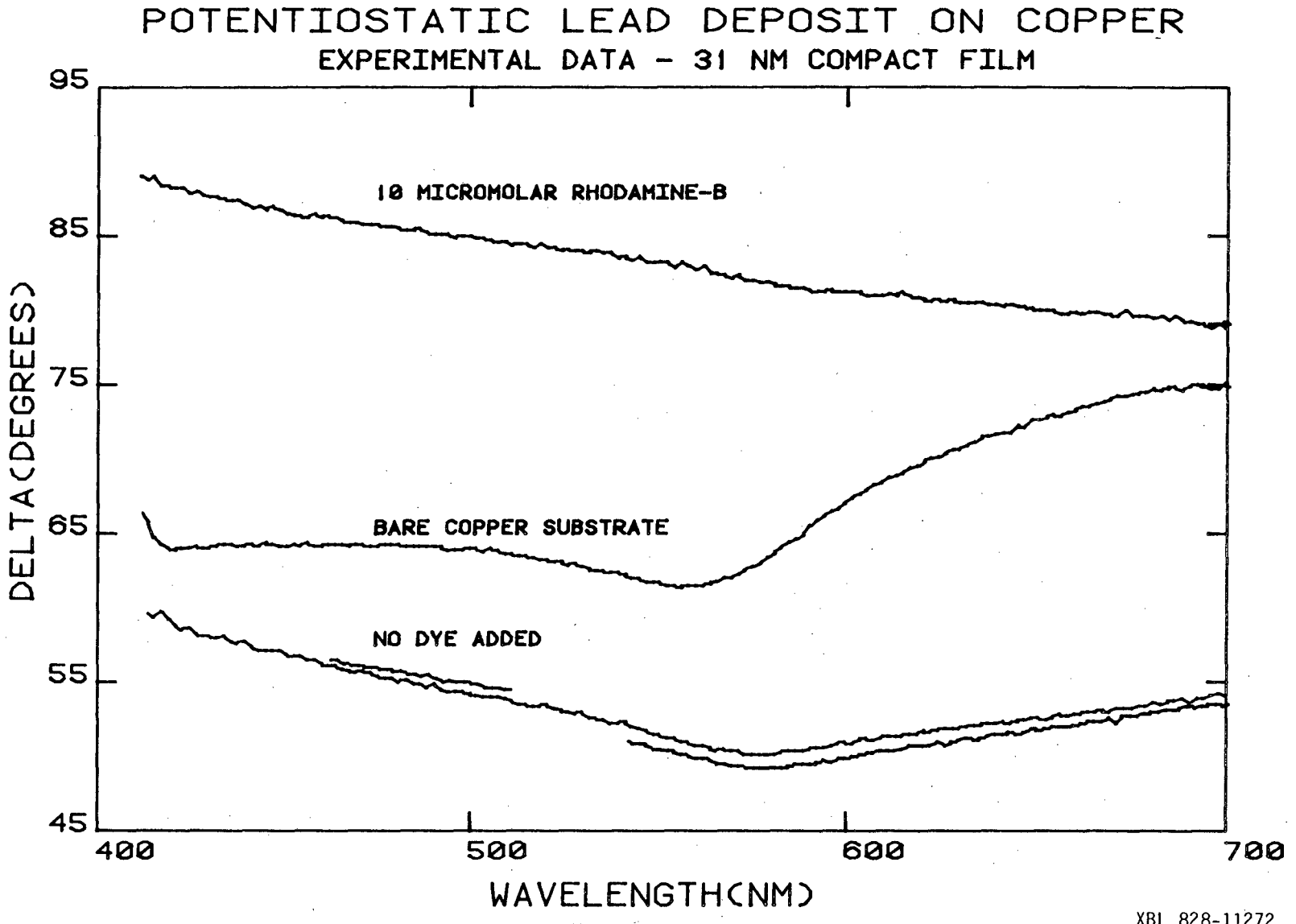

Fig. 7.a

XBL 828-11272

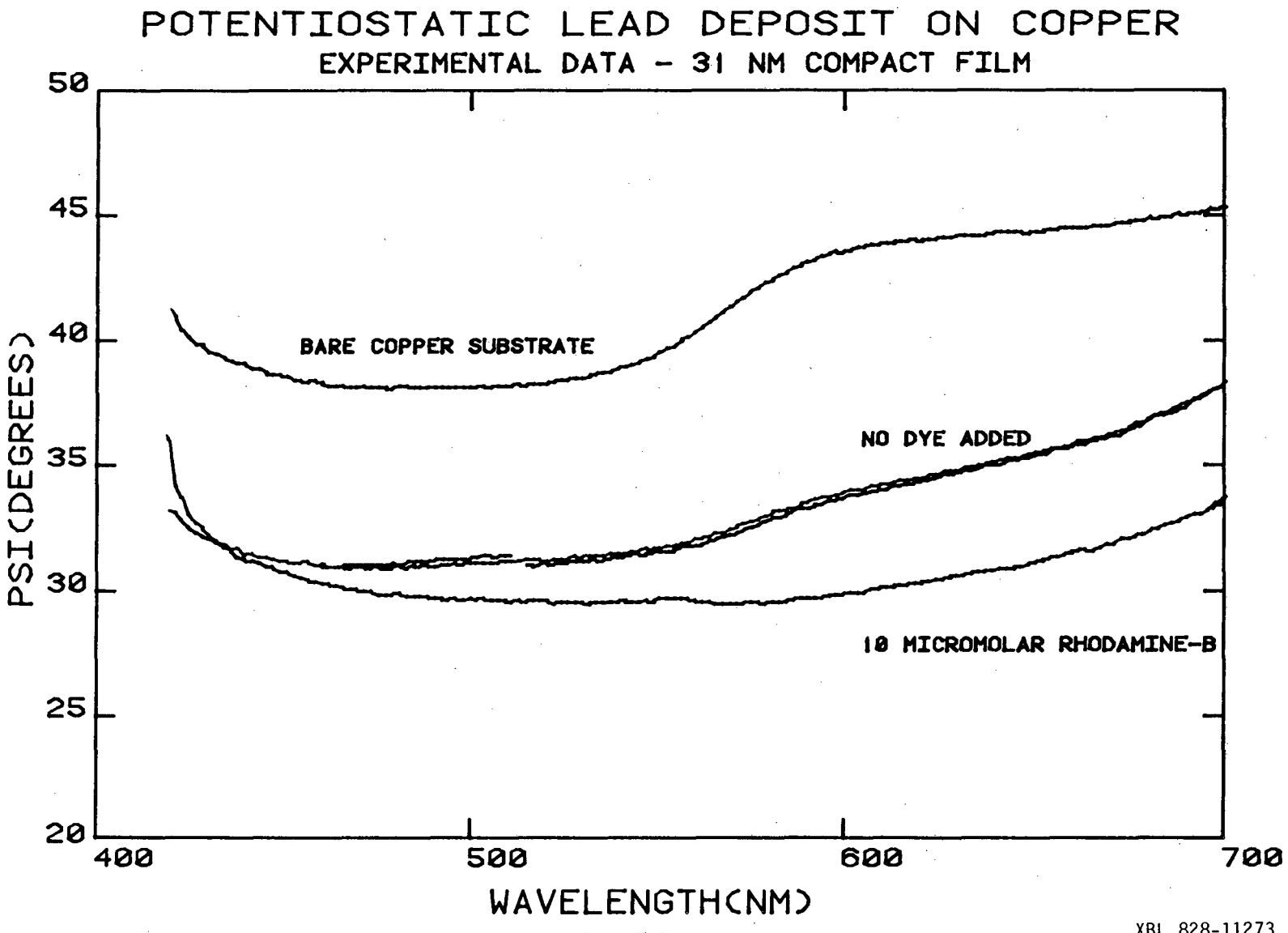

Fig. 7.b

XBL 828-11273

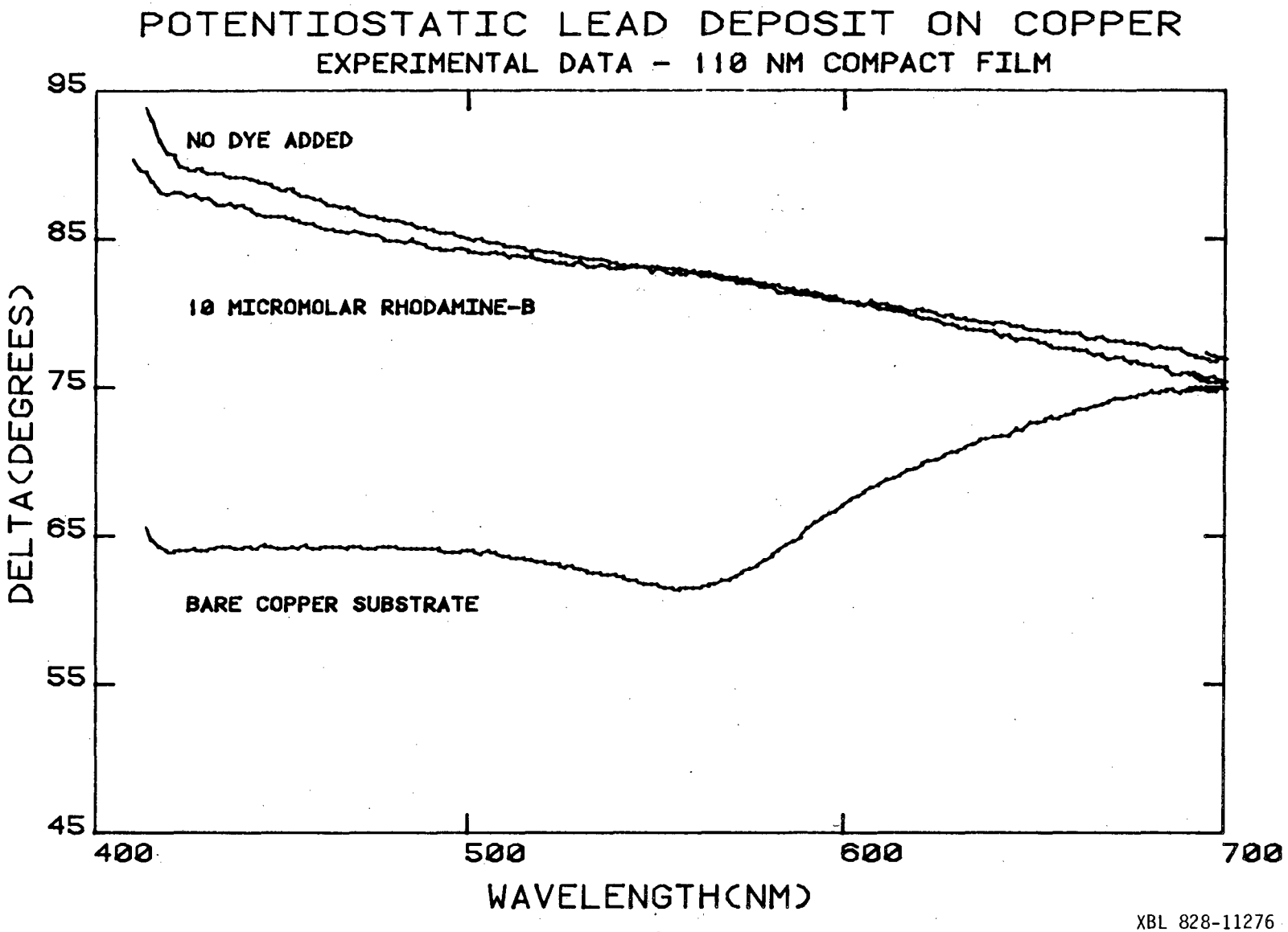

XBL 828-11276

Fig. 8.a

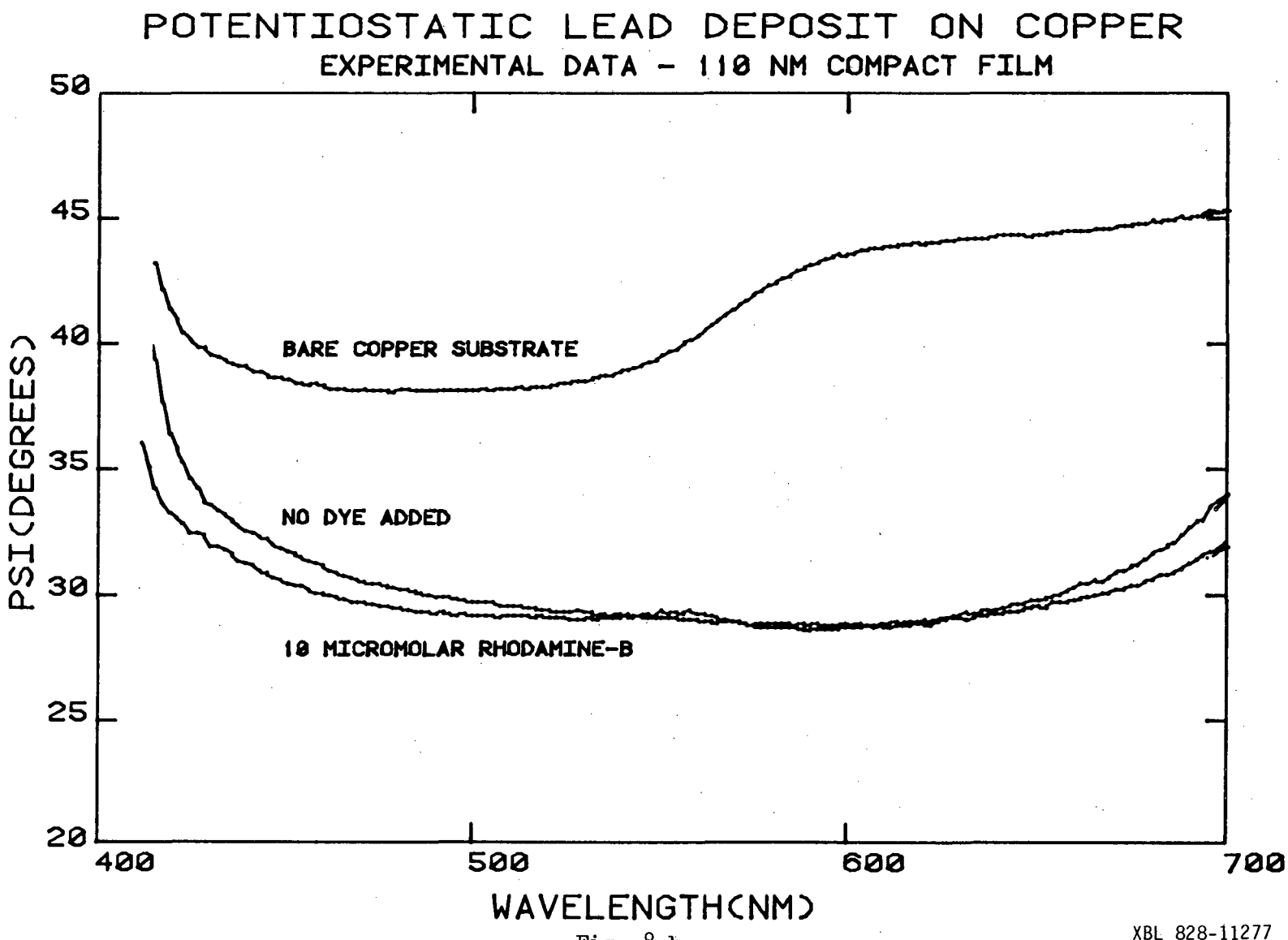

Fig. 8.b

XBL 828-11277

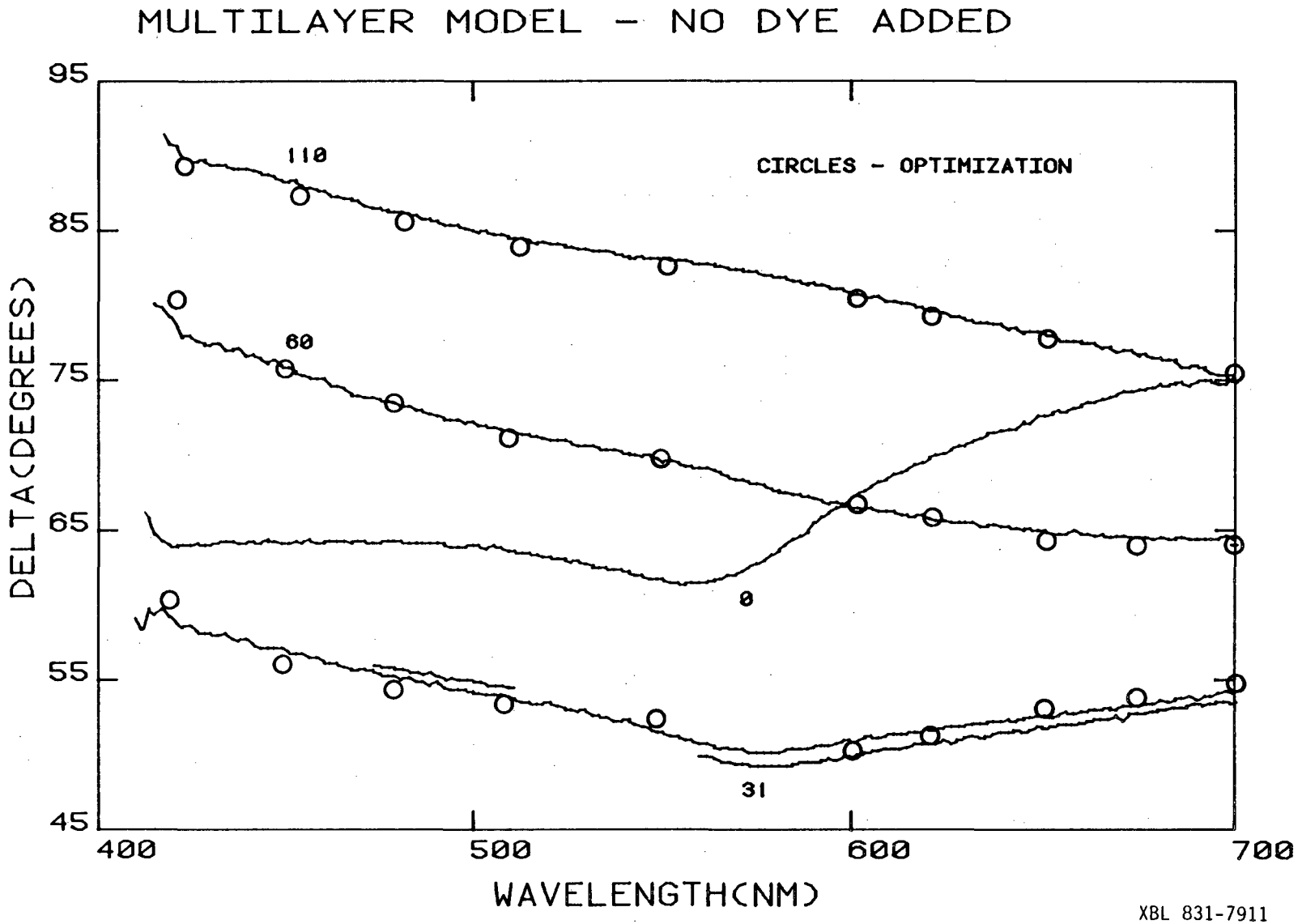

XBL 831-7911

Fig. 9.a

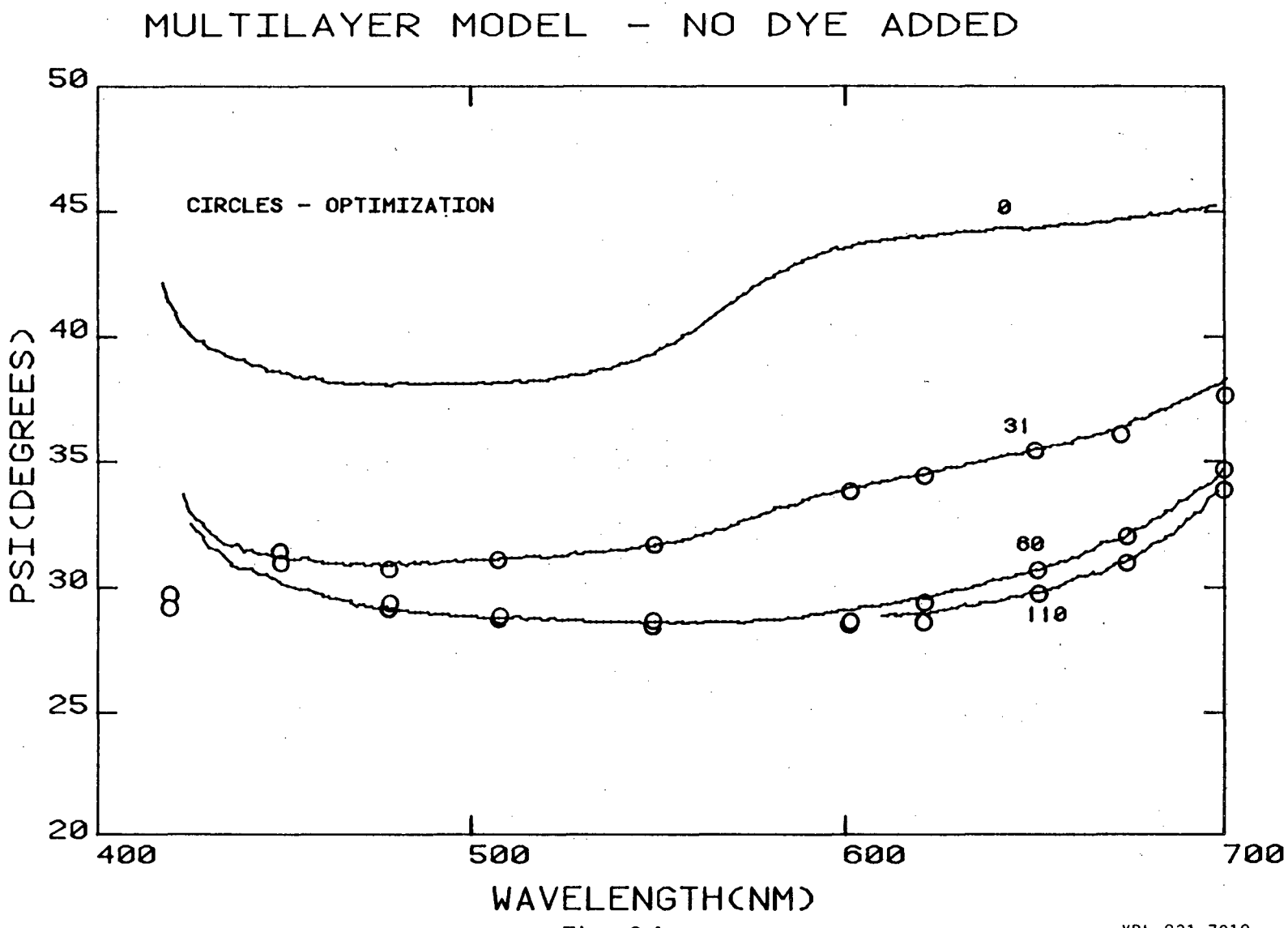

Fig. 9.b

XBL 831-7912

Rhodamine-B Relaxation Effect on Copper during Cyclic Voltametry with Lead

1 M $NaClO_4$, 5 mM Pb^{++}, 10 μM dye, pH 3, 2 V/min, Ag/AgCl ref., and 1.27 cm^2 electrode

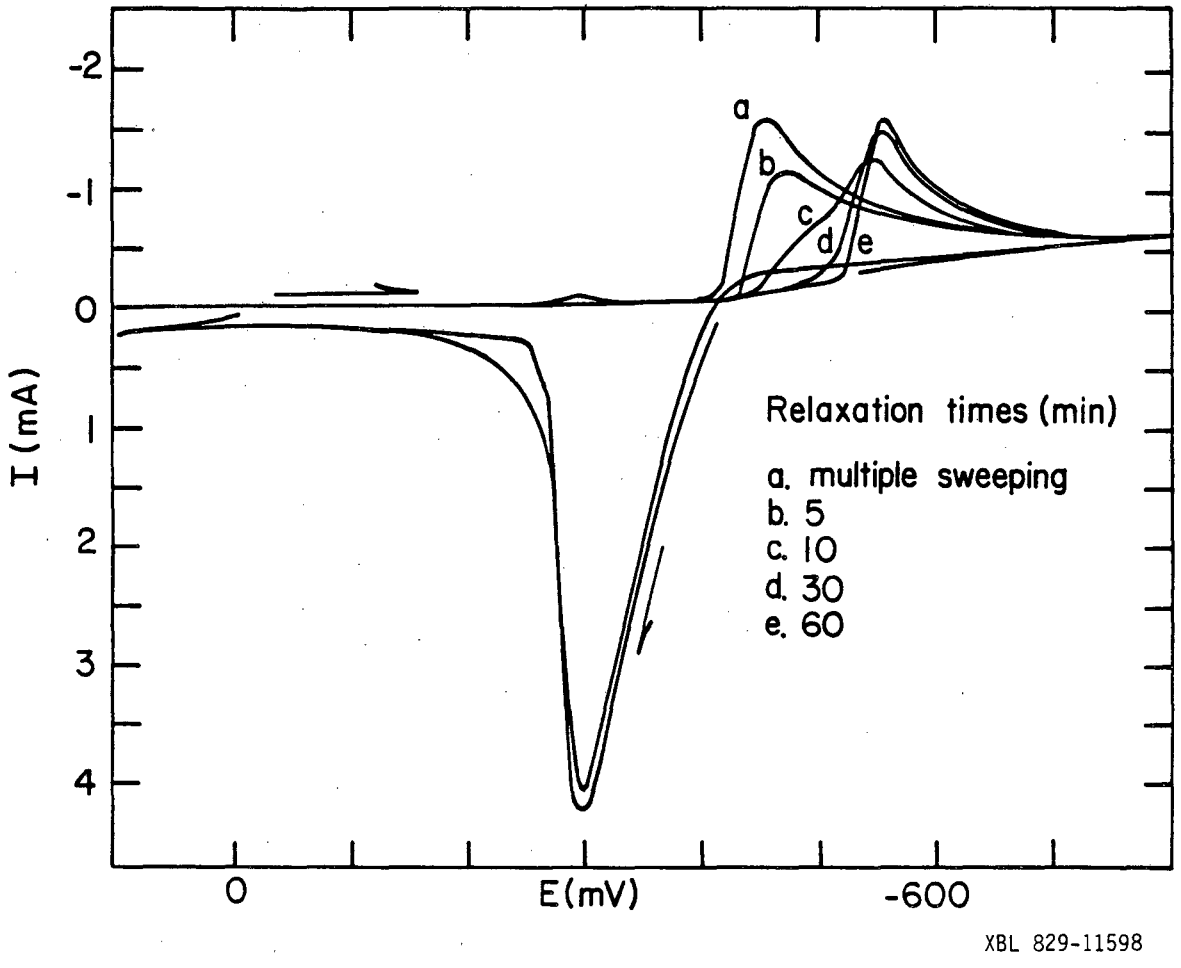

Fig. 10

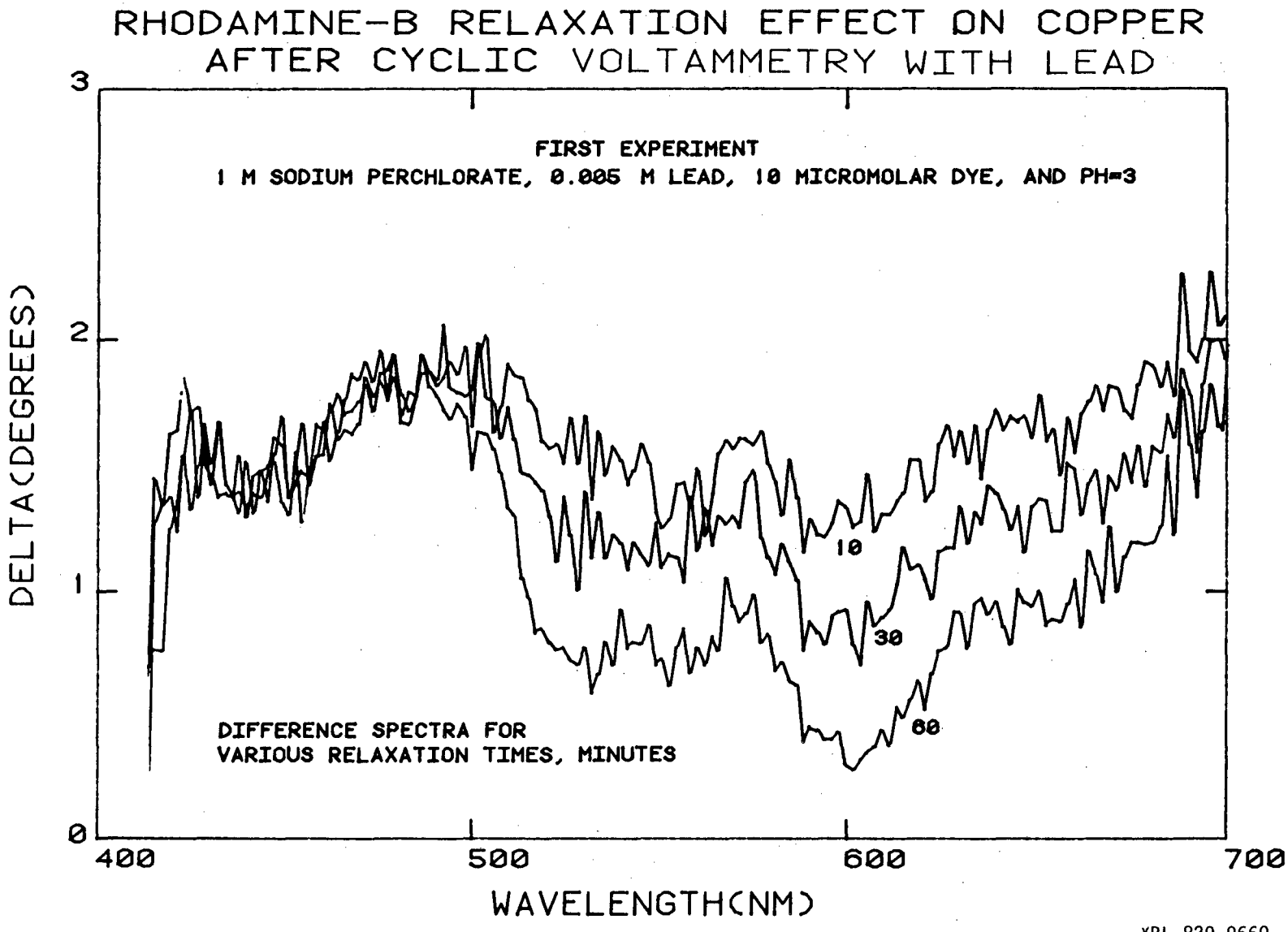

Fig. 11.a

XBL 829-9660

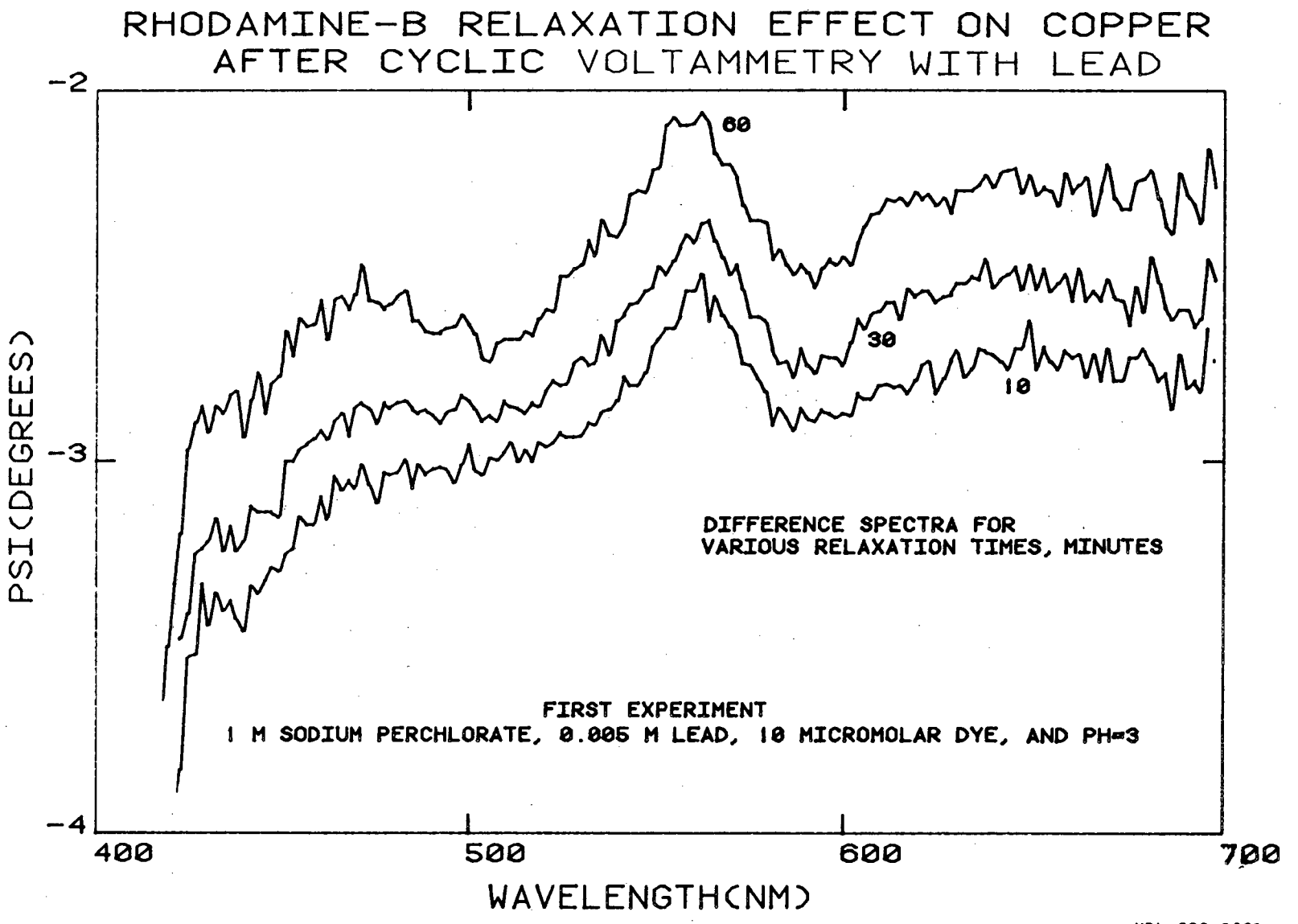

Fig. 11.b

XBL 829-9661

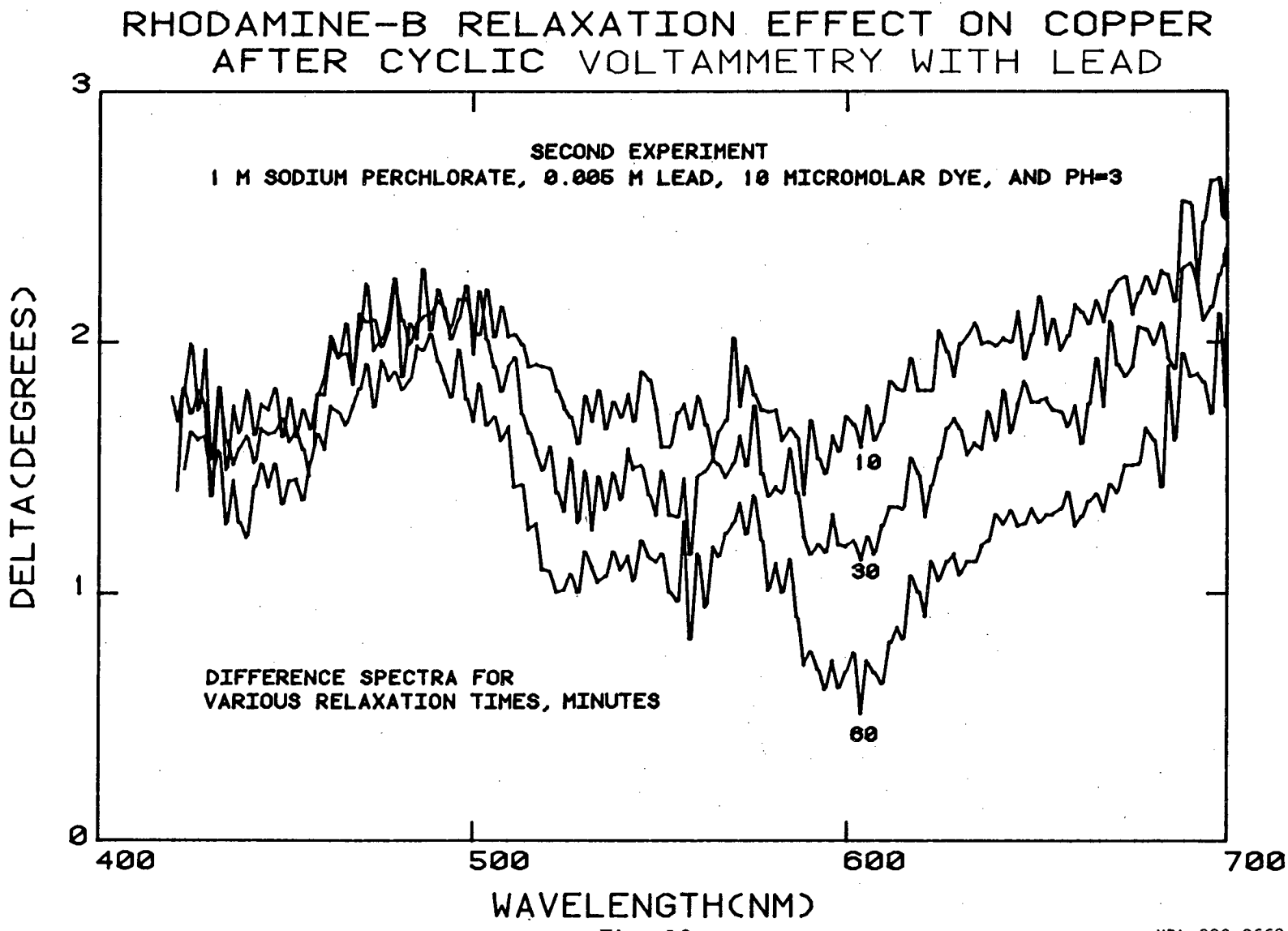

Fig. 12.a

XBL 829-9662

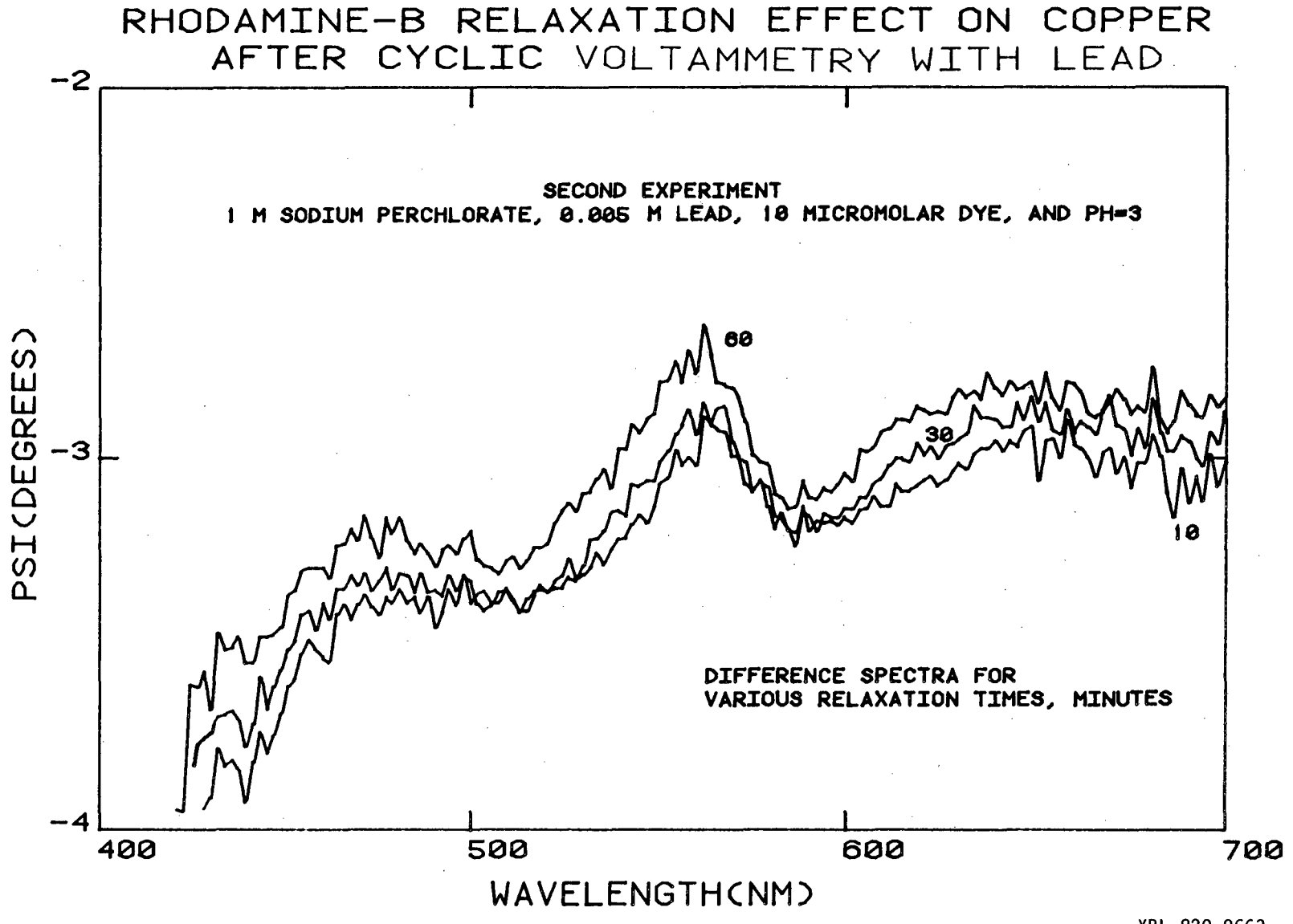

Fig. 12.b

XBL 829-9663

MODELING SECOND ORDER EFFECTS

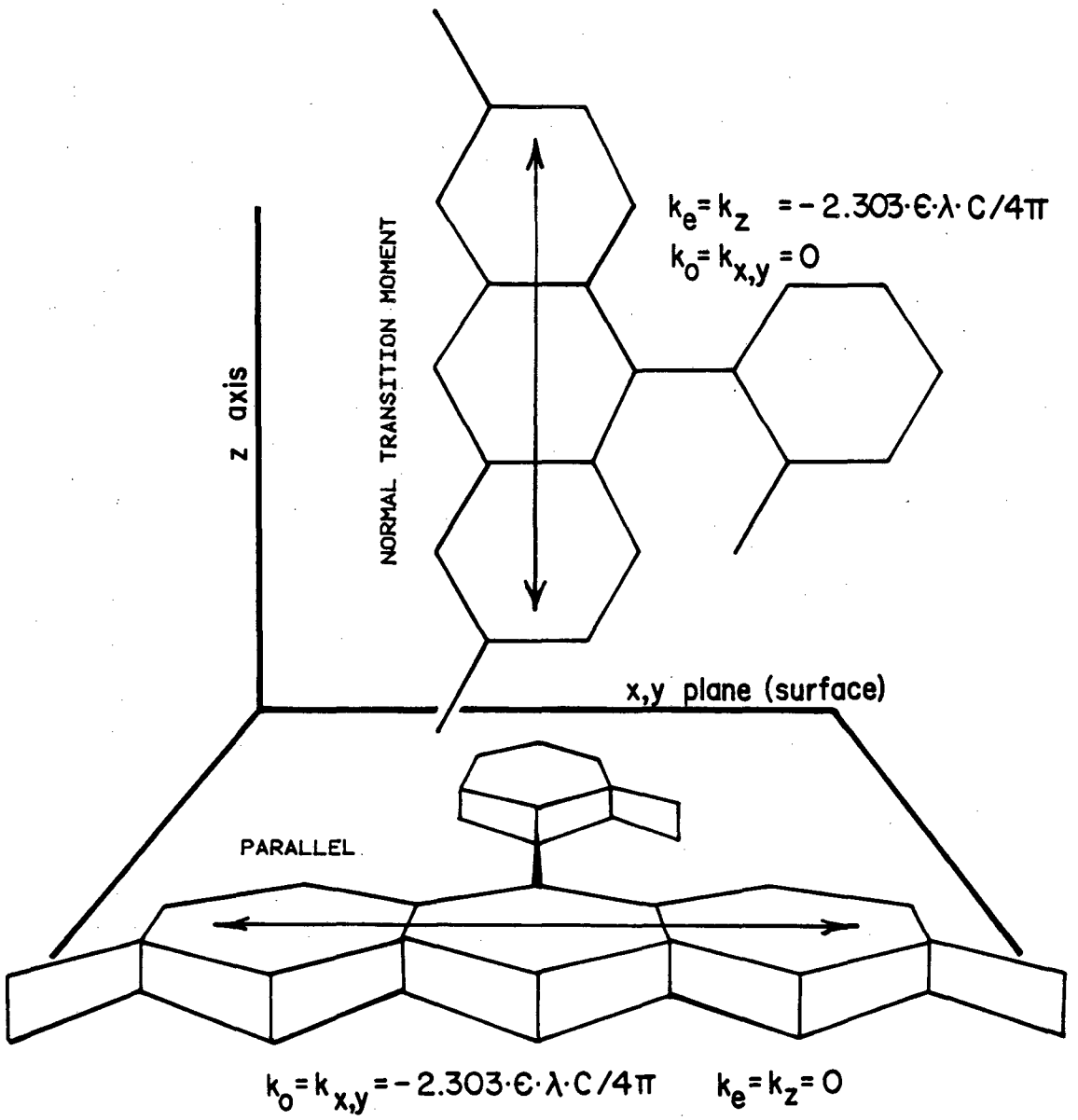

Fig. 13

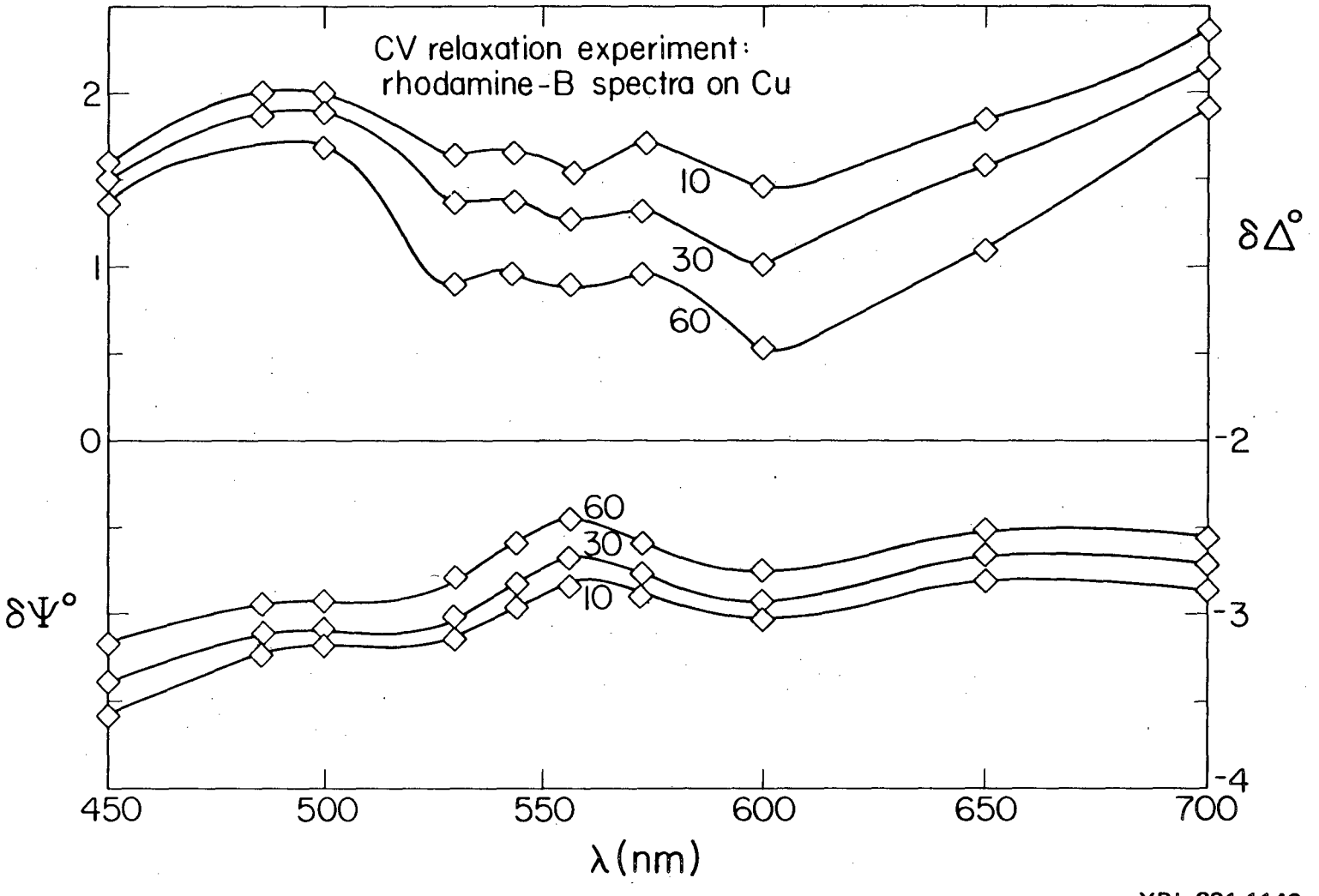

XBL 831-1140

Fig. 14.a

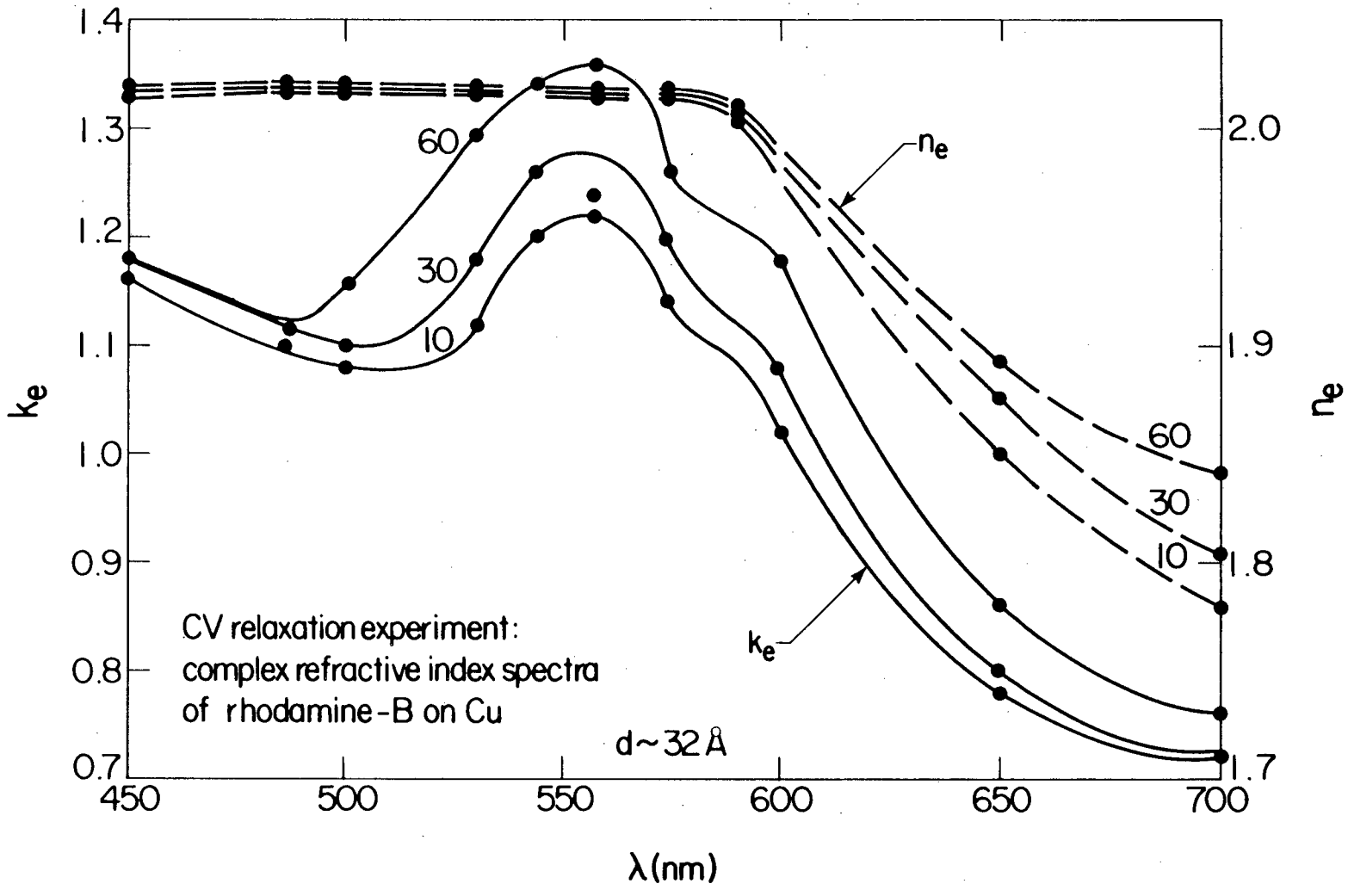

Fig. 14.b

XBL 831-1130

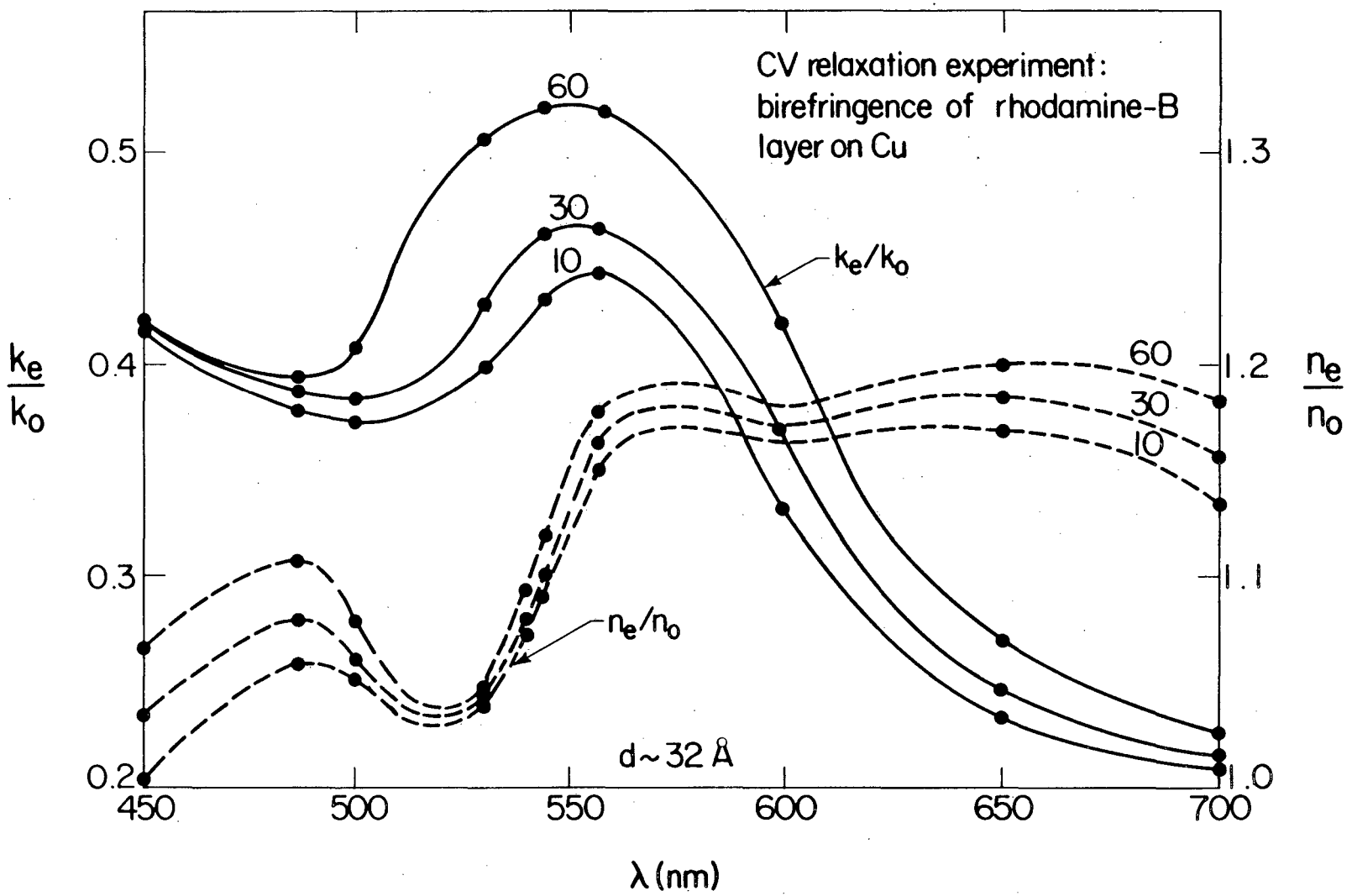

Fig. 14.c

XBL 831-1131

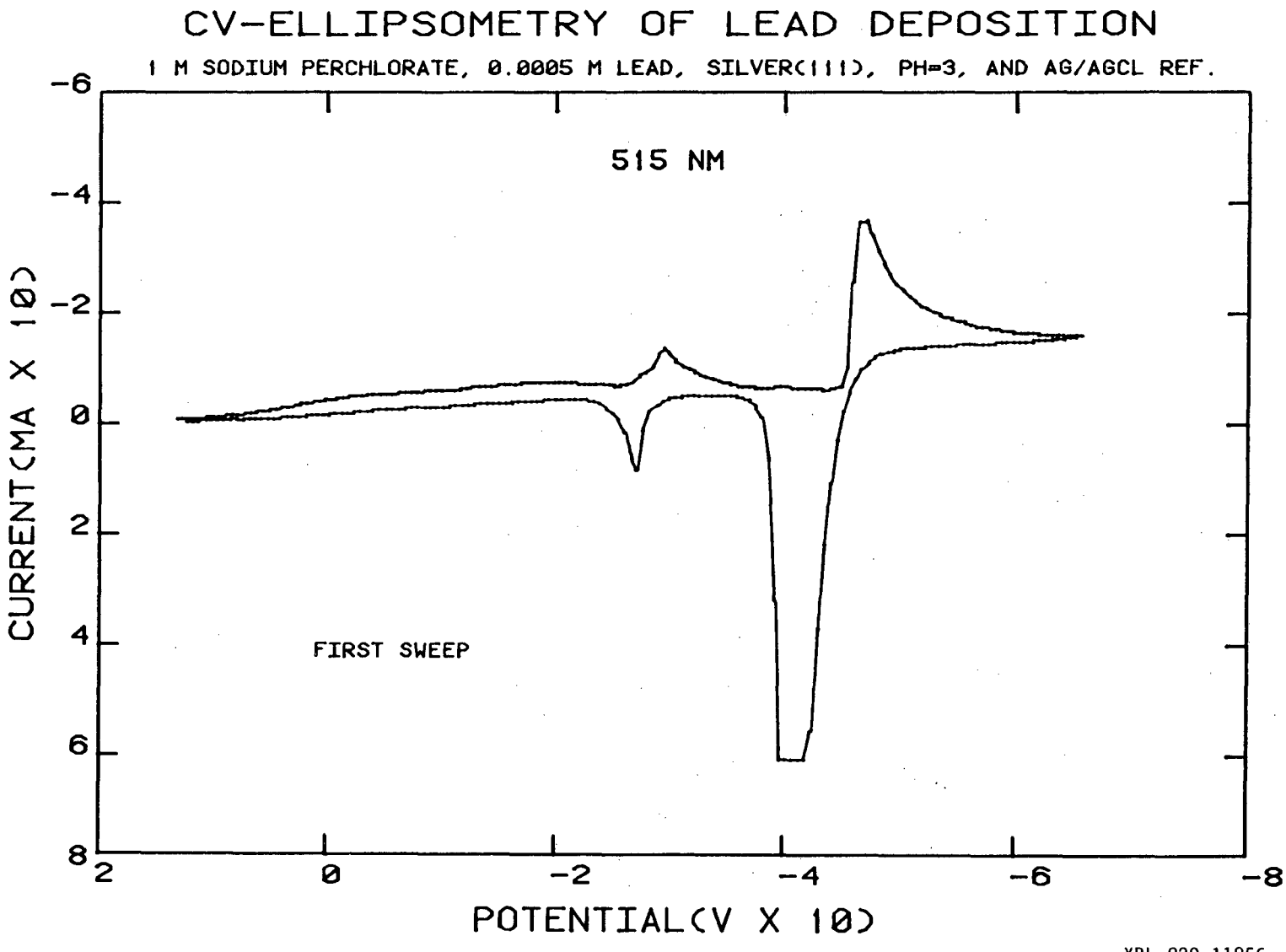

Fig. 15.a

XBL 829-11856

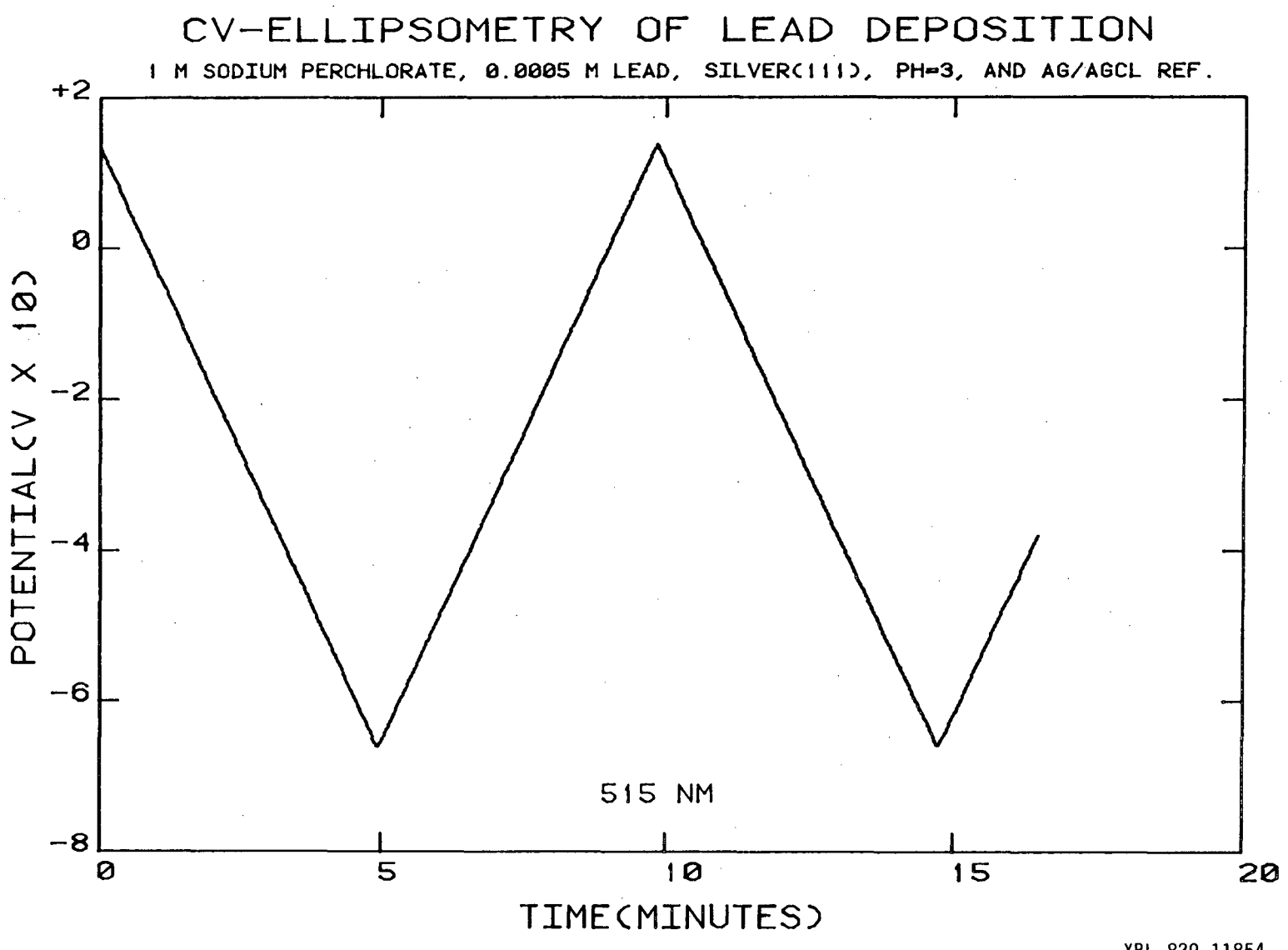

Fig. 15.b

XBL 829-11854

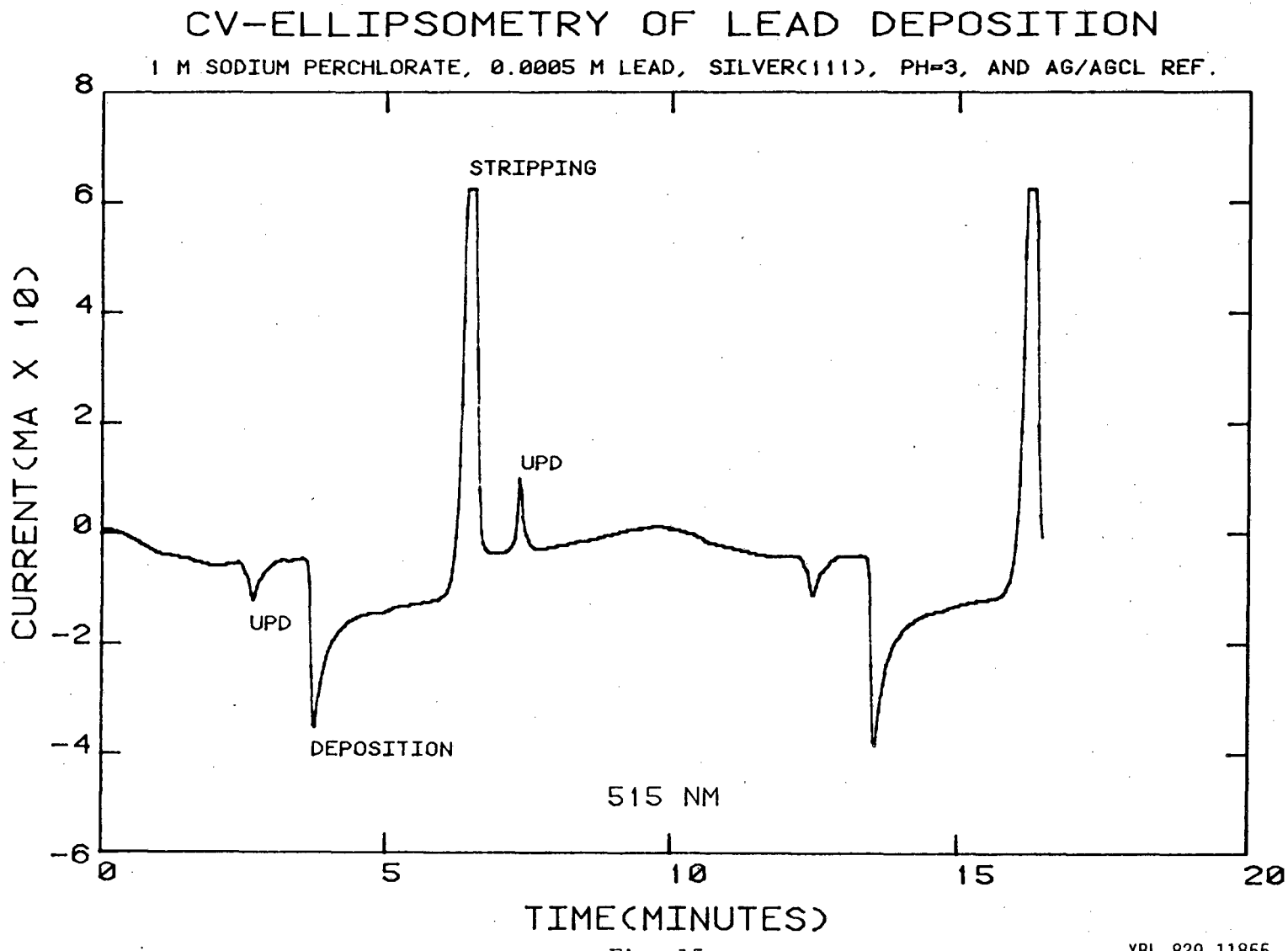

Fig. 15.c

XBL 829-11855

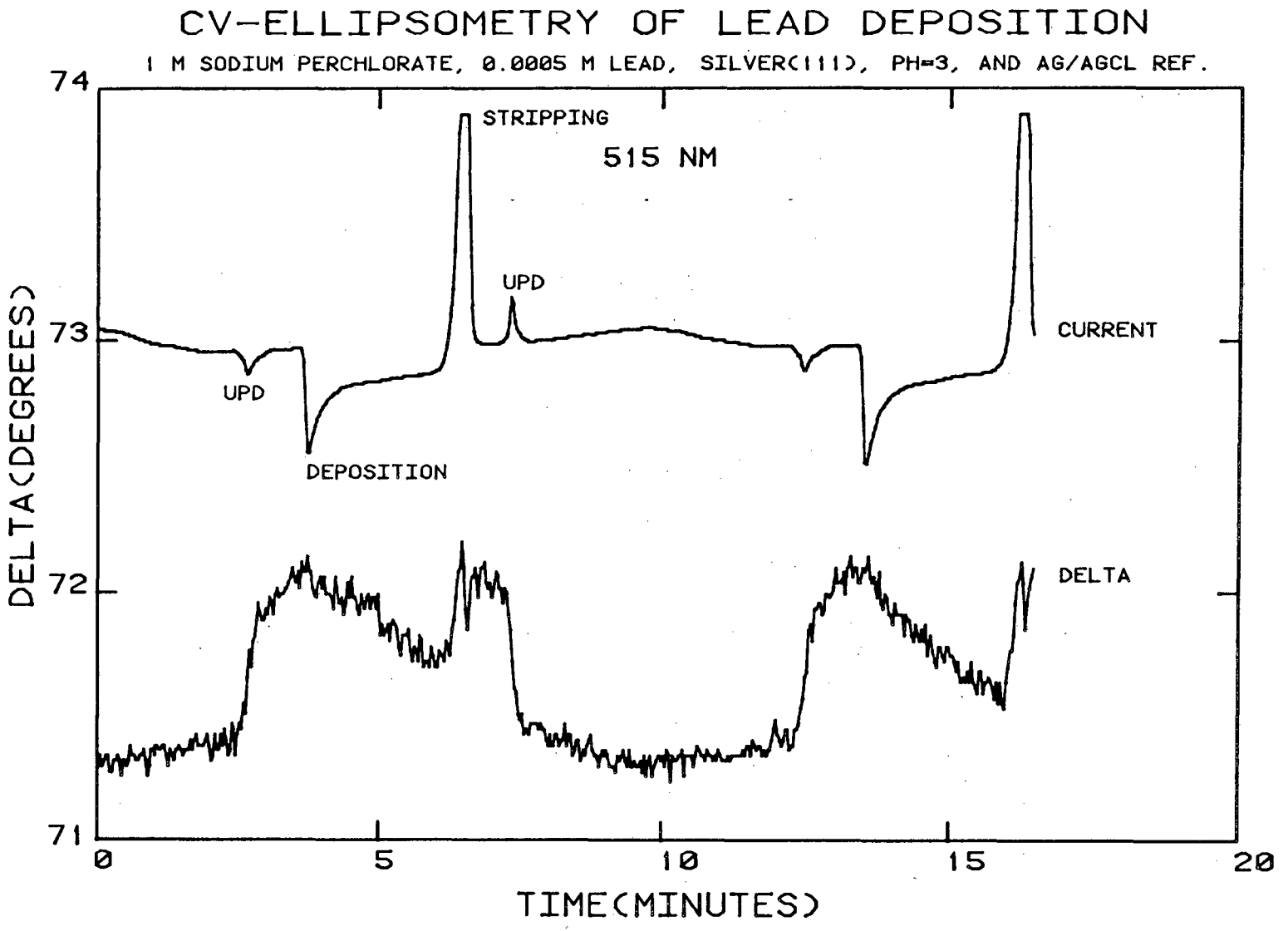

Fig. 15.d

XBL 829-11857

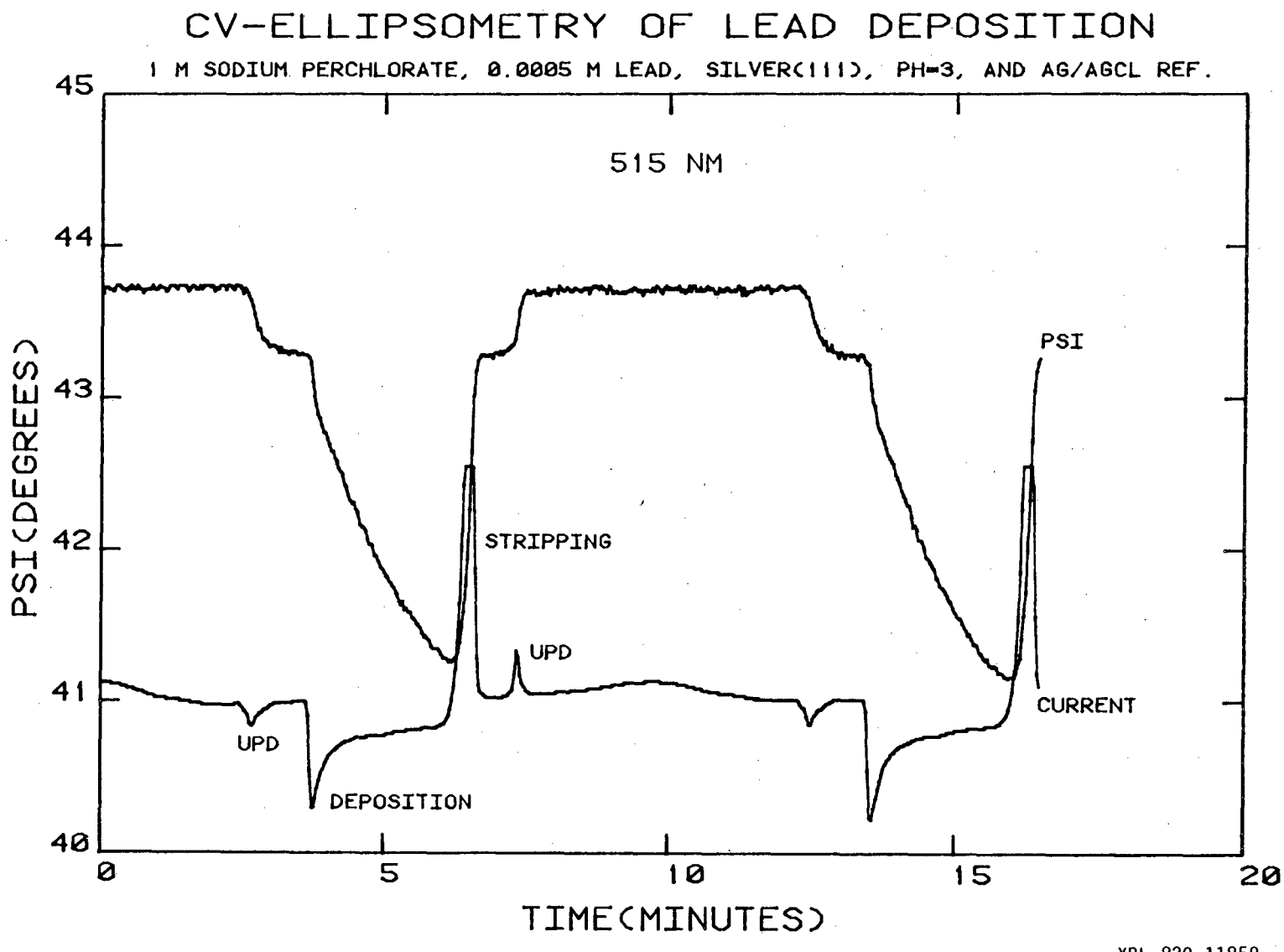

XBL 829-11858

Fig. 15.e

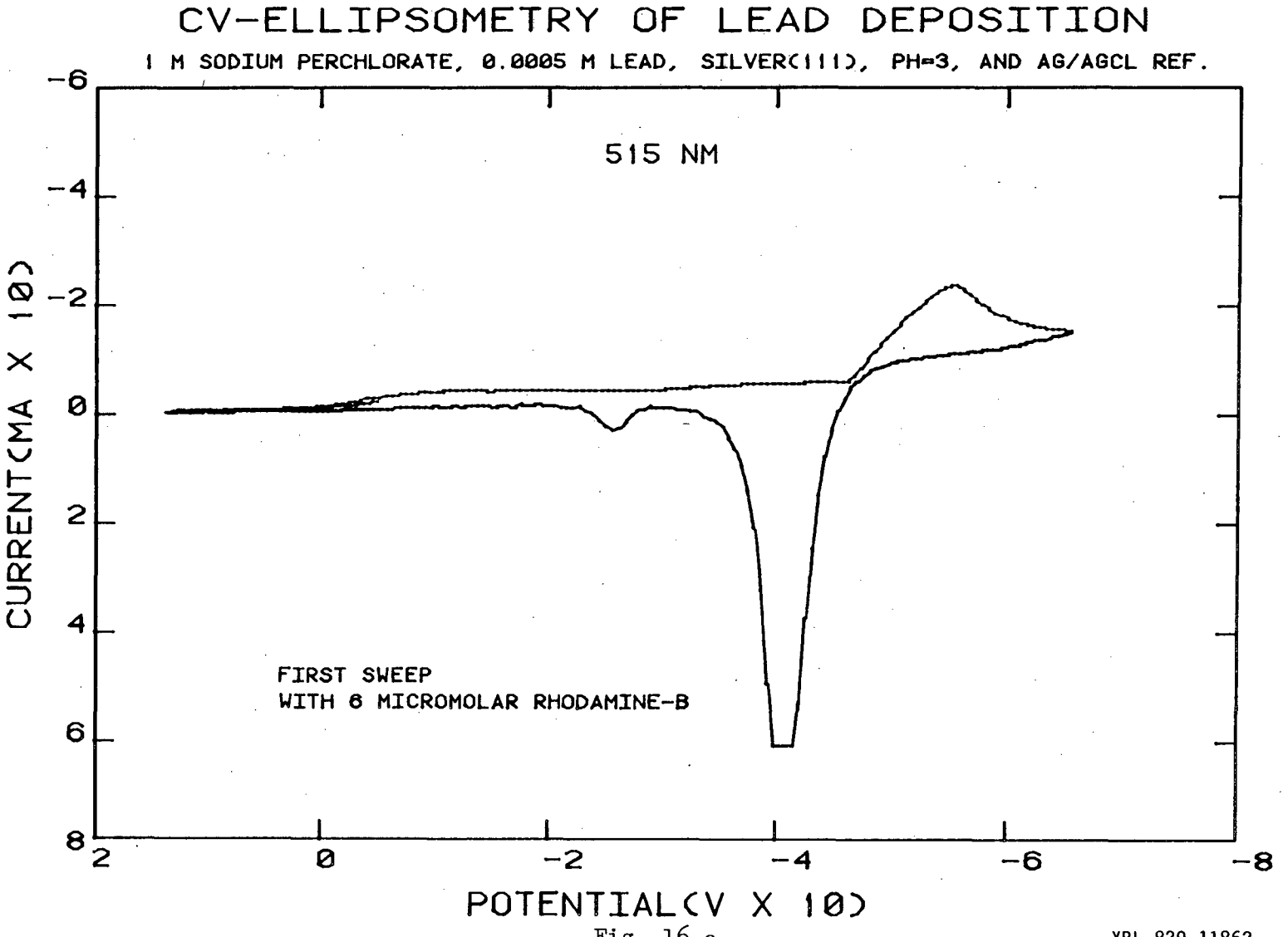

Fig. 16.a

XBL 829-11862

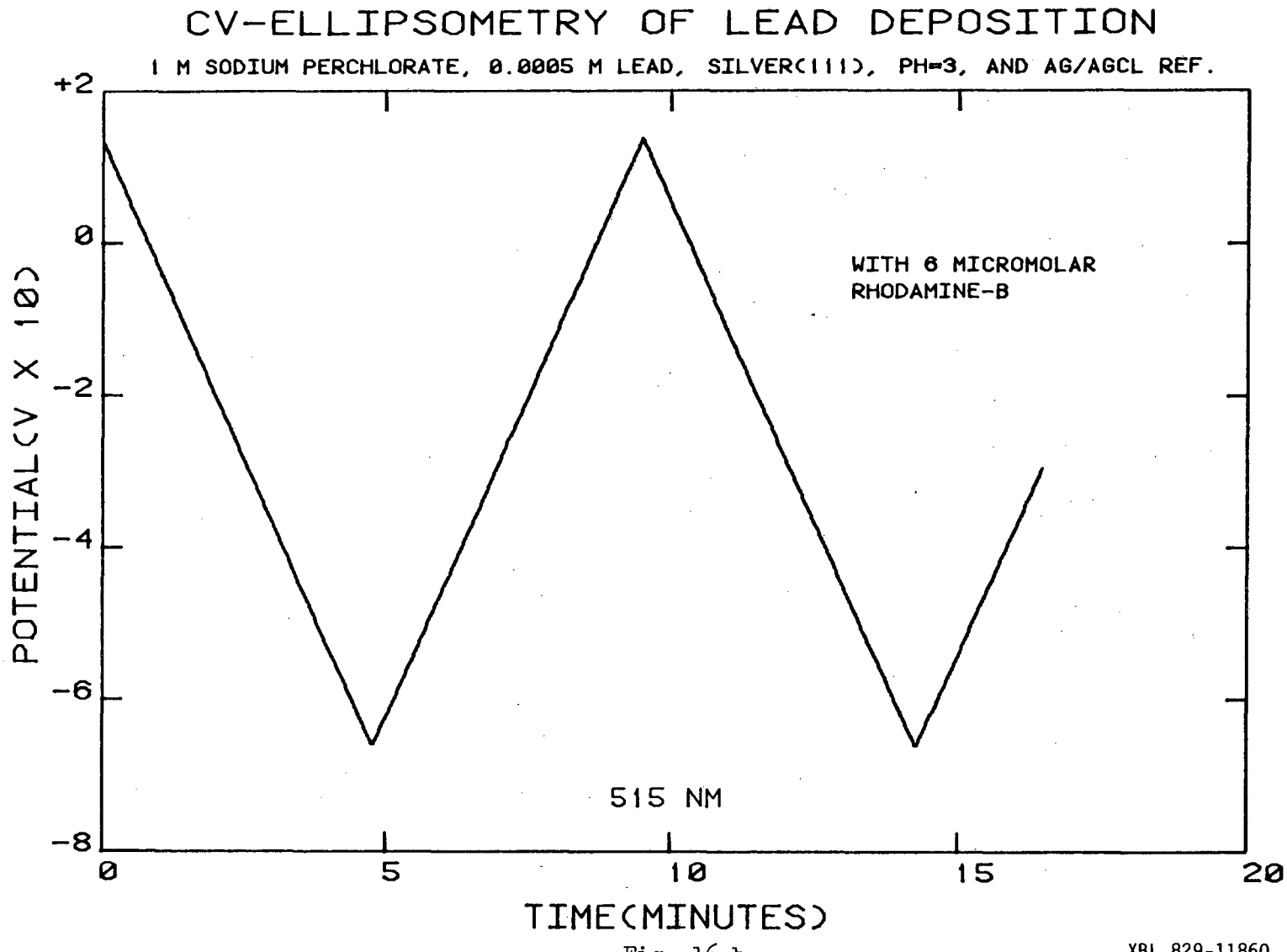

Fig. 16.b

XBL 829-11860

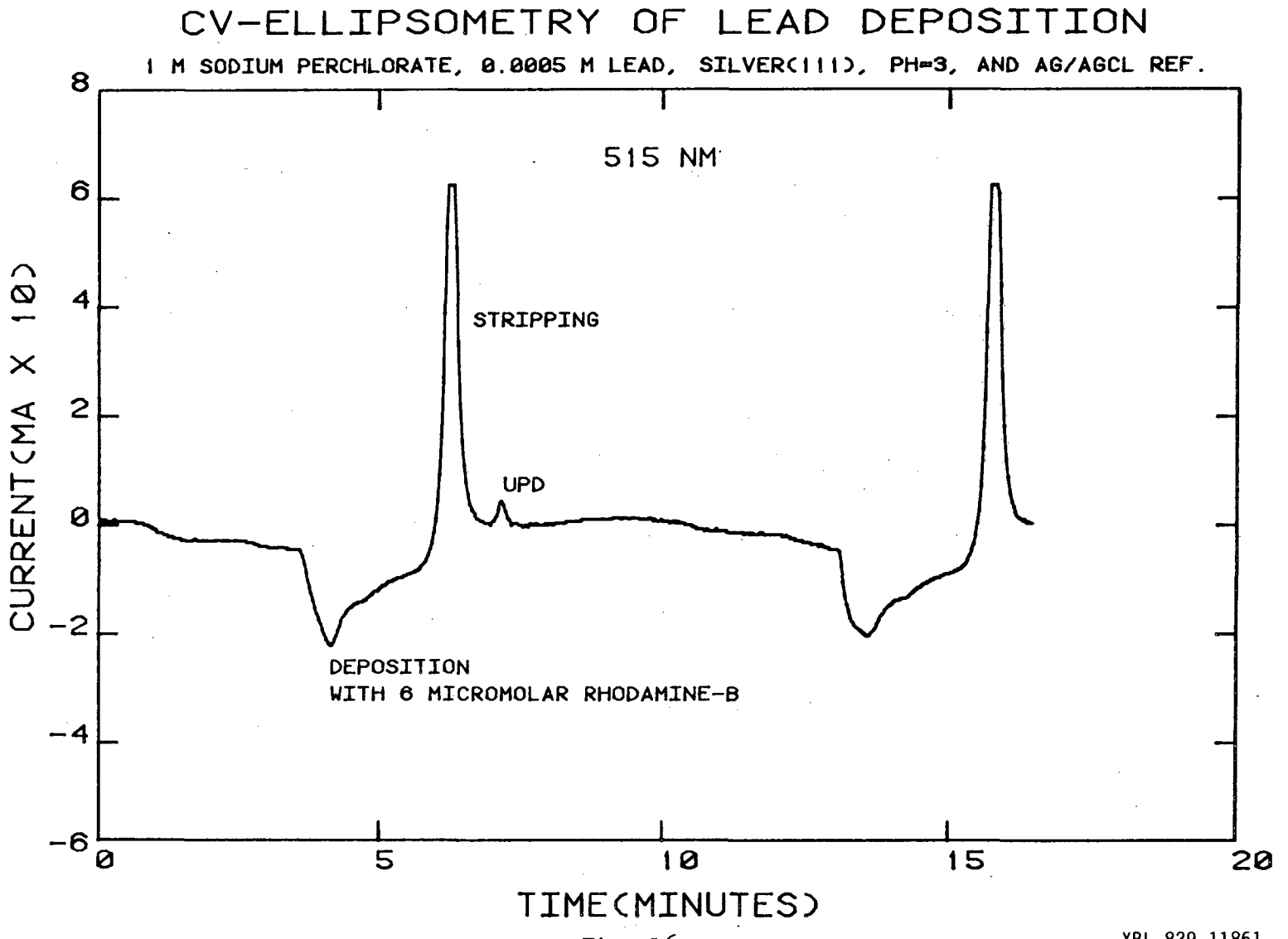

Fig. 16.c

XBL 829-11861

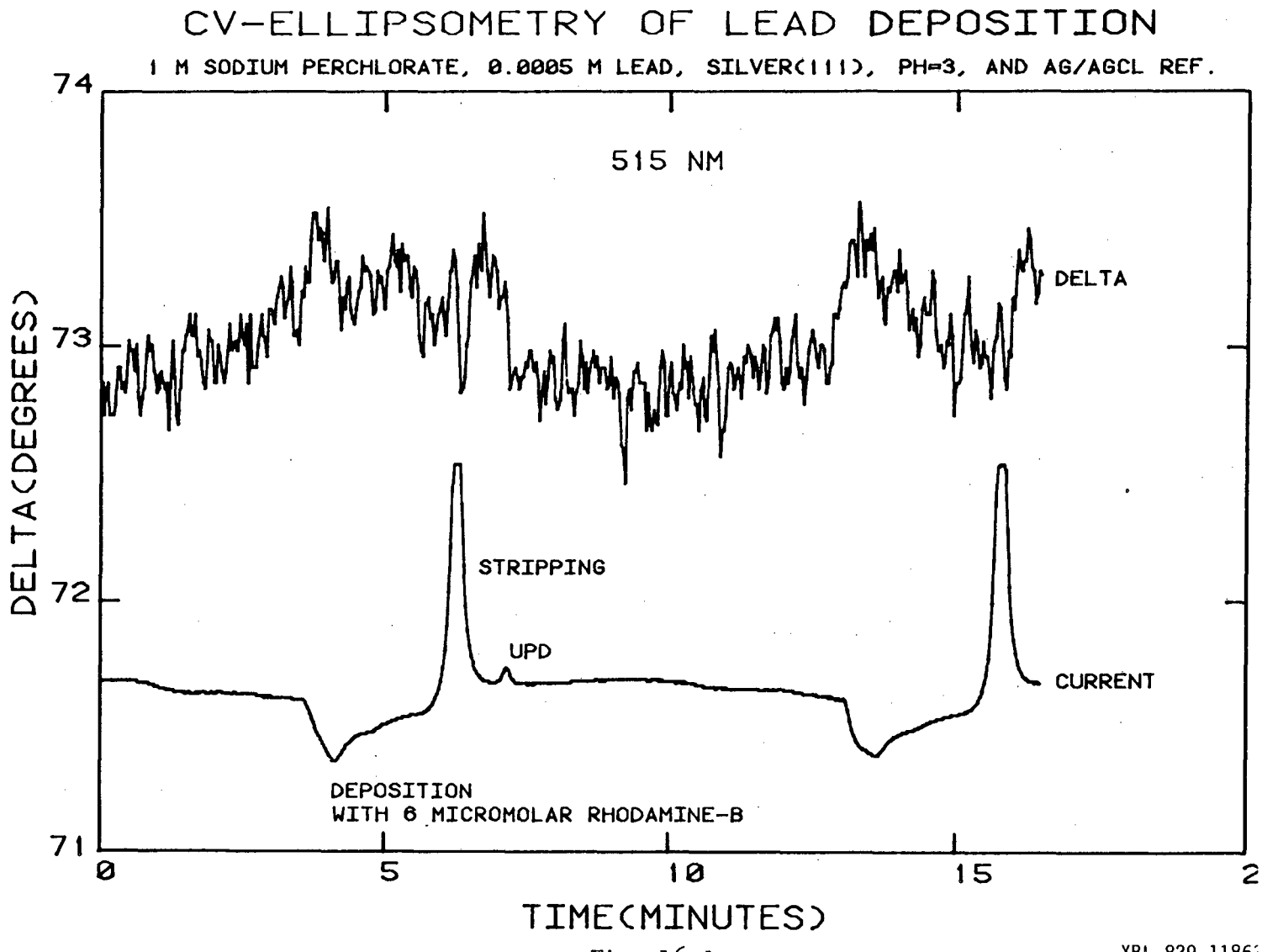

Fig. 16.d

XBL 829-1186

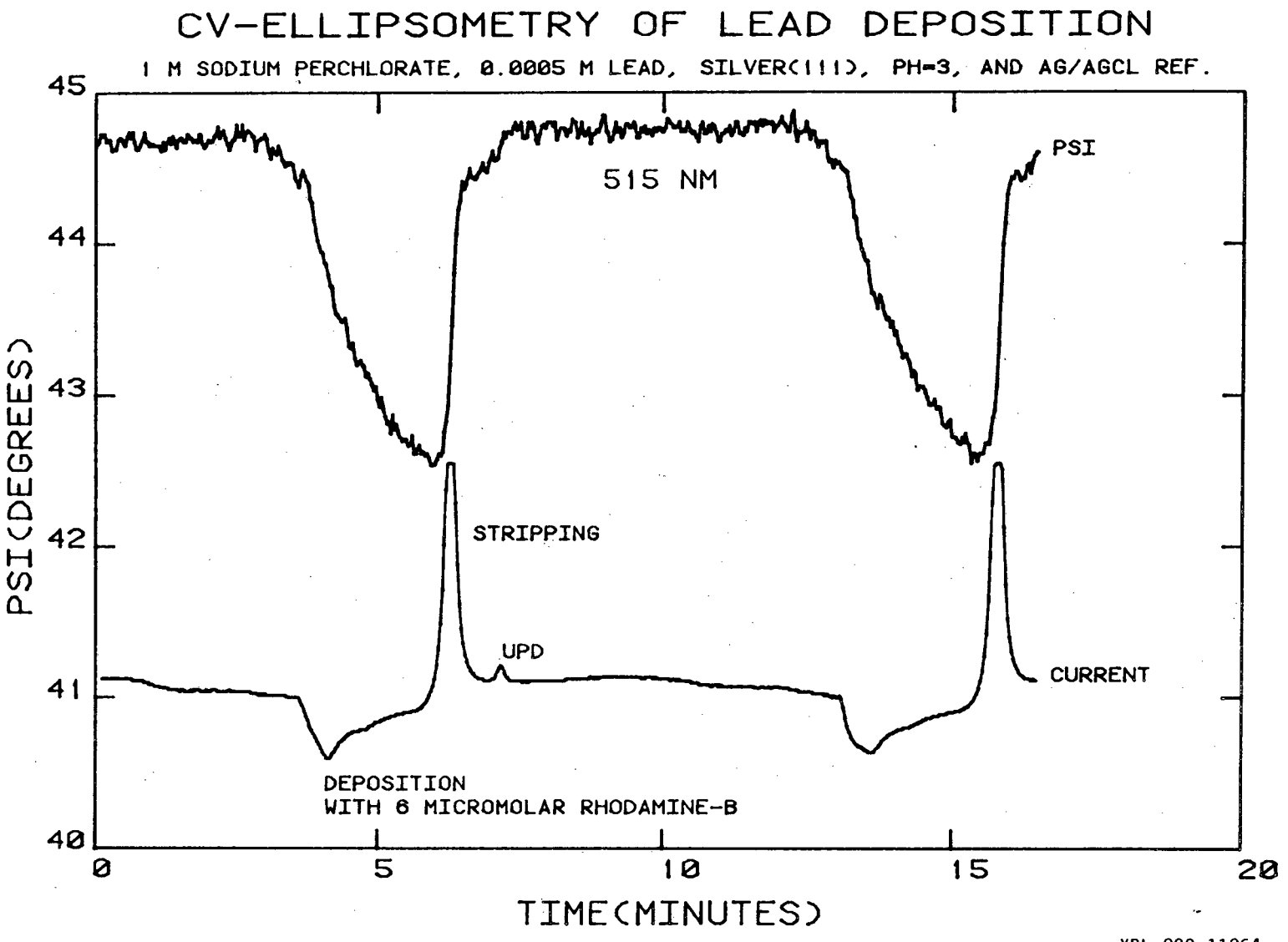

Fig. 16.e

XBL 829-11864

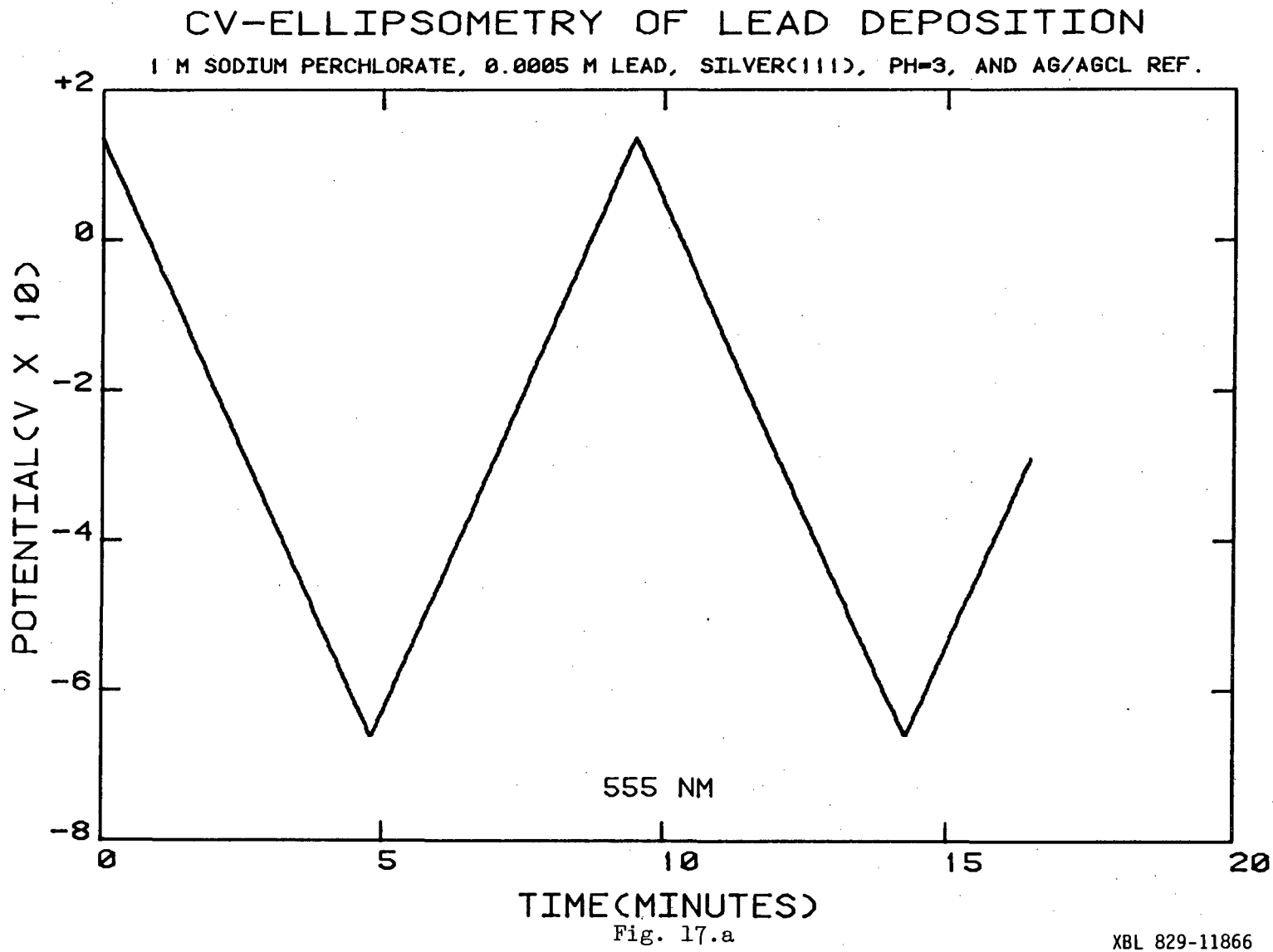

Fig. 17.a

XBL 829-11866

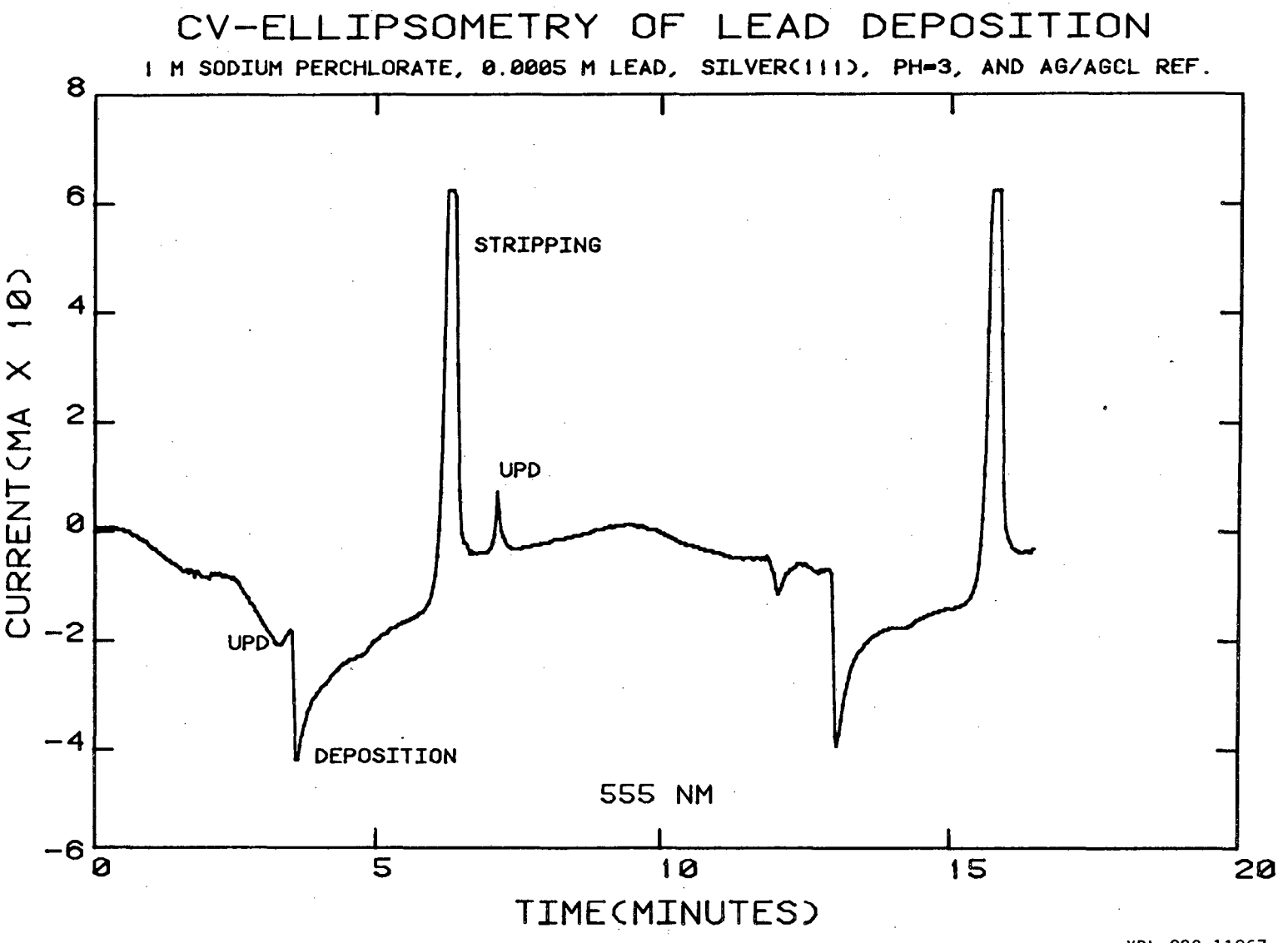

Fig. 17.b

XBL 829-11867

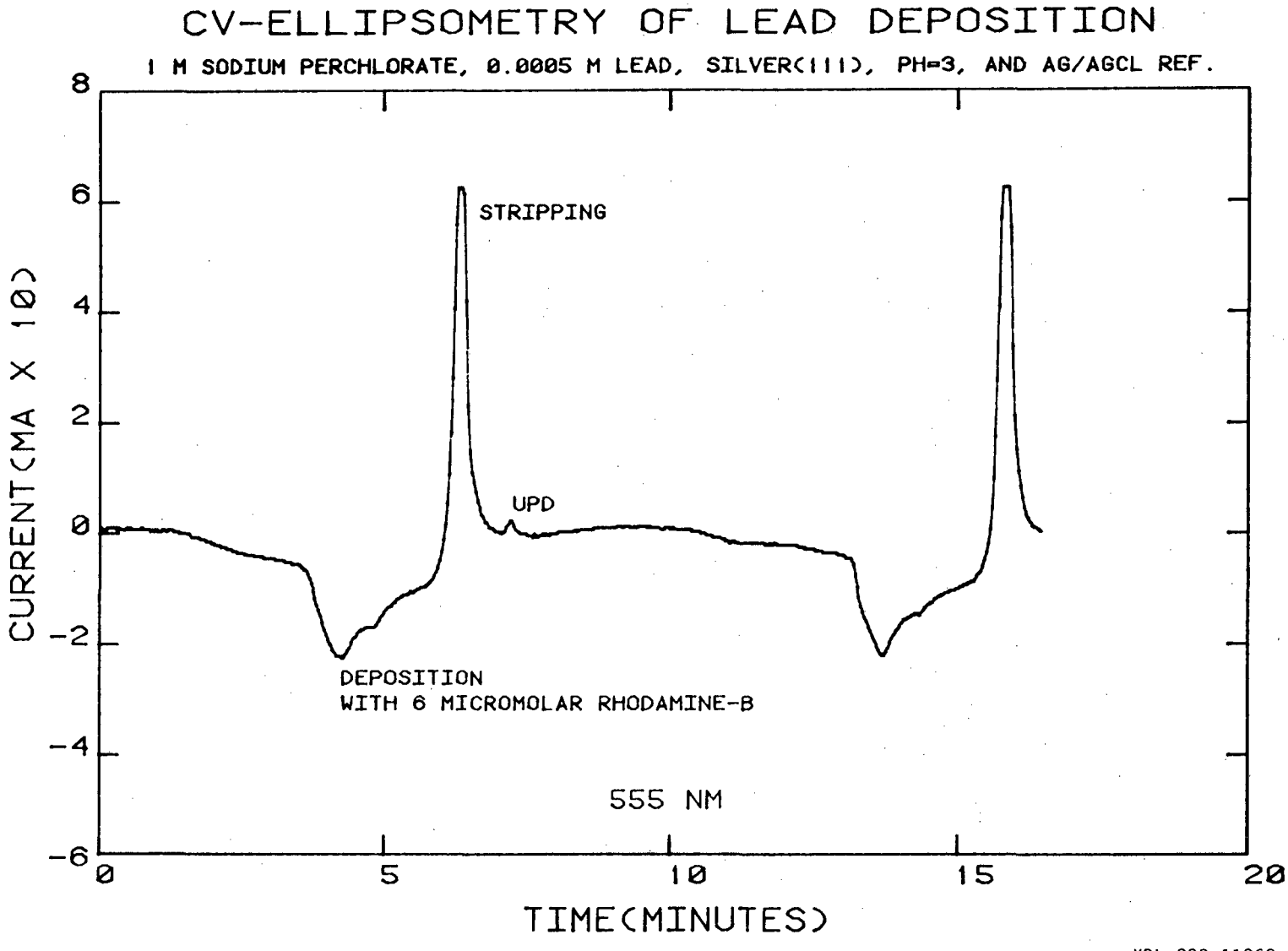

Fig. 17.c

XBL 829-11868

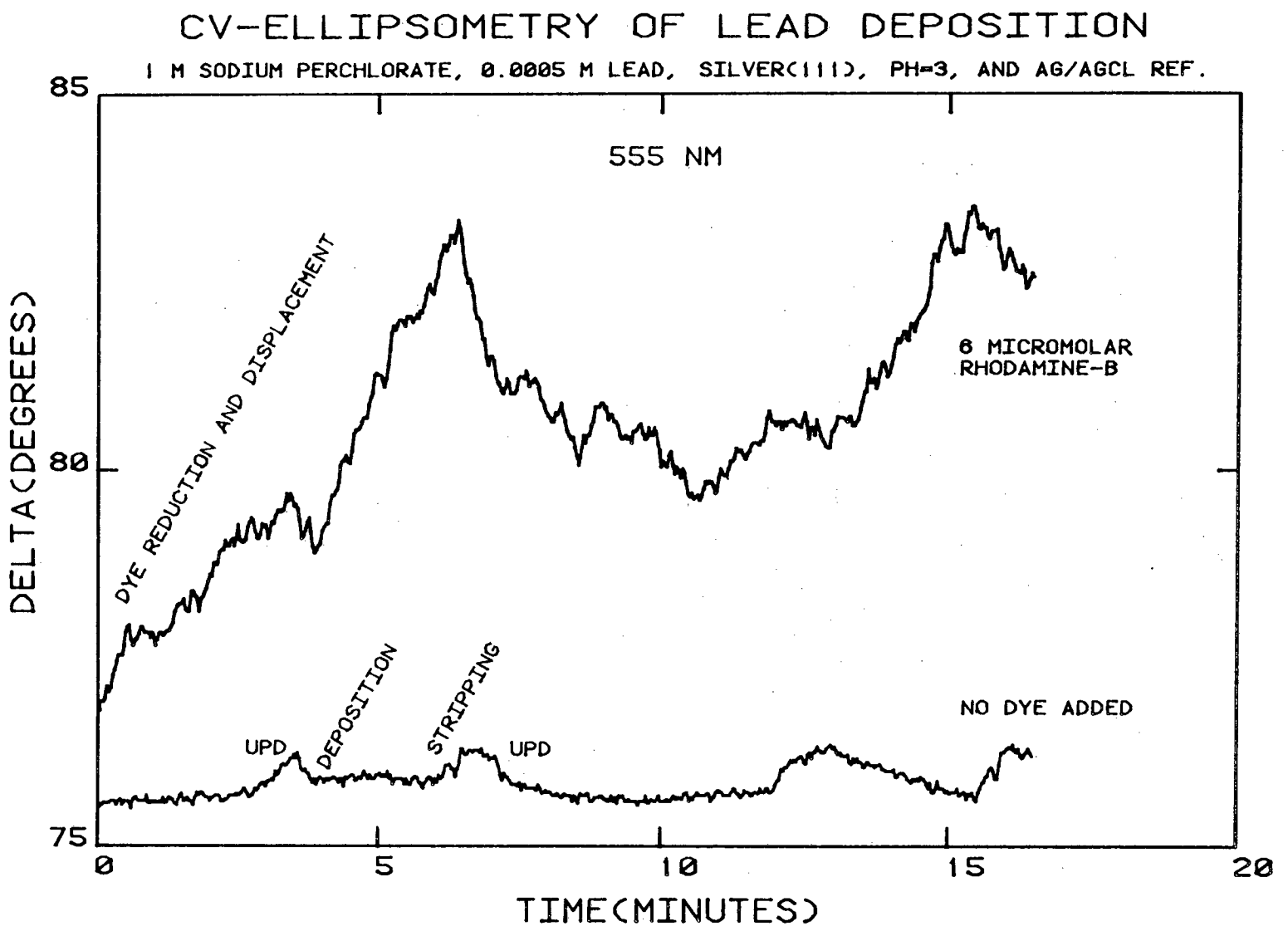

XBL 829-11869

Fig. 17.d

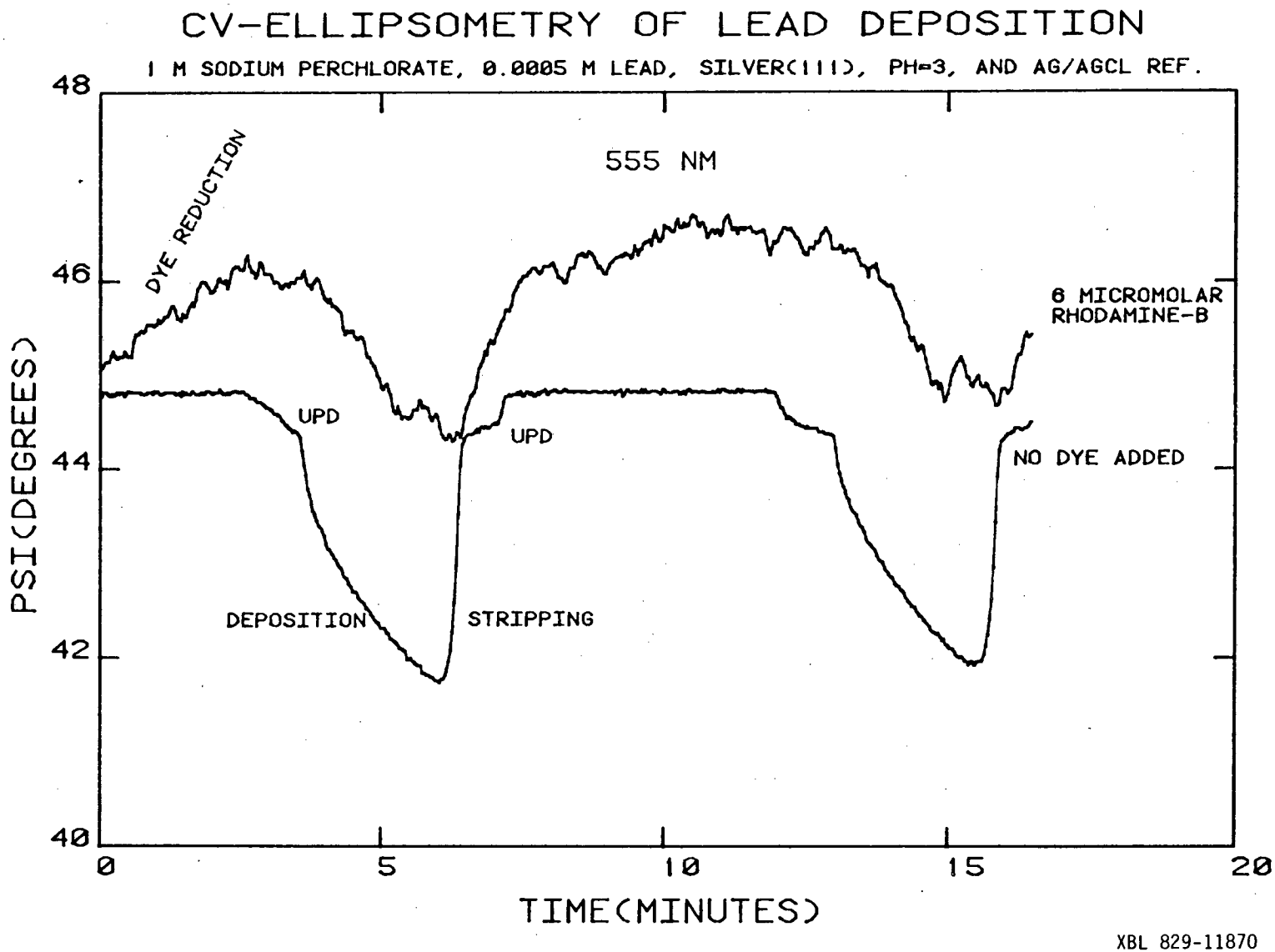

XBL 829-11870

Fig. 17.e

Chapter 7

MODELING FIRST ORDER OPTICAL EFFECTS: DEPOSIT MICROMORPHOLOGY

Abstract

A novel spectroscopic ellipsometer was (1) used in micromorphological determinations of electrochemically formed Pb thin films on Cu substrates. The thin films were deposited potentiostatically (-600 mV vs Ag/AgCl) from an electrolyte consisting of 5 millimolar $Pb(NO_3)_2$ and 1 M $NaClO_4$ at a pH of 3. Based upon deposited charge, the film thicknesses would have been 31, 60, and 110 nm if the deposits had formed uniformly and had been compact. It was found that the deposits were not homogeneous and compact, and multilayer ellipsometer models had to be used to explain spectroscopic ellipsometer measurements of the surfaces.

The best agreement between measurements and model predictions were obtained for a three-layer model. This multilayer model assumed a compact layer of Pb covered the Cu substrate. The compact layer was then covered by a granular, porous layer. Dendritic islands were assumed to exist on top of the second porous layer. A homogeneous, isotropic film model was used to explain the first layer; the optical constants of this layer were assumed to be those of underpotentially deposited (UPD) Pb. The second granular, porous layer had effective optical constants computed by the Bruggeman mixing rule (2); the microinclusions of deposit and/or electrolyte were assumed to be small compared to the wavelength of light. The third layer was composed of large dendritic island

structures, larger than the ellipsometer source wavelength but smaller than the transverse and longitudinal coherence lengths; the coherent superposition of reflection coefficients of bare surface (substrate plus first two layers) and the reflection coefficients of the island covered surface was used to predict the effect of these dendritic structures on ellipsometer responses at various wavelengths (3). This multilayer modeling has allowed determination of the distribution of Pb between compact, granular (porous), and dendritic-island layers.

Multilayer modeling has been applied to explain unusual optical measurements of complicated silver oxide films (4). This approach was different from the modeling of silver oxide films in that measurements were spectroscopic (400 to 700 nm), rather than fixed-wavelength (546.1 nm). It was demonstrated that one can use a single spectral scan of a film covered surface to determine the confidence intervals on model parameters which are independent of wavelength (thickness, porosity, etc.) and can justify the use of more sophisticated optical models on the basis of the greater number of degrees-of-freedom.

Thin film deposits were also made in the presence of a known inhibitor (5), 10 micromolar rhodamine-B, and differences in micromorphology due to the inhibitor measured insitu. Deposits formed with the inhibitor were more compact; optical measurements were easily explained by a simple compact film model.

Introduction

Historically, spectroscopic ellipsometry has been used to determine both the structure and composition of thin films on various surfaces. Aspnes and Theeten have used both light scattering and spectroscopic ellipsometry to determine the microroughness of both fine-grained polycrystalline silicon films and smoother, amorphous silicon films grown by chemical vapor deposition (6). They found that the microroughness, or micromorphology, can be accurately modeled as an equivalent film using either the Bruggeman or Maxwell-Garnett effective media theories. The applicability of the Maxwell-Garnett theory to rough surfaces has also been illustrated by Azzam and Bashara (7). However, in their experiments they varied angle-of-incidence instead of wavelength, and used a diffraction grating as a model rough surface. Muller and Smith have shown that the coherent superposition model, coupled with other formulations like the Maxwell-Garnett equation, can be used in multiple film models to explain unusual optical measurements of anodically formed silver oxide films (8); however, only single, fixed-wavelength measurements were used.

Here, spectroscopic ellipsometry has been used to determine the micromorphology of electrochemically deposited Pb thin films on Cu (9). It has been found that experimental measurements can be best predicted by a multilayer optical model which accounts for deposit porosity and the existence of dendrites on the surface. The evolution of the optical model used in interpretation of these data is discussed here.

Experimental

The spectral range of the spectroscopic ellipsometer extended from 400 nm to 700 nm with a band width of about 10 nm; the angle-of-incidence was fixed at 75 degrees.

The thin films were deposited potentiostatically (-600 mV vs Ag/AgCl) from an electrolyte consisting of 5 millimolar $Pb(NO_3)_2$ and 1 M $NaClO_4$ at a pH of 3. Details regarding the electrochemical cell are given elsewhere (10). For each deposit formed in the absence of inhibitor, an identical deposit was formed with rhodamine-B added to the electrolyte at a 10 micromolar concentration.

The spectroscopic ellipsometer measurements for the potentiostatic deposits are shown in Figs. 1.a through 4.b. In each figure three curves are shown which correspond to the bare Cu surface and Pb deposits formed with and without rhodamine-B (both deposits involving identical quantities of Pb). Fig. 1.a (delta vs wavelength) and Fig. 1.b (psi vs wavelength) are measurements for deposits which would have been 31 nm thick (based upon coulometry) if they had been uniform and compact. One curve in each figure represents a deposit formed with rhodamine-B added to the electrolyte, and shows the optical characteristics of a compact, uniform Pb deposit. Another curve represents a deposit formed in the absence of rhodamine-B; it has unusual optical properties which cannot be interpreted as a compact, uniform layer of Pb. Figs. 2.a and 2.b are comparable to Figs. 1.a and 1.b, except the compact deposit thicknesses (based upon coulometry) would have been 60 nm; here too the deposit formed with rhodamine-B appears compact and the deposit formed without

inhibitor appears nonuniform and noncompact. Figs. 3.a and 3.b contrast spectroscopic measurements for compact deposit thicknesses (based on coulometry) which would have been 110 nm; both deposits appear uniform and compact. Figs. 4.a and 4.b show all spectroscopic measurements of the three compact deposit thicknesses (31, 60, and 110 nm) formed with and without rhodamine-B together; progression of the spectroscopic measurements for Pb deposits formed in the absence of rhodamine-B is evident.

Single Layer Deposit Models

I. Compact Film Model

A simple, isotropic, homogeneous film model (14) was first used to explain the experimental spectroscopic ellipsometer measurements. This model is shown schematically in Fig. 5 and is referred to as the compact film model. This model assumes that the entire Pb deposit can be treated as bulk Pb; there is only one adjustable parameter, the deposit thickness. Figs. 6.a and 6.b (delta vs wavelength and psi vs wavelength, respectively) show spectroscopic simulations for various assumed thicknesses (solid lines labeled 0, 1, 5, 10 nm, etc.) in contrast to experimental measurements (dotted lines for 31, 60, and 110 nm compact thicknesses, no dye added). This model cannot explain the experimental observations; it is inadequate.

II. Effective Media Models

An additional degree of sophistication was incorporated into the optical model of the deposit by taking into consideration porosity. This model is shown schematically in Fig. 5 and referred to as the effective media approximation; it has two adjustable parameters, the deposit thickness and porosity. Either the Maxwell-Garnett or Bruggeman equations can be used as a basis for calculation of the porous deposit apparent optical properties from the properties of Pb and electrolyte; pores are treated as microinclusions of electrolyte in a Pb host medium. Once optical properties are computed, the isotropic homogeneous film model can be used to predict the ellipsometer response to this layer. The most general form of the rule for mixing dielectric properties of a medium is given in Eqn. 1. All symbols are defined in the list of nomenclature at the end of this chapter.

$$\frac{\hat{\varepsilon}-\hat{\varepsilon}_h}{\hat{\varepsilon}+2\hat{\varepsilon}_h} = \sum_{i=1}^{n} \frac{\hat{\varepsilon}_i-\hat{\varepsilon}_h}{\hat{\varepsilon}_i+2\hat{\varepsilon}_h} \qquad (1)$$

Each term in the summation represents a weighted contribution of the molecular polarizability of individual components of the medium. The Bruggeman equation is a special case of this general mixing rule; the host medium is assumed to be the same as the effective medium. This approach is different from the Maxwell-Garnett equation where the host medium is assumed to be the component present in the largest amount, and the Lorentz-Lorentz equation where the host medium is assumed to be vacuum. Both the Maxwell-Garnett and Lorentz-Lorentz equations lack

self-consistency over the complete range of volume fractions.

The porous deposit is a binary mixture of Pb and electrolyte, and the Bruggeman equation becomes a complex quadratic; the solution is given by Eqns. 2.a through 2.c.

$$\hat{\varepsilon}_f = \frac{1}{2}\left[-\hat{A} \pm (\hat{A}^2 - 4\hat{B})^{1/2}\right] \tag{2.a}$$

$$\hat{A} = \frac{1}{2}\left[\hat{\varepsilon}_{Pb}(1-3\theta_{Pb}) + \hat{\varepsilon}_{soln}(3\theta_{Pb}-2)\right] \tag{2.b}$$

$$\hat{B} = -\frac{1}{2}\left[\hat{\varepsilon}_{Pb}\,\hat{\varepsilon}_{soln}\right] \tag{2.c}$$

The complex refractive index is then calculated with Eqn. 2.d

$$\hat{n}_f = \hat{\varepsilon}_f^{\,1/2} \tag{2.d}$$

These equations for the two-component system are considerably easier to solve than those for the more general multicomponent case. For "n" components one would have to find the roots to an "n-th" degree complex polynomial, whereas for two components one uses the quadratic formula and selects the root having the greatest modulus (11). Pore dimensions are assumed to be smaller than the wavelength of reflected light.

Simulated spectroscopic ellipsometer measurements for this deposit model are shown in Figs. 7.a (delta vs wavelength) and 7.b (psi vs wavelength). The simulations in these figures are of a 31 nm thick, compact Pb deposit (based upon coulometric measurements) redistributed on a Cu substrate as deposits of various porosities. Porous deposit thicknesses are consistent with the coulometric measurement and assumed porosities. Simulations are represented as solid lines and experimental measurements are represented by dotted lines. From these simulations it is evident that this simple two parameter model is inadequate to explain experimental observations.

III. Coherent Superposition Model

The coherent superposition model assumes that the Cu surface is partially bare and partially covered with Pb islands (Fig. 5). Reflection coefficients are computed for both the bare and film covered surface (12). Then, provided that the dimensions of the islands are less than both the transverse and longitudinal coherence length of the ellipsometer source (13), overall reflection coefficients for both the "s" and "p" polarizations can be calculated by taking the weighted average of the reflection coefficients for the bare and film-covered surfaces (Eqn. 3).

$$r_\nu = \theta_f \, r_{\nu,f} + (1-\theta_f) r_{\nu,s} \qquad (3)$$

For the spectroscopic ellipsometer, the longitudinal coherence length ranges from 16 microns at 400 nm to 49 microns at 700 nm (12); the transverse (lateral) coherence ranges from 10 microns at 400 nm to 17 microns at 700 nm (13). These estimates assume (conservatively) a bandwidth twice that of the source (20 nm). From complementary SEM studies the dimensions of the dendritic islands have been found to be less than 15 microns, so the coherent superposition model is applicable. Details of the coherence length calculations are given in Chapter 2.

Spectroscopic simulations of a 31 nm thick, uniform, compact Pb deposit (based upon coulometric measurements) redistributed on a Cu substrate as compact islands are shown in Figs. 8.a (delta vs wavelength) and 8.b (psi vs wavelength); simulations of 60 and 110 nm thick deposits are shown in Figs. 9.(a & b) and 10.(a & b), respectively. The island model used for these simulations has two adjustable parameters, fractional surface coverage and island thickness. Island thicknesses are consistent with both the coulometric measurements and assumed fractional surface coverages (by islands). This model is incapable of explaining the experimental measurements.

Dendritic Pb structures on the electrode (observed by SEM) inspired the development of the island model. At first islands were assumed to be compact. After failure of the compact island model variations were considered. Next, the islands were assumed to have some effective size and porosity, since the dendrites are not actually compact structures. This model has three adjustable parameters, island porosity, fractional surface coverage, and island thickness. Optical constants of the

islands were computed by the methods described in the preceding section, "the effective media approximation. Simulations for the 31 nm thick compact deposit (comparable to Figs. 8.a and 8.b) assuming that the islands are 20% porous are shown in Figs. 11.a and 11.b, respectively; island porosities of 30% (Figs. 11.c and 11.d) and 40% (Figs. 11.e and 11.f) were also assumed. Similar calculations for the 60 nm thick compact deposit are shown in Figs. 12.a through 12.f. This model was also incapable of explaining the experimental measurements.

Since the dendrites are crystals with a particular orientation on the surface they are probably anisotropic; an anisotropic island model was considered, but it had too many adjustable parameters (six) and the physical meaning of these parameters was vague.

Multilayer Models

I. Description

(1) First Layer

The first layer was assumed to be compact Pb. An isotropic, homogeneous film model was used to predict the ellipsometer response to this layer, which was given the optical constants of the UPD Pb layer (usually). Apparent substrate optical constants were computed for the Pb covered Cu surface, and were used as the substrate optical constants for the second layer. Note that in some calculations the first layer was assumed to be much thicker than the UPD and was given the optical properties of bulk Pb. Interpretation of this layer as a compact monolayer

was consistent with the ellipsometry and light scattering measurements made during cyclic voltammetry; these experiments are discussed in Chapter 5.

(2) Second Layer

Optical constants of the second layer, assumed to be a granular, porous deposit, were computed from the properties of Pb and electrolyte; optical constants of the porous deposit were calculated by the methods discussed in the preceding section entitled "the effective media approximation." Once the porous deposit optical constants were calculated, the isotropic homogeneous film model was used to predict the ellipsometer response to this layer. Apparent substrate substrate optical constants were then calculated for the Cu surface covered by the first and second layers. Recall that incorporation of this layer into the optical model was motivated by the light scattering experiments discussed in Chapter 5.

(3) Third Layer

The third layer was assumed to be composed of dendritic Pb islands. Reflection coefficients were computed for areas covered with only the first two layers (discussed above) and areas covered by an additional layer of Pb deposit (dendritic islands). Overall reflection coefficients for the entire surface were calculated by coherent superposition of the reflection coefficients for both areas. The total Pb involved in the three layers was consistent with the coulometric measurements; the three-layer model alters the distribution of the Pb on the surface, but

does not alter the quantity. Incorporation of this layer into the optical model was motivated by the scanning electron micrographs presented in Chapter 9.

II. Results of Early Three-layer Model Simulations

A first attempt at improving the agreement between simulations and spectroscopic measurements (31 nm case) by using multilayer modeling are shown in Figs. 13.a (delta vs wavelength) and 13.b (psi vs wavelength). Simulations are represented as solid lines and experimental data are represented as dotted lines. Curves are labeled as (1), (1+2), and (1+2+3); these designate collective responses to the first layer, the first and second layers, and all three layers, respectively. The first layer was assumed to be compact and 10 nm thick; the second layer was assumed to be 20 nm thick with a porosity of either 60% (A) or 80% (B); the dendritic Pb islands were also assumed to be porous. Simulations like those shown in Figs. 13.a and 13.b are shown in Figs. 13.c and 13.d, respectively, except the second layer is assumed to be 40 nm thick and either 80% (A) or 90% (B) porous. None of these simulations agreed with spectroscopic measurements over the full spectral range; however, the agreement was better than could be achieved with a single layer model (either compact film, effective media, or coherent superposition). This simulation demonstrated the ellipsometer responds primarily to the first two deposited layers, even with as much as 2/3 of the deposited Pb distributed as islands (since the islands cover only between 5 to 10% of the surface).

III. Strategy for Using Spectroscopic Simulators

Spectroscopic simulations presented in this chapter were all generated with programs discussed in detail in Chapter 3. One first had to have knowledge of the refractive indices of interest (Pb, Cu, and electrolyte). The refractive indices of Pb and Cu were determined experimentally with the spectroscopic ellipsometer; polarizer and analyzer Faraday cell currents were measured as a function of wavelength using program SEV002; these measurements were then converted to polarizer and analyzer azimuths and to delta and psi by DSCONV; the complex refractive index as a function of wavelength was calculated from the output file of DSCONV using RISURF. Electrolyte optical constants were either measured by a refractometer or found in the literature and used to synthesize a data file of identical format to that generated by RISURF. These "refractive index spectra" were then read by either CSMSES (Coherent Superposition Spectroscopic Ellipsometer Simulator), EMASES (Effective Media Approximation Spectroscopic Ellipsometer Simulator), or BRGMAN (Bruggeman Model Calculation). CSMSES was based on the coherent superposition of reflection coefficients, EMASES was based upon the Maxwell-Garnett theory, and BRUGMN was based upon the Bruggeman theory for a binary system. The strategy for multilayer simulations was to sequentially operate on a single data file with RISURF and one of the simulators (CSMSES, EMASES, etc.). For example, the sequence of operations (after calculation of the substrate refractive index calculation) for the three-layer model would be:

1. Calculate delta and psi over spectral range for the compact deposit using BRUGMN. Required inputs are spectroscopic refractive index data files for the substrate, deposit, and electrolyte; deposit thickness and porosity are entered from the LSI-11 control consol keyboard. Zero porosity is assumed for the first layer.

2. Calculate a new apparent spectroscopic refractive index data file for the substrate using RISURF. RISURF reads the data file created in step 1 by BRUGMN.

3. Repeat step 1 using the new apparent substate optical properties generated in step 2; the porosity and thickness of the second layer are entered instead of those of the first layer.

4. Repeat step 2.

5. Calculate delta and psi over the spectral range using CSMSES for the layer composed of islands. The spectroscopic refractive index data file generated in step 4 is used for the substrate. If porous islands are to be simulated, corresponding spectroscopic refractive index data for the islands can be generated prior to step 5 using BRUGMN.

IV. Optimization of the Three-layer Model

Figs. 14.a (delta vs wavelength) and 14.b (psi vs wavelength) compare the several spectroscopic simulations that were used in attempts match the experimental measurements. The best qualitative agreement was obtained with the three-layer model; consequently, this model was chosen for optimization. As discussed in the preceding section, the

ellipsometer was not very sensitive to the large dendritic islands, even though they contained most of the deposited Pb and were the most striking features in scanning electron microphotographs (Chapter 9). Optimization of the adjustable parameters for all three layers resulted in a greater variance for each parameter than when only two layers were assumed. Therefore, the strategy used assumed that the third layer had an insignificant optical effect; it was ignored in model calculations and only the parameters required to specify the first two layers were optimized. All deposited Pb not accounted for in the first two layers after optimization was assumed to be distributed in the large dendritic islands (which have little effect on the ellipsometer response). This approach is referred to as the "two-layer simplification of a three-layer model."

Results of the optimization are shown in figures 15.a (delta vs wavelength) and 15.b (psi vs wavelength). The solid lines represent experimental measurements and the circles represent points calculated by the optimization routine WLGOGO which is described in Chapter 3. Nearly perfect agreement was obtained by optimization of the thickness and porosity of the second layer, which are wavelength-independent adjustable parameters. Table I summarizes the results of the optimization. Measured and calculated values of delta and psi at particular wavelengths are tabulated for three compact, uniform, film thicknesses (based upon coulometric measurements); these thicknesses are 31, 60 and 110 nm respectively. Only spectroscopic measurements for deposits formed in the absence of rhodamine-B were interpreted by this optimiza-

tion since deposits formed with rhodamine-B were easily explained by the simple compact film model (a limiting case of the model considered here). Table I also gives the values of the sum-of-squares error, the thickness and porosity of the second layer (bulk deposit), and corresponding parameter variances (in parenthesis). The optical constants and thickness of the first layer are values corresponding to the underpotential deposit discussed in Chapter 5. Note that the three sets of experimental spectroscopic ellipsometer measurements can be explained by second layer thicknesses and porosities of 31 nm and 41 percent; 50 nm and 22 percent; and 87 nm and 3 percent.

V. Calculation of Parameters and Variances

By minimizing the sum-of-squares error between the model predictions and measured values of delta and psi over the entire spectral range, the optimum values of the wavelength-independent adjustable parameters (thickness and porosity) were determined. This was done with the optimization routine called WLGOGO which optimized the objective subroutine ERROR. Subroutine ERROR calculated values of delta and psi at trial values of the adjustable parameters; the sum-of-squares error between the calculated and measured values of delta and psi was also computed. Subroutines directly involved in the calculation of delta and psi were EMA, FILM, CSFILM, and REFIND, and were called by ERROR. Both simplex and univariate search routines have been used and give the same results. Only the univariate search algorithm is given here. The simplex program is confidential Union Carbide software and was obtained while the author was employed at Union Carbide.

Eqn. 4 defines the sum-of-squares error for the model; the parameter variance is defined by Eqn. 5.

$$S = \sum_{i=1}^{n} [(\Delta_{C,i}-\Delta_{M,i})^2 + (\Psi_{C,i}-\Psi_{M,i})^2]^{1/2} \tag{4}$$

$$SE(p) = \frac{\sigma^2}{\frac{1}{2}\frac{\partial^s S}{\partial p^2}} \tag{5}$$

Parameter confidence intervals (Eqn. 6) were calculated from this variance and the student-t statistic for "2N-P" degrees of freedom, where "N" is the number of delta-psi measurements over the spectral range (from a single spectroscopic measurement) and "P" is the number of adjustable parameters. Wavelengths were spaced at intervals greater than the source bandwidth; measurements at each wavelength were treated as independent observations of the surface.

$$\delta(p) = t(2N-P,\ 1-2\alpha)[SE(p)]^{1/2} \tag{6}$$

Values of both the numerator and denominator of Eqn. 5 were required and were estimated numerically with Eqns. 7 and 8, respectively.

$$\sigma^2 = S_{MIN}/df = S_{MIN}/(2N-P) \tag{7}$$

$$\frac{1}{2}\frac{\partial^2 S}{\partial p^2} \sim \frac{S_{(+)} + S_{(-)} - 2S_{MIN}}{2(\Delta p)^2} \qquad (8)$$

Conclusions

Spectroscopic ellipsometry allows one to calculate confidence intervals of wavelength-independent parameters for micromorphological optical models since spectroscopic measurements have much greater information content. Measurements over a broad spectral range can be made much more rapidly than measurements at different angles-of-incidence, intended to give the same advantage. The advantage of angle-of-incidence modulation over spectroscopic ellipsometry lies in one's ability to also optimize complex refractive indices (wavelength dependent); however, the refractive indices can only be optimized at one wavelength; furthermore, one usually has knowledge of refractive indices so this advantage is unimportant.

Pb deposits of three different thicknesses were formed electrolytically. If the deposits had been uniform and compact the thicknesses would have been 31 nm, 60 nm, and 110 nm based upon coulometric measurements. However, it was found that the deposits were non-ideal and that multilayer ellipsometer models had to be used to explain spectroscopic measurements (consistent with the charge balances). Single-layer compact, porous, and island film models were inadequate when used separately, but were successful when used in combination.

The best agreement between measurements and model predictions was obtained for a three-layer model which assumed a compact Pb layer

covered the Cu substrate, which was covered by a porous Pb layer. Dendritic islands were assumed to exist on the porous layer. A simple film model was used to explain the first layer covering the Cu surface; the optical constants of this layer were assumed to be those of bulk Pb. The second porous layer had effective optical constants computed by the Bruggeman mixing rule (2); the microinclusions of deposit and/or electrolyte were assumed to be small compared to the wavelength of light. The third layer was composed of large dendritic island structures, larger than the ellipsometer source wavelength but smaller than the transverse and longitudinal coherence lengths; the coherent superposition of reflection coefficients (3) of bare surface (substrate plus first two layers) and the reflection coefficients of the island covered surface was used to predict the effect of these dendritic structures on ellipsometer responses at various wavelengths. This multilayer modeling have allowed quantification of the distribution of deposited material between compact, granular (porous), and dendritic island layers.

Multilayer modeling has been applied to explain unusual optical measurements of complicated silver oxide films (4). The approach presented here is different from that applied to silver oxide films in that measurements were spectroscopic (400 to 700 nm), rather than fixed-wavelength (546.1 nm). Here, it was demonstrated that one can use single spectroscopic measurements of a film covered surface to determine confidence intervals on model parameters which are independent of wavelength (thickness, porosity, etc.), and can justify the use of more sophisticated optical modeling on the basis of the greater degrees-of-

freedom. Thin film deposits were also made in the presence of a known inhibitor (5), 10 micromolar rhodamine-B, and differences in micromorphology due to the inhibitor measured insitu. Deposits formed with the inhibitor were more compact; optical measurements were easily explained by a simple compact film model.

References

1. Farmer, J. C., Muller, R. H. Intl. Conference of Ellipsometry and Other Optical Methods, Paris, France, June 7-10, 1983.

2. Aspnes, D. E. Theeten, J. B., "Investigation of Effective-media Models for the Interpretation of Ellipsometer Observations," Surf. Sci., 96, 375 (1980).

3. Smith, C. G., "Ellipsometry of Anodic Film Growth," Ph.D. Thesis, Department of Chemical Engineering, University of California, Berkeley, LBL-8082 (1978).

4. Muller, R. H., Smith, C. G., "Use of Film Formation Models for the Interpretation of Ellipsometer Observations," Surf. Sci., 96, 375 (1980).

5. Farmer, J. C., Muller, R. H., "The Effect Rhodamine-B on Pb Electrodeposition on Ag and Cu," Electrochem. Soc. Meeting, San Francisco, CA, May 8-13, 1983.

6. see reference 2.

7. Azzam, R. M. A., Bashara, N. M., "Polarization Characteristics of Scattered Radiation from a Diffraction Grating by Ellipsometry with Application to Surface Roughness," Phys. Rev. B 5, 4721 (1972).

8. see reference 4.

9. see Chapter 2 and reference 1.

10. see Chapter 6 and reference 5.

11. see Chapter 5.

12. Fowles, G. R., INTRODUCTION TO MODERN OPTICS, 2nd ed., Halt, Rinehart, and Winston, New York, 1968, pp. 74-75.

13. Born, M., Wolf, E., PRINCIPLES OF OPTICS, MacMillan, New York, 1964, p. 551.

14. Muller, R. H., "Principles of Ellipsometry," ADVANCES IN ELECTRO-CHEMISTRY, Vol. 9, Delahay, P. Tobias, C. W., ed., John Wiley & Sons New York, 1973, pp. 167-226.

Table I. Spectroscopic Ellipsometry of Pb Deposits: Optimization of 2-Layer Simplification Model

	30 nm		60 nm		110 nm		
λ(nm)	Δ°	ψ°	Δ°	ψ°	Δ°	ψ°	
4248	58.69	32.99	78.01	32.55	89.84	34.62	Measured
	60.54	28.92	81.97	29.30	94.25	29.61	Calculated
4492	57.24	31.12	76.02	30.14	88.42	31.81	etc.
	56.49	31.68	75.64	31.60	87.64	31.76	
4756	55.48	30.88	73.77	29.11	86.53	30.35	
	54.28	30.97	73.63	30.16	85.84	30.30	
5155	52.73	30.99	71.42	28.81	84.44	29.42	
	51.89	30.90	71.19	29.18	83.69	29.32	
5586	50.07	31.73	69.52	28.68	82.91	28.99	
	49.59	31.48	69.44	28.60	82.44	28.85	
5998	49.97	33.58	66.95	29.04	81.14	28.84	
	49.81	33.50	66.71	28.70	80.88	28.77	
6242	51.03	34.47	65.91	29.62	79.68	29.10	
	50.91	34.38	64.95	29.25	79.47	28.99	
6504	51.85	35.35	64.99	30.59	78.06	29.85	
	52.27	35.24	63.54	30.38	77.90	29.71	
6748	52.87	36.39	64.58	31.99	76.99	30.96	
	53.69	35.99	63.04	31.78	76.79	30.81	
6991	53.45	38.11	64.09	34.43	75.53	33.65	
	55.14	36.89	63.12	34.53	75.30	33.52	
ERROR (degrees)	5.359		6.049		6.835		
THICKNESS (Å)	310	(5.8×10^{2})	500	(9.0×10^{3})	870	(2.3×10^{6})	
VOL. FRACT. Pb	0.585	(6.7×10^{-3})	0.775	(9.5×10^{-3})	0.968	(2.6×10^{-2})	

NOTE: PARAMETER VARIANCE GIVEN IN PARENTHESES

Figures

1.a Experimental spectroscopic measurements of delta for 31 nm thick (based on coulometric measurement), uniform, compact Pb deposits formed with and without 10 micromolar rhodamine-B additions.

1.b Experimental spectroscopic measurements of psi corresponding to 1.a.

2.a Experimental spectroscopic measurements of delta for 60 nm thick (based on coulometric measurement), uniform, compact Pb deposits formed with and without 10 micromolar rhodamine-B additions.

2.b Experimental spectroscopic measurements of psi corresponding to 2.a.

3.a Experimental spectroscopic measurements of delta for 110 nm thick (based on coulometric measurement), uniform, compact Pb deposits formed with and without 10 micromolar rhodamine-B additions.

3.b Experimental spectroscopic measurements of psi corresponding to 3.a.

4.a A comparison of all experimental spectroscopic measurements of delta for 31, 60, and 110 nm thick (based upon coulometric measurements), uniform, compact Pb deposits formed with and without rhodamine-B inhibitor additions. The solid lines are measurements of deposits formed with rhodamine-B additions; the dotted lines are measurements of deposits formed without rhodamine-B present.

4.b Experimental spectroscopic measurements of psi corresponding to 4.a.

5. Schematic representation of the various ellipsometer models used in attempts to explain experimental spectroscopic measurements of thin film Pb deposits on Cu substrates. Numbers in parenthesis indicate the number of adjustable parameters involved in each model. General classes of models are (1) the compact homogeneous film, (2) the effective media approximation, (3) the coherent superposition model, and (4) multilayer models. Note that each model class has sub-classes regarding more detailed assumptions which were made.

6.a Spectroscopic simulations of thin layer Pb deposits of various thicknesses based upon the compact film model. Simulations (solid lines) are compared to experimental measurements (dotted lines); experimental data are given for 31, 60, and 110 nm equivalent compact Pb deposits on Cu (based upon coulometric measurements). Optical constants used are shown in Figs. 6.a and 6.b of Chapter 8.

6.b Psi vs wavelength corresponding to 6.a.

7.a Spectroscopic simulations of a 31 nm thick, uniform, compact Pb deposit (based upon coulometric measurements) redistributed on a Cu substrate as deposits of various porosities. Porous deposit thicknesses are consistent with the coulometric measurement and assumed porosities. Simulations are based upon the effective media approximation and are represented by solid lines; experimental measurements are represented by dotted lines. Delta vs wavelength.

7.b Psi vs wavelength corresponding to 7.a.

8.a Spectroscopic simulations of a 31 nm thick, uniform, compact Pb deposit (based upon coulometric measurements) redistributed on a Cu substrate as compact islands. Island thicknesses are consistent with both the coulometric measurement and assumed fractional surface coverages (by islands). Simulations are based upon the coherent superposition model and are represented by solid lines; experimental measurements are represented by dotted lines. Delta vs wavelength.

8.b Psi vs wavelength corresponding to 8.a.

9.a Spectroscopic simulations of a 60 nm thick, uniform, compact Pb deposit (based upon coulometric measurements) redistributed on a Cu substrate as compact islands. Island thicknesses are consistent with both the coulometric measurement and assumed fractional surface coverages (by islands). Simulations are based upon the coherent superposition model and are represented by solid lines; experimental measurements are represented by dotted lines. Delta vs wavelength.

9.b Psi vs wavelength corresponding to 9.a.

10.a Spectroscopic simulations of a 110 nm thick, uniform, compact Pb deposit (based upon coulometric measurements) redistributed on a Cu substrate as compact islands. Island thicknesses are consistent with both the coulometric measurement and assumed fractional surface coverages (by islands). Simulations are based upon the coherent superposition model and are represented by solid lines; experimental measurements are represented by dotted lines. Delta

vs wavelength.

10.b Psi vs wavelength corresponding to 10.a.

11.a Simulations comparable to 8.a, but assuming that the islands are 20% porous. These simulations represent a joint application of the effective media approximation (island porosity) and the coherent superposition model. Delta vs wavelength.

11.b Psi vs wavelength corresponding to 11.a.

11.c Simulations comparable to 8.a, but assuming that the islands are 30% porous.

11.d Psi vs wavelength corresponding to 11.c.

11.e Simulations comparable to 8.a, but assuming that the islands are 40% porous.

11.f Psi vs wavelength corresponding to 11.e.

12.a Simulations comparable to 9.a, but assuming that the islands are 20% porous.

12.b Psi vs wavelength corresponding to 12.a.

12.c Simulations comparable to 9.a, but assuming that the islands are 30% porous.

12.d Psi vs wavelength corresponding to 12.c.

12.e Simulations comparable to 9.a, but assuming that the islands are 40% porous.

12.f Psi vs wavelength corresponding to 12.e.

13.a A first attempt at improving the agreement between simulations and spectroscopic measurements (31 nm case) by using multilayer modeling. Simulations are represented as solid lines and experimental data are represented as dotted lines. Curves are labeled as (1), (1+2), and (1+2+3); these designate collective responses to the first layer, the first and second layers, and all three layers, respectively. The first layer was assumed to be compact and 10 nm thick; the second layer was assumed to be 20 nm thick with a porosity of either 60% (A) or 80% (B); the dendritic Pb islands were also assumed to be porous. None of the simulations agreed with spectroscopic measurements over the full spectral range; however, the agreement was better than could be achieved with a single layer model (either compact film, effective media, or coherent superposition). This simulation demonstrated the ellipsometer responds primarily to the first two deposited layers, even with as much as 2/3 of the deposited Pb distributed as islands (since the islands cover only between 5 to 10 % of the surface). Delta vs wavelength.

13.b Psi vs wavelength corresponding to 13.a.

13.c Analogous to 14.a, but assuming that the second layer was 40 nm thick and either 80% (A) or 90% (B) porous. The agreement, improved over that in 14.a, is still not acceptable. Delta vs wavelength.

13.d Psi vs wavelength corresponding to 13.c.

14.a A comparison of initial modeling attempts to match experimental spectroscopic measurements (31 nm case) with simulations; delta vs wavelength. Agreement was achieved with the multilayer model by trial and error.

14.b Psi vs wavelength corresponding to 14.a.

15.a Comparison of experimental spectroscopic measurements and predictions based on a three-layer model (two-layer approximation, after optimization of parameter values); delta vs wavelength.

15.b Psi vs wavelength corresponding to 15.a.

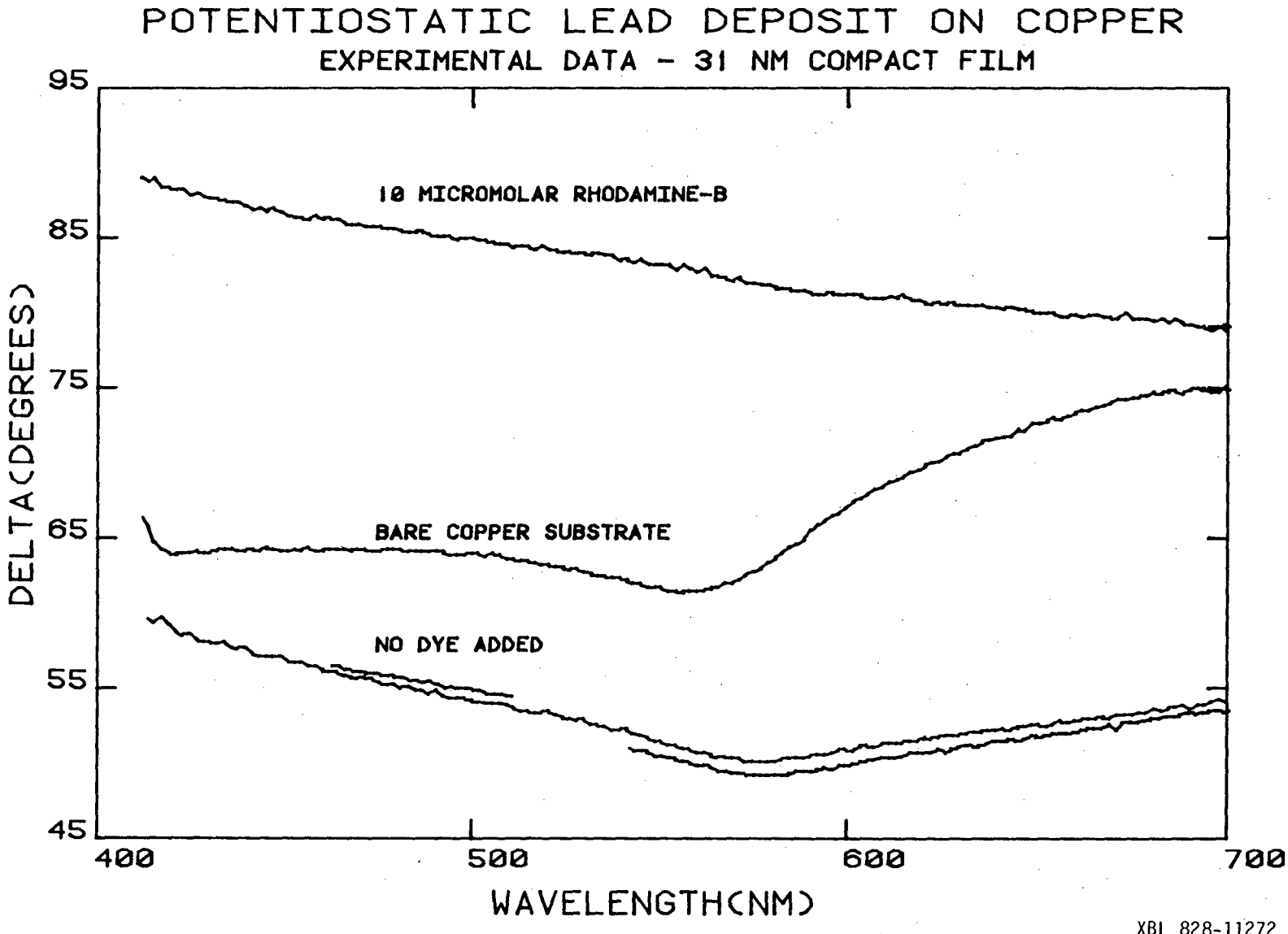

Fig. 1.a

XBL 828-11272

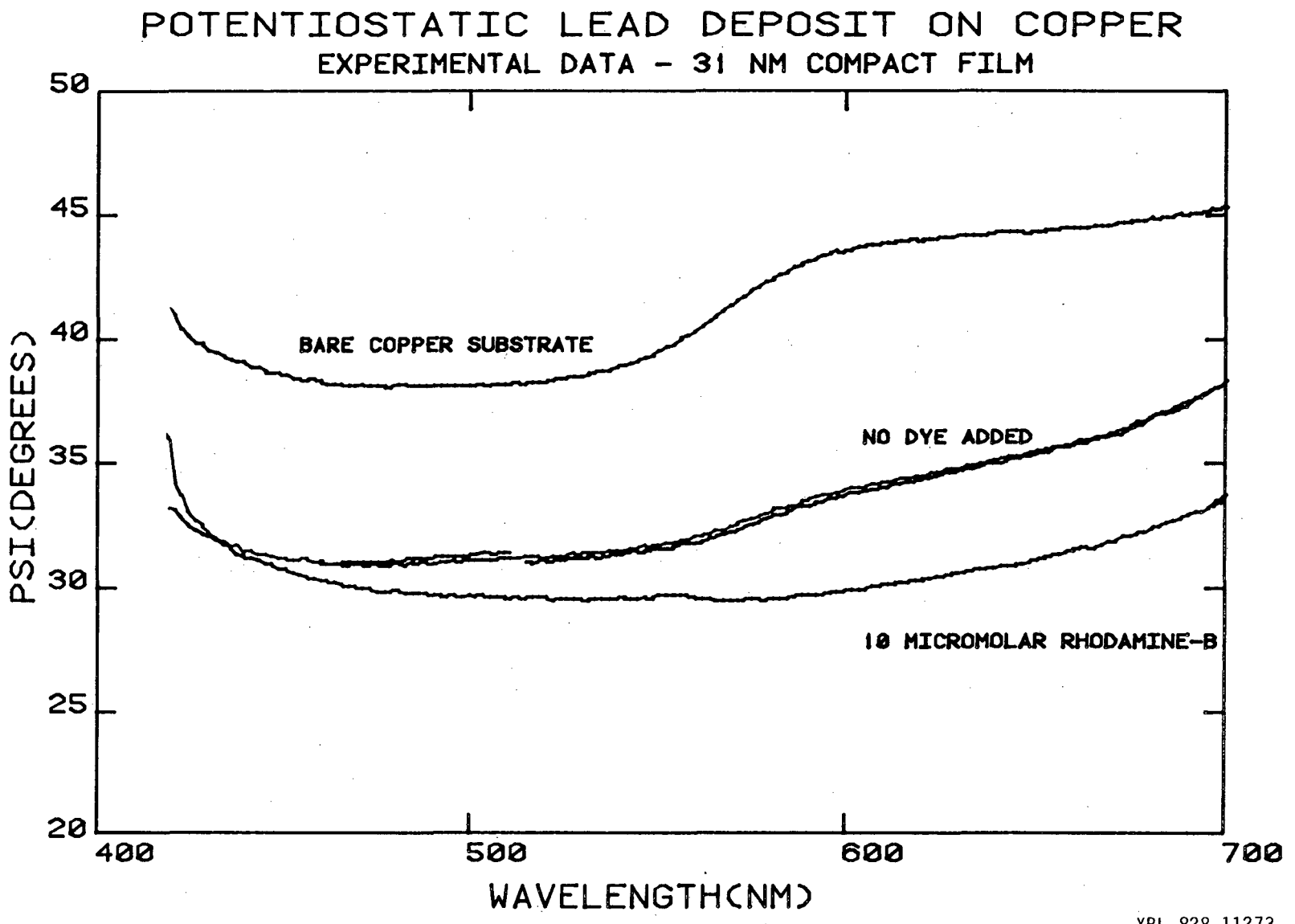

Fig. 1.b

XBL 828-11273

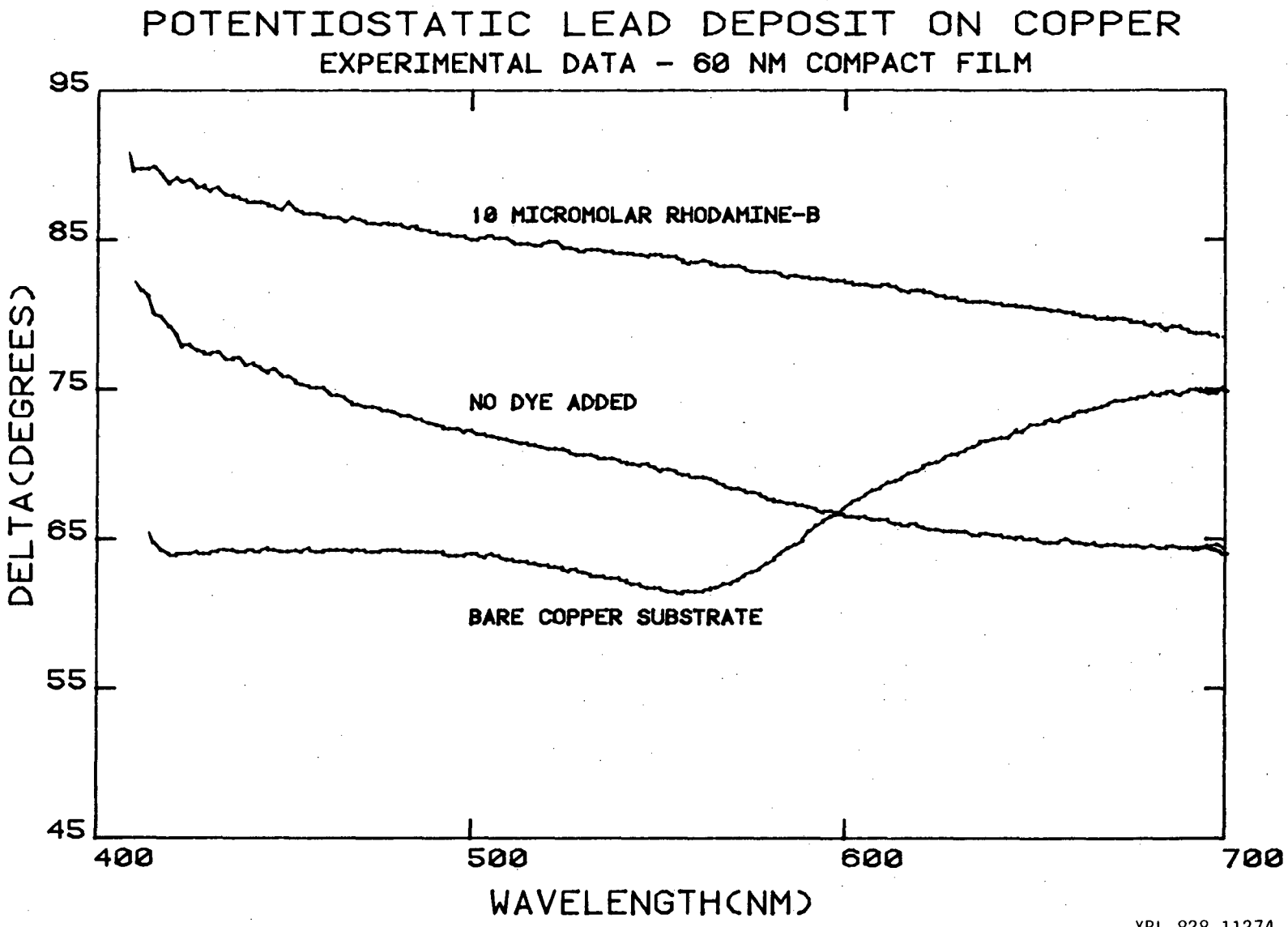

XBL 828-11274

Fig. 2.a

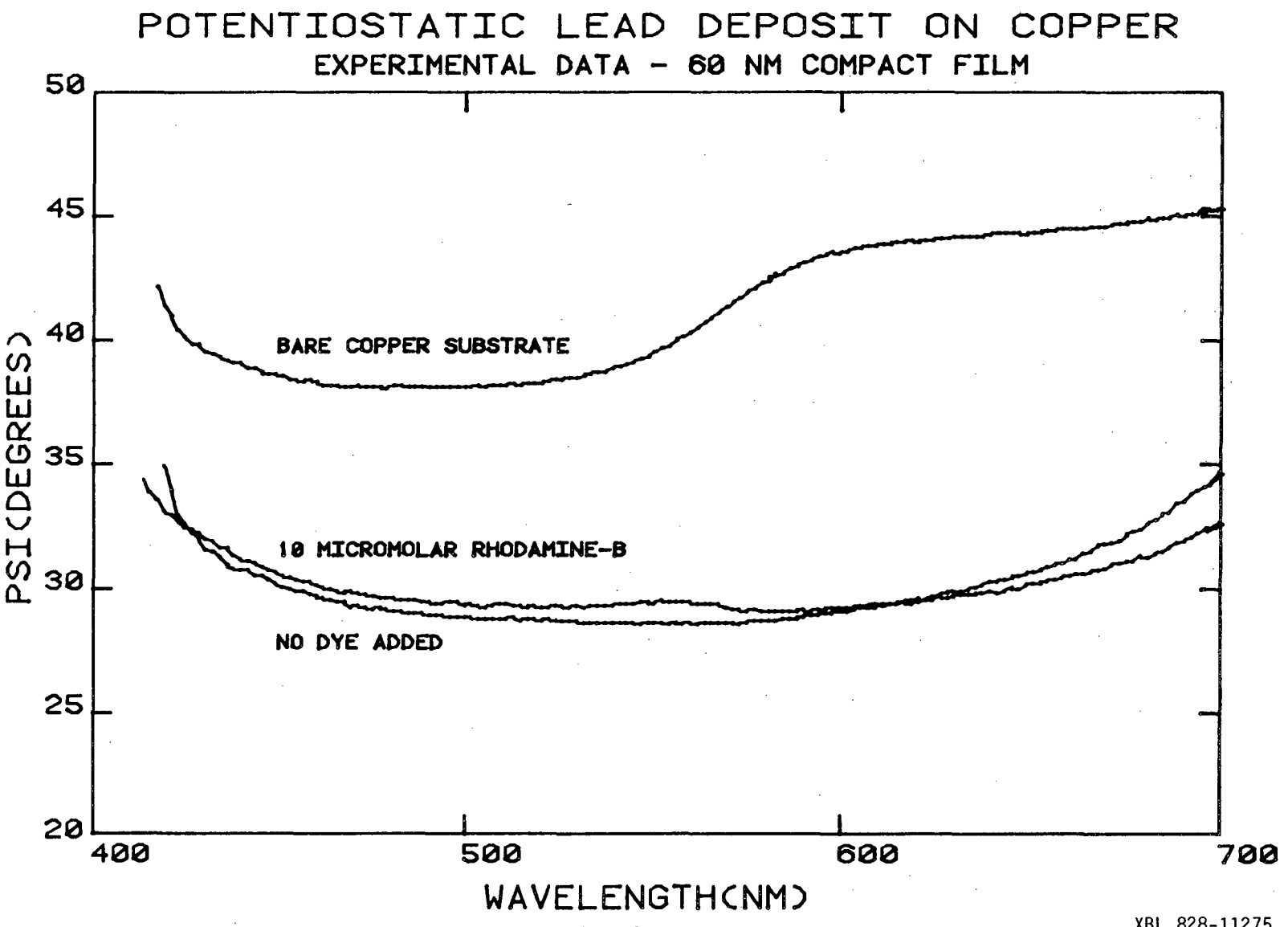

Fig. 2.b

XBL 828-11275

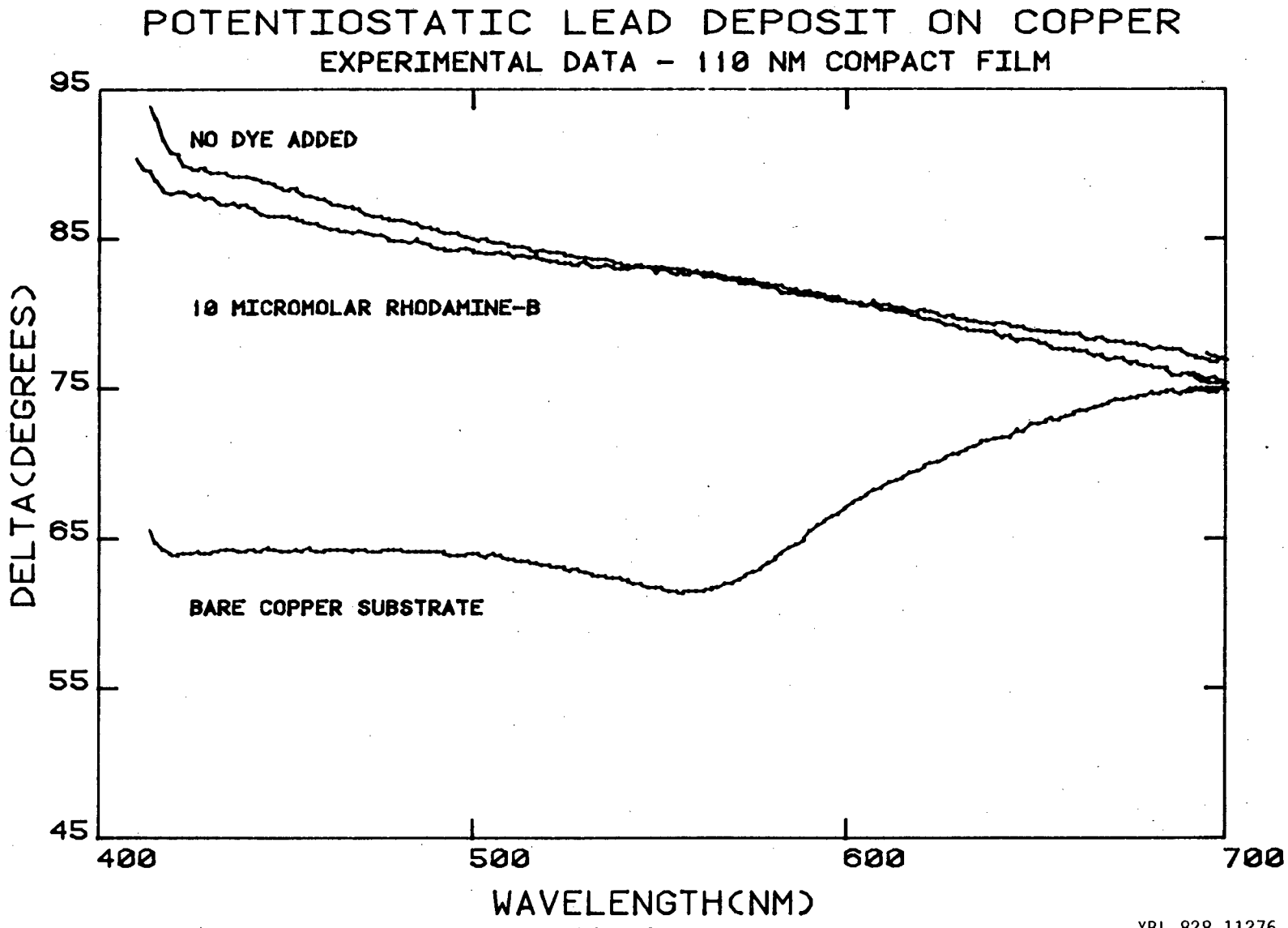

Fig. 3.a

XBL 828-11276

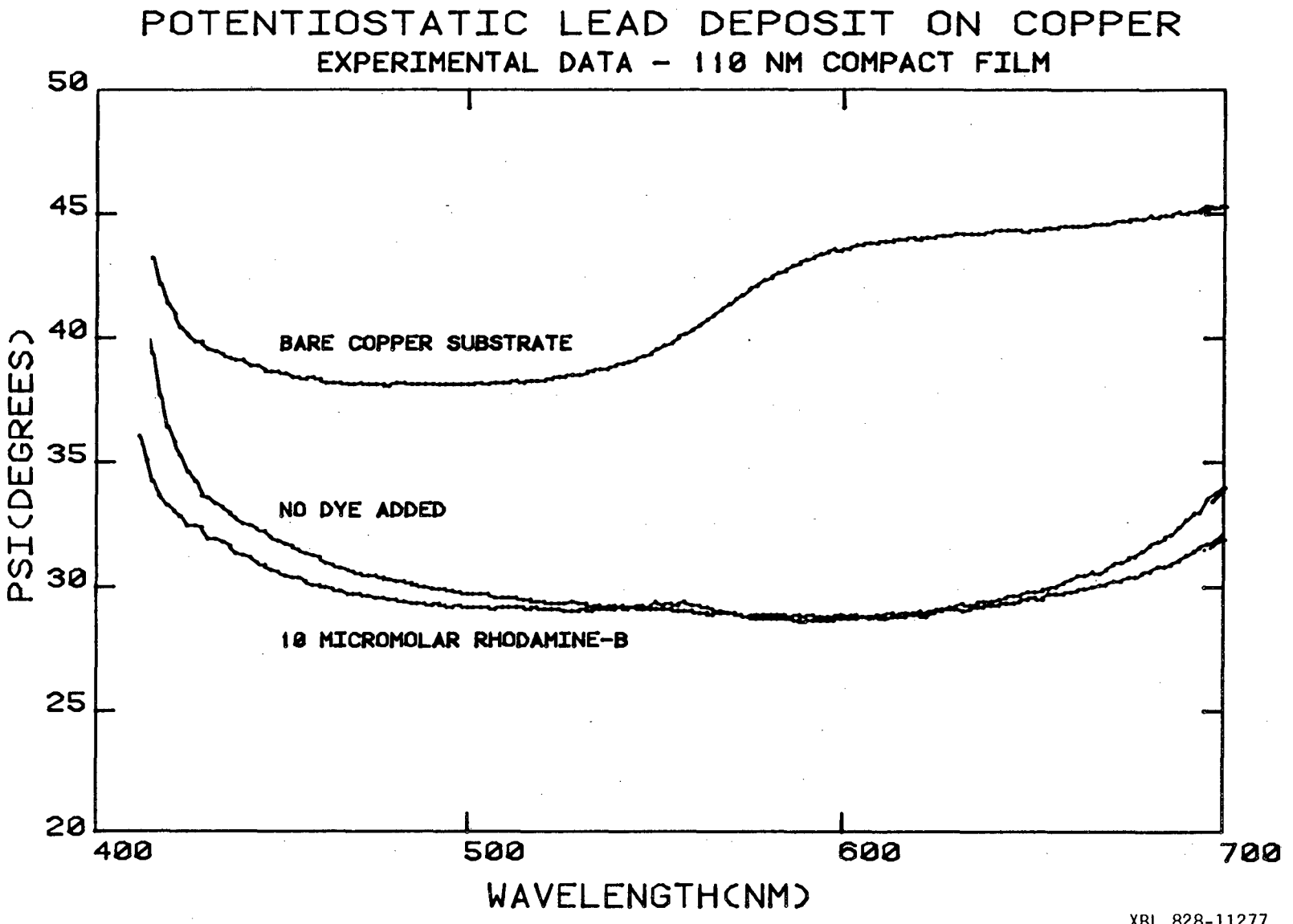

XBL 828-11277

Fig. 3.b

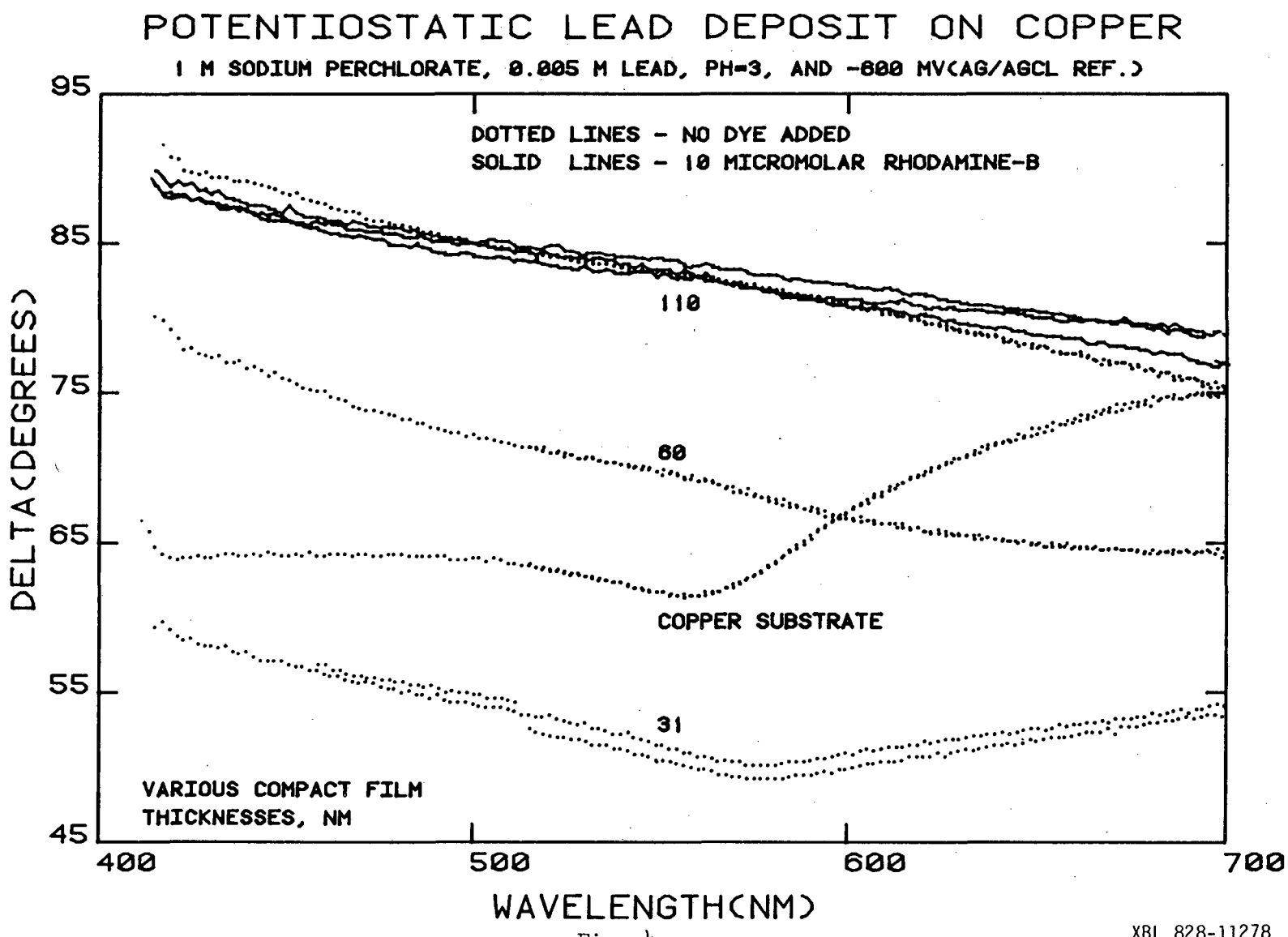

Fig. 4.a

XBL 828-11278

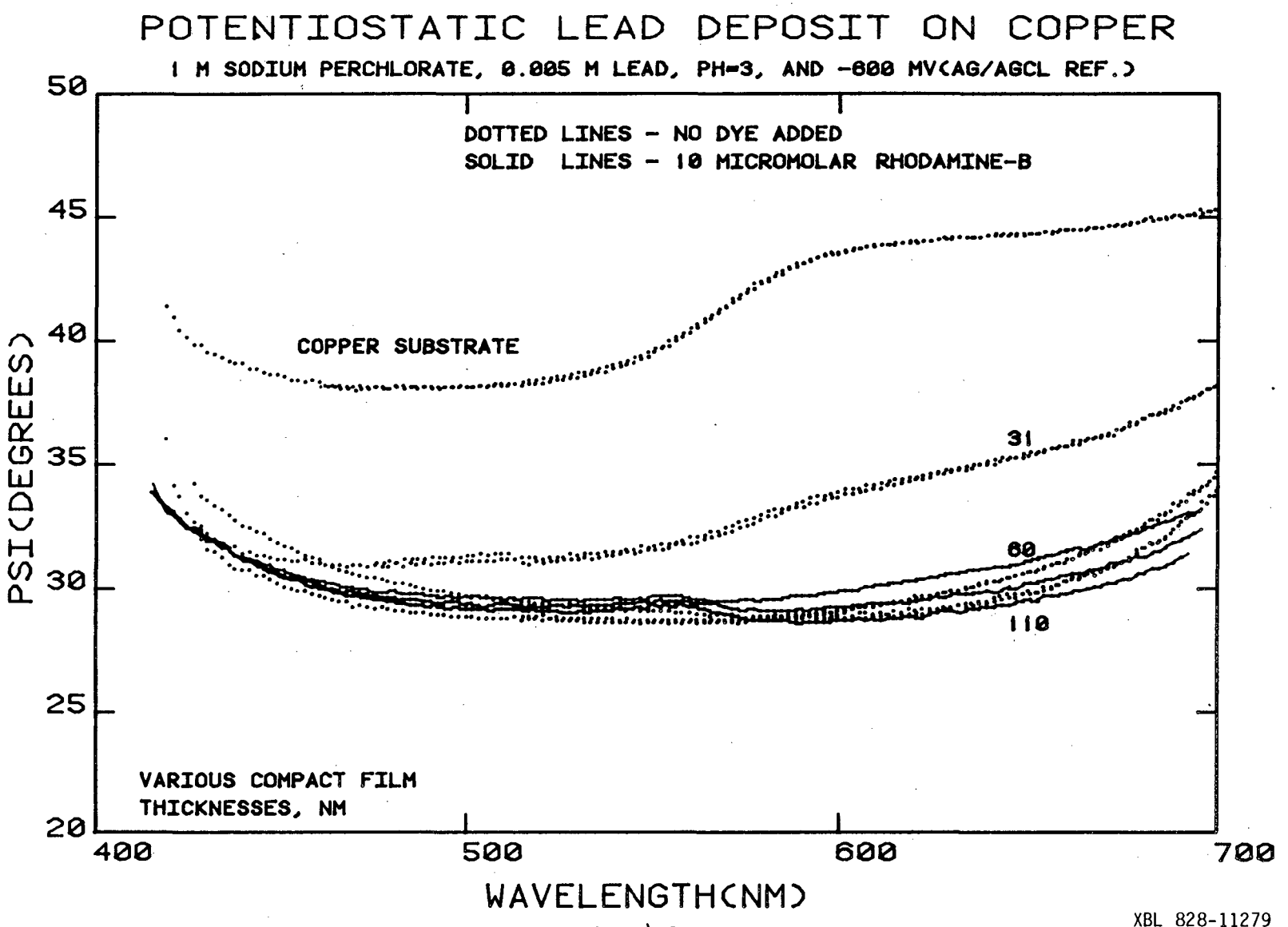

Fig. 4.b

XBL 828-11279

MODELING FIRST ORDER OPTICAL EFFECTS

COMPACT HOMOGENEOUS FILM

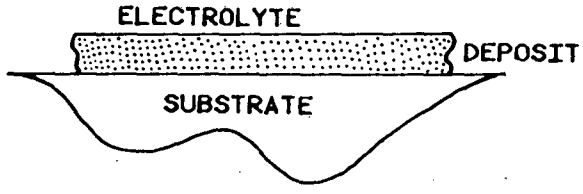

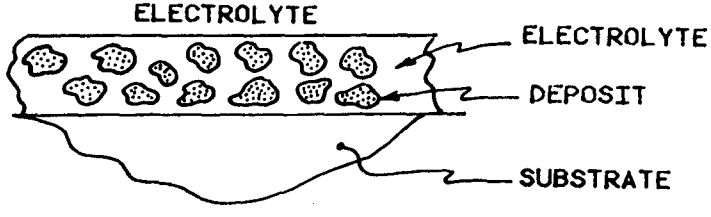

EFFECTIVE MEDIA APPROXIMATION

1. MAXWELL-GARNETT (2)
2. BRUGGEMAN (2)

COHERENT SUPERPOSITION

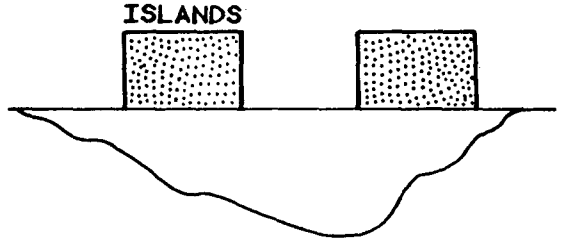

1. COMPACT ISLANDS (2)
2. POROUS ISLANDS (3)
3. ANISOTROPIC (6)

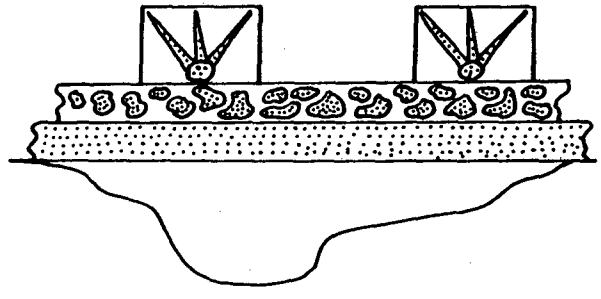

MULTILAYER MODELS

1. THREE LAYER (6)
2. TWO LAYER SIMPLIFICATION (3)

XBL 829-11873

Fig. 5

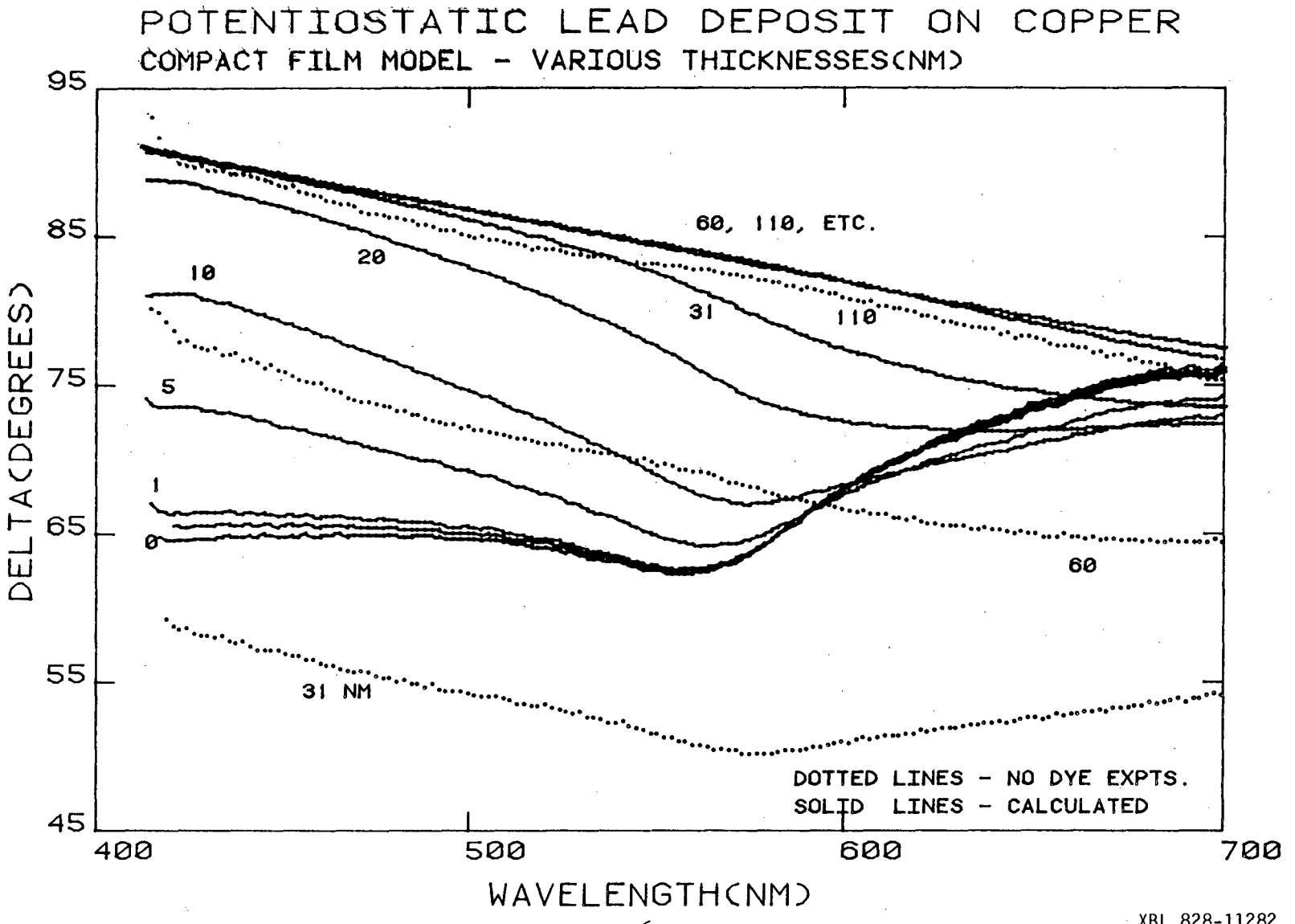

Fig. 6.a

XBL 828-11282

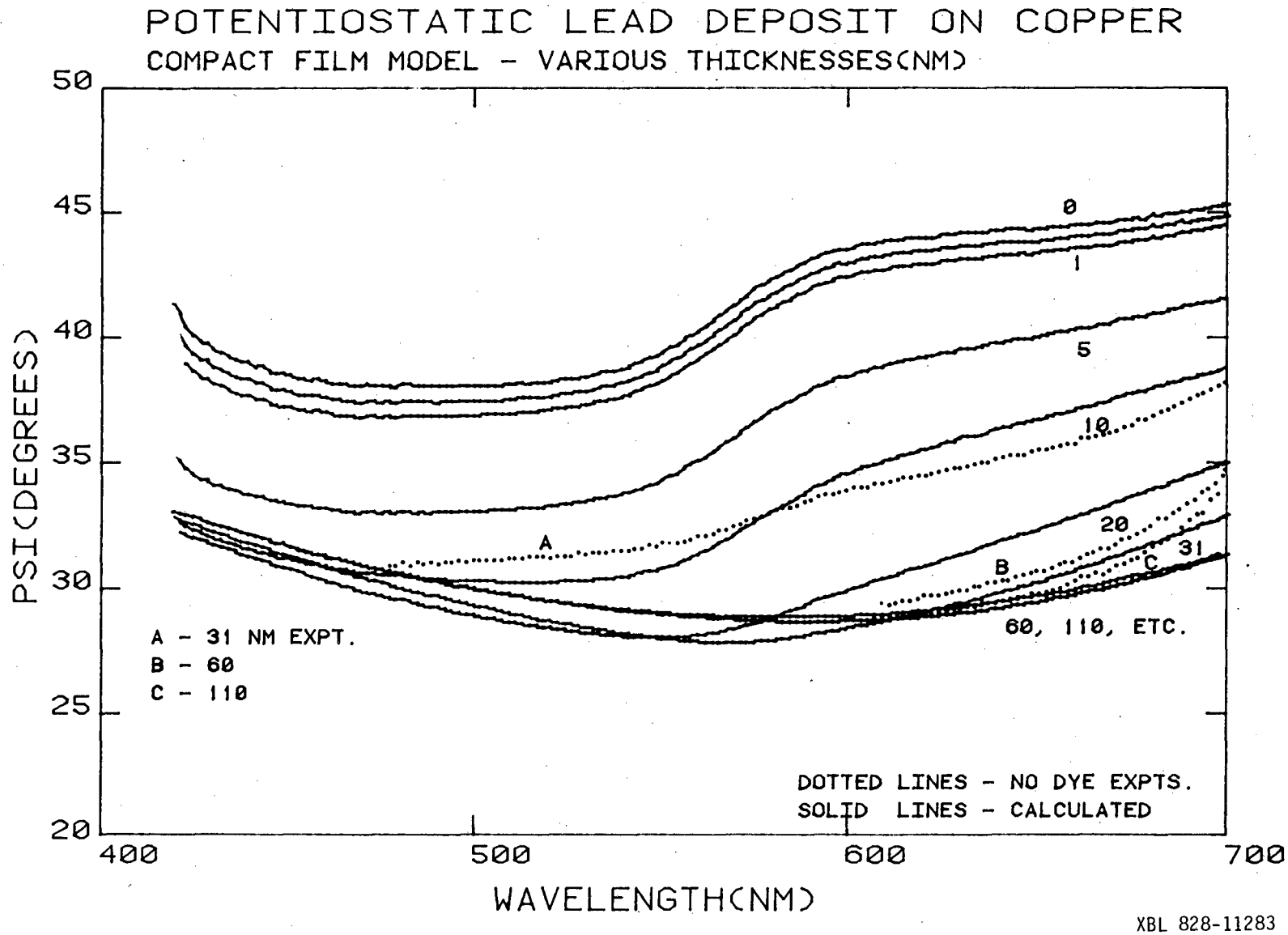

XBL 828-11283

Fig. 6.b

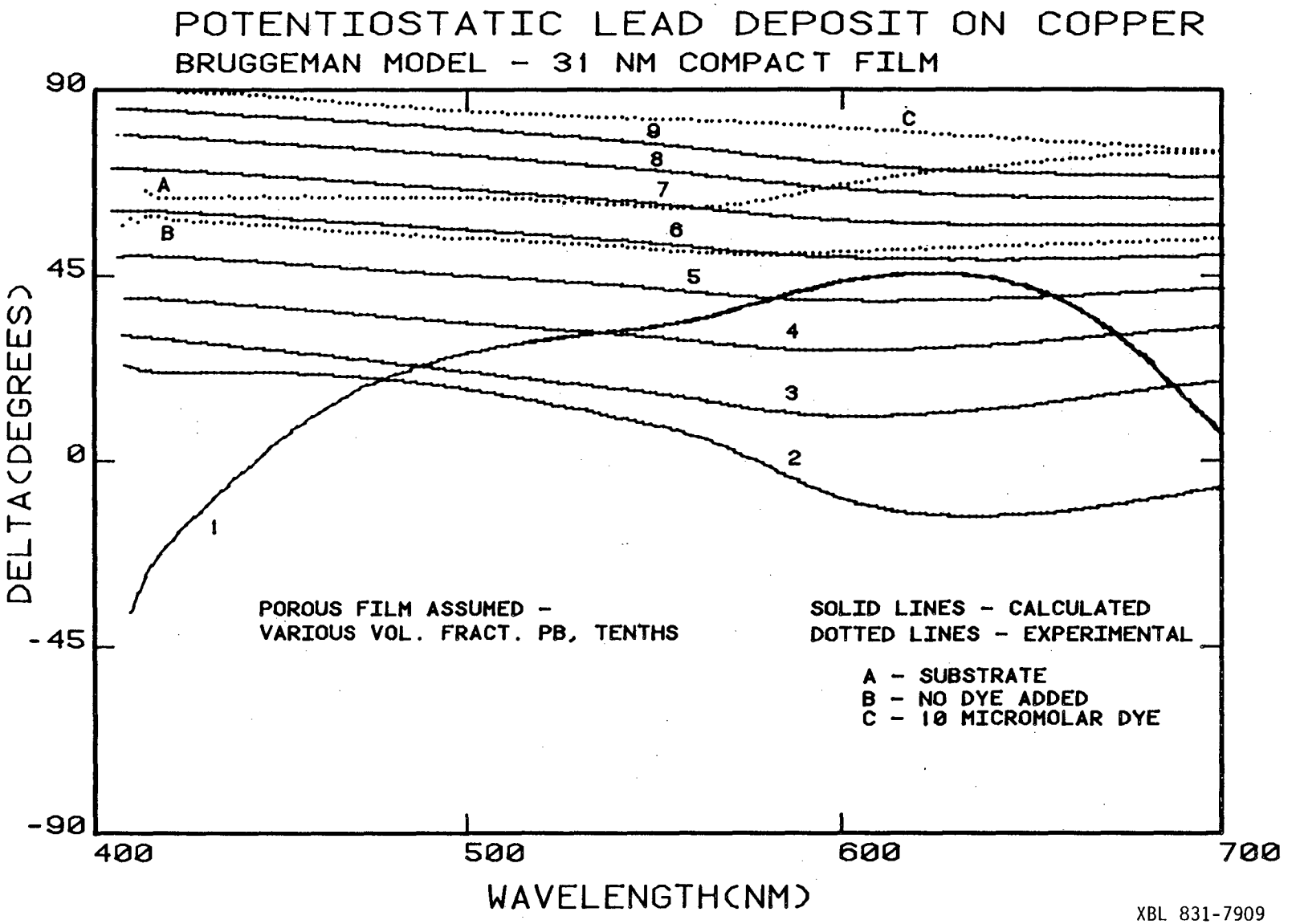

XBL 831-7909

Fig. 7.a

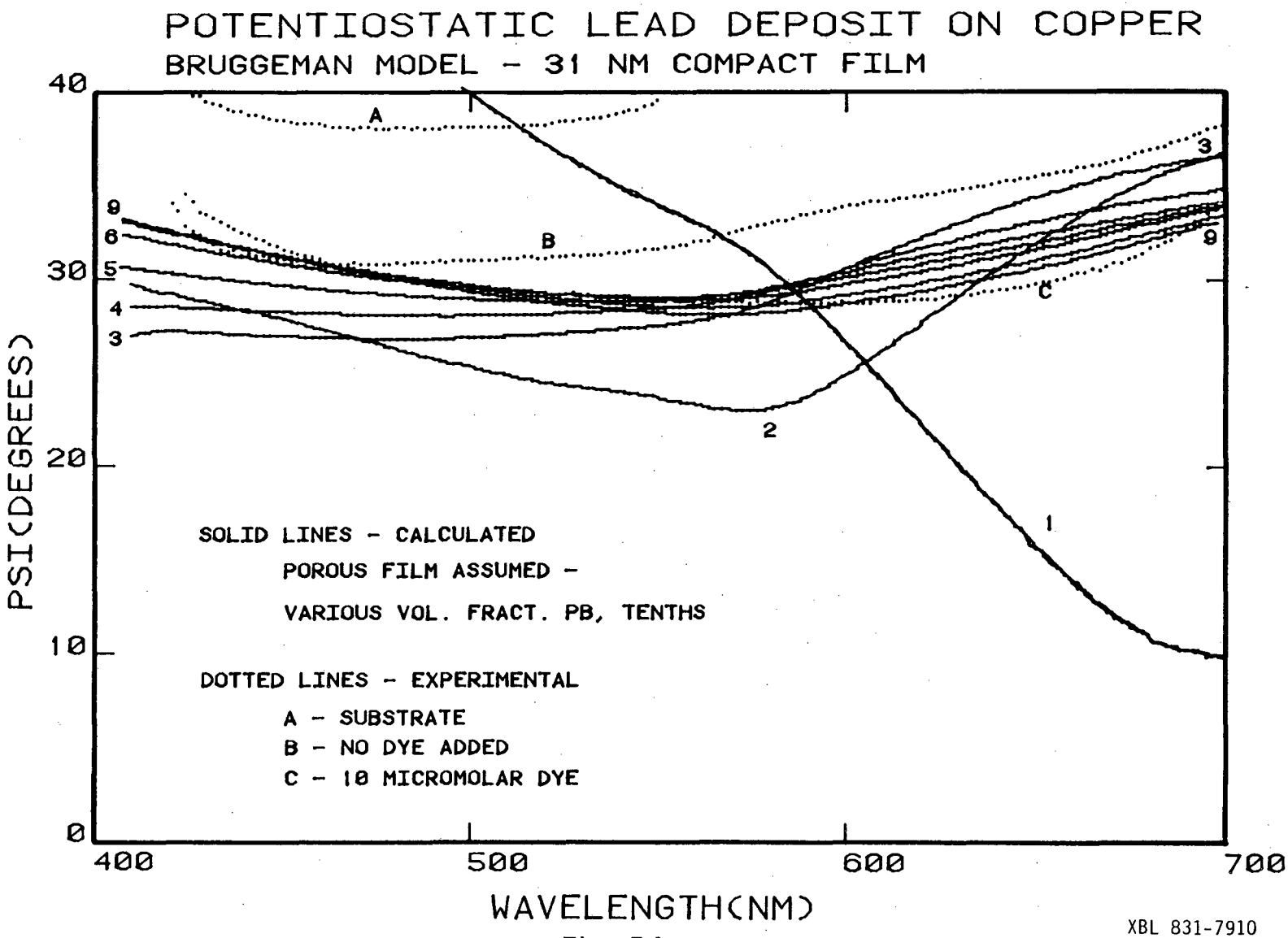

Fig. 7.b

XBL 831-7910

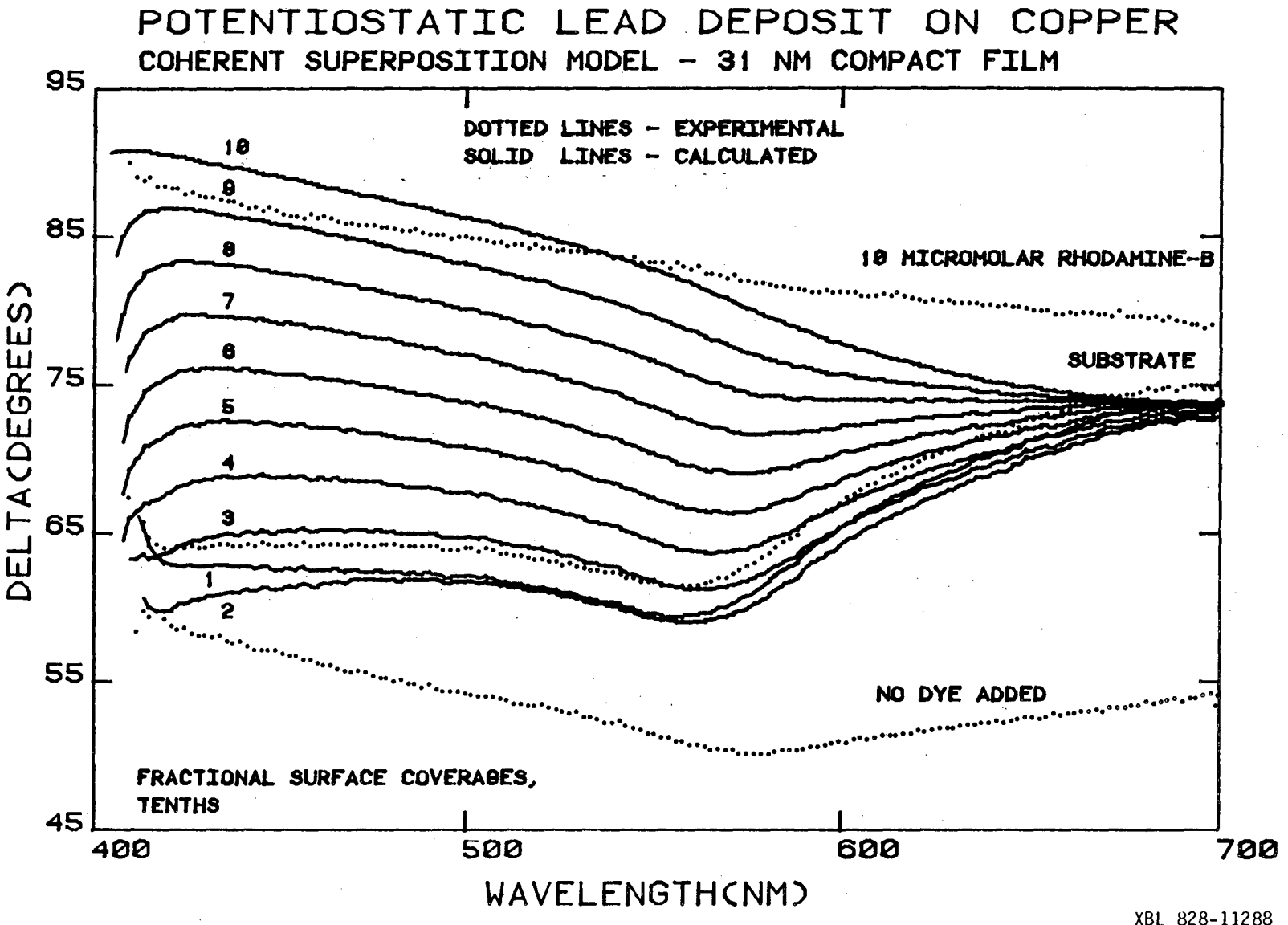

XBL 828-11288

Fig. 8.a

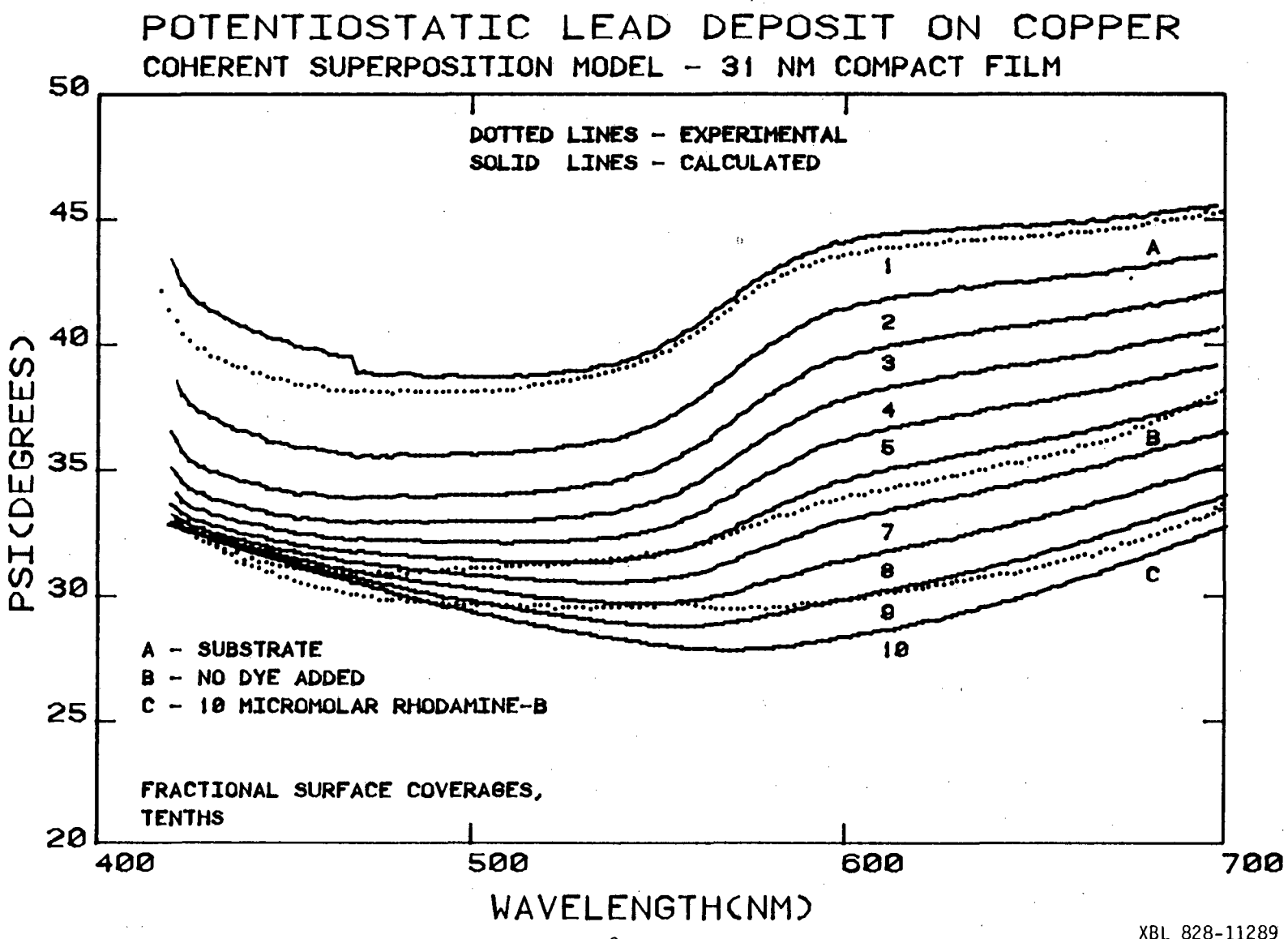

Fig. 8.b

XBL 828-11289

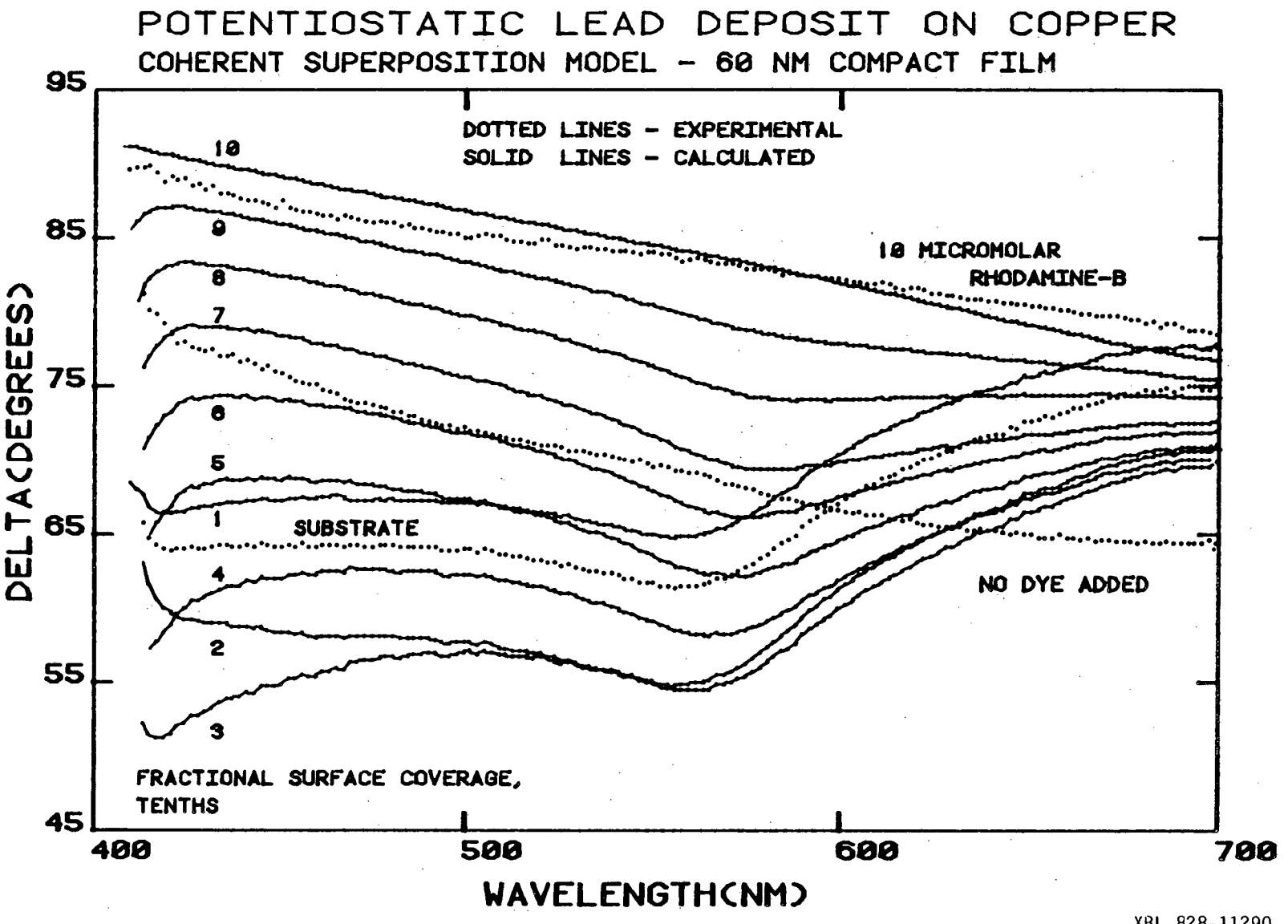

XBL 828-11290

Fig. 9.a

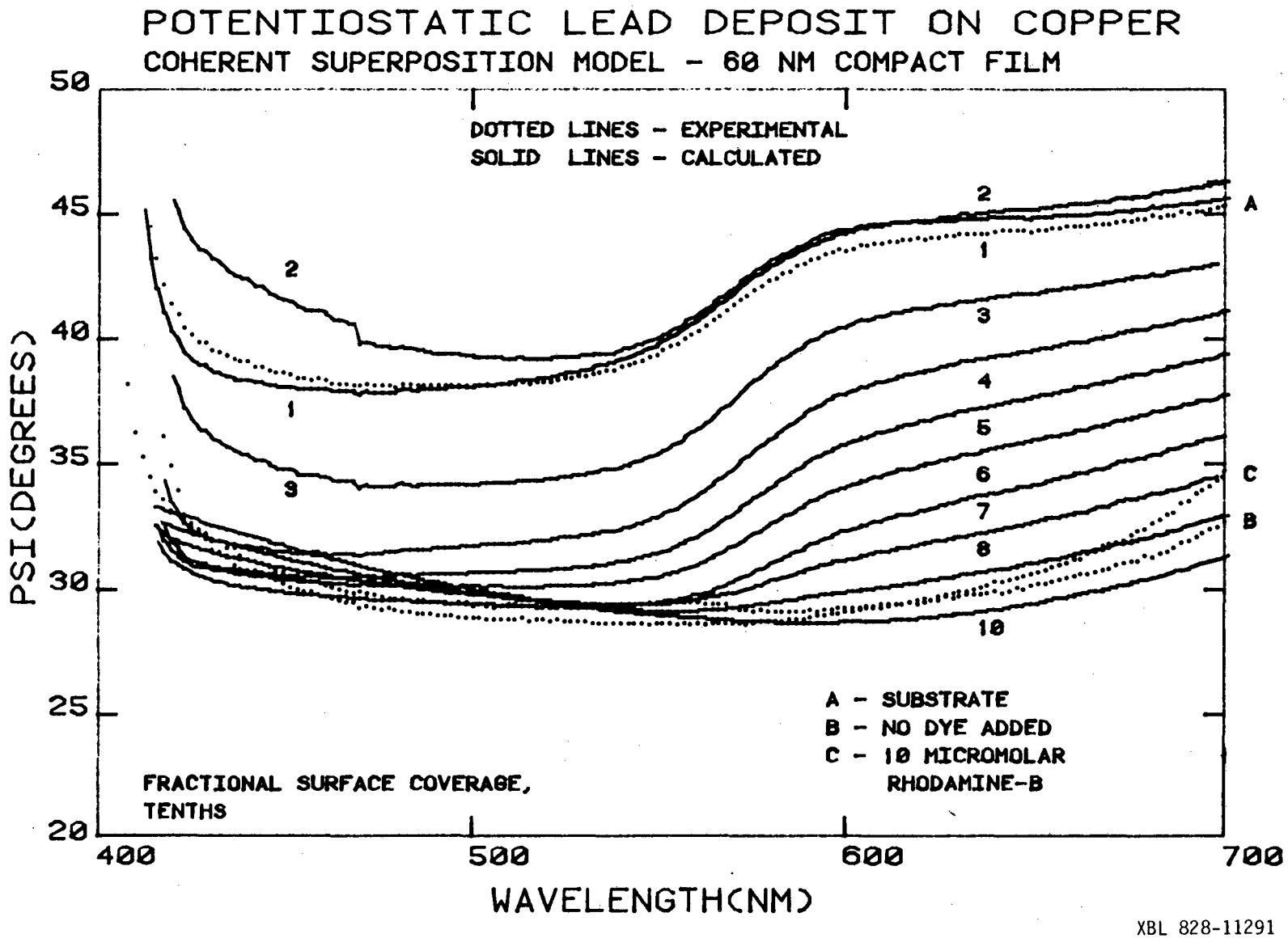

XBL 828-11291

Fig. 9.b

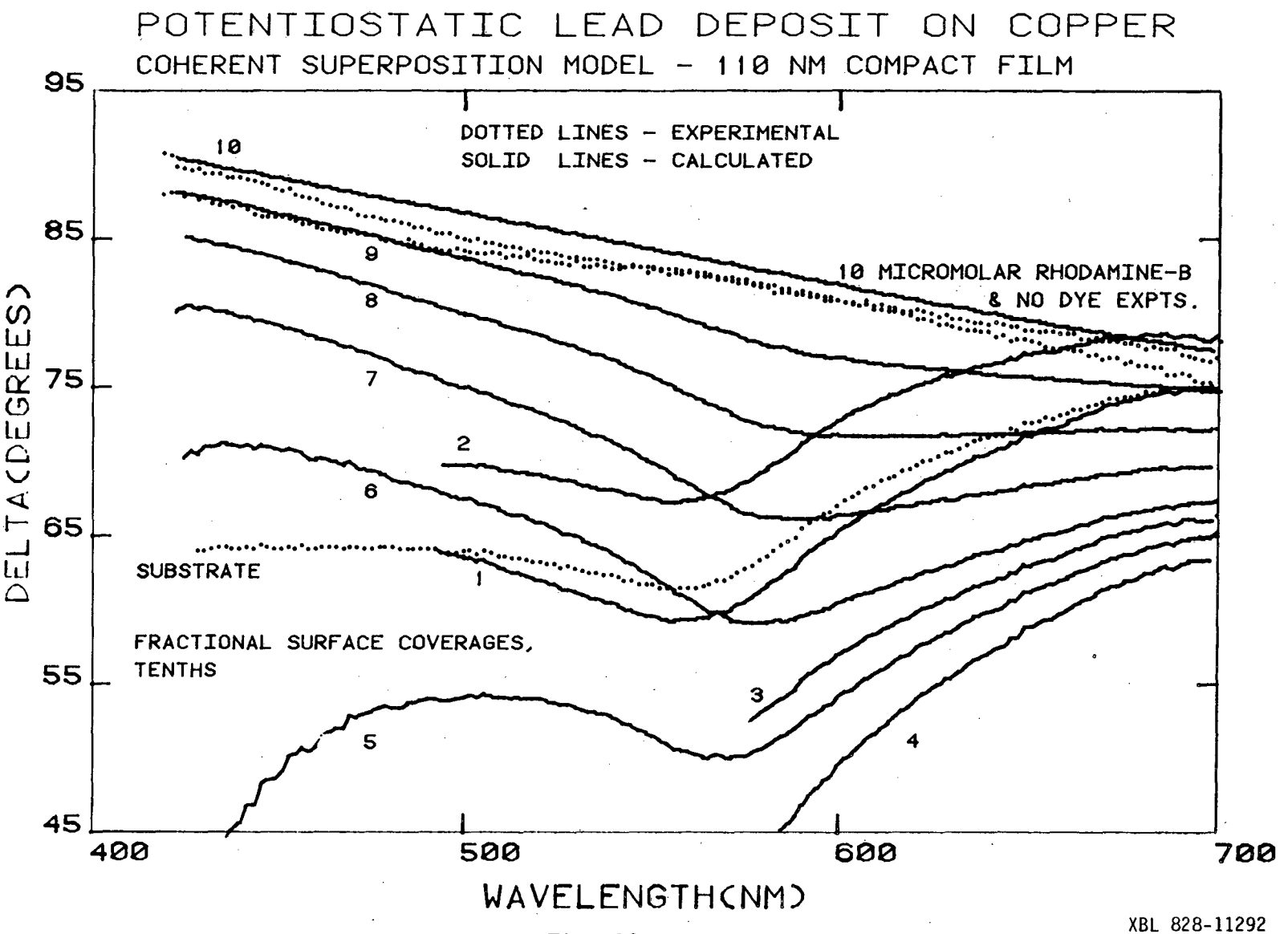

XBL 828-11292

Fig. 10.a

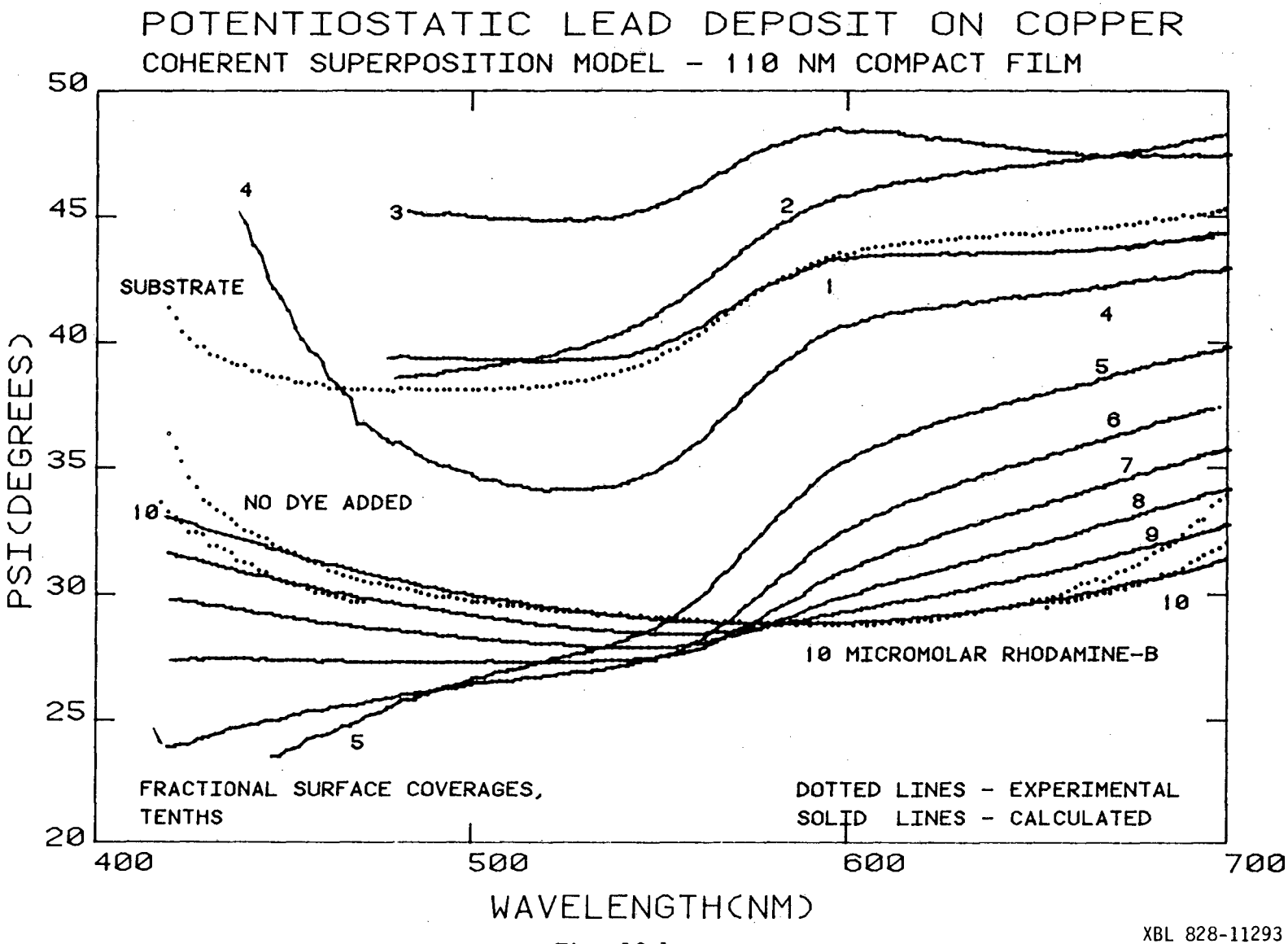

XBL 828-11293

Fig. 10.b

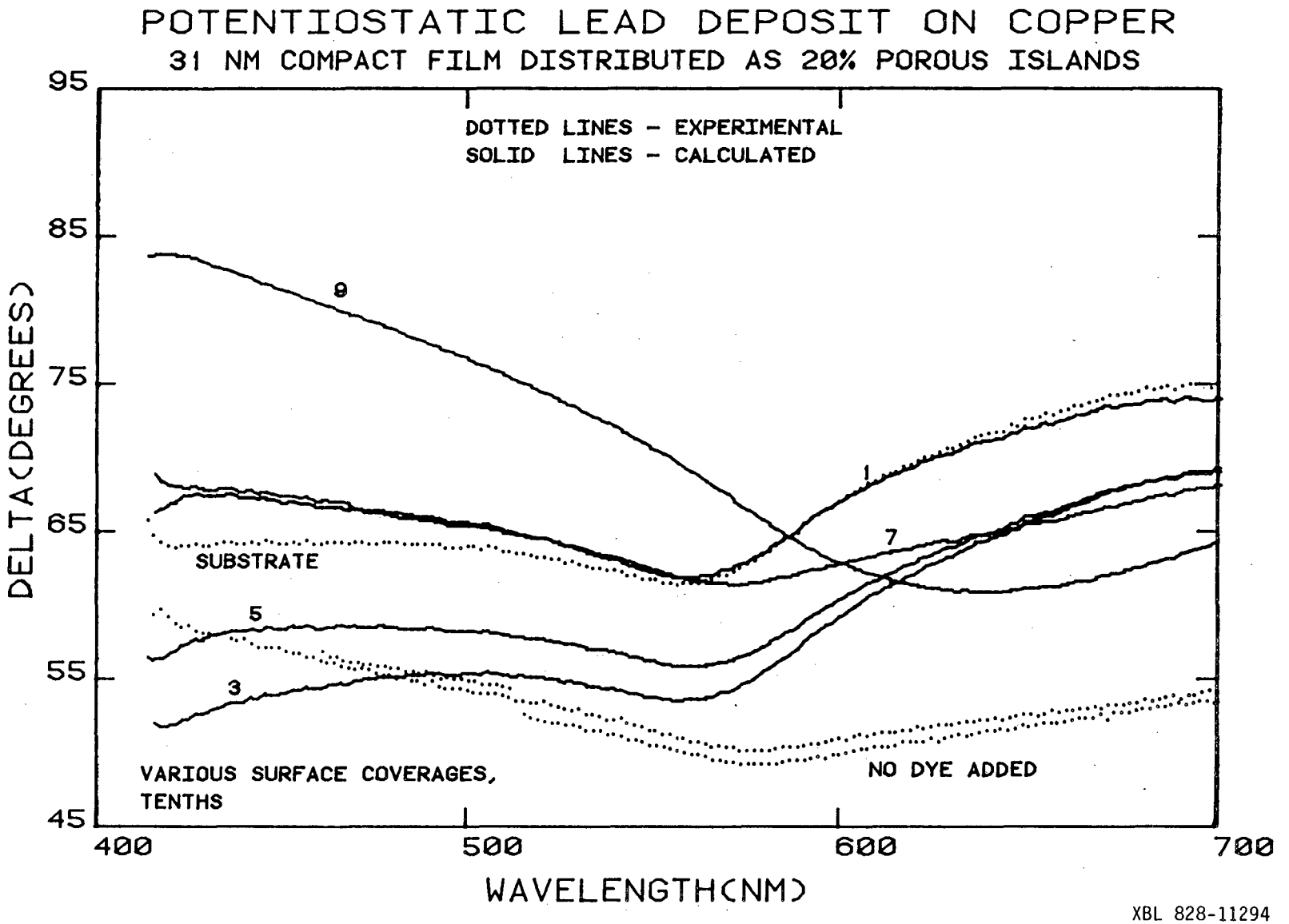

XBL 828-11294

Fig. 11.a

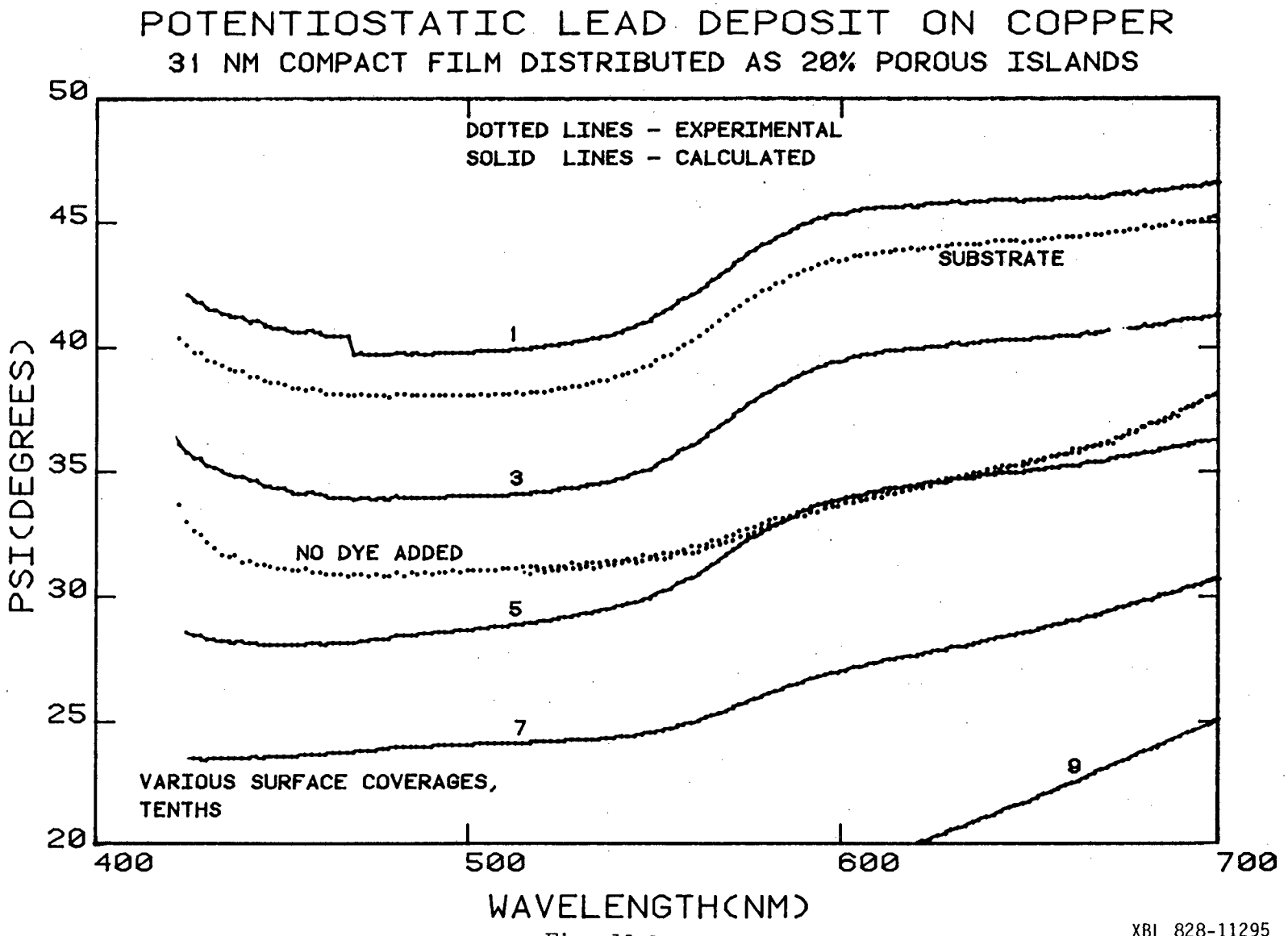

Fig. 11.b

XBL 828-11295

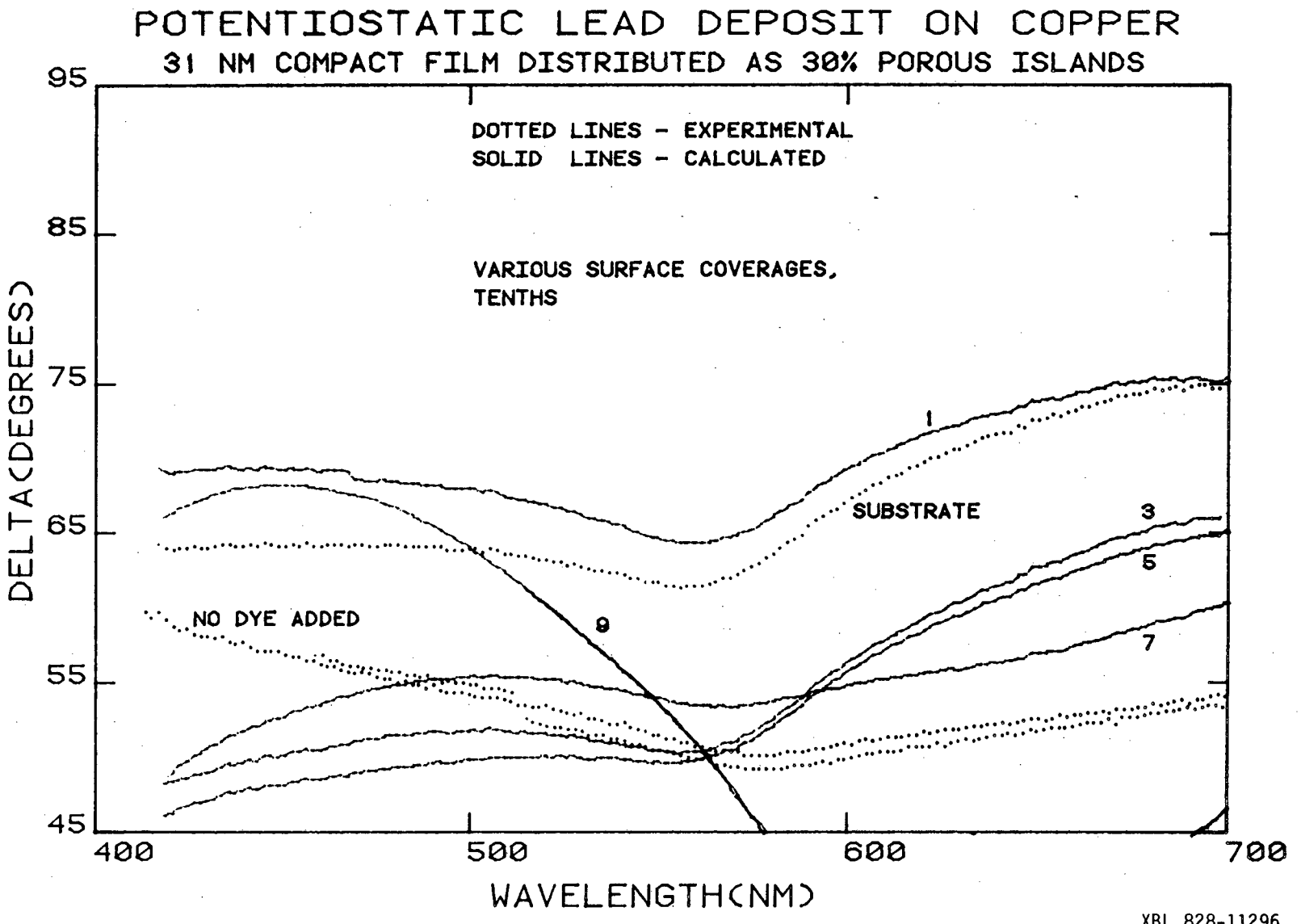

Fig. 11.c

XBL 828-11296

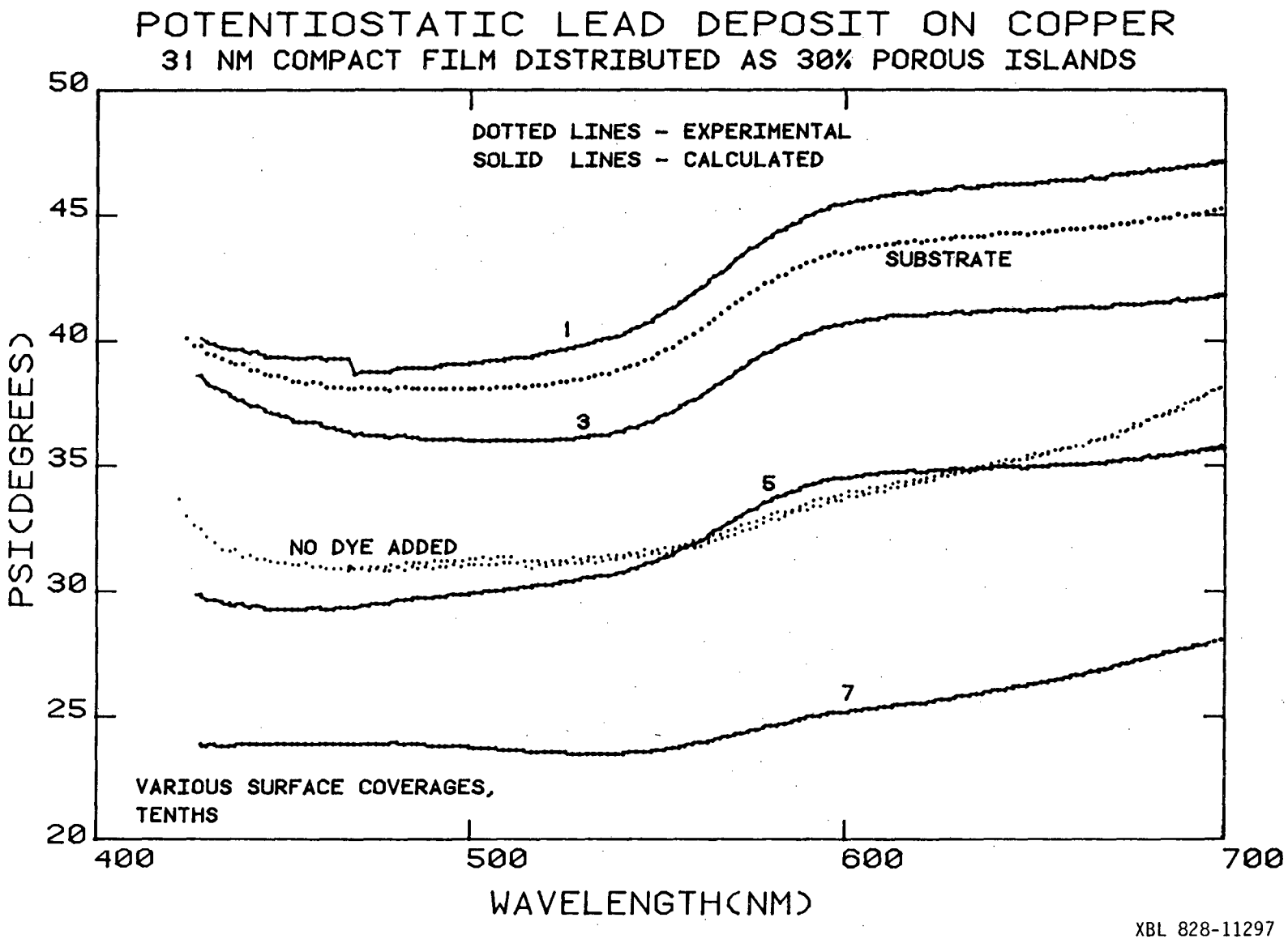

XBL 828-11297

Fig. 11.d

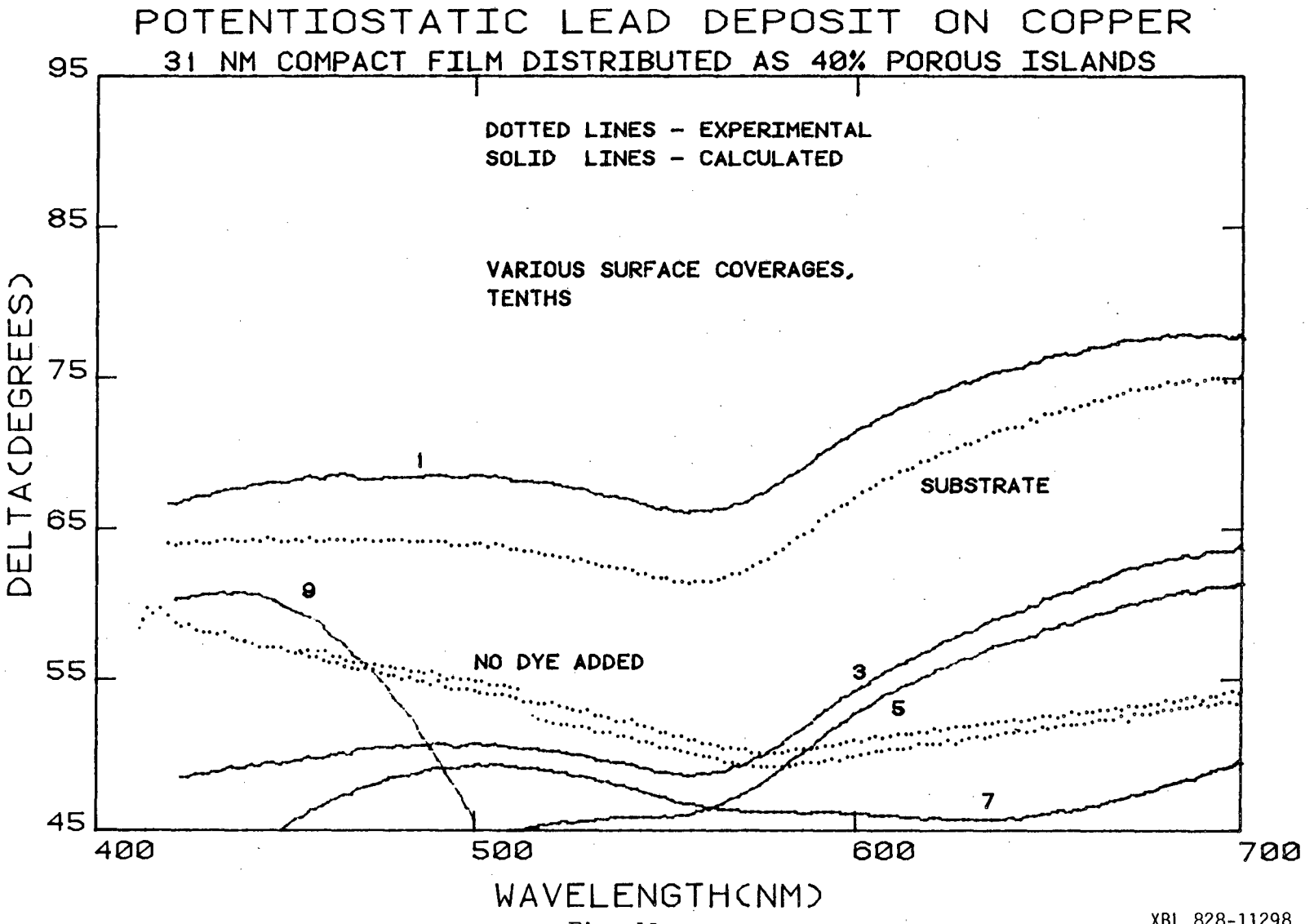

Fig. 11.e

XBL 828-11298

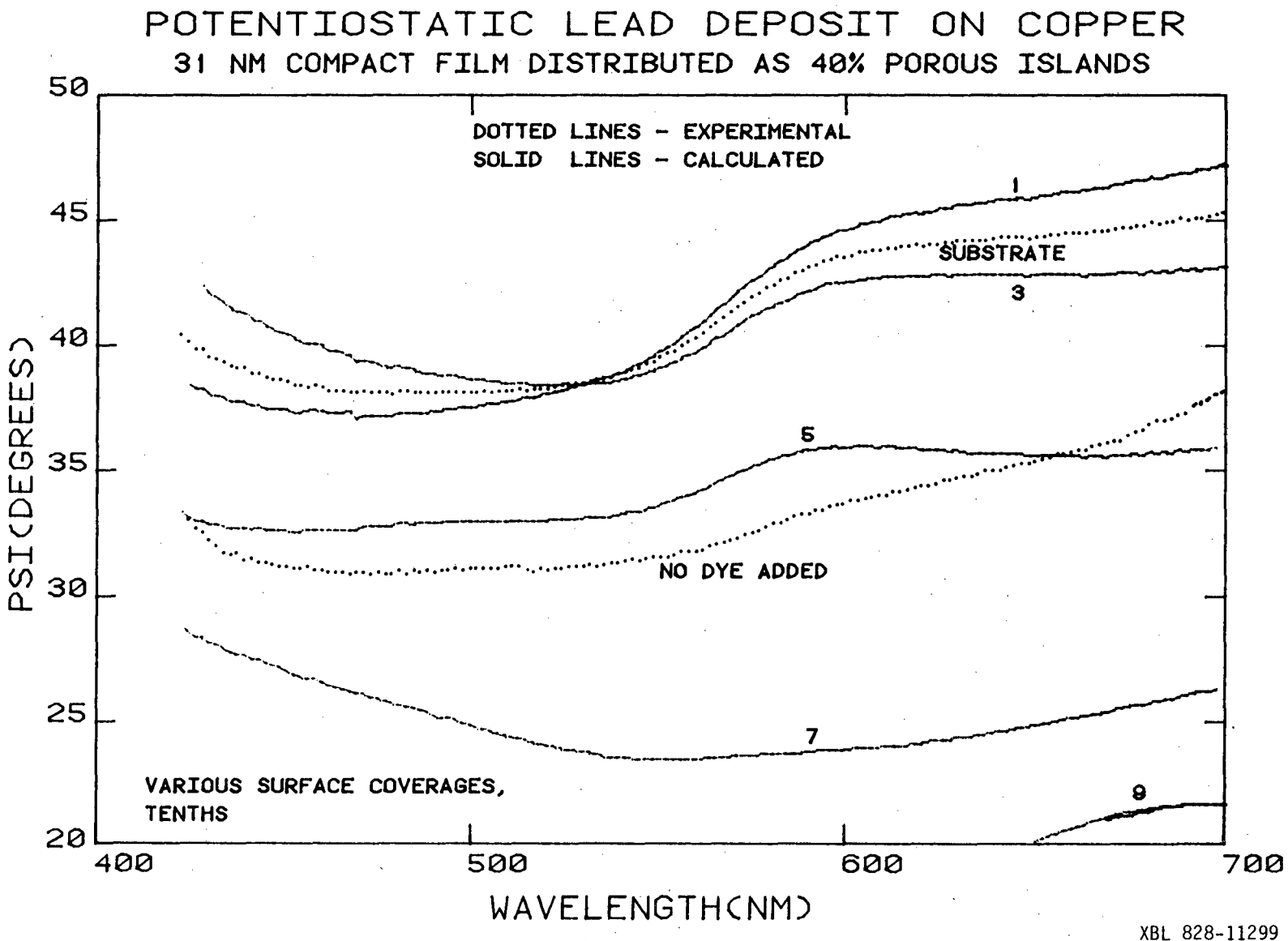

Fig. 11.f

XBL 828-11299

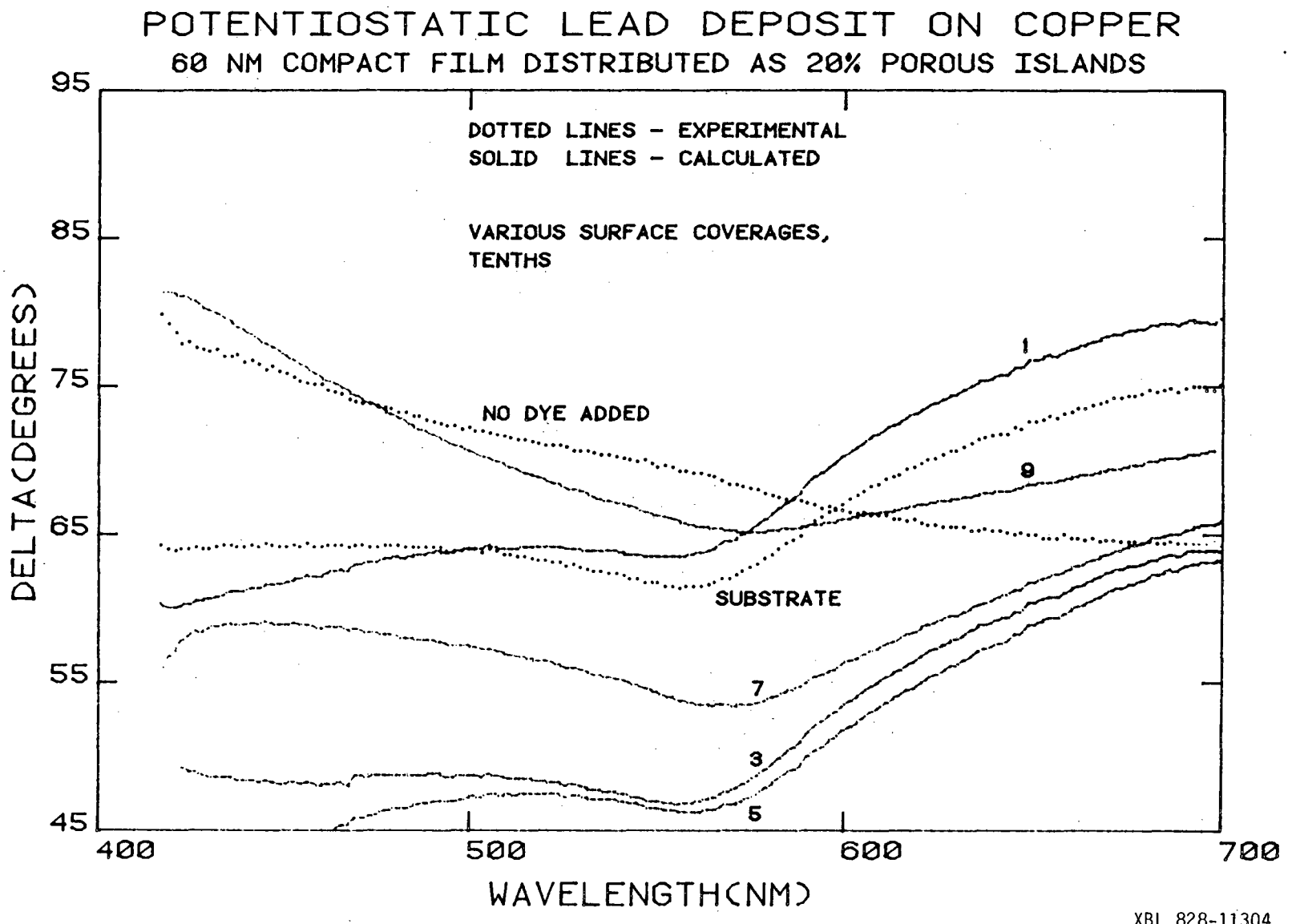

Fig. 12.a

XBL 828-11304

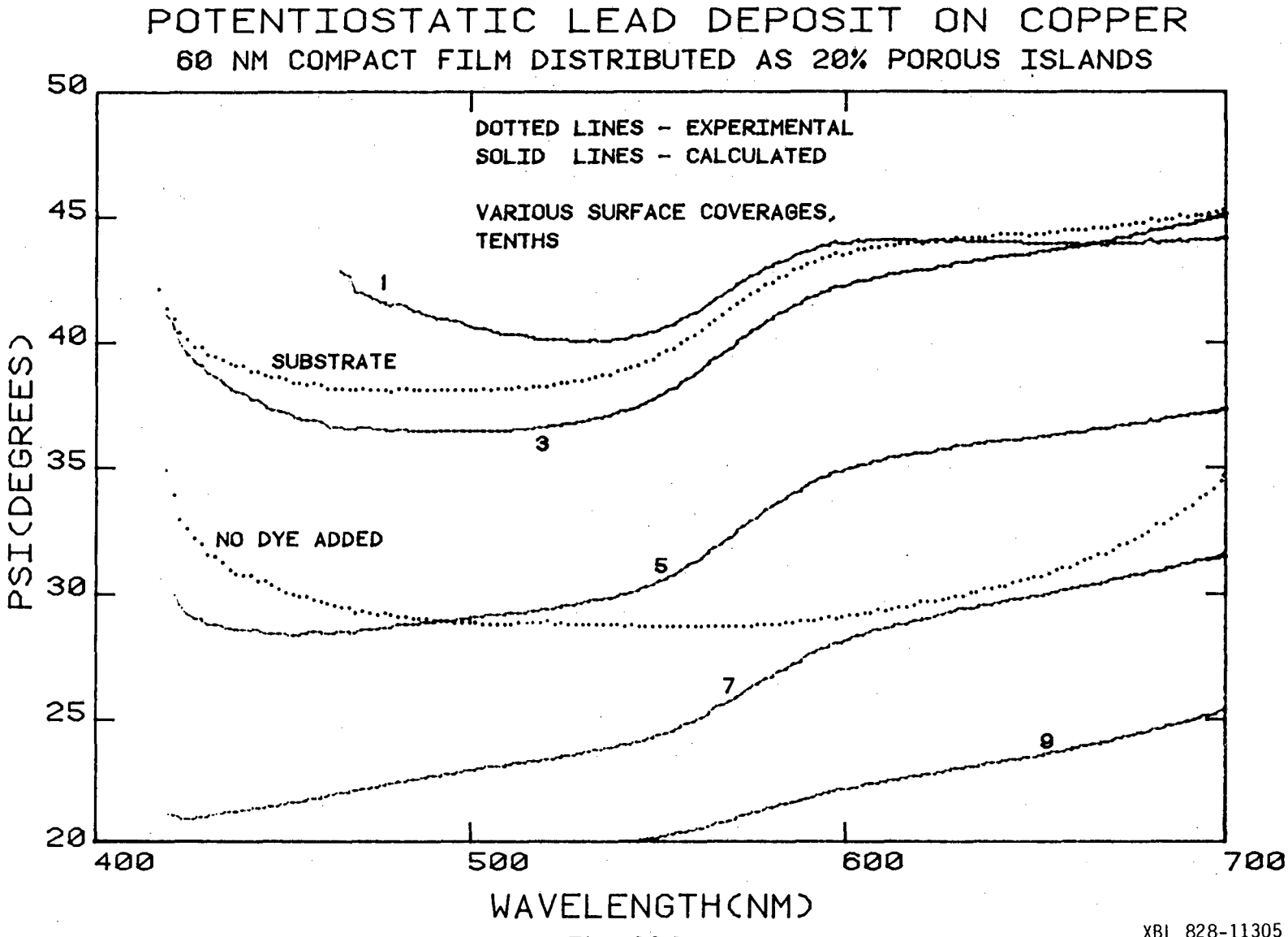

Fig. 12.b

XBL 828-11305

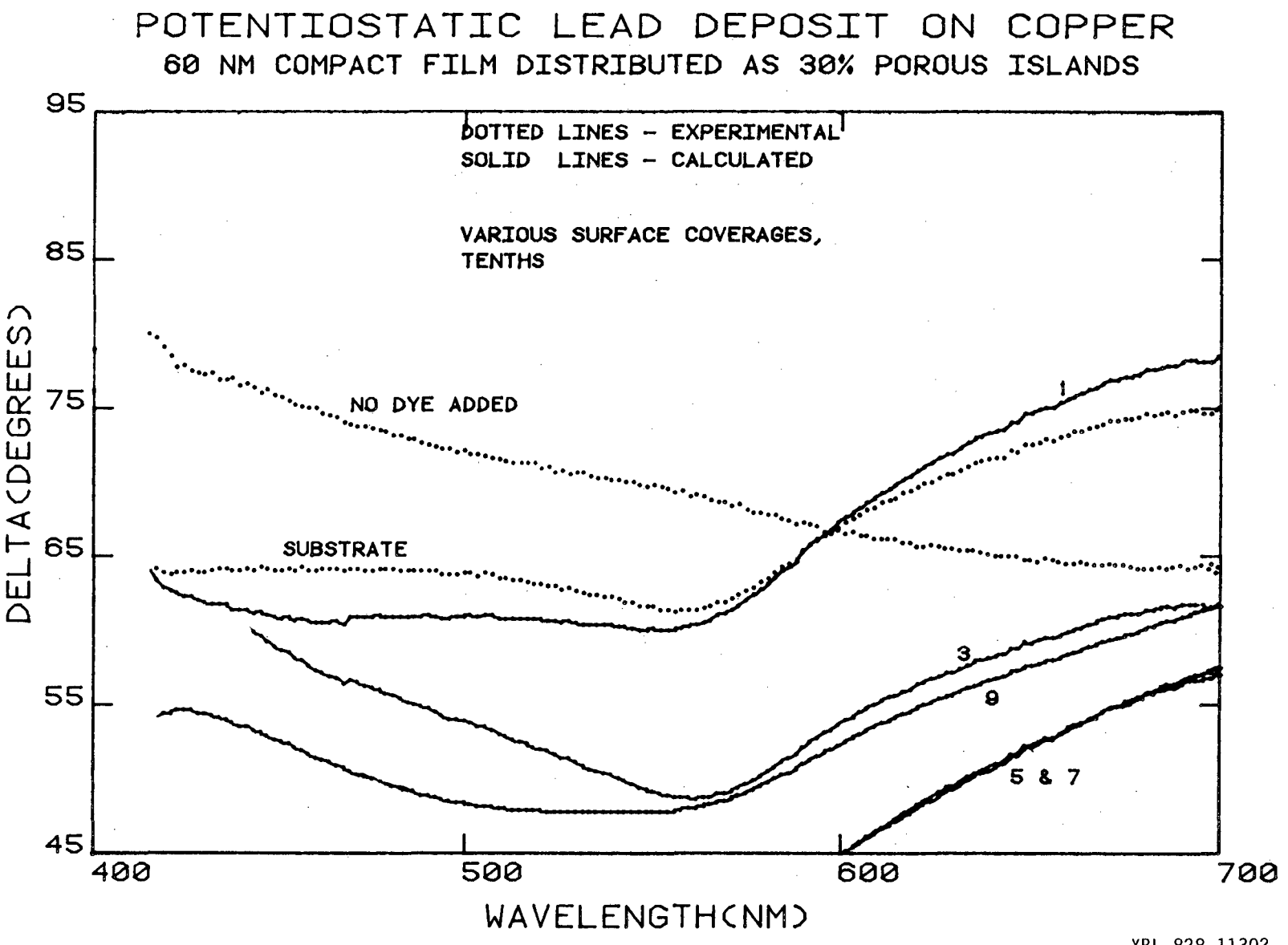

Fig. 12.c

XBL 828-11302

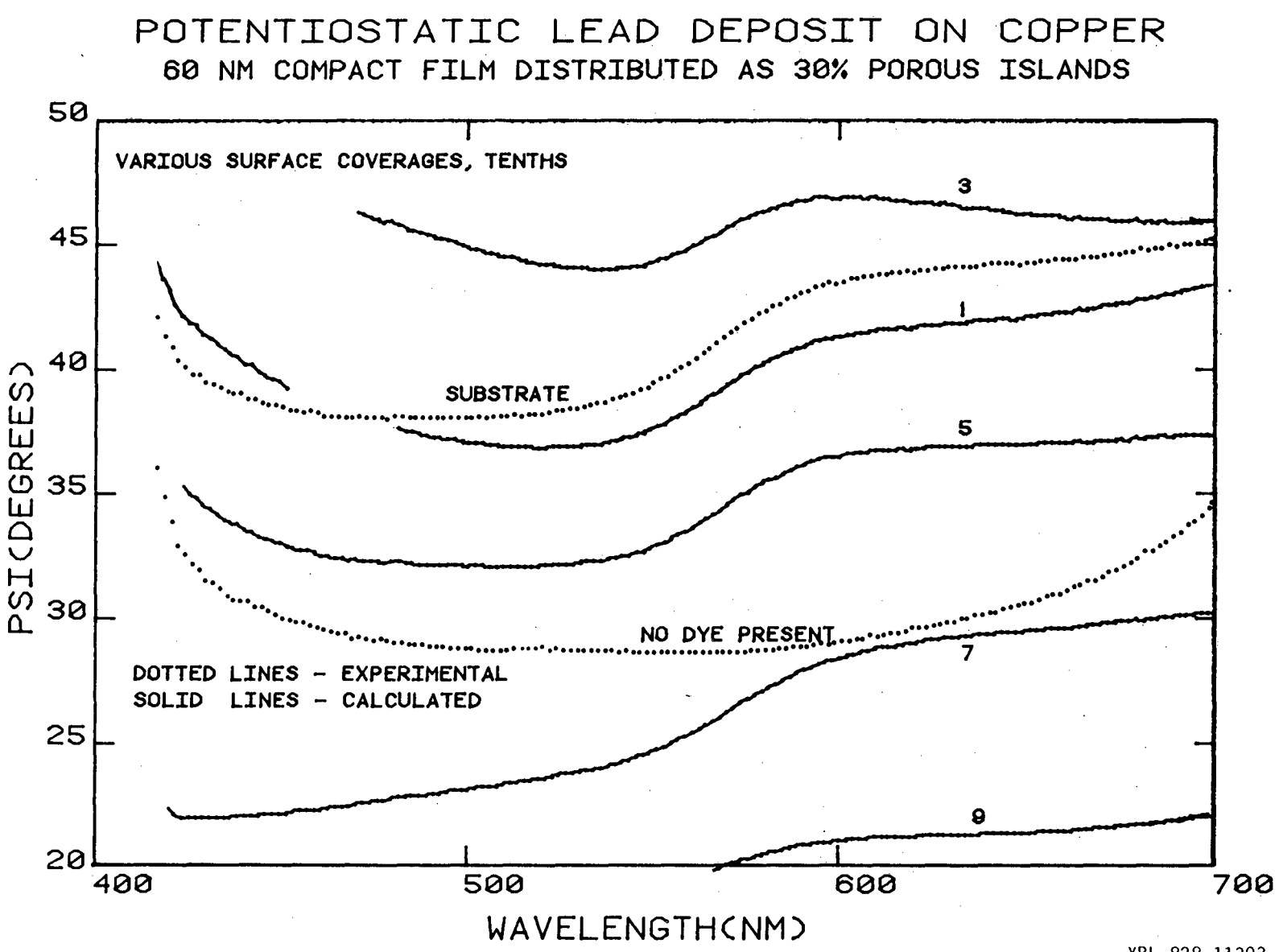

Fig. 12.d

XBL 828-11303

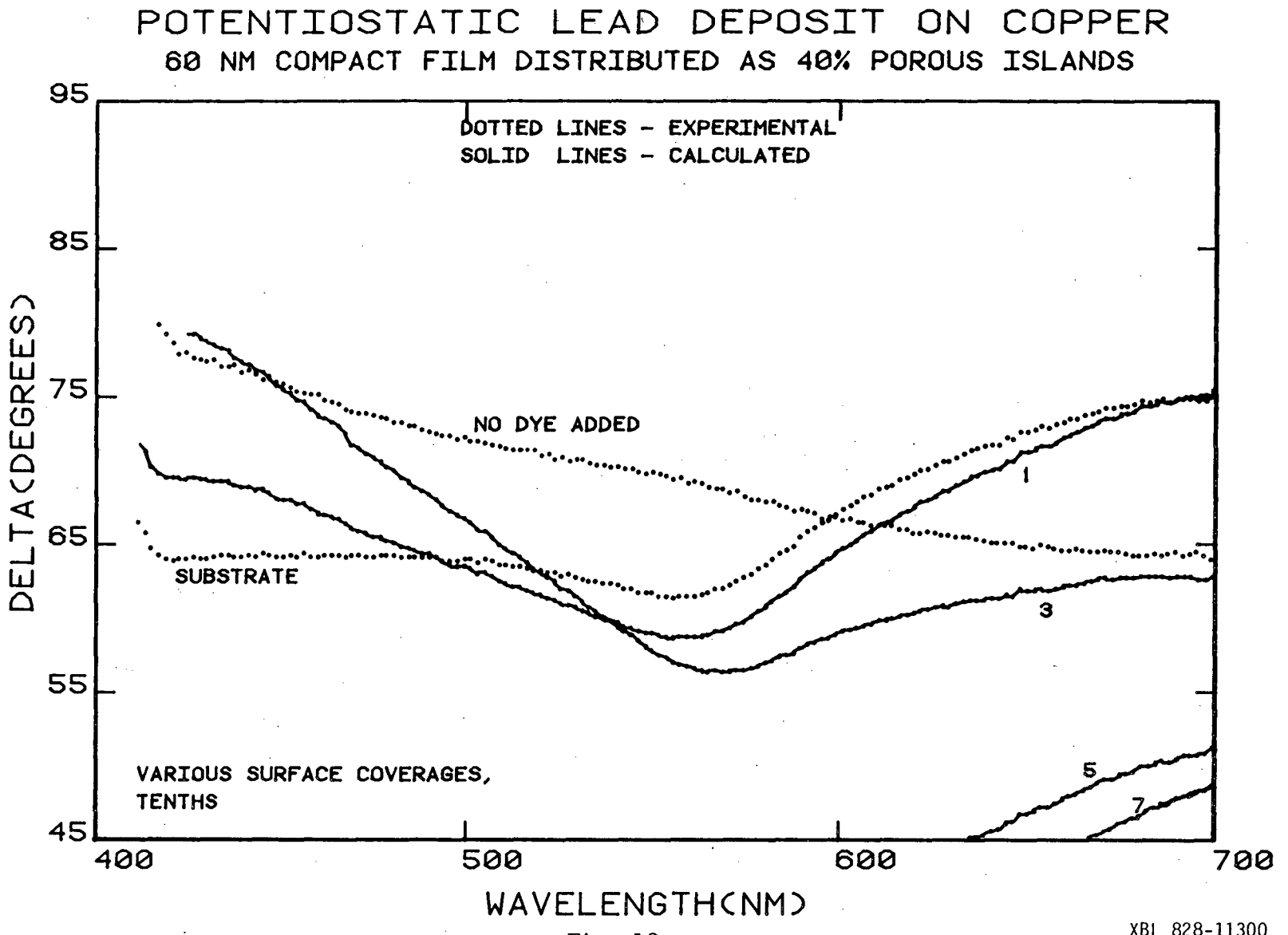

Fig. 12.e

XBL 828-11300

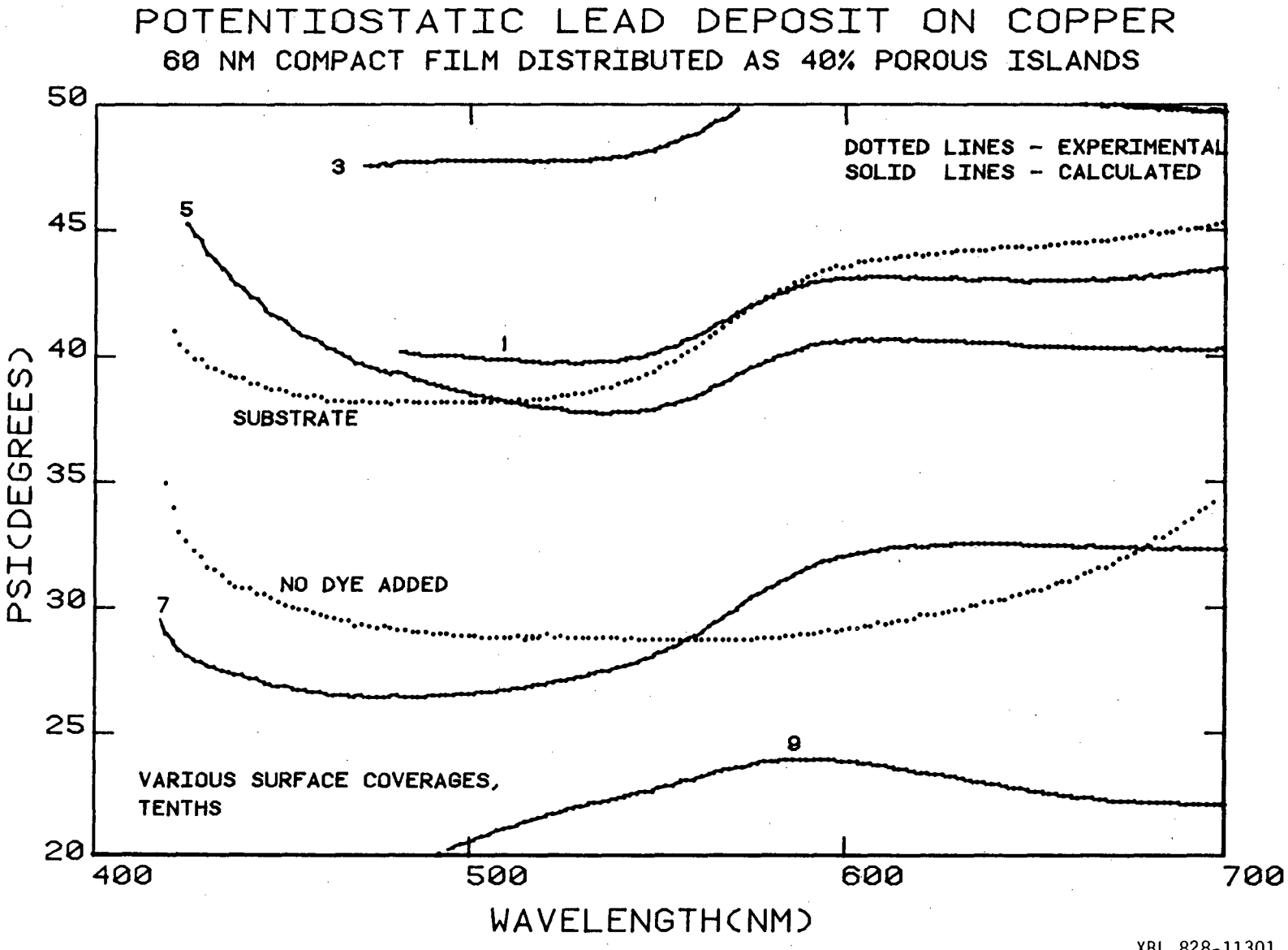

Fig. 12.f

XBL 828-11301

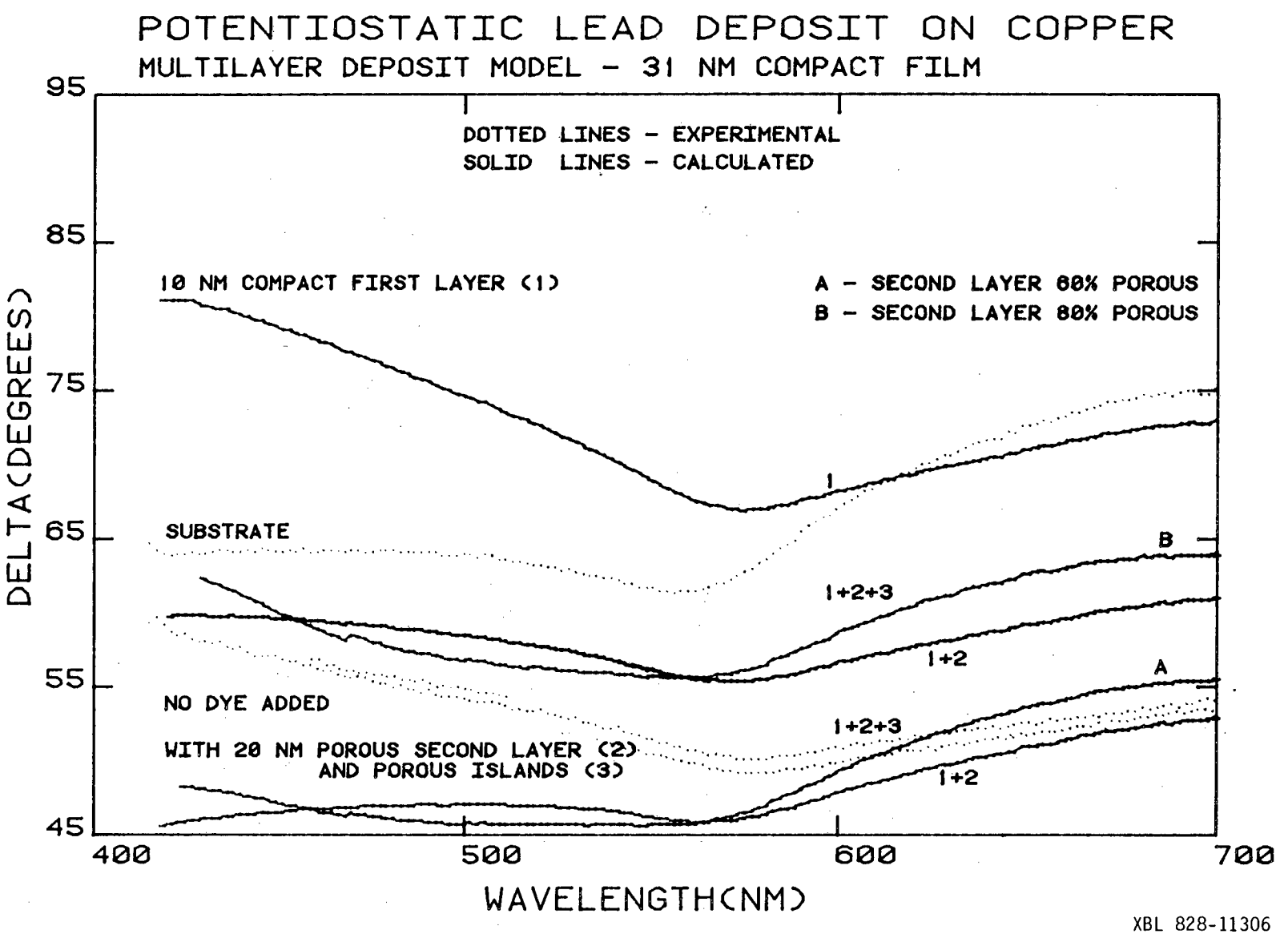

XBL 828-11306

Fig. 13.a

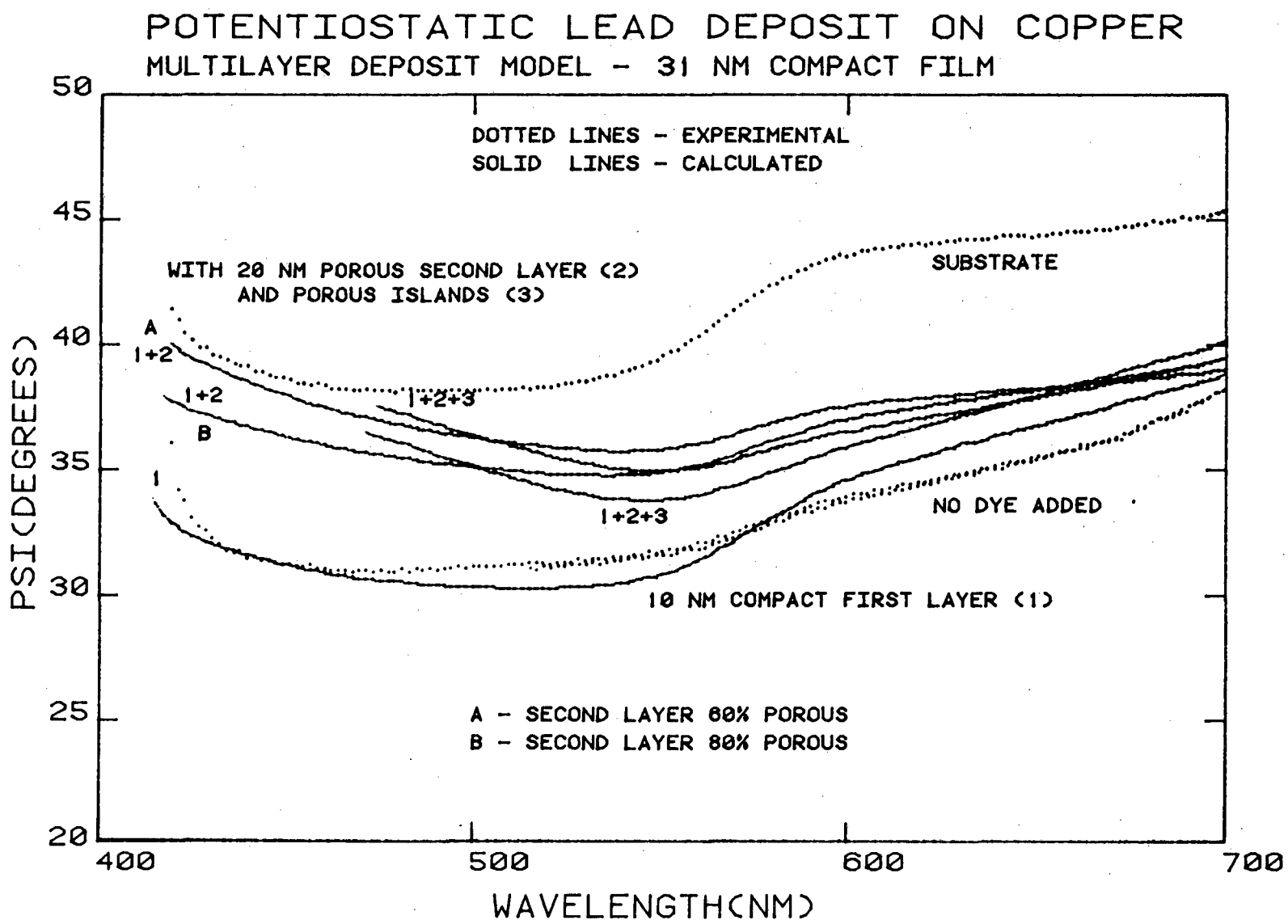

Fig. 13.b

XBL 828-11307

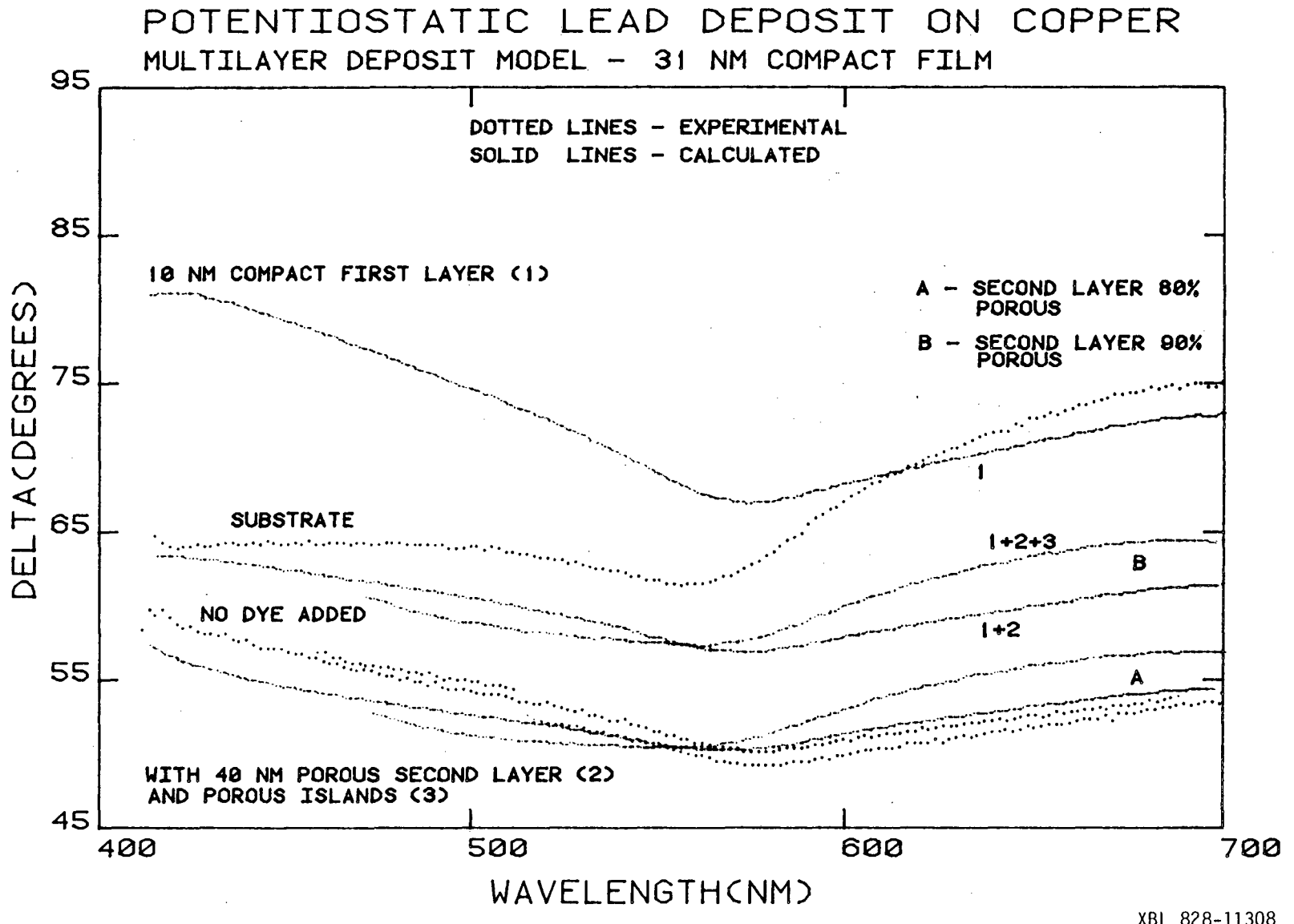

XBL 828-11308

Fig. 13.c

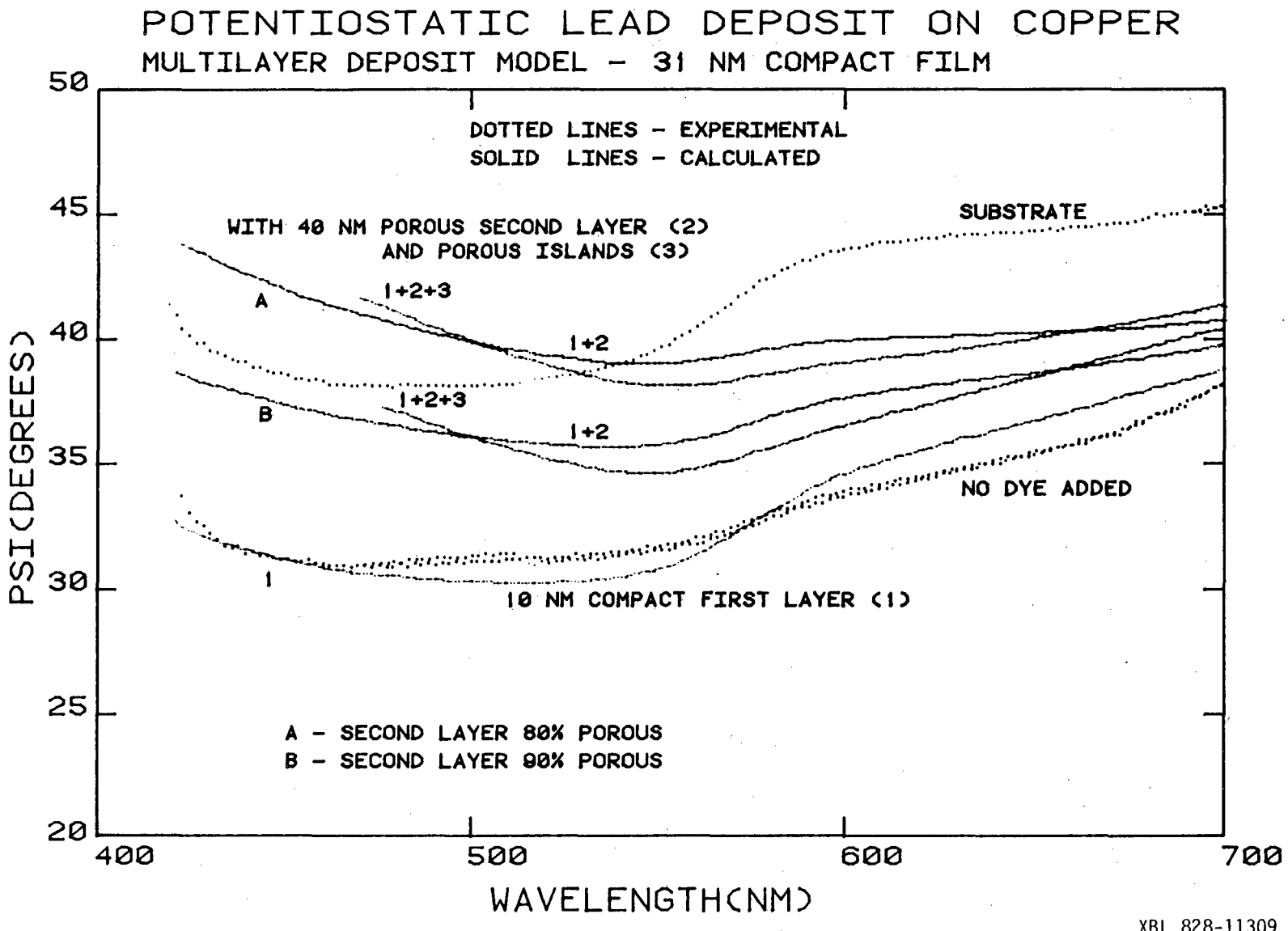

XBL 828-11309

Fig. 13.d

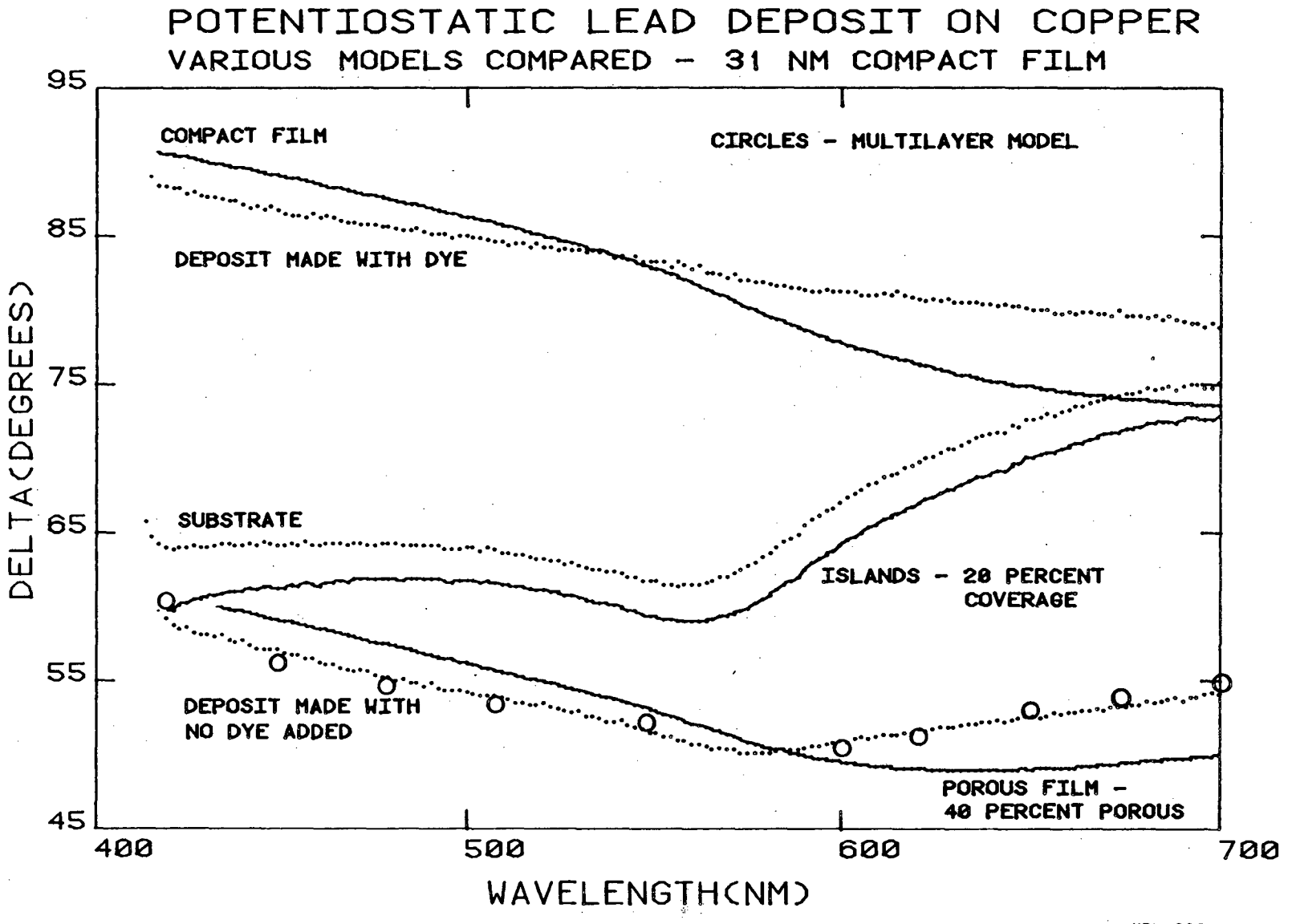

Fig. 14.a

XBL 828-11280

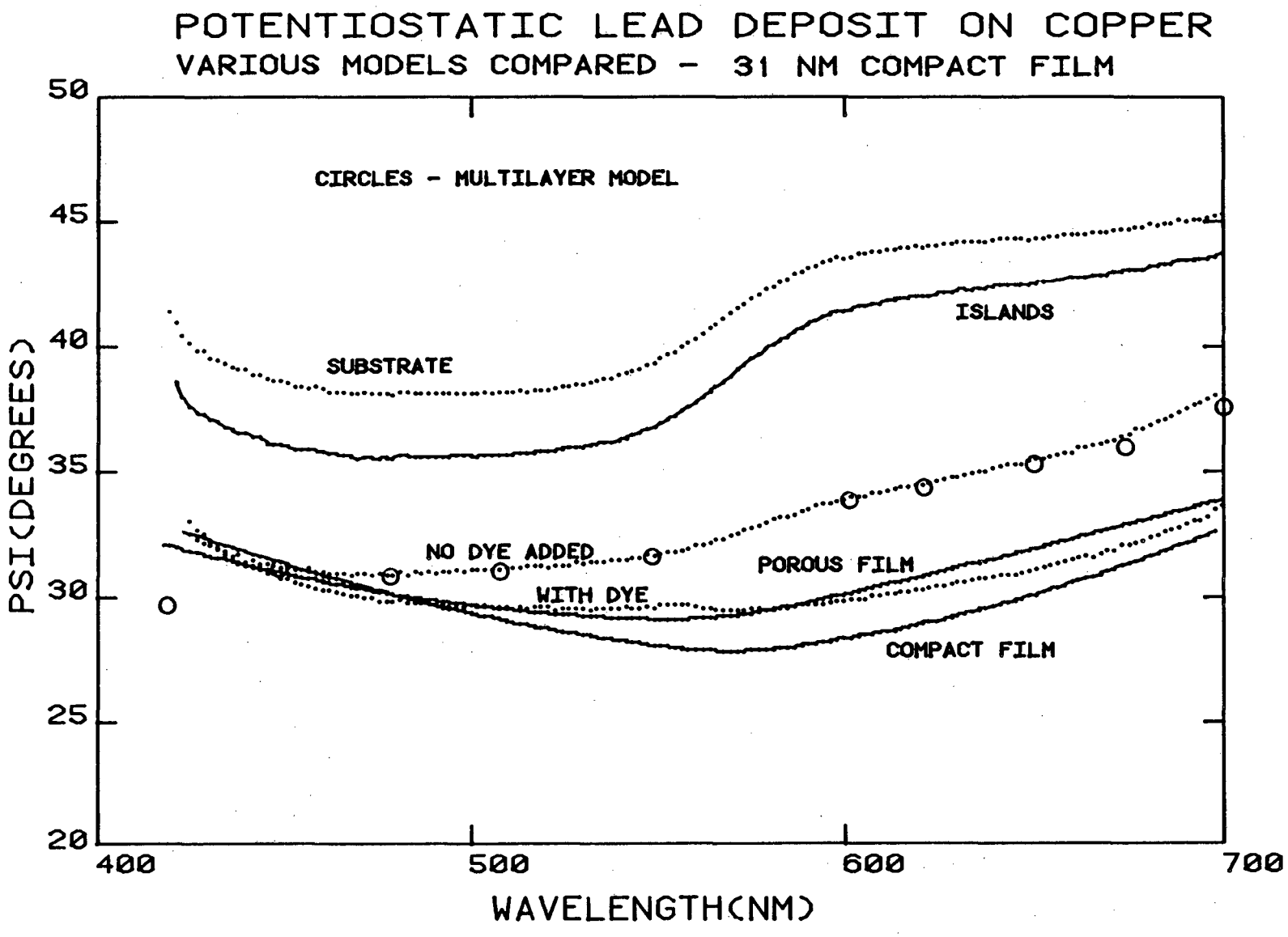

Fig. 14.b

XBL 828-11281

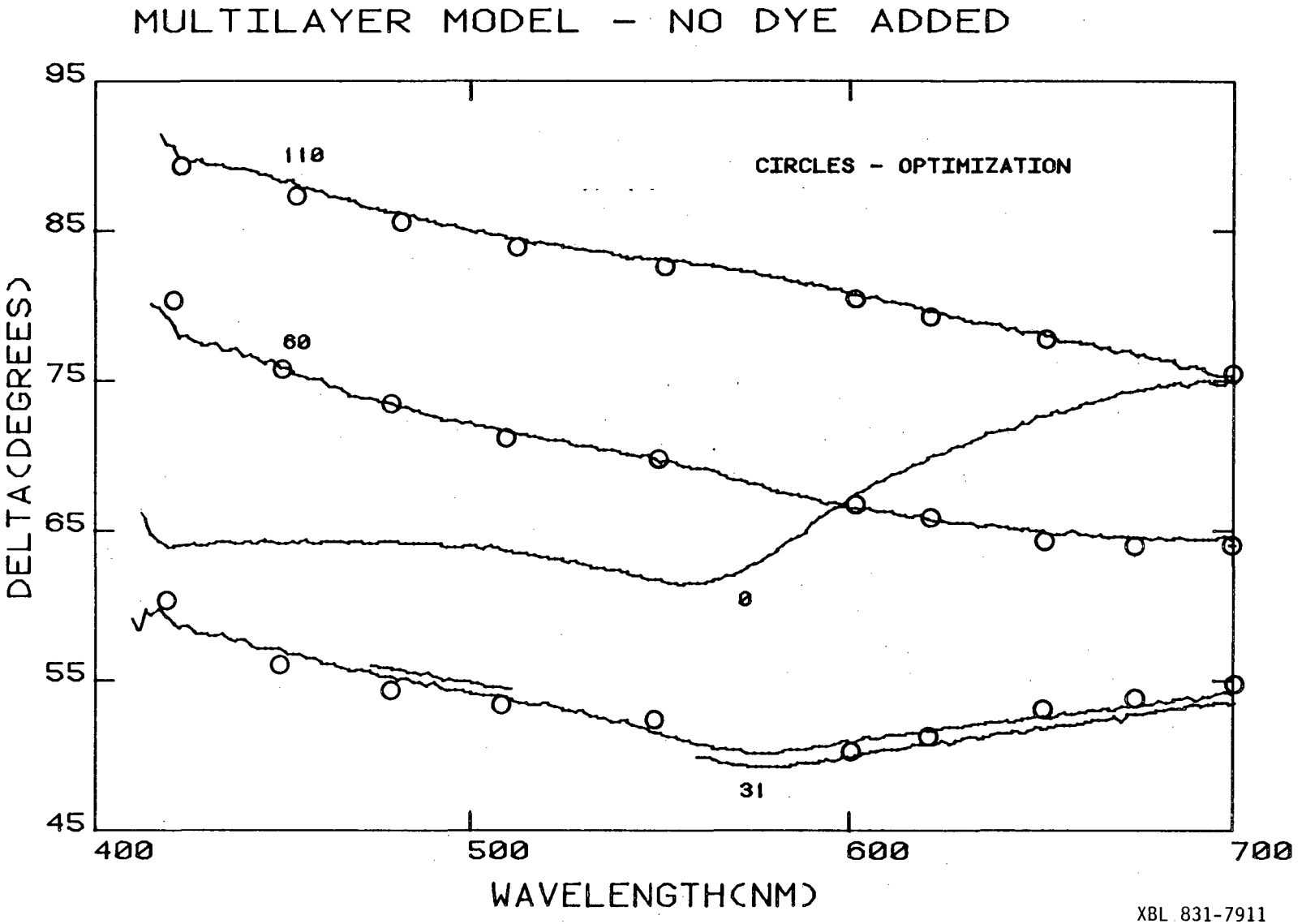

XBL 831-7911

Fig. 15.a

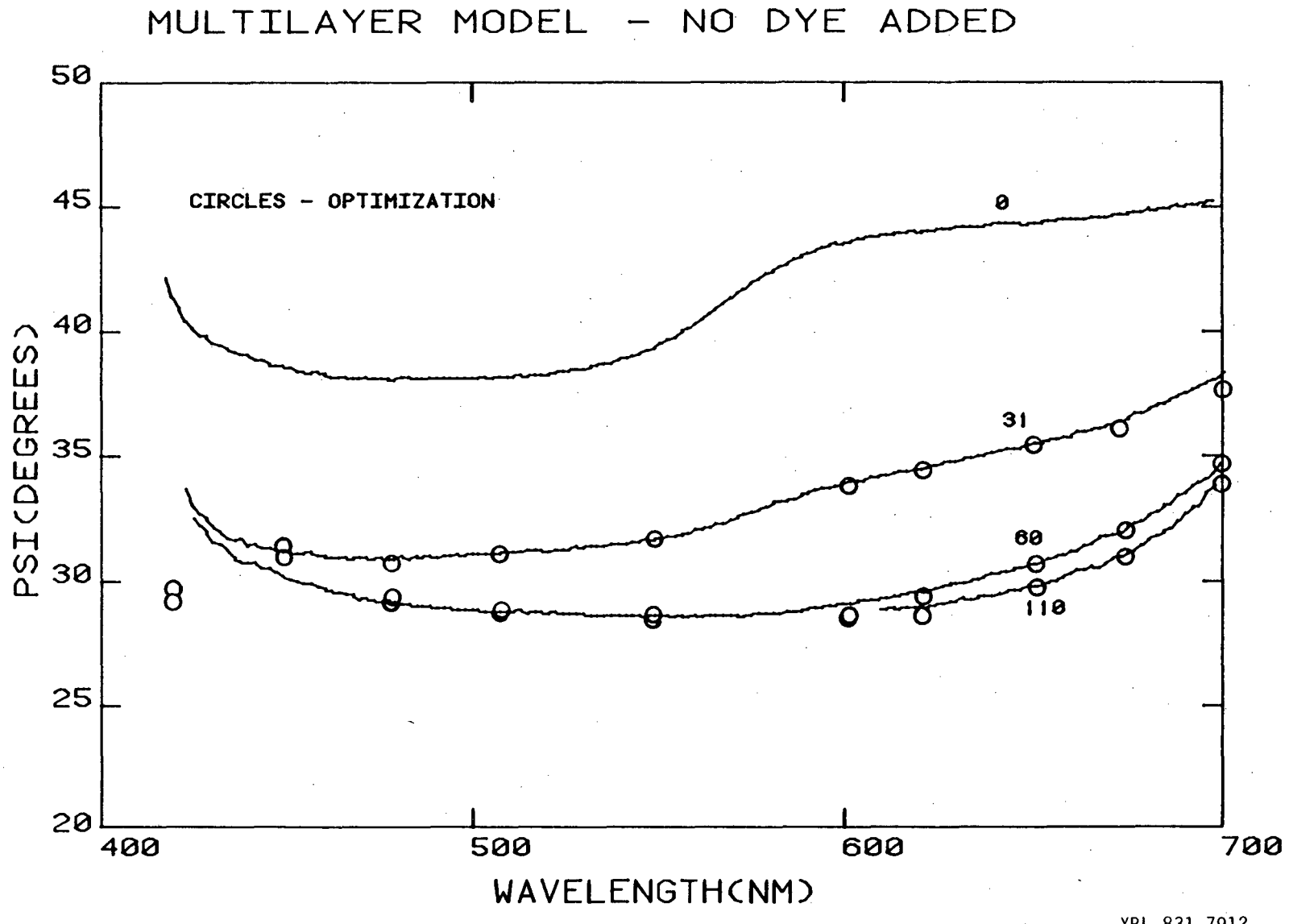

Fig. 15.b

XBL 831-7912

NOMENCLATURE

$\hat{\varepsilon}$	complex dielectric function of the effective medium
$\hat{\varepsilon}_h$	complex dielectric function of the host medium
$\hat{\varepsilon}_i$	complex dielectric function of the i^{th} component
$\hat{\varepsilon}_f$	complex dielectric function of the porous deposit
$\hat{\varepsilon}_{Pb}$	complex dielectric function of metallic Pb
$\hat{\varepsilon}_{soln}$	complex dielectric function of electrolyte
θ_{Pb}	volume fraction Pb in porous deposit
$\hat{n}_f$	film complex refractive index
S	sum-of-squares error between measured and calculated delta ($\Delta_{M,i}$ and $\Delta_{C,i}$ respectively), and between measured and calculated psi ($\Psi_{M,i}$ and $\Psi_{C,i}$ respectively) summed over all i^{th} wavelengths
σ^2	model variance
SE(p)	variance of parameter p
t(2N-P,1-2α)	student-t statistic
Δp	step size used in optimization of parameter p
$S_{(+)}$	S evaluated at the optimum parameter value plus Δp
$S_{(-)}$	S evaluated at the optimum parameter value minus Δp
S_{MIN}	minimum value of S at optimum parameter value

Chapter 8

MODELING SECOND ORDER EFFECTS: RHODAMINE-B ADSORPTION

Abstract

A uniaxial anisotropic film model has been used to simulate spectroscopic measurements of various metallic substrates covered by a monolayer of adsorbed rhodamine-B (dye). Two orientation of the electronic transition moment were assumed, parallel and perpendicular to the surface. The extraordinary and ordinary extinction coefficients of the dye layer were estimated on the basis of dissolved dye extinction coefficients measured by absorption spectroscopy. For a 75 degree angle-of-incidence and over the spectral range of interest (400 to 700 nm) it was found that (theoretically) ellipsometer responses are far greater for species oriented with their transition moment normal to the surface; empirical rules were developed for the interpretation of spectroscopic ellipsometry measurements of adsorbed dye monolayers based upon model calculations.

Experimental spectroscopic ellipsometry measurements for rhodamine-B adsorbed to Pt and Ag(111) are presented. Peaks due to adsorbed dye are interpreted on the basis of the emperical rules derived from spectroscopic simulations. Molecular orientation and surface saturation can be inferred from the spectroscopic ellipsometry measurements. Early measurements of rhodamine-B adsorbed to Cu(111) during Pb deposition are also presented and discussed.

Introduction

A spectroscopic ellipsometer was developed (1) for the purpose of measuring surface concentrations and orientations of adsorbed organic dyes during electrolytic metal deposition. Dyes were chosen as model inhibitors because they are well characterized optically and structurally; they are also available in high purity at low cost. Before more complicated spectroscopic measurements made during metal deposition could be interpreted in regard to adsorbed dye monolayers (second order optical effects), work had to be done in order to understand the sensitivity of the spectroscopic ellipsometer to such surface layers, and is discussed here.

Several dyes were considered for investigation (2); rhodamine-B had the most significant inhibitory effect on Pb electrodeposition and was chosen as the best model inhibitor. In solution, it absorbs light in the spectral range of interest. Substrates of interest were Pt, Ag, Cu, and Pb. The electrolyte (dye solvent) was 5 millimolar $Pb(NO_3)_2$, 1 M $NaClO_4$ acidified to a pH of 3 with $HClO_4$; the electrolyte composition was dictated by the metal ion to be deposited. The acidic electrolyte gave well separated bulk and UPD Pb peaks, and prevented oxidation of the substrates over the potential ranges investigated.

Optical Models of the Dye Monolayer

The theoretical aspects of modeling the dye monolayer are first reviewed. Almost all of the concepts presented here are discussed in a review article by Bootsma (3). This review article compares the Drude model to other, perhaps more correct models like those of Strachan, Sivukin, etc. In this work, the adsorbate layer is treated like a homogeneous, uniaxially anisotropic film.

I. Drude's Model - The Monolayer as a Simple Film of Variable Thickness

The ellipsometry equation describes the change in the state of polarization of a light beam due to reflection through two physical parameters, ψ and Δ, and contains relative amplitude and phase information, respectively (4).

$$\rho = \tan(\Psi)\exp(i\Delta) = r_p/r_s = (E_p^{(r)}/E_p^{(i)})/(E_s^{(r)}/E_s^{(i)}) \qquad (1)$$

$$\Delta = (\delta_p^{(r)} - \delta_s^{(r)}) - (\delta_p^{(i)} - \delta_s^{(i)}) \qquad (2)$$

$$\Psi = (A_p^{(r)}/A_p^{(i)})/(A_s^{(r)}/A_s^{(i)}) \qquad (3)$$

$$E_\nu^{(\ )} = A_\nu^{(\ )} \exp(i\delta_\nu^{(\ )}) \quad \& \quad \nu = s,p \ (\ ) = (r,i) \tag{4}$$

where the subscripts, s and p, refer to the polarization states normal and parallel to the plane of incidence for the propagating electromagnetic wave vector, $E_\nu^{(\ )}$; the superscripts, i and r, refer to the incident and reflected beams, respectively; $\delta_\nu^{(\ )}$ and $A_\nu^{(\ )}$ are the phase and amplitude of $E_\nu^{(\ )}$; and r_ν is the reflection coefficient for the specified polarization.

For reflection from a single, linear, homogeneous, and isotropic film covering some isotropic substrate, the reflection coefficients are given by the Drude equation

$$r_\nu = \frac{r_{1\nu} + r_{2\nu}\exp(-iD)}{1 + r_{1\nu}r_{2\nu}\exp(-iD)} \qquad \nu = s,p \tag{5.a}$$

The Fresnel reflection coefficients for ambient-film and film-substrate interfaces, denoted 1 and 2, and for s and p polarizations are given as Eqns. 5.b through 5.e.

$$r_{1p} = \tan(\phi - \hat{\phi}_f)/\tan(\phi + \hat{\phi}_f) \tag{5.b}$$

$$-r_{1s} = \sin(\phi - \hat{\phi}_f)/\sin(\phi + \hat{\phi}_f) \tag{5.c}$$

$$-r_{2s} = \sin(\hat{\phi}_f - \hat{\phi}_s)/\sin(\hat{\phi}_f + \hat{\phi}_s) \tag{5.d}$$

$$r_{2p} = \tan(\hat{\phi}_f - \hat{\phi}_s)/\tan(\hat{\phi}_f + \hat{\phi}_s) \tag{5.e}$$

The phase delay in the film is given by Eqn. 6.

$$D = 4\pi\ (d/\lambda_o)\ \hat{n}_f\ \cos(\hat{\phi}_f) \tag{6}$$

where the subscripts, 1 and 2, refer to the film and substrate, respectively; ϕ, $\hat{\phi}_f$, and $\hat{\phi}_s$ are the ambient-film angle-of-incidence, the film-substrate complex angle-of-incidence, and the substrate complex angle-of-incidence, respectively; d is the film thickness; λ_o is the vacuum wavelength; and $\hat{n}_f$ is the complex refractive index for the film. It is also necessary to relate the three angles of incidence through Snell's law.

$$n \sin(\phi) = \hat{n}_f\ \sin(\hat{\phi}_f) = \hat{n}_s\ \sin(\hat{\phi}_s) \tag{7}$$

where $\hat{n}_s$ is the substrate complex refractive index. From inspection of these equations, it is clear that the ellipsometer parameters, Δ and ψ, contain information on the physical nature of the film; i.e., its complex refractive index, $\hat{n}_f$, and its thickness, d. Experimentally, the substrate refractive index, $\hat{n}_s$, is a known quantity, determined from ellipsometric measurements of Δ and ψ by reflection from bare (film-free) substrate. As will be seen in subsequent discussion, the real-part of the refractive indices can be related to the molecular electronic polarizability of the medium, and the imaginary-part can be related to the light absorptive properties, the extinction coefficient. The pronounced spectral dependence of the extinction coefficient make molecule-specific ellipsometry possible through spectral scanning ellipsometry, as will be seen from the spectroscopic simulations and experimental data to be discussed subsequently.

At this point it is important to emphasize that the above equations only apply to isotropic systems; i.e., systems where the refractive index is independent of directionality. Generally, for monolayers this is not true, since electronic transitions responsible for light absorption occur in specific geometric planes (determined by how the molecule is oriented when bonded to the surface). Since molecules are anisotropic, so are monolayers.

Though the simple film model presented above is not the most appropriate for submonolayer measurement, due to its simplicity and linearizations of it for $d \ll \lambda_0$, it has been widely used for adsorption studies (5,6).

A linearization also introduced by Drude is presented below which includes only first order terms of d/λ_0 and assumes a nonabsorbing ambient (3).

$$\tan(\Psi)\exp(i\Delta) = \tan(\overline{\Psi})\exp(i\overline{\Delta})\ x \\ [1 - iF(4\pi\ \hat{n}_s^4\ \cos\phi\ \sin^2\phi)/(\hat{n}_s^2\ - 1)(\hat{n}_s^2\ \cos^2\phi - \sin^2\phi)] \tag{8}$$

$$F = (\hat{n}_f^2\ - 1)(\hat{n}_f^{-2}\ - \hat{n}_s^{-2}\ )d \tag{9}$$

It is important to note that upon inversion of this equation, an expression is obtained which is linear in the thickness, d. The exact functionality of f and g are also given by Bootsma (3).

$$\delta\Delta = d\cdot f(n,\phi,\hat{n}_f,\hat{n}_s) \tag{10}$$

$$\delta\Psi = d\cdot g(\hat{n},\phi,\hat{n}_f,\hat{n}_s) \tag{11}$$

This linearization, called the Drude approximation (not to be confused with the Drude equation), rests on the assumption that the fractional coverage, θ, is identical to some fraction of the thickness of and adsorbed monolayer, d. Since this equivalent thickness, d, is less than the dimension of the adsorbate normal to the interface, it has no physi-

cal significance (and disturbs many people). However, such a model has some merit in that in some special cases, Δ and ψ have been observed experimentally to vary linearly with θ, as predicted. However, other models too can account for such linear behavior in the monolayer region, which do not assume a variable thickness (7). Such a linear variation of delta and psi with surface concentration makes the following convention convenient for the presentation of spectroscopic measurements.

$$\delta\Delta = \overline{\Delta} - \Delta \tag{12}$$

$$\delta\Psi = \overline{\Psi} - \Psi \tag{13}$$

$$\delta\Delta, \delta\Psi \propto d(\theta) \tag{14}$$

This linearization is also the incentive for presenting spectroscopic measurements as differences from background values, as will be discussed subsequently.

Summarizing, Drude's approximation treats the adsorbate layer as if it were a homogeneous, isotropic film and uses interpretable macroscopic optical constants n and k, the refractive index and extinction coefficient, respectively. The model assumes that the film thickness, d, varies with the coverage, θ; consequently, the differences in delta and

psi, $\delta\Delta$ and $\delta\psi$, also vary linearly with coverage.

II. Strachan's Model - Adsorbate Molecules as 3-D Scattering Centers

The interfacial surface is assumed to be a two-dimensional distribution of Hertzian oscillators, characterized by scattering indices σ_x, σ_y, and σ_z where the z-axis is normal to the interface. Strachan does not give a microscopic interpretation of the scattering indices in terms of structure or molecular polarizabilities. Hence, one is at a loss with this model when trying to incorporate available optical property data for molecules into calculations from first principles. At very low coverages one might assume that the oscillator strength per element of interfacial area is linearly proportional to the number of oscillators present, so that σ_i ($i = x,y,z$) is proportional to θ. This is reasonable, if molecular interactions in the interface are ignored. In this case, the inverted Eqn. 8 still predicts a linear response of Δ and ψ. The parameter F above is now defined as

$$F = 4\pi(\sigma_z - \sigma_x/\hat{n}_s^2) \qquad (15)$$

The key advantage of this model is its ability to account for anisotropy. The disadvantage is that the scattering parameters can't be readily interpreted in terms of available optical data; i.e., refractive indices, extinction coefficients, etc.

Summarizing, Strachan's model assumes a biaxially anisotropic film, but has the disadvantage of uninterpretable optical constants, σ_x, σ_y,

and σ_z; it is assumed that these oscillator strengths vary with coverage, θ. The differences in Δ and ψ, $\delta\Delta$ and $\delta\psi$ are proportional to the oscillator strengths σ_i (i = x,y,z) which are in turn proportional to θ.

III. Sivukin's Model - Interfacial Polarizability Change due to Adsorption

Sivukin characterizes the interface by ratios of the interfacial polarizability, τ_i (i = x,y,z), to that of the substrate, P_i (i = x,y,z).

$$\gamma_i = \tau_i/P_i \qquad i = x,y,z \tag{16}$$

$$F = (\gamma_z - \gamma_x)(1-1/\hat{n}_s^2) \tag{17}$$

This model too allows for anisotropy normal to the surface and has the advantage of physically interpretable optical parameters. Note that isotropy has been assumed in the plane of the interface; i.e., $\gamma_x = \gamma_y$. Also, the substrate is assumed to be only uniaxially anisotropic, normal to the interface. Expressions for γ_z and γ_y are given by Bootsma in his review. These equations are very complicated in that they involve both cross-sectional and intermolecular distances for adsorbed atoms in the interface in such a way that makes γ_i (i = x,y,z) highly nonlinear in the fractional coverage, θ. This model was derived with a solid sub-

strate in mind and involves physical parameters such as the lattice sum and adsorbate molecule distance above the substrate atoms. In a liquid interface such physical interpretations are dubious since the "substrate," or lower phase solvent, also adsorbs to the interface to some extent, along with molecules from the ambient.

Summarizing, Sivukin's model assumes a uniaxial anisotropic film and has interpretable optical constants γ_z and $\gamma_{x,y}$ related to the polarizability of the film relative to the substrate. These optical constants vary with θ in a highly nonlinear fashion since γ_i ($i = x,y,z$) depends on both adsorbate molecular spacing and cross-section.

IV. Anisotropic Film - Adsorbate Layer as Film of Variable Birefringence

This approach is similar to the Drude model first presented, except it is assumed that the interfacial thickness is constant and equivalent to the adsorbate monolayer thickness. Instead of a variable film thickness, it is assumed that changes of the interfacial concentration result in changes in the apparent optical properties of this film of fixed thickness, d. Furthermore, the anisotropy of the adsorbate layer is taken into consideration by application of the equations presented by Azzam and Bashara (8) for a linear, homogeneous uniaxially anisotropic film with the optic axis normal to the interface. The ellipsometry equation is written as Eqn. 18.

$$\tan(\Psi)\exp(i\Delta) = \frac{R_{pp} + R_{ps} \div [\tan(\Psi^{(i)})\exp(i\Delta^{(i)})]}{R_{ss} + R_{sp} \times [\tan(\Psi^{(i)})\exp(i\Delta^{(i)})]} \tag{18}$$

where the reflection coefficients, R_{pp}, etc., are defined by the reflection matrix, Eqn. 19; the reflection matrix is then defined by Eqn. 20.

$$E^{(r)} = R\, E^{(i)} \tag{19}$$

$$R = \begin{vmatrix} R_{pp} & R_{ps} \\ R_{sp} & R_{ss} \end{vmatrix} \tag{20}$$

Because of symmetry, when the incident wave in the ambient is either p or s polarized, the excited wave in the isotropic substrate will posses the same polarization. The reflection matrix is therefore diagonal; this allows equation 18 to be simplified to the form given as Eqn. 21.

$$\tan(\Psi)\exp(i\Delta) = R_{pp}/R_{ss} \tag{21}$$

Note that Eqn. 21 is analogous in form to Eqn. 1. The reflection coefficients are defined by Eqn. 22.a and 22.b.

$$R_{pp} = \frac{r_{01_{pp}} + r_{12_{pp}} \exp(-i\beta_p)}{1 + r_{01_{pp}} r_{12_{ss}} \exp(-i\beta_p)} \tag{22.a}$$

$$R_{ss} = \frac{r_{01_{ss}} + r_{12_{ss}} \exp(-i\beta_s)}{1 + r_{01_{ss}} r_{12_{pp}} \exp(-i\beta_s)} \tag{22.b}$$

Eqns. 22.c and 22.d are the interfacial reflection coefficients for the p polarization at the ambient-film and film-substrate interfaces, respectively. The "pp" subscript denotes diagonal terms in the reflection matrix; no off-diagonal terms are necessary for a uniaxial film.

$$r_{01_{pp}} = \frac{\hat{n}_{fo}\hat{n}_{fe}\cos\phi - n(\hat{n}_{fe}^2 - n^2\sin^2\phi)^{1/2}}{\hat{n}_{fo}\hat{n}_{fe}\cos\phi + n(\hat{n}_{fe}^2 - n^2\sin^2\phi)^{1/2}} \tag{22.c}$$

$$r_{12_{pp}} = \frac{-\hat{n}_{fo}\hat{n}_{fe}\cos\hat{\phi}_s + \hat{n}_s(\hat{n}_{fe}^2 - \hat{n}_s^2\sin^2\hat{\phi}_s)^{1/2}}{\hat{n}_{fo}\hat{n}_{fe}\cos\phi_s + \hat{n}_s(\hat{n}_{fe}^2 - \hat{n}_s^2\sin^2\phi_s)^{1/2}} \tag{22.d}$$

Eqns. 22.e and 22.f are the interfacial reflection coefficients for the s polarization at the ambient-film and film-substrate interfaces, respectively.

$$r_{01_{ss}} = \frac{n\cos\phi - (\hat{n}_{fo}^2 - n^2\sin^2\phi)^{1/2}}{n\cos\phi + (\hat{n}_{fo}^2 - n^2\sin^2\phi)^{1/2}} \tag{22.e}$$

$$r_{12_{ss}} = \frac{-\hat{n}_s\cos\hat{\phi}_s + (\hat{n}_{fo}^2 - \hat{n}_s^2\sin^2\hat{\phi}_s)^{1/2}}{\hat{n}_s\cos\hat{\phi}_s + (\hat{n}_{fo}^2 - \hat{n}_s^2\sin^2\hat{\phi}_s)^{1/2}} \tag{22.f}$$

Snell's law, Eqn. 22.g, is also used.

$$n \sin\phi = \hat{n}_s \sin\hat{\phi}_s \tag{22.g}$$

The phase delays of the p and s polarizations are given as Eqns. 22.h and 22.i, respectively.

$$\beta_p = 4\pi(d/\lambda_o)(\hat{n}_{fo}/\hat{n}_{fe})(\hat{n}_{fe}^2 - n^2\sin^2\phi)^{1/2} \tag{22.h}$$

$$\beta_s = 4\pi(d/\lambda_o)(\hat{n}_{fo}^2 - n^2\sin^2\phi)^{1/2} \tag{22.i}$$

where n is the ambient refractive index; $\hat{n}_{fo}$ and $\hat{n}_{fe}$ the complex ordinary and extraordinary refractive indices, respectively; $\hat{n}_s$ is the complex substrate refractive index; ϕ is the ambient angle-of-incidence; and $\hat{\phi}_s$ the complex angle-of-refraction in the substrate. The film complex refractive indices are

$$\hat{n}_{fe} = n_{fe} + k_{fe}\, i \tag{23.a}$$

$$\hat{n}_{fo} = n_{fo} + k_{fo}\, i \tag{23.b}$$

Both the ordinary and extraordinary complex refractive index have a real and imaginary part, their respective refractive indices and extinction coefficients.

V. Coverage and Molecular Orientation from the Anisotropic Film Model

One is faced with the problem of estimating realistic optical constants for the dye adsorbate layer. Any of several strategies might be considered. For example, optical properties could be calculated from those of the dye and solvent adatoms by application of the Bruggeman theory.

However, in this special case the primary distinction of the dye adsorbate layer is its large extinction coefficient at the maximum absorption wavelength; at other wavelengths the optical constants are similar to those of the solvent (relatively small, practically zero extinction coefficient). As the dye populates the surface, the extinction coefficient at the maximum absorption wavelength would be expected to increase from zero to some value corresponding to complete coverage; one can use a Beer's law argument to estimate the increased absorption of the film at this specific wavelength. Application of Beer's law allows one to extrapolate the extinction coefficient of dissolved dye to volummetric concentrations comparable to the dye monolayer; this assumes that the maximum absorption wavelength is not shifted by electronic interactions with the surface. Furthermore, it is recognized that dissolved dye has random orientation in the liquid phase and probably has a specific orientation when adsorbed to a metallic surface, which is

manifested as dichroism in the adsorbate layer extinction coefficient (defined as $k_o - k_e$). The electric field vector parallel to the electronic transition moment of the dye molecule (responsible for light absorption) is attenuated to a greater extent than the normally oriented electric field vector; i.e., the extinction coefficient parallel to the electronic transition moment will be much greater than extinction coefficients in other directions (which will be approximately zero). So, by measuring both the magnitude and anisotropy of the extinction coefficient of the dye adsorbate layer at the maximum absorption wavelength relative to that at other wavelengths, one can determine coverage and molecular orientation, respectively. Parallel and perpendicular orientations of a rhodamine-B molecule adsorbed to a surface (x,y plane) are shown in Fig. 1 (geometric representation).

In order to calculate the adsorbate layer extinction coefficient, one must first know the volumetric concentration of dye molecules in the layer; this allows extrapolation of absorption measurements for dissolved dye concentrations (dilute relative to adsorbate layer) by application of Beer's law. The volumetric concentration of dye molecules in the adsorbate layer is calculated from the volume occupied by a single molecule and the total number of molecules that can be close-packed on the surface (limiting case); the volume occupied by a single molecule is calculated from the molecule's dimensions, which are based upon bond lengths. The following standard bond lengths were assumed for this calculation:

-C=C-	carbon-carbon double bonds	1.53 Angstroms
-C-C-	carbon-carbon single bonds	1.54 Angstroms
-C-O-	carbon-oxygen single bonds	1.47 Angstroms
-C=N-	carbon-nitrogen double bonds	1.43 Angstroms
-C-N-	carbon-nitrogen single bonds	1.47 Angstroms
-C-H-	carbon-hydrogen single bonds	1.10 Angstroms

Bond angles for the tertiary amine group and aromatic structure are taken as 120 degrees. The calculated length of the rhodamine-B molecule in the direction parallel to the transition moment (parallel to the line passing through the two nitrogen atoms) is 25 Angstroms; the thickness of the rhodamine-B molecule is taken to be the same as for a benzene ring, about 5 Angstroms; and the third dimension of the molecule is calculated to be approximately 10 Angstroms. The volume occupied by a single molecule is then assumed to be that of a box with dimensions of 5 x 10 x 25 cubic angstroms (1250 cubic Angstroms); the inverse of this number (for the close-packed case) is the volumetric concentration of molecules in the adsorbate layer. Note that the volumetric concentration of the adsorbate layer is independent of orientation (8×10^{20} molecules per cm^3 for close-packed case), though the surface concentration (molecules per unit surface area) is not. The thickness of the adsorbate layer also depends upon orientation.

Two molecular orientations are considered which are consistent with concepts of adsorption on a metallic surface. First, the dye molecule could bond to the surface with its pi-electrons, in which case it would lie with its electronic transition moment parallel to the electrode surface (9). The adsorbate layer thickness would then be about 5 Angstroms, the extinction coefficient parallel to the x,y-plane would be

non-zero, and the extinction coefficient parallel to the z-axis would be zero; the corresponding surface concentration would be 4×10^{13} molecules per cm^2.

Alternatively, the dye molecule could have its transition moment perpendicular to the surface if it acts as a cation (10); the cationic amine group would be closest to the surface due to attractive interaction with the image charge in the surface. The corresponding thickness would be 25 Angstroms, the extinction coefficient along the z-axis would be non-zero, and the extinction coefficient parallel to the x,y-plane would be approximately zero; the corresponding surface concentration would be 2×10^{14} molecules per cm^2.

Beer's law can be stated in terms of the entering and exiting light intensities, I_0 and I, the decadic molar extinction coefficient, ε, the molar concentration, [M], and the path length, d, by Eqn. 24 (11).

$$\log \frac{I}{I_0} = - \varepsilon [M]d \qquad (24)$$

It can also be stated in terms of the absorption coefficient, α, the extinction coefficient, k, and the wavelength, λ, by equations 25 and 26 (12).

$$\ell n \frac{I}{I_0} = - \alpha d \qquad (25)$$

$$\ell n \frac{I}{I_o} = - \frac{4\pi kd}{\lambda} \qquad (26)$$

Equating Eqns. 24 and 26 the relationship for converting dissolved dye absorption measurements (measured values of ε at a concentration of [M]) to extinction coefficient values at adsorbate layer volumetric concentrations is

$$k = - 2.303\ \varepsilon\lambda c/4\pi \qquad (27)$$

Absorption measurements for dissolved rhodamine-B at a wavelength of 554 nm, its maximum absorption wavelength, indicate that the extinction coefficient value for a close-packed monolayer would be about 1.7, which is comparable to values for other solid, absorbing materials (13).

It is worth summarizing this conceptualization of the dye adsorbate layer. Case I: the dye molecule is assumed to lie with its electronic transition moment parallel to the surface, has a layer thickness of about 5 Angstroms, and ordinary extinction coefficient (parallel to x,y-plane, the electrode surface) of 1.7 at the maximum absorption wavelength; the layer exhibits complete dichroism so the extraordinary extinction coefficient (parallel to z-axis, normal to the electrode surface) is zero at the same wavelength; the ordinary extinction coefficient also becomes zero at wavelengths far removed from the absorption band. Case II: the dye molecule is assumed to lie with its electronic

transition moment perpendicular to the surface, has a layer thickness of about 25 Angstroms, and an extraordinary extinction coefficient (parallel to z-axis) of 1.7 at the maximum absorption wavelength; the layer exhibits complete dichroism so the ordinary coefficient (parallel to x,y-plane) is zero at the same wavelength; the extraordinary extinction becomes zero at wavelengths far removed from the absorption band.

Measurements of the absorption cross-section for dissolved dye are for random orientations of the electronic transition moment relative to the two components (s and p polarizations) of the propagating electric field wave; molecules with transition moments parallel to the wave vector do not absorb. If all molecules had transition moments parallel to the s and p electric field vectors, greater absorption would be observed. This type of enhancement should be considered in extrapolation of dissolved dye extinction coefficients to a well-ordered adsorbate layer; either the extraordinary (normal to surface) or ordinary (parallel to surface) extinction coefficient will be slightly greater than the value calculated by extrapolation of dissolved dye absorption measurements, depending upon the orientation of the dye molecule on the surface. However, this enhancement is probably small due to other effects which are unaccounted for in this crude model; so, the correction was not made.

So far only the extinction coefficient of the adsorbate layer has been discussed. One must also select a value for the real part of the complex refractive indices, no and ne. The refractive index corresponding to the non-zero extinction coefficient (direction of greatest polar-

izability) was taken to be about 1.5 and independent of wavelength, a value typical of such aromatic molecules and the other refractive index was taken to be about 1.34, identical to the solution; the refractive indices and extinction coefficients were assumed to be unrelated.

Actually, the real and imaginary parts of the refractive index are interdependent, related through relationships like those given in Eqns. 28.a and 28.b (14).

$$n^2 - k^2 = 1 + \frac{Ne^2}{m\varepsilon_o} \frac{\omega_o^2-\omega^2}{(\omega_o^2-\omega^2) + \gamma^2\omega^2} \qquad (28.a)$$

$$2nk = \frac{Ne^2}{m\varepsilon_o} \frac{\gamma\omega}{(\omega_o^2-\omega^2) + \gamma^2\omega^2} \qquad (28.b)$$

where ε_0 is the permeability of free-space, ω, is the frequency of light at a specific wavelength, ω_0 is the resonance frequency of the medium (at the maximum absorption wavelength), and γ is the frictional damping constant for electronic oscillations (arising from the acceleration term, m γ dr/dt). These equations are derived by equating the real and imaginary parts of the square of the complex refractive index, Eqn. 29.

$$\hat{n}^2 = (n+ik)^2 = 1 + \frac{Ne^2}{m\varepsilon_o} \frac{1}{\omega_o^2-\omega^2-i\gamma\omega} \qquad (29)$$

These relationships predict that the real part of the complex refractive index will have a derivative-type response to peaks in the extinction coefficient at absorption wavelengths. Such behavior in metals is referred to as dispersion; however, in dyes the behaviour is somewhat different and referred to as anamalous dispersion. The absorption in metals can be due to either electronic transitions or plasmon resonances at discrete harmonics, whereas the absorption in the dye is due to electronic excitations.

Simulated Spectroscopic Ellipsometer Measurements

Spectroscopic ellipsometer responses were simulated based upon a 75 degree angle-of-incidence and the assumptions made in this chapter. Simulations are shown for Pt, Ag, Cu, and Pb substrates in Figs. 2.a & b, 3.a & b, 4.a & b, and 5.a & b, respectively. Both perpendicular (Case I) and parallel (Case II) orientations of the electronic transition moment relative to the surface were considered and are shown in the figures as solid and dotted lines, respectively. Responses to parallel orientations are much smaller (peak amplitudes) than responses to the perpendicular orientation; therefore, simulated responses for the parallel orientation are shown with expanded scales in Figs. 2.c through 5.c; in these figures delta is shown as solid lines and psi is shown as dotted lines. Two surface concentrations were computed; 100% and 50% close-packing of the surface, denoted as A and B, respectively.

These calculated spectroscopic ellipsometer responses (delta and psi as a function of wavelength) illustrate the sensitivity of the

instrument to an adsorbed monolayer of rhodamine-B; the following qualitative conclusions have been drawn. At the specified angle-of-incidence, the ellipsometer is most sensitive to perpendicular orientations of the dye transition moment, responses being at least an order-of-magnitude greater than for the parallel orientation. Furthermore, negative changes in delta due to the adsorbed dye are indicative of the perpendicular orientation; similar conclusions cannot be drawn about trends in psi. The absolute response of delta to perturbations in the extinction coefficient (imaginary part of the complex refractive index) at the maximum absorption wavelength is much larger than the corresponding response in psi. Changes in delta and psi at wavelengths removed from the absorption band are attributable to the refractive indices of the dye layer (real part of the complex refractive index). These conclusions are independent of substrate, and are treated as empirical rules for the interpretation of complicated peak structure in spectroscopic ellipsometer responses.

The simulations discussed here required complex refractive index data for the substrates over the spectral range of interest, obtained by making spectroscopic ellipsometer measurements of the bare metal surfaces and inverting delta and psi; the results are shown in Figs. 6.a and 6.b. Spectroscopic measurements were obtained using program SEV002; the data file created by SEV002 was then converted to refractive indices by program RISURF and the results stored on a floppy disk. Refractive indices for rhodamine-B were assumed and the extinction coefficients were calculated from an absorption spectrum, measured by the spectros-

copic ellipsometer while serving as a spectrophotometer (photocurrent was monitored by the computer rather than the nulling Faraday current level); these data were also obtained using program SEV002. These complex refractive index data files were then read by program AISPEC, the AnIsotropic SPECtroscopic simulator; this simulation program calculates delta and psi using the equations presented for a uniaxially anisotropic film and stores the results on a floppy disk. Software is discussed in Chapter 3.

Empirical Interpretation of Experimental Spectroscopic Measurements

The spectroscopic responses for rhodamine-B adsorbed on polycrystalline Pt are shown in Figs. 7.a (delta vs wavelength) and 7.b (psi vs wavelength). The dye solution contained 20 micromolar rhodamine-B, 5 millimolar Pb(NO3)2, and 1 M $NaClO_4$ acidified to a pH of 3 with $HClO_4$; no current was passed. Two peaks appeared, a small peak at 470 nm and a broad band centered at about 570 nm; the small peak was a positive change in delta from the value for the bare survace and the broad band was a negative deviation in delta; the responses of psi appears to have a derivative type relationship with the responses of delta (anomalous dispersion). Based upon the empirical rules presented, the broad band has been interpreted as being due to an adsorbed dye molecule with its electronic transition moment oriented perpendicular to the surface; only slight chemical shifting of the peak wavelength from the maximum absorption wavelength of the dissolved dye was noted. The smaller peak has been interpreted as a chemically shifted absorption due to a strongly chemisorbed species having its transition moment parallel to the

surface. Such chemical shifting of the peak wavelength could have resulted from either lowering the singlet ground state or raising the triplet excited state resulting from photon absorption. Similar peak shifting has been noted for rhodamine-B adsorption on Pt by Schmidt and Reich (15).

Rhodamine-B adsorption on Ag(111) was observed with spectroscopic ellipsometry and the measured responses are shown in Figs. 8.a through 8.e. The concentration of dye in solution was increased from 0 to 2.2 micromolar; spectroscopic measurements were made at each concentration level. This solution also contained 5 millimolar $Pb(NO_3)_2$ and 1 M $NaClO_4$ at a pH of 3. Figs. 8.a through 8.c show changes in delta at different wavelengths; Figs. 8.d throught 8.e show the corresponding changes in psi. The absorption band of the adsorbate layer was at about 560 nm, closer to the dissolved dye maximum absorption wavelength than the broad band observed for the Pt surface; the magnitude and direction of change in delta indicate that the adsorbed species had its transition moment oriented normal to the surface. At wavelengths removed from the peak wavelength, delta changed very little as the concentration was increased above the 1.2 micromolar level; however, the peak response continued to increase. Furthermore, continuous changes in psi were observed as the concentration was increased to the 1.2 micromolar level, with little change thereafter (Fig 8.f). It is therefore believed that the surface becomes saturated with rhodamine-B at a concentration of approximately 1.2 micromolar; increases in peak response above the 1.2 micromolar level may be due to instrument gain artifact (discussed in

reference 1). This experiment illustrates the application of spectroscopic ellipsometry to adsorption isotherm measurements.

Experimental spectroscopic measurements were made for rhodamine-B adsorbed on Cu(111) during Pb electrodeposition at -600 mV from 0.5 millimolar $Pb(NO_3)_2$, 1 M $NaClO_4$ at pH 3, and 10 micromolar dye. Results are shown in in Fig. 9.a (delta vs wavelength) and 9.b (psi vs wavelength), respectively. Curves marked A denote measurements made of the bare Cu(111) surface before either dye addition to the electrolyte or Pb electrodeposition; curves marked B denote measurements made of the surface with adsorbed rhodamine-B; and curves marked C denote measurements made of the surface with simultaneous electrodeposition and dye adsorption. The peak amplitude seen in the figure showing delta vs wavelength is smaller during Pb deposition than before; this may be due to dye displacement and reduction at the electrode surface. These data are presented with a lower degree of confidence than that for the Pt and Ag substrates since it was taken early in the project while significant development of the instrument was still in progress.

Conclusions

A uniaxial anisotropic film model has been used to simulate spectroscopic measurements of various metallic substrates covered by a monolayer of adsorbed rhodamine-B (dye). Two orientations of the electronic transition moment were assumed, parallel and perpendicular to the surface. The extraordinary and ordinary extinction coefficients of the dye layer were estimated on the basis of dissolved dye extinction coeffi-

cients measured by absorption spectroscopy. For a 75 degree angle-of-incidence and over the spectral range of interest (400 to 700 nm) it was found that (theoretically) ellipsometer responses are far greater for species oriented with their transition moment normal to the surface; empirical rules were developed for the interpretation of spectroscopic ellipsometry measurements of adsorbed dye monolayers.

Experimental spectroscopic ellipsometry measurements for rhodamine-B adsorbed to Pt and Ag(111) were presented. Peaks due to adsorbed dye were interpreted on the basis of the empirical rules derived from spectroscopic simulations. Molecular orientation and surface saturation were inferred from the spectroscopic ellipsometry measurements. Earlier measurements of rhodamine-B adsorbed to Cu(111) during Pb deposition were also presented and discussed.

References

1. Chapter 2.

2. Chapter 4.

3. Bootsma, G. A., Meyer, F., "Ellipsometry in the Submonolayer Region," Surf. Sci., 14, 52 (1969).

4. Muller, R. H., "Principles of Ellipsometry," ADVANCES IN ELECTROCHEMISTRY, Vol. 9, Delahay, P., Tobias, C. W., ed., John Wiley & Sons, New York, 1973, pp. 167-226.

5. Somorjai, G. A., CHEMISTRY IN TWO DIMENSIONS, Cornell University Press, Ithaca, NY, 1981, pp. 79-81.

6. see 3.

7. Chapter 5.

8. Azzam, R. M. A., Bashara, N. M., ELLIPSOMETRY AND POLARIZED LIGHT, North-Holland, New York, 1977, pp. 356-357.

9. Plieth, W. J., Gruschinske, P. Hensel, H. J., "Electronic Changes of Light Absorption by the Electric Field of the Electrolytic Double Layer," Ber. Bunsenges. Phys. Chem. 82, 615 (1978).

10. Bockris, J. O'M., Razumney, G. A., FUNDAMENTAL ASPECTS OF ELECTROCRYSTALLIZATION, Plenum Press, 1967, NY, pg. 111.

11. Birks, J. B., PHOTOPHYSICS OF AROMATIC MOLECULES, Wiley, London, 1970, pg. 47.

12. See 8, pp. 75, 76.

13. EASTMAN ORGANIC CHEMICALS CATALOG, No. 82, Eastman-Kodak, Rochester, NY 14650, 1981-1982.

14. Fowles, G. R., INTRODUCTION TO MODERN OPTICS, 2nd ed., Halt, Rinehart, Winston, New York, 1968, pp. 157-160.

15. Schmidt, S., Reich, R., Ber. Bunsenges. Phys. Chem., 76, 549 (1972).

Figures

1. Geometric representation of rhodamine-B adsorbed on a surface (x-y plane) with normal and parallel orientations of the electronic transition moment.

2.a Simulated spectroscopic ellipsometry of rhodamine-B adsorbed on Pt (delta vs wavelength). Data are presented as changes in delta due to adsorption. Dotted lines represent simulations assuming parallel orientation of the transition moment; the solid lines represent simulations assuming a normal orientation. Curves labeled A and B represent 100% and 50% close-packing of rhodamine-B molecules on the surface, respectively. Optical data used are shown in Figs. 6.a and 6.b.

2.b Psi vs wavelength corresponding to Fig. 2.a.

2.c Expanded scale for data in Figs. 2.a and 2.b; case of parallel orientation shown only.

3.a Simulated spectroscopic ellipsometry of rhodamine-B adsorbed on Ag (delta vs wavelength). Figure analogous to 2.a.

3.b Psi vs wavelength corresponding to Fig. 3.a.

3.c Expanded scale for data in Figs. 3.a and 3.b; case of parallel orientation shown only.

4.a Simulated spectroscopic ellipsometry of rhodamine-B adsorbed on Cu (delta vs wavelength). Figure analogous to 2.a.

4.b Psi vs wavelength corresponding to Fig. 4.a.

4.c Expanded scale for data in Figs. 4.a and 4.b; case of parallel orientation shown only.

5.a Simulated spectroscopic ellipsometry of rhodamine-B adsorbed on Pb (delta vs wavelength). Figure analogous to 2.a.

5.b Psi vs wavelength corresponding to Fig. 5.a.

5.c Expanded scale for data in Figs. 5.a and 5.b; case of parallel orientation shown only.

6.a Refractive indices for spectroscopic ellipsometer simulations. Data for Pt, Ag, Cu, and Pb were all determined experimentally; all data except that for Cu was smoothed numerically. The refractive index for rhodamine-B was assumed.

6.b Extinction coefficients for spectroscopic ellipsometer simulations. data for Pt, Ag, Cu, and Pb were all determined experimentally; all data except that for copper was smoothed numerically. The extinction coefficients for rhodamine-B were computed from an experimental absorption spectrum (see text).

7.a Experimental spectroscopic ellipsometry of rhodamine-B adsorbed on Pt from a 20 micromolar solution containing 5 millimolar $Pb(NO_3)_2$ and 1 M $NaClO_4$ at pH 3 (delta vs wavelength). Here, delta is presented on an absolute scale (these are not difference measurements). There is a broad band between 500 and 600 nm and a smaller peak at about 470 nm; these are believed to be due to two different adsorbed states of the dye molecule. The broad band is probably

due to a preferential normal orientation of the electronic transition moment, whereas the smaller peak is believed to be due to a species with a preferential parallel orientation of the transition moment and strong electronic interaction with the surface. Two spectral scans of the surface are superimposed, showing reproducibility.

7.b Psi vs wavelength corresponding to Fig. 7.a.

8.a Experimental spectroscopic ellipsometry of rhodamine-B adsorbed on Ag(111) from solutions of various dye concentrations (which are indicated by the numbers labeling the curves) containing 5 millimolar $Pb(NO_3)_2$ and 1 M $NaClO_4$ at pH 3 (delta vs wavelength). Here, delta is presented on an absolute scale (these are not difference measurements). The surface is believed to be completely saturated with adsorbed rhodamine-B (preferential normal orientation) at a concentration of about 1.2 micromolar; changes in delta at higher concentrations are believed to be due to variations in instrument gain (see Chapter 2).

8.b Expanded scale for Fig. 8.a. This figure illustrates how measured values of delta for concentrations between 1.0 and 1.2 micromolar change insignificantly, whereas the response between concentrations of 1.2 and 1.5 micromolar change (only on the maximum absorption wavelength) dramatically. Since delta only changes on the maximum absorption wavelength for concentrations greater than 1.2 micromolar, it is suspected that these changes are attributable to attenuation of the optical signal (reduced gain) by the light

absorbing incident medium (dye solution).

8.c Further expansion for Fig. 8.a.

8.d Psi vs wavelength corresponding to Fig. 8.a.

8.e Expanded scale for Fig. 8.d.

8.f A plot of spectroscopic ellipsometer responses (delta and psi) at the maximum absorption wavelength (570 nm) and removed from the absorption band (600 nm); note that little change in delta and psi was observed at 600 nm for concentration increments at concentrations greater than 1.2 micromolar; this is contrasted to the response at 570 nm (delta continued to change).

9.a Experimental spectroscopic ellipsometry of rhodamine-B adsorbed on Cu(111) during various stages of Pb deposition. Curve "A" represents measurements of the bare Cu surface before either dye addition or Pb deposition, curve "B" represents measurements after rhodamine-B addition at 10 micromolar concentration, and curve "C" represents the surface after polarization at -600 mV (vs Ag/AgCl) with some Pb deposition. There is a slight attenuation of the peak amplitude after polarization; this may be either due to lower bulk dye concentration (lowered due to reduction with effect on instrument gain) or some change in the surface concentration of the dye.

9.b Psi vs wavelength corresponding to Fig. 9.a.

MODELING SECOND ORDER EFFECTS

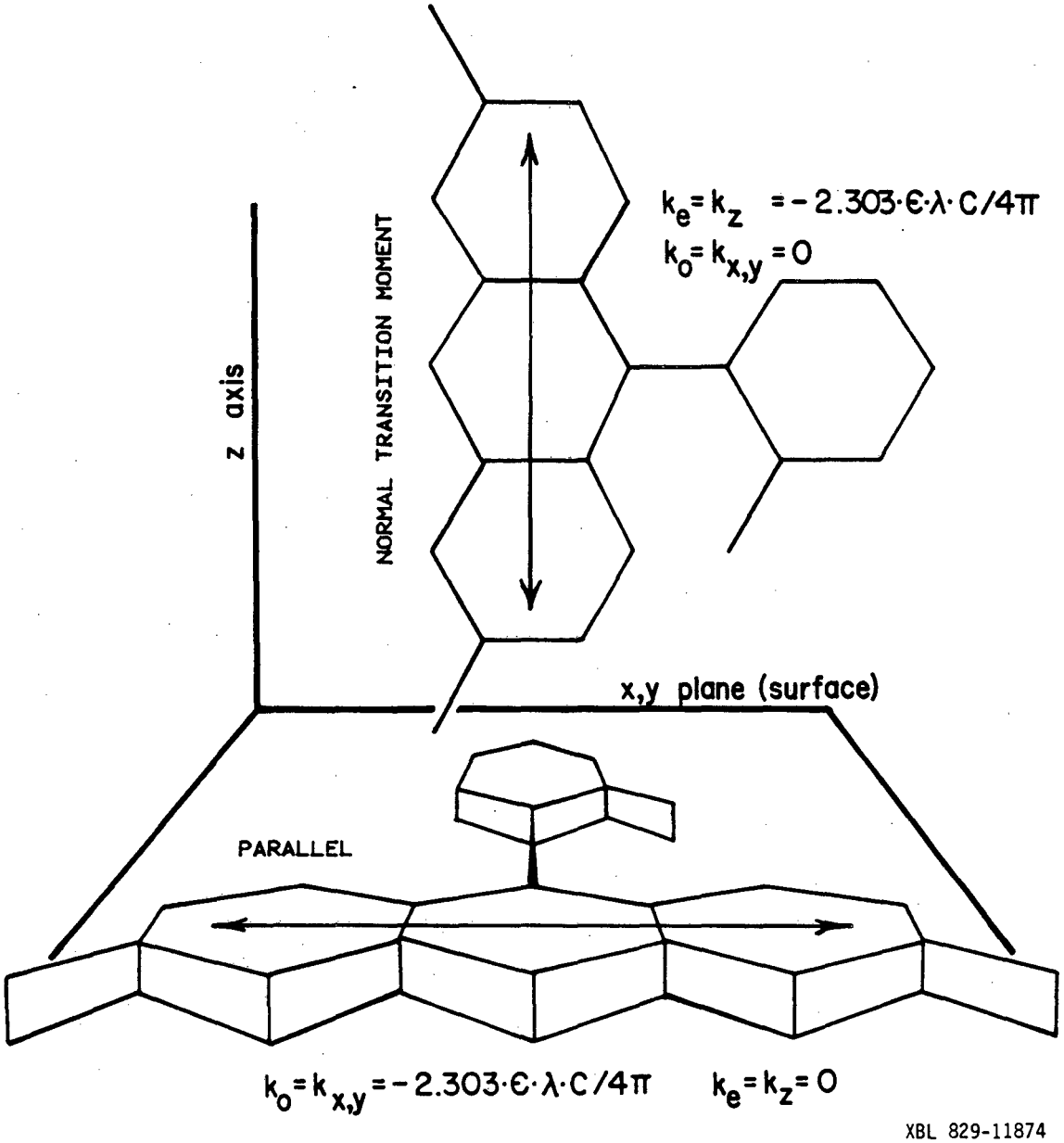

XBL 829-11874

Fig. 1

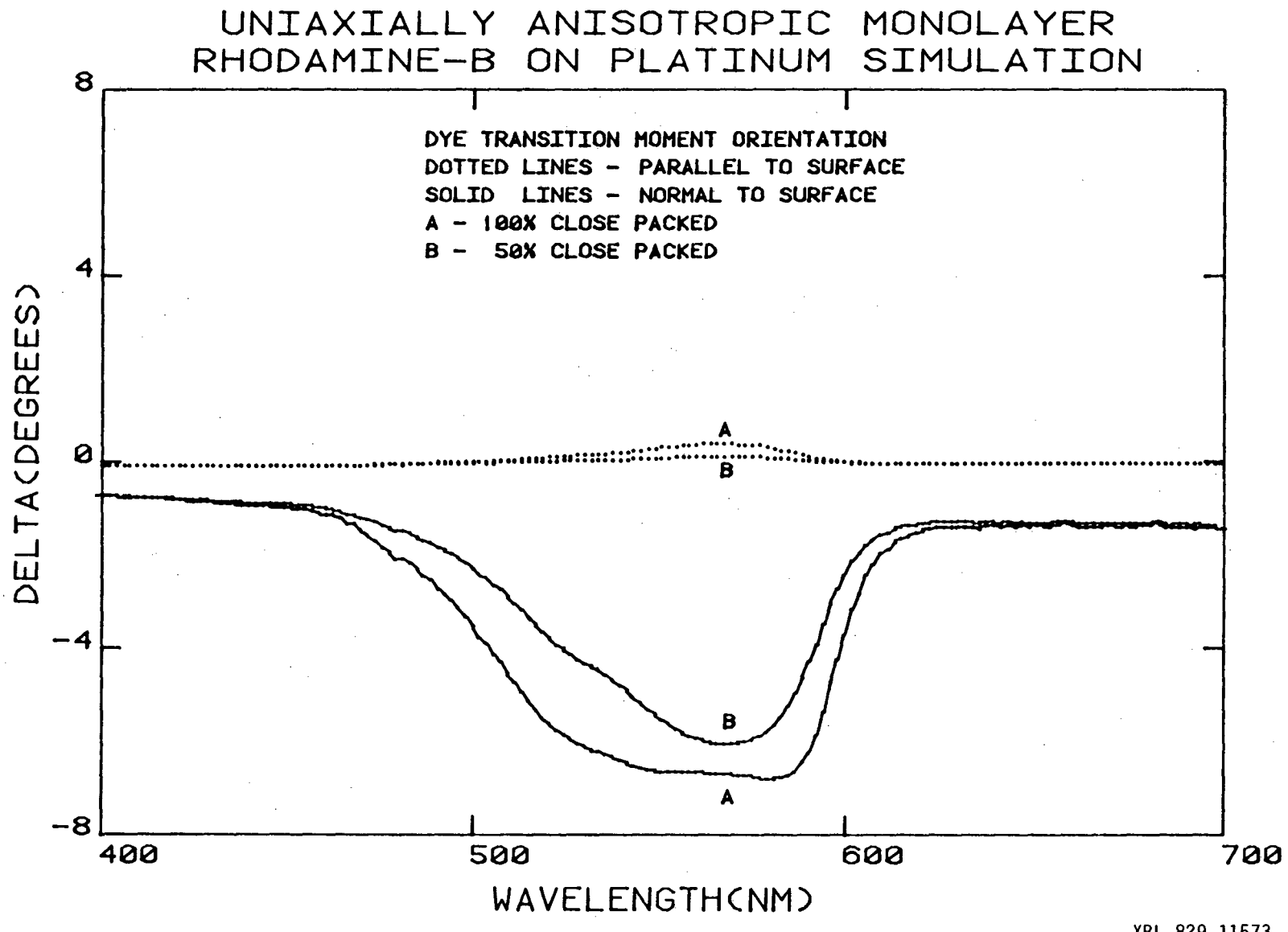

Fig. 2.a

XBL 829-11573

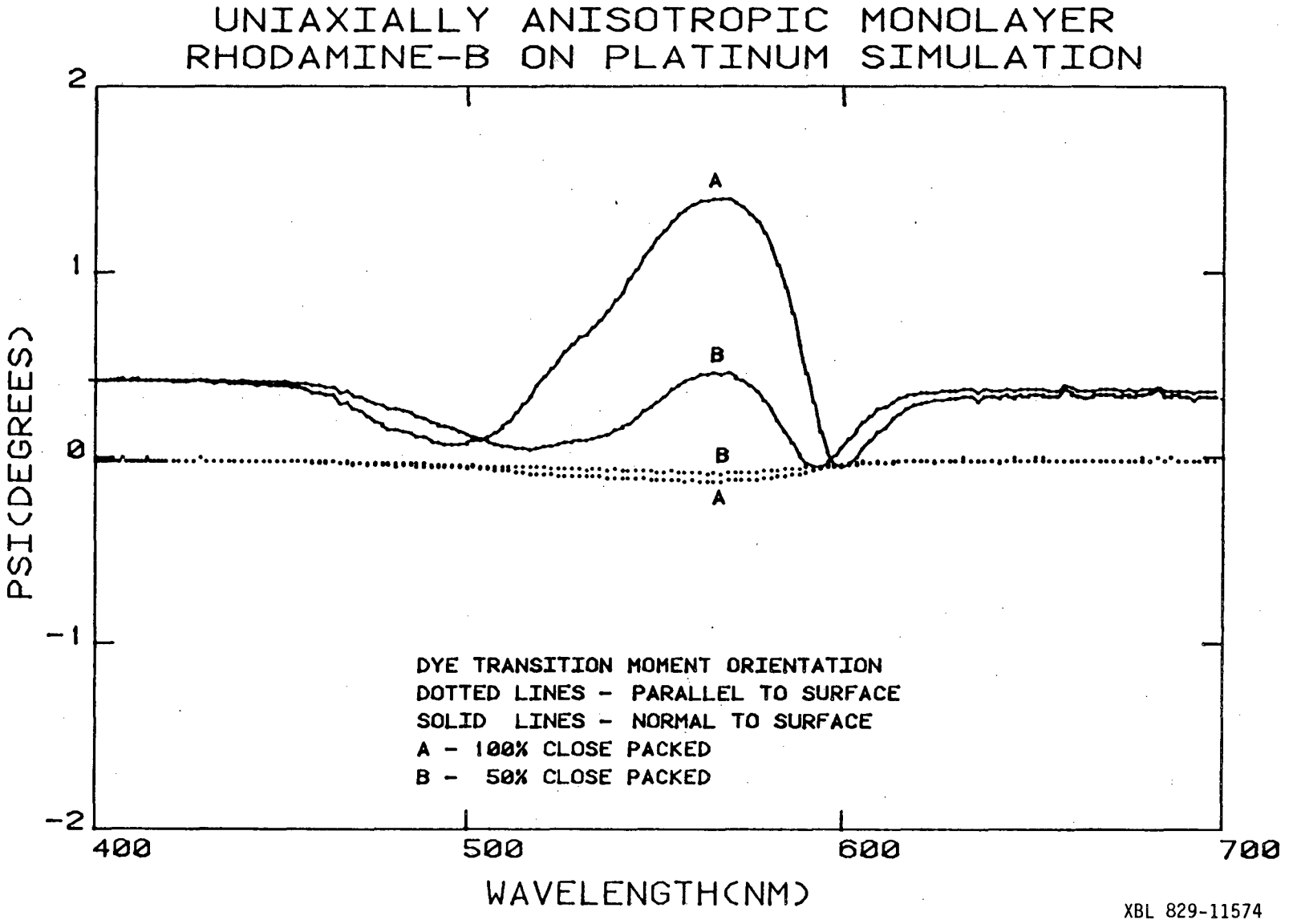

XBL 829-11574

Fig. 2.b

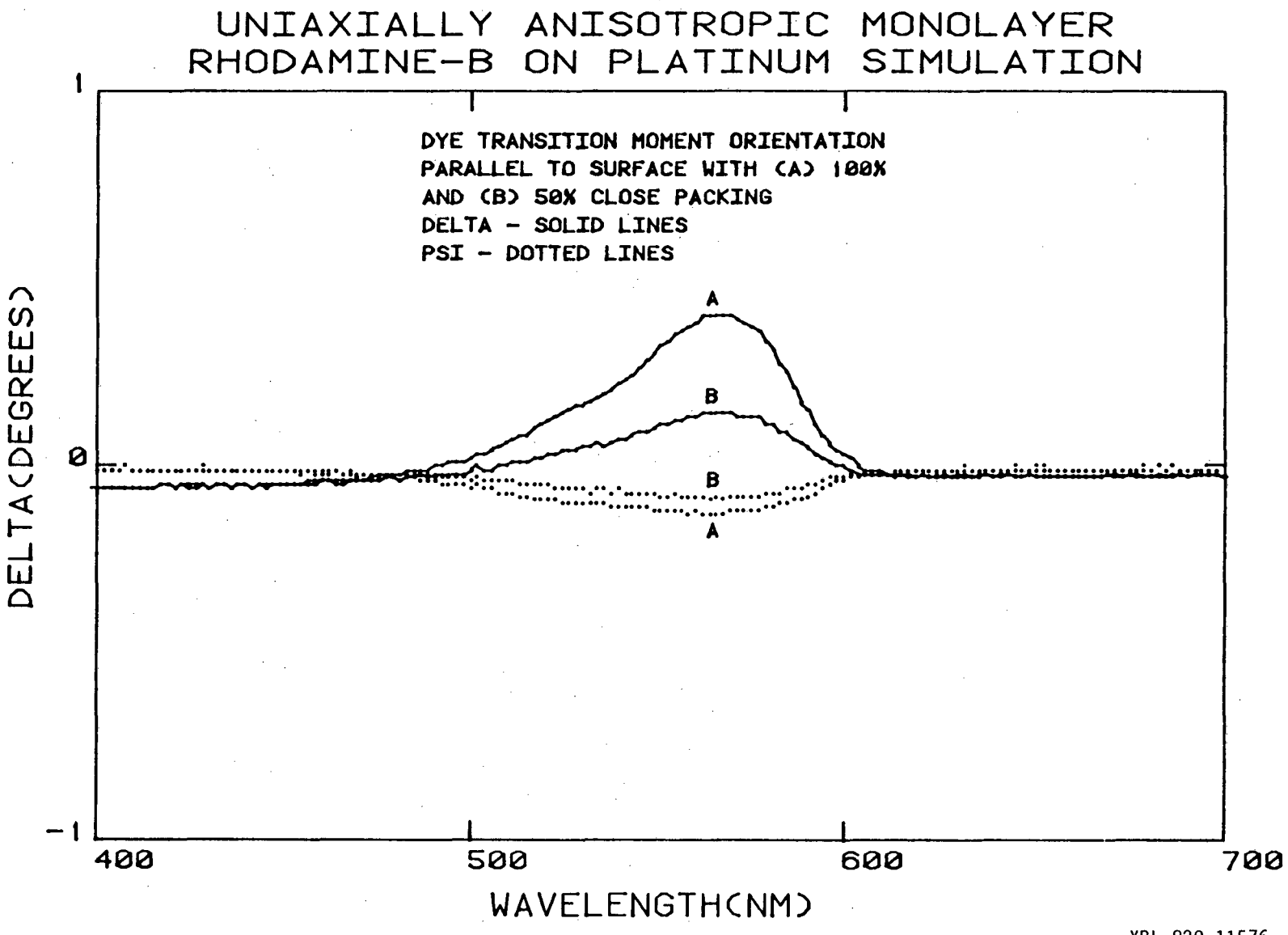

Fig. 2.c

XBL 829-11576

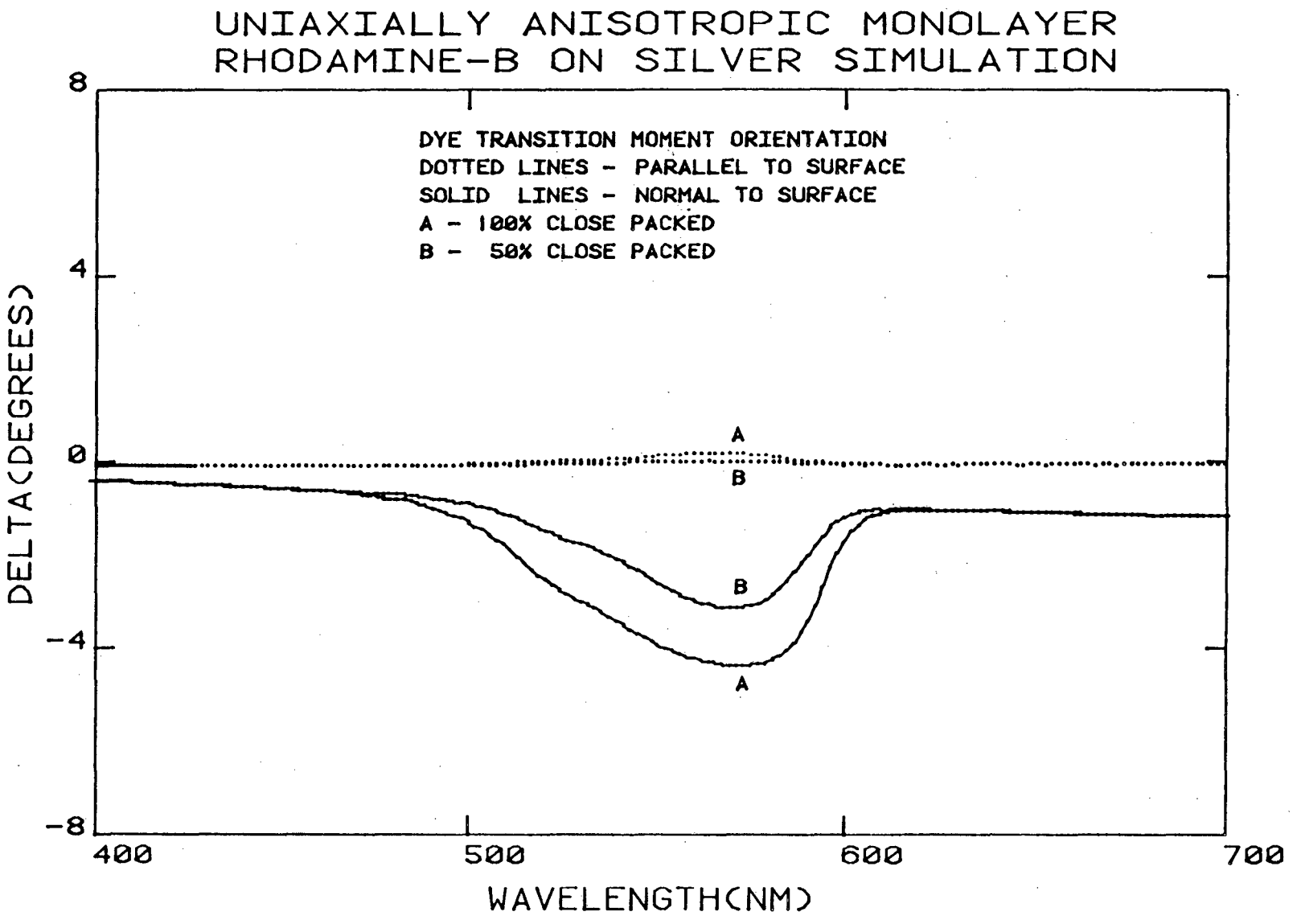

Fig. 3.a

XBL 829-11581

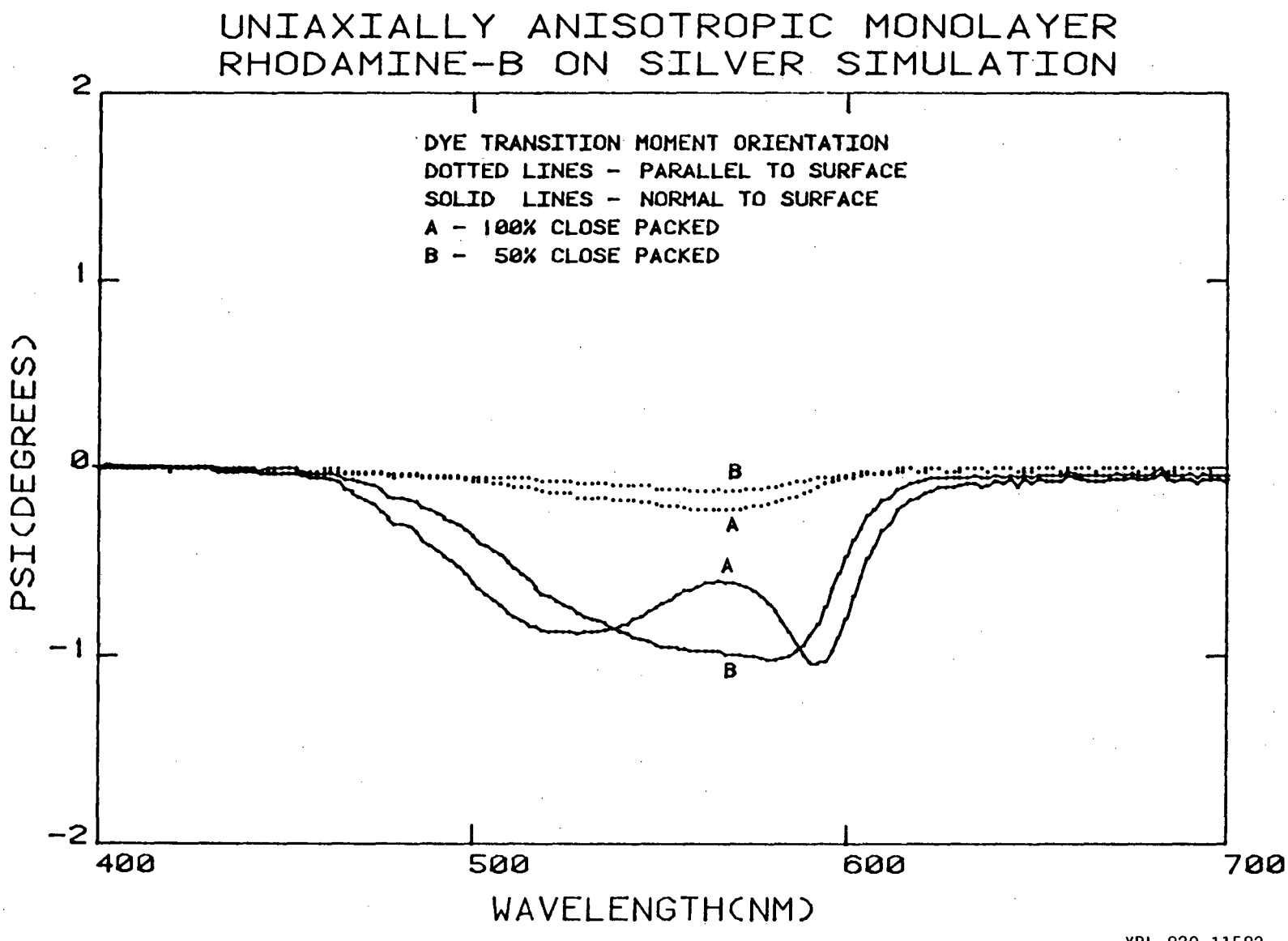

Fig. 3.b

XBL 829-11582

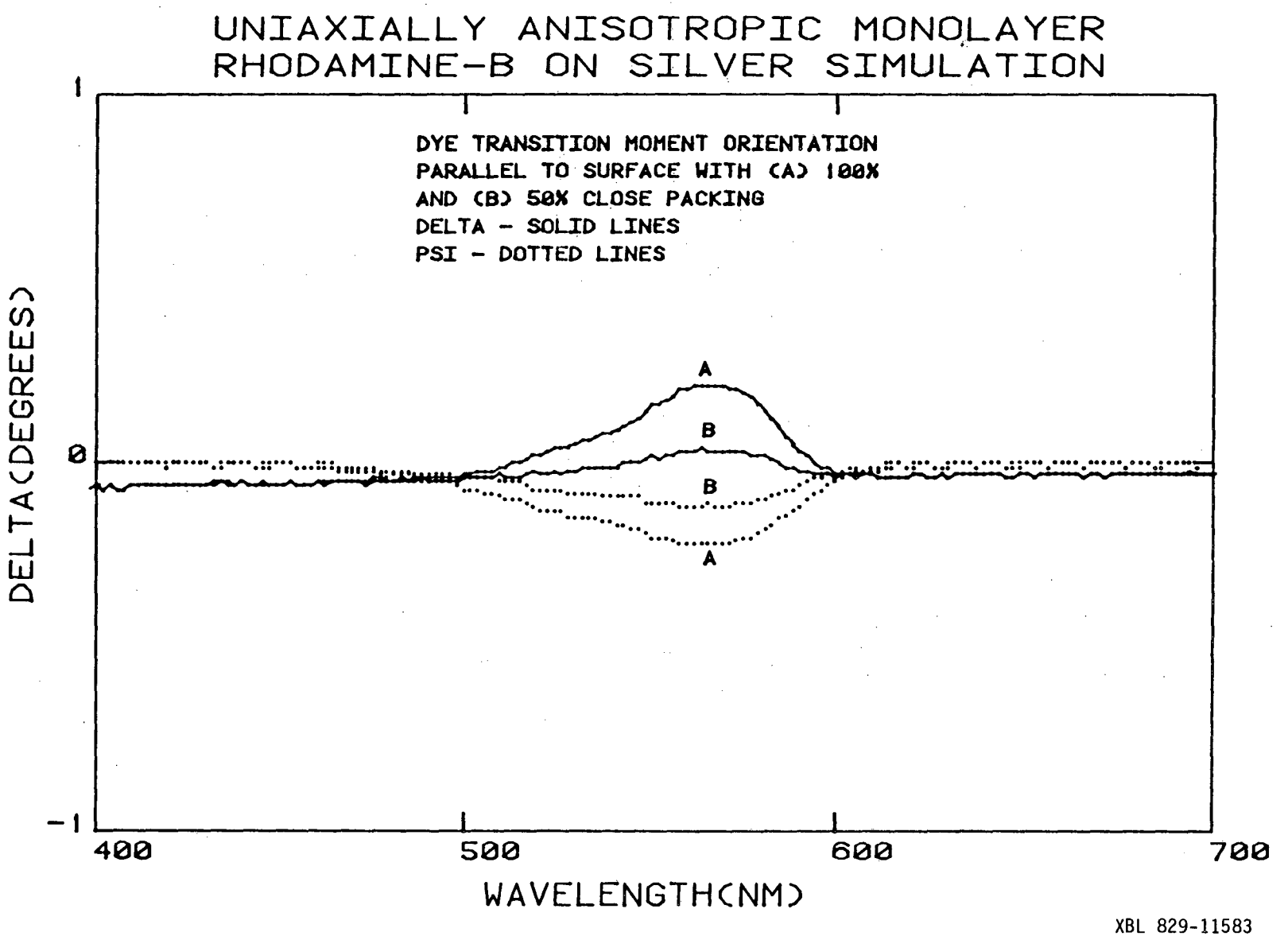

XBL 829-11583

Fig. 3.c

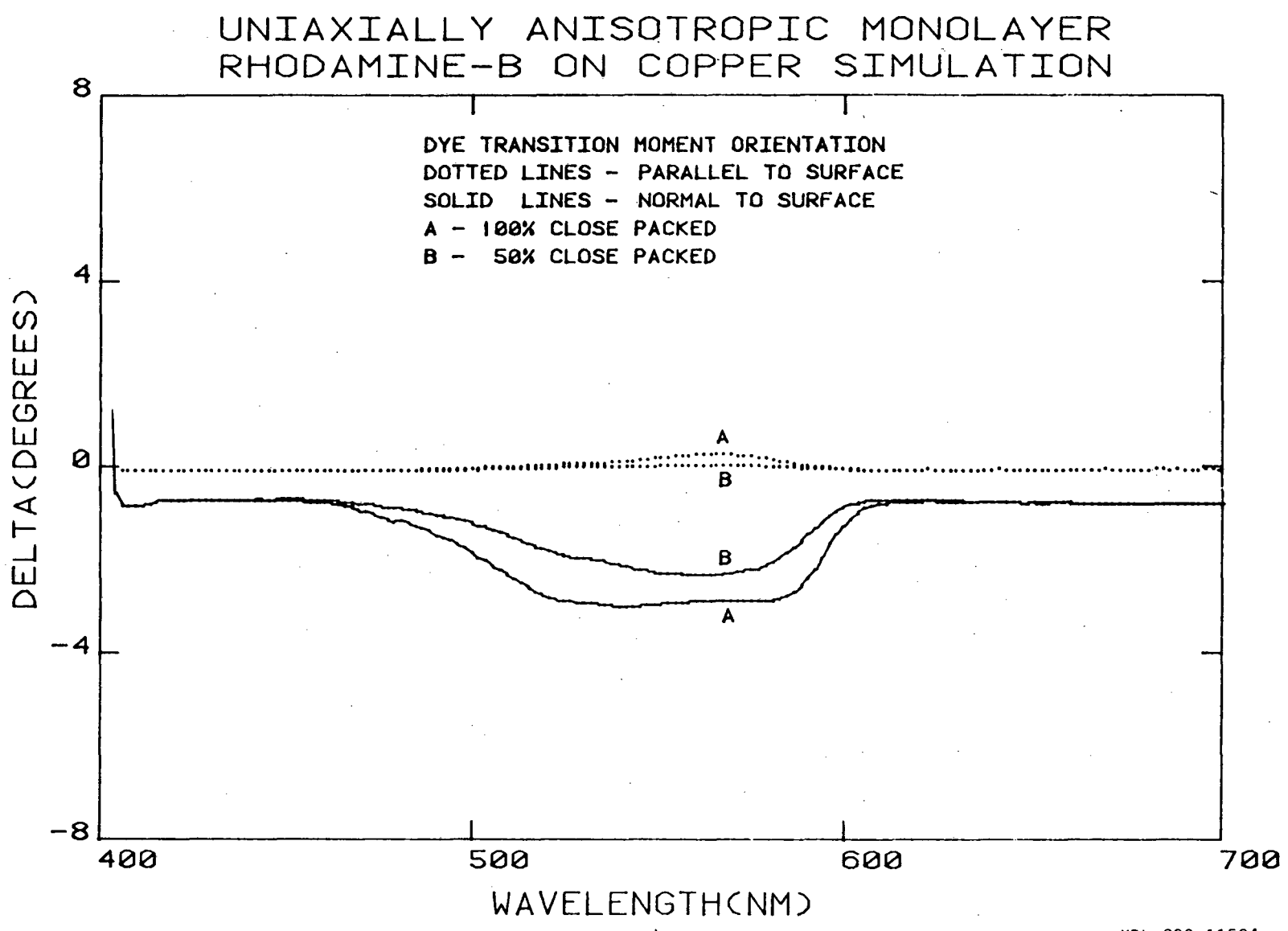

Fig. 4.a

XBL 829-11584

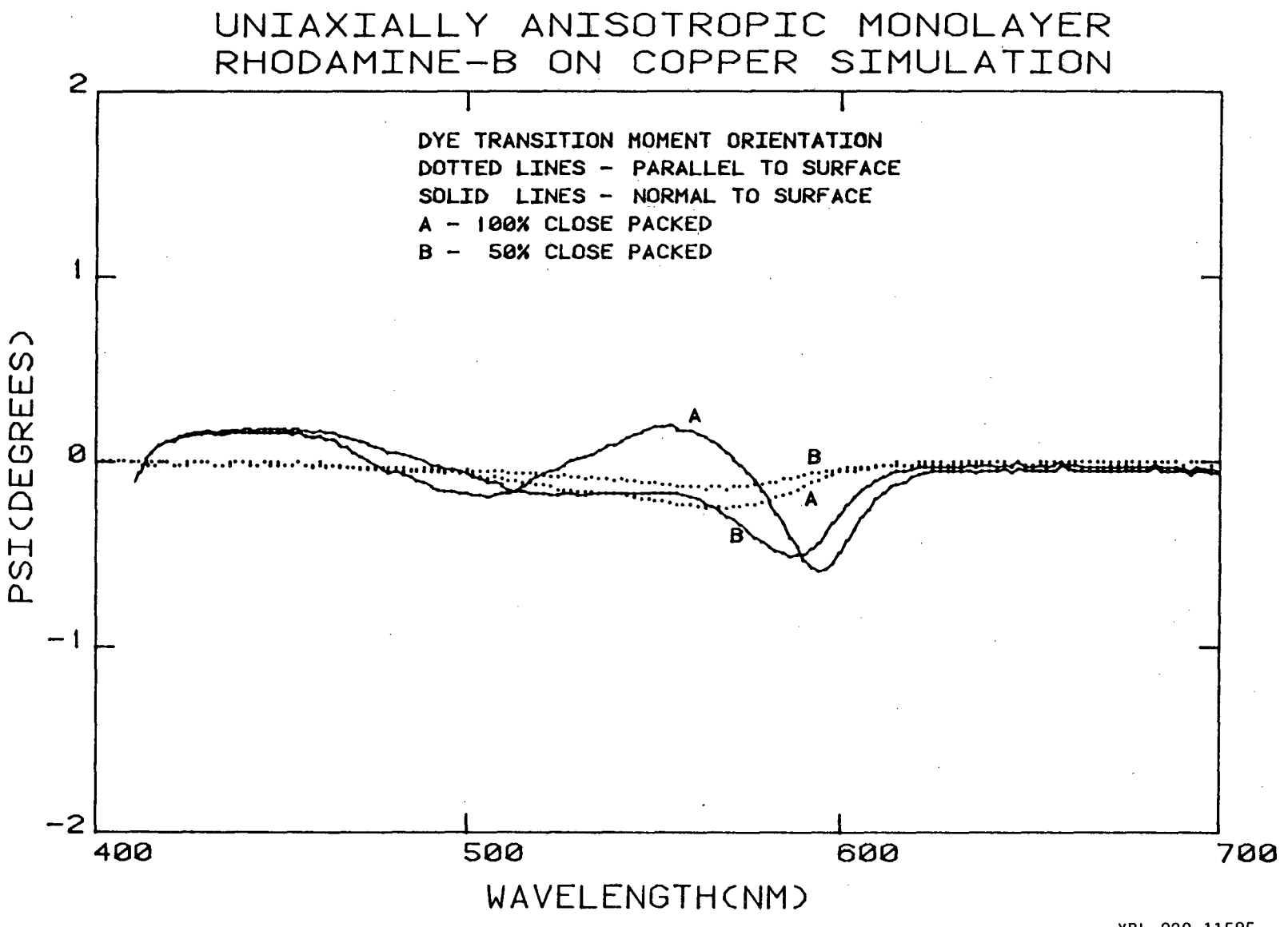

Fig. 4.b

XBL 829-11585

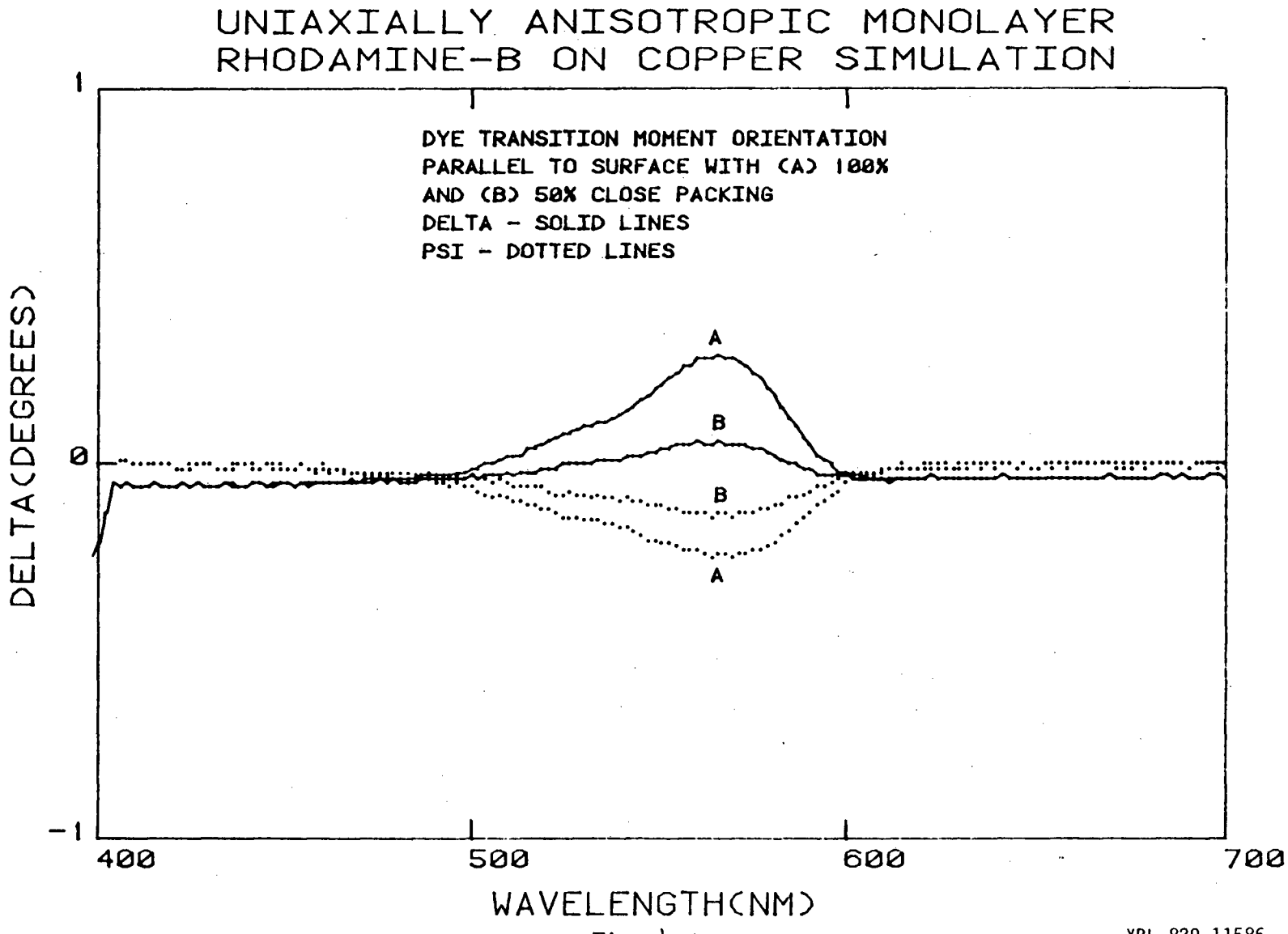

Fig. 4.c

XBL 829-11586

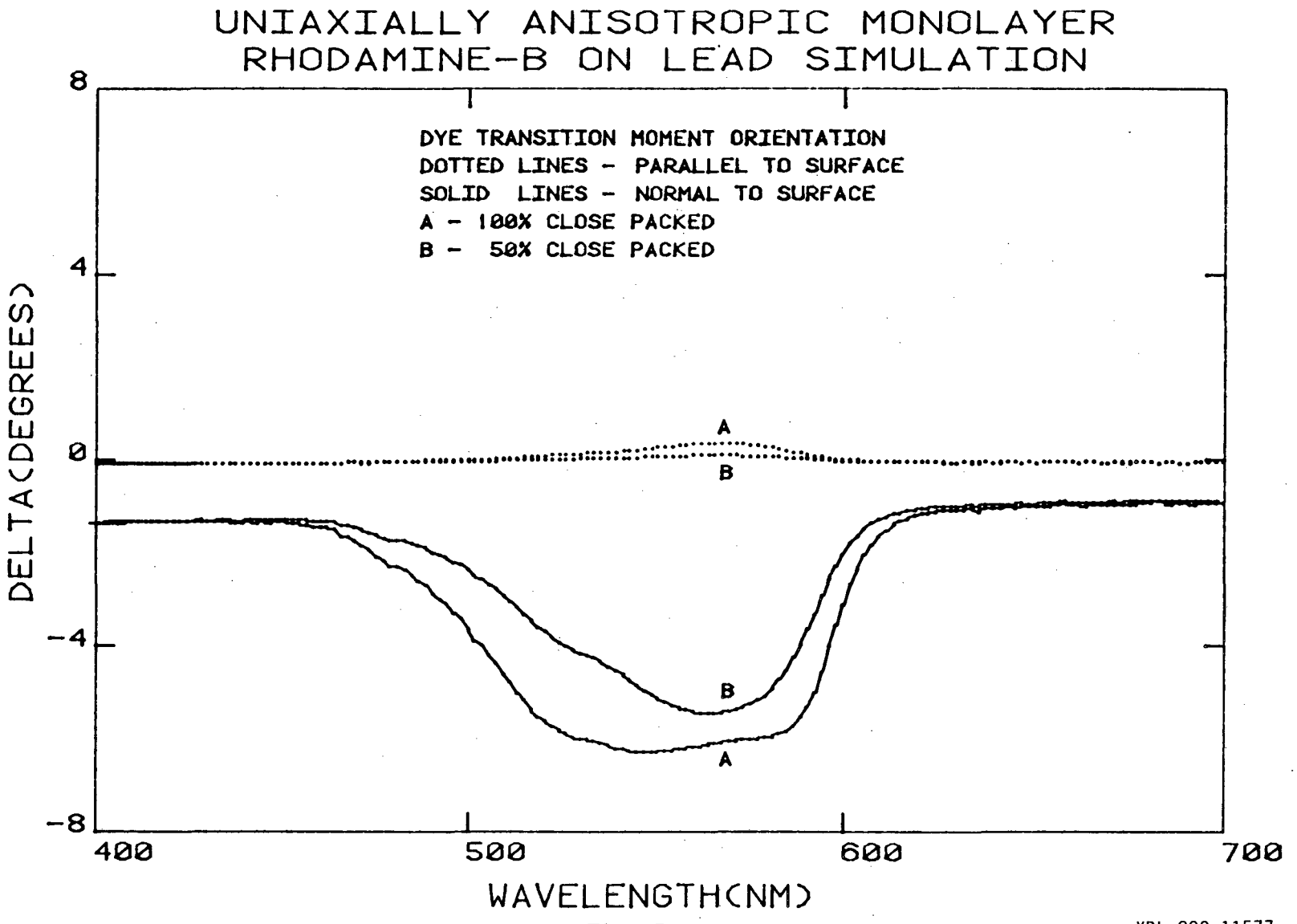

Fig. 5.a

XBL 829-11577

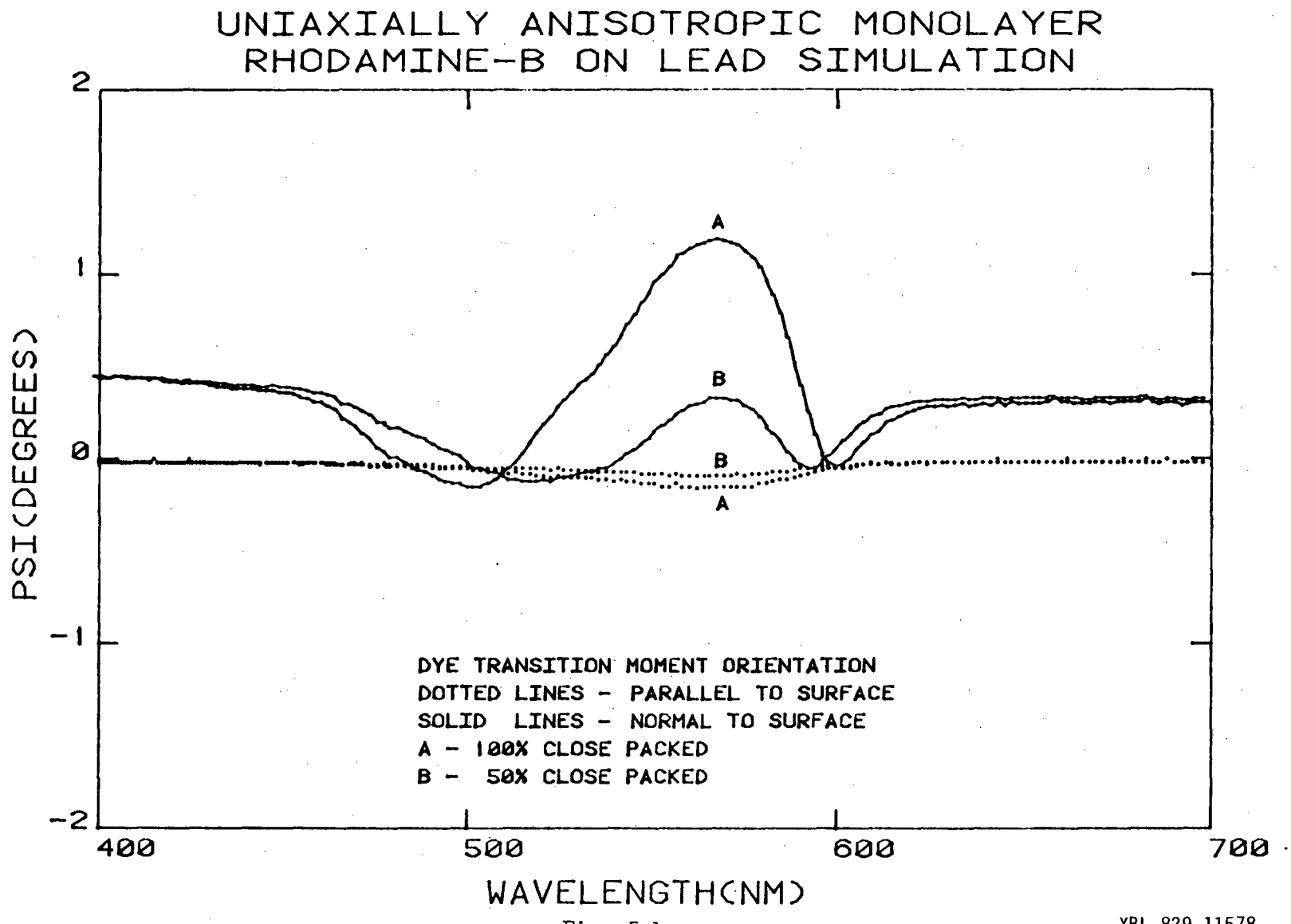

Fig. 5.b

XBL 829-11578

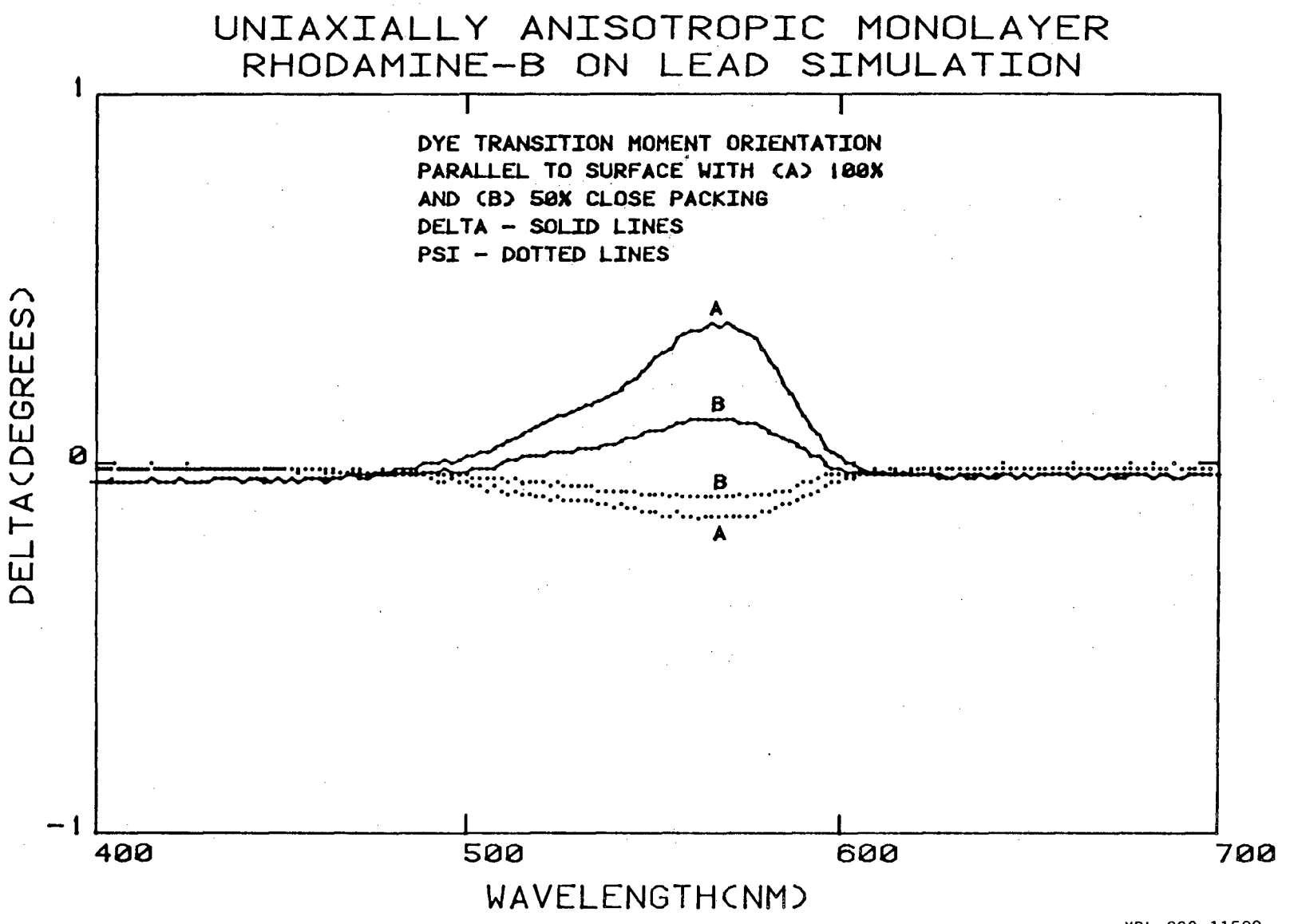

Fig. 5.c

XBL 829-11580

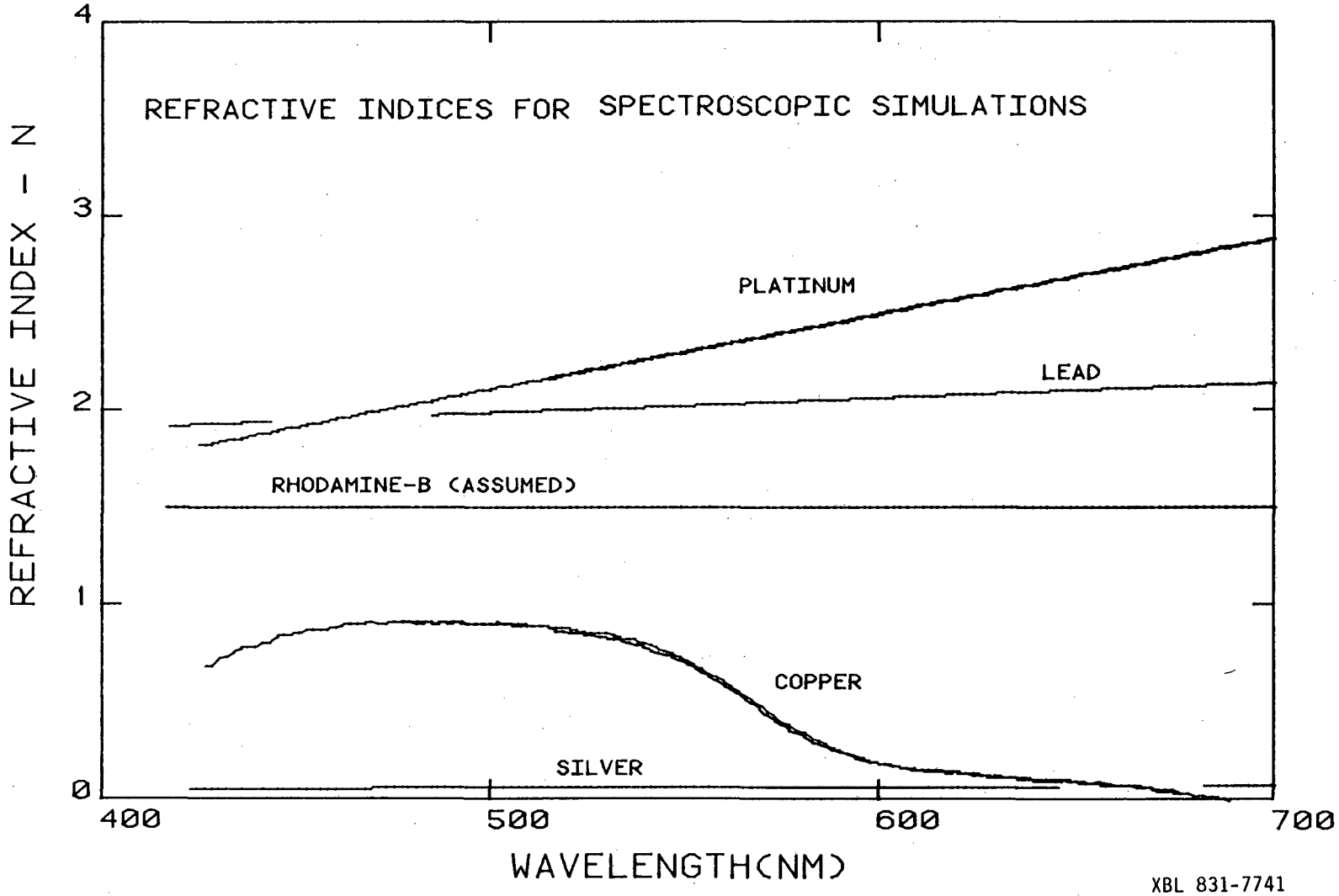

XBL 831-7741

Fig. 6.a

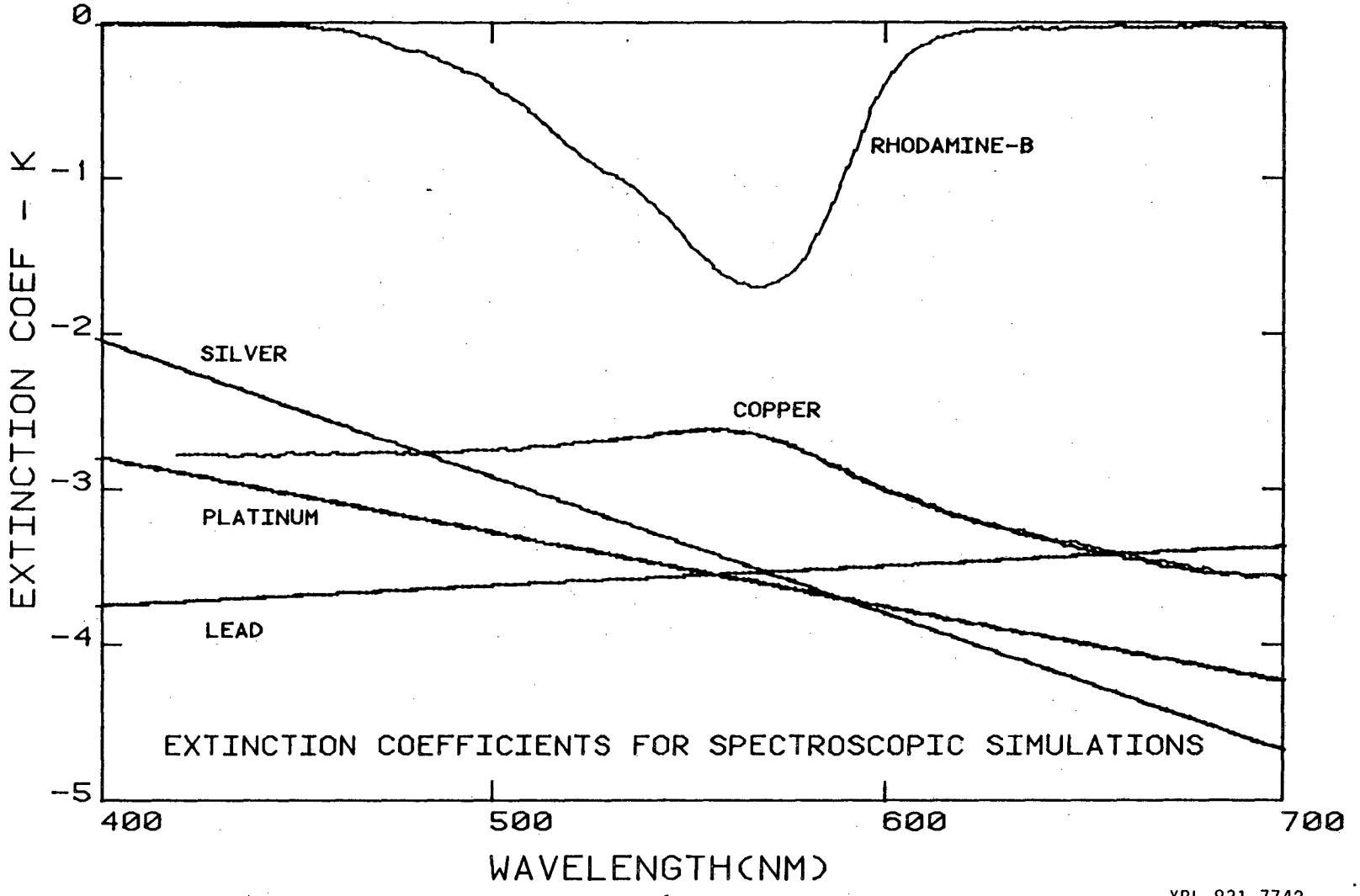

Fig. 6.b

XBL 831-7742

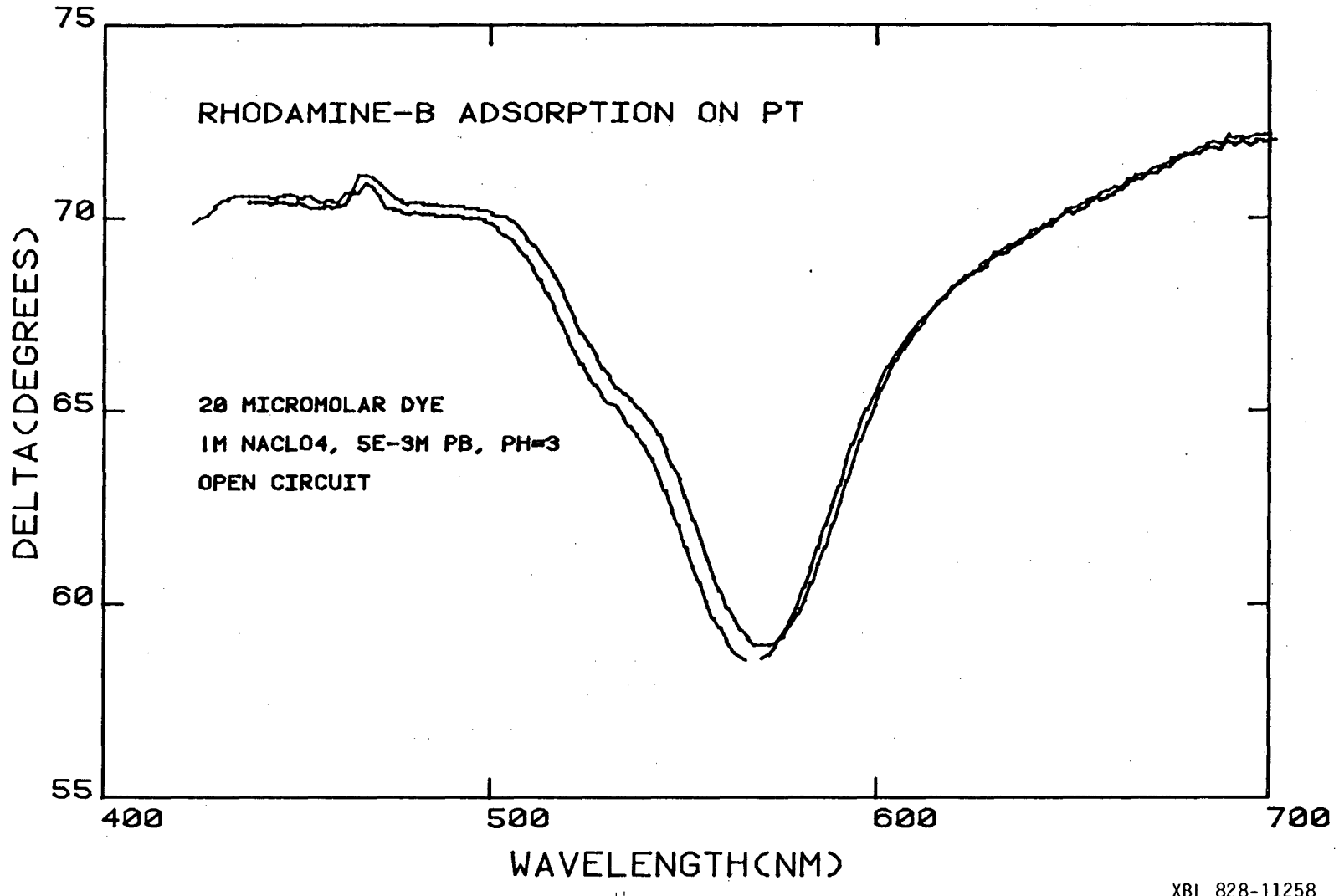

Fig. 7.a

XBL 828-11258

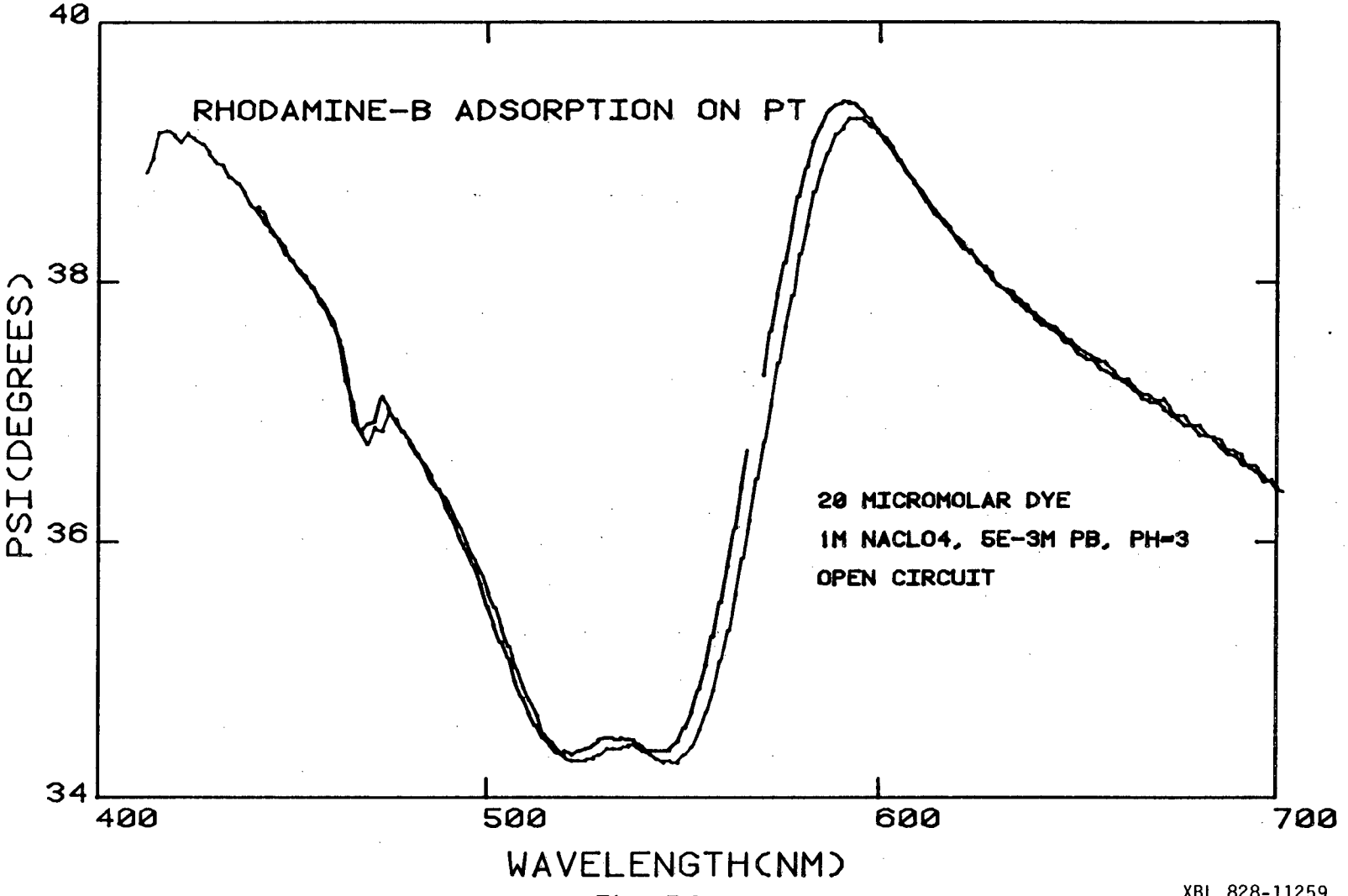

Fig. 7.b

XBL 828-11259

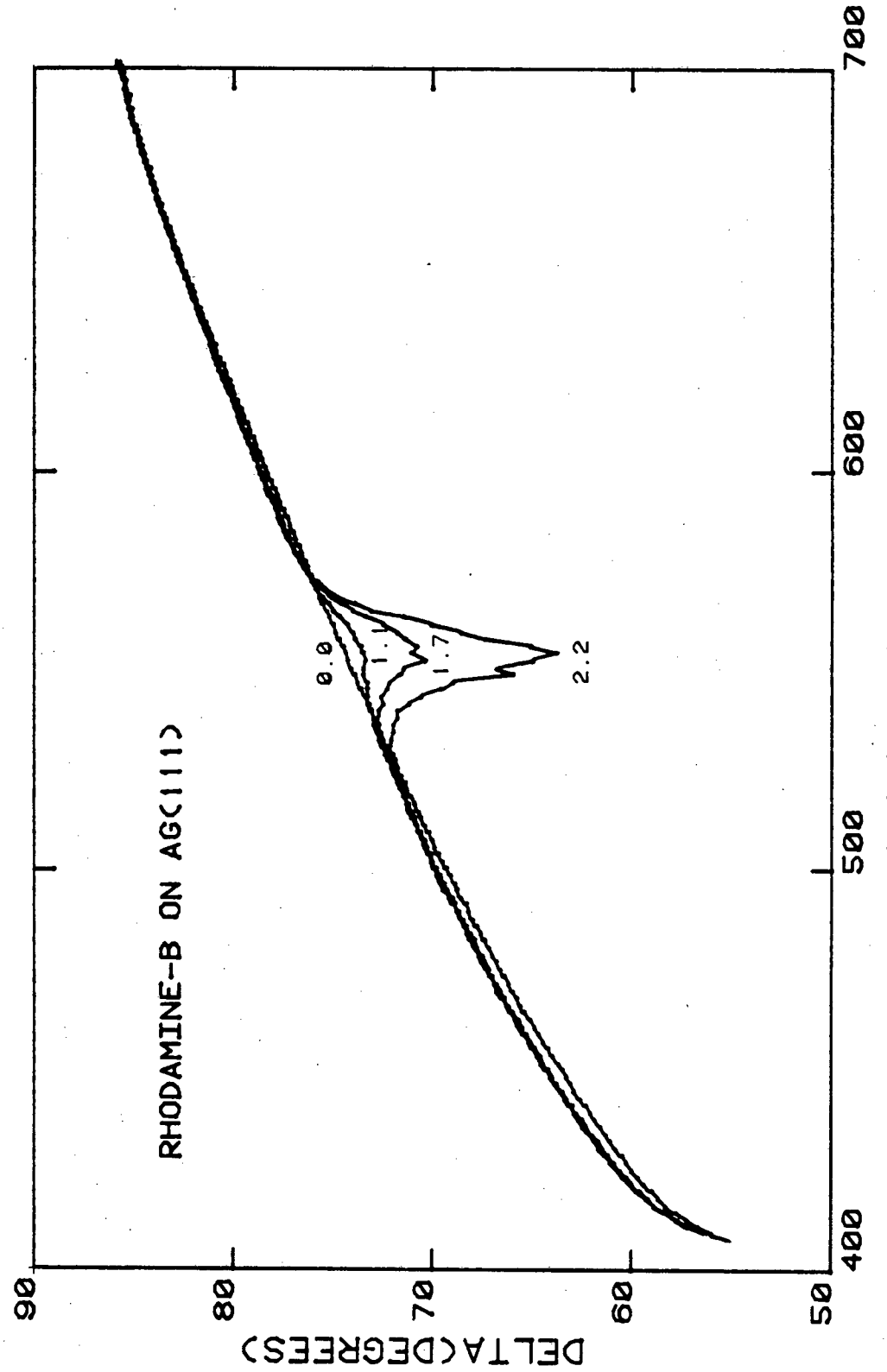

XBL 831-7743

Fig. 8.a

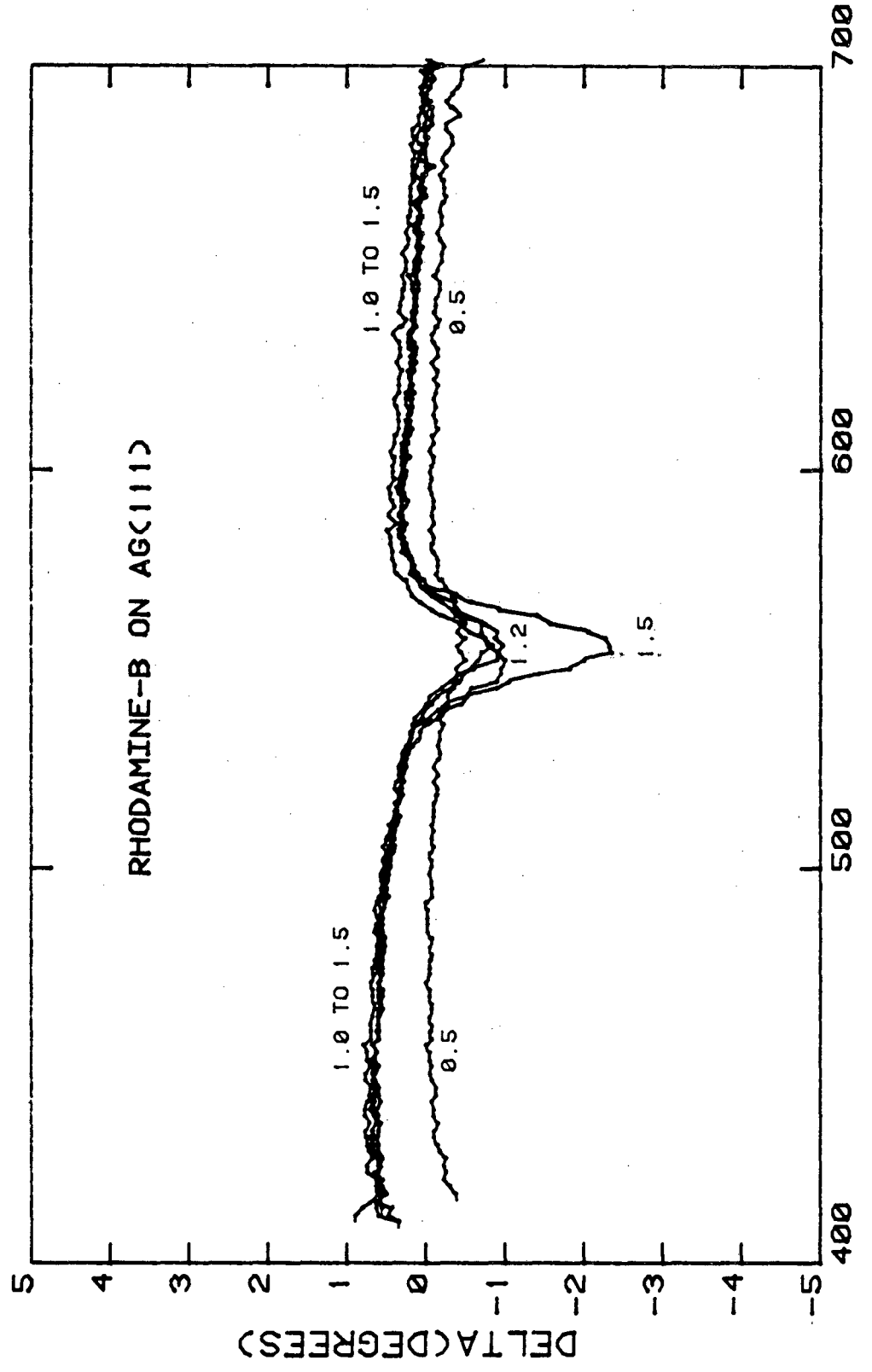

XBL 831-7744

Fig. 8.b

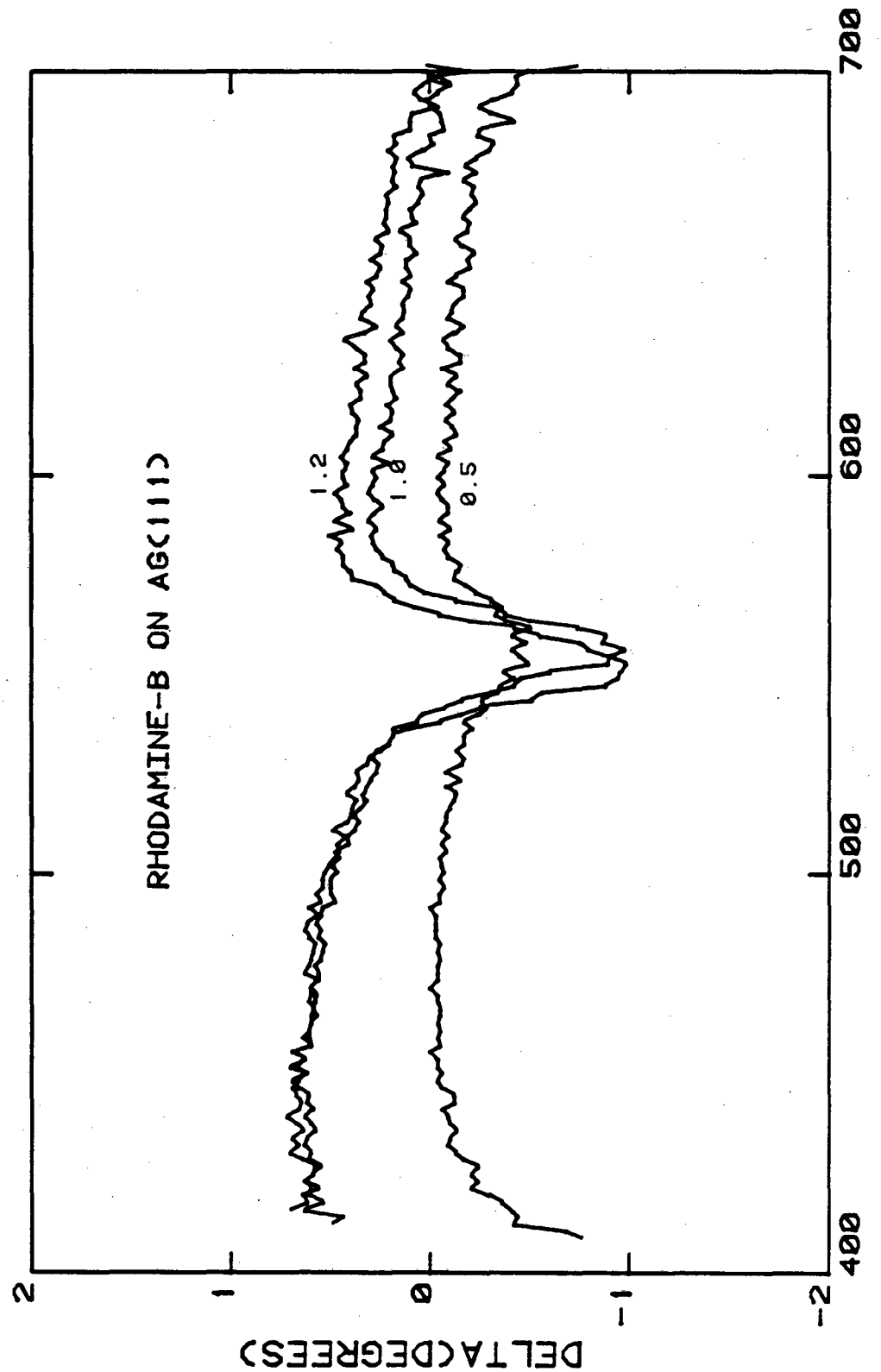

XBL 831-7745

Fig. 8.c

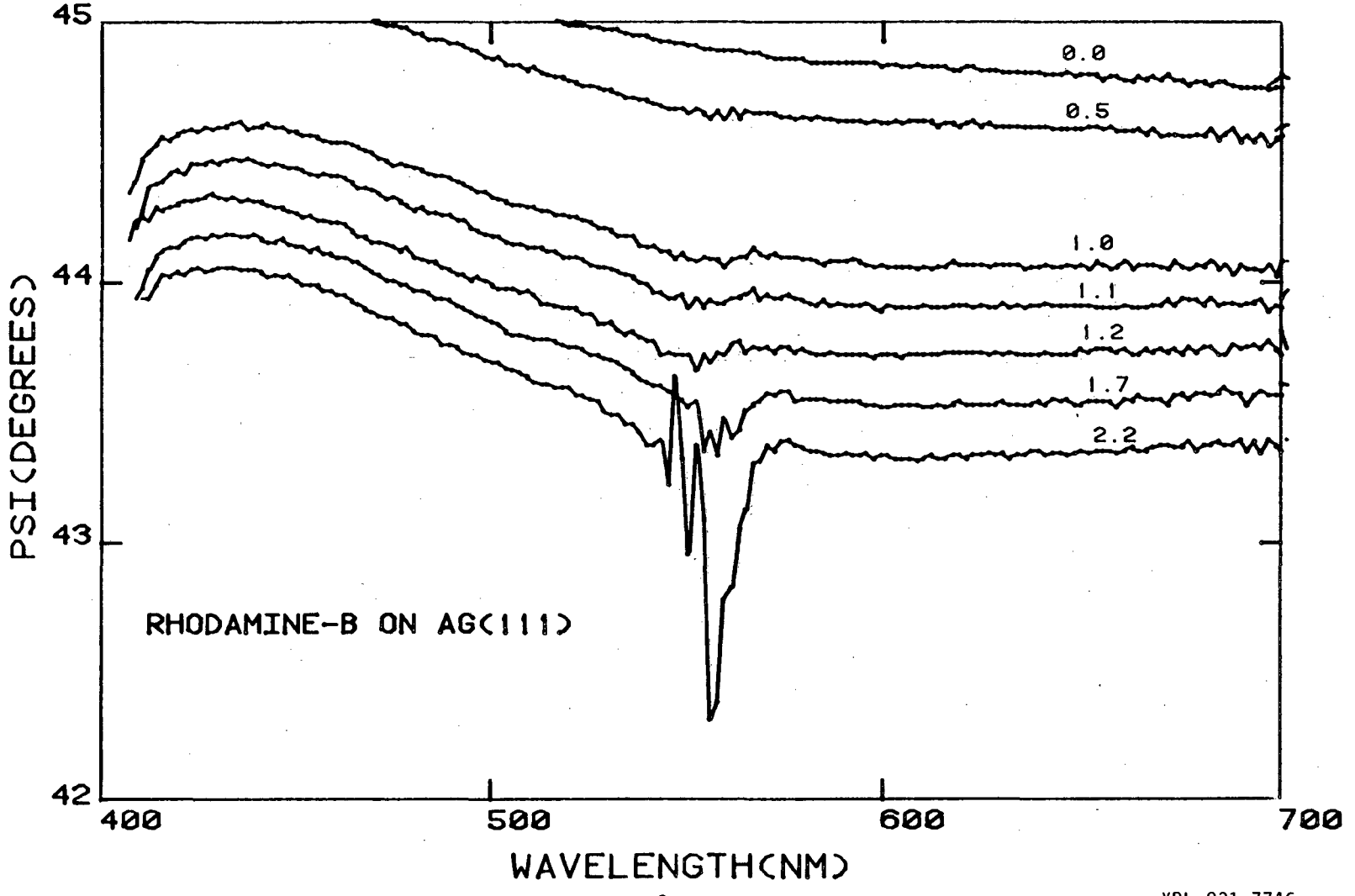

Fig. 8.d

XBL 831-7746

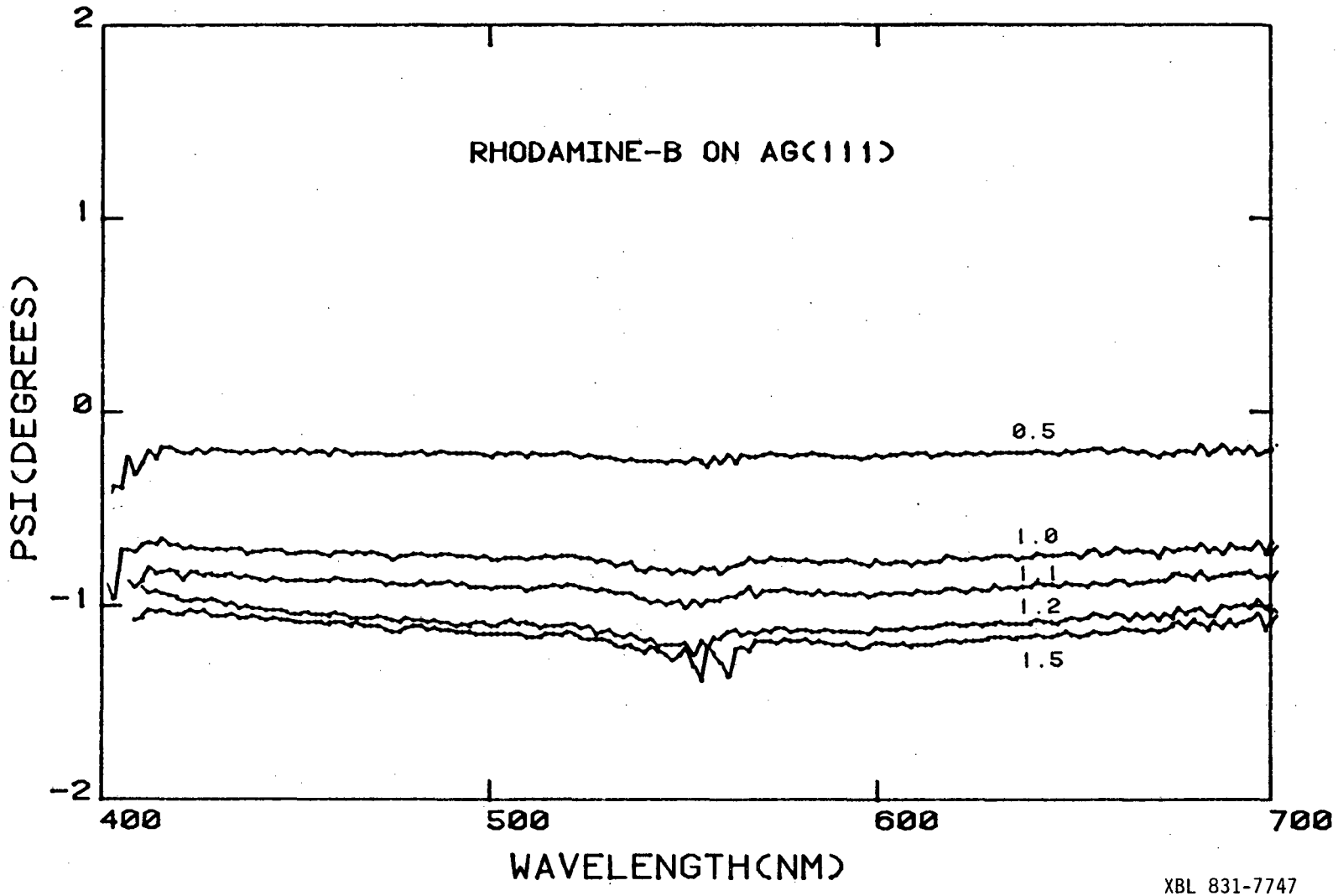

XBL 831-7747

Fig. 8.e

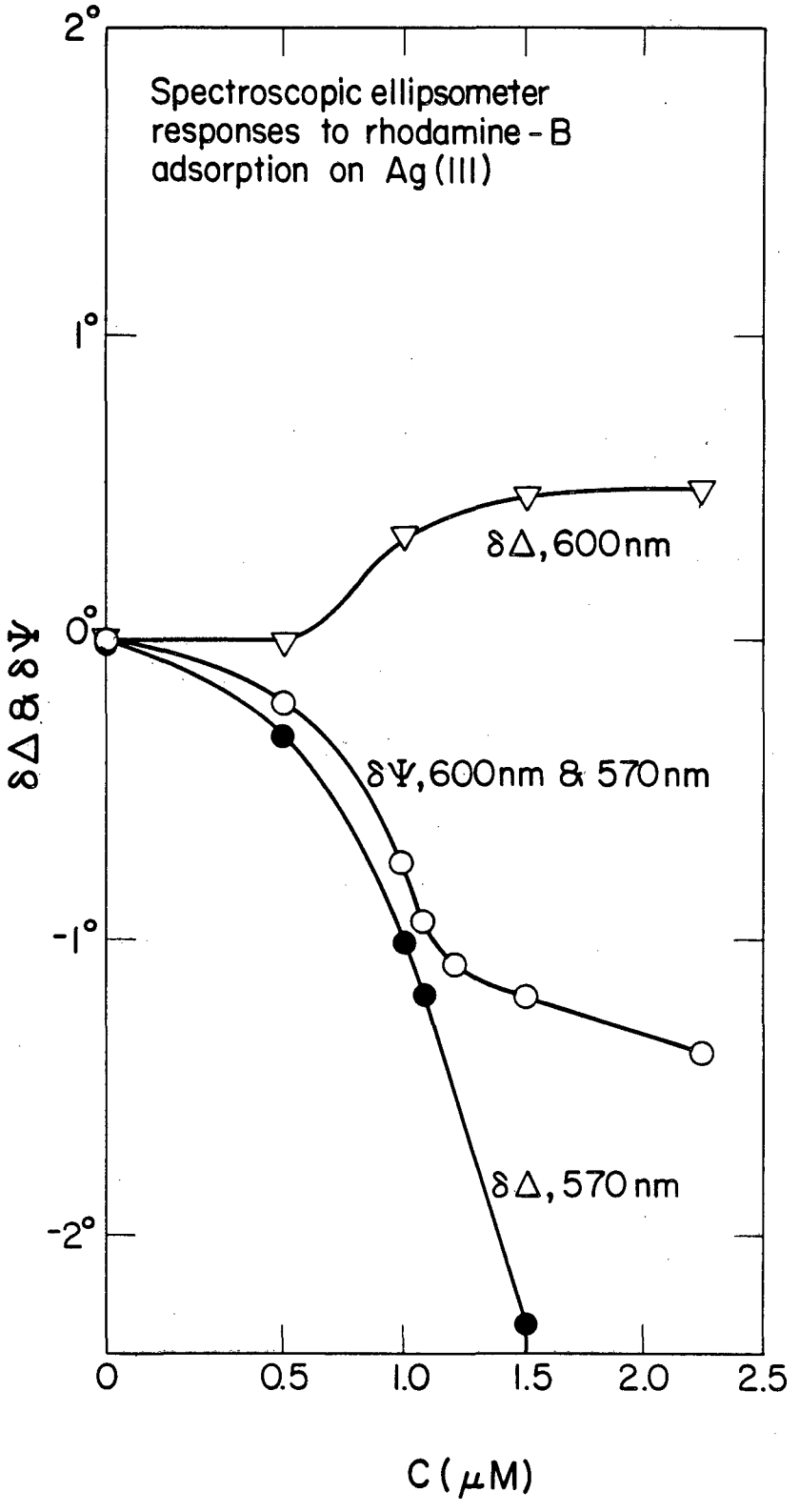
Spectroscopic ellipsometer
responses to rhodamine-B
adsorption on Ag(111)
2°
1°
0°
-1°
-2°
δΔ & δΨ
δΔ,600nm
δΨ,600nm & 570nm
δΔ,570nm
0
0.5
1.0
1.5
2.0
2.5
C(μM)
XBL 831-1133

Fig. 8.f

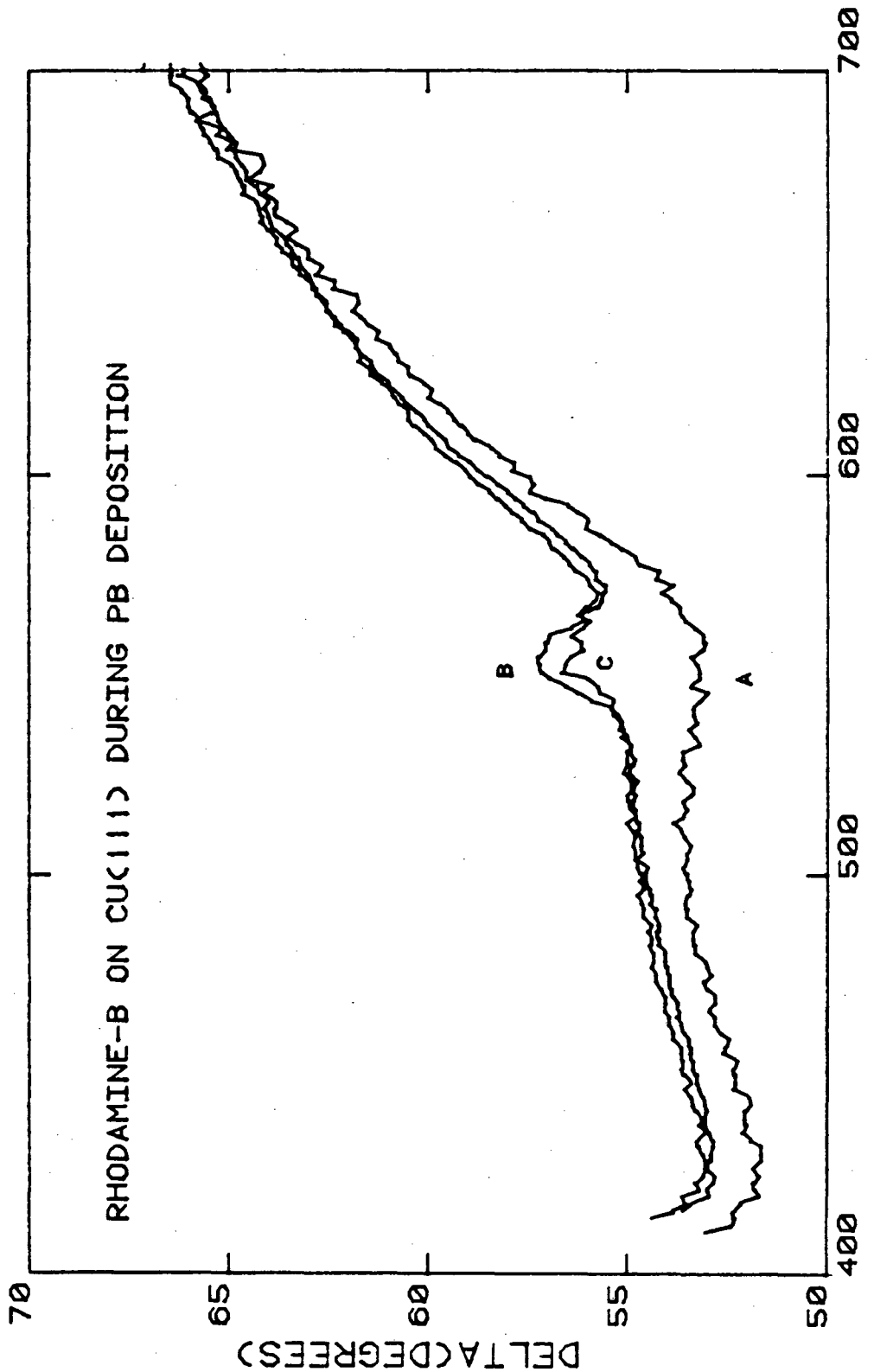

XBL 831-7748

Fig. 9.a

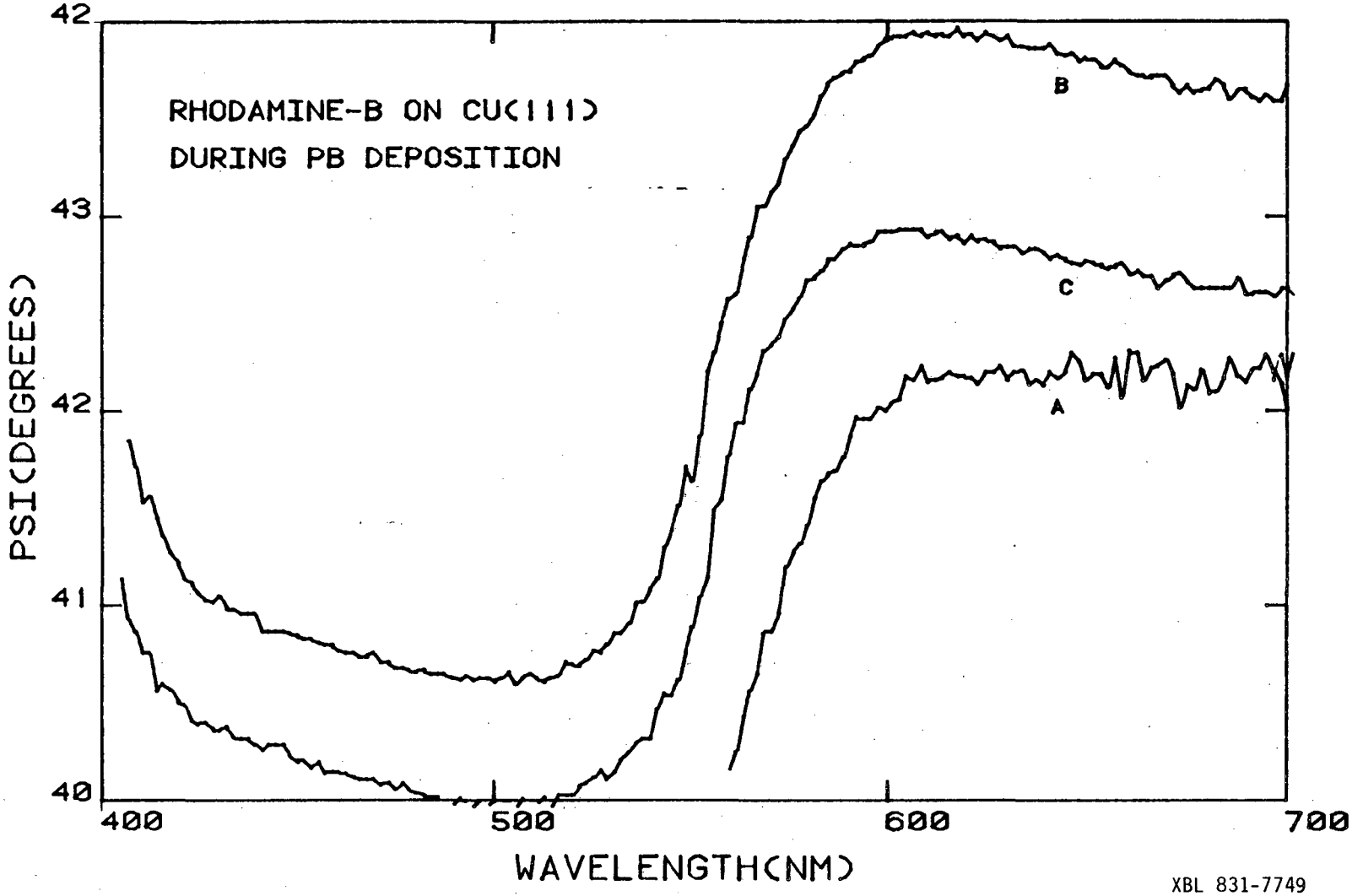

XBL 831-7749

Fig. 9.b

Chapter 9

SCANNING ELECTRON MICROSCOPY COMPLEMENTING ELLIPSOMETRY OF THIN LEAD ELECTRODEPOSITS

Abstract

Scanning electron microscopy was performed of thin Pb electrodeposits (less than 1000 Angstroms thick) on Cu to complement ellipsometry measurements taken during the formation of the Pb layers. In the absence of rhodamine-B inhibitor, deposits were found to consist of dendritic islands with a much fine granular distribution of Pb between the islands. This non-compact, non-homogeneous deposit structure was correlated with unusual ellipsometric observations. The addition of rhodamine-B was found to inhibit growth of the dendritic islands; consequently, all of the Pb deposited was distributed as a fine, granular deposit.

Introduction

Though the results presented in this chapter were obtained early in the study, they are presented last. The experimental techniques used, spectroscopic ellipsometry in particular, were still under development when these results were obtained. Furthermore, these results are all qualitative in nature. Results presented in earlier chapters were quantifiable and were obtained after a greater degree of experimental refinement was achieved.

Pb was deposited on Cu(111) from an electrolyte composed of 5 millimolar $Pb(NO_3)_2$ and 1 M $NaClO_4$ at pH 4 under potentiostatic conditions (-600 mV vs Ag/AgCl ref.). Ellipsometry at a fixed-wavelength (515 nm) was done during the depositions; spectroscopic ellipsometry of the deposits formed after different deposition times was also performed. Subsequently, deposits were removed from the electrochemical cell and investigated by scanning electron microscopy with energy dispersive analysis of X-ray emission (EDAX).

These studies help substantiate the interpretations of ellipsometry data presented in earlier chapters. Negative changes in delta during the initial stages of deposition in the absence of rhodamine-B were attributed to the formation of a porous, granualar deposit covered by relatively large, dendritic islands. Recall that if Pb covers a Cu substrate as a compact layer the corresponding changes in delta are positive. Though the most prominent features in SEM photographs are the dendritic islands, the unusual optical properties of the surface are primarily due to a fine, granular Pb deposit distributed between the islands (see Chapter 7).

Experimental procedures used for this study are similar to those discussed in Chapters 5 and 6, except here a potential step was applied to the working electrode rather than a potential ramp.

Results

Potential steps like the one pictured in Fig. 1 were applied to the working electrode. Corresponding responses of the cell current and of the ellipsometer are shown in Figs. 2, 3, and 4 respectively.

In Fig. 2 it is seen that rhodamine-B additions reduce the initial current passed upon polarization of the cathode by about 50 percent; however, after extended periods of time the current levels achieved with and without this inhibitor are more nearly the same. This observation may be attributable to the reduction of rhodamine-B at the cathode during Pb electrodeposition; the inhibitory effect would diminish with depletion of the dye from the surface.

Fig. 3 and 4 show the ellipsometer response to the potential step (delta and psi plotted against time, respectively). Data are shown for experiments with and without rhodamine-B additions. Initially, in the absence of rhodamine-B, delta changes in a direction opposite to that expected for a compact, homogeneous film.

Similar observations were made with spectroscopic ellipsometry of deposits. These measurements are shown in Figs. 5.a and b (no dye added) and in Figs. 6.a and b (10 micromolar rhodamine-B) for deposition times of 1, 3 and 8 minutes (30, 60, 110 nm), respectively. These deposition times give thicknesses comparable to those of spectroscopic data shown in Chapters 6 and 7. However, deposits made here with and without dye contain slightly different quantities of Pb, even though the deposition times are equivalent. These deposits were not stripped after spectroscopic measurements since they were to be removed from solution for

SEM investigations, so exact coulometric measurements were not made. Some corrosion dissolution of the deposit may have occurred between deposit formation and the spectroscopic ellipsometry measurements taken at open circuit. Peaks at the rhodamine-B absorption wavelength are artifact (see Chapter 2).

After electrodes were removed from the electrochemical cell they were rinsed with distilled water; after exposure to air they immediately oxidized. While submersed in electrolyte the surfaces were the same color as Pb, but slowly turned the color of Cu upon oxidation. Ellipsometry was done of the deposits formed after 8 minutes at -600 mV (Ag/AgCl ref.) in the electrochemical cell (Figs. 7.a and 7.b); electrolyte containing dye was displaced by fresh electrolyte containing no dye (because of the artifact peak problem). Note that the curves representing the deposit before oxidation (exposure to air) show no absorption bands associated with rhodamine-B. However, after oxidation the deposits (now lead oxide) are more transparent and a dye absorption peak appears in the spectroscopic measurements of the oxidized Pb layer formed in the presence of rhodamine-B. Evidently, the rhodamine-B is incorporated into the Pb electrodeposit and is not visible until the layer is made more transparent by oxidation.

Scanning electron micrographs of Pb electrodeposited layers on the Cu substrate are shown in Fig. 8 for deposition times of 1, 3, and 8 minutes; all three surfaces shown here were prepared in the absence of rhodamine-B and illustrate the growth of dendritic islands discussed in previous chapters. Again, recall that the ellipsometer is primarily

sensitive to the optical properties Pb distributed between the islands initially (1 minute and 3 minute deposits). Fig. 9.a and 9.b show the effect of introducing rhodamine-B into the electrolyte during Pb electrodeposition; initially, the deposit grows as a finer, granular deposit. At later times (8 minutes) dendrites eventually form, even in the presence rhodamine-B; this too may be attributable to depletion of this inhibitor at the electrode surface. EDAX data for the deposits shown in Fig. 9.a and 9.b are given in Fig. 10; these data are presented to confirm the assumption that the islands are indeed composed of Pb. These data eliminates the possibility of crystallization of supporting electrolyte on the surface, which could have left residue (islands) on the surface.

The peak corresponding to the Pb M lines were found to be more intense (relative to the peak corresponding to the Cu L lines) when the electron beam was positioned on islands rather than between islands. Though this Pb peak is of much lower intensity (relative to the Cu peak) in areas between islands, it is still present. This supports the notion that there is a fine, granular Pb deposit between the dendritic islands. Compare the two results for 1 minute referred to as "probe on dendritic islands" and "probe between islands."

Even though the Cu surface was completely Pb covered, Cu peaks were still observed by EDAX. This is probably due to the deep penetration of 20 KeV electrons into the sample surface; by extrapolation of the "universal curve" given in reference 1, the penetration depth is believed to be greater than 100 Angstroms (assuming a compact solid).

It is also noted that X-ray emission from the Cu substrate (Cu K line) induces X-ray fluorescence in the Pb dendrites sitting on the surface (Pb M line), causing some unpredictable amplification of the Pb peaks. Problems such as these make quantification of the EDAX analyses impractical.

Fig. 11 shows SEM photographs taken at a much later date than those shown in Fig. 9.a and 9.b with an electron microscope capable of better resolution. Furthermore, the deposits shown in Figs. 9.a and 9.b were formed with a Pt counter electrode and with the working electrode in a vertical position. The deposits shown in Fig. 11 were formed on a horizontal electrode (facing downward) in a cell with a Pb counter electrode. Qualitatively, results were similar. Dendrites formed in the absence of rhodamine-B, and were prevented when rhodamine-B was added to the electrolyte. Photograph A shows a dendrite formed on a surface after just a few minutes of deposition in the absence of rhodamine-B; B is a magnification of the area between large dendrites seen on the surface; C represents a position on the electrode at a later stage of deposition, also an area between dendrites. Comparable deposits were formed with rhodamine-B added to the electrolyte, and are represented by photographs D, E, and F, respectively. If the deposits had been uniform and compact, the thicknesses of the Pb layers in the cases of A, B, D, and E would have been about 30 nm; the thicknesses of the Pb layers in the cases of C and F would have been about 100 nm (on the basis of digital coulometry).

Conclusions

This portion of the study has shown that rhodamine-B prevents the formation of dendrites during the initial stages of Pb electrodeposition on Cu and results in a Pb layer of finer structure. Rhodamine-B also lowers the cell current under potentiostatic conditions. The unusual trends in ellipsometry data are related to the formation of non-uniform deposits on the surface. Rhodamine-B is incorporated into the Pb electrodeposit.

Reference

1. Somorjai, G. A., CHEMISTRY IN TWO DIMENSIONS, Cornell University Press, Ithaca, NY, 1981, pg. 40.

Figures

1. Potential step applied to Cu cathode during the electrodeposition of Pb from 5 millimolar $Pb(NO_3)_2$ and 1 M $NaClO_4$ at pH 3.

2. Current response corresponding to Fig. 1.

3. Ellipsometer response (delta vs time) corresponding to Fig. 1.

4. Ellipsometer response (delta vs time) corresponding to Fig. 1.

5.a Spectroscopic ellipsometry of Pb deposits formed during various deposition times at the conditions of Fig. 1 in the absence of inhibitor (rhodamine-B); delta vs wavelength.

5.b Psi vs wavelength corresponding to Fig. 5.a.

6.a Spectroscopic ellipsometry of Pb deposits formed during various deposition times at the conditions of Fig. 1 with the addition of rhodamine-B at a concentration of 10 micromolar. Peaks are artifacts. See text.

6.b Psi vs wavelength corresponding to Fig. 6.a.

7.a Spectroscopic ellipsometry of Pb deposits formed formed after 8 minutes at -600 mV (vs Ag/AgCl reference). Dotted lines represent the data for a deposit formed in the absence of rhodamine-B; one scan of the deposit submersed in electrolyte (before oxidation) and one scan of the deposit after exposure to air (after oxidation). Comparable data are shown for a deposit formed with 10 micromolar rhodamine-B. Delta vs wavelength. The compact deposit thickness (based on charge only) was about 1000 Angstroms.

7.b Psi vs wavelength corresponding to Fig. 7.a.

8. Scanning electron micrographs of deposits formed in the absence of rhodamine-B after 1, 3, and 8 minutes at -600 mV. This figure illustrates dendritic island growth of Pb on Cu.

9.a Scanning electron micrographs of Pb electrodeposits formed with and without rhodamine-B additions to the electrolyte.

9.b Comparable to Fig. 9.a, but at a lower magnification.

10. Energy Dispersive Analysis by X-rays (EDAX) of Pb electrodeposits formed on Cu in the absence of rhodamine-B. In each picture four peaks are shown; from left to right (low energy to high energy) these peaks correspond to the copper L lines (0.92 keV), the lead M lines (2.37 keV), the copper K lines (8.03 and 8.90 keV), and the lead L lines (9 keV). Note the change in the peak intensity of the lead M lines in the photographs.

11. Scanning electron micrographs of thin Pb electrodeposits showing porous deposit between larger dendrites (in the absence of rhodamine-B). The scales for the photographs are shown by the small bar.

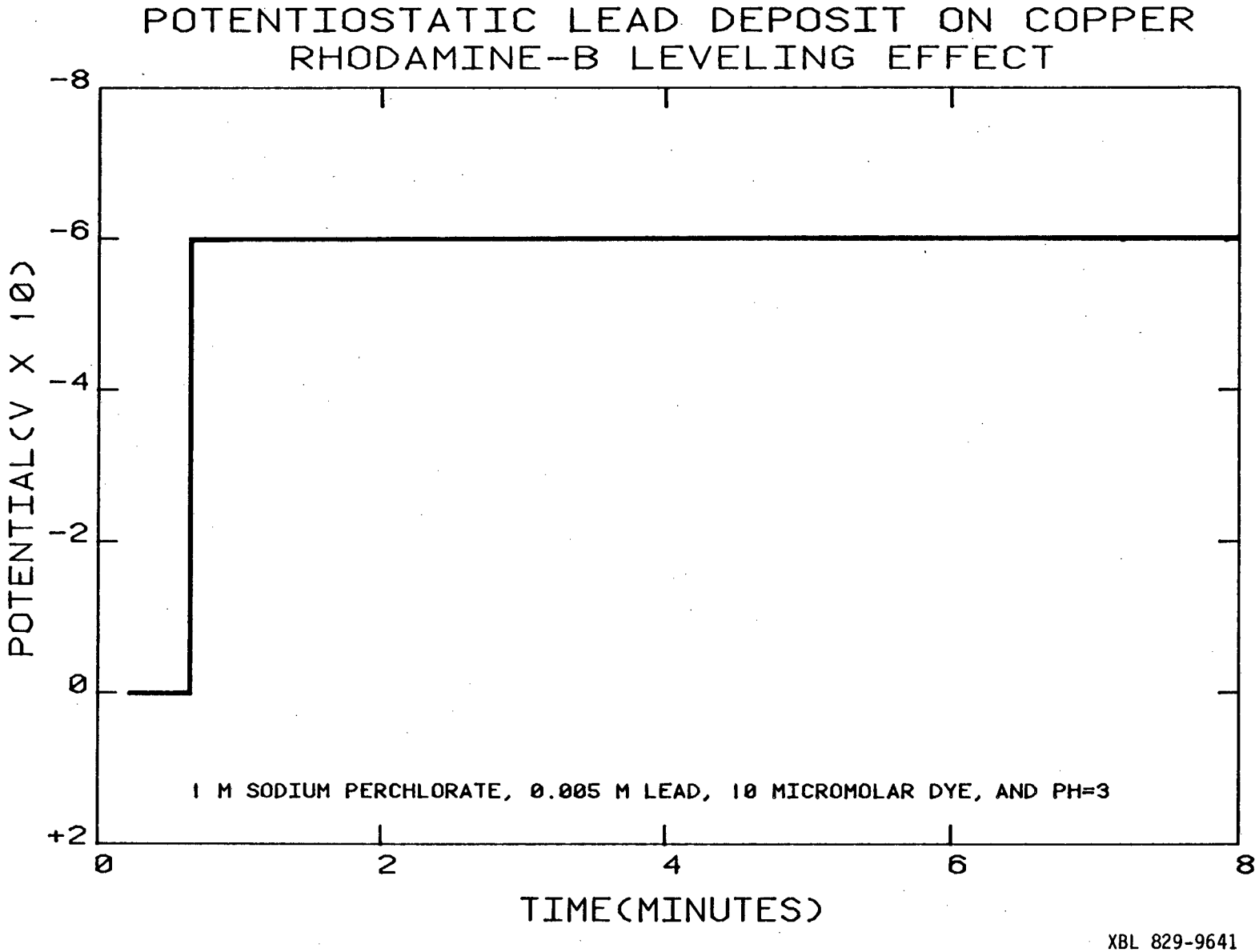
POTENTIOSTATIC LEAD DEPOSIT ON COPPER
RHODAMINE-B LEVELING EFFECT
POTENTIAL(V X 10)
-8
-6
-4
-2
0
+2
0
2
4
6
8
TIME(MINUTES)
1 M SODIUM PERCHLORATE, 0.005 M LEAD, 10 MICROMOLAR DYE, AND PH=3
XBL 829-9641

Fig. 1

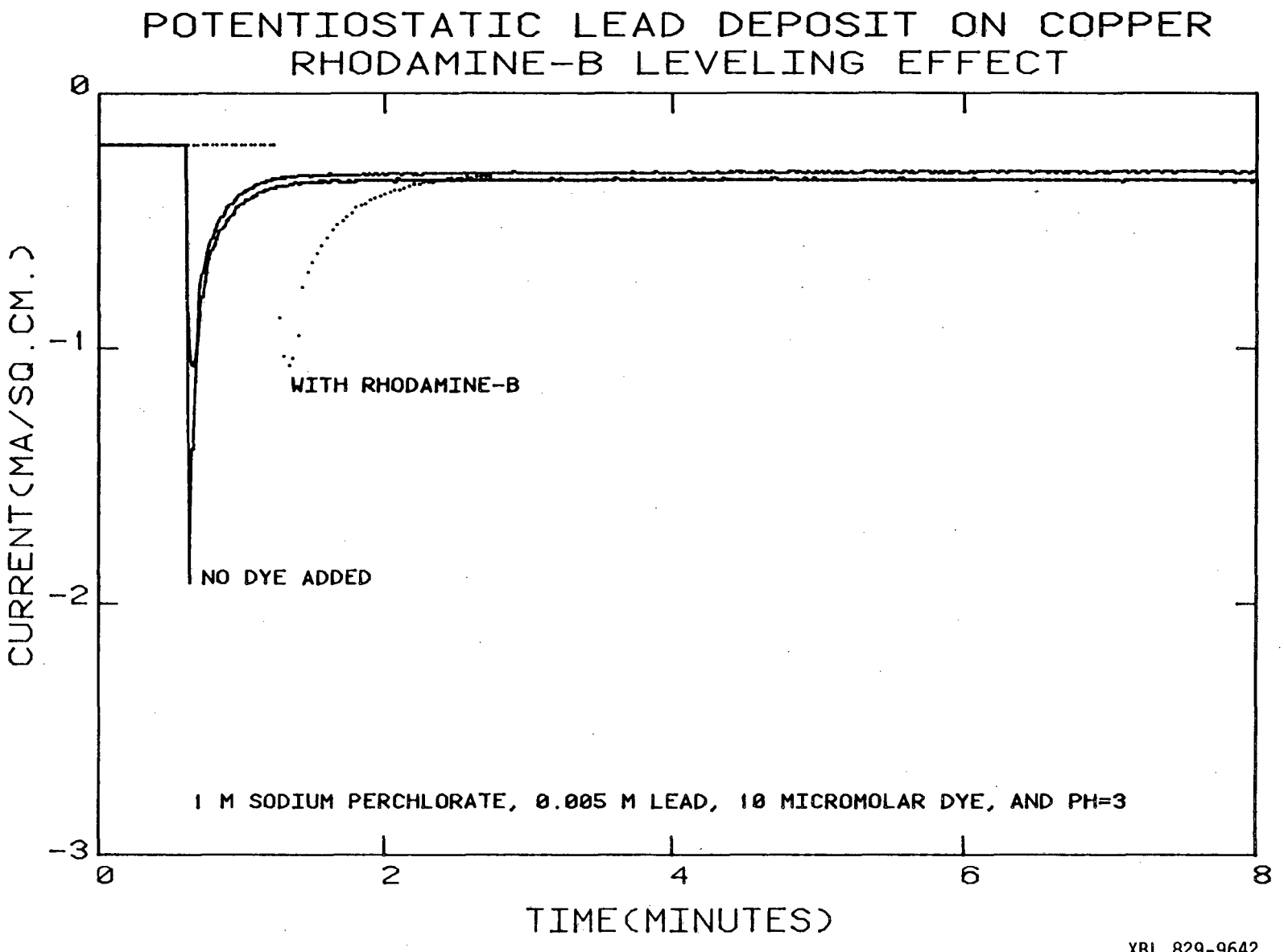

Fig. 2

XBL 829-9642

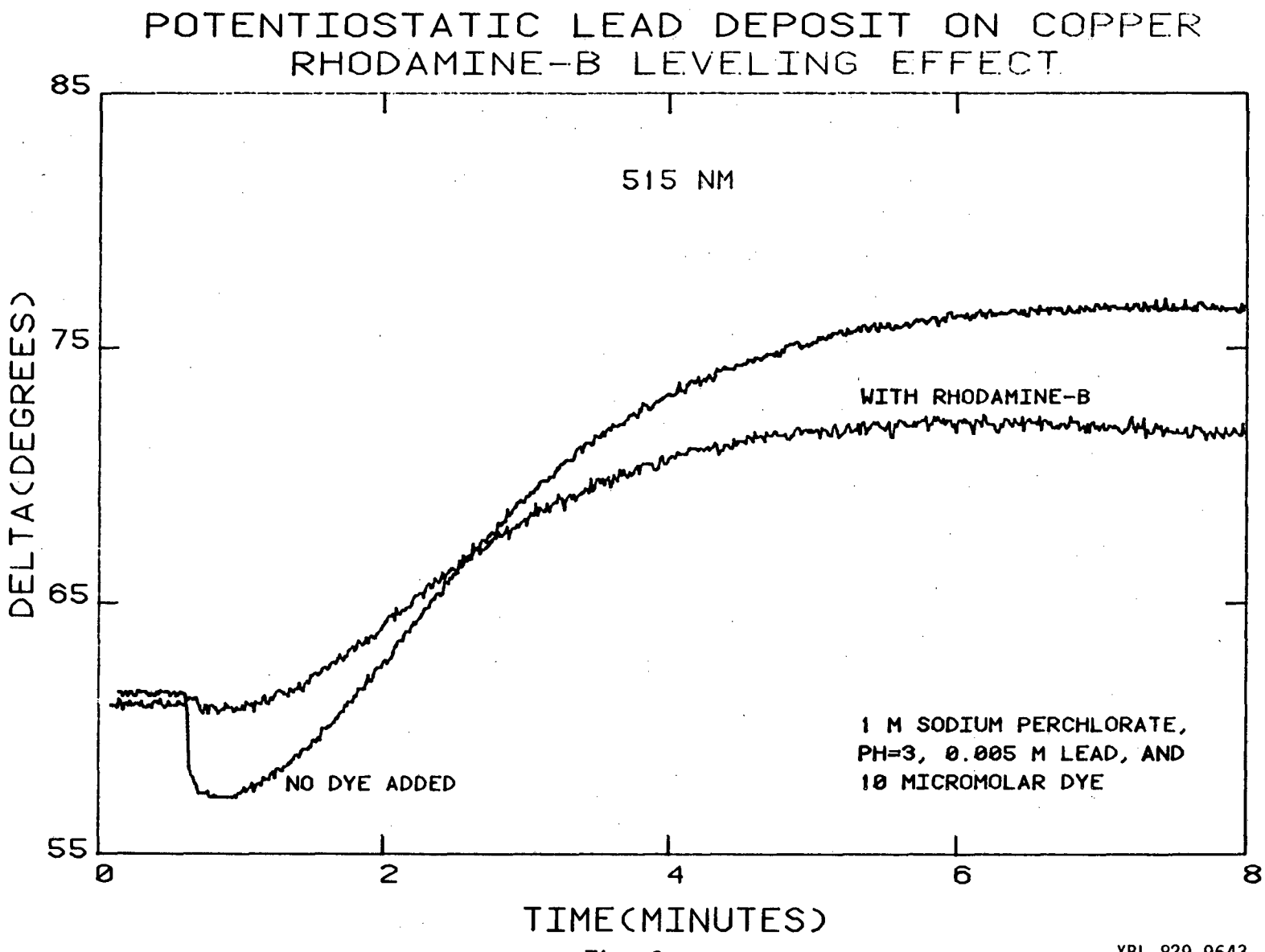

Fig. 3

XBL 829-9643

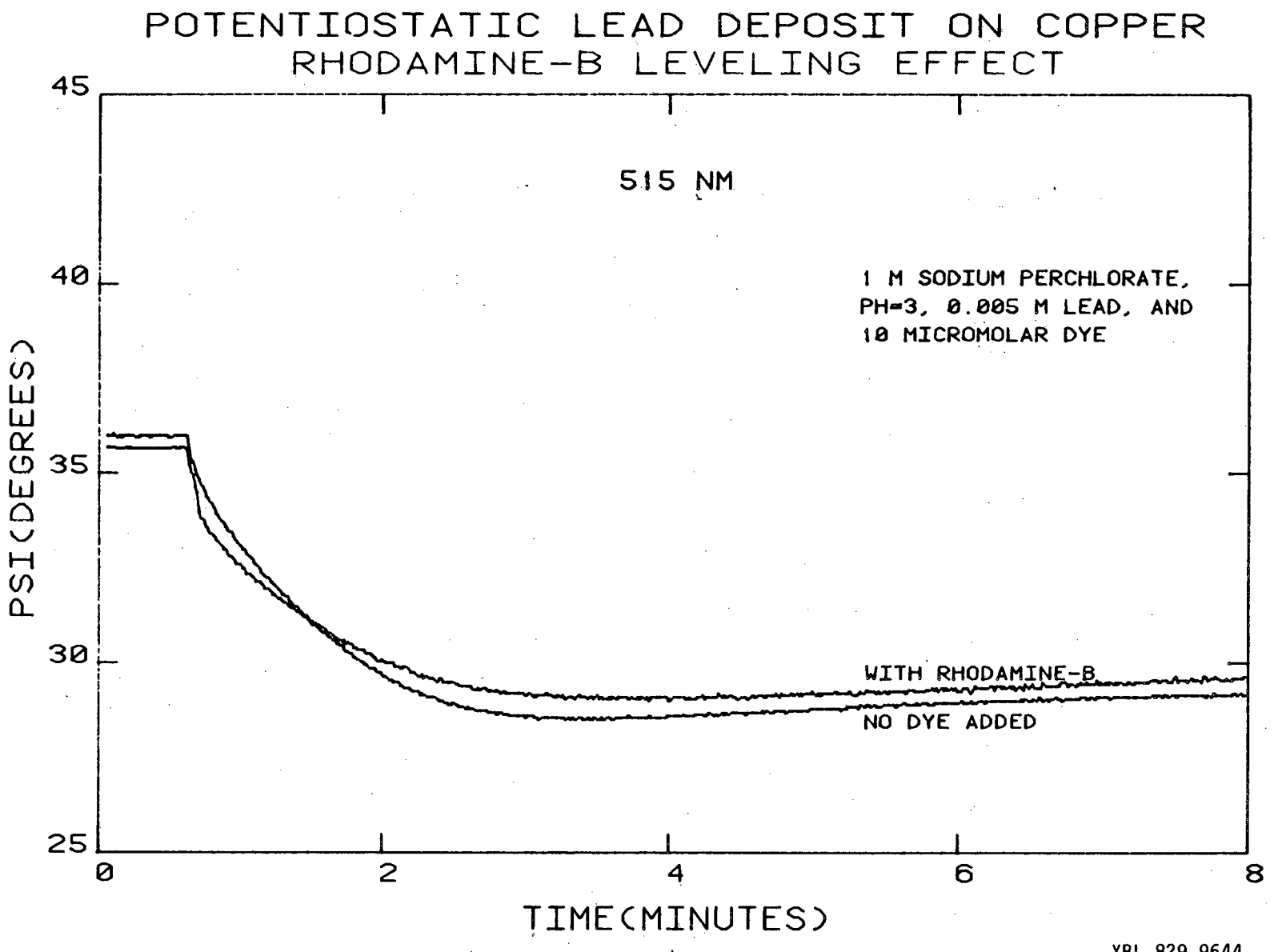

Fig. 4

XBL 829-9644

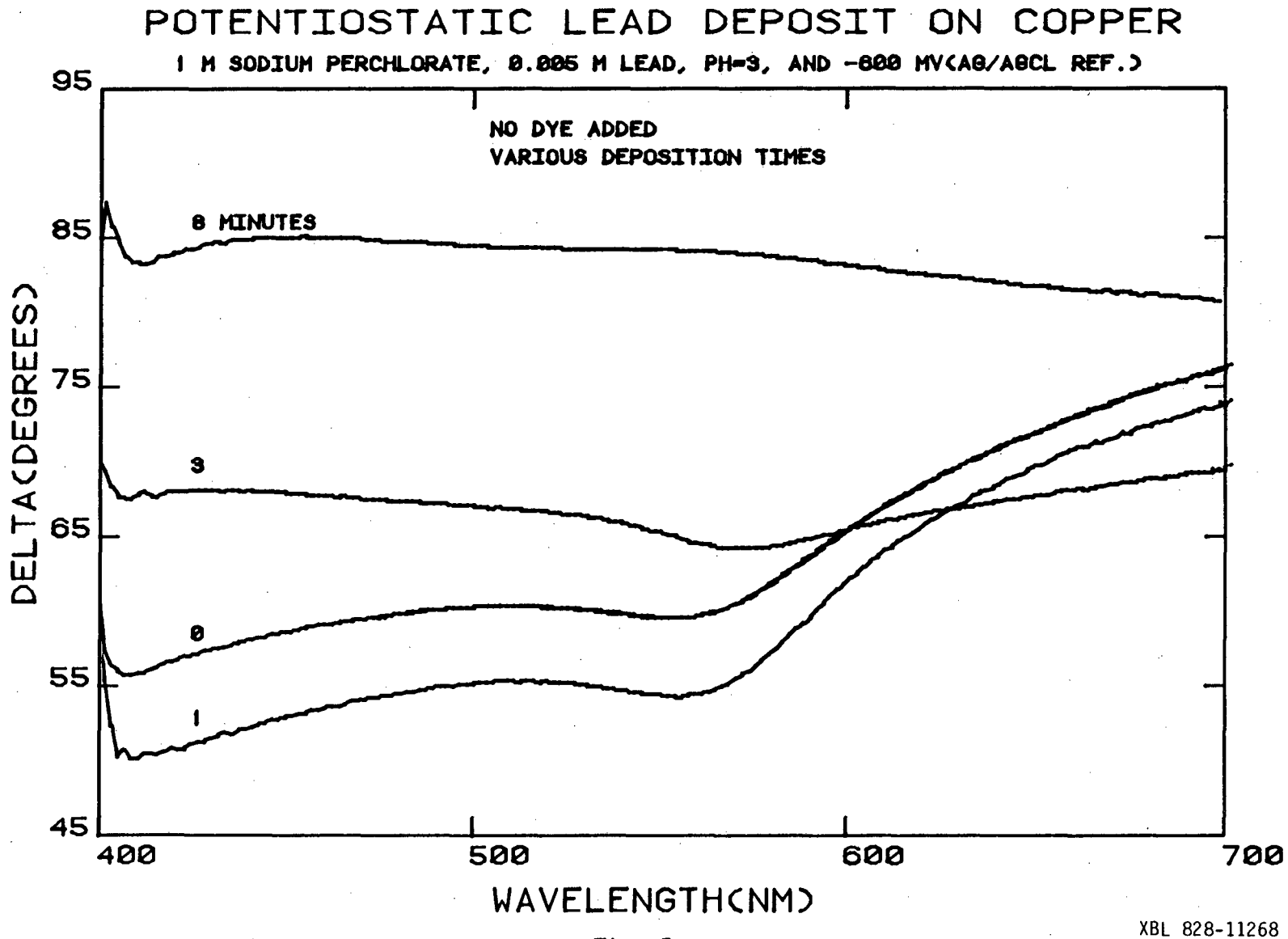

XBL 828-11268

Fig. 5.a

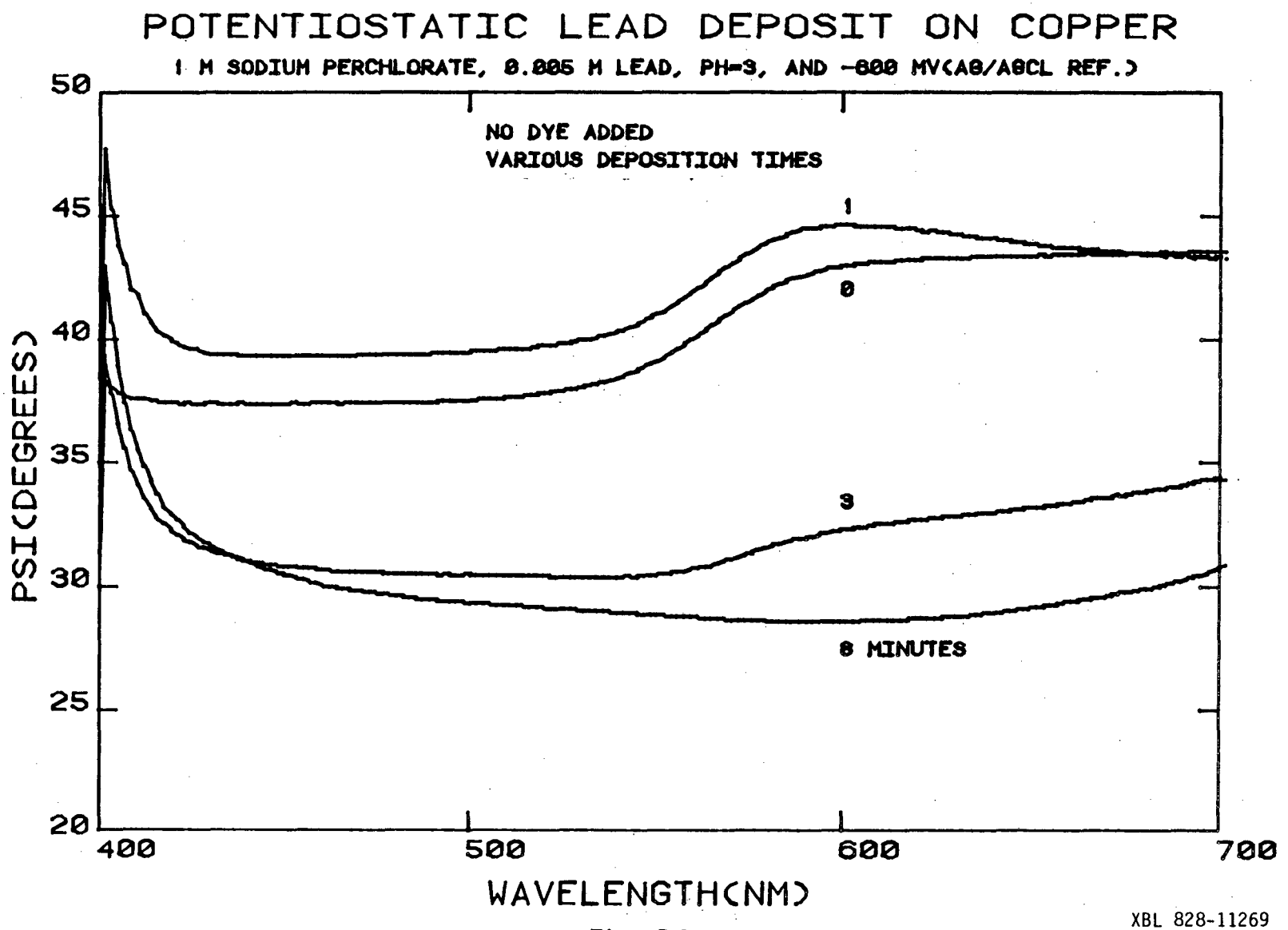

XBL 828-11269

Fig. 5.b

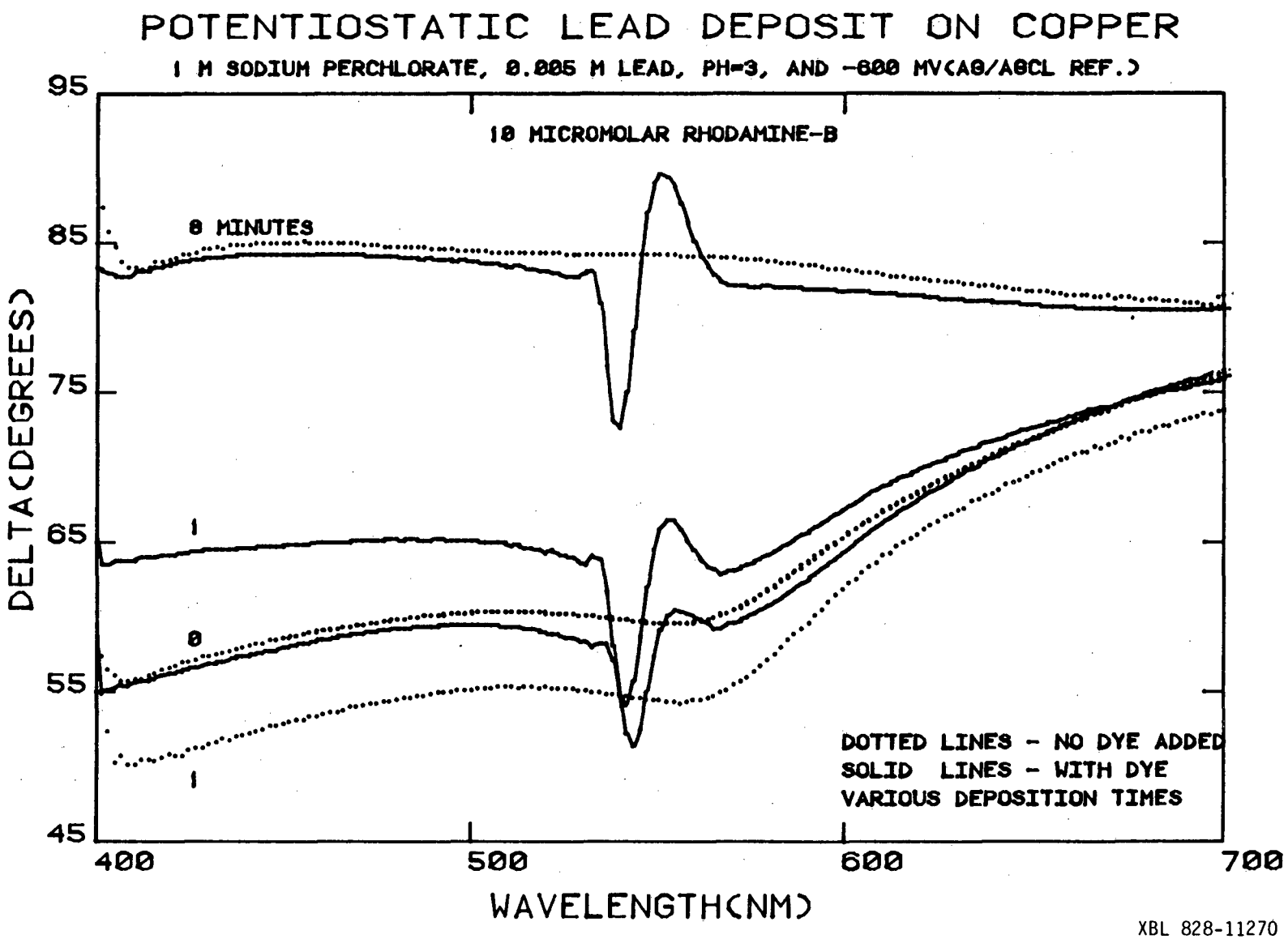

XBL 828-11270

Fig. 6.a

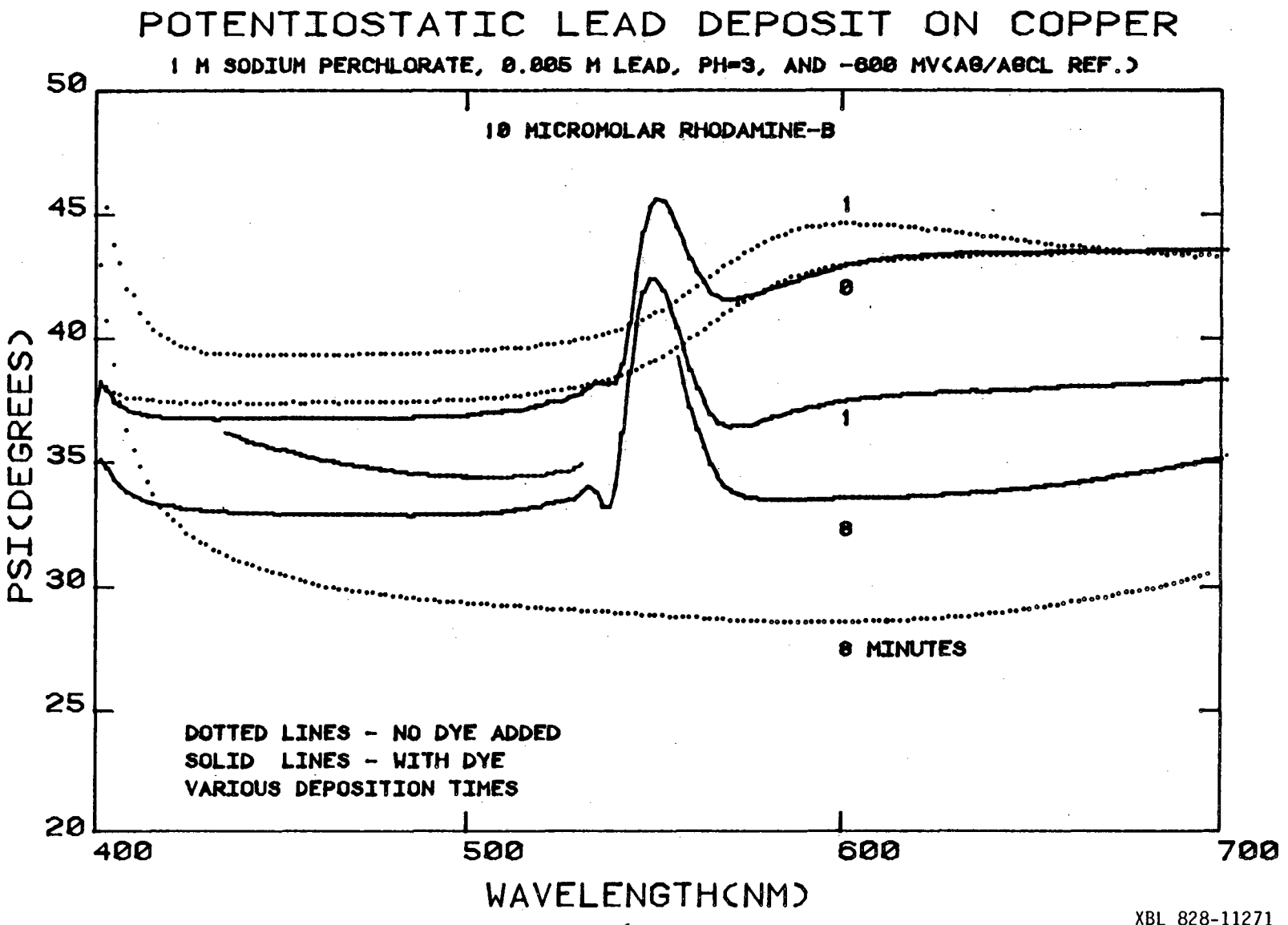

Fig. 6.b

XBL 828-11271

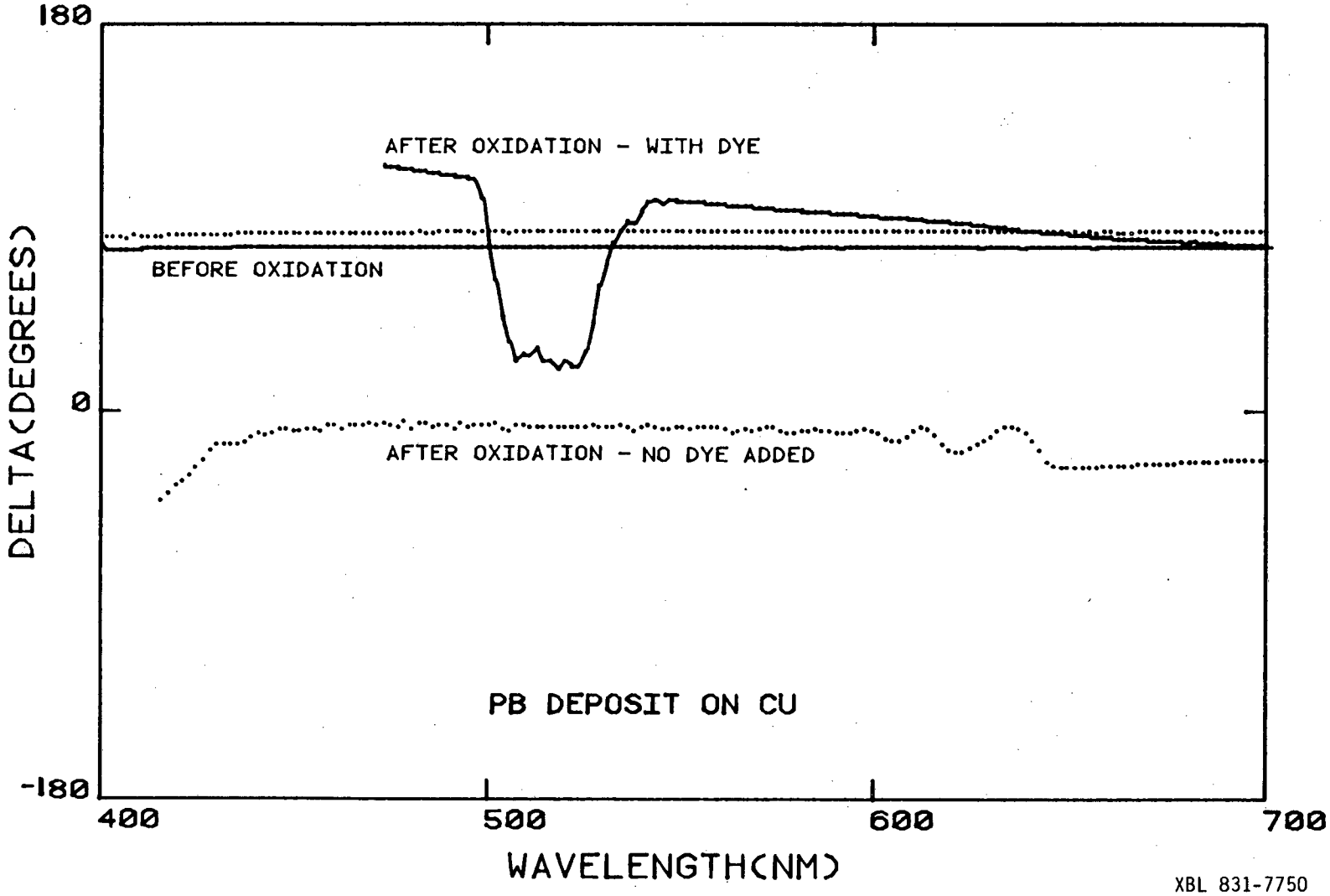

XBL 831-7750

Fig. 7.a

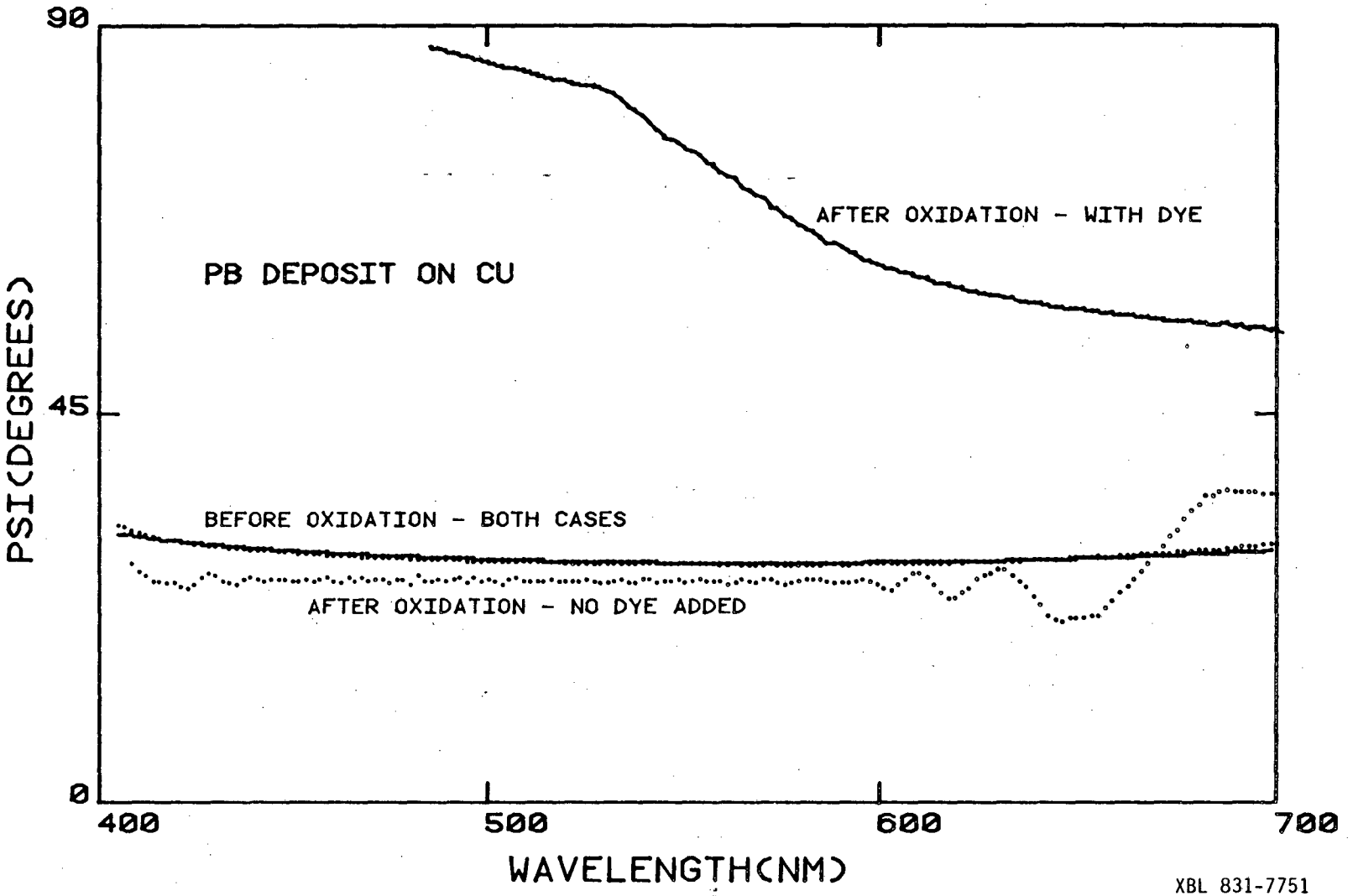

XBL 831-7751

Fig. 7.b

DENDRITIC ISLAND GROWTH OF LEAD ON A COPPER SUBSTRATE

NO DYE ADDED

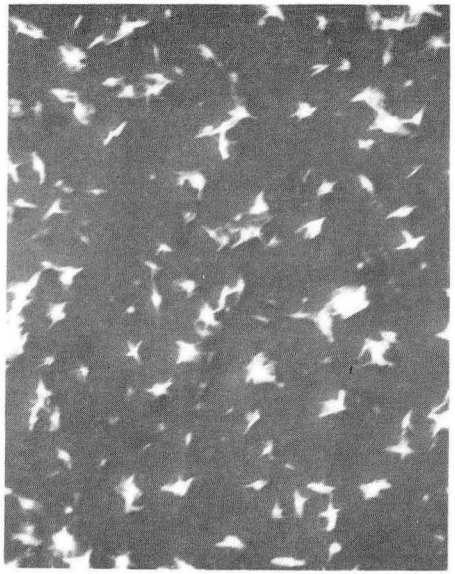

1 MIN DEPOSIT

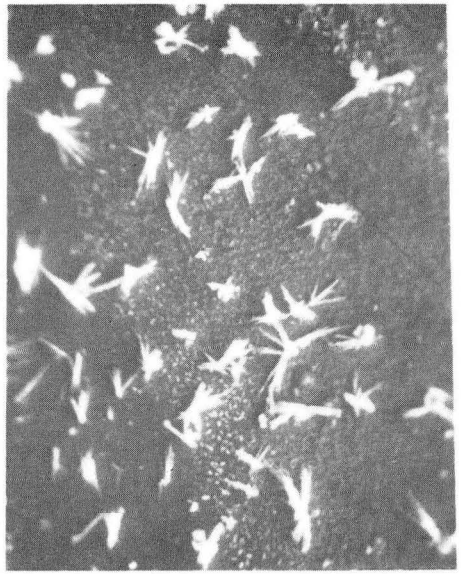

3 MIN DEPOSIT

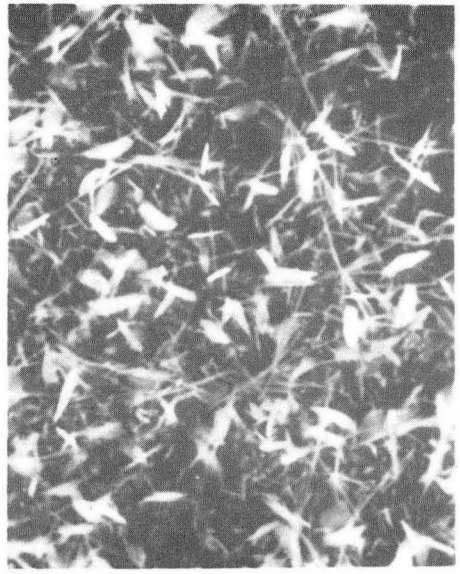

8 MIN DEPOSIT

SCALE: 10 MICRONS

XBB 825-4444

Fig. 8

EFFECT OF RHODAMINE-B ON
LEAD DEPOSIT MICROMORPHOLOGY

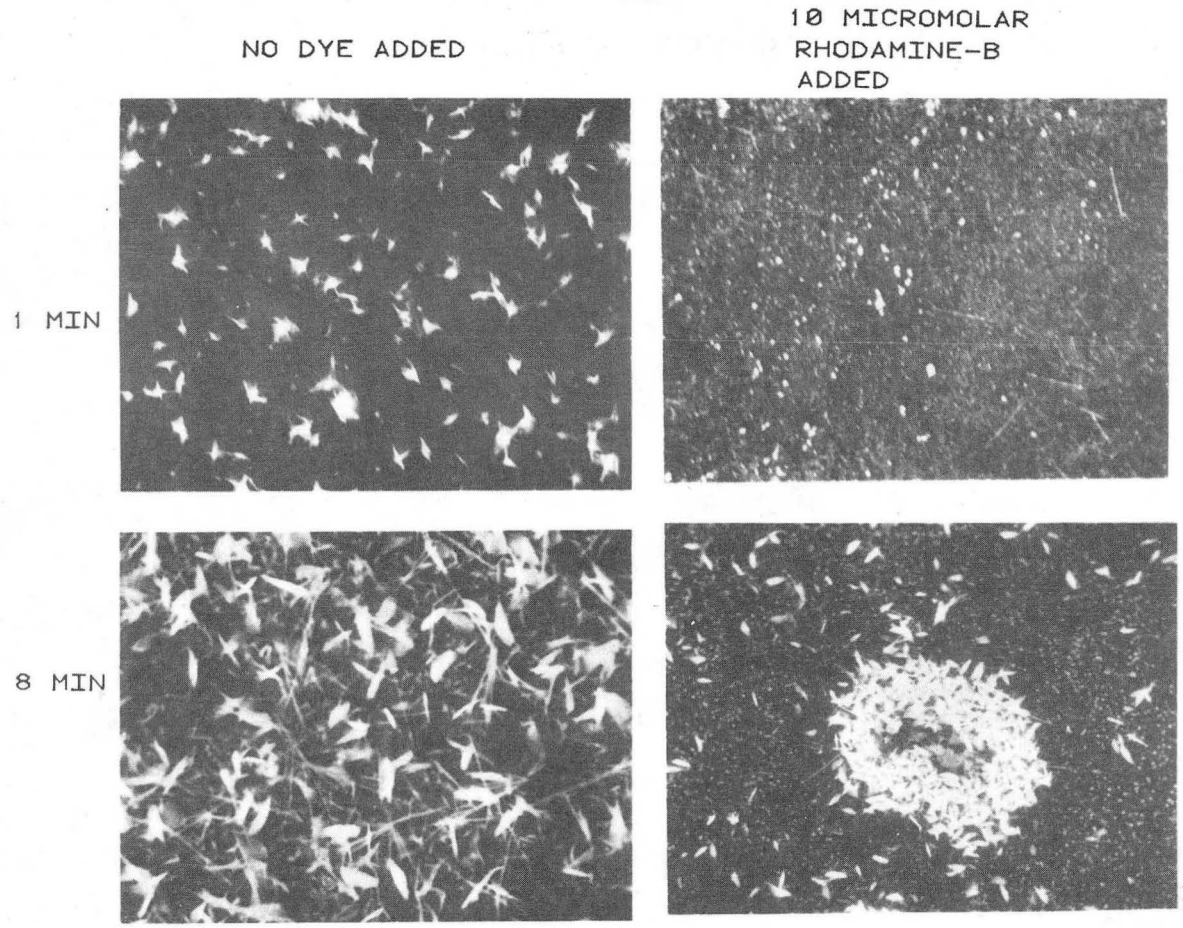

XBB 831-722

Fig. 9.a

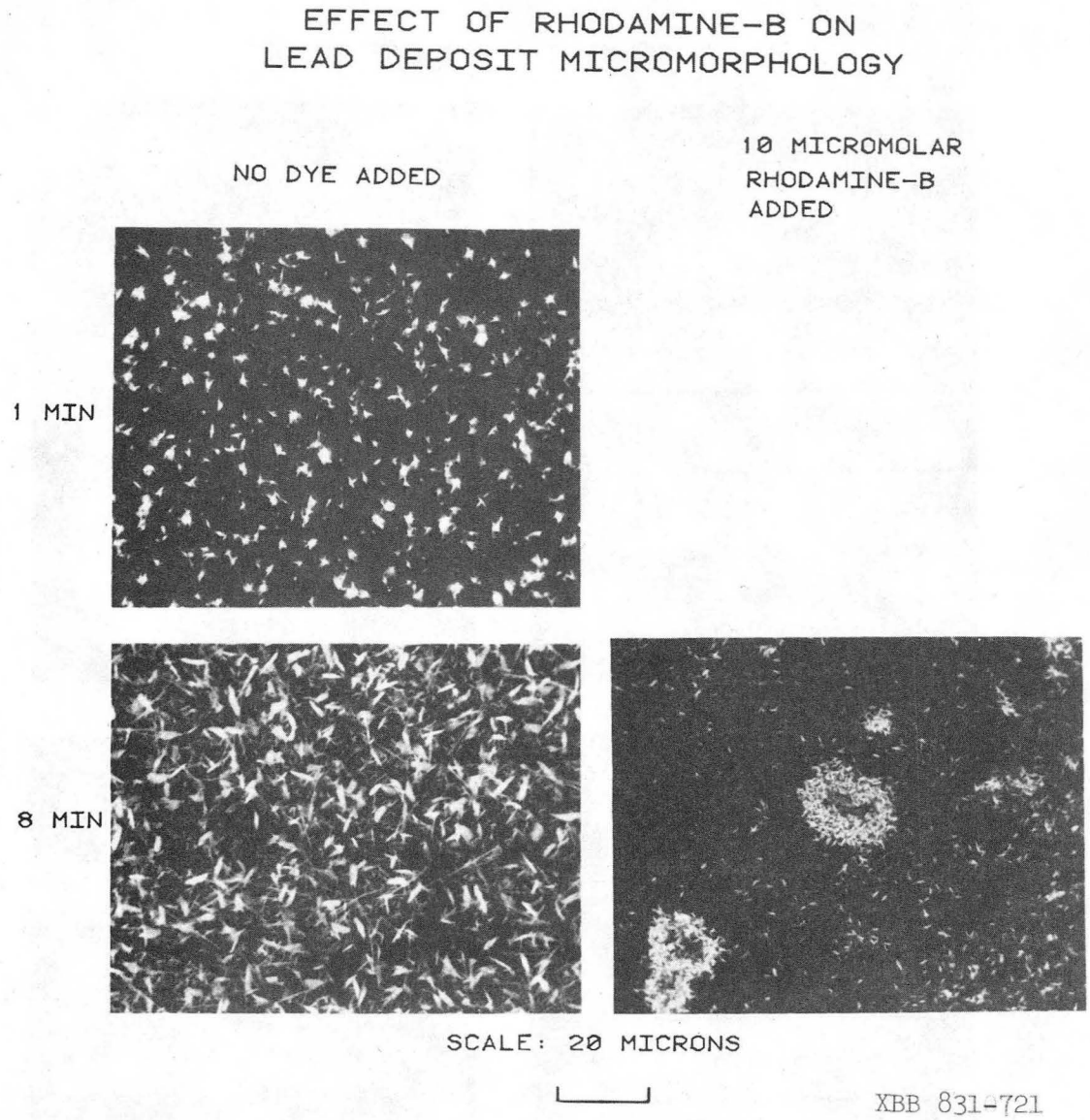
EFFECT OF RHODAMINE-B ON
LEAD DEPOSIT MICROMORPHOLOGY
NO DYE ADDED
10 MICROMOLAR
RHODAMINE-B
ADDED
1 MIN
8 MIN
SCALE: 20 MICRONS
XBB 831-721

Fig. 9.b

EDAX ANALYSIS

LEAD ON COPPER - NO DYE ADDED

1 MIN

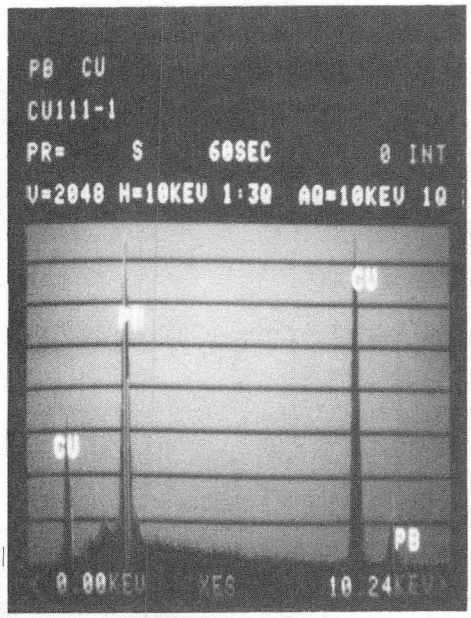

PROBE ON DENDRITIC ISLANDS

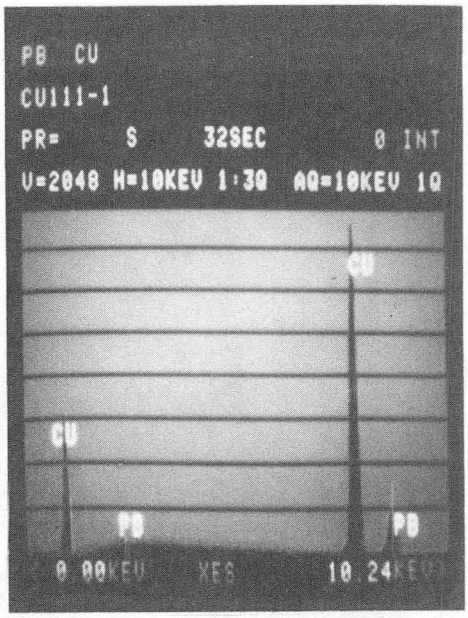

PROBE BETWEEN ISLANDS

8 MIN

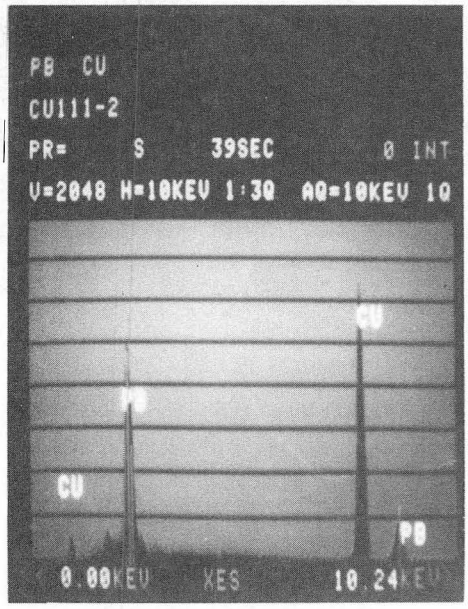

PROBE ON DENDRITIC NEEDLE

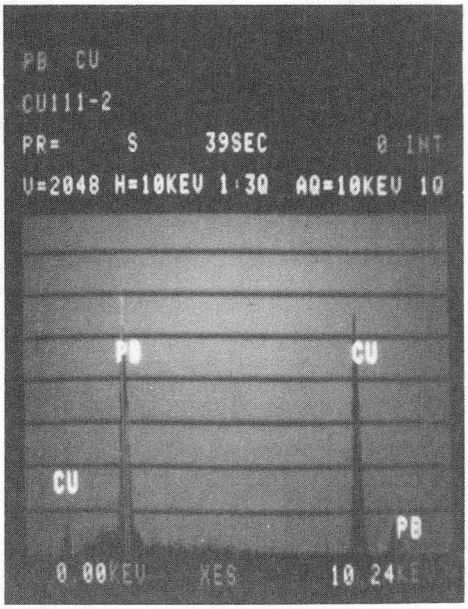

PROBE BETWEEN NEEDLES

XBB 831-723

Fig. 10

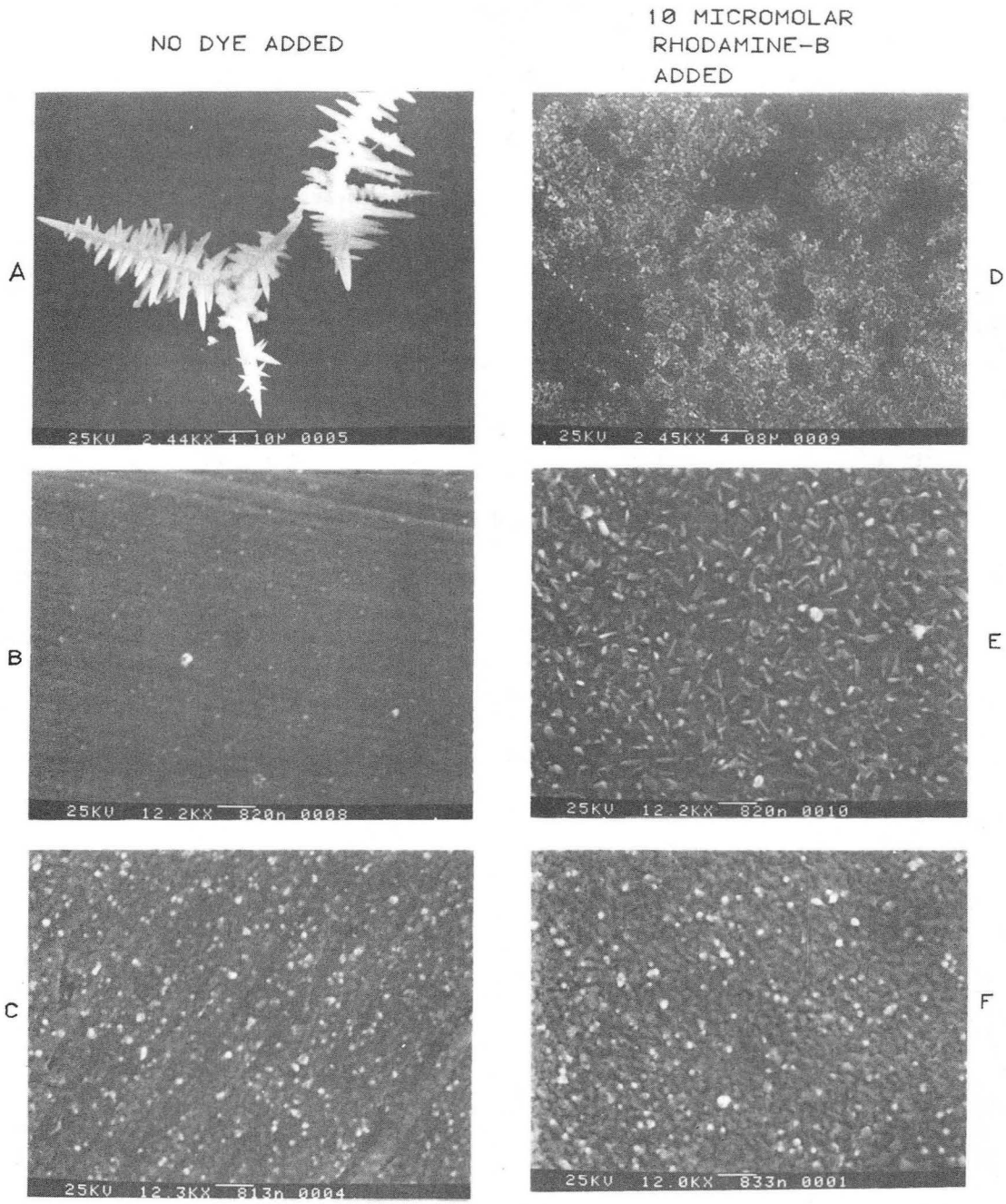

XBB 831-724

Fig. 11

ACKNOWLEDGMENTS

In the 6th Century B.C., Lao-Tzu wrote, "...the journey of a thousand miles began with a single step." A portion of my journey is through, and I want to thank those who have helped me along the way. My many devoted friends and family members have all made the last four years a little easier. This list of names is long and is not included here since it is in my heart.

This dissertation reflects the efforts of other staff and guests at Lawrence Berkeley Laboratory, as much as it does my own. These persons are acknowledged according to their specific contributions, all of which were essential: Phil Ross, Waldfried Plieth, Felix Schwager, Lee Johnson, Fred Wagner, Panos Andricacos and Jim Faltemier for their frequent discussions and tutorial sessions on electrochemistry and surface science; Jim Severns, Herb Riebe, Walter Giba, Joe Katz, Brian Ng and Greg Derry for advice and assistance in the development of hardware and software; Ken Gaugler for instruction in scanning electron microscopy and help in interpreting related data; Sandy Stewart and Cathy Sterling for purchasing the many hard-to-obtain supplies that I needed, and for doing it quickly and efficiently; Charles Tobias, Paul Richards and Dennis Hess for detailed proof reading of the text and important suggestions; Miriam Schwartz, George Huggard and Dick Gallant for drafting; and Gay Brazil, Stan Combs, Jean Wolslegel and Valerie Kelly for final preparation of the dissertation. Thanks also go to the photographic laboratory for their outstanding work.

Finally, this work is dedicated to my parents who helped me take my first step as a child, and to Rolf H. Muller who helped me take my first step as a scientist.

This work was supported by the Director, Office of Energy Research, Office of Basic Energy Sciences, Materials Sciences Division of the U.S. Department of Energy under Contract No. DE-AC03-76SF00098.

This report was done with support from the Department of Energy. Any conclusions or opinions expressed in this report represent solely those of the author(s) and not necessarily those of The Regents of the University of California, the Lawrence Berkeley Laboratory or the Department of Energy.

Reference to a company or product name does not imply approval or recommendation of the product by the University of California or the U.S. Department of Energy to the exclusion of others that may be suitable.

TECHNICAL INFORMATION DEPARTMENT
LAWRENCE BERKELEY LABORATORY
UNIVERSITY OF CALIFORNIA
BERKELEY, CALIFORNIA 94720